THE UNIVERSITY *of* EDINBURGH

The toxicology of high aspect ratio nanomaterials- How shape determines the biologically effective dose

Anja Schinwald

Presented for the degree of Doctor of Philosophy

The University of Edinburgh

2013

Declaration

I hereby declare that the presented thesis has been composed only by me the undersigned. The work contained within this thesis has been performed wholly by me except in certain circumstances, for which the contributors and level of contribution are clearly indicated.

I also declare that the work presented herein has not been submitted for any other degree or professional qualification.

Anja Schinwald

Abstract

Nanotechnologies are the fastest growing industry sector ever recorded. The US budget for nanotechnology is predicted to reach the 1 trillion dollar threshold in 2015, meaning that nanotechnologies will indeed be larger than all other technologies combined. High aspect ratio nanomaterials (HARN) become increasingly important in the nanotechnology industries, and show great promise, offering many advantages and improvements to a significant range of products. The main feature of HARN is the ratio of the width of a nanomaterial to its height which can be up to 1000, making the material fibre or platelet- shaped. However, this feature leads to comparison between HARN and other high aspect ratio materials including fibre shaped materials, such as asbestos fibres. Due to the structural similarities between fibrous HARN and asbestos the question arises- do HARN pose the same risk as asbestos?

This project aimed to assess the potential of a range of HARN to cause similar pathological effects as asbestos fibres. In order to address this aim a panel of HARN was tested against the fibre pathogenicity paradigm *in vivo* by examining the pulmonary and pleural responses as well as *in vitro* to reveal the mechanism of cell/HARN interaction.

The first part of the study focused on fibre-shaped HARN, including a panel of distinct length classes of silver nanowires (AgNW) which were injected directly into the pleural space, a target tissue for asbestos related diseases. Injection of high aspect ratio AgNW into the pleural space of mice revealed a length dependent inflammatory response in line with the fibre pathogenicity paradigm which explains fibre pathogenicity. AgNW from 5 µm in length and above led to a significant increase in granulocytes in the pleural space which is similar to that seen after treatment with long amosite asbestos. The use of additional HARN with different compositions allowed us to identify a threshold length for fibre-induced pleural inflammation, which is 5 µm. Frustrated phagocytosis has been stated as an important factor in the initiation of an inflammatory response after fibre exposure. A novel technique, backscatter scanning electron microscopy (BSEM), was used to study frustrated phagocytosis since it provides high-contrast detection of nanowires, allowing clear

discrimination between the nanofibres and other cellular features. Using this technique we showed that the onset of inflammation does not correlate with the onset of frustrated phagocytosis, with a fibre length of ≥5 μm and ≥10 μm, respectively, leading to the conclusion that intermediate length fibres fully enclosed within macrophages as well as frustrated phagocytosis are associated with a pro-inflammatory state in the pleural space. We further showed that fibres compartmentalise in the mesothelial cells at the parietal pleura as well as in inflammatory cells in the pleural space. To investigate the mechanism of the length-dependent inflammation caused by AgNW, the NALP3 inflammasome activation pathway was studied *in vitro*, however no clear correlation could be identified.

We further aimed to investigate the threshold length of fibre-induced inflammation in the lung and the effect of fibre length on macrophage locomotion in an *in vitro* macrophage migration assay. Pharyngeal aspiration of AgNW resulted in a length dependent inflammatory response in the lungs with threshold at a fibre length of 14 μm. Shorter fibres including 3, 5 and 10 μm elicited no significant inflammation. This identified threshold length differs from that in the pleural space which may be explained by differences in clearance mechanism of deposited fibres from the airspaces compared to the pleural space. Particle clearance from the lung is partly performed by migration of particle-laden macrophages to the mucociliary escalator. We investigated if uptake of longer fibres leads to restricted mobility and showed that exposure to AgNW in the length of ≥ 5 μm resulted in impaired motility of macrophages in the wound closure assay.

The second part of the study focused on HARN in the form of nanoplatelet-shaped particles since nanoplatelets may pose an unusual risk to the lungs and the pleural space because of their aerodynamic properties. We first derived the respirability of graphene nanoplatelets (GP) from the basic principles of the aerodynamic behaviour of plate-shaped particles which allowed us to calculate their aerodynamic diameter. This showed that the nanoplatelets, which were up to 25 μm in diameter, were respirable and so would deposit beyond the ciliated airways following inhalation. We therefore utilized models of pharyngeal aspiration and direct intrapleural installation of GP, as well as an *in vitro* model, to assess their inflammatory potential. These

large but respirable GP were inflammogenic in both the lung and the pleural space at an acute timepoint although they decreased in their inflammatory potential over a 6 weeks period. Oxidation of GP in the lung tissue was investigated in order to identify if GP degraded over the 6 week period in the lung tissue and therefore showed reduced inflammogenicity. Raman spectroscopy was used to measure the oxidation state and revealed that no change occurred over the observed timeframe. The mechanism underlying acute GP inflammation was studied in THP-1 macrophages exposed to GP. These investigations showed that GP exposure led to significant expression of IL-1β, which could be blocked via a number of inhibitors related to the NALP3 inflammasome activation.

This study highlights the importance of shape/length of HARN as a driver for *in vivo* and *in vitro* inflammogenicity by virtue of their respirable aerodynamic diameter, despite a considerable 2-dimensional size which leads to an inflammatory response when deposited in the distal lungs and the pleural space. The identification of the threshold length for nanofibre-induced pathogenicity in the pleura and the lung has important implications for the understanding of the structure–toxicity relationship for asbestos-induced mesothelioma. It also contributes to risk assessment by offering a template for production of safer synthetic nanofibres by the adoption of a benign-by-design approach.

The results of this work highlight the importance of testing new HARN to protect workers in nanotechnology industries and the public.

Acknowledgements

I would like to express my deepest gratitude to my supervisor Prof. Ken Donaldson.

Ken, thank you so much for your excellent supervision, support and help throughout these three years and for giving me the opportunity to work in you lab. I am especially grateful for your inspiration, advice and open ear at any time for all my questions. It has been a great experience and I could have not wished for any better!

Special thanks to my colleague, Dr Fiona Murphy who has been a great help and source of knowledge from the start of my PhD. All the stimulating discussions I had with Fiona during the *in vivo* procedures made the several hours in the animal facilities pass by quickly. My project was based on the excellent work of both, Fiona and Dr Craig Poland's whose scientific contributions have had an outstanding impact on the knowledge related to HARN toxicology, from which my project continued.

To everyone in the ELEGI lab for their help and support throughout the project and especially to Jennifer Raftis and Jen McLeish for the lovely time in the office and at lunch which always provided a nice distraction - it has been a great place to work.

To my collaborators, Dr Colin Campbell (School of Chemistry), Dr Alan Jones (IOM), Prof. Chris Jeffree (Institute of Molecular Plant Sciences), Dr Adriele Prina-Mello and Dr Fiona Byrne, Dr Rebecca Coll and Prof. Luke O'Neill and everybody in the LON lab (Trinity College Dublin) and Dr Tanya Chernova (MRC Leicester). Your contributions have been an invaluable addition to the project!

Special thanks to Dr Janet Dickerson, Dr James Glass and Dr David Schultz from Seashell Technology Company for providing the silver nanowire samples. I would also like to acknowledge the great technical support of Steve Mitchell, Shonna Johnston and Bob Morris and his histology team.

I want to express my gratitude to the Colt Foundation, especially to the director Jackie Douglas for their generous financial support of this project and the stimulating meetings.

Finally I would like to thank Jason, for being ever so motivating, encouraging and cheerful throughout the whole time. You made my stay in Edinburgh incredibly enjoyable and our adventurous trips through Scotland from midge fests to cycle trips in never-ending rain have been an unforgettable experience! Thank you for everything!

Dedication

Diese Arbeit widme ich in Liebe und Dankbarkeit meine Eltern, Annette und Friedrich, die mich ermutigt und unterstuetzt haben mein Studium in Edinburgh zu absolvieren und mir alle Moeglichkeiten eroeffnet haben. Ich bin unendlich Dankbar fuer euere Unterstuetzung!

Contents

Table Index

Figure Index

Abbreviations

ADP	Adenosin diphosphate
AgNW	Silver Nanowire
AgP	Silver nanoparticulate
AM	Alveolar macrophages
ANOVA	Analysis of variance
AO	Acridine orange
AP-1	Activator protein-1
ARF	Altering reading frame
ASC	Apoptosis-associated speck-like protein containing a C-terminal caspase recruitment domain
BAL	Broncho alveolar lavage
BED	Biologically effective dose
BMMs	Bone marrow derived macrophages
BSA	Bovine serum albumin
BSEM	Backscatter scanning electron microscopy
CB	Nanoparticulate carbon black
CBA	Cytometric bead aray
CCL2	CC-chemokine ligand
CNT	Carbon nanotubes
CRANN	Centre for Research on Adaptive Nanostructures and Nanodevices
CTGF	Connective tissue growth factor
CVD	Catalytic vapour discharge
D_{ae}	Aerodynamic diamter
DAMP	Damage associated molecular pattern
DMEM	Dulbecco's Modified Eagle Medium
DNA	Deoxyribonucleic acid
DPI	Diphenyleneiodonium Chloride
DPPC	Dipalmitoylphosphatidycholine
ECM	Extracellular matrix
EGFR	Epidermal growth factor receptor
ELEGI	Edinburgh lung and environment group initiative

ELISA	Enzyme-linked immunosorbant assay
EPR	Electron paramagnetic resonance
Erk	Extracellular-signal related kinase
FPP	Fibre pathogenicity paradigm
H_2O_2	Hydrogen peroxide
HARN	High aspect ratio nanoparticle
HCl	Hydrogen chloride
HMGB	High-mobility group box
hMPO	Human neutrophil myeloperoxidase
HRP	Horseradish peroxidase
IARC	International Agency for Research on Cancer
ICAM-1	Intracellular adhesion molecule-1
ICP-MS	Inductively coupled plasma mass spectroscopy
IFN	Interferon
IL	Interleukine
IRAK-4	IL-1 receptor-associated kinase-4
KCl	Potassium chloride
LAL	Limuluss Amoebocyte Lysate
LBP	LPS binding protein
LDH	Lactate dehydrogenase
LFA	Long fibre amosite asbestos
LFC	Long fibre chrysotile
LPS	Lipopolysaccharide
MAPK	Mitogen-activated protein kinase
MBB	Monobromobimane
MCP-1	Monocyte chemotactic protein 1
MIP	Macrophage inflammatory protein
miRNA	Micro ribonucleic acid
MMVF	Man-made vitreous fibre
mRNA	Messenger ribonucleic acid
MSU	Monosodium urate
MWCNT	Multi-walled carbon nanotubes

MyD88	Myeloid differentiation primary response gene 88
NADPH	Nicotinamide adenine dinucleotide phosphate
NALP3	Nucleotide-binding oligomerisation domain (NOD)-like receptors containing a pyrin domain 3
NF2	Neurofibromatosis type 2 gene
NF-κB	Nuclear-factor κB
NiNW	Nickel nanowire
NIOSH	National institute of occupational safety and health
NiP	Nickel nanoparticulate
NLRs	Nucleotide-binding oligomerisation domain (NOD)-like receptors
NO	Nitric oxide
NOD	Nucleotide-binding oligomerisation domain
NP	Nanoparticle
PARP	Poly (ADP-ribose) polymerase
PBS	Phosphate buffered saline
PDGF	Platelet derived growth factor
PMA	Phorbol 12-myristate 13-acetate
PMN	Polymorphonuclear leukocyte
PSR	Pico Sirius red
RANTES	Regulated on activation, normal T cell expressed and secreted
RIP1	Receptor-interacting protein 1
ROS	Reactive oxygen species
RPMI	Roswell Park Memorial Institute
SEM	Scanning electron microscopy
SFA	Short fibre asbestos
SP	Surfactant- associated protein
STAT	Signal transducer and activator of transcription
STR	Structure Toxicity Relationship
SV40	Simian Virus 40
SWCNT	Single-walled carbon nanotube
TEM	Transmission electron microscopy
TGF-α	Transforming growth factor α

TGF-β1	Tumour growth factor-1β
T_H	T-helper
TI	Type I alveolar epithelial cells
TII	Type II alveolar epithelial cells
TIR	Toll-interleukin-1 receptor
TLR4	Toll-like receptor 4
TNF-α	Tumour necrosis factor α
TRAF6	TNF receptor-associated factor 6
TRIF	TIR domain-containing adaptor inducing IFN-β
VC	Vehicle control
VCAM-1	Vascular cellular adhesion molecule
VEGF	Vascular endothelial growth factor
WHO	World health organisation
WT	Wild type
Z	Atomic number

Chapter 1: Introduction

1.1 Respiratory System

1.1.1 The anatomy of the respiratory system

The respiratory system is made up of structures responsible for the exchange of oxygen and carbon dioxide between the blood and the atmosphere. The anatomy of the human respiratory system consists of the external and internal nose and the paranasal sinuses; the pharynx, which connects the mouth and the nose to the larynx; the trachea where the air gets cleansed and moistened before entering the bronchi and lungs (Figure 1-1). Due to the asymmetrical position of the heart the right lung is slightly larger than the left lung, with 10 and 8 airway segments respectively. The left lung has two lobes whereas the right lung has three lobes which together make up to approximately 2,400 kilometres of airways (Frank and Netter 1979; Stone *et al.* 1992). Additional structures necessary for operation of the respiratory system include the pleura, the diaphragm, the thoracic wall and the muscles which raise and lower the ribs in inspiration and expiration.

The lower respiratory tract starts at the trachea which divides into two main bronchi that enter the right and the left lung. The main bronchus divides further into lobular bronchi at the hilus of the lung and bronchioles. The distinguishing feature between bronchi and bronchioles is the distribution of cartilage, whereby bronchioles are cartilage free. Three to five bronchioles make up a lobule including respiratory bronchioles, alveolar ducts and alveolar sacs. The respiratory unit of the lung is called acinus and comprises of respiratory bronchioles, alveolar ducts and alveolar sacs

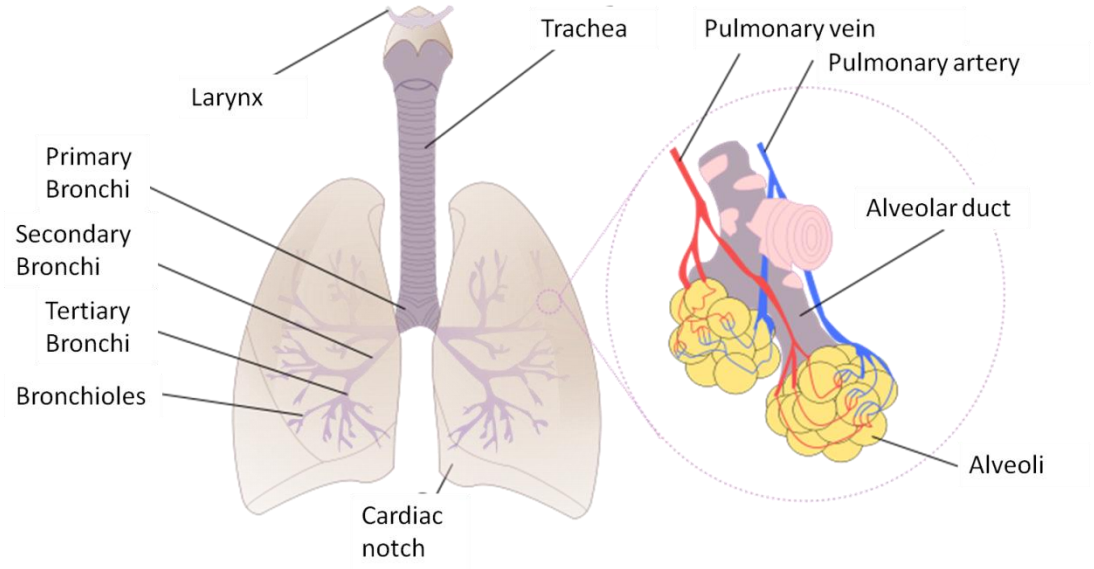

Figure 1-1: Gross anatomy of the respiratory system. Redrawn and adapted from a public domain image by Rastrojo.

1.1.2 Ultrastructure of the tracheal, bronchial and bronchiolar epithelium

The epithelium in the trachea and the large bronchi is made up of eight epithelial cell types, the basal and Kulchitsky cells that are attached to the basement membrane but do not reach the lumen as well as the ciliated cells, brush cell (secretory cells), goblet (mucous) cell, serous cell and Clara cell which all differentiate from one precursor intermediate cell (Roger, 2005). The distal epithelium towards the terminal bronchioles consists mainly of cuboidal epithelium containingClara cells with a decrease in ciliated cells, goblet cells and serous cells. Serous and Clara cells are the common secretory cells in the airways and upon irritation these cells can develop into mucus cells. Ciliated cells which are surrounded by a thin fluid film of mucus are present from the trachea to bronchioles and the cilia in the smaller airways are not as tall as in the central airways (Roger, 2005). The mucociliary escalator starts in the most distal region of the airway epithelium and is responsible for the transport of foreign particles and microorganism from the lower region of the respiratory tract towards the pharynx by coordinated movement of the cilia to propel rafts of mucus upwards whereby the deposited particles trapped in it are either swallowed or expectorated.

1.1.3 Alveolar capillary unit

The alveoli, 300- 500 million in the human lungs, are the primary gas exchange units of the lung with at least two cells, type I alveolar epithelial cells (TI) and endothelial cells forming the boundary between blood and the air. TI cells and endothelial cells are remarkable thin but make up to a total surface area of approximately 70 m^2 (Frank and Netter, 1979) which accounts for 99 % of internal surface of the lung (Stone et al., 1992). Additionally, the barrier between the blood and air is composed of extracellular material including a surfactant-lining layer, the basement membrane and surface coatings composed of mucopolysaccarides.

The intrapulmonary blood circulation is composed of two arterial systems, the pulmonary and the bronchial system. Oxygen depleted blood enters the pulmonary arteries from the heart via the semilunar valve, splitting into the right and the left pulmonary artery. The arteries are further divided into very fine capillaries which enrich the acinus. The bronchial system differs from the pulmonary system by supplying the lung tissue with oxygenated blood from the aorta.

TI cells are very large squamous-like cells with a surface area of approximately 5400 μm^2 (Stone et al., 1992) which make up more than 90% of the alveolar surface. They provide a tight barrier over the basement membrane which minimises transudation of interstitial fluid from interstitium to the airspaces. TI cells are terminally differentiated with a simplified cellular machinery which makes them sensitive to injury (Shields et al., 2009). TI cells are incapable of cell repair and mitosis after injury and are dependent on alveolar type II epithelial cells (TII) for their replacement (Shields et al., 2009). TII cells possess the ability to differentiate into TI cells to repair the injured alveolar epithelium or differentiate into new TII cells. TII cells are also called granular pneumocytes due to their intracellular stores of surfactant lining which gives them a distinct granular appearance (Shields et al., 2009). TII cells make up 15 % of the cell population in the distal lung and are, in contrast to TI cells cuboidal in shape. Their major function is the synthesis and secretion of surfactant lining.

The surfactant secreted by TII cells plays an important role in the reduction of surface tension in the alveoli during inspiration and expiration and prevents the lung from collapsing. Additionally the surfactant- associated proteins, especially SP-A and SP-D are opsonins and important modulators of immune and inflammatory regulation within the lung (Crouch et al., 2000). SP-A and SP-D are members of collagenous carbohydrate binding proteins which are also known as collectins (Crouch et al., 2000). SP-A is the most abundant protein in the surfactant which makes up 4 % of the total mass of surfactant. Recent data has shown that SP-A and SP-D can modulate phagocyte function *in vitro* by binding to carbohydrate structures on the surface of the microorganisms (Reid, 1998). Various different receptors have been identified on the surface of both endothelial and hematopoietic cells to interact with SP, among these are Toll-like receptors and their associated molecule CD14, signal regulating protein-α or calreticulin-CD91 receptor complex (Pastva et al., 2007). Exposure to particulate matter has also been shown to affect the expression of SP-A (Romieu et al., 2010). Another major component of lung surfactant are neutral lipids and phospholipids, 1,2- dipalmitoylphosphatidylcholine (DPPC) which form a closed bilayer on the surface of the epithelial cell layer.

1.1.4 Pulmonary and thoracic macrophage subpopulations

Lung macrophages are derived from a hematopoietic stem cell in the bone marrow and have monocytes as a putative precursor. Monocytes circulate for 1-3 days in the bloodstream before differentiating into mature macrophages in the tissue. Several subpopulation of macrophages can be found in the lower respiratory tract. Depending on their location they are divided into

1) airway macrophages on and in the epithelial lining of the conducting airways and in the bronchus associated lymphoid tissue;
2) alveolar macrophages (AM) which reside on the epithelial surfaces of the alveoli;
3) interstitial macrophages found in the perivascular, peribronchiolar, visceral pleura sites and the interstitium of the alveolar regions;

4) pleural macrophages present in the pleural space;
5) intravascular macrophages which have direct access to the circulating blood (Lehnert, 1992).

AMs are the most common type of immune cell in the alveolar airspaces and lie in close proximity to the air-liquid interface. The primary function of alveolar macrophages is scavenging particles and to eliminate deposited microorganism and insoluble particles from the lung surfaces, which occurs usually within a day or so of deposition. The turnover time of alveolar macrophages varies between species and has been reported to be 21-28 days in mice (van oud Alblas and van, 1979) and 81 days in human (Thomas et al., 1976). AM are a heterogeneous population, depending on their maturation/activation state. Mature macrophages are large in size, low in density, exhibit increased phagocytosis, superoxide anion and hydrolase activity. In contrast, less mature macrophages are less chemotactic and have an increased FcR activity (Geiser, 2010). Lavage of the bronchoalveolar region (BAL) of healthy humans yields ≥80 % macrophages, 18% lymphocytes and a few neutrophils and eosinophils (Spurzem et al., 1987). In comparison rodent BAL yields ≥95% macrophages with a few lymphocytes, neutrophils and eosinophils (Warheit et al., 1988). Differences in immune activity, as reflected in the lymphocyte infiltrate, very likely reflect the barrier-maintained pathogen-free status of laboratory mice. The average volume of human AM is 1474 μm^3 whereas mouse macrophages exhibit a volume of 493 μm^3 as summarized by (Geiser, 2010).

1.2 Pleural space

1.2.1 Anatomy of the Pleura

The lung parenchyma, the mediastinum, the diaphragm and the rib cage are covered by a serous membrane called the pleura. The pleura is divided into the visceral pleura which covers the lung parenchyma with its interlobar fissures and the parietal pleura which lines the inside of the thoracic cavities (Negrini and Moriondo, 2012). The parietal pleura is further subdivided into the costal, mediastinal and diaphragmatic parietal pleura. Visceral and parietal pleura consist of several layers which differ

from each other markedly in their anatomy. The parietal pleura is composed of a deep fibroelastic layer, loose connective tissue layer, a thin superficial elastic layer and a thin sub-mesothelial connective tissue layer which is covered by a single layer of mesothelial cells (Jantz and Antony, 2008). In the apical region, the mesothelial cells are characterised by a dense microvillous layer. The thickness of the visceral pleura differs among species (Lai-Fook and Kaplowitz, 1985). The connective tissue layer in the visceral pleura contributes to the elastic recoil of the lung and it restricts the volume to which the lung can be inflated. Within the pleura are blood vessels and lymphatic lacunae. The blood vessels are located in the main connective tissue layer. The visceral pleura is supplied by the bronchial circulation and the the parietal pleura is supplied by branches of the intercostal arteries (Lai-Fook, 2004). Lymphatic drainage from the pleural is via numerous lymphatic vessels in the pleural connective tissue layer which start off as gaps with endothelial lining called lymphatic stomata in the parietal pleura. These stomata have a diameter of 2-8 µm and are predominantly found in the dorsal caudal intercostal spaces and to a lesser degree in the ventro-cranial region of the pleura (Shinohara, 1997). Across mammalian species there is a remarkable consistency in the reported size of stomata on the diaphragm or parietal pleura as summarized in Table 1-1. Through stomata the pleural space communicates directly with the lumen of the lymphatic vessels (Mueller, 2002). The lymphatic vessels run along the intercostal spaces and drain towards nodes along the internal thoracic artery and the intercostal lymph nodes near the head of the ribs. The visceral lymphatic drainage occurs through a completely independent pathway via the lung parenchyma towards hilar nodes.

Table 1-1: Size of stomata across mammalian species.

Species	Stomatal size (µm)	Reference
Bat	0.8-2	(Azzali, 1999)
Hedgehog, Gerbil, Bat, mouse	1.8-6	(Azzali, 1999)
Monkey	3-8	(Oya et al., 1993)
Sheep	1-3	(Lai-Fook, 2004)
Human	6.2	(Li, 1993)
Rat, mouse, rabbit, hamster, human	4-10	(Abu-Hijleh et al., 1995)
Human	2-8	(Muller et al., 2002)

1.2.2 Pleural Fluid

The pleural space is the cavity between the visceral and parietal pleura and contains a film of fluid which acts as a lubricant during respiratory movements while avoiding direct contact between visceral and parietal mesothelial surfaces, thus preventing cell damage. The pleural surface has a sub-atmospheric pressure that keeps the lung expanded at the end-expiration and allows its inflation during inspiration (Negrini and Moriondo, 2012). If this pressure within the pleural space is altered, differences in regional lung expansion can occur which can lead to potentially life threatening conditions.

The pleural cavity contains about ~0.26 ml of fluid per kg body weight in healthy humans (Noppen et al., 2000) and ~2.5 ml/kg in rats (Miserocchi et al., 1984) and for a pleural surface are of ~90 cm^2/kg the thickness is approximately 5 µm over the flat coastal surface and up to 60- 100 µm in fluid pools (Negrini and Moriondo,

2012). The circulation and flow of the pleural fluid in the pleural space has been measured via different methods using fluorescently labelled beads injected into the pleural space of rabbits (Wang and Lai-Fook, 1993; Wang and Lai-Fook, 1992) and a model pump (Butler et al., 1995). The studies showed that the circulation consists of a gravity dependent downward flow on the costal lung surface, an upward flow of pleural fluid adjacent to a lobar margin and a transverse flow from lobar margins to the flat costal surfaces (Wang and Lai-Fook, 1992). The pleural fluid is a microvascular filtrate from the parietal pleural capillaries and in large mammals pleural fluid can also be filtered from the bronchial capillaries of the visceral pleura (Figure 1-2) (Lai-Fook, 2004). In smaller mammals pleural liquid might be reabsorbed by pulmonary capillaries underlying the visceral pleura (Noppen et al., 2000; Lai-Fook, 2004), otherwise the fluid is drained from the pleural space to the lymphatics via stomata in the parietal pleura.

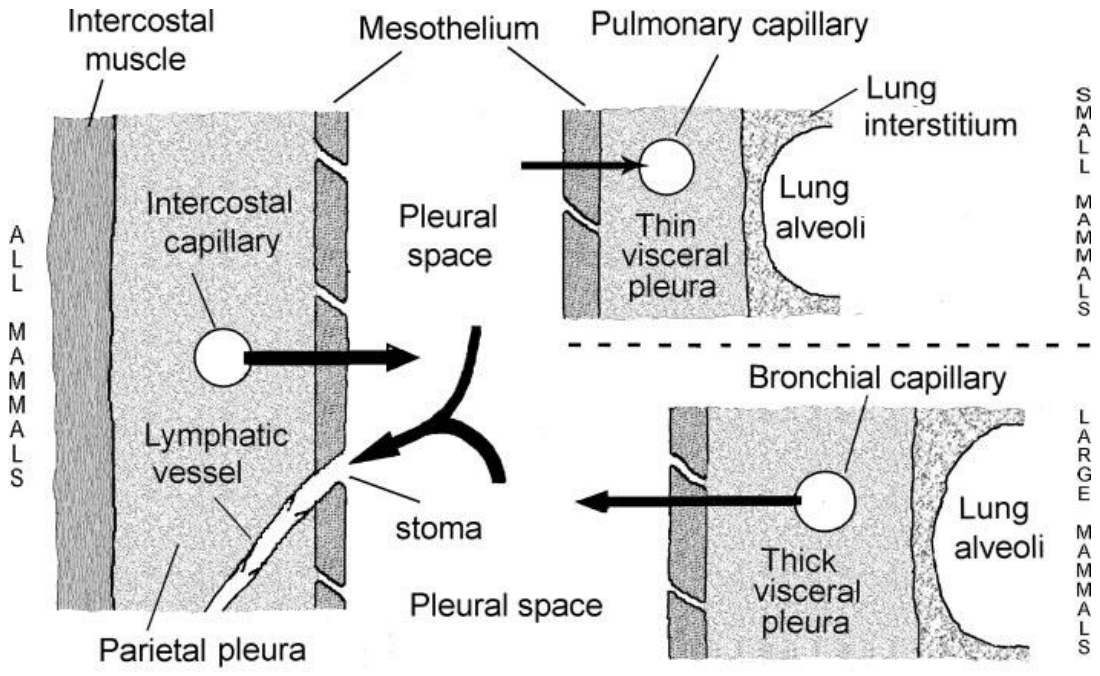

Figure 1-2: Pleural fluid turnover in small and large mammals. The fluid is a filtrate from the capillaries in the parietal pleura as well as from the bronchial capillaries of the visceral pleura in large mammals. In small mammals pleural fluid can be reabsorbed by pulmonary capillaries. Figure from (Lai-Fook, 2004) with permission from Lai-Fook Stephen.

The pleural fluid is composed of a number of proteins including albumin, globulin and fibrinogen, as well as a few detached mesothelial cells (1%), lymphocytes (23%), monocytes and macrophages (75%) (Lai-Fook, 2004). The cell number in the pleural fluid can be used as an indicator for pleural inflammation since the number of cells, especially macrophages and neutrophils increases.

1.2.3 Mesothelial cells

The parietal and visceral mesothelium consists of a monolayer of flat and cuboidal mesothelial cells (Mutsaers, 2004) with an average diameter of 25 µm (Wang, 1974), whereby the cuboidal mesothelial cells are predominantly found on the parietal mesothelial pleura and in specific areas including 'milky spots' (Mutsaers, 2004). Milky spots can act as a first line defence by increasing their number and size in inflammatory conditions (Michailova, 2004). The squamous-like flat cells have thickness of about 1-4 µm and contain few microtubules, microfilaments, mitrochondria, vacuoles and vesicles, compared to cuboidal mesothelial cells, as well as a poorly developed Golgi apparatus (Mutsaers, 2004). The luminal surface of the mesothelial cells is lined with a layer of microvilli which are 1-6 µm long (Lai-Fook, 2004). The function of microvilli is hypothesised to support the forces between the pleural surfaces and to trap hyaluronan, a boundary lubricant, on pleural mesothelial cells (Lai-Fook, 2004). In addition to hyaluronan, the surface of the mesothelium is covered by sialomucins (Jantz and Antony, 2008). Sialomucins have strong anionic sites which act as a protective layer against microbes, particles and invading cells and electro-statically repel the opposing sides of the pleural membranes (Jantz and Antony, 2008). Connection between adjacent mesothelial cells is via tight and adherens junctions in the apical portion and gap junctions as well as desmosomes on the basal side (Mutsaers, 2002).

Mesothelial cells in the pleura are multipotent and take part in the first line defence by recognising foreign substances and subsequently initiating the inflammatory response (Jantz and Antony, 2008). They produce fibronectin, a large glycoprotein which acts to prevent adherence of foreign organisms, release reactive oxygen

species and nitrogen intermediates and possess multiple pattern recognition receptors including CD14, integrins and mannose receptors to control infection in the pleural space (Jantz and Antony, 2008).

1.3 Particle lung interaction

The respiratory tract is in constant direct contact with the atmospheric environment, composed of numerous gases and particles. Human beings experience intentional and unintentional lifelong exposure to aerosol particles which deposit in the respiratory tract. Their clearance/retention is dependent upon their size and composition and the site of deposition within the respiratory tract and their pathogenicity. Some particles may be readily soluble in the lung fluid, whereas others are cleared via the mucociliary escalator, get taken up by alveolar macrophages or penetrate into the interstitium (Schulz et al., 2000); an unknown proportion, probably small, find their way to the pleural space (Donaldson et al., 2010). Aerosol particles are classified in three categories depending on their size. Particles with a diameter range of <0.1 µm are classified as ultrafine particles, 0.1-1 µm diameter as fine particles and particles 1-10 µm are defined as coarse particles (Schulz et al., 2000).

1.3.1 Deposition

The aerodynamic diameter of a particle is the most relevant parameter to determine deposition within the respiratory tract. The aerodynamic diameter is defined as the diameter of a unit density sphere (1 g/cm^3) with the same settling speed as the particle of interest (Jones, 1993). In other words, an irregular shaped particle has an aerodynamic diameter that equates to the diameter of a perfect sphere with a density of 1 g/cm^3 falling at the exact same rate as the irregular shaped particle. The aerodynamic diameter for particles with a size greater than 500 nm is

$$D_{pa}=d_{ps}\sqrt{Pp}$$

D_{pa}= Aerodynamic diameter (µm)

D_{ps}= Stokes diameter (µm)

P_p= Particle density (g/cm^3)

The stokes diameter is the diameter of a sphere that has the same density and settling velocity as the particle of interest. The aerodynamic drag force caused by the difference in the velocity of the particle and the surrounding medium determines the stokes value, whereby the Stokes diameter is identical to the actual diameter for smooth, spherical particles.

As mentioned above, particles characteristics are a major determinant for deposition. The nose is an effective filter for nanoparticles and for particles larger than ~2 µm (Figure 1-3) (Kreyling et al., 2007). The primary mechanisms for the deposition of inhaled particles are impaction, sedimentation, interception, diffusion and electrostatic deposition (Heyder, 2004). Impaction occurs when the airflow changes course but the particles, because of their mass, maintain trajectory and impact onto the airway wall in the upper respiratory tract and trachea-bronchial bifurcations which acts on particles > 1.5 µm D_{ae}. Sedimentation of particles occurs due to gravimetric force on the mass of the particle and takes place in area where the air flow is minimal. Particles with a D_{ae} of >0.5 µm are affected (Kreyling et al., 2007). Impaction and sedimentation are the main mechanism by which particles with a diameter ≥ 5µm deposit in the respiratory tract. For particles with a diameter ≤ 5 µm (< 0.5 µm D_{ae}) the deposition is mainly determined by diffusional transport. The smaller the particles are and the longer they remain in the respiratory system the higher is their probability to hit the airspace surface. Deposition fraction curve inside the respiratory system as shown in Figure 1-3 are generated from mathematical models which are based on experimental data. In general, deposition in the alveolar region is maximal for particles with a diameter of ~ 3 µm and minimal at a diameter of 0.5 µm due to mechanism of sedimentation and diffusion (Heyder, 2004). The sub-micron sized particles show the highest deposition in the pulmonary region (Figure 1.3). Interception is seen after inhalation of fibres which follow the airflow however may make contact with the airway walls at sides of bifurcation; interception increases with increasing fibre length. Lippmann M. performed extensive deposition

studies in humans and determined a maximal alveolar deposition for particles with an aerodynamic diameter of 3 µm (Lippmann, 1977; Jones, 1993).

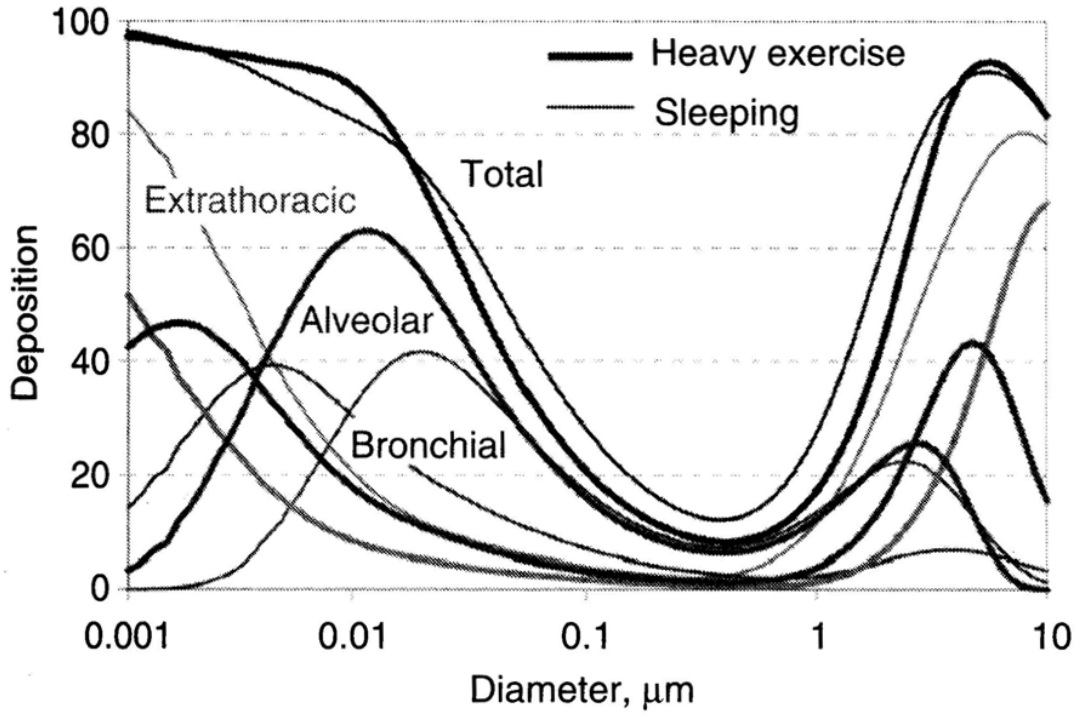

Figure 1-3: Deposition patterns of particles in the human respiratory tract. The deposition fraction of particles is shown for the tracheobronchial region, the pulomary region and the head airways in respect to their particle diameter. Reproduced from Kreyling et al.(Kreyling et al., 2007).

1.3.2 Deposition of fibres

A fibre is defined by the World Health Organisation (WHO) as a particle with a length greater than 5 µm, a diameter less than 3 µm and an aspect ratio (length to width ratio) greater than 3:1 (WHO, 1997). Taking these geometric properties of fibres into account it seems intuitively unlikely that a fibre would penetrate to the alveoli following inhalation.

The mechanisms by which particles deposit in the lungs can be applied, with few exceptions, to fibrous materials. The orientation of the fibres within the airways is a major determinant for the drag force and the settling speed of a fibre. As the inhaled

fibre is aligned parallel to the airways, due to the laminar flow of the air, the aerodynamic diameter is proportional to the fibre diameter for a constant fibre aspect ratio. Jones A.D calculated the aerodynamic diameter for a range of aspect ratios of fibres and showed that the aerodynamic diameter is between 2.5 to 4 times the actual diameter of a fibres with aspect ratios from 3 to 27 (Jones, 1993).

1.3.3 Particle clearance and translocation

Clearance of deposited particles from the respiratory tract depends on the site of deposition. In the nasopharyngeal region particles can either be swallowed or cleared via sneezing. Clearance of particles depositing in the trachea-bronchial region is facilitated by the mucociliary escalator. The cilia of the epithelial cells are covered with a layer of mucus, which is secreted by goblet cells and called the aqueous phase, and a surfactant film at the air liquid interface. Inhaled particles that deposit on the surfactant layer from air are displaced into the aqueous phase by the surfactant and are moved with the flow of mucus from the trachea-bronchial region towards the larynx where they get either swallowed or expectorated. The time take for clearance of micron-sized deposited particles in the trachea-bronchial region via the mucociliary escalator generally does not exceed 24 – 48 hours. Particles which are not cleared via the mucociliary escalator can penetrate through the mucus into the periciliary zone or deposit beyond the ciliated airways where clearance is mediated via phagocytosis by alveolar macrophages. The recognition of particles by phagocytes and their subsequent interaction determines the effectiveness of the clearance from the lung periphery. Macrophages recognise and ingest foreign particles via various receptor/opsonin interactions such as scavenger receptors, Fc receptors, complement receptors and integrins. Scavenger receptors are important modulators in the innate immune system and play a key role in the phagocytosis of unopsonized particles, in particular SR-A and MARCO (Sulahian et al., 2008).

It is known that particle surface characteristics including crystallinity, curvature, porosity, hydrophobicity, hydrophobility and zeta potential, contribute to the interaction with biological medium (Nel et al., 2009) and that particles are immediately covered by proteins/opsonins upon contact with the pulmonary

surfactant. In recent years, especially due to the increase in research into nanoparticles and lung interaction, the hypothesis was formed that the biological response to inhaled particles is dependent upon the proteins absorbed on the surface of the particles rather than the particles themselves (Lynch et al., 2007). However as seems likely, the nature of the particle surface dictates the nature of the corona and so the two are inseparable. The importance of the coating of particle surfaces with pulmonary surfactant which results in the so called 'protein corona' that mediates the biological interaction remains a controversial aspect. Proteins of particular importance in the pulmonary surfactant are the collectins SP-A and SP-D due to their immunological function as opsonins and scavenger molecules (Kishore et al., 2006). A recent study on the uptake of magnetite nanoparticles by alveolar macrophages showed that SP-A treatment of nanoparticles leads to an increase in cellular binding and phagocytosis compared to albumin coating (Ruge et al., 2011). In addition to the proteins, lipids constitute the major part in the pulmonary surfactant and can therefore modulate the protein-corona cell interaction and should be taken into consideration when studying these effects (Ruge et al., 2012).

The clearance rate via alveolar macrophages and transport to the larynx is species dependent and one order of magnitude lower in human compared to rodents (Kreyling and Scheuch, 2000). The transport of particle- laden macrophages toward the ciliated airways can either be via directed movement in reponse to chemotactic forces or random migration. Additional mechanisms for the elimination of slowly dissolving particles from the epithelium or the peripheral lung is transport to hilar lymph nodes, interstitial sites or the subpleural spaces, either as free particles or within phagocytes. Uptake of deposited particles by epithelial type I and type II cells and subsequent translocation to interstitial spaces and lymphatic system or phagocytosis of particle laden macrophages by interstitial macrophages accounts for additional clearance mechanisms. Particle translocation to the blood and accumulation in secondary organs is minimal for micron sized particles however does occur with ultrafine particles (Oberdorster et al., 2005; Geiser and Kreyling, 2010).

Dissolution of particles in extracellular fluid including epithelial lung lining fluid or interstitial fluid as well as intracellular dissolution within macrophages via fusion of the phagosome with acidic lysosomes play a major role in the clearance of soluble particles (Cho et al., 2011).

1.3.4 Translocation of particles to the pleura

There is ample evidence that particles depositing in the distal regions of the lung can translocate to the pleural space. This was shown in a number of autopsy specimens from former coal miners who had black foci of mixed dust on the parietal pleura (Muller et al., 2002). These intrapleural mixed dust accumulations were described as 'black spots' and are mainly seen near stomatas, in the regions of pleural lymphatics. Black spots have also been discussed in relation to asbestos fibre exposure as being the starting points for mesothelioma development (Boutin et al., 1996). Due to the elongated nature of fibres the passage through the visceral pleura, which is approximately 700 μm thick, may be slow which would account for the late development of pleural diseases after inhalation exposure. A study by Boutin *et al.* investigated the amount of asbestos fibres, their dimensions and distribution on the parietal pleura of human subjects exposed to asbestos fibres (Boutin et al., 1996). The results of this study showed that around 22 % of the fibres in the pleural space had a length of ≤ 5 μm, confirming the translocation of longer fibres to the pleural space. The mechanism and pathway of translocation of fibres through the visceral pleura to the pleural space is not understood. An increase in interstitial pressure and microvascular permeability due to a raise in lung inflammation leading to a reversal of the trans-endothelial pressure gradient has been proposed as a mechanism for fibre translocation to the pleural space (Miserocchi et al., 2008). Recent studies on the translocation of carbon nanotubes to the pleural space after aspiration exposure showed images of carbon nanotube penetrations through the visceral pleura suggesting a direct route of translocation (Mercer et al., 2010). The translocation of fibrous materials was further confirmed by Bernstein *et al.* demonstrating the penetration of amosite asbestos fibres in the pleural space after inhalation exposure with subsequent inflammation in the pleural space (Bernstein et al., 2010).

1.4 Asbestos

1.4.1 History of the toxicology of inhaled particles

The toxicology of inhaled particles in workplaces and the environment dates back to the 15th century and was first described by Georgius Agricola, reporting lung disease in mine workers although he failed to make a clear link between dust exposure and disease development. In 1700 Bernardino Ramazzini was the first to put lung disease in workers in context to the environmental exposure but it took until the early 20th century to protect the workforce, especially in mining, from exposure to hazardous dust in the workplace (Donaldson and Seaton, 2012). Coal, quartz and asbestos are recognized as the major hazardous particles in occupational exposure settings and have led to numerous cases of lung diseases over time up to the present. The fibrosing lung diseases caused by exposure to airborne dust are termed the pneumoconiosis. Workers in coalmines developed coalworker's pneumoconiosis which is characterised by the presence of nodular aggregations of macrophages and a minimal collagen network within the lungs in response to very high lung dust burdens and leading to progressive massive fibrosis in a few severe cases. Exposure to quartz (or crystalline silica) was most common where there was occupational generation of respirable quartz dust during mining, tunnelling and other occupations where the surface of the earth is penetrated or disturbed, since quartz is abundant in most rock types, notably granites, sandstones, sands and soils. Exposure to crystalline silica causes a severe fibrosing form of pneumoconiosis called silicosis. Quartz is also classified by the IARC as a group 1 carcinogen (Rice, 2000). In the 1920s the Hawks Nest Tunnel Disaster led to the death of hundreds of workers mining mineral silica. The tunnelers died from acute silicosis which in some cases developed rapidly, in some cases within a year. At the time the physicochemical properties of silica relevant to its pathogenicity were unknown and regulations for silica dust exposure were put in place based on mass. Since then a number of studies investigated the pathogenic potential of quartz and showed that the inflammatory potential ascribes to undissociated SiOH on the surface of quartz interacting via H-bonding with cell membrane components (Ghiazza et al., 2011). Modification of the

surface with aluminium lactate significantly reduced ability of quartz to generate hydroxyl-radicals and showed reduced inflammogenicity (Schins et al., 2002).

Asbestos is another major hazardous particle in occupational exposure settings and its use dates back to approximately 2500 B.C when anthophyllite was used as a reinforcement in clay utensils and pottery (Virta, 2002). Exploitation of asbestos fibres on an industrial scale began in the early nineteenth century in Italy and expanded throughout the world with Canada, South Africa and USSR being the major producing countries. Asbestos has a wide range of applications due to their fire-proof and insulating properties in building and construction materials including ships, roofing, bricks and asphalt as well as textiles. During World War II asbestos was used in a range of military applications for thermal insulation and fire protection which led to an increase in production. The growth of asbestos industry reached a maximum in the late 1960s with worldwide production of 5 million tons but was brought to a halt in the early 1970s due to the growing opposition to the use of asbestos fibre in response to an epidemic of disease caused by exposure to it. By the year 2000 the world production level had decreased to 2 million tons (Virta, 2002).

The first written report addressing the link between asbestos exposure and disease appeared in the *British Medical Journal* in 1924 by William Cooke (Cooke, 1924). This was a single case report of pneumoconiotic fibrosis (asbestosis) of the lungs in a worker in the asbestos industry. In 1925 the term asbestosis was first mentioned by Thomas Oliver and in the early 1930s a survey of occupational exposure to asbestos dust confirmed the relation between inhalation of asbestos and fatal asbestosis (Bartrip, 2004). In 1933 Home Office officials in Britain implemented asbestos industry regulations to control asbestos dust in workplaces; however these regulations were widely neglected by other countries. At the time silicosis was recognised as a major dust hazard and the regulations for dust measurement and control of silica in workplace were adapted for asbestos. In the 1960s several additional important connections were made linking exposure to asbestos with other disease including lung cancer and mesothelioma (Tweedale, 2002). A study by Wagner *et al.* highlighted that 28 out of 33 histologically proven mesothelioma cases

were identified in association with the asbestos fields in north western cape province, South Africa (Wagner et al., 1960). This relationship was strengthened by the fact that no such neoplasm was observed in 10000 lung examination from patients not subjected to asbestos exposure (Wagner et al., 1960). Subsequently it was shown that disease development was not restricted only to workers in asbestos industries, but it occurred also in insulation worker, in users of asbestos products and in individuals residing near asbestos factories. Finally the topic attracted media attention and led to law suits claiming compensation which resulted in the virtual demise of the asbestos industry and eventually the banning of asbestos in most Western countries. The mass-based standard first used for regulating exposure in workplaces was recognised to be deficient and in 1958 the Asbestos Research Council set the standard for asbestos fibre sampling and counting to be number-based and quantifying all airborne structures with a length of 5-100 µm with an aspect ratio of 3:1. This standard was chosen 'somewhat arbitrarily and was intended to allow a margin of safety below the limits of 10-20 µm for pathogenic fibres' (Walton, 1982). In 1968 the British Occupational Hygiene Society set a standard for air contaminants and measurement methods and included the definitions for 'fibres' as stated by the Asbestos Research Council in their regulation (Ogden, 2003) (Asbestosis Research Council, 1968); this forms the current worldwide WHO standard for measuring airborne fibre number in workplaces which counts all airborne fibres longer than 5 µm, thinner than 3 µm and with an aspect ratio greater than 3:1.

1.4.2 Structure of asbestos

Asbestos fibres are silicate minerals and classified into two categories, serpentine and amphiboles regarding their basic building blocks. Asbestos fibres have a basic silicate tetrahedral building block which occurs as double chains $(Si_4O_{11})^{-6}$ in amphiboles or in sheets $(Si_4O_{10})^{-4}$ in serpentine asbestos. Chrysotile, a hydrated magnesium silicate, is the only asbestiform mineral of the serpentine group and has a fibrillar, wavy, thread-like appearance and are extremely thin with an average diameter of 25 nanometers of a unit fibre with aggregations of chrysotile fibres up to 100 µm. The length of the fibres ranges from fractions of millimetres to several

centimetres. The stochiometric chemical composition of chrysotile asbestos is given as $Mg_3Si_2O_5(OH)_4$ however several mineral contaminates are present, including brucite as the most common.

Amphibole minerals consist of five asbestiform fibres including amosite (grunerite), crocidolite (riebeckite), tremolite, anthophyllite, and actinolite – of these only the first 3 are commercially mined and used. Compared to chrysotile asbestos, the amphibole fibres are straight and needle shaped. Their composition varies depending on the complexity of the environment but can be represented as

$$A_{0\text{-}1}, B_2C_5D_8O_{22}(OH, O, F, Cl)_2$$

where A= Na, K

B= Na, Ca, Mg, Fe^{2+}, Mn, Li

C= Al, Fe^{2+}, Fe^{3+}, Ti, Mg, Mn, Cr

D= Si, Al

Adapted from (Virta, 2002).

Crocidolite and amosite are hydrated silicates of iron and magnesium, are the most important amphibole asbestos fibres and together with chrysotile were industrially exploited to a significant degree (Virta, 2002).

1.4.3 Asbestos related diseases

1.4.3.1 Asbestosis

Asbestosis is defined as a bilateral diffuse interstitial fibrosis in the peripheral lung at the sites of asbestos fibre deposition. The clinical signs of asbestosis are similar to that of idiopathic interstitial fibrosis (Mossman and Churg, 1998) however differential diagnosis can be made due to the presence of asbestos or ferruginous bodies, fibres surrounded by an iron-protein coating. Epidemiologic studies on the incidence of asbestosis showed that a minimum exposure dose of approximately 25

to 100 fibres per ml per year are required for the development of the disease. The latency period of the disease can be as short as 5.2 years after extremely high exposure and up to 20.2 years at lower exposure levels (Mossman and Churg, 1998).

The alveolar type I and type II epithelial cells play a major role in the development of pulmonary fibrosis. Epithelial cell proliferation is a natural repair mechanism after injury which, if uncontrolled, can result in fibrogenesis and carcinogenesis. Molecular changes in the early response protooncogenes, c-fos, c-jun and c-myc after asbestos exposure are involved in epithelial cell proliferation (Janssen et al., 1994). Other important proliferative signals include tumour necrosis factor α (TNF-α), prostaglandins and monocyte chemotactic protein 1 (MCP-1) (Chapman, 2011). Epithelial cells have been shown to undergo epithelial-to-mesenchymal transition characterised by the downregulation of E-cadherin, loss of cell-cell contacts, actin reorganization and expression of α-smooth muscle actin after asbestos exposure with mitogen-activated protein kinase (MAPK) and extracellular-signal related kinase (Erk) being the main signalling pathway (Tamminen et al., 2012). Survival of mesenchymal cells (fibroblasts and myofibroblasts) determines the severity of the disease and is a key factor in determining the progress of a fibrotic response after toxic injury to the lung. Resistance to apoptosis is mediated by a number of growth factors and cytokine receptor expression including tumour growth factor-1β (TGF-β1), platelet derived growth factor (PDGF), connective tissue growth factor (CTGF) and receptor expression of interleukine 4 (IL-4), IL-13 and CC-chemokine ligand (CCL2) (Bonner, 2010).The phenotype of myofibroblasts is further determined by the T-helper 1 (Th1) or T-helper 2 (Th2) microenvironment, whereby interferon γ (IFN-γ) and IFN-β produced by Th1 cells leads to resolution of fibrosis via growth arrest and cell death (Bonner, 2010). The Th2 microenvironment in contrast leads to myoblast survival and matrix production via TGF-β1, IL-13 and platelet-derived growth factor (PDGF)-AA (Bonner, 2010).

1.4.3.2 Lung cancer

The first relation between asbestos exposure and lung cancer was reported in 1935 by Gloyne, and Lynch and Smith (reported in (Wikeley, 1992)). Since these tumours are histologically indistinguishable from those caused by other factors known to cause lung cancer, such as cigarette smoke, the exact incidence of lung cancer related solely to asbestos is unknown. An epidemiologic study showed that asbestos is a lung carcinogen because of its fibrogenicity (Hughes and Weill, 1991) and therefore asbestosis may be a necessary precursor to asbestos-related lung cancer (Nurminen and Tossavainen, 1994). Molecular pathways involved in malignant transformation of lung epithelial cells are similar to pathways linked to pulmonary fibrosis including TNF-α mediated activation of nuclear-factor NF-κB, epidermal growth factor receptor (EGFR) signalling and activation of c-jun and c-fos leading to cell proliferation and transformation via activator-protein (AP)-1 dependent genes (Heintz et al., 2010).

1.4.3.3 Pleural effusion and pleural plaques

Pleural effusion is a build-up of pleural fluid due to an imbalance of influx and efflux of fluid in the pleural space (Owens and Milligan, 1995). Benign asbestos pleural effusion develops between 5 to 30 years after exposure to asbestos, depending on the exposure concentration. It can either resolve or lead to pleural thickening, however is not followed by the development of malignancy (Jamrozik et al., 2011).

Pleural plaques are areas of hyaline fibrosis predominantly on the parietal pleura. They consist of acellular bundles of collagen with asbestos fibres enclosed in these areas and have a white and shaggy macroscopical appearance (Greillier and Astoul, 2008). Pleural plaques are mainly asymptomatic and are not pre-cancerous nor are they associated with impairment of pulmonary function (Greillier and Astoul, 2008).

1.4.3.4 Mesothelioma

Mesothelioma is an insidious cancer of the mesothelial cells lining the pleural and peritoneal cavities primarily seen in conjunction with asbestos exposure. Other causes for mesothelioma are rare but include exposure to erionite, a non- asbestos fibrous form of zeolite, radiation and simian virus (SV) 40 (Rascoe et al., 2012; Comar et al., 2012). Mesothelioma has a long latency period with clinical symptoms usually developing 20 to 40 years after exposure. A study by Peto *et al*. predicts a peak in mesothelioma incidence in Britain to be in the year 2020 with a number of 2700 to 3300 deaths per annum dating back to exposures in the 1960's and 1970' s (Peto et al., 1995). Mesothelioma is classified into various stages depending on its severity. T1a is a tumour limited to the parietal pleura whereas T1b tumours effect the parietal and visceral pleura (Mueller, 2002). The most severe version of mesothelioma is classified under T4 with spreading of the tumour to mediastinal organs, the spine, inner surface of the pericardium and destruction of the ribs (Mueller, 2002).

Extensive research has been performed investigating the molecular pathogenesis of malignant mesothelioma to identify potential target for therapeutics. TGF-β1 is associated with the development of various tumours and has been shown to be markedly suppressed in asbestos induced tumorigenic cells (Wen et al., 2011). Therefore, TGF-β1 suppression could be a potential target for therapeutics by preventing rogression via the PI3K/Akt signalling pathway (Wen et al., 2011). Studies on the role of microRNAs (miRNA) in regulating multiple genes in malignant mesothelioma have identified mRNA-34b/c as playing a major role in pleural mesothelioma pathogenesis (Kubo et al., 2011). Epigenetic silencing of miRNA-34b/c as seen in tumours was linked to proliferation, migration and invasion and over-expression of miRNA-34b/c induced anti-tumour effect such as cell cycle arrest and apoptosis (Kubo et al., 2011).

Other key molecular factors aberrant in mesothelioma include vascular endothelial growth factor (VEGF), epidermal growth factor receptor (EGFR) and Wnt pathway (Lee et al., 2007). VEGF is involved in angiogenesis, growth, metastasis and is a potent tumour inducer. It is seven-fold up-regulated in the serum of malignant

mesothelioma patients were it plays an important role in mesothelial cell transformation (Kumar-Singh et al., 1999) (Rascoe et al., 2012). Overexpression of IL-6 in tumours was linked to the increased expression of VEGF via the signal transducer and activator of transcription 3 (STAT3) pathway (Adachi et al., 2006). Epidermal growth factor receptor (EGFR) and its ligand transforming growth factor α (TGF-α) show over-expression in cancer leading to cell proliferation, differentiation and survival (Lee et al., 2007). Successful clinical trials have been performed on cytotoxic drugs to evaluate the anti-tumour activity of VEGF and EGFR inhibitors (Kindler, 2004). Chromosomal alterations, especially p53 and pRb are common in malignancies. In malignant mesothelioma the p53 and pRb alleles remain intact however allele loss is seen in 1p, 3p21, 6q, 9p21, 15q11-15 and 22q (Zucali et al., 2011). Loss of the 9p21 chromosome band results in the loss of the INK4a/ARF locus which encodes the proteins p16INK4a and p14ARF (Lee et al., 2007). Both proteins are essential regulators for tumour suppressor pathways and apoptosis regulation (Prins et al., 1998), which explains the unresponsiveness of mesothelioma treatment with drugs inducing apoptosis (Zucali et al., 2011). Loss of the proteins p16INK4a and p14ARF is linked to mutation in the gene neurofibromatosis type 2 gene (NF2) on chromosome 22q12, which is seen in nearly 100% of all mesothelioma patients (Cheng et al., 1999). An *in vivo* study on wild-type and heterozygote mutation of the NF2 gene in mice exposed to crocidolite asbestos fibres showed that NF2 gene mutation is involved in mesothelioma oncogenisis (Fleury-Feith et al., 2003).

Treatment of malignant mesothelioma is extremely difficult since a number of genetic mutations accumulate over the years of disease development and progression. Current therapies including surgery, chemotherapy and radiotherapy led to very little improvement in the patient's survival rate. However, new therapeutic approaches including immunotherapy and gene therapy of wild type (wt)-p53 gene delivery in the pleura space in the early stages of mesothelioma demonstrated promising results for clinical trials in the near-future (Haas and Sterman, 2012).

1.5 Fibre pathogenicity paradigm

Fibre toxicology is a sub-discipline of particle toxicology addressing the specialised nature of fibre effects. Studies on natural occurring fibres like asbestos, erionite and zeolite as well as man-made fibres like synthetic vitreous fibre (SVF) and refractory ceramic fibre (RCF1) have resulted in the fibre pathogenicity paradigm (FPP) (Donaldson, 2009). It was borne out of 25 years of research and has proven to be the most robust structure-activity relationship in particle toxicology (Donaldson et al., 2010). The FPP can be split into 3 main criteria, namely fibre dimensions, biopersistence and surface reactivity.

1.5.1 Dose

As in all branches of toxicology the dose is the most important factor driving a toxicological response as stated already by Paracelsus in his famous quotation "*All things are poison and nothing is without poison; only the dose makes that a thing is no poison*". A recent comprehensive review we discussed in detail the biologically effective dose (BED) in toxicology, focusing on nanotoxicology and high aspect ratio nanoparticles including nanofibres (Donaldson et al., 2012). The BED is a term describing the actual component of the total dose that drives adverse effects or in other words "*the entity within any mass dose of particles that drives a critical pathophysiogically relevant form of toxicity in tissue*" (Donaldson et al., 2012). In fibre toxicology, fibre dimension including length and diameter, and biopersistent are the accepted components used to describe the BED which are summarised in the fibre pathogenicity paradigm.

1.5.2 Fibre dimension

Fibre dimensions have been identified as one of the major determinants in particle toxicology. The width of a fibre determines the aerodynamic diameter which further governs the side of deposition of a fibre in the respiratory tract as discussed in chapter 1.3.2 (Ellison, 1993).

The first indication of the importance of fibre length in the development of respiratory disease in relation to asbestos exposure was reported by Beger in 1933 (quoted by (Holt, 1957)) who showed that asbestos fibres with a length of 25-109 µm were found in a patient who died on asbestosis. A series of animal inhalation studies and studies on lung material from asbestosis cases were performed to investigate the length fraction of asbestos fibres responsible for asbestosis (KNOX and BEATTIE, 1954; VORWALD et al., 1951). The inhalation models indicated a fibre length of 20-50 µm were necessary to cause peribronchiloar fibrosis whereas human asbestosis cases showed that fibres up to 15 µm caused severe. An extensive study by Stanton & Wrench in 1972 investigated the role of fibre length, diameter and composition of a range of fibrous materials including asbestos, fibrous glass and aluminium oxide on experimental pleural mesothelioma in rats. This study concluded that carcinogenicity was related to fibres with a length between 10 to 80 µm with a diameter below 2.5 µm (Stanton, 1973; Stanton and Wrench, 1972). Physiochemical properties of the fibre samples had no influence on the carcinogenicity outcome. In 1986 the 'Stanton' fibre threshold for pathogenic fibres of ≥ 10 µm had to be corrected according to the growing knowledge on asbestos fibre length and mesothelioma incidences in humans (Timbrell, 1983) and rats (Davis et al., 1986). Timbrell showed that asbestos fibres form the Northwest Cape in Africa had virtually no fibres greater than 10 µm however numerous mesothelioma cases had been reported (Timbrell, 1983). *In vivo* inhalation studies in rats showed that long fibre amosite with a size distribution of 30% >5 µm and 10% > 10 µm produced carcinomas in rats (Davis et al., 1986). These studies led to the conclusion that "*the critical fibres for mesothelioma induction have lengths between 5 and 10 µm*", whereby "*fibres shorter than 5 µm appear to be ineffective, while an appreciable fraction longer than 10 µm appears to be unnecessary*" (Lippmann, 1993). In 1997 the WHO included in their regulation of airborne dust the definition of fibres as particles with a diameter < 3µm and a length > 5 µm with an aspect ratio of 3:1, a definition which originated from the Asbestos Research Council meeting in 1958 (Asbestosis Research Council, 1968).

There are various proposed mechanism by which fibre length influences the development of lung and pleural diseases. The predominant mechanism is length dependent retention of longer fibres in the lung caused by inefficient clearance by

alveolar macrophages. Due to the aerodynamic properties of fibres as discussed in chapter 1.3.2, they bypass the normal clearance mechanism of the lung, which would restrict the deposition of foreign particles in the lower respiratory tract to a size fraction that can be phagocytosed by alveolar macrophages. Fibres, exceeding the maximal length for complete phagocytosis by macrophages, can cause 'frustrated phagocytosis', a term used to describe incomplete uptake of particles by cells as shown in Figure 1-4.

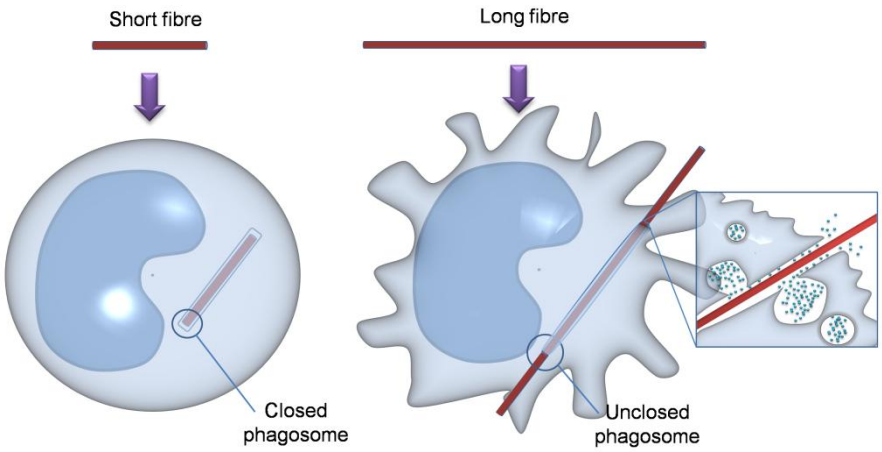

Figure 1-4: Diagrammatic representation of short fibre complete phagocytosis and long fibre –mediated frustrated phagocytosis. Short fibres can be fully phagocytosed by macrophages whereas long fibres are too long to be fully taken up leading to an unclosed membrane and leakage of cell content.

The retention of longer fibres in the lung is well documented. Coin *et al.* performed a study measuring the average fibre length of chrysotile asbestos over time retained in the peripheral and central regions in the lung after inhalation exposure and concluded that the average length of retained fibres increased over time with fibres ≥ 16 µm clearing very slowly (Coin et al., 1992). Another study by Searl *et al.* confirmed the hypothesis that short fibres are cleared by cells from the lower regions of the lung and longer fibres (> 20 µm) are retained (Searl et al., 1999).

In addition to the selective retention of longer fibres in the lung due to failed macrophage clearance, retention of longer fibres in the pleural and peritoneal space after translocation from the lung has also been reported (Moalli et al., 1987; Murphy et al., 2011). Clearance of fibres from the pleural- and peritoneal space is via the passive lymphatic flow through stomata, as discussed in chapter 1.2.1. Stomatal openings range from 2-8 μm and act as a sieve, preventing efficient clearance of fibres exceeding the size of the stomata. First evidence of the selective retention of asbestos fibres in the peritoneal caviety was given by Moalli *et al*. (Moalli et al., 1987). After intraperitoneal injections of short and long asbestos fibres, shorter fibres (90.6% ≤ 2μm) were readily cleared after 6 hours through the stomatal opening in the diaphragm whereas longer fibres (60.3% ≥ 2 μm) were retained at the lymphatic stomata (Moalli et al., 1987).

Phagocytosis of foreign material by macrophages leads to the generation of an oxidative or respiratory burst through which the invading pathogens are killed. Reactive oxygen species (ROS) are produced within the phago-lysosome by the multi-subunit NADPH-dependent phagocytic oxidase, whereby electrons are pumped into this compartment via NADPH oxidase to reduce oxygen to superoxide anion (O_2^-). O_2^- can spontaneously undergo dismutation in a pH and concentration dependent manner to form H_2O_2 and O_2. In the case of frustrated phagocytosis, release of ROS extracellularly, into the surrounding tissue, can occur with potential harmful effects (Bergstrand, 1990).

In recent years in-depth investigation of the mechanism of asbestos induced inflammation has led to a better understanding of the molecular pathways involved in frustrated phagocytosis. The NALP3 inflammasome has been identified as a key player in asbestos induced inflammation (Hornung et al., 2008; Hornung and Latz, 2010; Yang et al., 2010; Dostert et al., 2008). The NALP3 inflammasome, alternatively named NLRP3, is a member of the nucleotide-binding oligomerisation domain (NOD)-like receptors (NLRs) containing a pyrin domain 3 (NALP3) complex and consists of the adaptor protein, apoptosis-associated speck-like protein containing a C-terminal caspase recruitment domain (ASC) and the effector cystein protease caspase 1 (Tschopp and Schroder, 2010). ASC is alternatively named

PYCARD. Oligomerization of the NALP3 inflammasome and pro-caspase 1 clustering results in the auto-activation of caspase 1 and cleavage of pro-IL-1β to mature IL-1β (Tschopp and Schroder, 2010).A diverse range of pathogens, environmental and endogenously derived molecules can lead to the formation and activation of the NALP3 inflammasome, which potentially modulates innate immune functions. Among these are extracellular ATP (Petrilli et al., 2007; Mariathasan et al., 2006), viral RNA, whole viruses and fungi (Allen et al., 2009; Gross et al., 2009), pore forming toxins (Mariathasan et al., 2006) and particulates. Activation of the NALP3 inflammasome was reported after islet amyloid polypeptide (Masters et al., 2010), asbestos (Dostert et al., 2008), silica and monosodium urate crystals (MSU) (Martinon et al., 2006) exposure but not with diesel exhaust particles or cigarette smoke (Dostert et al., 2008), which strengthen the conclusion that the crystalline structure of the particles and frustrated phagocytosis are the driving factors for the observed response. In contrast to these reports, NALP3 activation has also been observed after exposure to nanosized CB (Reisetter et al., 2011), nano-sized TiO_2 and SiO_2 (Kumar-Singh et al., 1999; Sandberg et al., 2012),

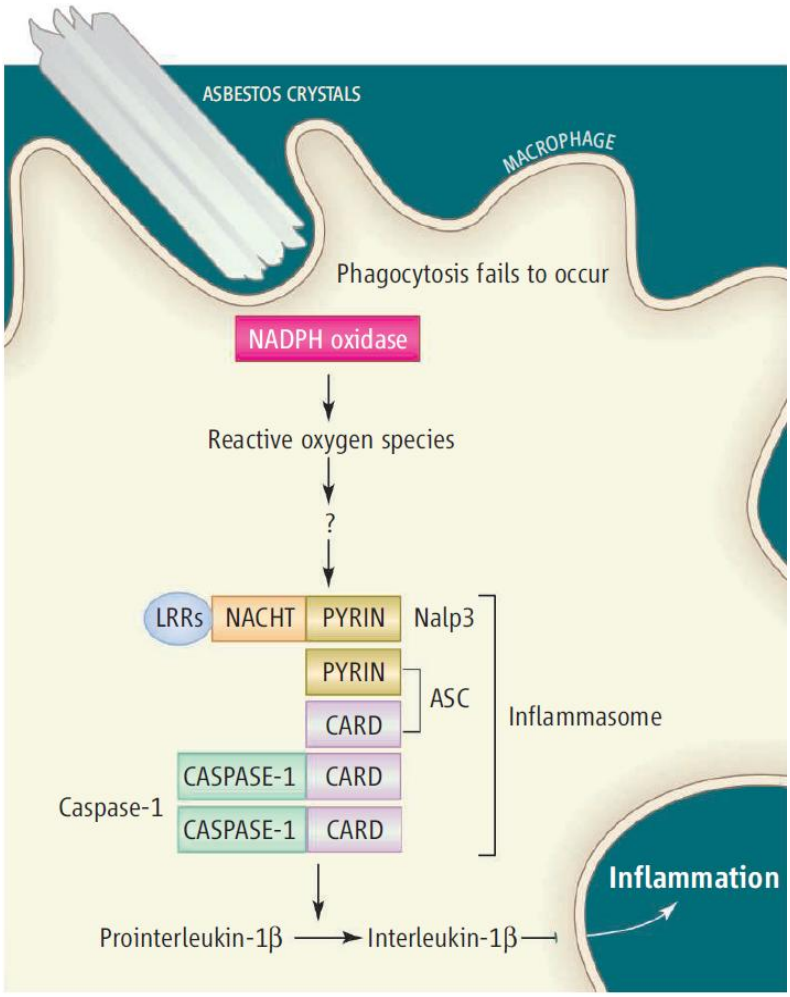

Figure 1-5: Diagrammatic representation of the NALP3 inflammasome activation by asbestos fibres. Frustrated phagocytosis of asbestos fibres by macrophages leads to the activation of NADPH oxidase and the generation of ROS, which was shown to be a mechanism for NALP3 inflammasome activation. Figure reprinted with permission from Science AAAS(O'Neill, 2008).

The activation of the NALP3 inflammasome is a two-step process whereby induction of pro-IL-1β in response to TLR, NLR, IL-1 or TNFα stimulation is a separate first step required for NALP3 signalling and release of IL-1β (Bauernfeind et al., 2011). The NALP3 inflammasome can be activated via various different mechanisms. The efflux of potassium from the cells via the P2X7 channel has been shown to be required for NALP3 activation (Petrilli et al., 2007). A further mechanism is

lysosomal rupture due to the phagocytosis of crystalline or particulate structures and subsequent release of cathepsin B (Tschopp and Schroder, 2010). A third proposed model is the activation via ROS, however it is not known whether ROS can directly be sensed by the NALP3 inflammasome (Bryant and Fitzgerald, 2009). Dostert *et al*. performed a in-depth study demonstrating NALP3 inflammasome activation after asbestos and silica exposure *in vitro* and *in vivo,* which could be blocked by using NALP3, ASC and caspase-1 knockdown mice (Dostert et al., 2008). The relation of IL-1β expression with the NALP3 inflammasome after asbestos exposure was further confirmed using potassium efflux inhibitors, ROS inhibitors and blockage of phagocytosis leading to a significant decrease of IL-1β expression (Dostert et al., 2008). Another study by Hornung *et al*. confirmed these results showing NALP3 activation to silica crystals and aluminium salt in conjunction with lysosomal destabilisation (Hornung et al., 2008).

So far, the activation and mechanism of NALP3 inflammasome has been studied mainly in macrophages. A recent study was focusing on the role of the inflammasome in neutrophils and showed a pivotal role of NALP3 in facilitating IL-1β cytokine release (Mankan et al., 2012). In addition, a study by Peeters et al. showed the activation of the NALP3 inflammasome by crystalline silica in human lung epithelial cells and identified a crucial link between inflammasome inactivation and blunted fibroblast proliferation (Peeters et al., 2013). The NALP3 inflammasome activation and chronic activation of IL-1β, which is directly relevant to fibroblast proliferation and fibrogenesis describes an important link between acute and chronic inflammation caused by particulates (Peeters et al., 2013).

1.5.3 Biopersistence

It has been widely accepted that biopersistence plays a major role in the pathological response to inhaled fibres since it determines the dissolution/ breakage of long fibres and their clearance rate. It is at the level of long fibres that biopersistence can be seen to be most important since they represent the pathologically-relevant length fraction.

A long fibre that is non-biopersistent will undergo weakening and breakage and can subsequently be phagocytosed by alveolar macrophages and cleared. Biopersistent long fibres on the other hand will accumulate due to incomplete phagocytosis and clearance resulting in a pathological response. Chrysotile asbestos has been shown to be less pathogenic compared to amphibole asbestos due to its less biopersistent chemical composition (Bernstein and Hoskins, 2006). The outer coating of chrysotile fibres is a rolled sheet composed of magnesium silicate and an external brucite layer which is soluble in the lung surfactant leaving the crystalline structure of silica to be readily attacked by acid within the phagolysosome when phagocytosed by macrophages (Bernstein and Hoskins, 2006). This process leads to destabilization of the chrysotile structure and ultimately its fragmentation into smaller fragments. In contrast, the double chain of silica tetrahedra in amphibole asbestos fibres provides tensile strength which is highly influenced by the iron content making them strong and durable (Virta, 2002). Studies have shown that amphibole asbestos fibres, mainly amosite, do not dissolve *in vivo* or *in vitro* at pH ranges that might be plausibly encountered in biological systems (Searl et al., 1999; Hesterberg et al., 1997). An extensive study was performed by Searl *et al.* comparing biopersistence and durability of nine mineral fibre types in rat lungs over a 12 month period (Searl et al., 1999). The studies on the clearance over the 12 month period showed that, for amosite, RCF-2 and RCF-4, the biopersistence increased with fibre length (Searl et al., 1999). For non-biopersistent fibres, man-made vitreous fibres, MMVF-10 and MMVF-22 the persistence decreased with increased fibre length showing the breakage/dissolution of longer fibres (Searl et al., 1999). In addition, *in vitro* durability studies were performed over a 12 month period whereby the same fibre samples were incubated in a pH 4.6 solution. The results obtained from *in vitro* durability studies paralleled the *in vivo* studies (Searl et al., 1999).

Extensive research was performed on p-aramid, a man-made organic fibre, first commercialised in 1970, which has fibril lengths up to 100 µm (Donaldson, 2009). P-aramid is a long chain synthetic polyamide used as advanced composite and in fabrics, body armour, etc and was manufactured in high quantities. Even though the fibres of p-aramid are long and respirable, inhalation exposure studies showed that these fibres have limited pathogenicity and fibrogenicity due to their non-

biopersistence with dissolution and shortening of longer fibrils into shorter fragments (Bellmann et al., 2000; Kelly et al., 1993).

Until recently research on the biopersistence of nanofibres focused on naturally occurring fibres as well as man-made synthetic vitreous and polyamide fibres. In recent years research into the biopersistence of carbonaceous nanomaterials, including fibrous carbon nanotubes (CNT) and graphene platelets attracted attention due to the increased production of these materials. The first study on the durability of CNT was performed by Osmond-McLeod comparing four different types of CNT, including single-walled as well as multi-walled CNT (SWCNT/MWCNT) to X607, a non-durable glass wool, long fibre amosite asbestos and long fibre chrysotile (Osmond-McLeod et al., 2011). Fibres were incubated in Gambles solution, a simulated biological fluid at a pH of 4.5 representing the acidic milieu within phagosomes, for up to 24 weeks and weight loss as well as length distribution and structural changes were recorded. Three out of four CNT tested showed nearly 100 % durability similar to that of amosite asbestos (Osmond-McLeod et al., 2011). In addition to the durability study, recent investigations have shown that carbon nanomaterials, including graphene oxide and oxidized carbon nanotubes, are degraded by oxidase enzymes including horseradish peroxidase and neutrophil myeloperoxidase (hMPO) *in vitro* and *in vivo* (Kagan et al., 2010; Graham et al., 1999; Kotchey et al., 2011; Shvedova et al., 2012) causing them to exhibit less inflammatory potential *in vivo*.

1.5.4 Surface reactivity

As mentioned above, studies on the toxicity of fibres, exhibiting entirely different chemical compositions, led to the conclusion that length and biopersistence are the dominating criteria in predicting the severity of fibre pathogenicities. However, not all long, biopersistent fibres show an equal degree of pathogenicity which is due to their difference in chemical composition, especially surface characteristics. At the end of the 1970s environmental exposure to erionite, a naturally occurring fibrous mineral, was found to be related to very high incidences of pleural mesothelioma in

Cappadocia, a region in Turkey where erionite was present in homes (Temel and Gundogdu, 1996). Erionite is a fine fibrous wool-like crystal and is a hydrated aluminosilicate minerals. It has similar morphology to amphibole asbestos however different chemical and physical properties and a 20 times larger internal surface compared to crocidolite asbestos (Metintas et al., 1999). The drastically increased surface-area- to –volume ratio could account for the enhanced pathogenicity.

It is known that these naturally occurring fibres possess a highly reactive surface due to their high iron content which is involved in iron-mediated redox chemistry and subsequently oxidative stress (Kamp et al., 1992).

Two mechanisms can lead to the production of reactive oxygen species (ROS) by asbestos. Firstly, the associated iron cations can promote the formation of highly reactive hydroxyl free radical ($HO^{\bullet}$) from hydrogen peroxide (H_2O_2) via the Fenton reaction (1) (Turci et al., 2011).

$$Fe^{2+} + H_2O_2 \rightarrow Fe^{3+} + HO^- + HO^{\bullet} \quad (1)$$

Biological reducing agents such as superoxide can reduce ferric iron (Fe^{3+}) back to ferrous iron (Fe^{2+}) which can further catalyze the formation of $HO^{\bullet}$ from H_2O_2 via the Haber-Weiss reaction (2) (Kamp and Weitzman, 1999).

$$O^{2-} + H_2O_2 \text{-> } HO^- + HO^{\bullet} + O_2 \quad (2)$$

Further reaction catalyzed by iron include alkoxyl radicals from organic hydroperoxides and ferryl (FeO^{2+}) (Kamp and Weitzman, 1999).

The production of ROS can cause oxidation and nitrosylation of proteins and DNA either by direct addition of $HO^{\bullet}$ to the DNA or by hydrogen abstraction (Byrnes, 1996). The second mechanism by which asbestos induce ROS is via stimulation of macrophages and neutrophils and their release of O_2^- and H_2O_2 catalyzed by iron (Kamp and Weitzman, 1999). There is strong evidence that this increase in ROS mediated by the iron content is linked to apoptosis, inflammation and proliferation and therefore enhanced asbestos induced lung injury (Shukla et al., 2003).

1.6 Inflammation in relation to inhaled particles

1.6.1 Lung inflammation

Inflammation is seen acutely and chronically in lungs exposed to harmful dusts and fibres and inflammation is a pathobiological process that leads to pathological change associated with particle exposure including fibrosis, airway inflammation and lung cancer. For these reasons inflammation is commonly studied as a way to identify harmful particles and to understand the features of particles that drive pathogenicity, the biologically effective dose. The cellular dynamics of the lung response to inhaled particles has been subject to intensive investigations in an attempt to identify the key mediators of the inflammatory response. From dust exposure experiments potent agents such as complement fragments C5a, prostaglandins, leukotrienes and other lipid mediators have been identified to act as chemoattractants and activators for macrophages and neutrophils (Finkelstein and Barrett, 2000). Alveolar macrophages whose evolved function is to take up deposited particles play a major role in the initiation of a pulmonary response to inhaled particles by up-regulating expression of a number of pro-inflammatory and pro-fibrotic cytokines. Among these, IL-1β and TNF-α have been identified as important mediators in the recruitment of neutrophils, lymphocytes, and macrophages. In addition, via cytokine growth factors, they induce fibroblast proliferation and granuloma formation as well as the release of acute phase proteins (Finkelstein and Barrett, 2000; Ohtsuka et al., 1995; Mohr et al., 1991; Piguet et al., 1993). Other cytokines involved in the recruitment of inflammatory cells are macrophage inflammatory protein 1 and 2 (MIP-1 α and MIP-2), which were shown to be upregulated after intratracheal installation of silica and titanium dioxide (Driscoll et al., 1993). In addition to the secretion of chemokines and cytokines by macrophages, direct interaction of epithelial type II cells with particles stimulates epithelial cells to produce inflammatory mediators such as granulocyte-macrophage colony-stimulating factor (GM-CSF), TGF-β, IFN, IL-8, MIP-2 and RANTES (Finkelstein and Barrett, 2000).

Intracellular signalling pathways leading to the activation of the above mentioned inflammatory mediators have been extensively studied, and the molecular pathways

leading to an acute inflammatory response in the lung are dependent on the type of particle exposure and a complex mixture of various pathways are involved. A well understood signalling pathway in lung inflammation is that of the endotoxin lipopolysaccaride (LPS). LPS stimulation is initiated by binding to LPS binding protein (LBP) which facilitates the association between LPS and CD14. CD14 facilitates further the transfer of LPS to the TLR4/MD-2 receptor complex (Lu et al., 2008). TLR4 undergoes oligomerization and recruits the TIR (Toll-interleukin-1 receptor) domain which is an adaptor protein for MyD88 (myeloid differentiation primary response gene 88). MyD88 recruits and activates IL-1 receptor-associated kinase-4 (IRAK-4) and TRAF6 (TNF receptor-associated factor 6) as well as the transcription factors NF-κB, AP-1 and IRF-5 further downstream leading to proinflammatory cytokine expression (Lu et al., 2008). TLR4 oligomerization via LPS can also stimulate a MyD88 independent pathway via TRIF (TIR domain-containing adaptor inducing IFN-β) signalling which induces type I interferons by recruiting TRAF3 and RIP1 (receptor-interacting protein 1) to activate transcription factor IRF3, as well as NF-κB and AP-1 (Lu et al., 2008).

The activation of the MAP kinase pathways has also been linked to asbestos and silica exposure (Tamminen et al., 2012; Heintz et al., 2010; Rimal et al., 2005). The extracellular signal related kinase (ERK1/2) pathway is the best characterised pathway in asbestos induced lung inflammation as well as mesothelioma (Heintz et al., 2010) and has also been shown to be activated ROS from ultrafine particulate matter (Weissenberg et al., 2010). The ERK pathway controls the expression and transcriptional activity of Fos and c-jun family members of the activator protein (AP)-1 transcription factor regulating genes for cell proliferation, transformation, migration, protein metabolism and immune response (Heintz et al., 2010). Similar signalling pathways activated in epithelial cells after asbestos exposure leading to lung cancer have been identified in pleural inflammation and the development of malignant mesothelioma (Heintz et al., 2010).

1.6.2 Inflammation in the pleural cavity

The onset of inflammation in the pleural space by either bacterial endotoxin, asbestos or other stimuli is characterised by an extensive influx of leukocytes from the vascular compartment (Mutsaers, 2004). The influx of leukocyteleukocytes requires a chemotactic gradient to the site of inflammation which is either generated by activated mesothelial cells or by residing macrophages in the pleural space. Expression of chemokines such as IL-8 and MCP-1 play a significant role in the chemotactic activity and are elevated in mesothelial cells after activation by LPS, IL-1β and TNF-α (Antony et al., 1995). Particulate stimuli such as talc and asbestos are also potent inducers in MCP-1 and IL-8 expression in pleural mesothelial cells and enhance intracellular adhesion molecule-1 (ICAM-1) expression (Nasreen et al., 1998; Tanaka et al., 2000). Other cell adhesion molecules expressed in activated mesothelial cells are vascular cellular adhesion molecule (VCAM-1), E-cadherin, N-cadherin, CD49a, CD49b and CD29 (Mutsaers, 2004). Increased expression of ICAM-1 on mesothelial cells leads to transmigration of leukocyteleukocytes via interaction with β2 integrin family receptors (Zeillemaker et al., 1996). IL-6 has also been shown to play an important role in pleural inflammation, as IL-6 knockout mice exhibit reduced polymorphonuclear leukocyte (PMN) migration and inflammation compared to wild type mice after intrapleural injection of carrageenan, a polysaccharide extracted from red seaweed (Cuzzocrea et al., 1999). IL-6 expression leads to additional expression of TNF-α and IL-1β, key cytokines in pleural inflammation expressed by activated resident macrophages in the pleural space (Frode et al., 2001). Little is known about the role of resident pleural macrophages in the initiation of inflammation and orchestration of PMN recruitment. A study by Cailhier *et al*. indicated that residential macrophages and their cytokines TNF-α, IL-6, MIP-2 and IL-10 are essential for the recruitment of PMN (Cailhier et al., 2006). A recent study by Murphy et al. investigated the pro-inflammatory responses of macrophages and mesothelial cells *in vitro* after CNT treatment and showed that CNT resulted in a significant release of IL-1β, TNF-α, IL-6 and IL-8 from macrophages but not mesothelial cells (Murphy et al., 2012b). However, pro-inflammatory mediators released by macrophages after CNT treatment led to an

significant increase in cytokine production of mesothelial cells (Murphy et al., 2012b).

Acute inflammation, release of cytokines and chemokines as well as production of mutagenic reactive oxygen species is known to be directly linked to the chronic inflammation and carcinogenesis caused by asbestos (Dai and Churg, 2001; Dostert et al., 2008; Nagai and Toyokuni, 2010; Unfried et al., 2002). It is also known that asbestos is cytotoxic to mesothelial cells via an apoptotic pathway; however, apoptosis is counterintuitive for a cell that is in the process of transformation. More recent studies by Yang *et al*. investigating the form of mesothelial cell death after asbestos exposure showed that mesothelial cells undergo programmed necrosis which is linked to carcinogenenis (Yang et al., 2010). In pleural inflammation ROS production, nitric oxide (NO) and reactive nitrogen species (NO·) production by mesothelial cells is seen in response to cytokines, bacteria and asbestos with concomitant increase in anti-oxidant gene expression (Mutsaers, 2004). A massive oxidative and nitrosative stress can cause poly (ADP ribose) polymerase (PARP) overactivation, depletion of ATP and promotion of cell necrosis (Virag and Szabo, 2002). PARP is a DNA nick-sensor enzyme that contributes to DNA repair, however during necrosis, PARP overreaction promotes the translocation of high-mobility group box (HMGB)-1 from the nucleus to the cytosol and the extracellular space which triggers an inflammatory response (Ditsworth et al., 2007). HMGB-1 is a damage-associated molecular pattern (DAMP) which, when released into the extracellular space activates adaptive immunity and initiates tissue repair programs (Bianchi and Manfredi, 2007). During exposure of human mesothelial cells to asbestos fibres, HMGB-1 translocates from the nucleus to the extracellular space where it triggers TNF-α release by macrophages, which protects human mesothelial cells from undergoing apoptosis and leads to chronic inflammation and potentially contributes to carcinogenesis (Yang et al., 2010).

1.7 Nanomaterials

Due to the unique properties of matter in the nanosize scale, research in developing new nanomaterials is proceeding remarkably fast and nanomaterials are being incorporated into a wide variety of consumer products. A material can be defined as a nanomaterial if at least one dimension is less than 100 nm and more specifically, on the 18th of October 2011 the European Comission adopted the recommendations on the definition of a nanomaterial to "*A natural, incidental or manufactured material containing particles, in an unbound state or as an aggregate or as an agglomerate and where, for 50 % or more of the particles in the number size distribution, one or more external dimensions is in the size range 1 nm - 100 nm" (European Commission, 2012).* According to the structure and nanoscale dimension of the material it can be further split into 3 different categories. One dimension nanoscale materials are referred to as nano-layers, -films or surfaces whereas two dimensional nanoscale materials are categorised as nanotubes, nanowires and nanorods; the third category consists of nanoparticles, which are nanoscale in all three dimensions (ISO/TS 27687, 2008).

1.7.1 High aspect ratio nanomaterials

The definition of a high aspect ratio in general terms describes the proportional relationship between the width and the height of an object. In terms of fibrous nanomaterials, the aspect ratio is determined by the ratio between the fibre length, which can be up to millimetre and its diameter, which is in the nanometer range. At present, fibrous high aspect ratio nanomaterials (HARN) include nanotubes, nanowires and nanorods which can be composed of various different elements and exhibit a large surface area (Figure 1-6). A new form of nanomaterial, also classifiable under the term 'high aspect ratio' are nanoplatelets made of graphene (Figure 1.5). Graphene nanoplatelets (GP) are completely different in their shape compared to the conventional fibrous HARN by exhibiting a planar geometry. Therefore the aspect ratio of a plate-like GP is determined by the diameter of the plate in relation to the thickness.

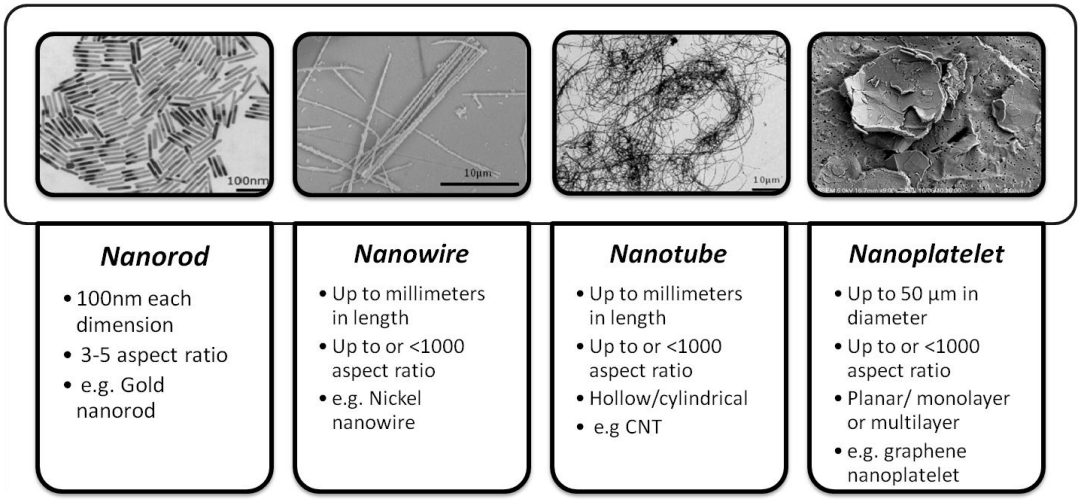

Figure 1-6: Images and characteristics of the different types of HARN. Gold Nanorod image was kindly provided by (Sharma et al., 2009).

1.7.1.1 Fibrous HARN

The terms nanowire and nanorod are used interchangeably in literature and the definition of these terms is still somewhat vague. The distinguishing feature between nanowires and nanorods is their length. Nanowires can be up to millimetres in length whereas each dimension of nanorods is within 100 nm. Therefore the standard aspect ratio of nanorods is 3-5 in comparison to the aspect ratio of nanowires which can be greater than 1000. Another term used in the literature for HARN is nanofibres which are occasionally used as an umbrella term for nanowires and nanotubes. Best known and most industrially utilised of all HARN are carbon nanotubes (CNT) which are long, thin cylindrical structures comprising single or multiple layers of concentric graphene sheets. CNT have been optimised for a huge range of applications by derivatisation of the surface with a range of chemical moities. Carbon, packed in the graphenic structure of CNT exhibits exceptional properties from electrical and thermal conductivity to tensile strength and rigidity. The development and optimization of CNT for a huge range of applications, from electronics to structural engineering has been a feature of the developing nanotechnologies industry (Aitken et al., 2006). There are a number of methods employed in the synthesis of CNT (Awasthi et al., 2005) however the advantages in

the production of non-carbon nanotubes, nanowires and nanorods over CNT could include controllability of length, diameter, geometry, surface functionality and purity during the production process. Various techniques have been developed to synthesise nanowires and nanorods based on different methods (e.g. evaporation-condensation, dissolution-condensation, vapour- liquid- solid), but the template-based approaches have proved the most versatile. Dependent on the material under use, different template- based synthesis methods can be utilised (Cao and Liu, 2008). For electrically conductive materials, the electrochemical deposition method is used and various nanowires and nanorods have been synthesised using this method, including metals such as Au, Ni, Co, Fe and Pb as well as semiconductors, conductive polymers and oxides. Other template-based synthesis methods are electrophoretic deposition from colloidal dispersion and template filling. A wide range of HARN has been produced using electrophoretic deposition method including polycrystalline oxides like ZnO, TiO_2 and SiO_2 (Cao and Liu, 2008).

The applications of nanofibres range from electronic devices, aerospace, automotive, sporting goods, textiles to tools for biology and medicine (Li and Tay, 2011; Prina-Mello et al., 2006; Uskokovic et al., 2012; futuremarketsinc.com, 2012). The application chart in Figure 1-7 summarises the number of nanotubes companies targeting a specific end user market.

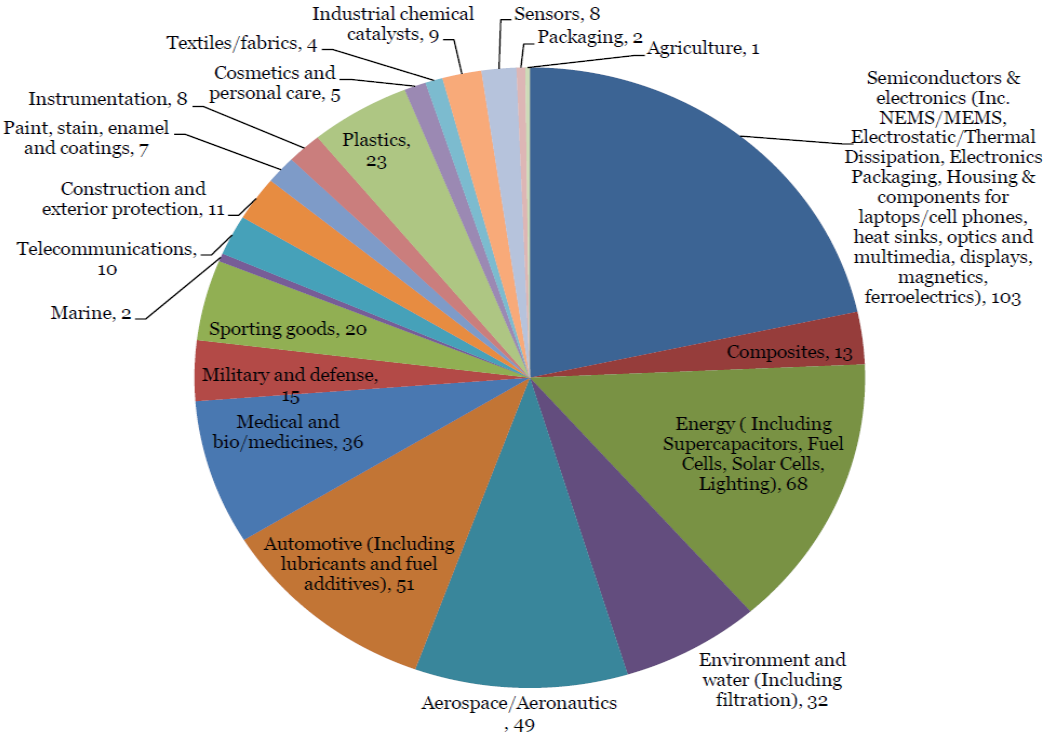

Figure 1-7: Application chart showing the number of nanotube companies worldwide targeting particular end user market. From Future Markets, Inc 2011 (futuremarketsinc.com, 2012).

With regard to nanomedicine applications, carbon nanotubes in particular have been identified for a number of potential uses including imaging, enhancement of bone growth and targeting and delivery of drugs (Pascu et al., 2010; Sahithi et al., 2010; Liang and Chen, 2010). Sharma *et al.* studied the neuroprotective efficacy of compounds attached to nanowires in comparison to normal compound delivery and reported an enhanced beneficial effect of the nanowire-drug delivered compound (Sharma et al., 2010). Uskokovic *et al.* showed that nanowire-coated microparticles are efficient transepithelial drug delivery devices due to their lager surface area compared to spherical counterparts (Uskokovic et al., 2012). Ceramic nanoparticles have drawn special attention in the fields of drug delivery, imaging, sensing and thermotherapy due to their biocompatibility, simple preparation and ease of surface modification. Additionally silica nanotubes combined with iron oxide seem to be a promising tool for image-guided drug delivery (Chen et al., 2012). The tubular shape

permits loading of large amounts of the desired molecule, whereas the outer surface can be modified using for example polyethylenglycol or targeting moieties (Son et al., 2006).

Year–by–year there is a near exponential increase in publications based on nanomaterials as well as a considerable expansion in the market potential. According to the data summarised in a recent report by 'Bcc Research-Market Forecasting', the global market for nanotechnology was valued at nearly $ 20.1 billion in 2011 with an annual growth rate of 18.7% (bccresearch.com, 2012). A search in Pubmed was performed to show the increase in the number of publications on the topics 'carbon nanotubes', 'nanoparticles' and 'nanofibre', 'nanotube', 'nanowire', 'nanorod', which are summarised under HARN excluding CNT (Figure 1-8). The number of HARN-related publications rose from 23 in the year 2000 to 5133 in the year 2012 (Figure 1.7).

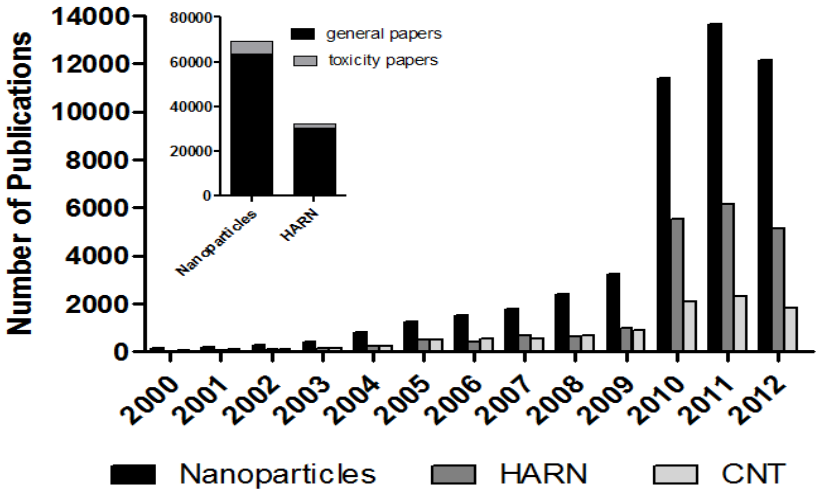

Figure 1-8: Number of publications on the topics of nanoparticles, high aspect ratio nanoparticles, excluding carbon nanotubes, and carbon nanotubes as well as the number of publications on the toxicity of nanomaterials. The graph shows the increase in the number of publications on the main three categories of nanomaterials from 2000 to 20012. HARN in this graph include nanofibres, nanowires, nanorods and nanotubes made of materials other than carbon. These data are based on publications in the PubMed database. The search in the database was performed

using the 'advanced search option' and 'limits' to specify the date range of publications in each field. Number of publication was revealed using the search terms 'carbon nanotubes' and 'nanoparticles'. HARN data was obtain by summing the number of hits from 'nanofibres', 'nanowires', 'nanorods' and 'nanotubes' using the 'Search Builder option NOT' to exclude CNTs. Insert shows the number of publications on nanoparticles/HARN in relation to the papers on their toxicity. CNT: Carbon nanotube; HARN: High aspect ratio nanoparticle.

The increasing growth of the HARN industry suggests considerable potential for human exposure to airborne HARN as these materials are handled in workplace during industrial preparation and use. However despite rapid growth in the publications reporting the development, optimization and potential applications of various HARN, the number of publications based on toxicity studies of HARN makes up only 5.6% of all publications. These data illustrate quite clearly the worrying mismatch between the increases in research focused on the development and use of HARN versus research concerned with potential health effects to exposure to HARN.

1.7.1.2 Planar HARN/ Graphene Nanoplatelets

Graphene is the youngest in the family of carbon nanomaterials being first isolated in 2004 by Andre Geim and Konstantine Novoselov by a somewhat unconventional method of using adhesive tape upon graphite, and stripping of a single layer of graphene (Geim and Novoselov, 2007). Graphene is a single layer of carbon packed in a hexagonal (honeycomb) lattice. The carbon atoms are covalently connected to three other carbon atoms with a distance of 0.142 nm resulting in a sp^2 bonding structure (Figure 1-9).

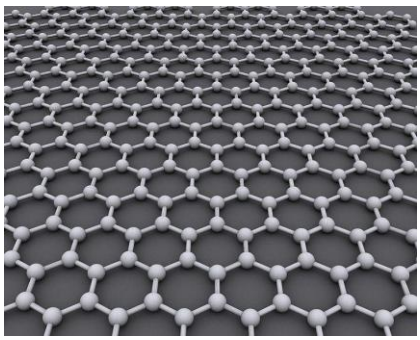

Figure 1-9: Honeycomb lattice of graphene. Adapted from a public domain image by AlexanderAIUS.

Graphene exhibits remarkable mechanical and electrical properties that make the material suitable for a number of applications. As stated by the Nobel Prize committee, '*a hammock made of graphene would be strong enough to support a 4 kg cat, with the hammock weighing only 0.77mg'* and has a breaking strength of ~40 N/m (Van, 2011; Geim and Novoselov, 2007). In regards to electrical conductivity, the hexagonal symmetry arrangement of the atoms in graphene allow the structure to conduct electricity much more efficient than silicon and can therefore act as a future replacement for versatile silicon in microchips (Van, 2011). The exceptional properties of graphene are reflected in the number of patents issued and papers published in 2010, being 400 and 3000 respectively. In addition, the European Union is giving 1,000 million euro funding for a 10 year coordination action on graphene, and the United Kingdom as well as South Korea are investing £ 50 million and $ 350 million, respectively in a new commercialization hub.

In the light of the increased production of graphene materials in recent years, it is of utmost importance to determine the potential hazard of the material and exposure of the workforce in manufacturing industries to determine the risk associated with graphene nanoplatelets.

1.7.1.3 Toxicology of HARN

HARN have useful and novel electro-physical properties which resulted in an increased production compared to other nanoscale materials, as a consequence of which, there is increasing potential for inhalation exposure. In light of the adverse effects of asbestos, some of which can be classified as high aspect ratio nanoparticle, albeit natural in origin the increasing production of HARN has triggered concern that, if HARN are inhaled into the lungs they may behave like asbestos. Exposure to asbestos fibres caused a worldwide epidemic of disease, although not all fibres that can be breathed into the lungs are as pathogenic as asbestos and the different forms of asbestos are not equally pathogenic. Therefore, if we can fully understand what features render a fibre pathogenic then we have the potential to develop HARN that are safe-by–design.

Regarding the unique geometry of nanoplatelets, their platelet-like structure, atomic thinness, extreme aspect ratio and extended lateral dimensions, nanoplatelets could pose a potential risk in relation to inhalation exposure similar to that seen with fibrous HARN, including asbestos fibres.

The term nanotoxicology was first mentioned by Robert Service in the Science journal in 2004, raising the awareness that the different properties of nanomaterials compared to their bulk form "*makes their potential health and environmental effects maddeningly difficult to predict" (Service, 2004)*. Donaldson et al. fully described the context of nanotoxicology within particle toxicology and set out major concerns raised by this new area in an Editorial in Occupational and Environmental Medicine in the same year (Donaldson and Tran, 2004; Donaldson et al., 2004).

A number of studies have been performed since then to evaluate the toxicological potential/risk of nanomaterials by identifying their hazard and assessing the exposure levels (Oberdorster et al., 2005). Figure 1-10 summarizes the key questions that need to be resolved to characterise the risk of nanomaterials.

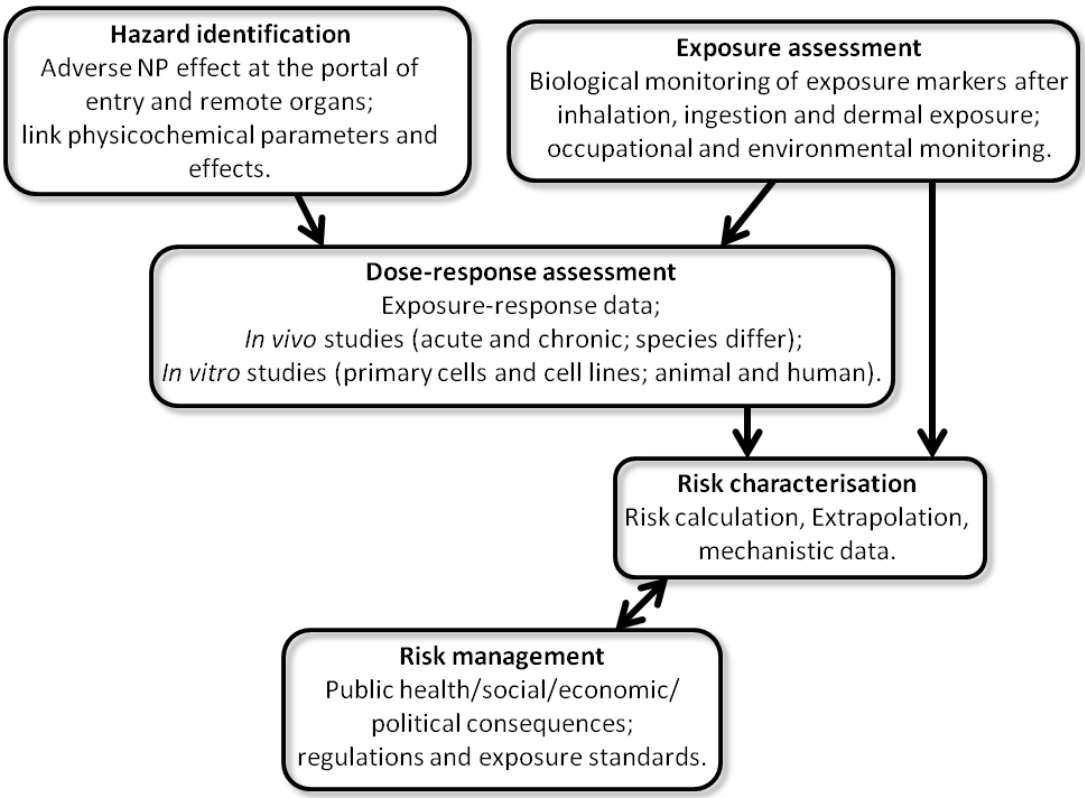

Figure 1-10: Risk assessment of nanomaterials. Hazard identification and exposure assessment are required in order to formulate exposure standards. Reproduced and adapted from (Oberdorster et al., 2005). NP= nanoparticle.

1.7.1.4 Hazard of HARN

The aim of the present thesis is to identify the potential hazard of HARN in relation to asbestos fibres. The basis of this comparison is the morphological similarity between HARN and asbestos fibres, both, in terms of length as well as diameter. From asbestos exposure history we know that the lung as well as the pleural/peritoneal cavity are the target sites for disease development. Therefore investigation of the adverse health effects of HARN should be directed towards these sites.

The first direct comparison between HARN and asbestos fibres in their ability to cause granuloma formation in the peritoneal cavity via the route of direct

intraperitoneal injection was performed by Poland *et a*l. (Poland et al., 2008). The study was comparing different forms of CNT, including two tangled CNT in the size range of 1-20 µm and two long fibrous CNT, with a mean length of 13 µm and up to 56 µm, to short and long amosite asbestos fibres (SFA/LFA) and nanoparticulate carbon black (CB) (Poland et al., 2008). This study demonstrated for the first time that CNT show asbestos-like length-dependent pathogenicity, whereby long CNT led to a substantial inflammatory response in the peritoneal space and granuloma formation on the diaphragm up to 7 days similar to the response observed after exposure to LFA fibres (Poland et al., 2008). No inflammatory response was measured after intraperitoneal injections of short/tangled CNT and SFA (Poland et al., 2008). At the same time a study by Takagi *et al*. reported the ability of MWCNT to induce mesothelioma in the peritoneal space after direct administration in p53+/- mice (Takagi et al., 2008). However this study received strong criticism due to the unrealistic high dose of 3 mg/ml that was used in this study leading to artifactual responses and questionable interpretation of the observed histological interpretation of mesothelioma (Donaldson et al., 2008).

In 2005 a study by Muller *et al.* investigated the respiratory toxicity of multi-wall CNT (MWCNT) (5.6 µm mean length) and ground MWCNT (0.7 µm mean length) in rats after intratracheal administration at a dose of 0.5, 2 and 5 mg up to 2 month post exposure (Muller et al., 2005). Due to a uniform dispersion of ground MWCNT, a fibrotic response was observed in the lung parenchyma whereas insufficient dispersion of non-ground MWCNT produced collagen-rich granulomas only in the bronchial lumen but not in the lung parenchyma (Muller et al., 2005). The observed toxicological effects of short/ground MWCNT in this study have been further examined by Fenoglio et al. (Fenoglio et al., 2008) showing that the structural surface defects, metals and oxygenated functionalities in the ground MWCNT sample governed the toxic potential of these CNTs. By reduction of oxygenated carbon functionalities and reduction of metallic oxides the toxic effect of short CNT could be eliminated (Fenoglio et al., 2008). To further test the hypothesis that MWCNT with defects have higher carcinogenic activity, MWCNT with and without defect were instilled into the peritoneal cavity of rats and the incidence of mesothelioma development was measured and compared to crocidolite asbestos

(Muller et al., 2009). No carcinogenic response was measured and no difference in the rate of mesothelioma was observed between the two MWCNT groups (Muller et al., 2009). These results can be explained by the shortness of the samples used and the clearance mechanisms from the peritoneal space with the efficient clearance of shorter fibres through stomata from the peritoneal space (Moalli et al., 1987; Poland et al., 2008).

Another study investigating the length dependent effect of CNT in the peritoneal space used ultrashort and full-length single-walled CNT (SWCNT) concluded that large aggregates of CNTs (> 10 µm) induce granuloma formation likely through a frustrated phagocytosis mechanism whereas smaller aggregates of SWCNT (< 10 µm) were sufficiently engulfed by phagocytes without granuloma formation (Kolosnjaj-Tabi et al., 2010).

So far, the studies reporting CNT toxicity focused on the peritoneal space as a surrogate for the more relevant pleural space in relation to mesothelioma development. Murphy *et al.* developed a technique for direct pleural installation to study the effects of short and long CNT in the pleural cavity (Murphy et al., 2011). The CNT panel used by Murphy *et al.* was the same as used by Poland *et al*. to directly compare the inflammatory response in the pleural space to that observed in the peritoneal space (Murphy et al., 2011; Poland et al., 2008). The results showed that the adverse effects reported in the peritoneal space were equivalent to the ones in the pleural space, whereby only long CNT as well as LFA resulted in extensive formation of granulomatous lesions on the parietal pleura mesothelial cell layer (Murphy et al., 2011).

The knowledge of the toxicity of CNT in a compact or particulate form increased extensively over the recent years reporting various pathological responses ranging from sustained elevations of neutrophils and collagen deposition in the lung (Pauluhn, 2010; Murphy et al., 2012a), DNA damage malignant transformation of epithelial cells (Yamashita et al., 2010) and tumourgenisis (Wang et al., 2011a) as well as *in vitro* studies investigating the inflammatory mediators and signalling pathways involved in CNT toxicity (Brown et al., 2007; Pacurari et al., 2008). *In vitro* studies on the alteration of molecular pathways in normal and malignant human

mesothelial cells after SWCNT exposure showed an activation of PARP, AP-1, NF-κB, p38, and Akt as well as enhanced DNA damage and increased cell death which indicates asbestos-like molecular changes (Pacurari et al., 2008). An advanced 3-D cell culture model has been developed to study granuloma formation of macrophages *in vitro* after CNT treatment showing a correlation between the high aspect ratio of CNT and granuloma formation (Sanchez et al., 2011).

The hazard assessment of HARN has been so far concentrated on CNT, due to their extensive market growth compared to other forms of HARN. However, as shown in Figure 1-8 HARN other than CNT underwent a substantial growth in use in the last 3 years measured as the number of publications. Therefore investigation of the toxicological potential of other forms of HARN is essential and aids the overall understanding of the biological effective dose of HARN. However, hardly any publications can be found on the toxicity of HARN other than CNT. Hamilton *et al*. demonstrated increased pathogenic potential of long titanium dioxide (TiO_2) nanowires compared to their shorter (< 5 µm) counterpart (Hamilton et al., 2009). In this study long TiO_2 nanowires elicited inflammation via the NALP3 inflammasome which was linked to lysosomal breakdown and release of cathepsin B (Hamilton et al., 2009). Another study by Poland *et al*. looked into the differential response of short (< 5 µm) and long (> 20 µm) nickel nanowires (NiNW) in the lung and the peritoneal cavity after aspiration exposure and direct intrapleural injection, respectively (Poland et al., 2012). The inflammatory response to NiNW in the peritoneal cavity was similar to that seen after CNT exposure, with a marked inflammation only after long NiNW exposure (Poland et al., 2012). The response in the lung had a similar pattern, showing extensive granuloma formation and collagen deposition in the lung after long NiNW exposure (Poland et al., 2012).

The first study on the hazard identification of multilayered graphene nanoplatelets was reported in 2010 by Zhang et al. (Zhang et al., 2010). Neural cytotoxicity of multi-layered graphene and SWCNT was tested in Phaeochromocytoma-derived PC12 cells, leading to the conclusion that shape plays the primary role in induction of cytotoxicity, whereby graphene treated cells showed higher levels of oxidative stress compared to SWCNT (Zhang et al., 2010). Graphene toxicity was further

studied on bacteria, showing anti-bacterial activity of reduced graphene nanowalls (Akhavan and Ghaderi, 2010) and on mice via intravenous administration of PEGylated graphene resulting in minimal toxicity at a tested dose of 20 mg/kg (Yang et al., 2011) as well as via direct administration into the lungs of graphene and graphene oxide demonstrating that oxidation of graphene is a major contributor to pulmonary toxicity (Duch et al., 2011).

1.7.1.5 Dose/Exposure

The use of a relevant/realistic dose for *in vitro* and *in vivo* toxicological studies on the hazard of nanomaterials is essential to perform dose-response assessment for real-world exposure scenarios (Oberdorster et al., 2005). In the case of aspiration-type delivery to the respiratory tract, a relatively high bolus is delivered to the lung within a few seconds in a very high dose-rate. In real-world inhalation exposure scenarios in occupational and environmental settings, a much lower dose is deposited over a prolonged time. A study was performed by Shvedova *et al*. to directly compare inhalation studies versus aspiration studies of single-walled carbon nanotubes in mice and showed that both ways of administration resulted in very similar responses (Shvedova et al., 2008). Aspiration experiments are therefore of value as proof of principle studies which can be used for extrapolation to inhalation studies. Dosimetry chosen for *in vitro* studies in relation to the respiratory tract is often based on 'hot spots' areas at bifurcations of the respiratory tract, which can receive massive doses, being hundred times higher than the average dose for the whole airway as calculated by Balashazy *et al.* (Balashazy et al., 2003). However, deposition enhancement greatly depends on the size of the particle as well as the patch size or area of deposition which has to be considered for nanoparticle dosimetry *in vitro*. As demonstrated by Oberdoerster *et al.* studies in 96 well plates with a total area of ~0.4 cm^2 only experience an enhancement factor of 2 and alveolar epithelial cells do not experience any enhanced deposition (Oberdorster, 2010).

Up to now relatively little information is available on the exposure level of nanomaterials, especially HARN in workplace settings. In regards to CNT exposure,

various different methods have been used to measure exposure concentration including condensation particle counters (CPC), optical particle counters (OPC) and scanning mobility particle sizers (SMPS). These techniques however do not distinguish between particle type and morphology and are therefore limiting for measurement of fibres concentration in the workplace. A recent study on the occupational exposure assessment in carbon nanotube and nanofibre primary and secondary manufacturers used a filter-based sampling method to perform a structure count analysis by transmission electron microscopy to assess exposure (Dahm et al., 2012). The vast majority of samples collected in this study were below the NIOSH recommended exposure limit for CNT in workplace, which is 7 µg/m^3 (Dahm et al., 2012). In two secondary manufacturing facilities, in which samples were collected during dry powder handling such as mixing and weighing, the concentration measured was above the proposed exposure limit (Dahm et al., 2012).

1.7.1.6 Risk characterisation and management

As shown in diagram 1.9 hazard identification and exposure assessment are essential to perform risk characterisation to subsequently formulate occupational exposure limits to minimize exposure to hazardous substances in the workplace, however for most nanomaterials occupational exposure limits are not available (Kuempel et al., 2012). The NIOSH centre for disease control and prevention developed a recommended exposure limit for CNT and carbon nanofibres based on subchronic and short-term animal studies investigating pulmonary inflammation and fibrosis (NIOSH, 2010). Extrapolation of the data to humans has been performed by accounting for species differences in the alveolar lung surface area and exposure concentration have been calculated for a working lifetime resulting in a upper limit of quantitation of 7 µg/m^3 (NIOSH, 2010).

Scope and Aims of the Thesis

The aim of this thesis was to investigate the biologically effective dose of HARN in the lung and the pleural space and evaluate their pathogenicity in relation to the fibre pathogenicity paradigm.

1) Investigate the validity of the fibre pathogenicity paradigm to various forms of HARN, other than CNT, which meet the fibre criteria.

2) Identify the threshold length for fibre-induced pleural and pulmonary inflammation.

3) Examine HARN/cell interaction *in vivo* and *in vitro* and mechanism of inflammation.

4) Evaluate the toxicological potential of platelet-shaped HARN.

Chapter 2: Materials and Methods

2.1 Acknowledgement

The silver nanowire samples were synthesis and provided by Seashell Technology, San Diego, USA with input from Dr James R. Glass, Dr Janet C. Dickerson and Dr David A. Schultz. Nickel nanowire synthesis was performed by Dr Adriele Prina-Mello and Dr Fiona Byrne, Centre for Research on Adaptive Nanostructures and Nanodevices (CRANN), Trinity College Dublin. ICP-MS and size distribution of the nickel nanowires and pH measurements of the AgNW and nickel nanowires was performed by Dr Adriele Prina-Mello and Dr Dania Movia. Measurement of the proteome profile in BMMs after AgNW treatment was performed by Tanya Chernova as part of a formal collaboration between the ELEGI Colt laboratories and the MRC Toxicology Unit, Leicester. Chemical oxidation of GP was performed by Dr Colin Campbell, School of Chemistry, The University of Edinburgh.

2.2 Particles

2.2.1 Silver nanowire panel

In order to evaluate the threshold length for fibre induced pathogenicity, a panel of nanowires and control fibres was assembled. Silver nanowires consisted of five different, distinct length categories, abbreviated in the text as $AgNW_3$, $AgNW_5$, $AgNW_{10}$, $AgNW_{14}$ and $AgNW_{28}$ according to their mean length in micrometre (μm). The AgNW panel were provided by Seashell Technology (http://www.seashelltech.com; California, USA) in isopropanol at a concentration of 30 mg/ml. They were synthesized using a polyol process as described in US patent number 7,922,787 B2 issued to Seashell Technology, San Diego. In brief, the polyol method is a solution based method whereby the polyol, e.g. ethylene glycol serves as a reducing agent that reduces a silver compound, mainly $AgNO_3$ to metallic silver (Wang and Dickerson, 2011). The silver compound can be any source of silver that produces silver metal when reduced.

1) $2HOCH_2CH_2OH \rightarrow 2CH_3CHO + 2H_2O$

2) $2Ag^{+}+ 2CH_3CHO \rightarrow CH_3CHO\text{-}OHCCH_3+2Ag+2H^{+}$ (Zhu et al., 2011)

When the concentration of silver atoms has reached a high saturation level, nucleation is initiated and growth of silver nanostructures begins. An organic protective agent, e.g. poly vinyl pyrrolidone (PVP) is used to shield nanostructures from each other to avoid aggregation (Wang and Dickerson, 2011). The silver metal that is formed produces various types of silver nanostructures, depending on the reaction conditions used. Additionally, the ratio between the concentrations of the organic protective agent to the concentration of the silver solution can affect the types of nanostructures formed (Wang and Dickerson, 2011).

However, synthesis of AgNW and reaction conditions to obtain different lengths did not affect the chemical composition of the different lengths of AgNW.

2.2.2 Control nanofibre panel

Nickel nanowires (NiNW) in two different length classes, short (4 µm/$NiNW_4$) and long (20 µm/$NiNW_{20}$) and short (2 µm/NT_2) and long (13 µm/NT_{13} and 36 µm/NT_{36}) multi-walled carbon nanotubes (MWCNT) were used as alternative forms of HARN.

NiNW were fabricated by electrochemical template synthesis at Trinity College Dublin (Ireland) as previously reported by Byrne *et al*. (Byrne et al., 2009) and Prina-Mello *et al*. (Prina-Mello et al., 2006). In brief, a three electron cell with a platinum counter electrode, a Ag/AgCl reference electrode and working electrode which consisted of a alumina membranes with 200 nm parallel pores was used for electrochemical template synthesis of the NiNW (Byrne et al., 2009). Deposition of metallic nickel into the pores via reduction of nickel ions resulted in the growth of NiNW (Byrne et al., 2009). The surface of these wires was coated with a layer of nickel oxide which is approximately of 3-4 nm thick, which acts as protective layer against the chemical dissolution (Prina-Mello et al., 2006). The different length of NW was achieved by altering the time of deposition. Size distribution data was obtained by scanning electron microscope (SEM, Carl Zeiss Ultra Plus, UK) performed by Dr Fiona Byrne.

The panel of MWCNT used in this project have been characterised previously by Dr Craig A. Poland (Institute of Occupational Medicine, Edinburgh, UK) and Dr Fiona Murphy (University of Leicester, UK) and reported in (Murphy et al., 2011; Poland et al., 2008). The MWCNT were produced by catalytic vapour discharge and were purchased from Nanostructured and Amorphous Materials, Inc. (NT_2) and Mitsui & Co. Ltd. in Japan (NT_{13}). The NT_{36} sample was produced in The Nanoscience Centre at the University of Cambridge.

Mixed length amosite asbestos enriched for long fibres (100% fibres ≥5 μm, 50.3% fibres >15 μm, 35.2% fibres >20 μm), hereafter referred to as long fibre asbestos (LFA), shortened amosite asbestos (SFA; 3.1% fibres ≥5 μm) (Donaldson et al. 1989) were used to link the response to asbestos pathogenicity. Both LFA and SFA were created from the same batch of South African amosite (Davis et al., 1986) obtained from the Manville Corporation (USA). SFA was prepared by grinding long fibres in a ceramic ball mill, and the resulting fibre preparation sedimented in water. The process of ball milling, used to shorten the LFA to make the SFA was associated with small changes in the iron chemistry (Graham et al. 1999; Tomatis et al. 2010). SFA contained a consistent fraction of non-fibrous particles based on the definition of a fibre by the WHO i.e., longer than 5 μm, thinner than 3 μm and with as aspect ratio greater than 3:1 (WHO, 1997).

2.2.3 Compact particle control

Material particulate control panel consisted of Ag-nanoparticle (AgP), Ni-nanoparticle (NiNP) and nanoparticle carbon black (CB). AgPs with a diameter of 35 nm, a purity of 99,5% and a specific surface area of 30–50 m^2/g and NiNPs with a diameter of 80 nm were purchased from Nanostructured & Amporphous Materials, Inc. Carbon Black (Printex 90®) was provided by Evonik Degussa GmbH in Germany. It was used as an amorphous carbon particle control.

2.2.4 Graphene Nanoplatelets

The graphene nanoplatelets grade 2 (GP) used in this project were purchased from cheaptubes.com. A chemical exfoliation process was used to retrieve GP, whereby natural graphite flakes and an acid are sonicated over time (Geng et al., 2009). GP had a surface area of about 100 m^2/g, a density of ~2.0 g/cm^3, an average thickness of approximately 10 nm and an average diameter of 5 µm based on manufacturers description. Each GP consisted of several sheets of graphene as determined by SEM and are therefore classified as few-layer graphene.

2.2.5 Dispersion

Particles were suspended in cell culture medium containing 0.5% bovine serum albumin (BSA; Sigma-Aldrich, Poole, UK) for *in vitro* experiments or sterile 0.9% saline (PAA Laboratories Ltd., UK) containing 0.5% bovine serum albumin for *in vivo* experiments. A particle stock concentration of 1 mg/ml was prepared. To ensure the carrier-solution of AgNWs, isopropanol, did not contribute to the observed response, the vehicle control solution contained isopropanol in the same concentration as in the AgNW solution used for *in vivo* and *in vitro* experiments. AgNW showed a uniform dispersion in both suspensions after brief vortex without further sonication. NT, CB and GP were dispersed by sonication in an ultra-sonicating water bath at 230V, 50Hz, 350W (FB11002, Fisherbrand, Thermo Fisher Scientific, Inc., MA, USA) for 1 hour (LFA, SFA, NiNW, AgP and NiNP), 2 hours (NT and CB) and 6 hours (GP) to break up aggregates. All suspensions were prepared fresh before each experiment.

2.2.6 Light microscopy

The length distribution of AgNWs and GP were determined using light microscopy. Whilst the limit of resolution of light microscopy would normally preclude the visualisation of 120 nm diameter nanowires, the surface plasmon resonance properties of AgNW means that they have a strong scattering cross section allowing

for sub 100 nm nanoparticles to be easily visualized with a conventional microscope (Schrand et al., 2010).

For light microscopy images a concentration of 50 µg/ml of particles was used to demonstrate the dispersion of the materials. Ten µl of particles (50 µg/ml) suspended in 0.5 % bovine serum albumin (BSA; Sigma-Aldrich, Poole, UK)/saline were mixed with 10 µl of glycerol (Sigma-Aldrich, Poole, UK) to reduce the flow of the particles. The suspension was placed on glass slide and covered with a glass coverslip and sealed (Murphy et al., 2011). Images were captured at x100 magnification using QCapture Pro software (Media Cybernetics). For AgNW length distribution 100 fibres from each batch were measured according to their length by using a graticule and by using measurement software (Image-Pro Plus; Media Cybernetics Inc., MD, USA). The length distribution was plotted as percentage fibre per length category and percentage of fibre greater than length. For GP size distribution 300 GP/GP-aggregates were measured according to their projected area diameter by using a graticule. The size was plotted per length category.

2.2.7 Scanning electron microscopy

Physical characterisation of CB and GP was determined by scanning electron microscopy (SEM). CB and GP were dispersed in 0.1% BSA (heat-shocked fractionate) (Sigma-Aldrich, Poole, UK)/saline at a concentration 5 µg/ml by ultrsonication. The suspension was filtered onto an Isopore™ membrane filter (Millipore), dried and gold sputter coated. Scanning electron microscopy was carried out using a Hitachi S-2600N digital scanning electron microscope (Oxford Instruments, Oxfordshire, UK). Preparation of particles samples for SEM was performed by Steven Mitchell (The University of Edinburgh).

2.2.8 Backscatter SEM

Physical characterisation of AgNW was determined by backscatter scanning electron microscopy (BSEM). See details for BSEM in chapter 2.3.17. For BSEM, 5 µg/ml

AgNW in saline suspension was filtered onto an Isopore™ membrane filter (Millipore), dried and rotary-coated with about 8 nm of carbon in an Edwards 306A vacuum coating system (Edwards High Vacuum, Crawley, UK). Backscatter SEM of carbon-coated specimens was carried out using a Hitachi 4700 II field emission SEM (Hitachi High-Tech, Maidenhead, UK) at a beam accelerating voltage of 10 kV and a working distance of about 8 mm. Preparation of particle samples for BSEM was performed by Steven Mitchell (The University of Edinburgh).

2.2.9 Electron paramagnetic resonance

Electron paramagnetic resonance (EPR) was used to detect oxygen-centred free radical generation from the particles in the absence of cells. EPR technique is based on the change in electromagnetic energy level of an unpaired electron spin by applying a magnetic field. The spin trap 1-hydroxy-2,2,6,6-tetramethyl-4-oxo-piperidine hydrochloride (Tempone-H, Alexis Biochemicals, San Diego, CA) was used to detect peroxynitrite, superoxide and peroxyl radicals via the oxidation of hyrdoxylamines from Tempone-H by superoxide to form stable nitroxide radicals (Dikalov et al., 1997; Rosen et al., 1982). In the Tempone-H assay no addition of H_2O_2 is necessary to start the reaction, compared to using DMPO as a spin trap (Lu et al., 2009). All AgNW including controls (AgP, SFA, LFA) were measured at a concentration of 100 µg/ml in Hanks Balanced Salt Solution (HBSS) (Sigma-Aldrich, Poole, UK). AgP, SFA and LFA were sonicated for 1 hour prior to addition of Tempone-H.

CB and GP were diluted to a final concentration of 50 µg/ml in HBSS and sonicated for 1 hour. HBSS and 1 mM Pyrogallol (benzene-1,2,3-triol) (Sigma), a known superoxide generator were diluted in HBSS and used as negative and positive controls, respectively. Tempone-H was added to the samples and controls to give a final concentration of 1 mM. EPR spectra were measured after 60 minutes incubation at 37°C using the following instrumental conditions: Microwave frequency: 9.39 GHz, Magnetic field: 3355 G, sweep width: 55 G, sweep time 30 seconds number of passes- 1; modulation amplitude- 1500 mG; receiver gain- 1E1; phase 180 ;

microwave frequency- 9,30-9,55 GHz (Miller et al., 2009). Intensity values of the highest spectra peak were recorded and graphed against each other (arbitrary units).

2.2.10 ICP-MS Analysis

For quantification of contaminating metals the supernatant of 50 µg/ml (AgP and AgNW samples) and 1 mg/ml (CB and GP) were analysed using the technique of inductively-coupled mass spectrometry (ICP-MS). The particles suspensions were made up in 0.5% BSA/saline to be consistent with experimental conditions. Supernatant was collected from each sample, after overnight mixing, by centrifugation at 13 000 rpm for 30 min. Samples were analysed by ICP-MS using an Agilent 7500ce (with octopole reaction system), employing an rf forward power of 1540 W and reflected power of 1 W, with argon gas flows of 0.82 L min^{-1} and 0.2 L min^{-1} for carrier and makeup flows, respectively. Sample solutions were taken up into the Micro mist nebuliser by peristaltic pump at a rate of 0.06 rps (approximately 1.2 mL min^{-1}). The gas flow for Helium mode was 6.5 mL min^{-1}. Skimmer and sample cones were made of nickel. The instrument was operated in spectrum multi-tune acquisition mode and five replicate runs per sample were employed. Each mass was analysed in fully quant mode (three points per unit mass). ^{107}Ag, ^{27}Al, ^{111}Cd, ^{59}Co, ^{52}Cr, ^{63}Cu, ^{56}Fe, ^{55}Mn, ^{60}Ni, ^{208}Pb and ^{64}Zn were analysed in 'nogas' mode then ^{56}Fe, ^{60}Ni, ^{52}Cr, ^{63}Cu, and ^{66}Zn were further analysed in Helium mode to remove any polyatomic interferences. ICP-MS measurement and analysis was performed by Dr Lorna Eades (School of GeoSciences, The University of Edinburgh).

2.2.11 Endotoxin contamination

The levels of gram-negative bacteria endotoxin in all particle suspensions were evaluated by the Limulus Amoebocyte Lysate (LAL) assay (Lonza, Walkersville, MD) according to manufacturer's description using supernatant of the particle suspensions to avoid interference of particles with the assay. A 1 mg/ml solution was

prepared in certified endotoxin free LAL reagent water (Lonza, Walkersville, MD) and mixed for 24 hour prior to ultracentrifugation (13,000 g). In brief, the assay is based on an enzymatic reaction of a clottable protein in the presence of endotoxin in the circulation of amebocytes of Limulus polyphemus whereby gram-negative bacterial endotoxin catalyzes the activation of a proenzyme in LAL (Young et al., 1972). The rate of activation is proportional to the amount of endotoxin in the sample which is measured photometrically. Quantitative analysis of the endotoxin concentration in particles samples was performed using a comparison against a standard curve of known concentration of endotoxin in the range of 0.1-1 EU/ml.

2.2.12 Dissolution of nanowires

Dissolution of AgNW and NiNW was measured via the change in pH compared to vehicle control across a 24 h exposure. Russell RL060P Portable pH Meter (Thermo Electron Corporation, USA) + Semi-micro with a Pellon junction microelectrode (VWR, Ireland) was used for pH measurements. Sodium chloride topical irrigation sterile solution (sodium chloride 0.9 % w/w) (Johnson & Johnson, UK) was used as a control and for NW dilutions. NW solution was prepared by adding stock NWs solution to saline (final NWs concentration: 50 µg/mL) into a clean, dry eppendorf (1.5 mL). pH measurements were repeated every 2 hours for 24 hours (n=3). Measurements were carried out under the same environmental conditions (21 degree Celsius, RH =64 %). A linear fitting on the averaged data of each NW and solution measured were applied. The linear fitting associated to the saline pH variations was compared to those of the NWs solutions. This data allowed identifying time-dependent pH variations. pH measurements were performed by Dr Adriele Prina-Mello and Dr Dania Movia at the Trinity College Dublin.

2.2.13 Calculation for equalised fibre length

Since fibre exposure is regulated on the basis of the fibre number, we calculated the number of fibres per treatment for AgNW. Following equation was used for the calculation of nanowires per treatment.

Length of NW (average) [µm] $= l$

Diameter of NW [µm] $= d$

Density of NW [µg/ml] $= 1.05\text{x}10^{7} = \rho$

Volume of NW [ml] $= l * \prod * \left(\frac{d}{2}\right)^{2} = V$

Weight of NW [µg] $= V \times \rho$

Dose [µg] per mouse $= D$

Number of NW $= \frac{\text{D}}{V \times \rho} = \cong mln\ wires$

2.3 *In vitro*

2.3.1 THP-1 monocyte cell line

The immortalised human monocytic cell line THP-1 was used for *in vitro* studies. The THP-1 cell line is cultured from the blood of a boy with acute monocytic leukemia and was obtained from ATCC (Product: TIB-202) (Tsuchiya et al., 1980). The monocytic nature of THP-1 cells was characterised by their ability to phagocytose latex particles and sensitized sheep erythrocytes, lysosome production and the ability to restore T-lymphocyte response to Con-A (Tsuchiya et al., 1980). THP-1 cells were cultured in Roswell Park Memorial Institute (RPMI) media supplemented with 10% heat inactivated FBS, 1% penicillin/streptomycin and 1% L-Glutamine (PAA, Austria). Prior to each treatment the cells were differentiated to macrophages using 10 ng/ml phorbol 12-myristate 13-acetate (PMA) (Sigma) for 2 days at 37°C in 5% CO_2 atmosphere (Park et al., 2007). Differentiation of monocytes into macrophages was characterised by their change in size using flow cytometry as well as their adherence to the cell culture flask, whereas undifferentiated cells remained in suspension and were removed by washing. Supernatant of the cells was

tested for Mycoplasma infection at the start and the end of the *in vitro* experiments and no infection was detected. Mycoplasma test was performed by Dr Forbes Howie, Centre for Inflammation Research, Edinburgh.

2.3.2 Cell culture treatment

Prior to each treatment THP-1 cells were seeded in at a specified density in medium containing 10% FBS and differentiated with 10 ng/ml PMA for 48 hours. Prior to treatment the cells were washed with PBS and RPMI medium without serum was added to each well.

2.3.2.1 GP in vitro study on THP-1 cells

THP-1 cells were differentiated at a cell density of $5x10^5$/ml in 24 well plates and treated for 24 hour with either lipopolysaccharide (LPS) at a final concentration of 1 µg/ml, CB at 1 µg/cm² or 5 µg/cm² and GP at a concentration range of 1 µg/cm², 5 µg/cm² and 10 µg/cm² in cell culture media and/or media supplemented with either Cytochalasin D at a final concentration of 0.2 µM (Enzo Life Sciences), potassium chloride at a final concentration of 30 mM (Sigma) and diphenyleneiodonium chloride at a final concentration of 15 µM (Sigma). After the treatment the supernatant was centrifuged for 5 min at 2000 g, transferred, centrifuged again for 5 min at 13000 g and used for subsequent analysis.

2.3.2.2 AgNW in vitro study on THP-1 cells

THP-1 cells were differentiated at a cell density of $5x10^5$/ml in 24 well plates prior to AgNW treatment. Nanofibres were uniformly dispersed in cell culture medium (RPMI 1640) supplemented with 1% penicillin/streptomycin and 1% L-Glutamine (PAA, Austria) and 0.5% bovine serum albumin (BSA; Sigma-Aldrich, Poole, UK) and briefly vortexed. Cells were treated with AgNW equalised to fibre number since fibre exposure is regulated on the basis of the fibre number and so relative

potency needs to be determined on a per-fibre basis. To equalise for fibre number a dose of 2 µg/cm² for $AgNW_{14}$ was chosen as the standard *in vitro* dose based on measurement of membrane integrity and proliferation of THP-1 cells. Based on 2 µg/cm² for $AgNW_{14}$, concentrations for the other length classes AgNW panel were calculated assuming that fibres thickness was constant in the different length classes (Table 2-1). After the treatment the supernatant was centrifuged for 5 min at 2000 g, transferred, centrifuged again for 5 min at 13000 g and used for subsequent analysis.

Table 2-1: Calculation for the mass adjustments for equalisation of number.

Length class [µm]	**Calculation to equalise for the same fibre number**	**Dose (µg/cm^2)**	**Total fibre number**
3	3/14 x 2	0.4	$1.2x10^6$
5	5/14 x 2	0.6	$1.1x10^6$
10	10/14 x 2	1.4	$1.1x10^6$
14	Standard	2.0	$1.3x10^6$
28	28/14 x 2	4.0	$1.3x10^6$

2.3.3 Lactate Dehydrogenase

The conversion of lactate to pyruvate was detected using the Cytotoxicity Detection Lactate Dehydrogenase kit (Roche Diagnostics Ltd., Burgess Hill, UK) following the manufacturer's instructions. In brief, upon damage of the plasma membrane of cells cytoplasmatic lactate dehydrogenase (LDH) is released into the supernatant. LDH in the test sample leads to the reduction of NAD^+ to $NADH/H^+$ and the oxidation of lactate to pyruvate. In the second step of the assay a diphorase catalyst transfers H/H^+ from $NADH/H^+$ to the tetrazolium salt 2-p- iodophenyl-3-p-nitrophenyl-5-phenyl tetrazolium chloride reducing it to formazan, which is a red compound. The amount of colour formed in the assay is proportional to amount of membrane damaged cells.

Seventy microliters of cell supernatant from THP-1 cells (see chapter 2.3.2.1 and 2.3.2.2) and bone marrow derived macrophages (BMMs) (see chapter 2.3.11) exposed to the particles panel was added in triplicates to a 96 well plate (Corning, Amsterdam, The Netherlands). Thirty microliters of phosphor buffered saline (PBS) and 100 µl of LDH test reagent (diaphorase/NAD+ mixed with iodotetrazolium chloride and sodium lactate at a ratio of 1:45) was added to each well and incubated for 30 minutes at room temperature. Triton X (Sigma), a nonionic detergent, was used as a positive control at a concentration of 0.1% and the cells were incubated with Triton X for 30 min to obtain 100 % cell lysis. A microplate reader (BioTek® SynergyHT, Inc. VT, USA) was used to measure the optical density at 490 nm. The level of LDH release in the sample was expressed as a percentage of the total LDH released after cell lysis using Triton X (positive control) and the untreated control.

$$\% \text{ LDH release} = \frac{\boldsymbol{sample\ value - untreated\ control}}{\boldsymbol{positive\ control - untreated\ control}}$$

2.3.4 Alamar blue assay

After treatment to particles as described above, adherent cells in the culture dish were used to measure their metabolic activity via a chemical reduction of AlamarBlue® (Invitrogen). Resazurin is the active ingredient in alamarBlue® which is a nontoxic, cell permeable compound. In metabolic active cells resazurin is reduced to resorufin converting the non-fluorescent blue compound to a very bright red fluorescent compound which can be measured photometrical. 150 µl of PBS and 15 µl of AlamarBlue® was added to each well and incubated for 3 hours at 37°C in 5% CO2 atmosphere. Absorbance was monitored at 570 nm and 600 nm as a reference wavelength (BioTek® SynergyHT, Inc. VT, USA). Data are normalized to 600 nm value.

2.3.5 BD™ Cytometric Bead Array Flex Set

The supernatant of untreated THP-1 macrophages and THP-1 macrophages treated with 5 µg/cm² CB and GP as well as 2 µg/cm² (based on $AgNW_{14}$) for AgNW (details on the dose used see Chapter 2.3.2.2) as described above was used to screen for a number of 11 cytokines important in acute inflammation and apoptosis to identify cytokines unregulated after treatment. The cytokine levels were measured using BD™ Cytometric Bead Array Flex Set. The flex set included the human soluble protein buffer master kit and beads number D9, A7, A9, B4, D8, D4, B9, C5, E6, B6 representing the cytokines TNF, IL-6, IL-8, IL-1, CCL-2 (MCP-1), CCL-5 (Rantes), CCL-3 (MIP-1α), basic FGF, IL-13 and TGF-β.

Twenty-five microliters of mixed capture antibodies were added to 50 µl of each supernatant or standard in a 96 well plate and incubated for 1 hour at room temperature. Detection reagent was added to each well and incubated for 2 hours at room temperature. After centrifugation at 1500 g for 5 min the supernatant was removed and wash buffer was added to each well and agitated for 5 min for resuspension of the beads. BD FACSArray Bioanalyzer (BD Biosciences, San Jose, CA) was used to measure the fluorescence intensity and FACP array software was used for analysis. The concentration of each cytokine was calculated using the standard curve and expressed as pg/ml.

2.3.6 Enzyme-linked immunosorbent assay (ELISA)

The supernatant of all treatments from chapter 2.3.2.1 was further used to measure the expression of IL1-β using human IL1-β/IL-1F2 DuoSet (R&D Systems Europe Ltd., Abingdon, UK) according to manufacturer's description. One-hundred micro-litre of capture antibody raised against IL1-β was incubated over night in a 96 well micro-titre plate. The wells were washed 3 times with 0.05% Tween-20 in PBS (pH 7.2) and blocked using reagent diluent (1% BSA in PBS; R&D systems, Abingdon, UK) for 1 hour at room temperature with subsequent washing and addition of 100 µl test samples and standards in triplicate. After 2 hour incubation the wells were washed and a biotinylated detection antibody added and incubated for 2 hours. After

washing the wells 100 µl of horseradish peroxidase conjugated streptavidin solution was added. The wells were washed again and developed by adding 3,3',5,5' - tetramethylbenzidine (TMB) substrate solution (Sigma-Aldrich, Poole, UK). H2SO2 at a concentration of 0.5 M was added after 20 min to stop the reaction by changing the blue byproduct to a yellow colour which can be measured using a plate reader at a wavelength of 450 nm. Concentration of IL1-β was calculated using an appropriate standard curve.

2.3.7 Lysosomal membrane integrity

Lysosomal membrane stability was assessed using acridine orange (AO), a lysosomotropic base which accumulates in lysosomes via proton trapping, as described previously (Sohaebuddin et al., 2010). The assay is based on the principle that AO is a metachromatic fluorophore and a lysosomotropic base which accumulates preferentially in the lysosomes and becomes protonated and trapped in the organelle (Sohaebuddin et al., 2010). Differentiated THP-1 cells were used for lysosomal membrane integrity studies. Prior to each treatment the cells were seeded and differentiated in µ-Dishes (35mm, high) (ibidi, Germany) at a density of $6x10^4$ cells/ml in 400 µl medium containing 10% FBS and 10 ng/ml PMA (Sigma) for 2 days at 37 °C in 5 % CO_2 atmosphere (Park et al., 2007). Fibres were uniformly dispersed in cell culture medium (RPMI 1640) supplemented with 1% penicillin/streptomycin and 1% L-Glutamine (PAA, Austria), 0% FBS and 0.5% bovine serum albumin (BSA; Sigma-Aldrich, Poole, UK, heat shock fractionated). The cells were then loaded with AO (5 µg/ml) in culture medium, rinsed with RPMI and incubated with control (SFA, LFA, Ag-P) and Ag-NW panel (5 µg/cm²). Additionally, sphingosine, a positive control for lysosomal rupture was included and used at a concentration of 10 µM (Kagedal et al., 2001). Sphingosine, a detergent is lysosomotropic accumulates in lysosomes via proton trapping where it exerts its detergent properties (Kagedal et al., 2001). After 4 hour treatment images were obtained from live cells using a Leica SP5 C confocal scanning microscope at a 63x oil immersions objective lens (485 nm excitation, 530 nm green emission, 620 nm red emission). For quantitative analysis, the area of each cell and the area of

lysosomal red staining of each cell were selected and measured using Image-Pro Plus software (Media Cvbernetics Inc., MD, USA). The percentage of lysosomal staining per cell was calculated for 50 cells per treatment group (n=4) and expressed as % lysosomal staining per cell.

2.3.8 Detection of reduced glutathione (GSH) as indicator of the oxidative status of cells

Glutathione (GSH), a tripeptide (γ-glutamyl-cysteinyl-glycine) is the most abundant low-molecular-weight thiol and together with glutathione disulfide (GSSG) a major antioxidant present in the lung lining fluid (Wu et al., 2004). Two cytosolic enzymes, γ-glutamylcysteine synthetase and GSH synthetase are responsible for sequentially catalysing GSH from glutamate, cysteine and glycine (Wu et al., 2004). Approximately 90% of GSH is present in its reduced form and the ratio between reduced and oxidised GSH determines the antioxidative capacity of cells. The major roles of GSH in regards to the antioxidant mechanism are effective scavenging of free radicals and ROS directly and indirectly through enzymatic reactions and scavenging of xenobiotics via glutathione-S-transferase. The shift of the GSH/GSSG ratio toward an oxidizing state can activate several signalling pathways involved in the pathogenesis of many diseases (Wu et al., 2004). The oxidative status of glutathione can be detected via monobromobimane (MBB), which becomes fluorescent after binding nonenzymatically free thiol groups. THP-1 cells were seeded in 12- well plates at a density of 0.5 x 10^5/ml in 2.5 ml medium containing 10% FBS and differentiated as described above. Prior to treatment the cells were washed with PBS and 2.5 ml of 1% FBS RPMI medium was added to each well. Cells were treated for 4 hour with either CB or GP at 1 µg/cm² or 5 µg/cm² in cell media. 100 µM N-ethyl-maleimide (NEM) (Sigma-Aldrich) was used as a positive control for the depletion of reduced glutathione (Palmen and Evelo, 1996). NEM is an alkene that is reactive towards thiol groups which leads to the depletion of glutathione. Supernatant and cells were transferred into falcon tubes and centrifuged for 3 min at 1500 g. PBS was added to the pellet and centrifuged for 3 min at 1500 g and repeated twice. 150 µl of 50 µM MBB (Sigma-Aldrich) was added to the

pellets and incubated for 10 min at 37ºC. Controls were included in all measurements and comprised of untreated/unstained and untreated/stained samples as well as treated/unstained samples. The dye was detected using a BD LSRFortessa™ flow cytometer. MBB was excited by a violate laser (405nm, 50 mW) and the emission was detected through a 450/50 filter. FlowJo software (Tree Star Inc.) was used for analysing the data. Gating was based on FSC/SSC and the data is expressed as mean fluorescence intensity. The mean value of the blank sample was subtracted of the stained samples.

2.3.9 Generation of bone marrow derived macrophages

Bone marrow-derived macrophages (BMMs) were used for studies on macrophage migration *in vitro*. BMMs were generated from 8 week old wild-type C57/Bl6 mouse femurs and tibias. In brief, the bone marrow was flushed with PBS using a 24 gauge needle, resuspended, passed through a cell strainer and centrifuged at 15000 rpm for 3 min. Cells were resuspended in red blood cell lysis buffer Hybrid Max™ (Sigma-Aldrich, UK) for 5 min at room temperature. Cells were centrifuged, resuspended in DMEM (Dulbecco's Modified Eagle Medium, Life Technologies) containing 10% FCS, 1% penicillin/ streptomycin and 20% L929 cell media and plated in a 10 cm^2 non tissue coated dish and cultured for 7 days.

2.3.10 Macrophage migration assay

Migratory ability of BMMs after AgNW treatment was measured using a macrophage migration assay. After 7 day differentiation BMMs were seeded in 24 well plates at a density of $5x10^5$/ml in DMEM containing 10% FCS, 1 % penicillin/ streptomycin and 20% L929 cell media and culture for 2 days as a confluent monolayer. The medium was replaced with serum free DMEM containing 1% penicillin/ streptomycin. Cells were treated with AgNW equalised to fibre number. To equalise for fibre number a dose of 2.5 μg/cm² for $AgNW_{14}$ was chosen as the standard *in vitro* dose based on measurement of membrane integrity and metabolic

activity for BMMs. Based on 2.5 µg/cm² for $AgNW_{14}$, concentrations for the other length classes AgNW panel were calculated assuming that fibres thickness was constant in the different length classes (Table 2-2). The panel was dispersed in 0.5% BSA/ cell culture medium (serum free DMEM) and added to the cells. An artificial wound was created by scraping with a pipette tip and the number of cells migrating into the wound was monitored microscopically and photographs were taken immediately and after 30 hour. Images were acquired through a Zeiss Axiover S100 microscope equipped with a 30x objective lens and were captured using RS Photometrics CoolSnap. The number of cells migrated into the wound was counted and expressed as percentage compared to vehicle control.

Table 2-2: Calculation for the mass adjustments for equalisation of fibre number in vitro for the migration assay.

Length class [µm]	Calculation to equalise for the same fibre number	Dose ($\mu g/cm^2$)	Total fibre number
3	3/14 x 2.5	0.5	$1.5x10^6$
5	5/14 x 2.5	0.9	$1.5x10^6$
14	Standard	2.5	$1.6x10^6$
28	28/14 x 2.5	5	$1.6x10^6$

2.3.11 NALP3 inflammasome study

2.3.11.1 Cell treatment for NALP3 inflammasome study

Murine bone marrow derived macrophages were derived from tibia and fermoral bone marrow cells from C57Bl/6J wild type and $NALP3^{-/-}$ mice as described in chapter 2.3.10. Female C57Bl/6J mice were obtained from Harlan Olac (Bicester, United Kingdom) and were used at 9 weeks old. $NLRP3^{-/-}$ breeding pairs were provided by the late Prof. Jurg Tschopp (Department of Biochemistry, University of

Lausanne, Switzerland) and bred in the TCD Bioresources Unit. Information on the generation of NALP3$^{-/-}$ mice can be found in Martinon et al. (Martinon et al., 2006). Animals were maintained according to the regulations of the European Union and the Irish Department of Health.

After 7 day differentiation BMMs were seeded in 6 well plates at a density of 10^6/ml in DMEM containing 10% FCS, 1% penicillin/ streptomycin and 20% L929 cell media and culture for 2 days as a confluent monolayer. The medium was replaced with serum free DMEM containing 1% penicillin/ streptomycin. Two distinct treatment conditions were used:

1) Prior to treatment with the fibre panel, cells were primed with LPS at a concentration of 10 ng/ml for 3 hours. Cells were treated with AgNW at a range of doses. For $AgNW_3$ and $AgNW_{14}$ a low (0.5 μg/cm²), medium (2.5 μg/cm²) and high (10 μg/cm²) dose was used. For $AgNW_5$ a range of doses from low (0.5 μg/cm²), medium (1 μg/cm²), high (5 and 10 μg/cm²) was used. The concentration of LFA used was 100 μg/ml (~26 μg/cm²) based on a previous study (Dostert et al., 2008). The panel was dispersed in 0.5% BSA/ cell culture medium (DMEM, 0% FCS) and added to the cells. Alum, aluminium hydroxide (Brenntag Biosector), was used as a positive control for NALP3 inflammasome activation and was used at a concentration of 100 and 200 μg/ml. BMMs were treated for 24 hours.

2) Prior to treatment with the fibre panel, cells were primed with LPS at a concentration of 10 ng/ml for 12 hours. Cells were treated with AgNW and LFA equalised to a fibre number dose (

Table 2-3) which was based on 100 μg/ml LFA as reported in Dostert *et al*. (Dostert et al., 2008). The panel was dispersed in 0.5% BSA/ cell culture medium (DMEM, 0% FCS) and added to the cells. Alum, aluminium hydroxide (Brenntag Biosector), was used as a positive control for NALP3 inflammasome activation and was used at a concentration of 20 μg/ml. BMMs were treated for 6 hours. This treatment was used on wild type (n=6) and NALP3-/- (n=3) mice.

Table 2-3: Calculation for the mass adjustments for equalisation of fibre number in vitro for the NALP3 study. xDose is based on LFA as reported by Dostert et al. (Dostert et al., 2008).

	Calculation to equalise for the same fibre number	Dose ($\mu g/cm^2$)	Total fibre number
$AgNW_3$	3/14 x 26	5.5	$16.8x10^6$
$AgNW_5$	5/14 x 26	9.2	$16.0x10^6$
$AgNW_{14}$	Standard- based on 100 µg/ml for LFAx	26	$17.0x10^6$
SFA	Equalised to $AgNW_3$	5.5	$25.9x10^6$
LFA	Standard	26	$4.6x10^6$

2.3.11.2 Preparation of secreted proteins in the supernatant

After treatment of the BMMs with the AgNW panel and controls, the supernatant was collected and the protein content concentrated using StrataClean™ resin (Agilent Technologies, USA). One microliter of the resin was added per 100 µl of supernatant and the mixture was vortexed for 1 min. The mixture was then centrifuged for 1 min at 40x g and the supernatant aspirated and 25 µl of 5x Laemmli sample buffer was added to the pellet. The samples were then boiled for 5 min at 99°C.

Laemmli sample buffer:

- 10 % (v/v) glycerol (Sigma-Aldrich)
- 2% (w/v) sodium dodecyl sulphate (SDS) (Sigma-Aldrich)
- 200 µg/ml bromophenol blue (Sigma-Aldrich)
- 125 mM Tris pH 6.8 (Sigma-Aldrich)
- 28.75 ml dH_2O
- Add 50 µl DTT (Dithiothreitol) at a final concentration of 50mM to 950 µl of Laemmli buffer (Sigma-Aldrich)

2.3.11.3 Preparation of whole cell lysates

All procedures were performed on ice. Cells were washed with PBS and cell lysates were prepared by direct lysis in 5x Laemmli sample buffer and boiled for 5 min at 99°C.

2.3.11.4 Sodium dodecyl sulphate- polyacrylamide gel electrophoresis (SDS-PAGE)

Gels were prepared in a Biorad apparatus. The resolving gel was prepared and the stacking gel added after the resolving gel was set. The gels were placed in a Biorad gel running apparatus containing running buffer. The protein samples and molecular weight standard (Prestained Protein Marker, Broad Range (7-175 kDa); New England BioLabs® Inc.) were added to the gels. The gels were electrophoresed using a constant current at 25 mA per gel until the dye front from the sample buffer ran off the end of the gel.

<u>15 % resolving gel (15 ml):</u>

- 3.5 ml H_2O
- 7.5 ml 30% (v/v) Acrylamide mix (29.2% acrylamide and 0.8% N,N'-methylene-bis-acrylamide) (UltraPure Protogel)
- 3.8 ml 1.5M Tris-HCl (pH 8.8)
- 150 µl 10% SDS
- 150 µl 10% ammonium persulfate (APS) (Sigam-Aldrich)
- 6 µl N,N,N',N'- tetramethylethylenediamine (TEMED) (Sigma-Aldrich)

<u>Stacking gel (1ml):</u>

- 0.68 ml H_2O
- 0.17 ml 30% (v/v) Acrylamide mix (29.2% acrylamide and 0.8% N,N'-methylene-bis-acrylamide) (UltraPure Protogel)
- 0.13 ml 1.5 M Tris-HCl (pH 8.8)
- 10 µl 10% SDS

- 10 µl 10% ammonium persulfate (APS)
- 1 µl N,N,N',N'- tetramethylethylenediamine (TEMED)
- 10x SDS-PAGE running buffer:
- 30.3 g 25 mM Tris
- 144 g 192 mM glycine
- 10 g 0.1% SDS
- Make to 1 litre with dH_2O

2.3.11.5 Electrophoretic transfer of proteins

The resolved proteins were transferred to an Immobilon™ polyvinylidene diflouride (PVDF) membrane via a wet transfer system. The membrane was soaked in methanol to activate it and all other components were soaked in transfer buffer. The gel was placed between two filter-papers each side and a sponge. The setup was filled with transfer buffer and a constant current of 150 mA was applied to the transfer chamber for 2 hours.

10x transfer buffer:

- 58 g 48 mM Tris
- 29 g 39 mM glycine
- 3.7 g 0.037% SDS
- Make up to 1 litre with dH_2O
- Add 200 ml of methanol and 700 ml of dH_2O to 100 ml to make 1x solution

Blocking of non-specific binding sites

The membrane was blocked in 5% (w/v) Marvel in 0.01% (v/v) Tris buffered saline (TBS)- Tween20® for 1 hour at room temperature to block non-specific binding sites.

10x Tris buffered saline-tween (TBST):

- 12.11 g Tris
- 87.6g NaCL (pH 8.0)

- 5ml Tween-20
- Bring up to 1 litre with dH_2O

2.3.11.6 Antibody probing

Antibodies of interest were diluted 1 in 1000 in 5% (w/v) non-fat dried milk powder (Marvel) in 0.1% TBST. The membrane was incubated over night at 4°C with constant rotating. The membrane was then washed 4x in 0.1% TBST for 5 min each at room temperature and subsequently incubated with a secondary horse-radish peroxidise conjugated antibody (depending on the primary antibody) for one hour at room temperature. The secondary antibody was diluted 1 in 2000 in 5 % Marvel in 0.1% TBST. After this incubation the membrane was washed 3x in 0.1% TBST for 5 min each and a chemiluminescence substrate (20x LumiGLO® Reagent and 20x Peroxide) (Cell Signaling Technology®) was added and developed using Scientific Imaging Film.

<u>Antibodies used:</u>

- Anti-mouse IL-1β/IL-1F2 antibody, goat IgG, R&D Systems
- Peroxidase-conjugated AffiniPure Bovine Anti-Goat IgG (H+L) (Jackson ImmunoResearch Laboratories, Inc.)
- Caspase-1 p10 (M-20): sc-514, affinity purified rabbit polyclonal antibody (Santa Cruz Biotechnology, Inc.)
- Peroxidase-conjugated AffiniPure Goat Anti-Rabbit IgG (H+L) (Jackson ImmunoResearch Laboratories, Inc.)

2.3.11.7 ASC complex isolation

The activation of NALP3 inflammasome involves the recruitment of an adaptor protein, apoptosis-associated speck-like protein containing a CARD (ASC), which forms a complex to activate procaspase 1 (Taniguchi and Sagara, 2007). To determine the formation of the ASC complex, a protocol for ASC complex isolation

was obtained from Dr Rebecca Coll, Trinity College Dublin (Coll and O'Neill, 2011b).

Murine bone marrow derived macrophages were derived as described in chapter 2.3.10. After 7 day differentiation BMMs were seeded in 6 well plates at a density of 10^6/ml in DMEM containing 10% FCS, 1% penicillin/ streptomycin and 20% L929 cell media and culture for 2 days as a confluent monolayer. The medium was replaced with serum free DMEM containing 1% penicillin/ streptomycin. Prior to treatment with the fibre panel, cells were primed with LPS at a concentration of 10 ng/ml for 3 hours. For the initial experiments cells were treated with $AgNW_5$ and $AgNW_{14}$ at 1, 5 and 10 µg/cm². For subsequent experiments, a dose of 10 µg/cm² was used for $AgNW_{3,5,14}$ as well as SFA and LFA. Alum was used at a dose of 100 µg/ml. The panel was dispersed in 0.5% BSA/ cell culture medium (DMEM, 0% FCS) and added to the cells. BMMs were treated for 6 hours. 45 minutes before end of the particle treatment 5 mM of ATP disodium salt (Sigma-Aldrich) was added.

After treatment the supernatant was removed and the cells were rinsed in ice-cold PBS and 500 µl of ice-cold buffer was added to each well. Cells were removed using a cell scraper, transferred in a microcentrifuge tube and lysed by shearing gauge needle. 50 µl was removed for Western blot analysis, the rest was centrifuged at 330 x g for 10 min at 4°C. The pellets were washed twice in 1 ml ice-cold PBS and centrifuged after each wash and respuspended in 500 µl PBS. 2 mM of disuccinimydyl suberate (DSS) (Thermo Scientific), prepared from a fresh stock of 100 mM DSS equilibrated to room temperature and diluted in dry dimethyl sulfoxide DMSO (Sigma-Aldrich) was added to the pellet and incubated at room temperature for 30 min with rotation. DSS is an N-hydroxysuccinimide ester that reacts efficiently with primary amino groups to form stable amide bonds and therefore can be used to demonstrate the formation of ASC dimers and higher order oligomers in the cell pellet. The samples were centrifuged for 10 min at 330 x g at 4°C. The supernatant was discarded and the cross linked pellets were resuspended in 30 µl Laemmli buffer and boiled for 5 min at 99°C for Western blotting.

Buffer for ASC-complex isolation:

- 20 mM Hepes-KOH, pH 7.5
- 150 mM KCl
- 1% NP40 (Igepal CA-630) (Sigma-Aldrich)
- 0.1 mM Phenylmethanesulfonyl fluoride (PMSF) (Sigma-Aldrich)
- 1 µg/ml leupeptin (Sigma-Aldrich)
- 11.5 µg/ml aprotinin (Sigma-Aldrich)
- 1 mM sodium orthovanadate (Na_3VO_4) (Sigma-Aldrich)

Antibody for ASC-complex Western blotting:

- ASC, pAb (AL177), from rabbit (Enzo Life Sciences)

2.3.11.8 ASC confocal microscopy

For confocal analysis of the ASC-complex formation, stably transfected ASC-CFP macrophages kindly gifted from Prof. Luke O'Neill, Trinity College Dublin were used. ASC-CFP cells were cultured at $2x10^5$/ml in DMEM supplemented with 10% FCS and 1% P/S on a 35 mm glass bottom culture dish the day prior to cell treatment. The medium was replaced with serum free DMEM containing 1% penicillin/ streptomycin. Prior to treatment with the fibre panel, cells were primed with LPS at a concentration of 10 ng/ml for 3 hours. Cells were treated with AgNWs at 1 µg/cm² for 6 hours. The panel was dispersed in 0.5% BSA/ cell culture medium (serum free DMEM) and added to the cells. 20 mins before confocal microscopy 5 mM ATP was added for 20 mins. Imaging was performed using a 458 nm laser on an Olympus FluoView™ FV1000 Microscope equipped with a temperature and CO_2 controlled chamber.

2.3.12 Proteome Profiler Array

A screening of the phosphorylation sites of 46 kinases was performed to identify if a change in the kinase profile could be an involved in the inhibition of BMMs

migration *in vitro* after AgNW treatment. BMMs were differentiated and seeded at $5x10^5$/ml in DMEM containing 10% FCS, 1% penicillin/ streptomycin and 20% L929 cell media and culture for 2 days as a confluent monolayer in a 60 mm tissue culture dish. The medium was replaced with serum free DMEM containing 1% penicillin/ streptomycin and the particle panel was added at the concentrations described above and treated for 30 h. The cells were rinsed with cold phosphate-buffered saline (PBS) and immediately solubilised in lysis buffer by pipetting up and down and rocking the cell lysate at 4ºC for 30 min. The lysate was centrifuged at 14,000 x g for 5 min, the supernatant was transferred into new test tubes and the protein concentration was measured using the bicinchoninic acid protein assay (Sigma-Aldrich, Poole, UK) following the manufacturer's instructions (see chapter 2.4.7). 500 µg of lysates were diluted and incubated with the human Phospho–MAPK Array Kit (Proteome Profiler™, R&D Systems) as per manufacturer's instructions. In brief, a nitrocellulose membrane has been spotted with capture and control antibodies on which the diluted cell lysate mixed with biotinylated detection antibodies were incubated over night. Blots were washed and developed on X-ray films following exposure to streptavidin-HRP and chemiluminescent reagents. MAPK array was performed by Dr Tanya Chernova at the MRC Toxicology Unit at the University of Leicester.

2.3.13 Scanning Electron Microscopy

THP-1 cells were differentiated and seeded in 24 well plates on Thermanox® Plastic Coverslips (NUNC™, Rochester, NY USA) at a density of 1 x 10^6/ml. The cells were treated with 1 µg/cm² and 5 µg/cm² CB and GP for 4 hours days at 37°C in 5% CO_2 atmosphere and washed 5 x with 0.1 M sodium cacodylate (pH 7.2) buffer. Overnight fixation was done in 3% glutaraldehyde/ 0.1 M sodium cacodylate (pH 7.2) buffer. After fixation the cells adherent to the coverslips were washed in sodium cacodylate buffer, post-fixed in 1% Osmium Tetroxide in 0.1 M sodium cacodylate buffer for 45 min, critical point dried and gold sputter coated and viewed using a Hitachi S-2600N digital scanning electron microscope (Oxford Instruments, Oxfordshire, UK).

2.3.14 Transmission Electron Microscopy

Samples for TEM on THP-1 cells after GP treatment (1 and 5 μg/cm²) were prepared as described for scanning electron microscopy (chapter 2.3.14). After overnight fixation and subsequent washing the samples were embedded in Araldite resin. Sections, 1 μm thick were cut on a Reichert OMU4 ultramicrotome (Leica Microsystems (UK) Ltd, Milton Keynes), stained with Toluidine Blue and viewed in a light microscope to select suitable areas for investigation. Ultrathin sections, 60nm thick were cut from selected areas, stained in Uranyl Acetate and Lead Citrate then viewed in a Phillips CM120 Transmission electron microscope (FEI UK Ltd, Cambridge, England). Images were taken on a Gatan Orius CCD camera (Gatan UK, Oxon, England). Samples for SEM were gold sputter coated. Preparation of the samples for TEM was performed by Steve Mitchell, The University of Edinburgh.

2.3.15 Backscatter electron signals in SEM

In backscatter scanning electron microscopy (BSEM) an electron beam is scattered across the surface of the sample by magnetic lenses. The electrons are accelerated to typically 10 keV and are scattered in a drop shaped region at the surface of the sample. Secondary electrons (SE) are emitted from the surface of the sample due to a collision between primary electrons and electrons within the sample. These electrons are low-energy electrons and penetrate only short distances about 2- 30 nm in the sample. Backscatter electrons are elastically scattered further inside the sample (~ 0.1-1 μm) and are collected less efficiently then SE (Figure 2-1). However the efficiency of BSE reflection is a function of the atomic number (Z) of the samples atoms. Elements with high atomic number such as silver reflect or back-scatter electrons more strongly than the lower Z light elements (predominantly H, C, N, O, P) of which cells are composed. BSEM is therefore a useful way to study frustrated phagocytosis since it provides high-contrast detection of nanowires, allowing clear discrimination between the nanofibres and other cellular features. Since the BSE signal from the fibres is attenuated by overlying cellular material, the method allows a clear distinction to be made between fibres that are, or are not, membrane-bounded,

and can allow detection of fully phagocytosed fibres, which would not otherwise be detected in an SE image, provided they are at shallow depth within the cell. This principle has been used widely for detection of colloidal gold markers in immunocytochemistry (Soligo et al., 1985; Jeffree et al., 2003).

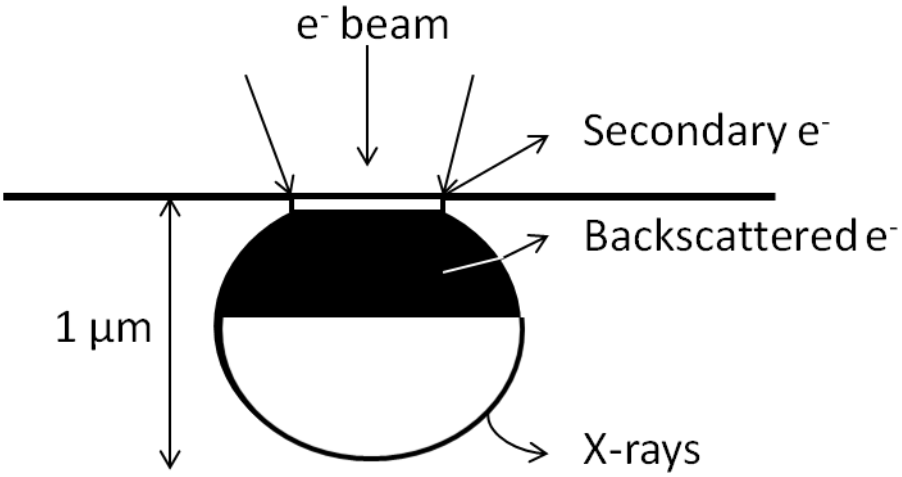

Figure 2-1: Section through a specimen illustrating the variation of electron scattering. High atomic number materials have a much greater scattering close to the specimen surface. The incidence electrons are scattered 90° and emerge as backscattered electrons. Illustration adapted from (Krinsley et al., 1998).

2.3.15.1 Cell culture for BSEM

BSEM was used to study cell-nanowire interaction and frustrated phagocytosis in THP-1 and macrophage migration in BMMs *in vitro*. For the study of cell nanowire interactions and frustrated phagocytosis THP-1 cells and BMMs were prepared as described in chapter 2.3.2.2 and 2.3.10 and seeded into 24 well plates on Thermanox® Plastic Coverslips (NUNC™, Rochester, NY USA) at a density of $0.5x10^6$/ml. The THP-1 cells were treated for 4 hours at a dose of 2 µg/cm² for $AgNW_{14}$ (dose equalised for fibre number see Table 2-1) and BMMs were treated for 30 hours at a dose of 2.5 µg/cm² for $AgNW_{14}$ (dose equalised for fibre number see Table 2-2) at 37°C in 5% CO2 atmosphere. After the treatment they were washed 5x with 0.1 M sodium cacodylate (pH 7.2) buffer. Overnight fixation was done in 3% glutaraldehyde/ 0.1 M sodium cacodylate (pH 7.2) buffer. After fixation the cells

adherent to the coverslips were washed three times in sodium cacodylate buffer. Fixed samples were dehydrated in 50%, 70%, 90% and 100% normal grade acetones for 10 minutes each, then for a further two 10 minute changes in analar acetone. Dehydrated samples were critical point dried and mounted on SEM aluminium stubs and rotary-coated with about 8 nm of carbon in an Edwards 306A vacuum coating system (Edwards High Vacuum, Crawley, UK).

2.3.15.2 BSEM on THP-1 and BMMs

SEM of carbon-coated specimens was carried out using a Hitachi 4700 II field emission SEM (Hitachi High-Tech, Maidenhead, UK) at a beam accelerating voltage of 10 kV and a working distance of about 8 mm. SE and BSE images were taken simultaneously using an annular YAG crystal BSE detector and the upper SE detector to produce perfectly-synchronised image pairs. The two images were superimposed using Adobe Photoshop. The SE and BSE image were converted to grayscale, the BSE image was pasted into the SE image by using the layer function "lighten". This newly merged image and the SE image were converted to RGB mode, and overlaid by pasting the red channel of the BSE image into the red channel of the greyscale SE image, thus colour coding in red the strong BSE signal from the nanowires, the SE image appearing in grey.

2.3.15.3 Methodology for quantifying unphagocytosed fibres

Image-Pro plus software (Media Cybernetics Inc., MD, USA) was used to measure the amount AgNW outside macrophages. The intensity of red pixels of the nanofibres differs if the fibre is taken up by a cell and therefore covered by a cell layer (lower intensity) or if the fibres is unphagocytosed (higher intensity). Using Image-Pro software, it was possible to specifically select the red pixel intensity of unphagocytosed cells which was expressed as object and area count. The number of objects (unphagocytosed fibres) was divided by the number of cells per image and

expressed as unphagocytosed fibres per cell. Approximately 100 cells per image were counted (n=3).

2.3.16 Bright- field microscopy

Phagocytotosis of AgNW by THP-1 cells were differentiated in a µ-dish (35mm) (ibidi, Germany) and treated for 4 hours at a dose of 2 µg/cm² for $AgNW_{14}$ (dose equalised for fibre number see Table 2-1). Bright-field microscope images were taken using Leica confocal laser scanning microscope SP5 at a 60x oil immersion objective lens.

2.3.17 Oxidation study on GP *in vitro*

2.3.17.1 Incubation of GP with horseradish peroxidase and H_2O_2

The potential of biodegradation of GP was examined *in vitro* using enzymatic oxidation of GP via horseradish peroxidase (HRP). Following protocol for HRP oxidation of GP was adapted from Kotchey et al. (Kotchey et al., 2011). Two milliliter of 0.125 wt% GP were dispersed in double distilled water and dispersed by sonication in an ultrasonicating water bath at 230 V, 50 Hz, 350W (FB11002, Fisherbrand, Thermo Fisher Scientific, Inc., MA, USA) for 2 h to break up aggregates. Lyophilized HRP type VI was solubilized in 1x phosphate buffered saline (PBS) (PAA, Austria) at 0.390 mg/ml and 4 ml were added to the GP dispersion and 3.5 ml of PBS for a total volume of 9.5 ml. H_2O_2 (Sigma Aldrich, Poole, UK) was added to give a final concentration of 40 µM. For the 24 hour incubation time H_2O_2 was added every hour for 12 hours, for 1 week incubation time H_2O_2 was added daily. Controls included GP incubation with HRP (- H_2O_2) (control I) and GP incubation with H_2O_2 (-HRP) (control II).

Chemical oxidation of GP was performed in a SPI Plasma Prep III plasma etcher, at 60W, for 5, 10, 15, 40 and 60 mins.

2.3.17.2 Raman spectroscopy

Raman spectroscopy is widely used for the characterization of carbon products since it is highly sensitive for symmetric covalent bonds with little or no natural dipole moment. As a result, Raman spectroscopy is capable of discerning slight changes in the structure and therefore gives information about the molecular morphology of carbon materials.

In brief, Raman spectroscopy measures the difference in molecular vibrational or rotational energies after inelastic collision between an incident photon and a molecule. The laser beam with the frequency v_o interacts with the molecule and induces an electrical dipole moment and vibration with a characteristic frequency v_m. The molecule can interact with the laser in three different ways:

1. The molecule has no Raman- active modes, it absorbs a photon and emits light with the same frequency v_o as the excitation source.

2. The photon is absorbed by a Raman-active molecule, which is at the basic vibrational state at the time of interaction. This results in the transformation of part of the photon's energy to the Raman-active mode and the resulting frequency of the scattered light is reduced to v_o-v_m, which is called Stokes frequency.

3. The photon is absorbed by a Raman-active molecule, which is in an excited vibrational state at the time of interaction. The excessive energy is released and the molecule returns to the basic vibrational state which results in the frequency of the scattered light to go up to v_o+v_m. This is called Anti-Stokes frequency.

The vibrational frequency corresponds to the position of a bond within the molecule and gives information on its orientation and can therefore be used for the detection of slight changes in the orientation of C-C bonds. Graphene consists of stacks of sp^2 bonded planar sheets which have a characteristic spectrum with the main band at 1582 cm^{-1}, which is known as the G-band (graphite or tangential band) and at 2700cm^{-1}, which is known as G' band. In graphene with a defective structure, another band, the D-band is measured at ~1350 cm^{-1} (Figure 2-2). This band is therefore often referred to as the disorder band or the defect band and its intensity

relative to the G band is used as a measure of the quality of graphene. Another disorder induced Raman D'-band at 1620 cm^{-1} indicates imperfect crystalline order (Malard et al., 2009) (Figure 2-2).

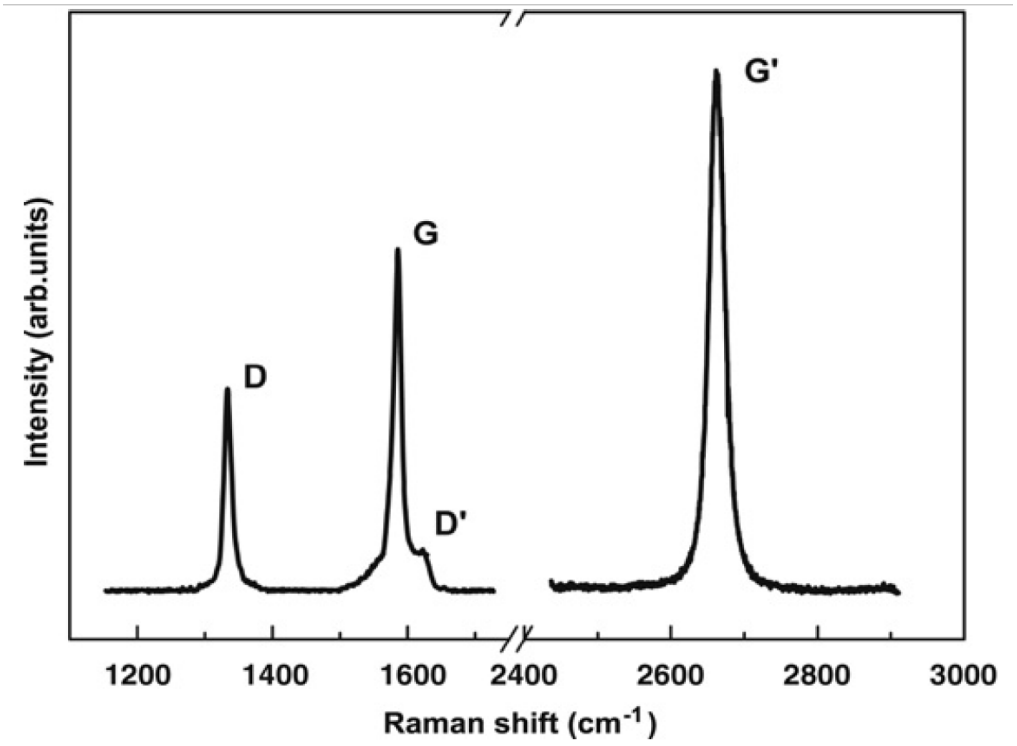

Figure 2-2: Raman spectra of graphene. This spectra shows the main Raman features, the D, G and G' as well as D' bands. Figure with permission from (Malard et al., 2009).

2.3.17.3 Raman spectroscopy on GP

Samples for *in vitro* oxidation of GP via HRP and H_2O_2 were prepared by adding 10 µl of GP at day 0, 1 and 7 on a quartz microscope slide and dried. All spectra were collected on a Renishaw *inVia* Raman microscope using an excitation wavelength of 514 nm of an argon ion gas laser. Exposure time was 250/sec, laser power was used at 30%, and a 50x objective was used with a numerical aperture of 0.45. Samples were scanned from 1000 to 2000 cm^{-1} to visualize D and G bands. Spectra were collected with a 120 s exposure; for pristine GP a total of 20 locations were selected per sample. For *in vitro* oxidation via HRP and plasma oxidation a total of 6 locations were selected per sample.

2.4 *In vivo*

2.4.1 Experimental animals

Eight to nine week old female C57Bl/6J strain mice (Harlan, UK) were used in this project. Animals were maintained according to the regulations of the European Union and the Irish Department of Health. For NALP3$^{-/-}$ experiments mice were provided by the late Prof. Jurg Tschopp (Department of Biochemistry, University of Lausanne, Switzerland) and bred in the TCD Bioresources Unit. Mice were used at 9 weeks old. NLRP3$^{-/-}$ breeding pairs were Information on the generation of NALP3$^{-/-}$ mice can be found in Martinon et al. (Martinon et al., 2006). Animals were maintained according to the regulations of the European Union and the Irish Department of Health.

Mice were kept in a group size of five in standard caging with sawdust bedding within a pathogen-free Home Office approved facility. Mice were maintained on a normal 12 hour light and dark cycle. Prior to the treatment mice were kept for 7 days in the facility to acclimatise. The work was carried out by staff holding a valid UK Home Office personal licence under a Home Office approved project licence. The experimental unit is here described as each individual mouse rather then based per cage and each cage contained a vehicle control mouse.

2.4.2 Pharyngeal aspiration

The given particle dose for pharyngeal aspiration was 50 µg per mouse for graphene platelet study and ranged from 10.7 to 50.0 µg per mouse for the AgNW study. An initial dose response series was performed which comprised of the doses 5, 10, 25 and 50 µg per mouse. The dose for the AgNW study was adjusted to reach an equal fibre number and calculations to reach the equal fibre number is shown in Table 2-4.

Mice were anesthetized with Isoflurane (2-chloro-2-(difluoromethoxy)-1,1,1 trifluoroethane) and the tongue was gently held in full extension while 50 µl of particle suspension was pipette onto the base of the tongue (Rao et al., 2003). The tongue was held extended until at least two breaths were complete. To stimulate

inhalation and to induce a gasp reflex the nasal cavities of the mice were covered. Mice were observed until full recovery.

Table 2-4: Calculation for the mass adjustments for equalisation of fibre number for the AgNW aspiration study.

Particles	Calculation to equalise for the same fibre number	Dose (µg/mouse)	Total fibre number
SFA	Short fibre control	10.7	50.48×10^6
$AgNW_3$	3/14 x 50	10.7	32.71×10^6
$AgNW_5$	5/14 x 50	17.9	31.19×10^6
$AgNW_{10}$	10/14 x 50	35.7	28.17×10^6
$AgNW_{14}$	Standard	50.0	32.76×10^6
LFAx	Long fibre control	50.0	8.24×10^6

2.4.3 Intrapleural Injection

Particle panel were prepared at a concentration of 50 µg/ml in 0.5% BSA/saline. For AgNW study, VC and Ag-P were made up in 600x diluted isopropanol and 0.5 % BSA/saline solution. 600x diluted isopropanol was included in VC and AgP since the stock solution (30 mg/ml) of AgNW panel was isopropanol and diluted 600x to reach the final concentration. The panel was injected at a dose of 5 µg and a volume of 100 µl per mouse into the pleural cavity of un-anaesthetised female C57BI/6 mice (aged 8 weeks) using a sleeve over the tip of a 27G to prevent the needle to pass through the pleural space into the lung (Figure 2-3 II) (Murphy et al., 2011). For a dose response series, the dose used for $AgNW_3$ was increased to 7.5 and 10 µg per mouse and the dose for $AgNW_5$ was decreased to 1 and 2.5 µg per mouse. The animals were humanly restrained by scuffing to expose the site of injection, which was the right upper quadrant of the thorax (Figure 2-3 I and III). No anaesthetic was used during this procedure and animals behaved normally when placed back into the cage.

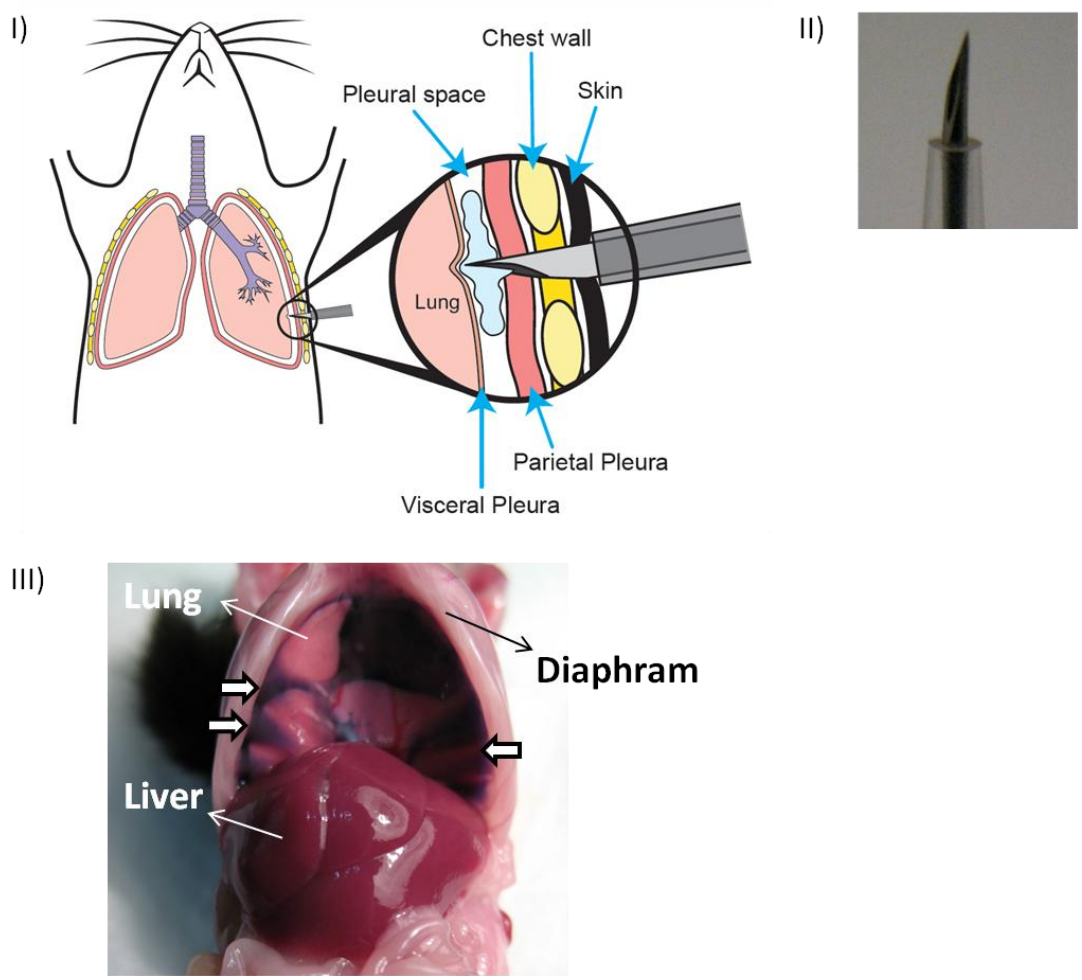

Figure 2-3: Intrapleural injection. I) Illustration of the intrapleural injection method. II) Modified needle for intrapleural injection. III) Intrapleural injection of trypan blue dye to illustrate the distribution of the injected volume in the pleural space as indicated by the white arrows.

2.4.4 Broncho alveolar lavage

Mice were sacrificed 24 hour, 1 week and 6 weeks post exposure of a single dose by terminal anaesthesia by injection of 0.5 ml of pentobarbitone (200 mg/ml) into the peritoneal cavity followed by exsanguinations via the abdominal aorta. The thoracic cavity was exposed via removal of the diaphragm and the right portion of the rib cage and cutting through the clavicle. The trachea cannulated using a 23 gauge needle and ligated. The lungs were lavaged three times with 800 µl of ice-cold sterile

saline. The first lavage was retained separately and the subsequent lavages were pooled and kept on ice for the entire duration of the processing.

2.4.5 Pleural lavage

Mice were euthanized at each timepoint by asphyxiation in 100% CO_2. An incision was made into the skin of the mice at the base of the abdomen and the skin was removed to expose the underlying tissue. The abdominal wall was removed and the xiphoid process was held up to remove the ligament connecting the diaphragm and the liver. A small incision was made directly inferior to the xiphoid process (Figure 2-4). The pleural space was lavaged through the incision using a Pasteur pipette with three 1 ml washes of sterile saline. The first wash was kept separately for further biochemical analysis.

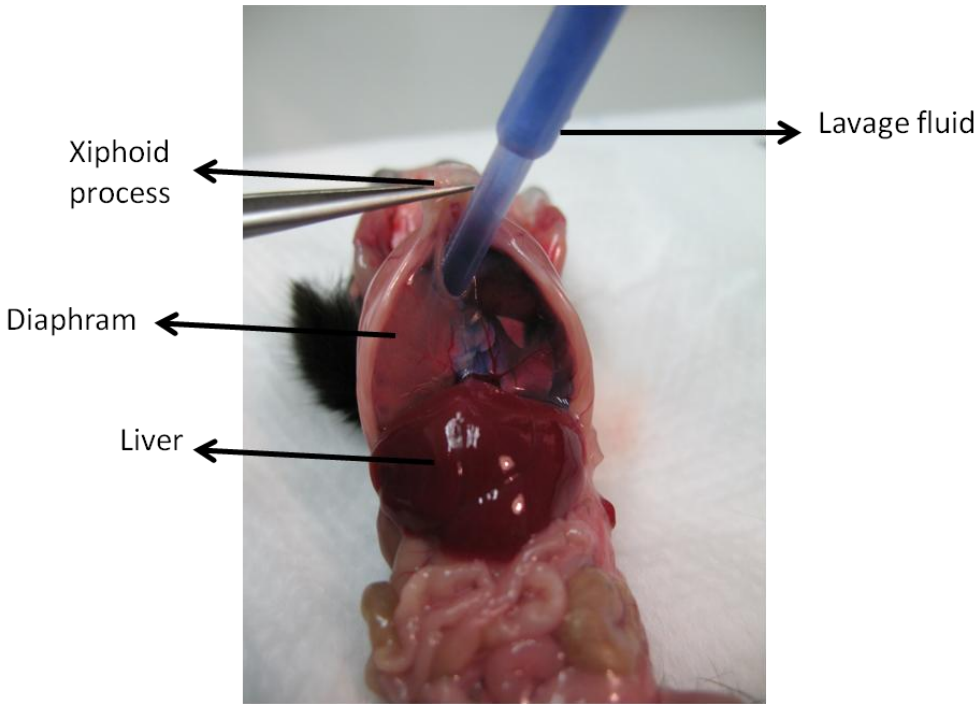

Figure 2-4: Illustration of a pleural lavage.

2.4.6 Differential cell count

To separate the cellular fraction from the supernatant, the lavage fluid from the lung and the pleural was centrifuged for 5 minutes at 2000 g at 4°C in a Mistral 3000i centrifuge (Thermo Fisher Scientific, Inc., MA, USA). The supernatant was kept for LDH, total protein and cytokine analysis. The cell pellets were resuspended in 0.5ml of 0.1% BSA/ ssaline solution. Total cell count was performed using a NucleoCounter (ChemoMetec, 7 A/S, Allerød, Denmark). For differential cell count cells were diluted in 0.1% BSA/ saline to reach a concentration of ~ 40,000 cells per slide. Cyto-centrifugation was performed at 300 rpm for 3 min using Cytospin 4 cytocentrifuge (Thermo Scientific, UK). Cells were fixed with 100% methanol and Diff-Quick staining was performed using Diff-Quick stainset (Dade Behring Gmbh, Marburg, Germany).

2.4.7 Total protein measurement

Total protein content in the supernantant was measured using the bicinchoninic acid (BCA) protein assay (Sigma-Aldrich, Poole, UK). The samples and a bovine serum albumin standard (BSA, Sigma-Aldrich, Poole, UK) in a range of 0-1000 µg/ml were incubated with 1 part of Cu^{2+} sulphate solution (4% w/v) and 50 parts bicinchoninic acid (Sigma-Aldrich, Poole, UK) for 30 min at 37°C. The protein bonds in the sample solution reduce Cu^{2+} to Cu^{+} which is subsequently chelated by two molecules of bicinchoninic acid forming a purple coloured product. The absorbance was read at 570 nm using Synergy HT microplate reader (BioTek Instruments, Inc VT, USA) and the protein concentration of the sample was established via extrapolation from the BSA standard curve.

2.4.8 Dissection

2.4.8.1 Lung

For histological examination the lungs and heart were removed on-block and fixed by installation of 10% ice-cold formalin without lavage and submerged in fixative for a period of 4 hours prior processing. The heart was removed and the lung separated into individual lobes and transferred to 70% ethanol for 24 hour. The tissue was embedded in paraffin, sectioned and stained with H&E to show gross pathology and Pico-Sirius Red (PSR) to show collagen deposition. Serial images were taken at 2.5x magnification using QCaputre Pro software (Media Cybernetics, Inc., MD, USA) and seamlessly re-aligned using Adobe Photoshop CS3 Version 10.0.1 (Adobe systems Inc.) to show the entire section of the lungs. Images at 20x magnification were taken to show higher magnification areas of the lung sections.

2.4.8.2 Chest wall

The whole chest was resected from the mice after lavage, washed in ice-cold saline and fixed for 4 hours in 10 % formalin. The lower right posterior portion of the chest wall was separated from the rest which had an area of approximately 10 mm x 10 mm adjacent to the spine including the lower 6 ribs and intercostals space. According to Shinohara *et al.* (Shinohara, 1997; Shinohara, 1997) this region is rich in stomata. Mediastinal lymph nodes were separated from the upper thoracic cavity. The chest wall was excised from the surrounding tissue, dehydrated through graded alcohol (ethanol) and imbedded on-edge in paraffin, sectioned (4 µm) and stained with Haematoxylin & Eosin (H&E) and picrosirius red (PSR) for gross pathology (n=2 per treatment for chest wall). Representative images of chest wall samples and lesion area were obtained by taking serial images at 10x magnification using QCapture Pro software (Media Cybernetics Inc., MD, USA). For SEM the tissue was prepared using tetroxide staining, critical point dried and gold sputter coated. SEM was carried out using a Hitachi S-2600N digital scanning electron microscope (Oxford Instruments, Oxfordshire, UK). For BSEM specimens were fixed and dehydrated as above and mounted on SEM aluminium stubs and rotary-coated with about 8 nm of

carbon in an Edwards 306A vacuum coating system (Edwards High Vacuum, Crawley, UK). SEM of carbon-coated specimens was carried out using a Hitachi 4700 II field emission SEM (Hitachi High-Tech, Maidenhead, UK) at a beam accelerating voltage of 10 kV and a working distance of about 8 mm. SE and BSE images were taken simultaneously using an annular YAG crystal BSE detector and the upper SE detector to produce perfectly-synchronised image pairs (more detail see chapter 2.3.16). The steps of tetroxide staining, critical point drying and gold sputter coating was performed by Steve Mitchell.

2.4.8.3 Methodology for lesion quantification

Serial images along the chest wall section were taken at 10x magnification using Zeiss Axioskop microscope fitted with a Micropublisher 3.3 RTV camera using QCapture Pro software (media Cybernetics Inc., MD, USA). Photoshop CS3 (Adobe systems Inc., CA, USA) was used to seamlessly re-align the images to give a high resolution image of the large sections of chest wall. To quantify the lesion area per unit chest wall length (mm^2/mm) the length of the each section along the mesothelium and the lesion area, identified by histology as lymphatic aggregates adhering to the mesothelial surface were measured using calibrated Image-Pro Plus software (Media Cybernetics Inc., MD, USA).

2.4.8.4 Lymph nodes

After 4 hour fixation mediastinal lymph nodes were separated from the upper thoracic cavity. The lymph nodes were excised from the surrounding fatty tissue, dehydrated through graded alcohol (ethanol) and imbedded in paraffin, sectioned (4 µm) and stained with picrosirius red (PSR). For lymph node CB and GP burden quantification of four sequential sections were taken from each lymph node. Images were taken at x10 magnification using QCapture Pro software (Media Cybernetics Inc.).

2.4.9 Cytometric bead array

The pleural lavage fluid as well as the BAL fluid from mice treated with AgNWs, GP and CB was used to screen for a number of 11 cytokines important in acute inflammation and apoptosis to identify cytokines unregulated after treatment. The cytokine levels were measured using BD™ Cytometric Bead Array Flex Set. The flex set included the human soluble protein buffer master kit and beads number A9, C8, B4, C4, B8, E5, B7, D8, C7, D4 representing KC, TNF, IL-6, IL-10, IL-13, IL-1β, MCP-1, RANTES, MIP-1α, G-CSF and IL-4.

Twenty-five microliters of mixed capture antibodies were added to 50 µl of each supernatant or standard in a 96 well plate and incubated for 1 hour at room temperature. Detection reagent was added to each well and incubated for 2 hours at room temperature. After centrifugation at 1500 g for 5 min the supernatant was removed and wash buffer was added to each well and agitated for 5 min for resuspension of the beads. BD FACSArray Bioanalyzer (BD Biosciences, San Jose, CA) was used to measure the fluorescence intensity and FACS array software was used for analysis. The concentration of each cytokine was calculated using the standard curve and expressed as pg/ml.

2.4.10 Chemokine and Cytokine measurement

Chemokines MCP-1 and MIP-1α and cytokines MIP-2 and IL-1β were measured in non-diluted BAL and pleural lavage fluid using a quantitative sandwich enzyme immunoassay technique (Quantikine kit of R&D systems). An affinity purified polyclonal antibody specific to the protein of interest was pre-coated onto a microplate. Fifty microliter of assay diluents and 50 µl of standard, control and samples were added per well, mixed gently for 1 min and incubated for 2 hours at room temperature. After 4 washes 100 µl of polyclonal antibody conjugated to horseradish peroxidase were added to each well and incubated for 2 hours. Wash step was repeated and 100 µl of substrate solution (hydrogen peroxide and tetramethylbenzidine) added to each well and incubated for 30 mins. After addition of 100 µl stop solution (hydrochloric acid) the absorbance was measured at 570 nm

and 450 nm using Synergy HT microplate reader (BioTek Instruments, Inc VT, USA). The reading at 570 nm was subtracted from 450 nm to adjust for optical imperfections and the sample concentration was established via extrapolation from the standard curve.

2.4.11 Raman Spectroscopy of lung tissue

Raman spectroscopy on lung tissue embedded in paraffin was used to measure oxidation of pristine GP *in vivo* in lung tissue after 24 hour, 1 week and 6 weeks aspiration exposure. For *ex-vivo* measurement, lung tissue embedded in paraffin was used to record GP oxidation. Areas of GP deposited in lung tissue were identified. All spectra were collected on a Renishaw *inVia* Raman microscope using an excitation wavelength of 514 nm. Samples were scanned from 1000 to 2000 cm^{-1} to visualize D and G bands. Spectra were collected with a 120 s exposure; for *ex-vivo* measurements and pristine GP at 0h a total of 20 locations were selected per sample.

2.5 Statistical analysis

All data was analysed using GraphPad Prism 5 (Version 5.03; GraphPad Software Inc. USA). Results were expressed as the mean + S.E.M. and multiple comparisons were analysed using one-way analysis of variance (ANOVA) with a Tukey-HSD method post-test and two sample comparisons were made using the Student's t-test. In all cases, values of $P < 0.05$ were considered significant. For pH measurement statistical analysis is measured as difference in the slope of the linear fitting of each measurement (Student’s t-test).

Chapter 3: The threshold length for fibre induced pleural inflammation

The following results have been published in

Schinwald A, Murphy F, Prina-Mello A, Poland C, Byrne F, Glass J, Dickerson J, Schultz D, Movia D, Jeffree C, Macnee W, Donaldson K. The threshold length for fibre-induced acute pleural inflammation: shedding light on the early events in asbestos-induced mesothelioma., Toxicological Sciences. 2012 May 12; 128(2):461-70.

and

Schinwald A & Donaldson K. Use of back-scatter electron signals to visualise cell/nanowires interactions *in vitro* and *in vivo*; frustrated phagocytosis of long fibres and compartmentalisation in mesothelial cells. Particle and Fibre Toxicology. 2012 Aug 28; 9(1):34.

3.1 Acknowledgements

The silver nanowire samples (AgNW) were produced by Seashell Technology™ and kindly provided by Dr Janet Dickerson from Seashell Technology™. The nanoparticulate carbon black sample Printex 90 was gifted by Evonik Degussa GmbH, Düsseldorf, Germany. Data on the CNT samples was kindly provided by Dr Fiona Murphy, which added to the overall interpretation of the data in regards to the threshold length in pleural inflammation. Nickel nanowire synthesis was performed by Dr Adriele Prina-Mello and Dr Fiona Byrne at the Centre for Research on Adaptive Nanostructures and Nanodevices (CRANN), Trinity College Dublin. The size distribution of all the nickel nanowires and dissolution measurement of AgNW and NiNW was performed by Dr Adriele Prina-Mello and Dr Dania Movia. Size distribution for CNT used in this study has been performed by Dr Craig Poland and Dr Fiona Murphy. I thank Steve Mitchell (University of Edinburgh) for sample

preparation for SEM and BSEM technical assistance. Prof. Chris Jeffree was deeply involved in the set up of the BSEM experiments and gave specialist input in preparation and detection of AgNW in tissue/cells.

3.2 Aims and Hypothesis

Suspicion has been raised that high aspect ratio nanoparticles or nanofibres might possess asbestos-like pathogenicity. The pleural space is a specific target for disease in individuals exposed to asbestos and, by implication nanofibres. Pleural effects of fibres depend on fibre length and as previously recorded, direct exposure of the peritoneal (Poland et al., 2008; Poland et al., 2012) and the pleural mesothelial surfaces (Murphy et al., 2011) to a range of different length of CNTs produced inflammatory and fibrotic effects only with long (>10 μm) samples of CNT. However, the key threshold length beyond which adverse effects occur has never been identified up to now since all asbestos and vitreous fibre samples containing longer fibres are heterogeneously distributed in their length.

Nanotechnology advantageously allows the production of nanofibres with highly defined length distributions which enable the in depth investigation of the threshold length for fibre-induced pleural inflammation.

This study utilised this advance in nanotechnology and aimed to investigate the threshold length for fibre effects in the pleural space with nano-fibrous structures in tightly defined length categories. From the information available on fibre induced inflammation in the pleural space, we hypothesised that the threshold length will lie somewhere between a fibre length of 5-10 μm.

3.3 Results

3.3.1 Morphology and size distribution of the fibre panel

To assess the role of fibre length in pleural inflammation a thorough characterisation of the length distribution of the fibre used in the study was performed. AgNW length distribution was characterized by light microscopy as well as backscatter scanning electron microscopy (BSEM), to additionally demonstrate the diameter of the fibres (Figure 3-1 I and II). Light microscopy can be used to visualise AgNW even though they are nominally ~100 nm in diameter and below the threshold of resolution of the light microscope because they show surface plasmon resonance (Schrand et al., 2008) which renders them visible by light microscope (see chapter 2.2.6). AgNW showed a uniform dispersion, consistent diameter and tight length distribution for each class as shown in Figure 3-2 and Table 3-1. The AgNW had an aspect ratio ranging from 50 up to 280 for $AgNW_5$ and $AgNW_{28,}$ respectively and therefore conform to the WHO classification of a fibre (WHO, 1997).

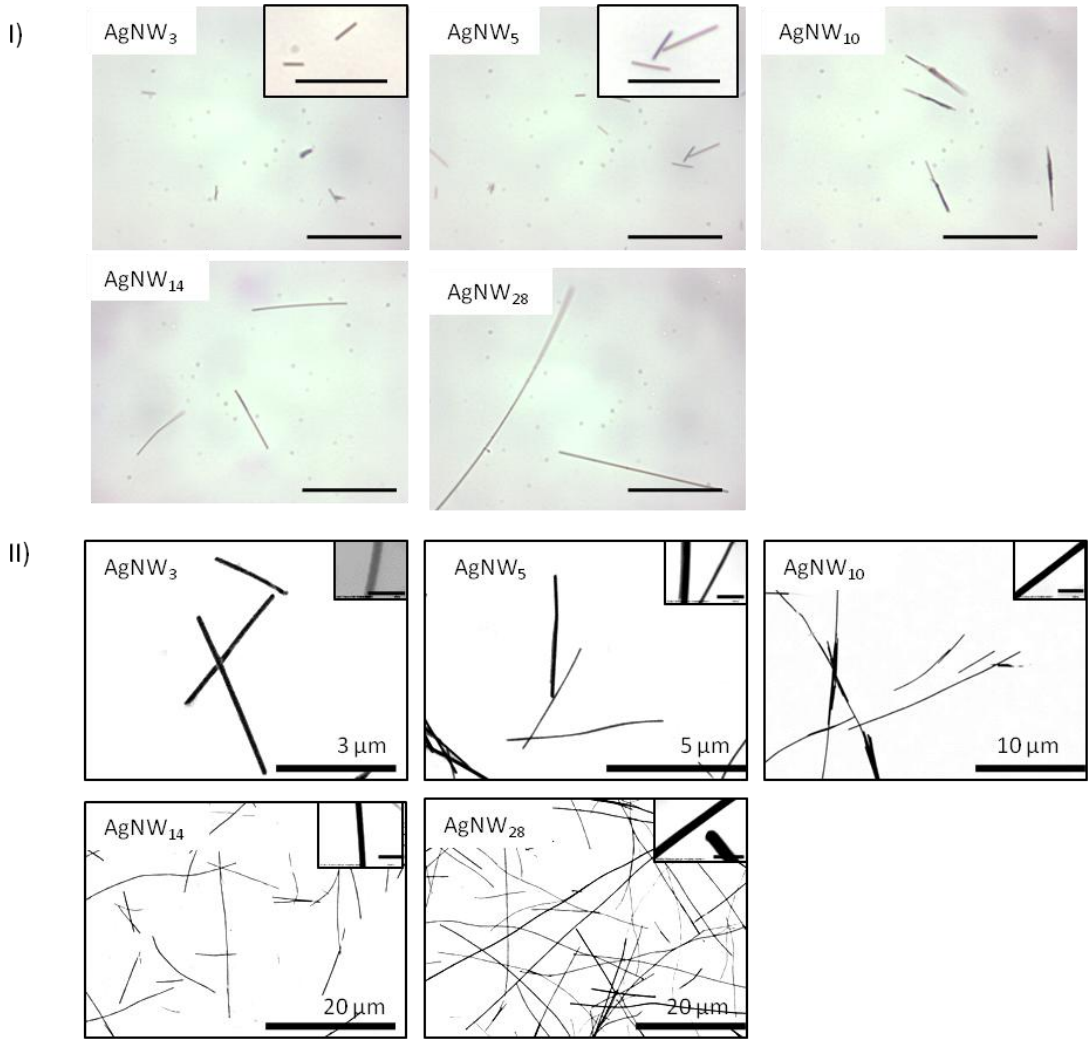

Figure 3-1: Light microscope and BSEM images of the AgNW panel. I) Light microscopy images of AgNW panel in 0.5% BSA/saline at a concentration of 50 µg/ml. Scale bar 20 µm, insert 10 µm. II) BSEM of 5 µg/ml AgNW in saline. Insert shows the diameter of each AgNW sample (scale bar 500nm).

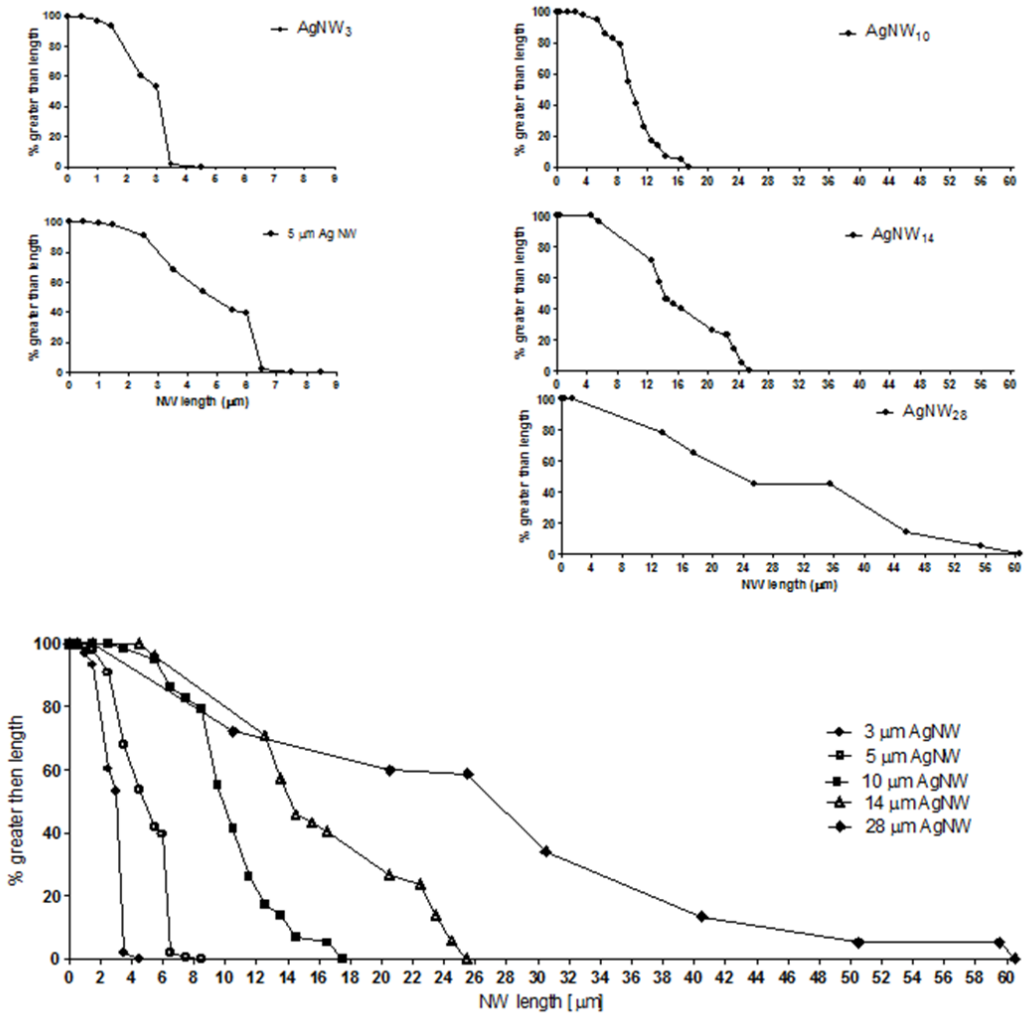

Figure 3-2: Fibre length distribution of AgNW. Length distribution of AgNWs plotted as % greater than any length. 100 fibres were calculated for each group.

Table 3-1: Characterisation of AgNW length distribution and diameter.

		$AgNW_3$	$AgNW_5$	$AgNW_{10}$	$AgNW_{14}$	$AgNW_{28}$
Mean length (µm)		**3**	**5**	**10**	**14**	**28**
% fibre per length category (µm)	**0.5-1.5**	6	2	0	0	0
	1.5-2.5	39	7	0	2	0
	2.5-3.5	53	22	2	2	0
	3.5-4.5	2	14	0	0	0
	4.5-5.5		12	3	0	0
	5.5-6.5		40	9	0	0
	6.5-7.5		2	4	2	0
	7.5-8.5		1	4	2	0
	8.5-9.5			24	23	0
	9.5-10.5			14	14	0
	10.5-15.5			34	17	22
	15.5-20.5			6	26	13
	20.5-30.5				12	20
	30.5-40.5					31
	40.5-50.5					9
	50.5-60.5					5
Diameter (nm, mean±s.e.m.)		115±3	118±3	128±2	121±3	120±4

For all additional nanofibres and control particles used in this study, the mean length is summarised in Table 3-2. Size distribution for CNT used in this study (NT_2, NT_{13} and NT_{36}) was performed by Dr Craig Poland and Dr Fiona Murphy (Poland et al., 2008; Murphy et al., 2011). The short CNT sample, NT_2, consisted of extremely short but straight fibres whereas long CNT samples, NT_{13} and NT_{36}, consisted of long straight fibres as defined by the WHO with a length greater than 5 µm and an aspect ratio of 3:1. NiNW size distribution was performed by Dr Adriele Prina-Mello Figure 3-3.

*Table 3-2: Mean length + S.E.M. and source of additional nanofibres and control particles. *Courtesy of Murphy et al. (Murphy et al., 2011).*

	Length (mean, µm) ± s.e.m.	Source
AgP	0.035	Nanostructured & Amorphous Materials, Inc.
NPCB (Printex 90®)*	0.014	Evonik Degussa GmbH
NT_2*	2 ± 0.2	Nanostructured & Amorphous Materials, Inc.
NT_{13}*	13 ± 6.1	Mitsui & Co. Ltd., Japan
NT_{36}*	36 ± 3.4	University of Manchester [Dr. I. Kinloch]
Ni-P	0.8	Nanostructured & Amorphous Materials, Inc.
$NiNW_4$	4.2 ± 0.9	CRANN - Trinity College Dublin [Prina-Mello A. and Drs Byrne F.]
$NiNW_{20}$	20.3 ± 5.5	CRANN - Trinity College Dublin [Prina-Mello A. and Drs Byrne F.]
SFA	1	Manville Corporation (USA)
LFA	15	Manville Corporation (USA)

The tightly defined length categories of the nanofibres used in this study, especially AgNWs and NiNWs allowed investigating the threshold length for fibre effects in the pleural space. This has been so far not been feasible since all naturally occurring fibres such as asbestos fibres and other man made vitreous fibres have a wide distribution of length.

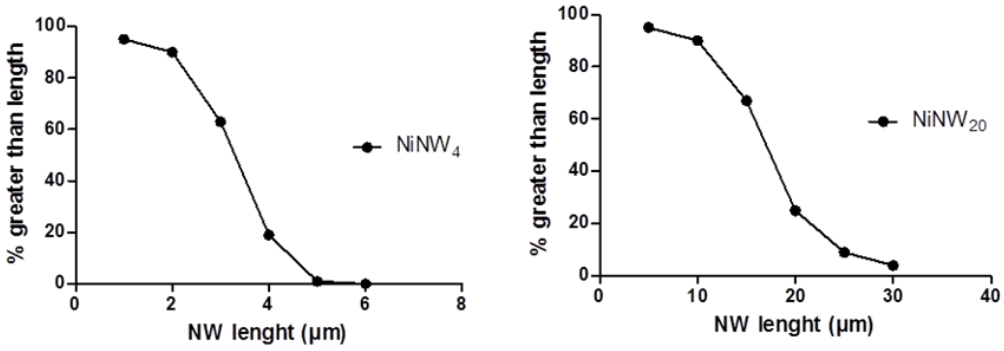

Figure 3-3: Nickel nanowire size distribution. Size distributions of nickel nanowire were carried out by measuring the lengths of at least 100 fibres under scanning eletron microscope. Average length for short NiNW is 4.2 + 0.9µm, average of long NiNW is 20.3 + 5.5µm. Size distribution was performed by Dr Adriele Prina-Mello.

3.3.2 Metal contamination and soluble metals

The presence of transition metals and the release of soluble metals from the nanowires, have been stated as a driver for inflammation due to their ability to generate free radical species via redox cycling with biological reductants. Redox-active metals are defined as those containing an unpaired electron in their d-orbital (Kelly and Mudway, 2006). The release of soluble metals into the aqueous extract (saline) of the different fibre lengths of AgNW and NiNW as well as AgP was measured using Inductive Coupled Plasma Mass Spectrometry (ICP-MS). The concentration of soluble metals was expressed as ng/g (Table 3-3 I and Table 3-4 I) as well as the amount (fg/g) per injected dose in the *in vivo* intrapleural injection experiment of a dose of 5 µg/mouse (Table 3-3 II and Table 3-4 II). The concentration of silver ions in the AgNW samples ranged from 1007 ng/g for $AgNW_{14}$ to 1666 ng/g for $AgNW_5$, however due to the formation of insoluble silver chloride the data is confounded. The concentration of soluble nickel in the samples was approximately 1200 ng/g. When comparing these concentrations to the soluble iron metal concentration in LFA, which is approximately 3200000 ng/g (Osmond-McLeod et al., 2011) and reported to contribute to pathogenicity observed with asbestos (Donaldson et al., 1996), negligible amounts of contaminating metals were measured for all nanowire and nanoparticle samples that would not be biologically active.

Table 3-3: Concentration of soluble metal in AgNW and AgP**.** *I) Concentration (ng/g) of soluble metal associated with* AgP *and AgNWs in the supernatant of a 50 µg/ml solution. II) Calculated concentration (fg) of soluble metals per injected dose (5 µg/mouse).*

I) Concentration (ng/g) of soluble metal associated with AgP and AgNWs

	^{107}Ag	^{27}Al	^{111}Cd	^{59}Co	^{52}Cr	^{63}Cu	^{56}Fex	^{55}Mn	^{60}Ni	^{208}Pb	^{64}Zn
AgP	1123	39.03	<0.01	0.03	0.17	13.01	3.69	0.30	0.46	0.98	7.18
$AgNW_3$	925.80	1.51	<0.01	0.01	0.26	2.56	3.88	0.24	0.68	0.18	2.23
$AgNW_5$	1666	4.27	<0.01	0.04	0.19	4.30	60.62	2.31	1.46	0.16	4.98
$AgNW_{10}$	830.10	5.38	<0.01	0.01	0.13	2.23	6.70	0.15	0.45	0.10	0.89
$AgNW_{14}$	1007	2.62	<0.01	<0.01	0.17	2.65	6.93	0.29	0.32	0.31	0.44
$AgNW_{28}$	1078	3.72	<0.01	0.03	0.17	6.30	15.32	0.29	0.58	0.38	7.78

xcomparison of soluble metals in LFA: Fe~3200000 ng/g (Osmond et al., 2010).

II) Concentration (fg/g) of soluble metal converted to amount per injected dose (5 µg/mouse)

	^{107}Ag	^{27}Al	^{111}Cd	^{59}Co	^{52}Cr	^{63}Cu	^{56}Fe	^{55}Mn	^{60}Ni	^{208}Pb	^{64}Zn
AgP	5615	195.15	<0.01	0.14	0.87	65.05	18.46	1.49	2.31	4.92	35.88
$AgNW_3$	4629	7.57	<0.01	0.02	1.28	12.81	19.41	1.20	3.42	0.92	11.16
$AgNW_5$	8330	21.36	<0.01	0.18	0.96	21.48	303.10	11.57	7.32	0.79	24.84
$AgNW_{10}$	4150.5	26.88	<0.01	0.06	0.67	11.17	33.52	0.76	2.26	0.47	4.48
$AgNW_{14}$	5035	13.08	<0.01	<0.01	0.82	13.23	34.66	1.434	1.62	1.55	2.23
$AgNW_{28}$	5390	18.60	<0.01	0.16	0.84	31.50	76.60	1.44	2.88	1.91	38.90

Table 3-4: Concentration of soluble metal in NiNW and NiNP. I) Concentration (ng/g) of soluble metal associated with NiNP and NiNWs in the supernatant of a 50 µg/ml solution. II) Calculated concentration (fg) of soluble metals per injected dose (5 µg/mouse).

I)	**Concentration (ng/g) of soluble metal associated with NiNP and NiNWs**										
	^{107}Ag	**^{27}Al**	**^{111}Cd**	**^{59}Co**	**^{52}Cr**	**^{63}Cu**	**^{56}Fe**	**^{55}Mn**	**^{60}Ni**	**^{208}Pb**	**^{64}Zn**
NiNP	0.71	80.12	0.09	0.71	0.57	0.29	173.62	0.27	**1146.1**	0.18	10.51
$NiNW_4$	10.59	211.03	0.09	0.18	0.43	3.43	168.15	0.32	**1197.4**	0.02	6.62
$NiNW_{20}$	30.13	202.54	0.08	0.57	0.71	17.73	186.81	0.10	**1314.4**	0.23	13.25

Values subtracted from BSA/saline sample (blank control)

II)	**Concentration (fg/g) of soluble metal converted to amount per injected dose (5 µg/mouse)**										
	^{107}Ag	**^{27}Al**	**^{111}Cd**	**^{59}Co**	**^{52}Cr**	**^{63}Cu**	**^{56}Fe**	**^{55}Mn**	**^{60}Ni**	**^{208}Pb**	**^{64}Zn**
NiNP	3.55	400.60	0.45	3.57	2.86	1.43	868.10	1.36	**5730.5**	0.89	52.55
$NiNW_4$	52.95	1055.15	0.47	0.91	2.14	17.14	840.75	1.60	**5987.3**	0.11	33.10
$NiNW_{20}$	150.65	1012.70	0.38	2.86	3.57	88.64	934.05	0.50	**6572.4**	1.13	66.25

Values subtracted from BSA/saline sample (blank control)

3.3.3 Dissolution measurement of AgNW and NiNW

Biopersistence of fibres in biological fluids is a major contributing factor to their pathogenicity as discussed in chapter 1.5.3. Dissolution of AgP/AgNW and the subsequent release of silver ions into the surrounding media are hypothesised to contribute to the severity of inflammation seen after silver exposure. Therefore, the dissolution kinetics of AgNW were measured via change in pH compared to vehicle control across the 24 h exposure. Dissolution of AgNW occurred to a modest extent as shown by the almost flat slope of the curve across the 24h exposure and no difference in dissolution was observed between all AgNW (Figure 3-4 I). To confirm that the AgNW retain their shape over the 24 hour period, AgNWs were incubated for 24 hour in pH 5.0 saline solution and rotated during this time. Images of the

AgNW structure were taken before and after the incubation time and showed no dissolution of the fibres over 24 hour (Figure 3-4 III).

Measurements for the kinetics of the dissolution of NiNW was modest over 24 hour detected using pH change measurement, compared to saline solution reference curve plotted below at the used concentration (Figure 3-4 II).

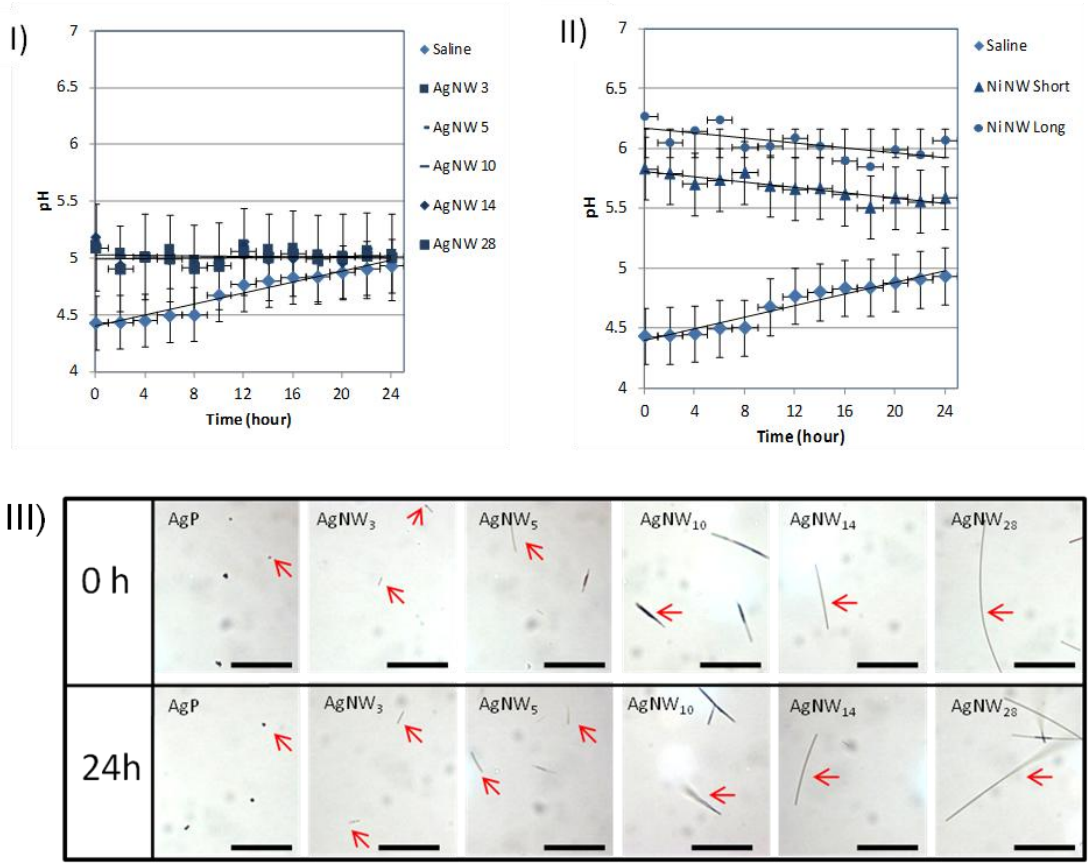

Figure 3-4: Dissolution measurement of NW. I) Comparison between sterile saline solution (as baseline) and $AgNW_{3,\ 5,\ 10,\ 14,\ 28}$ dispersed in sterile saline solution. Average value of pH and standard deviation calculated for every time point up to 24h (interval 2 h) (n = 3). No statistical difference between Ag samples. Statistical significance AgNWs vs saline ($p<0.01$). II) Comparison between sterile saline solution (as baseline) and nickel nanowires long and short dispersed in sterile saline solution. Average value of pH and standard deviation calculated for every time point up to 24h (interval 2 h) (n = 3). Statistical significance saline vs NiNW $p<0.01$, NiNW long VS short (>0.05). III) Light micrograph images of AgP and AgNW at 0 hour and 24 hour after rotation in pH 5.0 saline solution. No dissolution or change

in morphology was observed after 24 hour. Red arrows indicate AgP and AgNW. Scale bar 10 µm.

3.3.4 Electron Paramagnetic Resonance

Intrinsic release of oxygen-centred free radical by the AgNWs, AgP and SFA/LFA was measured via Electron paramagnetic resonance (EPR). The spin trap Tempone-H was used to detect superoxide and peroxyl radicals and pyrogallol was used as a positive control. Pyrogallol, the positive control for superoxide generation as well as SFA, LFA and $AgNW_5$ produced a signal significantly greater than that of the vehicle control (Figure 3-5).

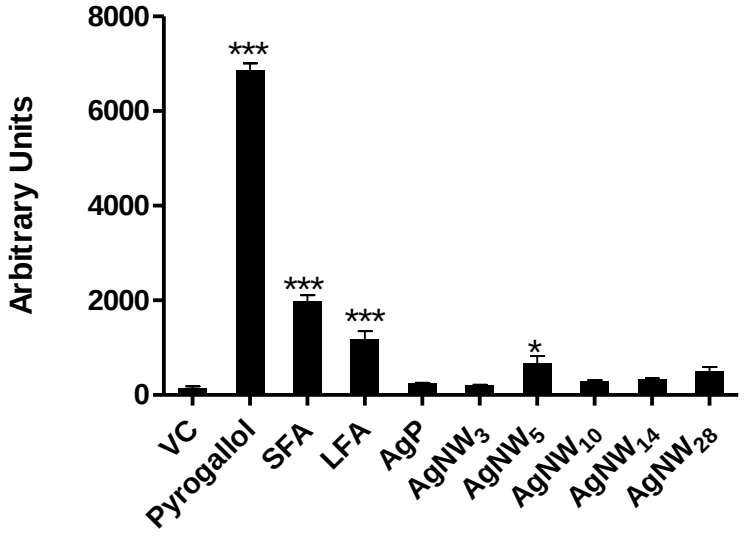

*Figure 3-5: Intrinsic free radical generation. Electron paramagnetic measurement of oxygen centred free radicals released by nanowires. Significance vs. vehicle control indicated by *p<0.05, ***p<0.0001. Data represent mean + S.E.M. of n=3.*

3.3.5 Acute inflammatory response to AgNW and AgP

The aim of this study was to identify any length dependent inflammatory response in the pleural space to AgNWs and AgP. Five microgram of AgNW and AgP were

injected into the pleural space and the pleural cavity was lavaged 24 hours later. The acute inflammatory reaction was measured as the total cell number and total granulocytes (predominantly neutrophils plus a low proportion of eosinophils) in the lavage (Figure 3-7). There was a clear length-dependent inflammatory response to AgNW, with significant increase in both total cell and total granulocyte number after treatment with $AgNW_5$, $AgNW_{10}$, $AgNW_{14}$ and $AgNW_{28}$ (Figure 3-6 I, II, III). In contrast, neither the very short fibre, $AgNW_3$ nor the compact nanoparticles (AgP) elicited a significant inflammation compared to the vehicle control (Figure 3-6). The length-dependent response reveals that the total granulocyte number induced was significantly increased ($p<0.01$) with $AgNW_5$ compared to $AgNW_3$ (Figure 3-6 III). Moreover, there was no significant difference in inflammatory response (granulocytes) as length increased between $AgNW_5$, $AgNW_{10}$ and $AgNW_{14}$, demonstrating an all-or-nothing type of response between 3 µm fibre length and 5 to 14 µm fibre length. This was not reflected in the total cell count, since a significant increase was observed between 5, 10 and 14 µm. For fibre length longer than 28 µm, there was a significant increase in total cell number and granulocyte cell number compared to $AgNW_5$ (Figure 3-6 III). This all-or-nothing response in granulocyte number, observed between 3 µm and 5-14 µm was confirmed by a dose effect series using 1, 2.5, 5, 7.5 and 10 µg/mouse for $AgNW_3$ and $AgNW_5$ (Figure 3-8 I and II). $AgNW_3$ did not lead to a significant increase in inflammatory cells up to a tested dose of 10 µg per mouse, however $AgNW_5$ showed a significant increase at a dose of 2.5 µg/mouse onwards (Figure 3-8 I and II).

In addition to the inflammatory response, the total protein concentration was measured in the lavage fluid as an indicator of the amount of inflammatory molecules present. The two longest fibres, $AgNW_{14}$ and $AgNW_{28}$ led to a significant increase in total protein (Figure 3-9).

I)

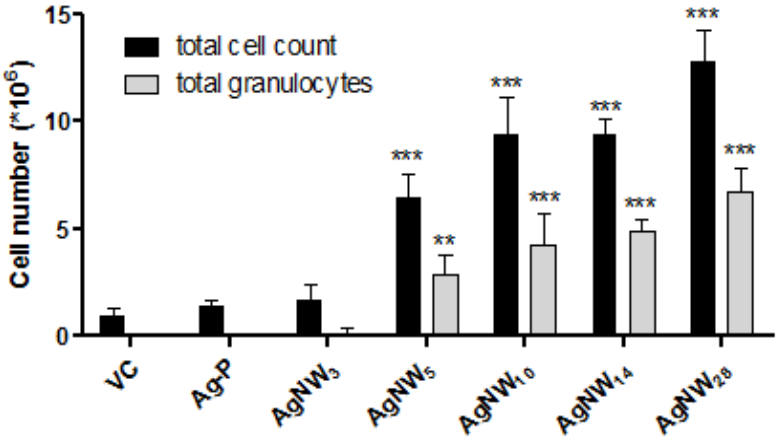

II)

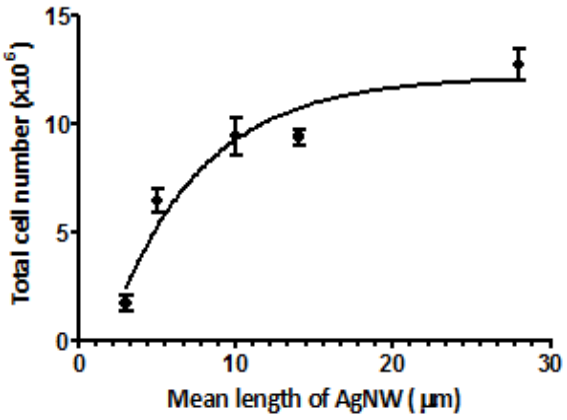

Comparison	p value
$AgNW_3$ vs $_5$	***
$AgNW_3$ vs $_{10}$	***
$AgNW_3$ vs $_{14}$	***
$AgNW_3$ vs $_{28}$	***
$AgNW_5$ vs $_{10}$	*
$AgNW_5$ vs $_{14}$	*
$AgNW_5$ vs $_{28}$	***
$AgNW_{10}$ vs $_{14}$	ns
$AgNW_{10}$ vs $_{28}$	**
$AgNW_{14}$ vs $_{28}$	**

III)

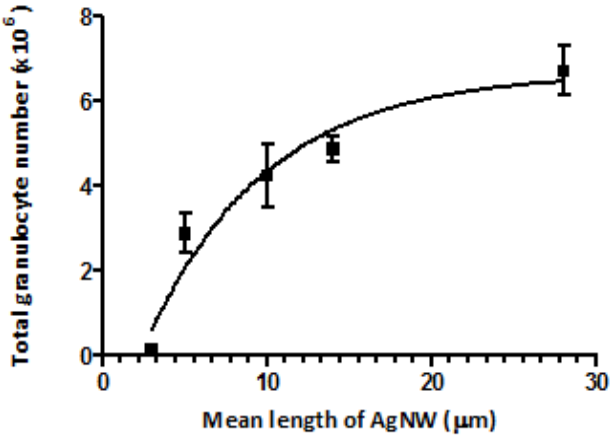

Comparison	p value
$AgNW_3$ vs $_5$	**
$AgNW_3$ vs $_{10}$	***
$AgNW_3$ vs $_{14}$	***
$AgNW_3$ vs $_{28}$	***
$AgNW_5$ vs $_{10}$	ns
$AgNW_5$ vs $_{14}$	ns
$AgNW_5$ vs $_{28}$	***
$AgNW_{10}$ vs $_{14}$	ns
$AgNW_{10}$ vs $_{28}$	*
$AgNW_{14}$ vs $_{28}$	ns

Figure 3-6: Length dependent response to AgNW in the pleural space 24 hour post injection. I) Count of total cell number and total granulocyte number in relation to fibre length of AgNW and AgP *after 24 hour treatment in female C57Bl/6 mice. The*

*influx of total cells and granuloctyes (neutrophil and eosinophil) is dependent on fibre length of AgNW. All length were significantly greater than $AgNW_3$ ($p<0.001$). Significance vs. vehicle control indicated by **$p<0.001$, ***$p<0.0001$. II) Mean length of AgNW and* AgP *plotted against the total cell number. Significant difference of $AgNW_5$ vs $AgNW_{10}$ ($p<0.05$), $AgNW_5$ vs $AgNW_{14}$ ($p<0.05$) and $AgNW_5$ vs $AgNW_{28}$ ($p<0.001$). III) Mean length of AgNW and* AgP *plotted against the total granulocyte number. All lengths were significantly greater then $AgNW_3$ ($p<0.01$-0.001). No significant difference of $AgNW_5$ vs $AgNW_{10}$ and $AgNW_5$ vs $AgNW_{14}$, significant difference of $AgNW_5$ vs $AgNW_{28}$ ($p<0.001$). Data represent mean + S.E.M. of n=4 mice.*

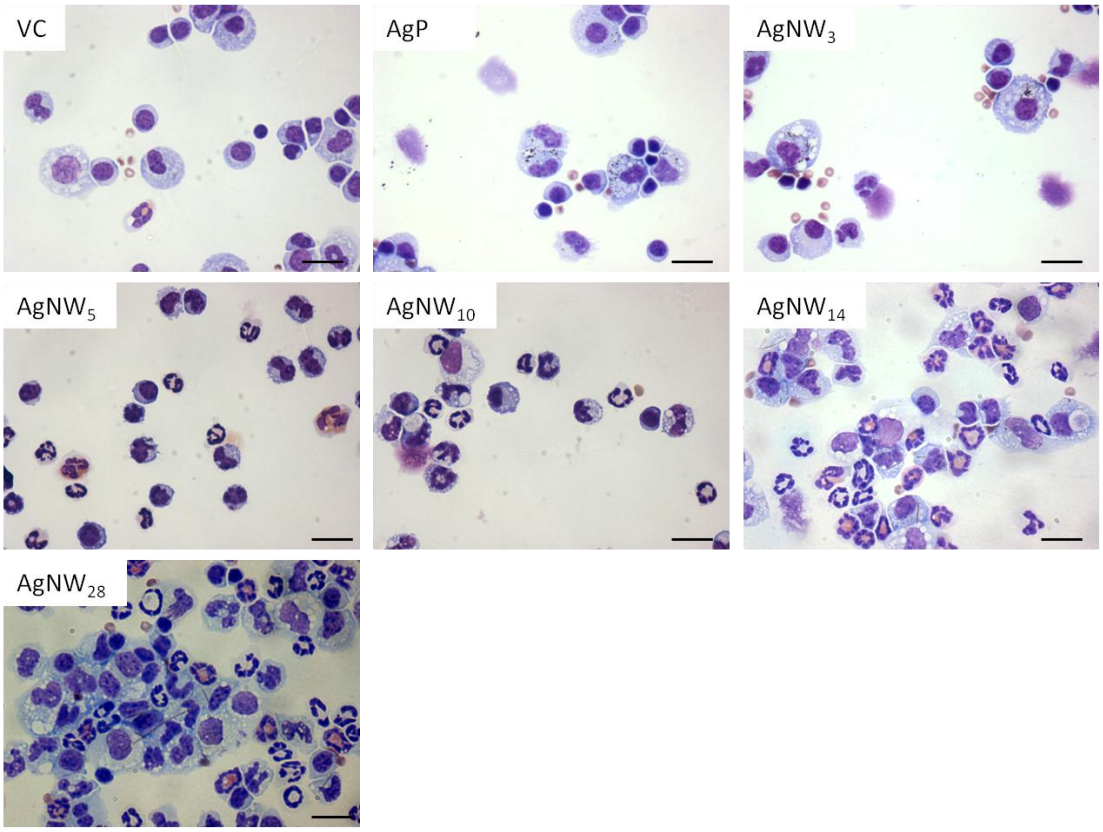

*Figure 3-7: Cytospins of the pleural lavage fluid 24 hour post injection of vehicle control (VC) and AgNW/*AgP*. Inflammatory cells are present in $AgNW_{5\text{-}28}$. Scale bar indicates 20 µm.*

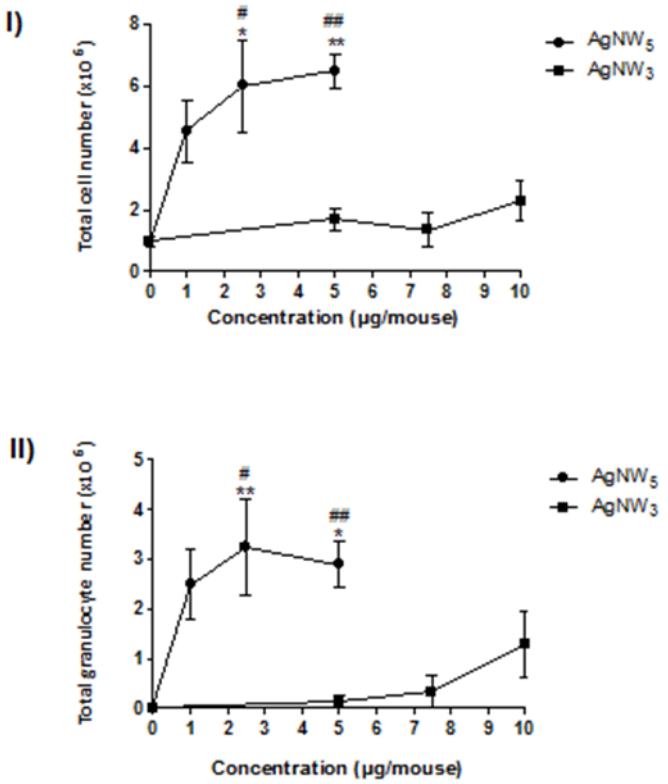

*Figure 3-8: Dose effect series for $AgNW_3$ and $AgNW_5$ measuring the acute 24 hour inflammatory response. Total cell number (I) and total granulocyte number (II) of $AgNW_5$ at a dose of 1.0, 2.5 and 5.0 µg/mouse and $AgNW_3$ at a dose of 5.0, 7.5 and 10.0 µg/mouse. Significance versus vehicle control (0 µg/mouse), * indicates $p<0.05$, ** indicates $p<0.01$. A) # indicates $p<0.05$, significance of $AgNW_5$ (2.5 µg/mouse) vs $AgNW_3$ (7.5 µg/mouse), ## indicates $p<0.05$, significance of $AgNW_5$ (5 µg/mouse) vs $AgNW_3$ (5.0, 7.5 µg/mouse); B) # indicates $p<0.05$, significance of $AgNW_5$ (2.5 µg/mouse) vs $AgNW_3$ (5.0, 7.5 µg/mouse), ## indicates $p<0.05$, significance of $AgNW_5$ (5.0 µg/mouse) vs $AgNW_3$ (5.0 µg/mouse). Data represent mean + S.E.M. of n=4 mice.*

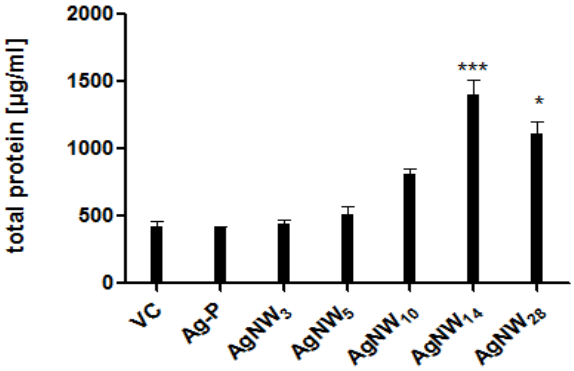

*Figure 3-9: Total protein in the lavage fluid after 24 hour intrapleural injection of AgNW and AgP. $AgNW_{14}$ and $AgNW_{28}$ led to a significant increase in the amount of total protein. Significance vs. vehicle control indicated by *p<0.05, ***p<0.0001. Data represent mean + S.E.M. of n=4.*

The general design of this study used equal fibre mass, therefore many more short fibres than long fibres were injected, yet still this greater number of short fibres in the dose of $AgNW_3$ was much less inflammogenic than the fewer long fibres in the dose of $AgNW_5$. Since fibre exposure is regulated in workplaces on the basis of the fibre number, the number of fibres per treatment was calculated for $AgNW_3$ and $AgNW_5$, the key lengths spanning the threshold value. Based on fibre number calculations the inflammatory response was re-expressed 'per fibre' and this clearly showed that the fibre-specific inflammatory potency of the $AgNW_3$ fibres is negligible compared to the marked specific inflammogenicity of $AgNW_5$ fibres (Figure 3-10).

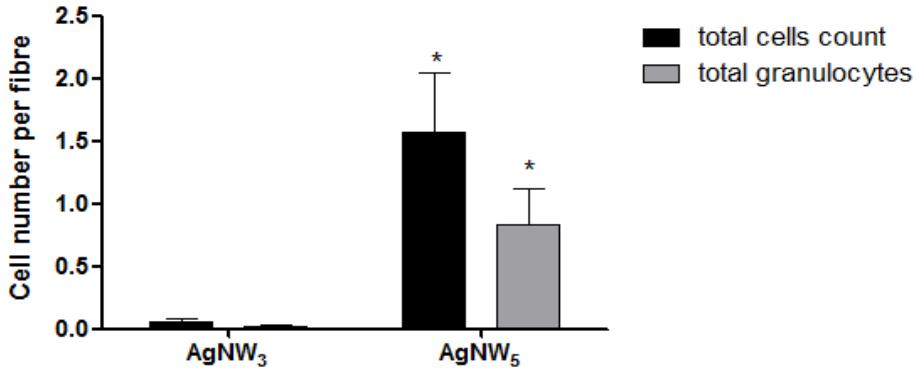

Figure 3-10: Acute inflammatory response expressed per fibre. The inflammatory response was expressed per fibre. The equalisation to fibre number reinforced the identified threshold value. Data represent mean + S.E.M. of n=4 mice.

3.3.6 Role of silver ion toxicity and soluble metals

To preclude a role of the soluble, ionic fraction of AgNWs, additionally to the measurements of ionic fraction and dissolution, supernatant was collected from a 5 µg dose of $AgNW_5$ and $AgNW_{14}$ in BSA/saline after overnight mixing and injected into the pleural space. This soluble fraction produced no significant inflammatory response in the pleural space after 24h (Figure 3-11) further confirming that soluble Ag ions were not responsible for the long fibre effects.

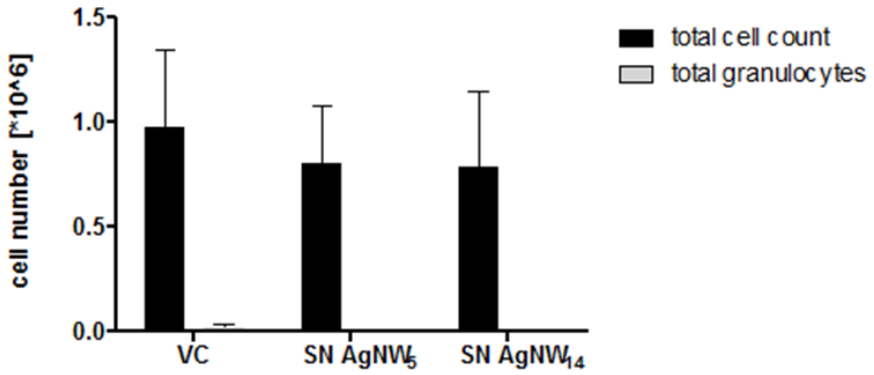

Figure 3-11: Total cell number and total granulocyte number from pleural lavage fluid after 24 hour treatment with supernatant (SN) of $AgNW_5$ and $AgNW_{14}$. Cell number shown as total cells and total granulocytes was counted from mice treated with the supernatant of $AgNW_5$ and $AgNW_{14}$ at 24 hour post-injection. Data represent mean + S.E.M. of n=3 mice.

3.3.7 Acute inflammatory response to intrapleural injection a range of HARN

The acute inflammatory response of AgNW in the pleural space after intrapleural injection was compared to other forms of HARN including and SFA and LFA, NT_2, NT_{13} and NT_{36} (Murphy et al., 2011) and $NiNW_4$ and $NiNW_{20}$ using the same method. Nanoparticle carbon black (CB) and nickel nanoparticle (NiNP) were included as material nanoparticulate controls (Table 3-2). Particulates and short fibres (CB, NiNP, SFA, NT_2, $NiNW_4$) produced no significant increase in total cell or granulocyte number 24 hour post intrapleural injection (Figure 3-12 I). In contrast all long fibre samples including LFA, NT_{13}, NT_{36} and $NiNW_{20}$ produced an inflammatory response (Figure 3-12 I). The amount of total protein was measured in SFA/LFA and NiNWs/NiNP and showed a significant increase after treatment with LFA as well as long NiNWs (Figure 3-12 II).

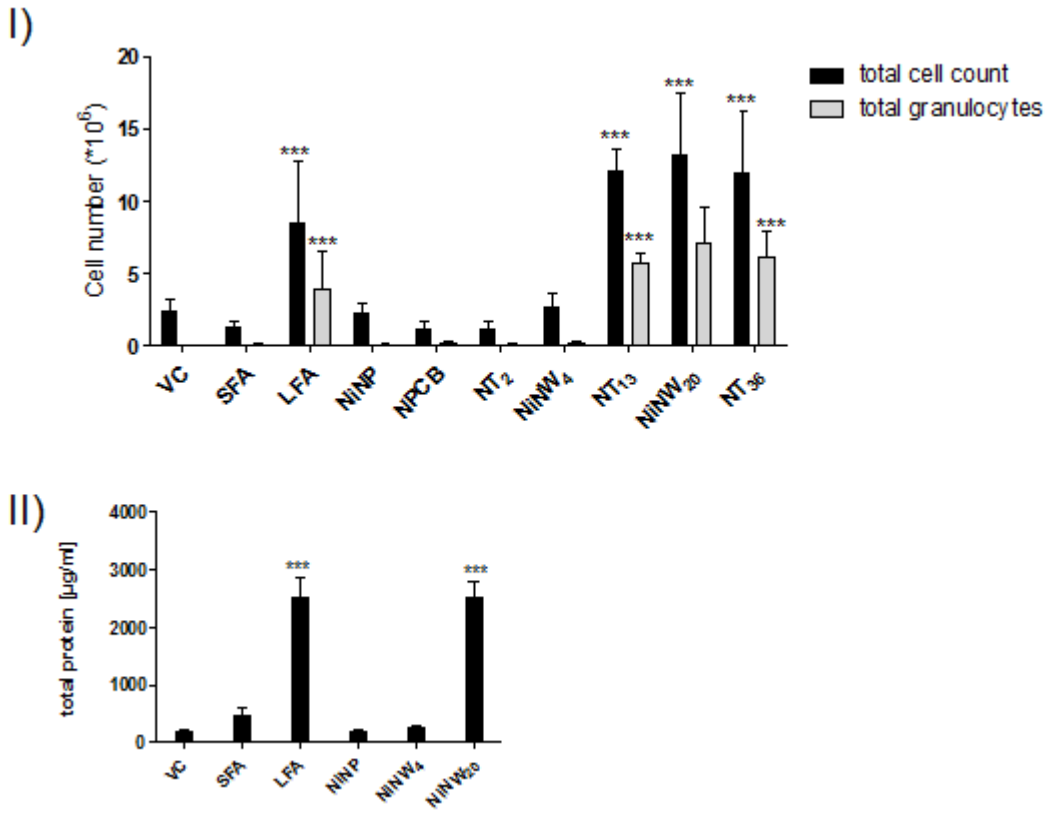

Figure 3-12: Acute inflammatory response in the pleural space 24 hour after treatment with all control fibres and particles. I) Total cell number and total granulocyte number in the lavage fluid of mice treated at a concentration of 5 µg/mouse with the material control panel SFA, LFA, NiNP, NiNWs, CB *and NTs at 24 hour post-injection. II) Total protein measured in the lavage fluid. Significance versus vehicle control *** indicates p<0.001. Data represent mean + S.E.M. of n=5 mice. NT data from Murphy et al. 2011 (Murphy et al., 2011).*

3.3.8 The threshold length for pleural inflammation

To identify the threshold length for pleural inflammation, the mean length of all nanofibre and control particles were plotted against the total granulocyte number (Figure 3-13). Particulates and short fibres (CB, Ni-P, Ag-P, NT_2, $AgNW_3$, $NiNW_4$) produced no significant increase in total cell number and granulocytes 24 hour post intrapleural injection. In contrast all fibre samples that were 5 µm and longer

produced an inflammatory response (NT_{13}, NT_{36}, $AgNW_{5/10/14/28}$, $NiNW_{20}$) (Figure 3-13). The data clearly show that the threshold length for long fibre effects in the pleural space is 5 µm. The difference in response to $NiNW_4$ and $AgNW_5$ is dramatic but can be explained by their size distribution curves which are illustrated in Figure 3-13 II. Hardly any $NiNW_4$ are longer than 5 µm, however ~40% $AgNW_5$ are ≥5 µm (Figure 3-2 and Figure 3-3).

I)

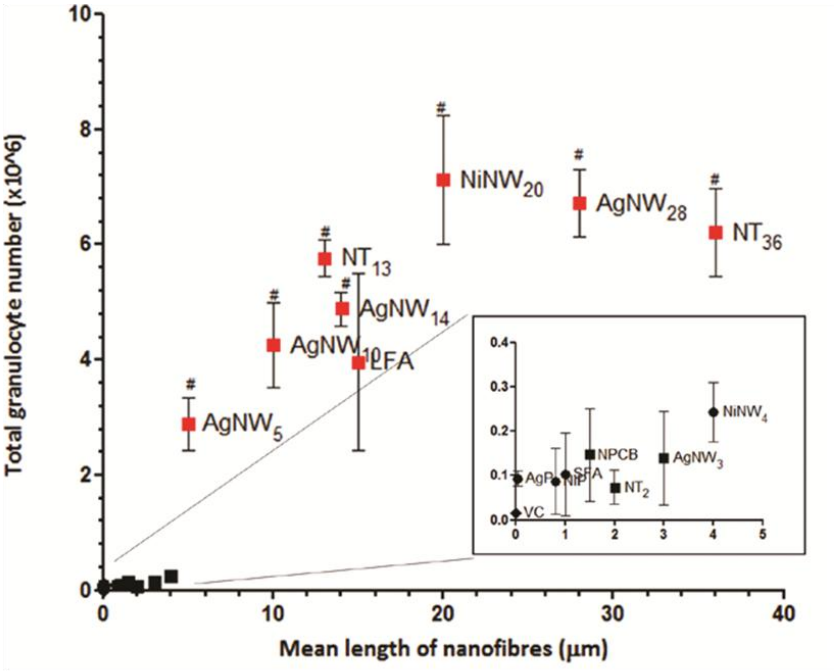

II)

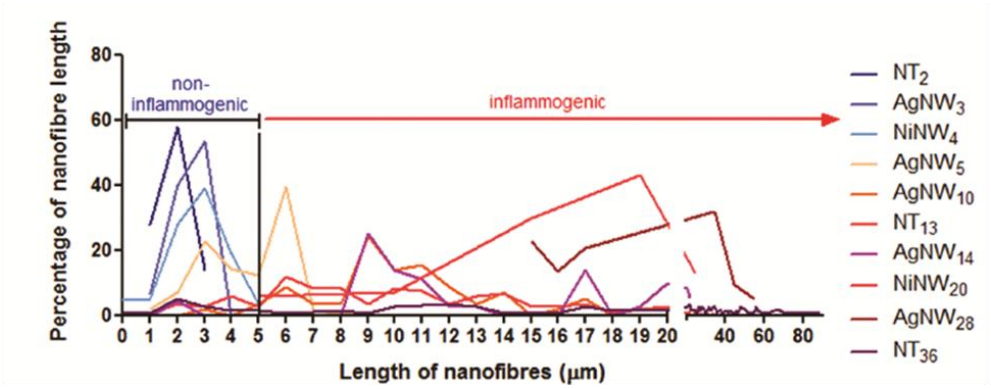

Figure 3-13: The acute pleural response to CNT, NiNW and AgNW in various lengths. I) Female C57Bl/6 mice were intrapleurally instilled with 5 µg/mouse of CB *(14nm),* NT_2, NT_{13}, NT_{36}, *Ni-P,* $NiNW_4$, $NiNW_{20}$, *AgP (35nm),* $AgNW_3$, $AgNW_5$, $AgNW_{10}$, $AgNW_{14}$, $AgNW_{28}$, *SFA and LFA. Total granulocyte number is shown from pleural lavage after 24 hour post exposure. A clear length- dependent threshold response in the pleural space to different sources and compositions of high aspect ratio nanomaterials from 5 µm in length is evident;* CB/NT_2/NT_{36} *data from Murphy et al. (Murphy et al., 2011). Length is shown as mean. Data represent mean + S.E.M. of n=4 mice. II) The percentage of nanofibres per length are plotted to illustrate their length distribution in relation to the cut-off length for fibre induced pleural inflammation.*

3.3.9 Histology and SEM of the parietal pleura 24 hour post injection

The mesothelial lining of the parietal pleura is uniquely sensitive to fibre exposure and it has been shown that pathological lesion after fibre exposure arise near stoma-rich regions on the parietal pleura (Shinohara, 1997) due to retention of particles that are too large to negotiate the stomata. To investigate the pathogenic response to AgNW, the surface of the parietal pleura was examined by light microscopy and by Scanning Electron Microscopy (SEM) at 24 hours post-exposure at the regions identified as being rich in stomata. In the vehicle control treated mice the mesothelium of the parietal pleura was a single, continuous layer of mesothelial cells overlaying the muscular tissue as shown in the histological sections as well as via SEM (Figure 3-14). Normal appearance of the mesothelial cell layer was observed after treatment with the panel of short fibres and particle control, Ag-P, $AgNW_3$ and SFA as identified via histological sections (Figure 3-14 top row) and SEM (Figure 3-14 bottom row). In contrast, sections of the parietal pleura from mice injected with LFA and $AgNW_{5/10/14/28}$ showed lesions comprising of macrophages and granulocytes on the mesothelial cell layer at the parietal pleural surface (Figure 3-14). SEM of the whole chest wall section is illustrated for each treatment in Figure 3-15.

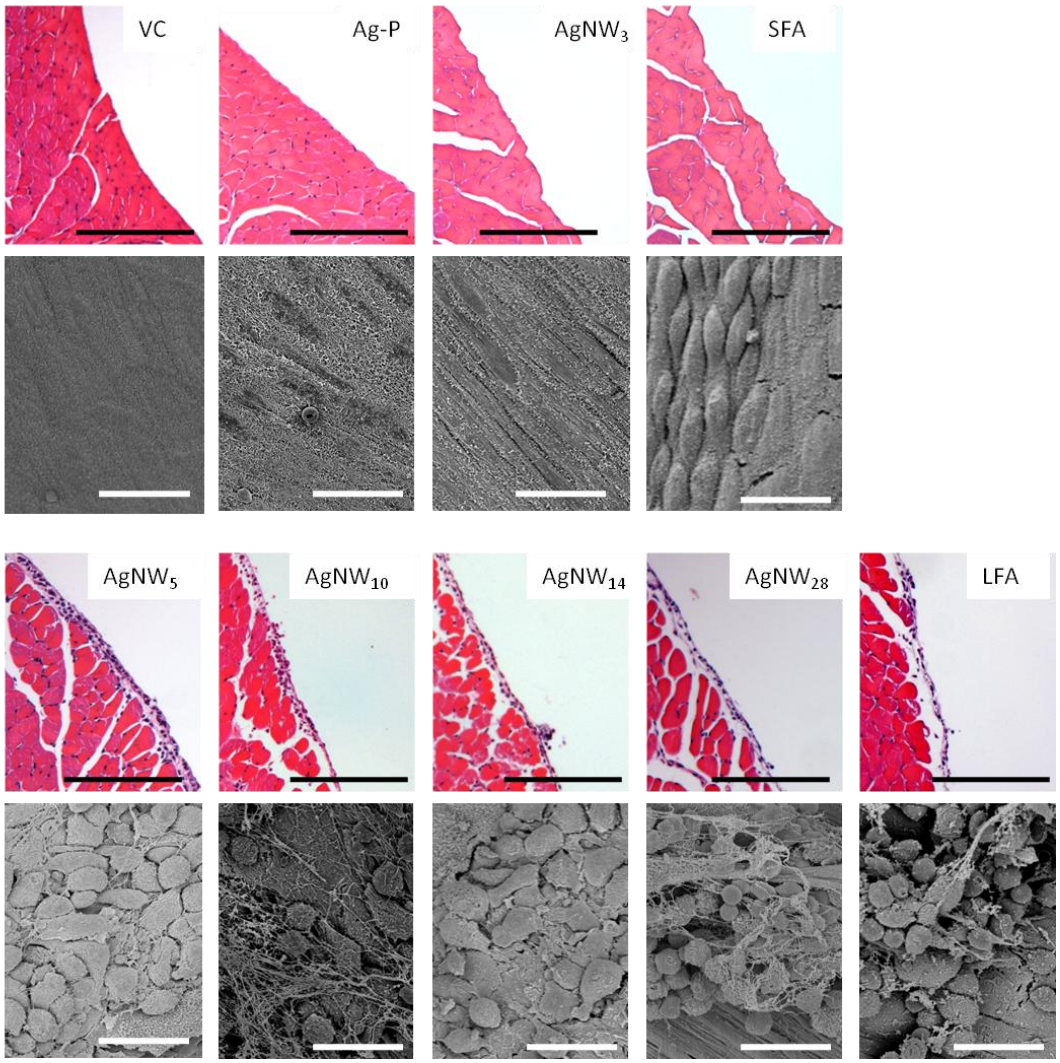

Figure 3-14: Length dependent response of AgNW and control particles on the parietal mesothelial surface 24 hours post injection. Haematoxylin and eosin (H&E) histology sections (top row) and SEM images (bottom row) of VC and mice treated with Ag-P, $AgNW_3$, SFA, $AgNW_5$, $AgNW_{10}$, $AgNW_{14}$, $AgNW_{28}$ and LFA. No alteration on the mesothelial surface can be seen in the mice treated with Ag-P, $AgNW_3$ and SFA. Normal mesothelial cells on the parietal pleura appear either flat as seen in the image of VC-exposed mesothelium or in a more rounded or raised form in areas called the lacunar regions, such as that seen in the image of SFA-exposed mesothelium (Donaldson et al., 2010). Accumulation of inflammatory cells was observed on the mesothelial lining in mice treated with long AgNW (≥5 µm) and LFA. Scale bar: black 100 µm; white 20 µm.

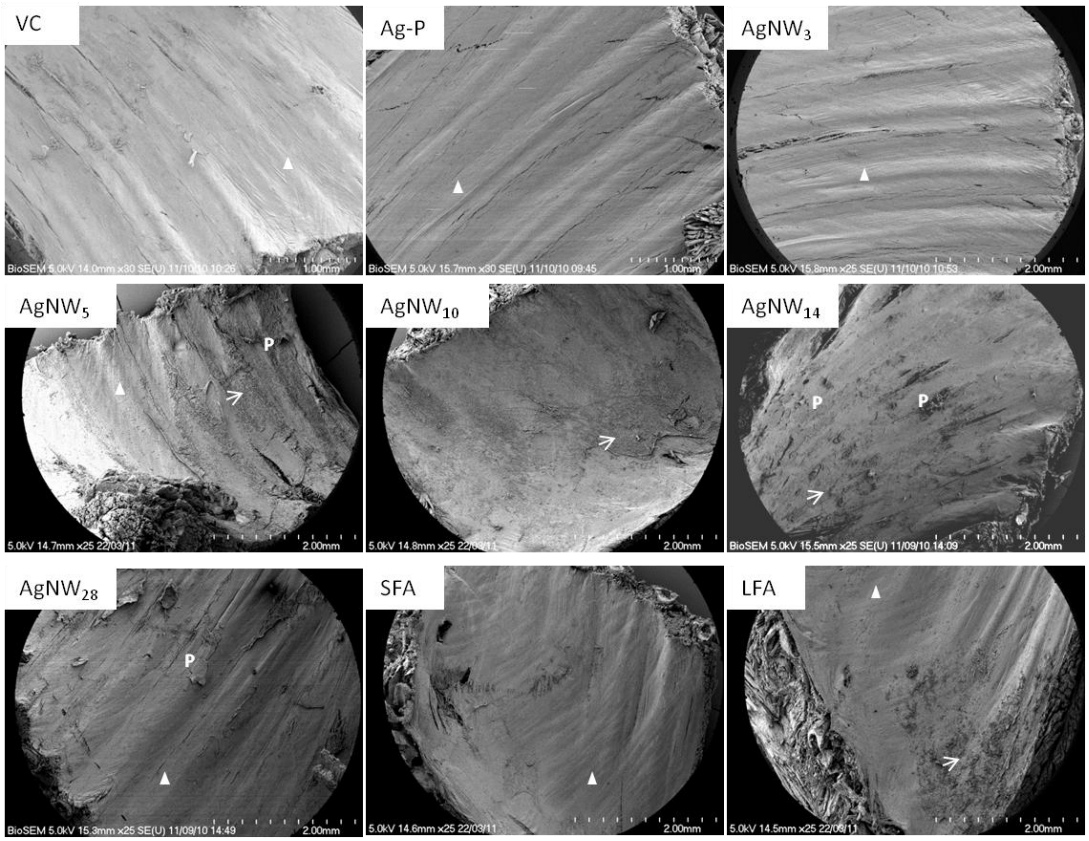

Figure 3-15: Length dependent response of AgNW and control particles on the parietal mesothelial surface 24 hour post injection. Overview of whole chest wall section at low magnification. Triangle indicates normal mesothelial cell layer, arrow indicates lesion areas of accumulated inflammatory cells and P indicates papillae or tongue-like structures made up of cell aggregates, which extend from the surface of the mesothelium.

3.3.10 Frustrated phagocytosis *in vivo* in the lavage fluid and on the parietal pleura surface 24 hour post exposure

Incomplete uptake of fibrous material by macrophages, termed frustrated phagocytosis has been stated as an important factor in the initiation of an inflammatory response after fibre exposure. The degree of phagocytosis of different length of AgNW in pleural macrophages was assessed in by light microscopy in cytospin preparations and by backscatter scanning electron microscopy (BSEM) in lesions on the parietal pleura. Cytospin images showed that $AgNW_3$ and $AgNW_5$

could, for the most part, be fully phagocytosed inside pleural macrophages recovered in the lavage fluid (Figure 3-16 I). In contrast $AgNW_{10/14/28}$ led to frustrated phagocytosis in the pleural macrophages as indicated by incomplete uptake of the fibres and accumulation of multiple macrophages to phagocytose the deposited fibres (Figure 3-16 I). The percentage of macrophages showing frustrated phagocytosis in the cytospin sections of the lavage fluid was counted (Figure 3-16 II). $AgNW_{28}$ was not counted since too few very long fibres could be seen on the cytospin preparation. This can be explained by physical retention of 28 µm long fibres at the side of injection in the pleural space, which has a thickness of approximately 7 µm in mice (Lai-Fook, 2004).

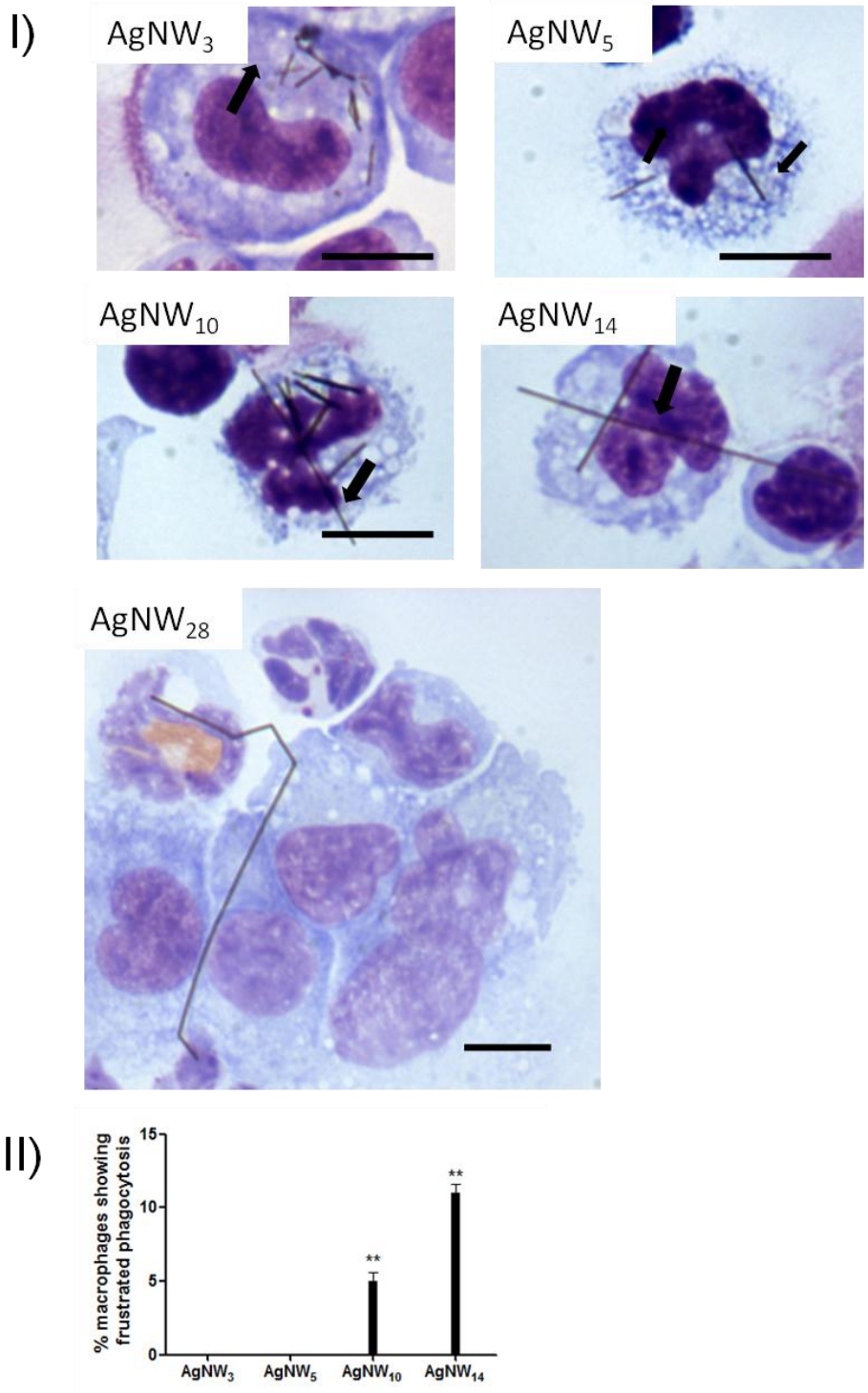

Figure 3-16: Phagocytosis of AgNW in pleural lavage fluid. I) Cytospin preparation of the pleural lavage fluid from mice treated with $AgNW_3$ and $AgNW_5$ showed complete phagocytosis of nanowires in pleural macrophages (nanowires indicated by the arrow); $AgNW_{10}$ are not entirely phagocytosed, showing the ends of a nanowire protruding from a cell (indicated by two arrows); Frustrated phagocytosis of

*macrophages was observed after $AgNW_{14/28}$ treatment. A number of macrophages can be seen sharing a single fibre indicated by the arrow. All cytospin images are x100 magnification. Scale bar for all images 10 µm. II) Percentage of frustrated phagocytosis of pleural macrophages. 50 fibre- containing macrophages were counted in the lavage fluid from $AgNW_3$, $AgNW_5$, $AgNW_{10}$, $AgNW_{14}$ treatment. The percentage of macrophages showing frustrated phagocytosis (not fully enclosed fibres) was calculated by comparing to the number of macrophages with completely enclosed fibres. Macrophages from $AgNW_{10}$ and $AgNW_{14}$ treatment show a significant increase in frustrated phagocytosis compared to $AgNW_3$ (** indicates $p<0.01$). Data represent mean + S.E.M. of n=4 mice. $AgNW_{28}$ was not counted since too few very long fibres could be seen on the cytospin preparation.*

BSEM examination was carried out on the macrophage accumulations on the parietal pleura samples from mice injected with $AgNW_3$, $AgNW_5$ and $AgNW_{10}$ at 24 hour post intrapleural instillation in order to examine retention of AgNW in the pleural space and their interaction with inflammatory cell in terms of phagocytosis/ frustrated phagocytosis. No $AgNW_3$ could be observed on the parietal pleura surface 24 hour post treatments confirming that short fibres are readily cleared from the pleural space. In contrast to $AgNW_3$, both $AgNW_5$ (Figure 3-17 top row) and $AgNW_{10}$ (Figure 3-17 bottom row) led to an aggregation of inflammatory cells on the surface of the parietal pleura with accumulation of nanowires within the lesion area (Figure 3-17 I and III). Most $AgNW_5$ were fully phagocytosed by pleural macrophages (Figure 3-17 I, II and insert, star). In comparison, $AgNW_{10}$ showed a number of fibres only partly phagocytosed and therefore leading to frustrated phagocytosis (Figure 3-17 II, IV white arrow). Some $AgNW_5$ and $AgNW_{10}$ were not taken up by macrophages as indicated by the yellow arrows (Figure 3-17 I and III). By looking at the surface with higher magnification unclosed membrane could be visualised in pleural macrophages phagocytosing $AgNW_{10}$ (Figure 3-17 IV and insert, black arrows). Additional higher magnification images of phagocytosis of $AgNW_5$ and frustrated phagocytosis of $AgNW_{10}$ can be seen in Figure 3-18.

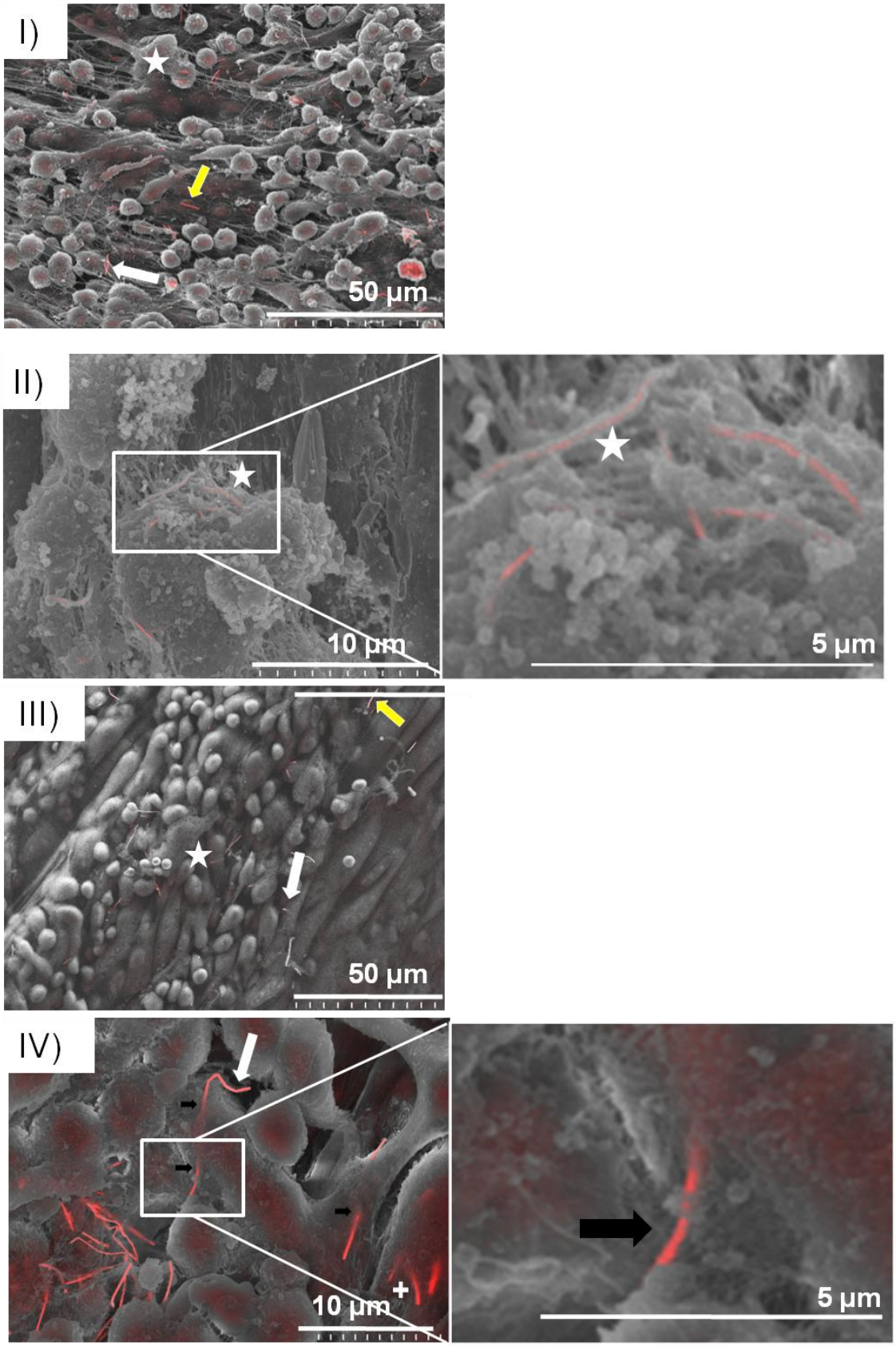
I)
50 µm
II)
10 µm
5 µm
III)
50 µm
IV)
10 µm
5 µm

Figure 3-17: Images of the parietal pleura surface 24 hour post pleural instillation of $AgNW_5$ and $AgNW_{10}$. Overview of the lesion area on the surface of the parietal pleura with $AgNW_5$ (I) and $AgNW_{10}$ (III). The yellow arrow indicates a nanowire which is not taken up by inflammatory cells whereas the star indicates a fibre that is fully phagocytosed but can be visualised underneath the surface of the cell. The white arrow indicates nanowires which are protruding out of cells. II) This figure shows $AgNW_5$ that are fully phagocytosed by pleural macrophages but can be visualised underneath the surface as indicated by the star. IV) $AgNW_{10}$ is causing frustrated phagocytosis in a macrophage in the centre of the image. The unclosed cell membrane is indicated by the black arrows and exposed fibre surface is indicated by the white arrow. The cross on the lower right of the image indicates fibres which are largely internalised but whose tips rise vertically to penetrate the cell surface adjacent to the other long fibre.

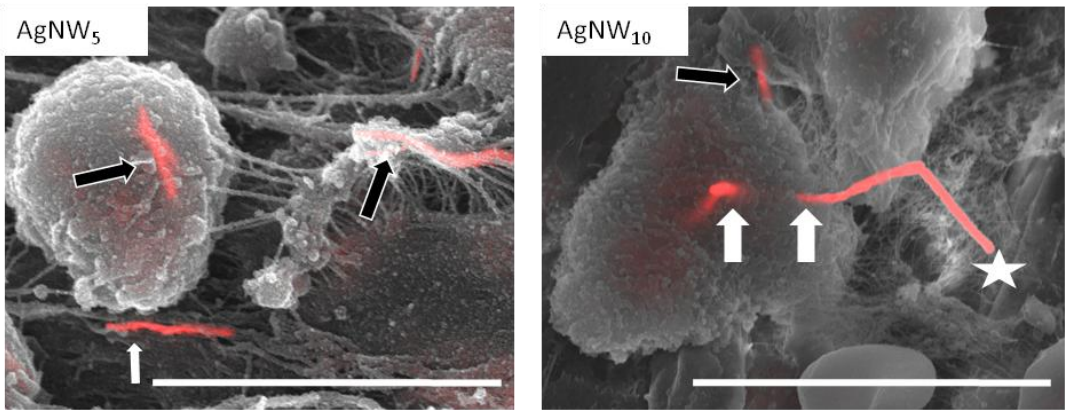

Figure 3-18: Merged secondary electron and backscatter electron SEM images lesions surface of the parietal pleura from mice treated with $AgNW_5$ and $AgNW_{10}$. For $AgNW_5$, two fibres are shown which are fully phagocytosed by pleural macrophages (black arrows). The white arrow shows a fibre on the surface in the lesion area; For $AgNW_{10}$, the star indicates frustrated phagocytosis of macrophages with $AgNW_{10}$. The loci where unclosed phagosomes must be present are indicated by the white arrows. The black arrow shows a fibre that is shared by two cells each of which must have an unclosed phagosome. Scale bar is 10 µm.

3.3.11 Quantification of pro- inflammatory mediators in the pleural lavage fluid after 24 hour exposure

To determine the inflammatory mediators present in the pleural space after AgNW treatment a screening of 11 cytokines and chemokines was performed from the pleural lavage fluid using the BD™ Cytometric Bead Array Flex Set. The cytokines measured in the screening included IL-4, IL-6, IL-10, IL-13, IL-1β, CCL2 (MCP-1), G-CSF, TNF and the chemokines measured included CCL-5 (Rantes), CCL-3 (MIP-1α) and CXCL-1 (KC). No significant increase in the amount of the cytokines and chemokines was detected in the lavage fluid at any treatment; however a trend in the increase of CCL-2 after treatment with $AgNW_{10/14/28}$ was observed (Figure 3-19 I). Dilution of the concentration levels of the pro-inflammatory mediators during the lavage fluid could be responsible for the low concentration measured in the samples. The concentration of CCL-2 and CCL-3, important mediators in the inflammatory response were further investigated by a more sensitive assay, the R&D Quantikine kit in the pleural lavage fluid. For this measurement the pleural lavage fluid of further control particles were included, namely $NT_{2/36}$ and $NiNW_{4/20}$. CCL-2 showed increased expression after long fibre treatment including LFA, $AgNW_{10/14/28}$ and NT_{36} and $NiNW_{20}$, however statistical significance was only reached after $AgNW_{28}$ treatment (Figure 3-19 II). Similar pattern was observed for the detection of the chemokine CCL-3 but no significant values were detected (Figure 3-19 III).

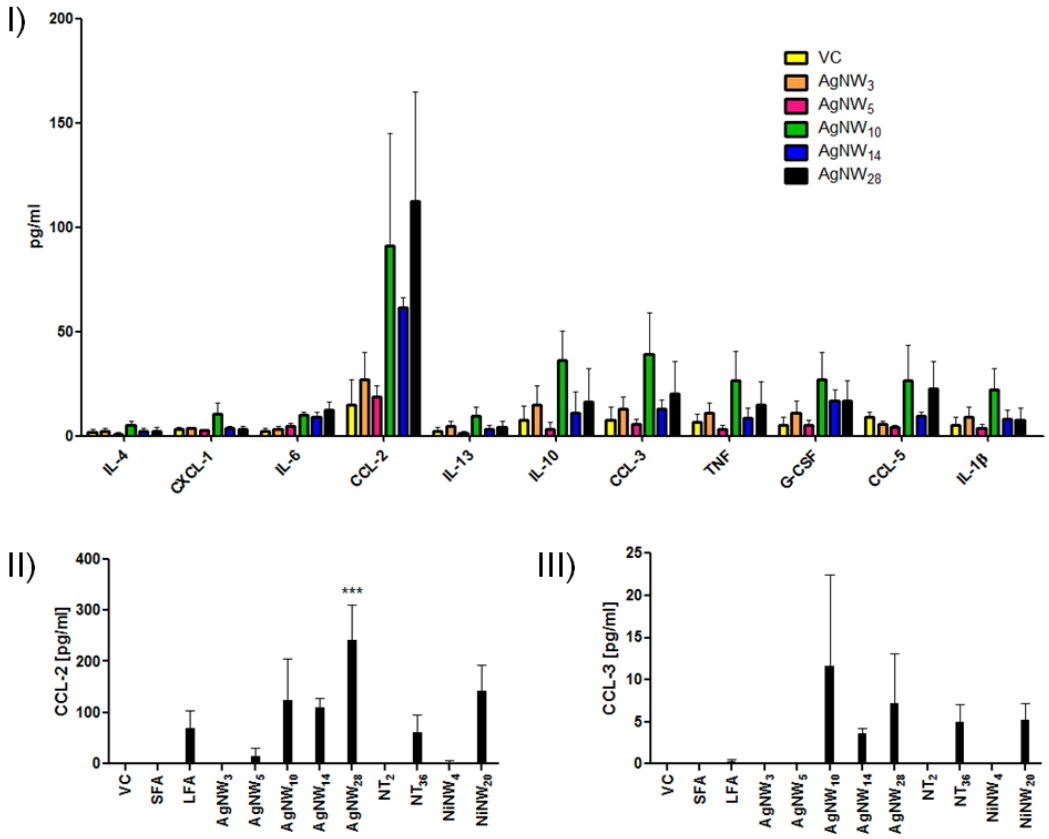

*Figure 3-19: Detection of pro-inflammatory mediators in the pleural space 24 hour post injection of NWs. I) The concentration of the measured cytokines IL-4, IL-6, IL-10, IL-13, IL-1β, CCL2 (MCP-1), G-CSF, TNF and chemokines CCL-5 (Rantes), CCL-3 (MIP-1α) and CXCL-1 (KC) is shown after 24 hour treatment with the AgNW panel. No significant difference was detected. II) The concentration of the cytokine CCL-2 was measured via R&D Quantikine kit and showed significant increase in expression after treatment with $AgNW_{28}$. III) The chemokine CCL-3 was measured via R&D Quantikine kit and showed no significant increase in expression after any treatment. Significance versus Vehicle control *** indicates $p<0.001$. Data represent mean + S.E.M. of n=3 mice.*

3.3.12 Inflammatory response of AgNW in the pleural space at a 1 week timepoint

To address the course of the response, mice were injected with a single dose of 5 µg AgNW and control particles and the inflammatory response was assessed at a 1 week time point. The acute inflammatory response had largely resolved at this time point although there was still a length-dependent effect detectable at $AgNW_{14/28}$ (Figure 3-20 I). The amount of total granulocytes was significantly increased with $AgNW_{14}$ and $AgNW_{28,}$ however no change in total cell number was detected across all treatments (Figure 3-20 I). Histological sections of the chest wall at 7 days continued to show thickening of the sub-mesothelial cell layer in the same length-dependent pattern as the acute inflammation i.e. with a threshold at 5 µm (Figure 3-20 II). This pattern was confirmed by SEM of the parietal pleura chest wall section, whereby normal appearance of the mesothelial cell layer was detected after VC, Ag-P, $AgNW_3$ and SFA and granulomatous regions were found on chest wall sections after treatment with $AgNW_{5,10,14}$ and LFA (Figure 3-21).

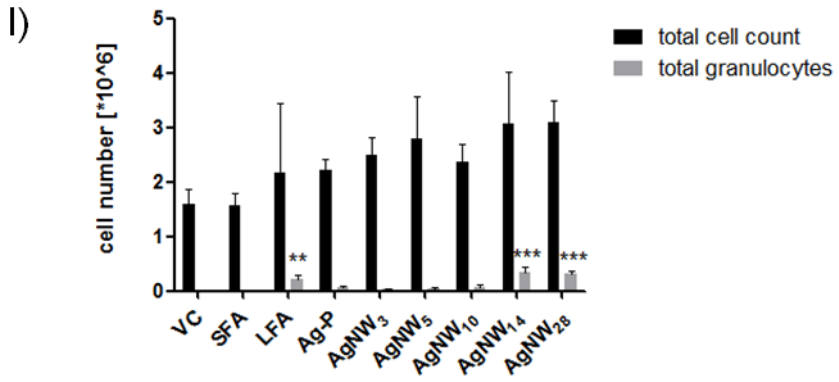

II)

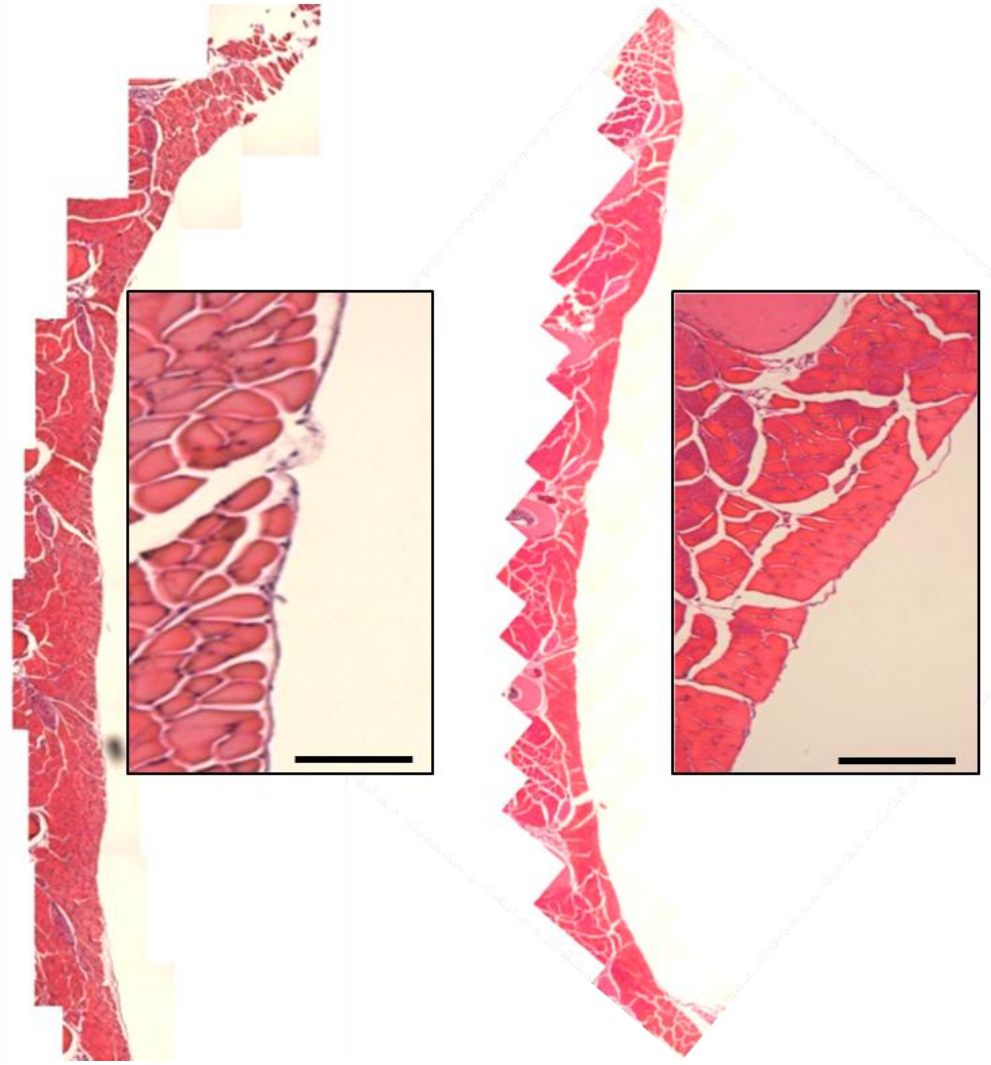

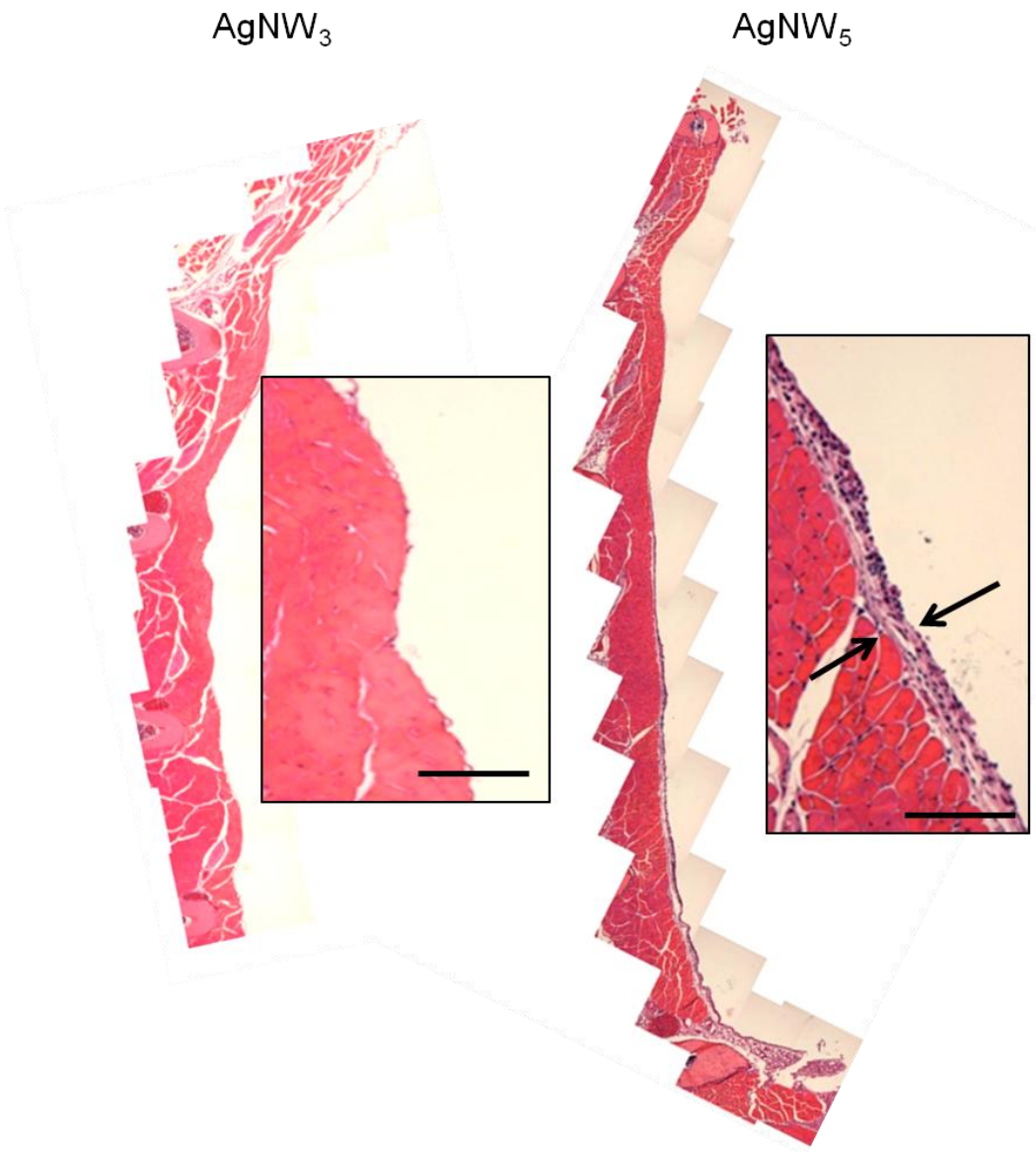
AgNW3
AgNW5

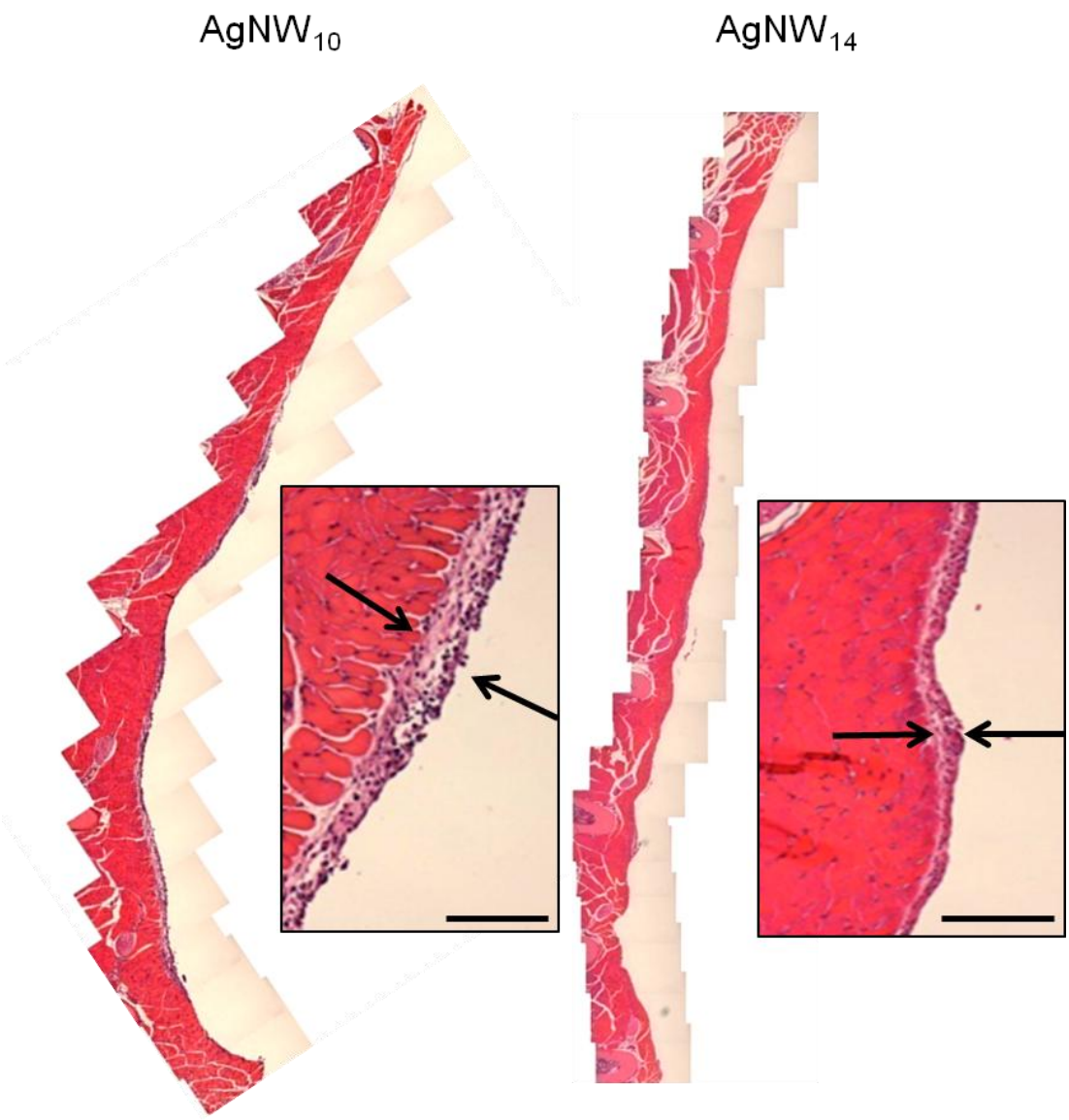
AgNW10
AgNW14

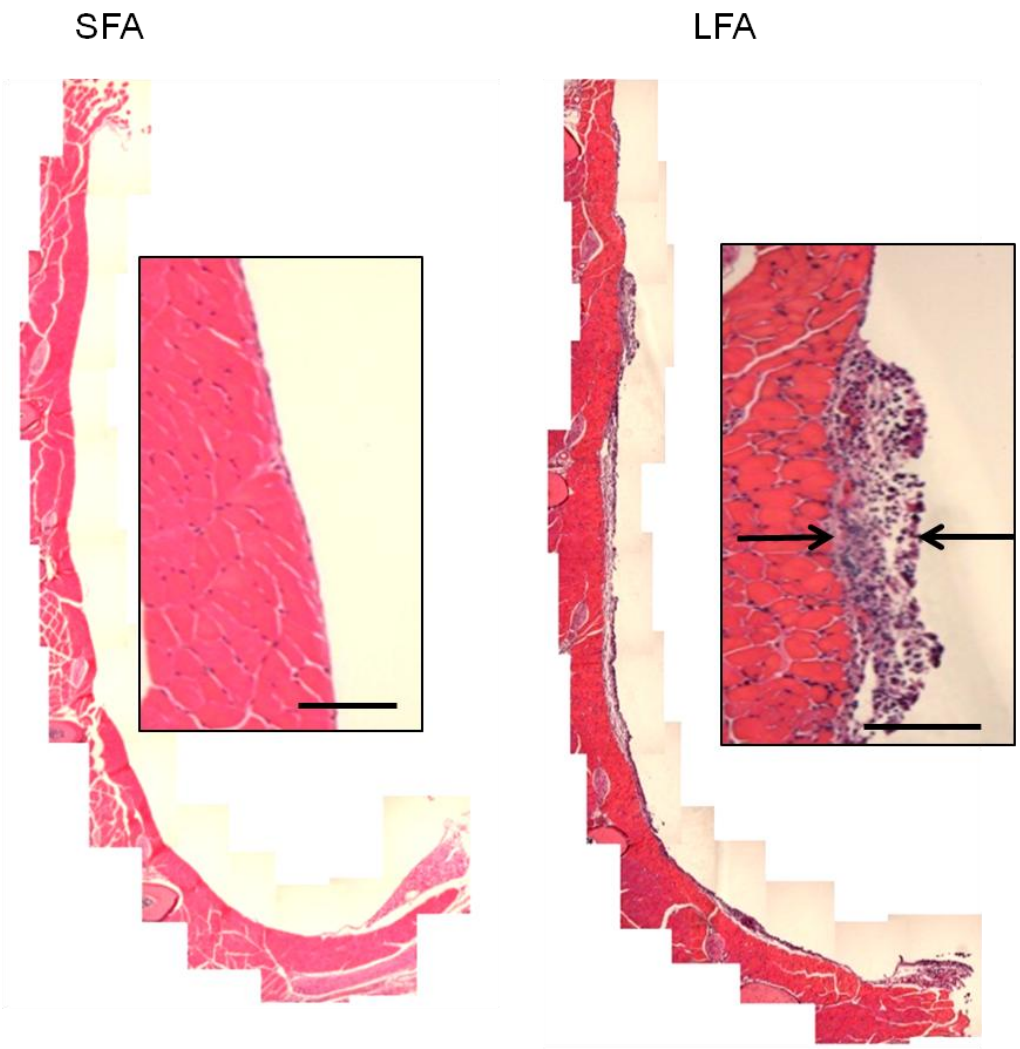

*Figure 3-20: Total cell number and total granulocyte number from pleural lavage fluid and H&E stained histology section of parietal pleura 1 week post exposure. I) Total cell number and total granulocyte number 1 week post exposure to 5 µg/mouse of SFA, LFA, Ag-P and AgNW panel. Significance versus Vehicle control * indicates $p<0.05$, ** indicates $p<0.01$, *** indicates $p<0.001$. Data represent mean + S.E.M. of n=4 mice. II) Normal appearance of mesothelial lining after VC, Ag-P, $AgNW_3$ and SFA exposure but thickening of the pleural sub-mesothelial layer can be seen in mice exposed to $AgNW_{5-14}$ and LFA as indicated by the black arrows. No thickening of the mesothelial cell layer could be seen after $AgNW_{28}$ exposure at 1 week (not shown). This was most likely due to retention of these very long fibres at the site of injection. Scale bar insert 100 µm.*

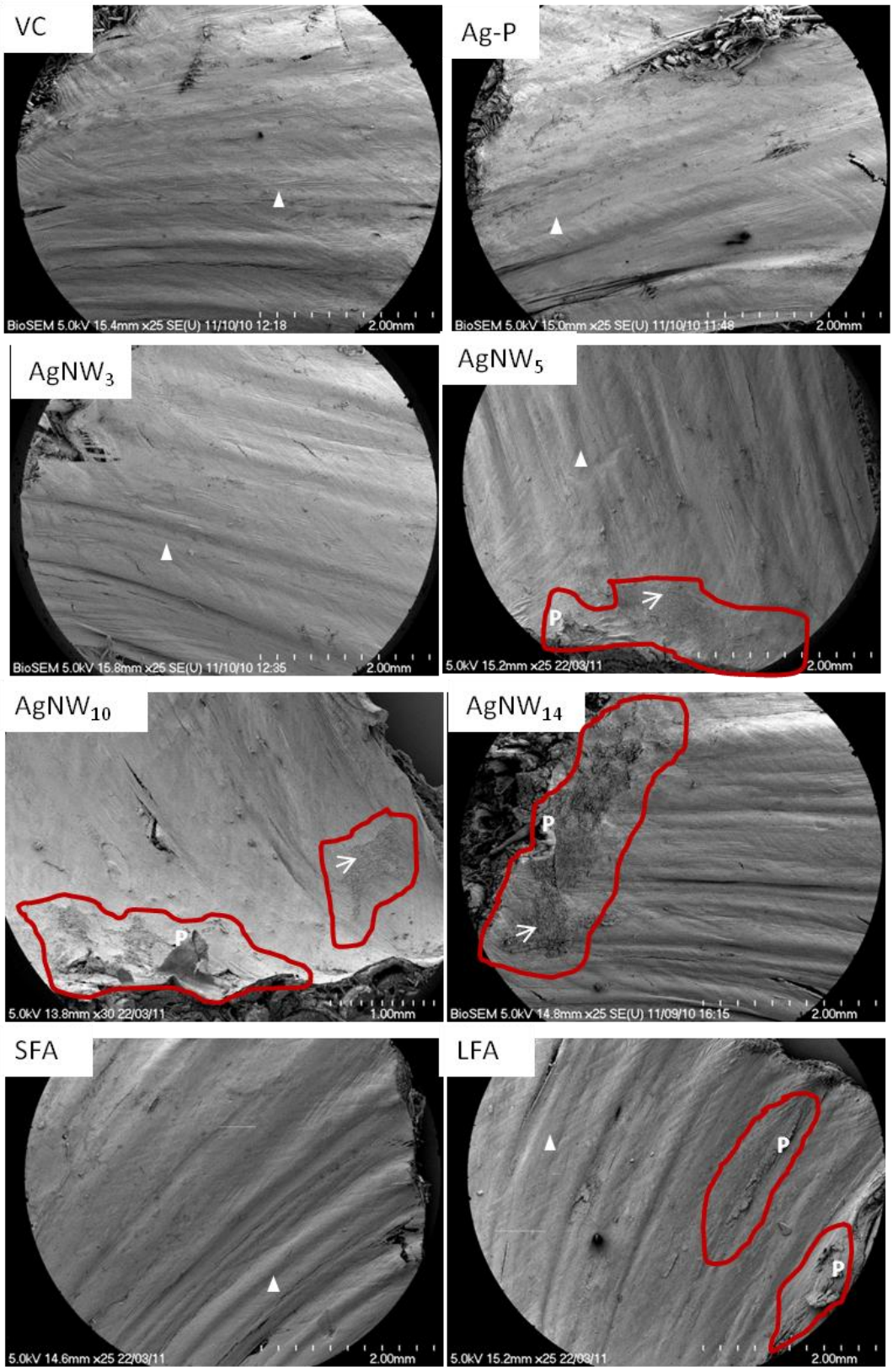
VC
BioSEM 5.0kV 15.4mm x25 SE(U) 11/10/10 12:18
2.00mm
Ag-P
BioSEM 5.0kV 15.0mm x25 SE(U) 11/10/10 11:48
2.00mm
AgNW3
BioSEM 5.0kV 15.8mm x25 SE(U) 11/10/10 12:35
2.00mm
AgNW5
P
5.0kV 15.2mm x25 22/03/11
2.00mm
AgNW10
P
5.0kV 13.8mm x30 22/03/11
1.00mm
AgNW14
P
BioSEM 5.0kV 14.8mm x25 SE(U) 11/09/10 16:15
2.00mm
SFA
5.0kV 14.6mm x25 22/03/11
2.00mm
LFA
P
P
5.0kV 15.2mm x25 22/03/11
2.00mm

Figure 3-21: Length dependent response of AgNW and control particles on the parietal mesothelial surface 1 week post injection. Overview of whole chest wall section at low magnification. Triangle indicates normal mesothelial cell layer, arrow indicates lesion areas of accumulated inflammatory cells and P indicates papillae or tongue-like structures made up of cell aggregates, which extend from the surface of the mesothelium. Granulomatous areas are indicated by red areas.N=2.

3.3.13 Integrity of AgNW and frustrated phagocytosis *in vivo* on the parietal pleura surface 1 week post exposure

Backscatter scanning electron microscopy (BSEM) examination was carried out on the macrophage accumulations on the parietal pleura samples from mice injected with $AgNW_5$ and $AgNW_{10}$ at 1 week post intrapleural instillation in order to examine the development of interaction between the mesothelial cell layer/inflammatory cells on the surface and the integrity of the AgNW. BSEM of parietal pleura after 1 week treatment with $AgNW_5$ are shown in Figure 3-22 I, II, III and $AgNW_{10}$ in Figure 3-22 IV, V, VI. By 1 week, $AgNW_5$ started to lose their integrity, presumably in the acidic conditions within a phagosome as seen in Figure 3-22 I, II indicated by the black arrow. Non-dissolved fibres overlying the mesothelial cell layer appear intact in their morphology (Figure 3-22 II, white arrow). Ghost-like structures of nanofibres which are covered by microvilli (Figure 3-22 II, III star) could be seen. $AgNW_{10}$ could be found either in accumulations of inflammatory cells which appeared denser and more granulomatous after 1 week (Figure 3-22 IV cross), or in the mesothelial cell layer (Figure 3-22 IV triangle). $AgNW_{10}$ also started to lose integrity inside the phagocytic compartments of pleural macrophages (Figure 3-22 V cross). Figure 3-22 VI shows $AgNW_{10}$ partly membrane bound on the mesothelial cell layer. Direct comparison between the dissolution of $AgNW_5$ at 24 hour and 1 week is shown in Figure 3-23.

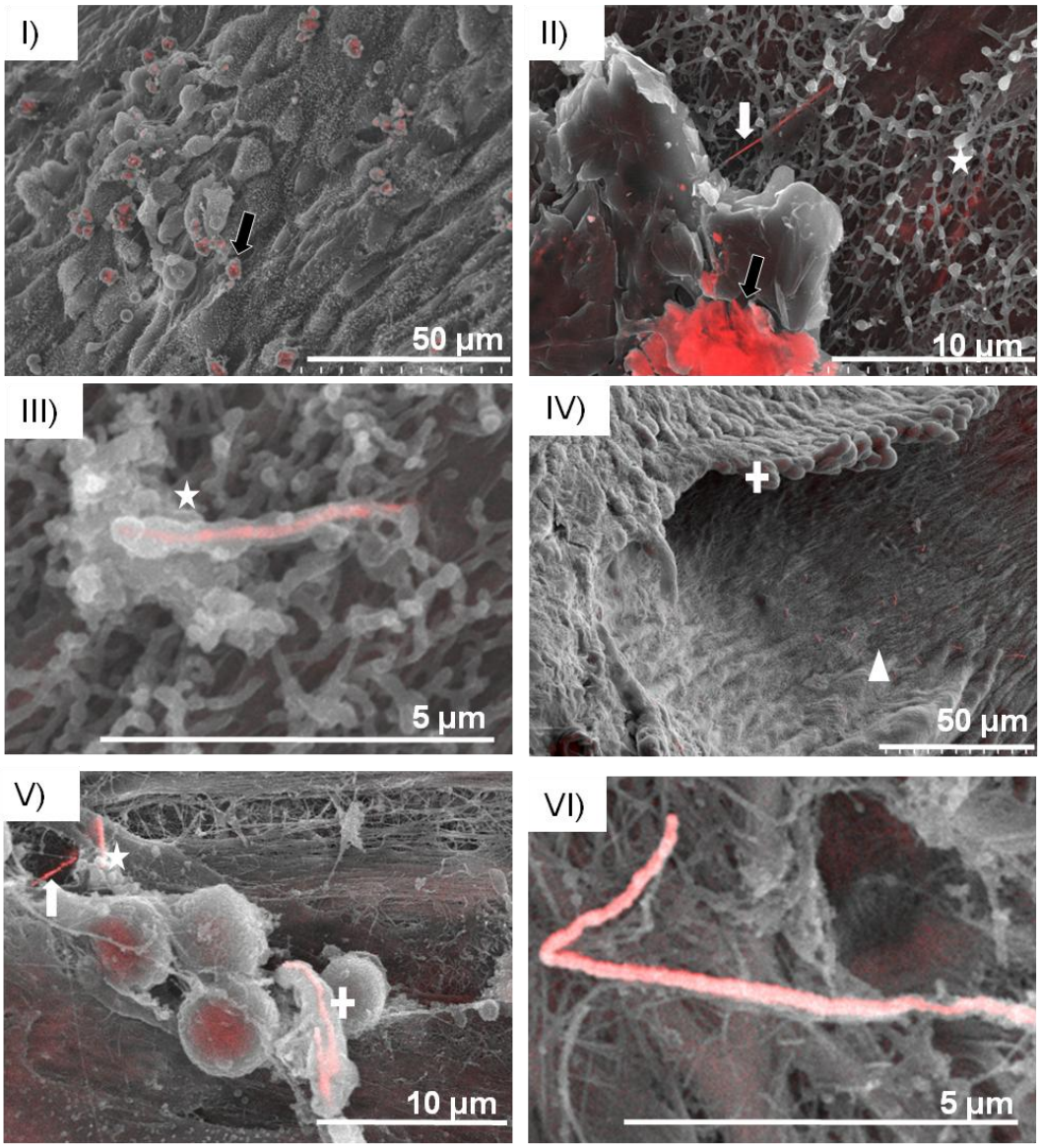

Figure 3-22: Images of macrophages on the parietal pleura 1 week post pleural instillation of $AgNW_5$ and $AgNW_{10}$. Lesion area showing $AgNW_5$ (I) dissolving inside macrophages, as can be seen by the loss of fibre structure (black arrow) (II). Intact nanofibres on the mesothelial cell layer as indicated by the white arrow (II) and membrane bound as indicated by the star (II,III). IV) Lesion area appears denser and more granulomatous after 1 week treatment $AgNW_{10}$ and occasional nanowires can be seen in these granulomatous areas as indicated by the white cross. Surprisingly, a large part of the nanowires were seen on and within the mesothelial cell layer indicated by the triangle. These nanowires appeared structurally intact whereas nanowires fully phagocytosed by macrophages as seen in V) indicated by

the cross on the right side start to dissolve under the acidic condition within a macrophage. On the top left of this image, a fibre is partly internalised (star) and partly exposed (white arrow). VI) $AgNW_{10}$ which is partly membrane bound on the mesothelial cell layer.N=2.

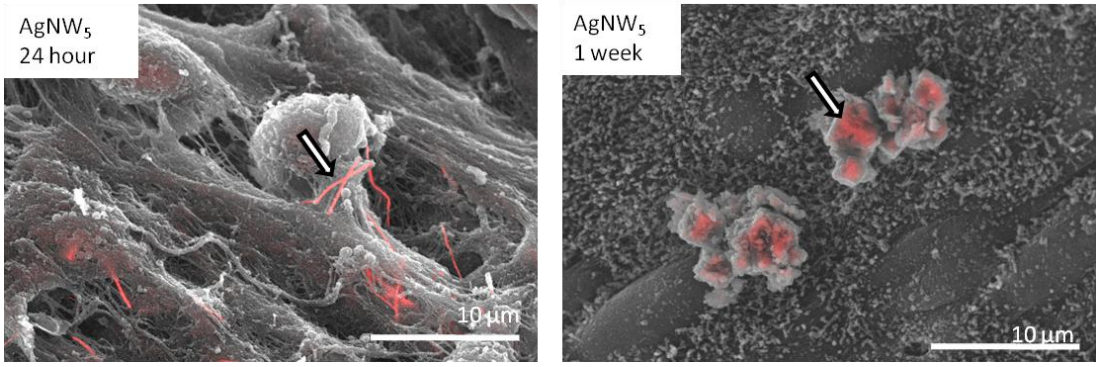

Figure 3-23: Integrity of $AgNW_5$ at 24 hour and 1 week. Merged secondary electron and backscatter electron SEM images of the parietal pleura from mice treated with $AgNW_5$. AgNWs appear intact in their morphology inside pleural macrophages 24 hour post-exposure, however after 1 week dissolution can be seen, evident as a more diffuse and 'ghost-like appearance of the AgNW (arrows) inside macrophages. N=2

3.3.14 Compartmentalisation of nanowires into mesothelial cells

So far, we hypothesised that after a prolonged exposure to fibres in general up to 7 days, the instilled fibres in the pleural space would either be cleared from the pleural space and enter the lymphatic drainage system or be accumulated in a granulomatous lesion on the parietal pleura at stomata (Boutin et al., 1996). By using backscatter imaging, for the first time it was possible to visualise nanowires in the mesothelial cell layer of the parietal pleura. Both treatments, $AgNW_5$ and $AgNW_{10}$ (but not $AgNW_3$ which were not observed as they had been cleared) showed nanofibres either on the surface of the mesothelial cells (black arrow Figure 3-24) or taken up by these cells (white arrow Figure 3-24 II). This is especially surprising for $AgNW_5$, since pleural macrophages are able to phagocytose these fibres completely under the applied treatment dose, as shown in Figure 3-17 II and Figure 3-18. By comparing

the structure/shape of the nanowires associated with the mesothelial layer (Figure 3-24) and within macrophages (Figure 3-22 II and V), it can quite clearly be seen that the nanowires are still intact after 1 week in the mesothelial layer whereas within the phago-lysosome of a macrophage the fibres start to degrade and lose integrity. These images show evidence that not all fibres longer than 5 µm are internalised by macrophages during the early inflammatory reaction, and that some are compartmentalised into the mesothelial layer which could lead to direct effects on the mesothelial cells that might pleural diseases in a later stage if they are biopersistent.

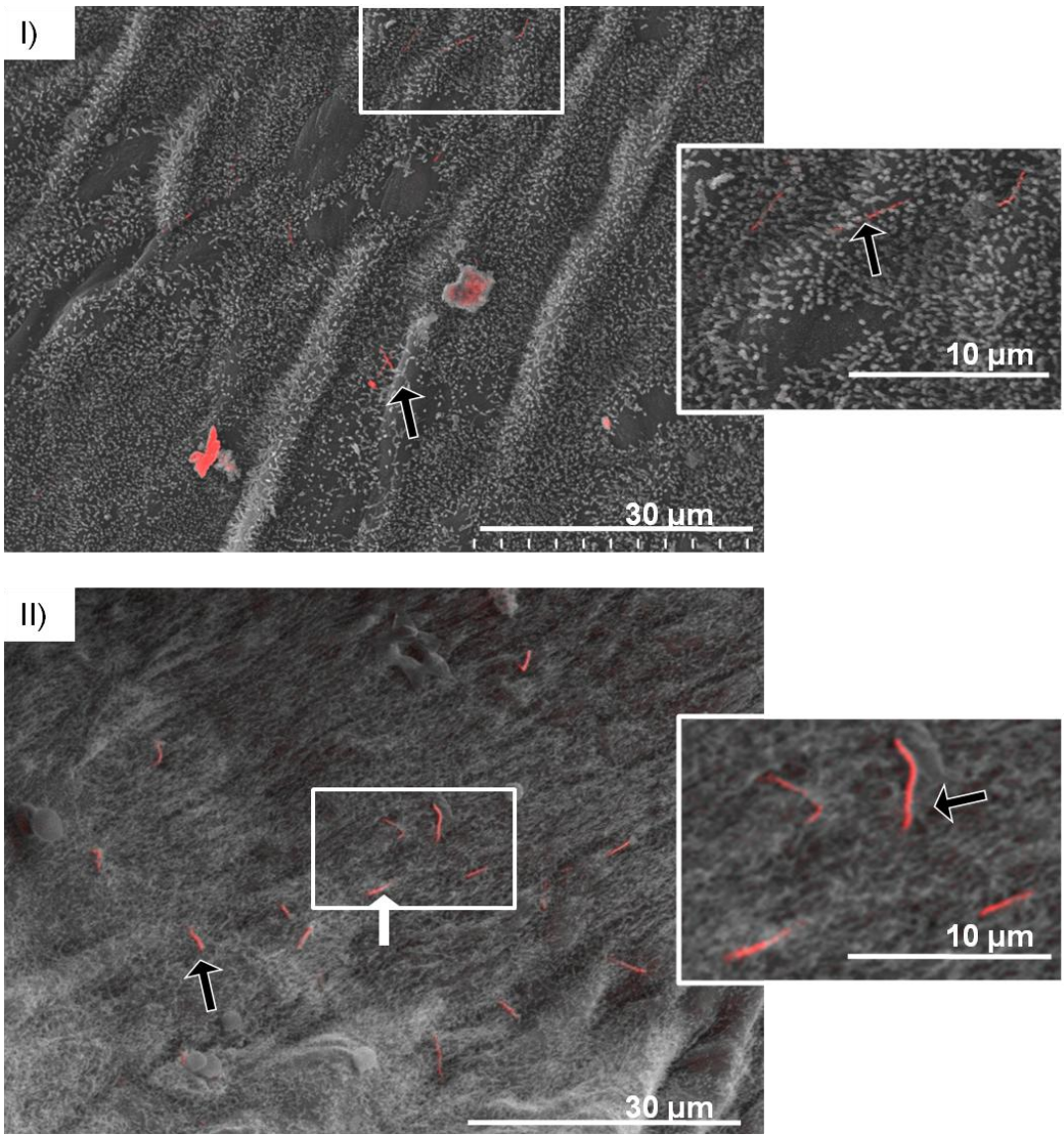

Figure 3-24: Mesothelial surfaces of the parietal pleura 1 week post injection of $AgNW_5$ and $AgNW_{10}$. Mesothelial cell layer of the parietal pleura after $AgNW_5$ (I) and $AgNW_{10}$ (II) exposure. AgNWs can be seen on the surface of the mesothelial layer as indicated by the black arrow. These AgNW are also partly taken up by mesothelial cells as indicated by the white arrow. The morphology of the nanofibres on the mesothelial layer appears intact.N=2.

3.4 Discussion

Thus far, the polydispersity of fibre length in samples including naturally occurring fibres and synthetic vitreous fibres prohibited the accurate investigation of the toxicity of various fibre lengths. In this study, the use of defined length classes of nanofibres allowed to quantify the threshold length for inflammatory effects in the pleural space, the key site for fibre pathogenicity.

A method of intrapleural injection of particles, previously described by Murphy *et al.* (Murphy et al., 2011) was used to measure acute inflammation in the pleural space.

A very specific panel of AgNW in different length classes was used and characterised according to their length, diameter, size distribution, concentration of soluble metals, dissolution behaviour and generation of free radicals. In depth characterisation of the material was essential to be able to link the pathological response observed after exposure to the material characteristics. From the fibre length distribution measurement, it can be seen that all AgNW length classes used in this study displayed a very tight distribution of length around their mean length which allowed the investigation of fibre length in relation to pleural inflammation. The concentration of soluble metals was determined in order to account for their effects in relation to pathophysiological response observed. This is especially important in the context of silver and its release of silver ions which could account for the observed effects from silver nanowires exposure. The role of silver ion in mediating a toxicological effect has been discussed extensively in the literature however the results are contradictory. Information about the role of Ag ion release in observed toxicity of silver particulates is mainly based on *in vitro* experiments at extremely high doses and cannot be correlated with *in vivo* observations (Johnston et al., 2010) and recent studies could not identify a significant health effect in *in vivo* studies after nanosilver exposure (Stebounova et al., 2011). If soluble silver was the explanatory factor for the pattern of inflammation after intrapleural silver nanowire injection, differences in the amount of soluble Ag release from the AgNWs should be observed. This was shown not to be the case and in fact all samples give off negligible amounts of silver ions or other contaminating metals in femto to pico grams dilutions that would not be biologically active. To confirm the integrity of the

AgNW fibre shape over the 24 hour exposure time, dissolution experiments were performed which showed a minimal extent of dissolution measured via pH change and no difference in morphological integrity could be detected after incubation of AgNW over 24 hour in a pH 5 solution.

NiNW were used as a control fibre to account for differences in the pathological response in terms of composition of the fibre samples. To preclude a role of the soluble, ionic fraction of NiNWs in the assay, the amount of Ni released was measured by ICP-MS. Thus, $NiNW_{4/20}$ and Ni-P were incubated with BSA/saline for 24 h and measured. The amount of soluble nickel detected in the supernatant solution did not differ between the short and long fibre sample and the Ni-P control. In addition, soluble Ni ions from the NiNW are unlikely to play a role since previous studies have shown that degradation of NiNW in biological media is minimal (Raphael et al., 2010).

The NiNW used in this study are covered by a 3-4 nm layer of nickel oxide (Prina-Mello et al., 2006) which is insoluble and so would prevent dissolution of the underlying nickel metal surface (Raphael et al., 2010); we also previously showed that the soluble products from NiO NP were not inflammogenic (Cho et al., 2012) in the lung. Following injection into the peritoneal cavity of NiNW from the same source as those used in the present study, only long NiNW produced a significant inflammatory response and not Ni nanoparticles or short NiNW (Poland et al., 2012). To completely rule out the effect of soluble Ni an aqueous extract of long NiNW was instilled into the peritoneal cavity and did not cause inflammation. We have previously shown that the response of the pleura and peritoneal cavities are identical in terms of the response to fibre length (Poland et al., 2012; Murphy et al., 2011), since the response is based on retention at stomata in the mesothelial lining in both cases. Therefore the release of Ni ions from long NiNW cannot explain any differences seen in the response to NiNW in the present study.

After careful characterisation of the AgNW samples, it was shown that the fibres differed only in their length distribution but were otherwise identical in composition, diameter and solubility. To measure the inflammatory potential of the nanofibre panel, intrapleural injections were performed. This method is justified on the basis

that a fraction of all inhaled particles and fibres that deposit in the peripheral lung translocate into the pleural space (Miserocchi et al., 2008; Walton, 1982; Mitchev et al., 2002; Mercer et al., 2010). By using the model of direct pleural instillation we bypassed various mechanisms of fibre clearance throughout the respiratory tract. However, recently rodent pharyngeal aspiration and inhalation models using CNT (Ryman-Rasmussen et al., 2009; Mercer et al., 2011) verified the translocation of inhaled CNT to subpleural region where they caused pleural inflammation. In the study by Ryman-Rasmussen *et al*. (Ryman-Rasmussen et al., 2009) MWCNTs were found sub-pleurally in macrophages, in sub-pleural mesenchymal cells and free in the collagen matrix of the sub-pleura. In the study by Mercer *et al*. the 'pleural penetrations' of CNT could be free fibre or fibres in macrophages (Mercer et al., 2011). However, so far the length threshold for fibres to reach the pleural space after inhalation exposure in rodent model is not known. Studies investigating the dimensions of asbestos fibres in mesothelial tissue from mesothelioma patients revealed that fibres up to a length of 62 µm were found in tumour tissue, with an average of 4.55 µm (Suzuki and Yuen, 2002). These data show that even the longest AgNW used in this study could potentially reach the subpleural tissue in humans after inhalation exposure. Long fibres translocated to the pleural space, both free or inside macrophages are retained because they cannot negotiate the stomata in the parietal pleura, through which the efferent flow of pleural fluid passes (Donaldson et al., 2010). We believe that this explains the propensity of long fibres to cause pleural effects including mesothelioma when compact particles and short fibres do not. However up to this point there has been no quantitative data on the threshold length for retention at the parietal stomata.

In this study, a dose of 5 µg was selected for intrapleural injection to allow comparison of the results with previously published data investigating the length dependent effect of CNT in the pleural space (Murphy et al., 2011).

The results from the intrapleural injection study using a range of different length of silver nanowires demonstrated a clear length threshold value for fibre pathogenicity in the pleural space of 5 µm. Significant increase in total cell number and granulocytes in the pleural space was observed after exposure to fibres of a length

including 5 µm and longer. Injecting a single dose into the pleural space, as we have done here, massively over-represents the number of fibres that reach the stomata compared to inhalation, yet there was no inflammatory effect of any of the short nanofibres. The fact that the huge dose and high dose rate of short fibres produced by instillation into the pleura proved non-inflammatory argues that the short fibres would be non-inflammatory to the pleura following inhalation, when the dose reaching the pleura and the dose-rate to the pleura would be vastly less than used here. To confirm this statement, a dose response series was performed whereby the dose of $AgNW_3$ was increased up to 10 µg/mouse and the dose of $AgNW_5$ was decreased to 1 µg/mouse. Even the highest dose of $AgNW_3$ used did not lead to a significant inflammation however the lowest dose of $AgNW_5$ showed increased inflammation which reached significance at a dose of 2.5 µg/mouse. As discussed earlier, the role of Ag ions released by AgNW might have accounted for the observed inflammatory response. Therefore, the supernatant of the AgNW solution was injected into the pleural space but not inflammatory reaction was detected. Although we found no difference between soluble extracts of short and long AgNWs measured by ICP-MS as reported above and no inflammation was detected after exposure to the soluble fraction of AgNW, the results may have been confounded by the formation of silver chloride. The issue of the potential formation of silver chloride from silver ions and chloride ions raises an important question as to whether silver ions could ever be toxic *in vivo* because of their rapid removal by formation of insoluble silver chloride following reaction with chloride ions, which are ubiquitous in biological systems. Furthermore it seems to be impossible to measure silver ion release from silver nanoparticles into biological media because chloride ions would always be present in biological media with formation of silver chloride.

We set out to determine whether length was a unifying factor in pleural inflammation across a range of HARN in addition to AgNW to rule out material-specific effects and to further determine the length threshold for pleural inflammation. We obtained good support for the contention that, for acute pleural inflammation, length is the predominant structural explanatory variable across a range of fibrous nanomaterials and asbestos.

In addition to measuring the acute inflammatory response in the pleural space via cell count, the mesothelial cell layer on the parietal pleura was examined in histological sections and via SEM. These investigations confirmed the observed inflammatory response since accumulations of inflammatory cells were detected after treatment with fibres ≥ 5µm.

The need for macrophages to internalise and clear fibres from the lung and the pleural space has long been accepted (Lehnert, 1992). In terms of clearance of long fibres it has been postulated that incomplete uptake of fibres, frustrated phagocytosis plays a major role in the development of an inflammatory milieu after exposure to fibres. An *in vivo* study performed by Oberdorster *et al.* assessed the clearance of small (~3 µm in diameter) and large (~10 µm in diameter) polystyrene microspheres in rat and identified minimal clearance of larger spheres after a 200 days post position period (Oberdorster et al., 1988). This was considered to be due to impaired clearance of particles when the macrophage particle load is 60% of its normal volume. It was recently demonstrated that frustrated phagocytosis is a major factor in the genesis of inflammation in the peritoneal and pleural space after deposition of long fibres whereby macrophages undergoing frustrated phagocytosis of the long fibres (Poland et al., 2008; Murphy et al., 2012b). However, so far frustrated phagocytosis has not been fully visualised *in vivo* in the pleural and the cut-off length below which complete internalisation of particles/fibres occurs is unknown. The use of a novel technique, backscatter electron microscopy allowed to distinguish between membrane bound fibres and unphagocytosed fibres and to visualise the interaction of inflammatory cells with different length of nanofibres on the parietal pleura, the site of fibre retention *in vivo*.

Here nanofibres in tight size ranges enabled us to show that true frustrated phagocytosis, where fibres actually protrude from the surface of the cell, is not necessary for long fibre-induced inflammation in the pleural space. This is argued on the basis that $AgNW_5$ caused inflammation in the pleural space but was for the most part phagocytosed by pleural macrophages. These results show that frustrated phagocytosis is not solely responsible for the onset of an inflammatory reaction in the pleural space after exposure to fibrous particles and that fibres around 5 µm can

be fully phagocytosed but nonetheless cause sufficient cellular stress to induce pro-inflammatory effects.

To investigate the time course of the response, a single intrapleural injection of the nanofibre panel was performed and the inflammation measured after a 1 week timepoint. The amount of inflammatory cells in the pleural lavage fluid was reduced compared to the 24 hour timepoint showing only a significant increase of granulocytes after longest fibre treatment LFA, $AgNW_{14}$ and $AgNW_{28}$. However, histology and SEM showed a similar pattern to the 24 hour data with inflammatory aggregates on the mesothelial cell surface after treatment with fibres ≥ 5 µm.

Investigations of the parietal pleura revealed that nanofibres started to lose their integrity at the 1 week timepoint and dissolve within macrophages and start to loose their integrity between the 24 hour and 1 week timepoint. Intact nanofibres were found on the normal mesothelial cell layer after 1 week exposure. So far, we hypothesised that fibres, which are retained in the pleural space would be accumulated in lesions on the parietal pleura. In this study the mesothelial cells did not seem to be pro-inflammatory in this position as they have not attracted leukocytes to their vicinity and so their main effect may be by direct genotoxic or cytotoxic effects on the mesothelial cells. A lack of direct pro-inflammatory effect of the nanowires on the mesothelial cells would be consistent with the study by Murphy *et al.* (Murphy et al., 2012b) on the interactions between long carbon nanotubes, macrophages and mesothelial cells in the genesis of inflammation. Work with long carbon nanotubes show that fibres interacting with macrophages cause the macrophages to release factors that evoke large scale production of inflammatory mediators by adjacent mesothelial cells (Murphy et al., 2012b). Activated mesothelial cells produce a number of pro-inflammatory mediators including prostaglandins, nitric oxide, reactive oxygen species, cytokines and growth factors. Prolonged release of these pro-inflammatory mediators due to retention of fibres on the mesothelial surface may play a role in stimulation tumour growth (Mutsaers, 2002). Further studies have investigates the signalling pathways and aberrant transcriptional responses involved in mesothelial cell proliferation after asbestos exposure and showed an induction of c-fos and c-jun protooncogene mRNA and

protein in pleural mesothelial cells as well as an increase in AP-1 DNA binding (Heintz et al., 1993). In addition, asbestos fibres have been shown to activate EGFR in mesothelial cells leading to the downstream activation of ERKs involved in the regulation of cell survival, motility and cell transformation (Zanella et al., 1996).

In contrast direct interaction between carbon nanotubes and mesothelial cells *in vitro* produced very little pro-inflammatory cytokine release by the mesothelial cells however led to significant membrane damage at higher carbon nanotube concentrations at a similar extent to that seen in macrophages (Murphy et al., 2012b). A study by Adamson reported that exposure to long (≤ 20 μm) crocidolite asbestos fibres led to increased pleural mesothelial cell proliferation in mice however no uptake of fibres in mesothelial cells was observed and again an indirect effect of mitogens released by cells in the sub-pleural lung tissues was implicated (Adamson, 1997). Therefore nanofibres that escape macrophage phagocytosis and take up residence in the mesothelium may be relatively non-inflammatory but represent a direct genotoxic threat. The interaction of AgNW with mesothelial cells changed their biopersistent characteristics, since AgNW appeared intact in their shape compared to compartmentalisation in macrophages where dissolution is observed.

The greater pathogenic potency of long asbestos fibres in asbestos-induced pathology was identified in animal studies in the first half of the 20th century and with special reference to mesothelioma in the later studies of Stanton *et al. (Stanton and Wrench, 1972)* and Davis *et al* (Davis et al., 1986). A mechanistic basis for the extra pathogenic effect of long asbestos fibres is evident in the greater retention of long fibres in the pleural space compared to short fibres and the greater potency of long fibres in general at eliciting pro-inflammogenic effects *in vivo* (Poland et al., 2008) and *in vitro (Poland et al., 2012).* The data here suggest that 5 μm, and above in length, are likely to be retained at the stomata where they can elicit inflammation. However, there is no doubt that a high enough dose of the shorter fibres would be inflammogenic in the pleural cavity due to artefactual aggregation into mats and clog in the stomata. This was shown previously by Goodglick *et al*. in the peritoneal cavity which possesses identical stomatal mechanism for fibre clearance (Goodglick and Kane, 1990). In the study the inflammatory response in the peritoneal cavity was

measured after injection of 120 µg short (24 % of fibres between 1.1-5.0 µm) and long (55 % of fibres between 1.1-5.0 µm) crocidolite asbestos fibres over 5 days. The study showed that the short fibres used in this study elicited an inflammatory response after the 5 day exposure due to a saturation of clearance mechanism and therefore accumulation of fibres, however no further examination was performed to investigate whether the uncleared short fibres are cytotoxic, fibrogenic, or carcinogenic (Goodglick and Kane, 1990).

Naturally, for purposes of extrapolating to the human risk relating to fibre length, the size of human parietal pleural stomata, the site of long fibre retention, is most relevant. Across mammalian species there is a remarkable consistency in the reported size of stomata on the diaphragm or parietal pleura (Table 1-1). This suggest that the findings of a general threshold for fibre retention that is applicable to humans is well-served by the mouse model described here. One can only speculate on the events that follow from first retention of a long fibre at a stoma but the lodging of a long fibre at a stoma and recruitment of inflammatory cells to it may enhance the likelihood of further retention of long fibres and led eventually to effective blockage of the stoma.

It is worth mentioning that the global regulation of fibres is based on a standard definition of a fibre as an object that has a length greater than 5 µm, a width less than 3 µm and an aspect ratio of greater than 3:1. The 5 µm length regulatory standard was defined in the middle of the last century and its origin was described in 1983 by Walton (Walton, 1982). It is fortuitous that the length of 5 µm was chosen, albeit without recourse to any scientific knowledge on length-dependent parietal pleural retention, as a margin of safety from long fibres (10-20 µm) that were known, even then, to be the most pathogenic fraction (Walton, 1982).

This study is of course a study of a short-term response, however short term response is rationally related to long-term pathology in the pleural space and the argument for this is twofold. The first is the argument of dose, by which we mean that the model we put forward relies on acute inflammation as both a marker of – and a response to - retention in the pleural space and we confirm here that short fibres transit out of the pleural space. So long fibres must represent the only dose that could be related to the

acute- but importantly also the chronic - responses seen in the pleural space to fibres. The second argument is based on the fact that the endpoint studied, inflammation is known to be directly related to fibrosis and cancer caused by asbestos through well-understood pathways and mechanisms (Dostert et al., 2008; Dai and Churg, 2001; Nagai and Toyokuni, 2010; Unfried et al., 2002).

The fact that the silver nanowires used here were not biopersistent beyond a few days does not detract from the relevance of the length-dependent effects demonstrated here. Biopersistent fibres of the same dimensions would have the same acute effect as silver nanowires but, in contrast, would evoke an ongoing chronic inflammatory response that would lead to pathological change as we have reported for long biopersistent multi-walled carbon nanotubes (Murphy et al., 2011). A clear link therefore exists between fibre length and the potential to cause acute inflammation; additionally there is a link between fibre biopersistence and ability for the acute inflammation to become chronic and a link between chronic pleural inflammation and the common pleural pathologies associated with asbestos exposure -pleural fibrosis and mesothelioma.

Biopersistence therefore remains a key factor in determining pathogenic effects of long nanofibres and warrants further elucidation if the biopersistent nanofibres in narrowly defined length classes similar to the AgNW can be obtained. This data suggest that any long biopersistent fibre will be retained on the parietal pleura and is likely to engender chronic inflammation.

The conclusion of the threshold length of this study is mainly based on linear straight single fibres. However long fibres that are tangled and agglomerated in their overall morphology, as is often the case with tangled CNT, have been shown to cause less inflammation due to their tightly packed spherical agglomerated state (Murphy et al., 2011; Poland et al., 2008). Therefore the aggregation state of nanofibres has to be considered on order to assess their toxicity.

In summary, our data provides for the first time a quantitative threshold for respirable fibre length in inducing pleural inflammation using a range of nanofibres. The threshold length for inducing pleural inflammogenicity in a range of fibres

including amosite asbestos is 5 µm in the mouse which we suggest can be extrapolated to humans. This knowledge is a valuable addition to our understanding of the mechanism of asbestos–related pleural disease especially for mesothelioma and its relationship to fibre length. We recognise that this research was carried out in a mouse model and with a necessarily restricted range of nanofibres and that extrapolation to humans is not straightforward. Therefore, for regulatory purposes, we urge further research on the important issue of the threshold length for safe fibres as regards the mesothelioma hazard to the pleura and the role of biopersistence. From the present data however we may conclude that, for acute inflammation, there is good evidence that short fibres less than 5 µm form the basis of safer- by- design nanofibres and this has important implication for fibre and nanofibre risk assessment.

Chapter 4: *In vitro* studies on the mechanism of the length dependent inflammation caused by AgNW.

Some of the following results have been published in

Schinwald A & Donaldson K. Use of back-scatter electron signals to visualise cell/nanowires interactions *in vitro* and *in vivo*; frustrated phagocytosis of long fibres and compartmentalisation in mesothelial cells. Part Fibre Toxicol. 2012 Aug 28;9(1):34.

4.1 Acknowledgement

The study on the NALP3 inflammasome was performed at Trinity College Dublin, School of Biochemistry and Immunology under the supervision of Prof. Luke O'Neill. NALP3 $^{-/-}$ mice were provided by Dr Ed Lavelle and Prof. Luke O'Neill. Protocols for the study on the NALP3 inflammsome and ASC complex formation in BMMs were obtained from Dr Rebecca Coll. *In vivo* studies on NALP3 $^{-/-}$ were performed under the supervision and help of Dr Sinead Corr. ASC-CFP stable transfected cell line was obtained from Prof. Luke O'Neill.

4.2 Aims and Hypothesis

In the previous chapter we have shown that nanofibres cause a length dependent inflammation in the pleural space, however didn't elicit the cellular mechanism leading to inflammation caused by nanofibres.

Here, we focused on cell/nanofibre interactions *in vitro* to examine the ability of long fibres to elicit a pro-inflammatory response in macrophages derived from the human monocyte cell line (THP-1) and murine bone marrow derived macrophages, by direct exposure to AgNW. Frustrated phagocytosis, cytokine and chemokine expression as well as the mechanism of the NALP3 inflammasome activation including IL-1β and

caspase 1 expression as well as ASC complex formation were measured as an indicator of the pro-inflammatory potential of AgNWs. We hypothesised that the length dependent inflammation seen *in vivo* will be reflected by a length dependent activation of cells *in vitro*.

4.3 Results

4.3.1 Membrane integrity and metabolic activity in THP-1 macrophages after AgNW treatment

The *in vitro* experiments were based on a treatment dose which was non/low-toxic to THP-1 cells in culture and was adjusted for fibre length to ensure approximately the same fibre number for each treatment (Table 2-1). The 2 µg/cm^2 dose based on $AgNW_{14}$ was determined by measuring the membrane integrity via the release of lactate dehydrogenase (LDH) into the supernatant and cell proliferation/metabolic activity of the THP-1 cells after 24 hour treatment. All treatments, with exception of $AgNW_{28}$ showed no significant increase in membrane integrity and loss of proliferation and metabolic activity (Figure 4-1).

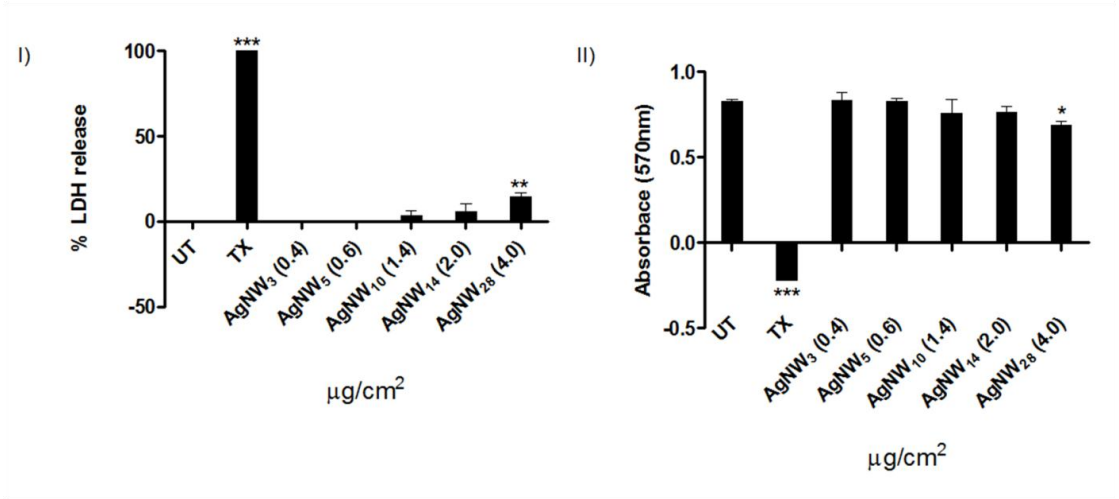

Figure 4-1: THP-1 membrane integrity and proliferation/metabolic activity. I) Measurement of membrane integrity plotted as % LDH release based on the positive and negative control. Only $AgNW_{28}$ led to a significant release of LDH into the supernatant. II) Proliferation and metabolic activity was measured using

*alamarBlue®. Cells treated with $AgNW_{28}$ showed decreased proliferation. Significance versus vehicle control *P <0.05, **P <0.01. Data represent mean+ S.E.M. of n=5.*

4.3.2 Bright field microscopy of THP-1 cells after 4 hour exposure *in vitro*

THP-1 cells were exposed to the panel of AgNWs for 4 hours and bright field images were taken using a 60x magnification. THP-1 cells completely phagocytose $AgNW_3$ (Figure 4-2 I) and $AgNW_5$ (Figure 4-2 II). The fibres were fully taken up as indicated by the yellow circle. $AgNW_{10}$ were mostly phagocytosed with only a small percentage of fibre-ends protruding out of the cells as indicated by the red arrow (Figure 4-2 III). Frustrated phagocytosis was observed after treatment with $AgNW_{14}$ (Figure 4-2 IV) and $AgNW_{28}$ (Figure 4-2 V). In Figure 4-2 IV the black arrow indicates a fibre shared by two cells and another fibre only partly enclosed by the cell (red arrow Figure 4-2 IV and V).

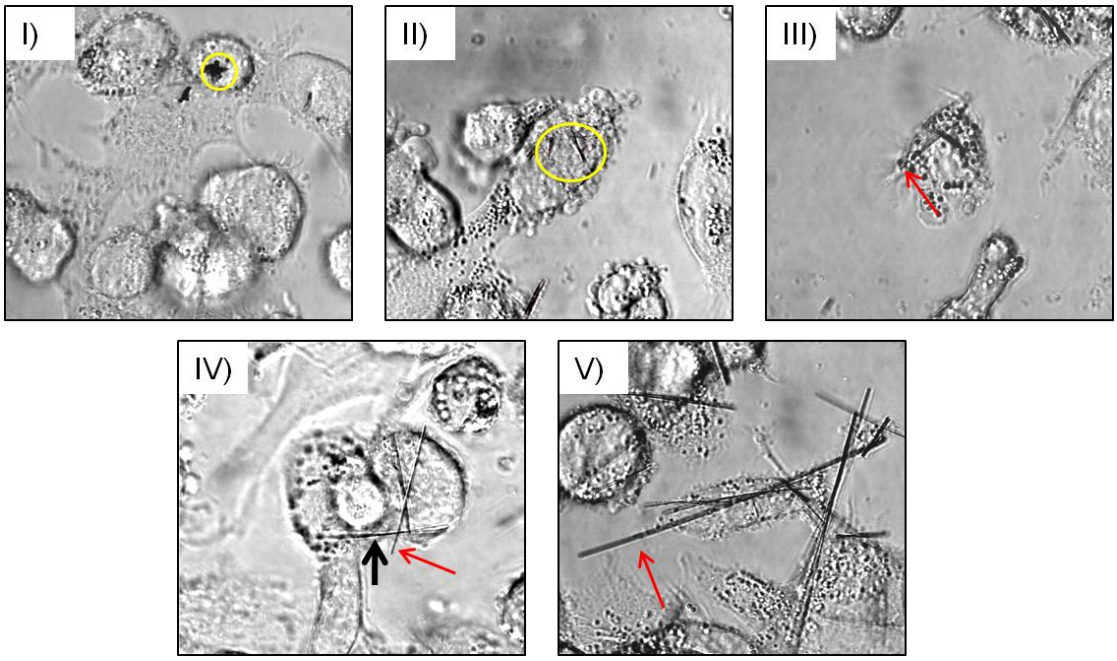

Figure 4-2: Bright-field microscope images of THP-1 cells treated with AgNWs. I) $AgNW_3$ and II) $AgNW_5$ were fully enclosed by the cell as indicated by the yellow circle. III) $AgNW_{10}$ were mostly taken up, however a small number of fibres were not fully enclosed and fibre ends were protruding out of the cells as indicated by the red arrow. IV) $AgNW_{14}$ and III) $AgNW_{28}$ caused frustrated phagocytosis. Red arrows indicate fibres partly taken up by THP-1 cells and the black arrow indicates sharing of a fibre between two adjacent cells. Scale bar 20µm. Images are representative of an n=3.

4.3.3 Characterisation of cell/nanowire interaction *in vitro* using BSEM

Backscatter electron microscopy (BSEM) enabled us to visualise the interaction of THP-1 macrophage cells with AgNW. We mainly focused on the uptake/phagocytosis of the five different size categories of AgNW to identify the cut-off value, at which frustrated phagocytosis occurs *in vitro*. Figure 4-3 I-V show differentiated THP-1 macrophages after 4 hour treatment with $AgNW_3$ (I), $AgNW_5$ (II), $AgNW_{10}$ (III), $AgNW_{14}$ (IV) and $AgNW_{28}$ (V). In Figure 4-3 I one external $AgNW_3$ can be seen (white arrow) and a few $AgNW_3$ can be seen just underneath the surface of a macrophage as indicated by the black arrow (Figure 4-3 I insert). After treatment with $AgNW_5$, nanowires were fully taken up by macrophages as indicated by the white arrow (Figure 4-3 II insert). A small proportion of cells showing incomplete uptake of $AgNW_{10}$ fibres could be observed as indicated by the white arrow (Figure 4-3 III) however, most of the fibres were membrane bound (black/white arrow) and therefore phagocytosed by the cells. Obvious frustrated phagocytosis could be observed from a nanowire length of 14 µm (Figure 4-3 IV) and 28 µm (Figure 4-3 V). A much greater amount of AgNW was observed protruding through cells or shared between adjacent cells, indicating frustrated phagocytosis (white arrow). The number of unphagocytosed fibres per cell was quantified and significantly increased with $AgNW_{14}$ ($p>0.05$) and $AgNW_{28}$ ($p>0.001$).

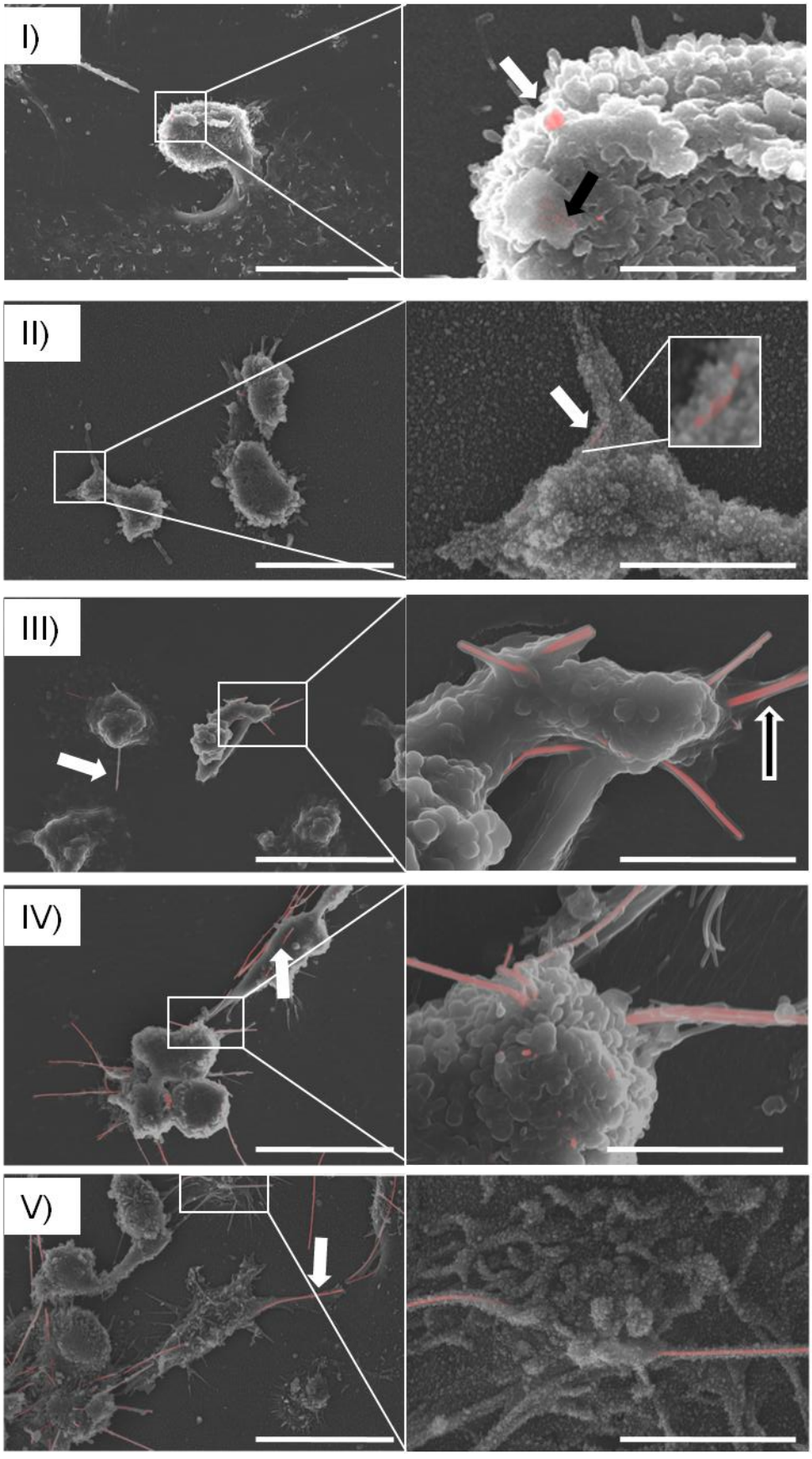
I)
II)
III)
IV)
V)

Figure 4-3: BSE images of differentiated THP-1 cells treated for 4 hours with AgNW. I) $AgNW_3$ treated macrophages showed full phagocytosis of the nanowires. Only one nanowire could be visualised outside a cell (white arrow) and a few underneath the surface indicated by the black arrow. II) After $AgNW_5$ treatment all nanowires were phagocytosed by cells after 4 hours (white arrow). III) A big proportion of $AgNW_{10}$ appear membrane bound and therefore phagocytosed by cells (black/white arrow), however a few fibres could be seen protruding out of cells (white arrow). Frustrated phagocytosis was observed after $AgNW_{14}$ (IV) and $AgNW_{28}$ (V) treatments, since most of the fibres can be seen protruding out of the cells or shared between cells (white arrow and insert). BSE merged image with a scale bar of 10µm and 5µm for the inserts.Images are representative of an n=3.

4.3.4 Screening of cytokines and chemokines involved in the inflammatory response to AgNW exposure

To assess which cytokines/chemokines were involved in acute inflammation after particle exposure a cytometric bead array was performed. THP-1 macrophages were exposed to a dose of 2 µg/cm^2 based on $AgNW_{14}$ (see Table 2-1) and SFA/LFA (0.4 and 2 µg/cm^2 , respectively) and a selected panel of cytokines and chemokines; TNF, IL-6, IL-8, IL-1β, CCL-2 (MCP-1), CCL-5 (RANTES), CCL-3 (MIP-1α), basic FGF, IL-13 and TGF-β were measured. Out of this range of cytokines, CCL-2, CCL-3 and IL-8 were significantly increased after $AgNW_{28}$ and LFA exposure with no significant effect of shorter AgNW exposure on these mediators (Figure 4-4).

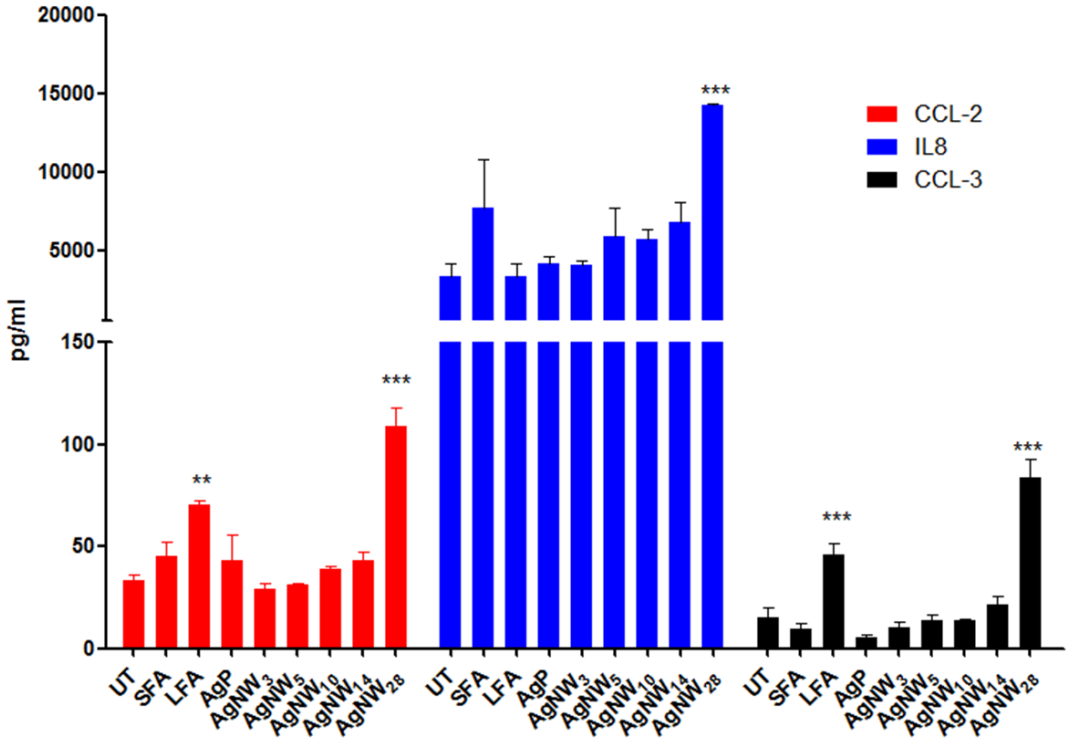

Figure 4-4: Screening of a panel of 10 cytokines/chemokines after exposure to AgNW and SFA/LFA. Three cytokines (CCL-2, IL-8 and CCL-3) out of 11 tested were significantly upregulated after a 24 hour exposure to $AgNW_{28}$ and LFA. Shorter fibre treatment did not led to a significant increase in any of the cytokines measured. Data expressed as mean + s.e.m, n=3. (**) P < 0.01, (***) P < 0.001 compared to vehicle control.

4.3.5 Lysosomal destabilisation in THP-1 macrophages after AgNW treatment

Lysosomal destabilisation has been linked to the inflammogenicity of long fibres as well as cholesterol crystals and silica (Rajamaki et al., 2010; Palomaki et al., 2011; Hornung et al., 2008), in relation to activation of the NALP3 inflammasome. Lysosomal membrane stability was assessed in macrophages *in vitro* after treatment with AgNWs using acridine orange (AO). THP-1 macrophages were treated for 4 hours with AgNWs and controls. After 4 hour treatment, images were obtained from live cells and the area of red lysosomal staining in each cell was quantitatively analysed. A significant decrease in lysosomal membrane integrity was observed after

exposure to $AgNW_{5-28}$ and sphingosine, a positive control for lysosomal rupture (Figure 4-5 I and II). AgP and $AgNW_3$ had similar amounts of lysosomal staining compared to vehicle control (Figure 4-5 I and II).

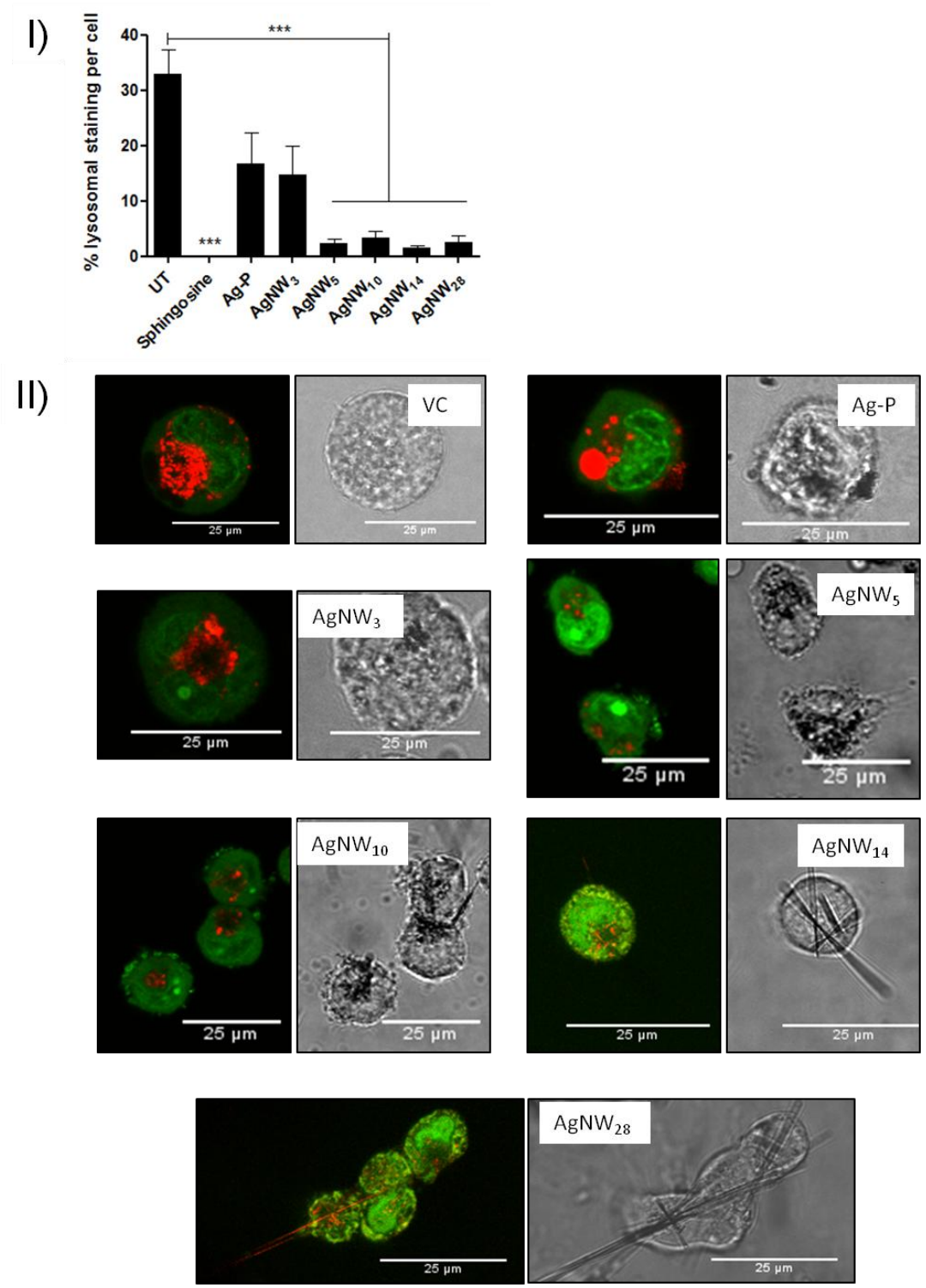

*Figure 4-5: Loss of lysosomal integrity as a marker for inflammasome activation. I) Quantification of lysosomal membrane destabilisation expressed as percentage of lysosomal staining (AO) per cell. A significant decrease in lysosomal membrane integrity in THP-1 cells could be observed after exposure of $AgNW_{5-28}$ at a concentration of 5 µg/cm² and sphingosine, a positive control for lysosomal rupture (*** indicates p<0.001). Data represent mean + S.E.M. of n=4. II) Representative confocal microscopy images (left panel) and brightfield images (right panel) of each treatment to visualise loss of lysosomal membrane integrity using AO. VC, Ag-P and $AgNW_3$ showed no significant decrease of lysosomal membrane integrity after 4 hour treatment, however $AgNW_5$, $AgNW_{10}$, $AgNW_{14}$ and $AgNW_{28}$ led to a significant loss of membrane integrity as seen by the decrease in lysosomal red staining.*

4.3.6 Activation and secretion of the pro-inflammatory cytokine IL-1β

Secretion of the pro-inflammatory cytokine IL-1β has been reported in macrophages after exposure to various fibres such as CNTs, silica, asbestos and TiO_2 (Murphy et al., 2012b; Hornung et al., 2008; Hamilton et al., 2009). To assess the secretion of IL-1β after exposure to AgNW, murine BMMs were exposed to a range of concentrations from 0.5 to 26 µg/cm^2 of AgNW (see details in chapter 2.3.12.1 and Table 2-3). Control particles comprised of SFA (5.5 µg/cm^2), LFA (26 µg/cm^2) and aluminium hydroxide (Alum) (100 and 200 µg/ml). Prior to the treatment BMMs were stimulated with LPS (10 ng/ml). Western blot analysis for the detection of IL-1β was performed at various different conditions, by changing the exposure time of AgNWs and controls as well as the LPS- priming time, the concentrations used for exposure as well as cell number used for the experiment but no consistent results could be obtained. The results as shown below are merely to give an indication of the extent of variation between results and are not representative for the whole study on IL-1β expression.

The extent of pro- IL-1β and IL-1β was measured in the cell lysate and the supernatant (Figure 4-6 I). 24 hour exposure of BMMs to AgNW led to the production of active IL-1β in the cell lysate at all concentrations measured. In

addition, secreted IL-1β was measured in the supernatant after exposure to $AgNW_5$ at 10 µg/cm^2 (H1) and $AgNW_{14}$ at all concentrations. For the control fibre LFA, IL-1β was measured in the cell lysate and to a lesser extent in the supernatant (Figure 4-6 I). Alum was used as a positive control for IL-1β activation and secretion which was shown in the supernatant (Figure 4-6 I). The experiment was repeated 6 times, showed however varying results in regards to the extent of mature IL-1β expression in the cell lysate as well as the supernatant with an n=3 showing similar results as shown in Figure 4-6 I. The experiment was repeated using a 6 hour exposure to AgNW and controls (see details for concentrations Table 2-3) but showed no production of active IL-1β nor secretion of IL-1β in the supernatant (Figure 4-6 II) (n=6). In addition to wild-type mice, NALP3 $^{-/-}$ mice were used to assess the production and secretion of IL-1β after treatment to AgNW and controls. NALP3$^{-/-}$ mice showed no production of mature IL-1β at any treatment, which was replicated in three independent experiments (Figure 4-6 III).

I) Cell lysate

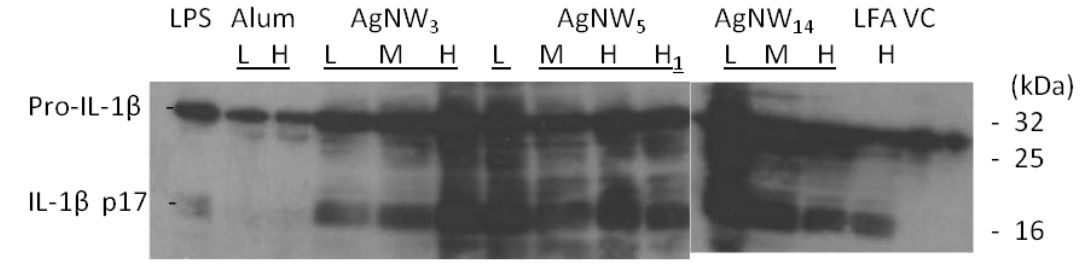

Supernatant

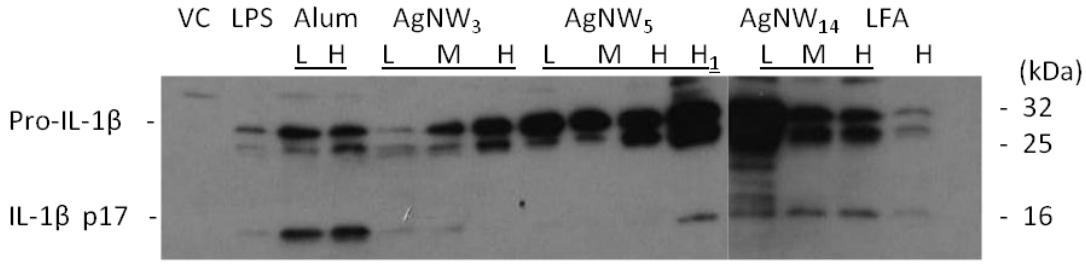

II) Cell lysate

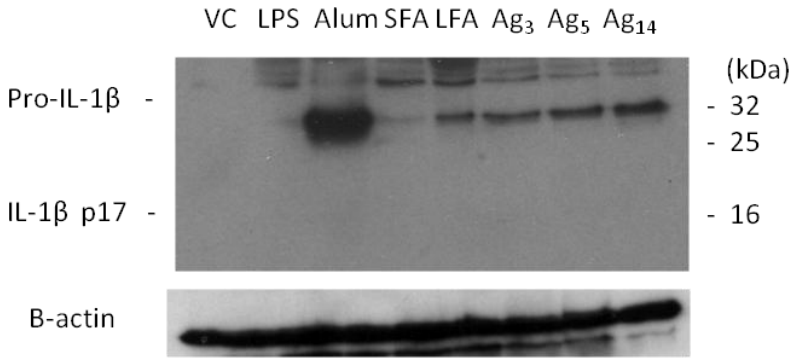

Supernatant

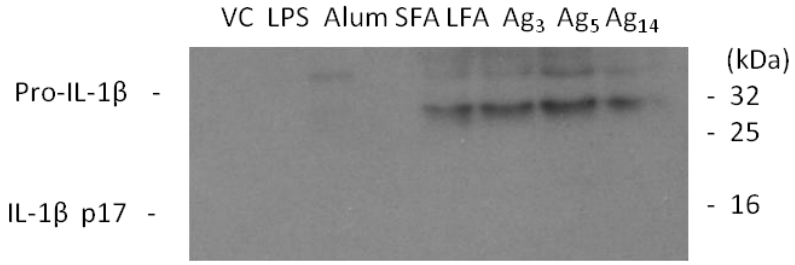

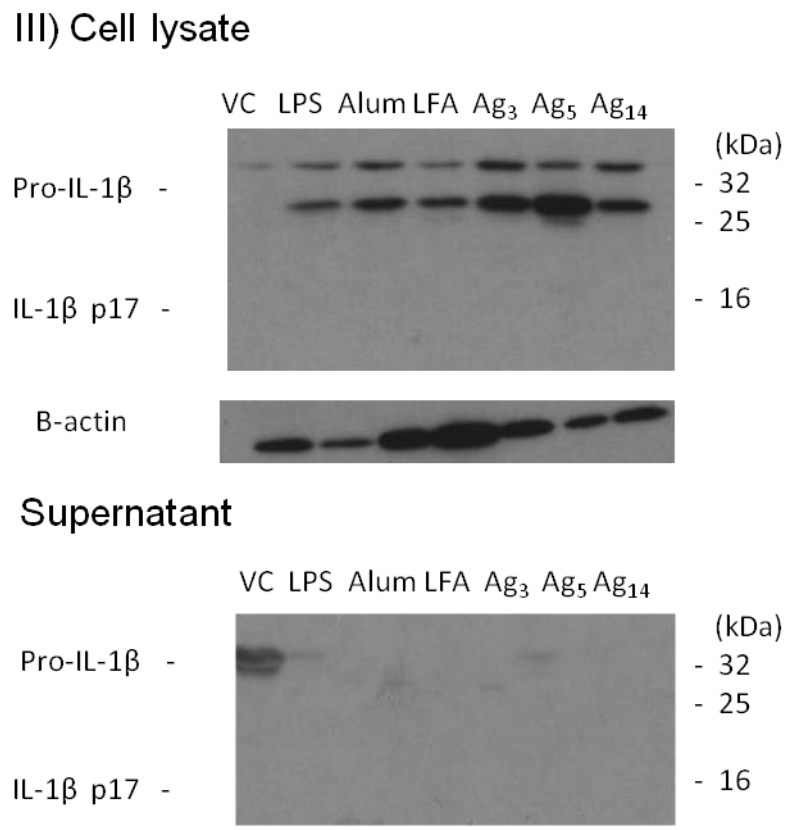

Figure 4-6: Detection of IL-1β activation and secretion in BMMs of WT and NALP3$^{-/-}$ mice after treatment with AgNWs and controls. I) BMMs were treated for 24 hours with $AgNW_3$ and $AgNW_{14}$ at a low (0.5 µg/cm²), medium (2.5 µg/cm²) and high (10 µg/cm²) dose. For $AgNW_5$ a range of doses from low (0.5 µg/cm²), medium (1 µg/cm²), high (5 and 10 µg/cm²) was used. The concentration of LFA used was 100 µg/ml (~26 µg/cm²) based on a previous study (Dostert et al., 2008). Alum was used as a positive control for NALP3 inflammasome activation and was used at a concentration of 100 and 200 µg/ml. Prior to treatment with the fibre panel, cells were primed with LPS at a concentration of 10 ng/ml for 3 hours. Active IL-1β was detected in the cell lysate as well as in the supernatant after treatment with AgNWs and LFA. Alum showed strong secretion of IL-1β in the supernatant (n=3). II) BMMs were treated for 6 hours with AgNW at a dose based on fibre number ($AgNW_3$- 5.5 µg/cm^2, $AgNW_5$ 9.5 µg/cm^2, $AgNW_{14}$ 26 µg/cm^2). Concentration for SFA and LFA was 5.5 and 26 µg/cm^2, respectively. Alum was used at a concentration of 20 µg/ml. BMMs were treated for 6 hours. Prior to treatment with the fibre panel, cells were

primed with LPS at a concentration of 10 ng/ml for 12 hours. No production of IL-1β was detected in the cell lysate and the supernatant(.n=6). III) BMMs from Nalp3$^{-/-}$ mice were treated as described for II but no production of mature IL-1β was detected in the cell lysate and the supernatant (n=3).

4.3.7 Detection of caspase 1

The formation of the NALP3 inflammasome leads to the activation of pro-caspase 1 to its mature form which consequently activates pro- IL-1β to form IL-1β (Taniguchi and Sagara, 2007). Pro-caspase 1 and the formation of caspase 1 was detected via Western blotting in cell lysate and supernatant of BMMs treated with AgNWs and controls. Treatment conditions were the same as described above (see chapter 2.3.12.1 and

Table 2-3). Western blot analysis for the detection of caspase 1 was performed at various different conditions, by changing the exposure time of AgNWs and controls as well as the LPS- priming time, the concentrations used for exposure as well as cell number used for the experiment but no consistent results could be obtained. The results as shown below are merely to give an indication of the extent of variation between results and are not representative for the whole study on caspase 1 expression.

A length- and dose-dependent activation of caspase 1 was detected after AgNW and LFA treatment at a 24 hour timepoint, whereby $AgNW_3$ at 10 μg/cm² (high dose) showed a slight increase in caspase 1 production in the cell lysate compared to VC (Figure 4-7 I). $AgNW_5$ showed a dose- dependent increase with highest production of caspase 1 in the cell lysate at 10 μg/cm² which was similar in $AgNW_{14}$ and LFA treated BMMs (Figure 4-7 I). In the supernatant, caspase 1 was detected only after treatment with Alum, in a dose-dependent manner (Figure 4-7 I). The experiment was repeated 6 times, showed however varying results in regards to the extent of mature caspase 1 expression in the cell lysate as well as the supernatant with an n=2 showing similar results as shown in Figure 4-7 I. At a 6 hour timepoint, alum led to a production of caspase 1 in the cell lysate and the supernatant (Figure 4-7 II).

Caspase 1 was also detected after $AgNW_{3,5,14}$ treatment in the cell lysate and $AgNW_5$ and $AgNW_{14}$ in the supernatant (Figure 4-7 II) (n=2). In addition to wild-type mice, NALP3 $^{-/-}$ mice were used to assess the production of caspase 1 after treatment to AgNW and controls. NALP3$^{-/-}$ mice showed no production of mature caspase 1 at any treatment, which was replicated in three independent experiments (Figure 4-7 III).

I) Cell lysate

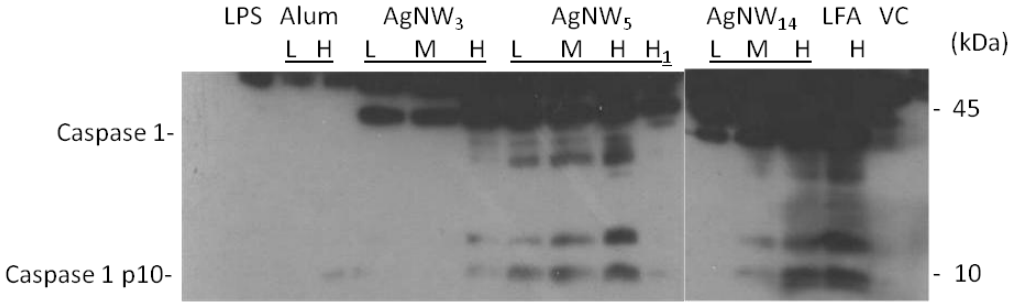

Supernatant

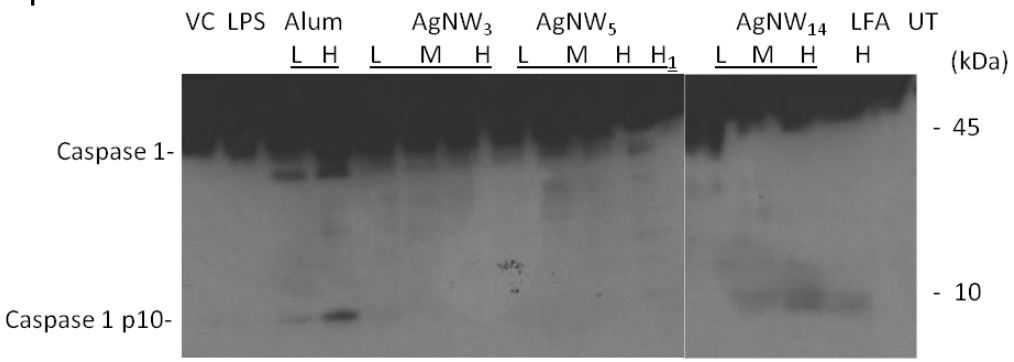

II) Cell lysate

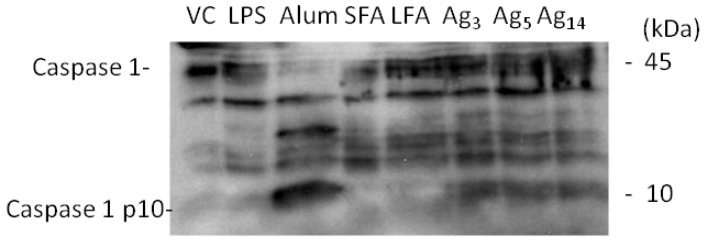

Supernatant

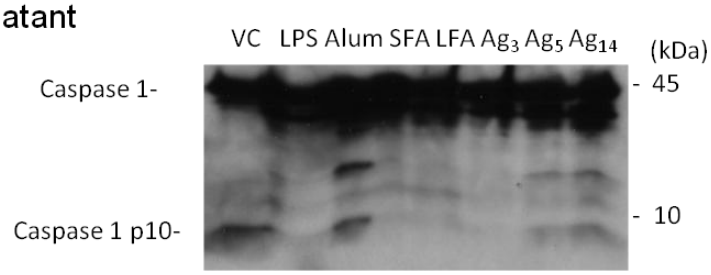

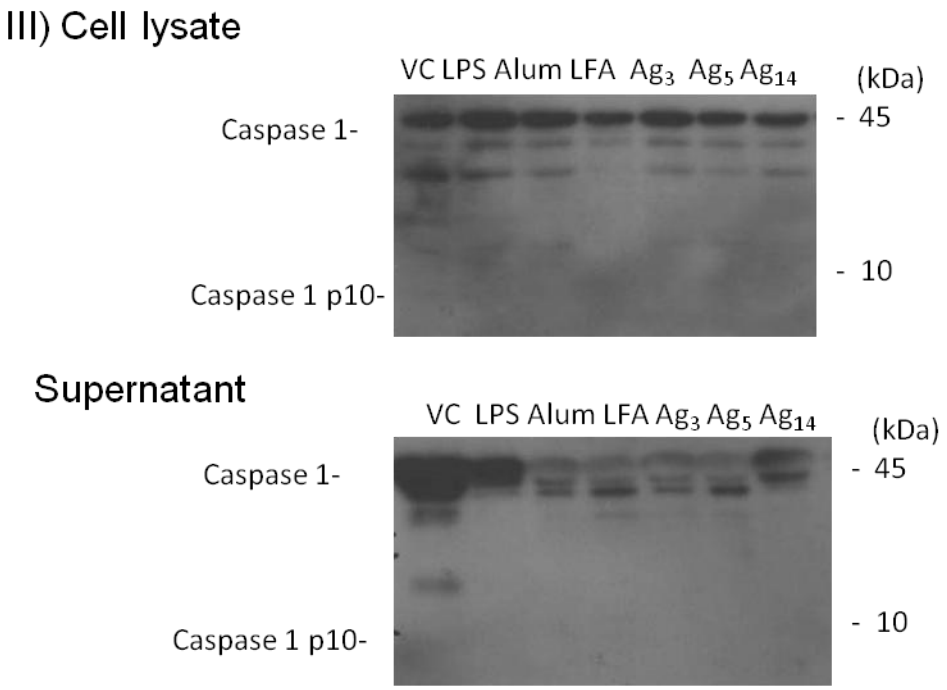

Figure 4-7: Detection of caspase 1 activation in BMMs after treatment with AgNWs and controls. I) BMMs were treated for 24 hours with $AgNW_3$ and $AgNW_{14}$ at a low (0.5 µg/cm²), medium (2.5 µg/cm²) and high (10 µg/cm²) dose. For $AgNW_5$ a range of doses from low (0.5 µg/cm²), medium (1 µg/cm²), high (5 and 10 µg/cm²) was used. The concentration of LFA used was 100 µg/ml (~26 µg/cm²) based on a previous study (Dostert et al., 2008). Alum was used as a positive control for NALP3 inflammasome activation and was used at a concentration of 100 and 200 µg/ml. Prior to treatment with the fibre panel, cells were primed with LPS at a concentration of 10 ng/ml for 3 hours. Caspase 1 was detected in the cell lysate after treatment with AgNWs and LFA in a dose and length dependent manner. Alum treatment produced strong secretion of caspase 1 in the supernatant. (n=2) II) BMMS were treated for 6 hour with AgNW at a dose based on fibre number ($AgNW_3$-5.5 µg/cm2, $AgNW_5$ 9.5 µg/cm^2, $AgNW_{14}$ 26 µg/cm^2). Concentration for SFA and LFA was 5.5 and 26 µg/cm^2, respectively. Alum was used at a concentration of 20 µg/ml. BMMs were treated for 6 hours. Prior to treatment with the fibre panel, cells were primed with LPS at a concentration of 10 ng/ml for 12 hours. Production of caspase 1 was detected in the cell lysate and the supernatant after treatment with

alum. A strong band for caspase 1 was also detected for the VC in the supernatant.(n=2). III) BMMs from Nalp3$^{-/-}$ mice were treated as described for II but no production of mature caspase 1 was detected in the cell lysate and the supernatant (n=3).

4.3.8 ASC-complex formation

The NALP3 inflammasome activation is described via the formation of the apoptosis associated Speck like protein containing a CARD (ASC) cluster together with the PYD domain and CARD-domain, which is responsible for the recruitment of procaspase 1 (Schroder and Tschopp, 2010). The formation of the ASC dimers and higher order oligomers was detected via Western blotting using anti-ASC antibodies and showed ASC oligomerisation (ASC dimer at 47.5 kDa) in BMMs after treatment with ATP (5 mM) and $AgNW_{14}$ at a concentration of 5 µg/cm^2 (Figure 4-8 I). For VC, LPS, $AgNW_5$ at 1 (L), 5 (M) and 10 (H) µg/cm^2 as well as $AgNW_{14}$ at 1 (L) and 10 (H) µg/cm^2, no oligomerisation could be detected (Figure 4-8 I). Cell lysates were analysed and showed uniform expression of ASC in all treatments (Figure 4-8 I). The assay was repeated using the highest dose (10 µg/cm^2) for AgNWs including Alum (100 µg/ml), LFA and SFA as a control, whereby only LFA showed ASC oligomerisation (Figure 4-8 II). Further repeats of the assay, were performed, showed however no consistency of the observed results (n=4).

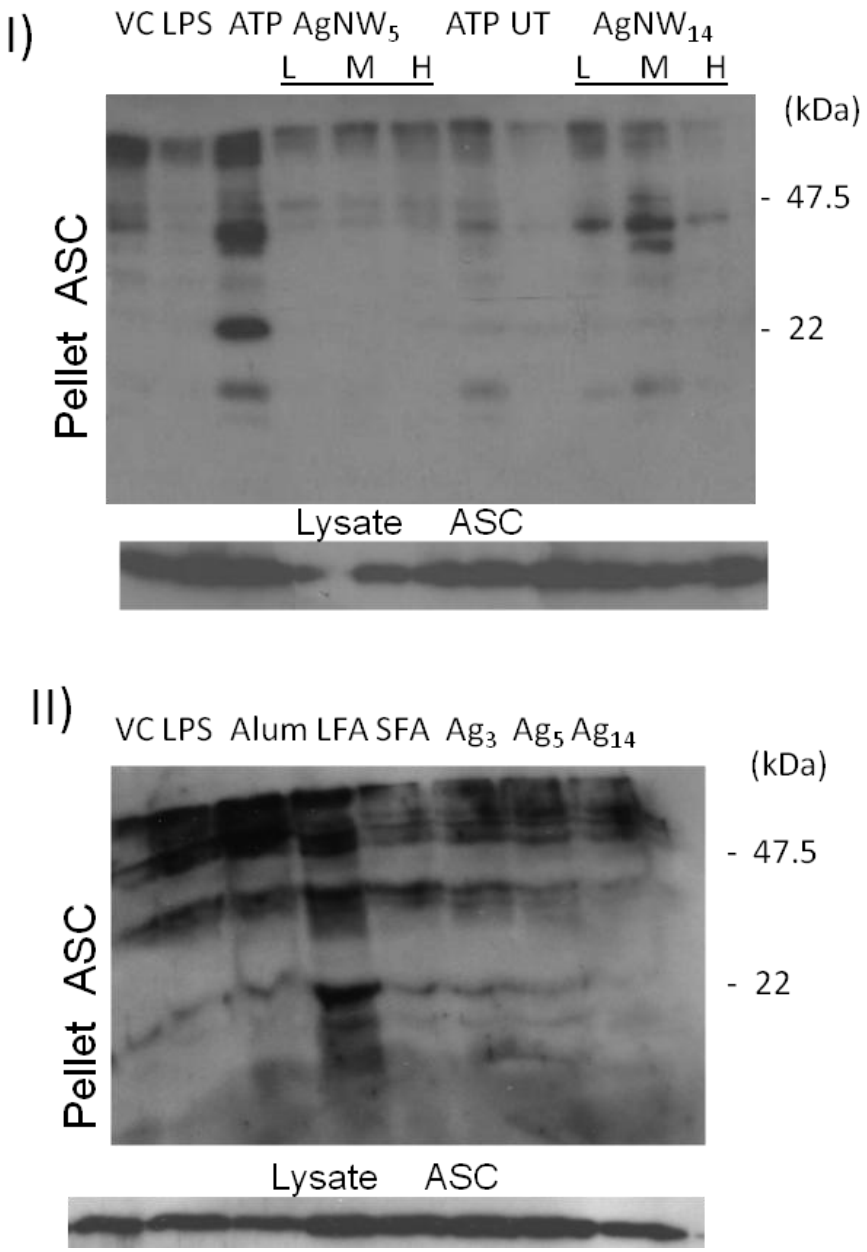

Figure 4-8: Detection of the ASC complex formation via Western blotting. BMMs were treated with $AgNW_5$ and $AgNW_{14}$ at 1, 5 and 10 µg/cm² for 6 hours. Prior to treatment with the fibre panel, cells were primed with LPS at a concentration of 10 ng/ml for 3 hours. 45 minutes before the end of the particle treatment, 5mM of ATP were added. ASC complex formation can be seen after treatment with ATP and $AgNW_{14}$ at 5 µg/cm² by blotting against ASC (ASC dimer at 47.5 kDa). In the cell lysate, uniform ASC expression was detected.(n=1). II) BMMs were treated with a dose of 10 µg/cm² for $AgNW_{3,5,14}$ as well as SFA and LFA for 6 hours. Alum was used at a dose of 100 µg/ml. LFA treatment led to the formation of ASC oligomers (n=1).

An additional assay was employed to examine the activation of ASC oligomerisation by NALP3. Immortalized murine macrophages that stably express ASC-CFP were used to analyse the formation of ASC oligomers or 'Specks'. In untreated cells and cells primed with LPS the CFP-ASC is diffuse throughout the cytosol of the cells, but in response with LPS and ATP (Figure 4-9) or AgNWs as well as SFA and LFA the CFP-ASC condensed into a large, bright Speck. 300 cells were counted for each treatment and analysed for the number of Specks formed but only a very small proportion of cells (~ 2%) showed Speck formation after AgNW and control treatment and therefore the assay couldn't be used as a reliable indicator for Speck formation.

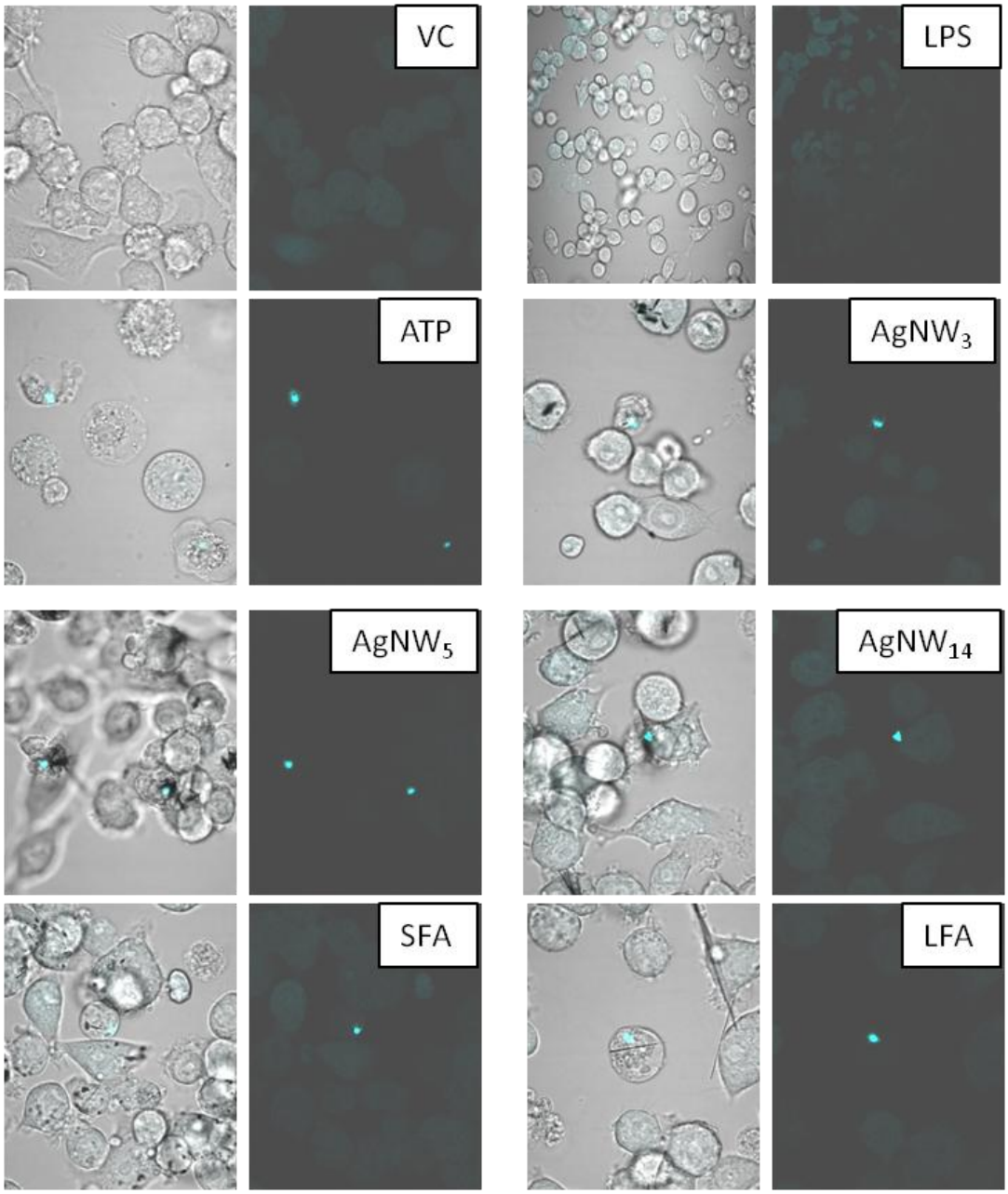

Figure 4-9: Confocal microscopy to identify ASC-complex formation in a murine macrophage cell line stably transfected with CFP-ASC. VC cells were unstimulated and showed uniform dispersion of CFP-ASC throughout the cytoplasma. For all other treatments cells were primed for 3 hours with 10 ng/ml LPS and 1 µg/cm^2 of AgNW and control fibres as well as 5 mM ATP. LPS alone showed no formation of Specks whereas Specks could be identified on all other treatment groups. Left hand side of each treatment groups shows phase contrast image and right hand image shows CFP-ASC image. These results are representative of three independent experiments.

4.3.9 Pleural inflammation in NALP3$^{-/-}$ mice

The aim of this study was to identify if the length dependent inflammatory response to AgNWs in the pleural space of wild type C57/Bl6 mice was similar in NALP3$^{-/-}$ C57/Bl6. Five microgram of $AgNW_5$ and $AgNW_{14}$ were injected into the pleural space of NALP3$^{-/-}$ mice and the pleural cavity was lavaged 24 hours after the intrapleural injection. The acute inflammatory reaction measured as the total cell number and total granulocytes in the lavage. The total cell number and granulocyte number were significantly decreased compared to the response seen in wild type mice after $AgNW_5$ treatment however no significant difference was detected in NALP3$^{-/-}$ mice treated with $AgNW_{14}$ (Figure 4-10 I and II).

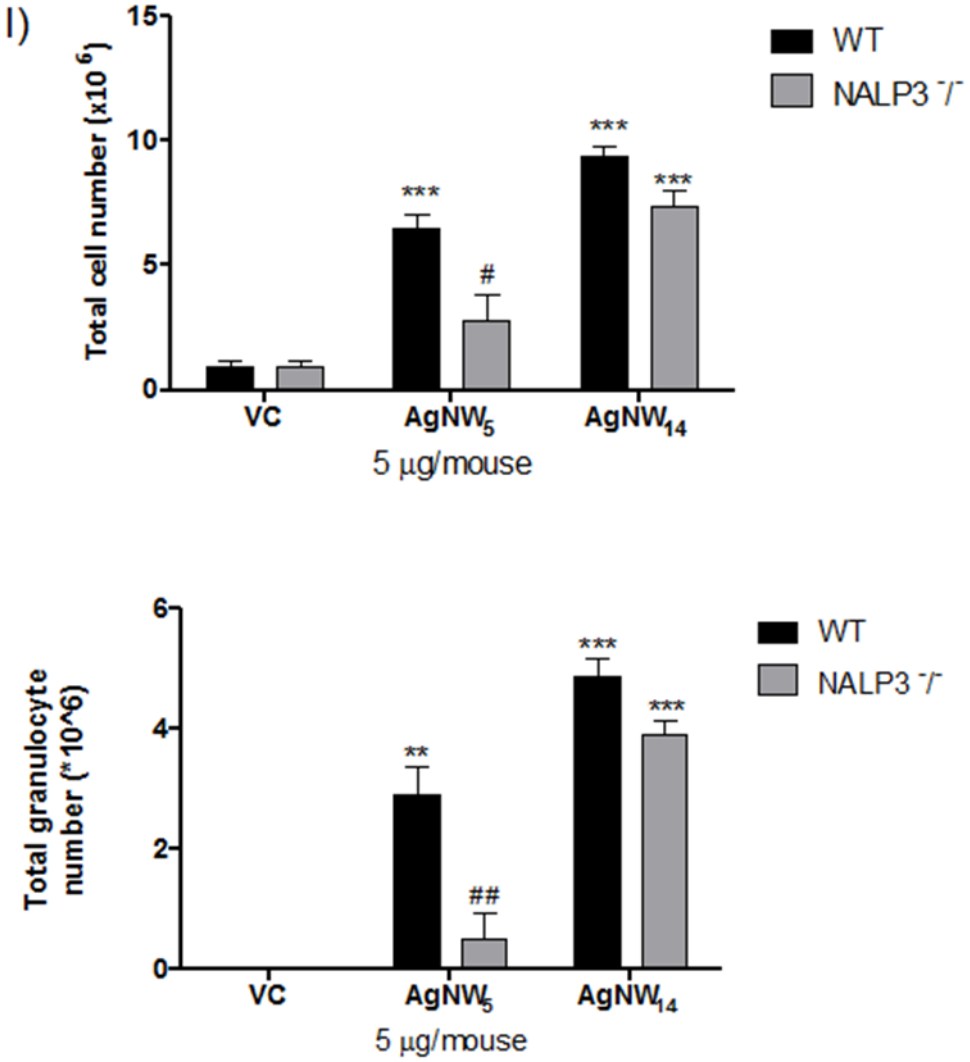

*Figure 4-10: Length dependent response to $AgNW_5$ and $AgNW_{14}$ in the pleural space of NALP3$^{-/-}$ mice compared to wild type mice 24 hour post injection. I) Count of total cell number and (II) total granulocyte number after 24 hour treatment with $AgNW_5$ and $AgNW_{14}$ in female C57Bl/6 wild type and NALP3$^{-/-}$ mice. The influx of total cells and granuloctyes were decreased after $AgNW_5$ treatment in NALP3$^{-/-}$ mice compared to wild type mice but no difference was detected after $AgNW_{14}$ treatment. Significance vs. vehicle control indicated by **p<0.001, ***p<0.0001. Significance compared between wild type (WT) and NALP3$^{-/-}$ mice #p<0.05, ##p<0.001.*

4.4 Discussion

In this study we focused on elucidating the mechanism of nanofibre induced inflammation *in vitro* using THP-1 macrophages and murine BMMs. We started off investigating the uptake efficiency of nanofibre by THP-1 macrophages. The need for macrophages to internalise and clear fibres from the lung and the pleural space has long been accepted (Lehnert, 1992). In terms of clearance of long fibres it has been postulated that incomplete uptake of fibres, frustrated phagocytosis plays a major role in the development of an inflammatory milieu after exposure to fibres. An extensive study has investigated the phagocytic capacity of murine bone marrow-derived macrophages to engulf various sizes of latex beads in a range of 13 µm to >30 µm in diameter (Cannon and Swanson, 1992). By measuring the bead diameter they calculated a phagocytosis capacity of 19.8 µm, which is 1.44 times the actual diameter of the cell. In regard to the phagocytosis of fibres by macrophages, Ye *et al*. investigated the role of glass fibre length in TNF-α production and NF-κB activation in a mouse macrophage cell line and correlated and increase in both cytokine level and transcription factor to incomplete phagocytosis of long fibres (17 µm) whereas short fibres (7 µm) were fully phagocytosed and therefore had less expression of the measured endpoints (Ye et al., 1999).

Here we showed that the threshold length value at which long fibres can be fully phagocytosed by macrophages *in vitro* is 14 µm, which was identified using BSEM. In the previous chapter we reported that *in vivo* inflammatory cells on the parietal

pleura showed incomplete uptake and frustrated phagocytosis of 10 µm fibres. There are a number of potential explanations for this anomalous difference between *in vivo* and *in vitro* length-dependent effect. Firstly the *in vivo* model is a pleural granuloma model in mice and this is very different from the *in vitro* situation where the cells human; secondly they are a cell line and thirdly they are not in the granulomatous milieu but are spread out singly on plastic, submerged in medium with 10% serum, a very abnormal environment. We conclude that investigations on frustrated phagocytosis and its relation to the pathological effects of fibres need to be carried out *in vivo* although future work could be focussed on trying different cell lines and culture conditions with the aim of finding a better *in vitro* model that mimics the *in vivo* findings.

Inflammasomes are believed to be early warning systems for danger to the innate immune system (Bryant and Fitzgerald, 2009). It has been recently implicated that frustrated phagocytosis is involved in the NALP3 inflammasome activation (O'Neill, 2008). The underlying mechanism by which frustrated phagocytosis of long fibres induces acute and chronic inflammation is poorly understood. Recent studies however identified the NALP3 inflammasome complex as an important component of the molecular pathway by which cells sense foreign bodies like asbestos fibres and initiate an inflammatory response (Hornung et al., 2008; Palomaki et al., 2011; Dostert et al., 2008; Winter et al., 2011). The inflammasome is a multiprotein complex consisting of nucleotide-binding oligomerization domain (NOD)-like receptors (NLR) which is activated via damage-associated molecular patterns (DAMPs) and forms a complex with apoptosis-associated Speck-like protein containing a caspase- recruiting domain (CARD) (ASC) and pro-caspase 1. Activation of caspase 1 leads to expression of IL-1β and IL-18, which mediate pro-inflammatory effects (Tschopp and Schroder, 2010). The inflammasome can be activated via different pathways including low intracellular potassium concentration (Petrilli et al., 2007), reactive oxygen species produced by NALP3 activators via NADPH oxidase (Martinon, 2010), frustrated phagocytosis (O'Neill, 2008) and phagosomal/lysosomal destabilisation (Hornung et al., 2008).

Recently, lysosomal destabilisation has been implicated in the inflammogenicity of long fibres of asbestos and TiO_2, as well as cholesterol crystals and silica (Rajamaki et al., 2010; Palomaki et al., 2011; Hornung et al., 2008), linked to activation of the NALP3 inflammasome. We therefore investigated the length–dependent loss of lysosomal membrane integrity in a macrophage cell line exposed to the different lengths of AgNW. Our studies showed a significant, length-dependent decrease of lysosomal membrane integrity at a fibre length of ≥ 5 μm, following the same pattern as seen in the *in vivo* pleura inflammation study. We interpret this to mean that 5 μm long nanofibres, which can be enclosed without fibre ends protruding from the cell, produce sufficient lysosomal stress to be pro-inflammatory even though 'classical' frustrated phagocytosis, with protruding fibre ends, did not occur. This signifies a potentially new mechanism for long fibre–induced inflammation for 5 μm length fibres that deserves further research. However, frustrated phagocytosis remains the likely predominant pro-inflammogenic mechanism since it would apply for all fibres longer than 5 μm.

We went on to investigate if IL-1β and caspase 1, two major components of the NALP3 inflammasome, are upregulated in a length dependent manner after AgNW exposure in murine BMMs. Mature IL-1β and caspase 1 are known to be upregulated after asbestos, silica and CNT exposure (Dostert et al., 2008; Hornung et al., 2008; Murphy et al., 2012b) via a NALP3 dependent mechanism. The results from our study on the expression of IL-1β and caspase 1 in BMMs after AgNW treatment showed no consistent results in the production of IL-1β and caspase 1, whereby a high degree of variability between each experiment was observed. We therefore cannot conclude that caspase 1 and subsequent cleavage of pro-IL-1β to mature IL-1β was involved in the pro-inflammatory response seen in the pleural space after AgNW exposure.

The formation of the ASC complex is a necessity for the recruitment of pro-caspase 1 and subsequent cleave of caspase 1 to its active form (Bryant and Fitzgerald, 2009). In addition to the significance of ASC in the NALP3 inflammasome activation, it plays important roles in regulating innate and adaptive immune responses via regulating the NF-κB pathway and mitogen-activated protein kinase

(MAPK) activation (Hassan and Amer, 2011). We investigated the formation of the ASC complex after AgNW treatment using a protocol as described by Coll et al. (Coll and O'Neill, 2011a) based on the detection of ASC dimers and higher oligomers via Western blotting as well as visualising ASC formation using confocal microscopy. The formation of the ASC complex was observed in both assays after treatment of BMMs with controls and fibre panel, however the results obtained via Western blotting were not reproducible and too little percentage of cells showed Speck formation in the confocal microscopy assay to form a valid conclusion.

Since the *in vitro* studies on the NALP3 inflammasome as an underlying mechanism in fibre-induced inflammation didn't show convincing results, we performed a 'proof-of-principle' study by using NALP3$^{-/-}$ mice to study the extent of inflammation *in vivo* after intrapleural injection of AgNWs. Interestingly, we observed a significant reduction of inflammation after $AgNW_5$ exposure in NALP3$^{-/-}$ mice however only a slight decrease but no significant change in inflammation was observed after treatment with $AgNW_{14}$. This leads to the conclusion that the NALP3 inflammasome is involved in the inflammation seen after fibre exposure and inflammation can be reduced by blocking the NALP3 inflammasome, however only in the case of inflammation caused by fibres that do not cause frustrated phagocytosis. This observation shows that the all-or-nothing response in the pleural space as discussed in the previous chapter, which was linked to the retention of longer fibres in the pleural space, can be extenuated by interfering with the NALP3 inflammasome pathway.

In summary, the study on the mechanism of the pro-inflammatory response to AgNW showed that the NALP3 inflammasome could be an underlying mechanism however an in depth study has to be performed to elucidate this mechanism further and different methods/experimental setups considered.

Chapter 5: The threshold length for fibre induced pulmonary inflammation

Some of the following results have been published in

Schinwald A, Chernova T, Donaldson K. Use of silver nanowires to determine thresholds for fibre length-dependent pulmonary inflammation and inhibition of macrophage migration *in vitro*. Particle and Fibre Toxicology. 2012 Dec 2;9:47

5.1 Acknowledgement

Phospho-kinase array was performed by Dr Tanya Chernova at the MRC Toxicology Unit in Leicester.

5.2 Aims and Hypothesis

Despite the knowledge that fibre length plays a crucial role in the development of asbestos related diseases, the threshold length for the induction of lung diseases after fibrous exposure is unknown.The objective of this study was to examine the threshold fibre length for the onset of pulmonary inflammation after aspiration exposure in mice to four different lengths of AgNW. We hypothesized that exposure to longer fibres shows a defined threshold length which will differ from the threshold length identified in the pleural space due to differences in the clearance mechanism of the lung and the pleural space.

The normal lung clearance mechanisms provide a defense mechanism for removing fibre dose and yet selective retention of longer fibres is well-documented (Coin et al., 1996; Searl et al., 1999). For the key fraction of fibres that deposit beyond the ciliated airways and are slowly cleared, macrophages are the central cells involved in phagocytosing and transporting the fibres to the foot of the mucociliary escalator for clearance. We therefore hypothesized that the uptake of long fibres impairs the ability of macrophages to migrate whilst short fibres do not, providing a mechanism

for selective retention of long fibres. We addressed this hypothesis using the samples with different fibre length classes and assessed their effects on macrophage migration in an *in vitro* wound closure assay.

5.3 Results

5.3.1 Length dependent inflammatory response to AgNW in lung at 24 hour

The inflammatory response to the panel of AgNW and control fibres as assessed by the bronchoalveolar lavage fluid (BAL) profile was measured 24 hour post aspiration. An initial dose response series was performed with $AgNW_{14}$ at a dose of 5, 10, 25 and 50 µg/mouse (n=2) (Figure 5-1 I, II) and SFA and LFA at a dose of 10 and 50 µg/mouse (n=2) (Figure 5-1 III, IV). The dose of 50 µg/mouse was chosen since it gave a persistent inflammatory response with $AgNW_{14}$ and LFA. The dose was adjusted so that each of the different treatments (Table 2-4) comprised of the same fibre number, whereby for $AgNW_3$, $AgNW_5$, $AgNW_{10}$, $AgNW_{14}$, SFA and LFA a dose of 10.7, 17.9, 35.7, 50.0, 10.7 and 50.0 µm, respectively was used. No change in total bronchoalveolar cell number was measured after exposure to equal numbers of the different fibre lengths compared to vehicle control (Figure 5-2 I). However, the total number of granulocytes was significantly increased after exposure to $AgNW_{14}$ (Figure 5-2 II). $AgNW_{3\text{-}10}$, SFA and LFA produced no significant increase in granulocyte number, although the LFA produced a trend to more inflammation than SFA. The effect of length on inflammation was demonstrated by plotting AgNW length against inflammation and it is clear that the relationship is not linear and that there is a discernible step–increase in granulocyte recruitment at a length between 10 and 14 µm (Figure 5-2 III). Total amount of protein and increase in membrane permeability by the release of LDH was measured but showed no significant difference between the treatments (data not shown).

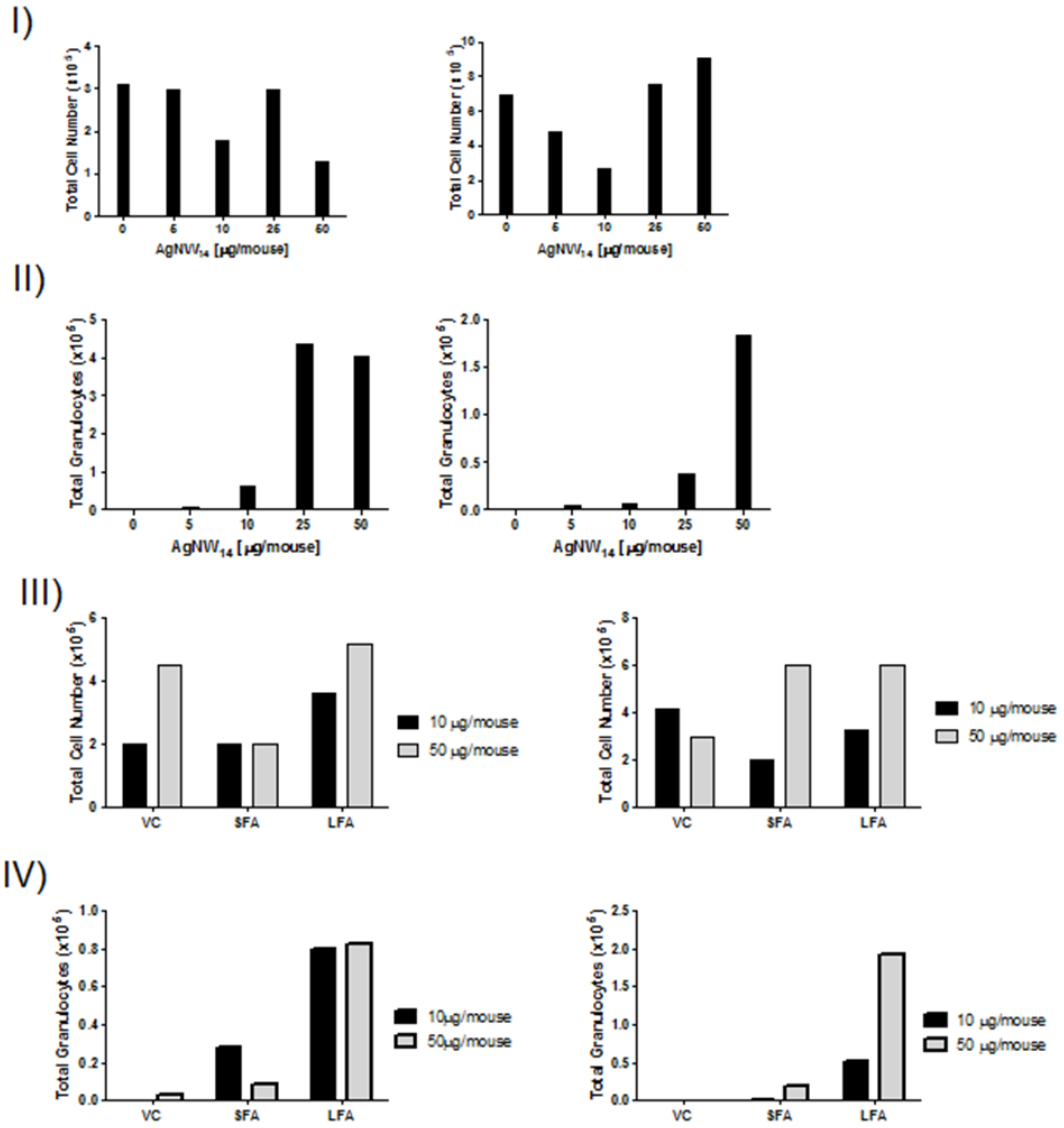

Figure 5-1: Dose response series for $AgNW_{14}$, SFA and LFA in the lungs at 24 hour. C57/Bl6 mice were exposed to $AgNW_{14}$ at a dose of 5, 10, 25 and 50 µg/mouse (I, II) and control particles SFA and LFA at 10 and 50 µg/mouse (III, IV) by pharyngeal aspiration. At 24 hour post exposure the lungs were lavaged and total cell number (I, III) and total granulocyte number (II, IV) were measured. Data of n = 2 mice.

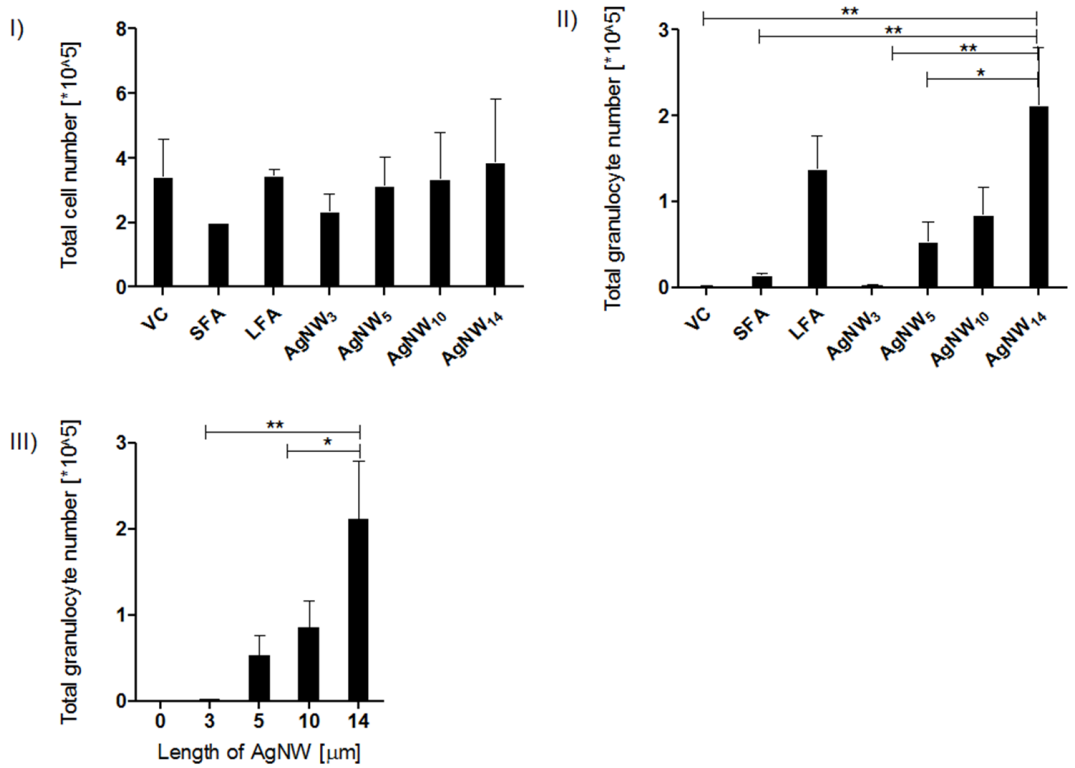

*Figure 5-2: Length dependent inflammatory response to AgNW in the lungs at 24 hour. C57/Bl6 mice were exposed to AgNW and control panel by pharyngeal aspiration. At 24 hour post exposure the lungs were lavaged and total cell number (I) and total granulocyte number (II) were measured. III) The acute inflammatory increase was plotted against length of AgNW. Significance indicated compares treatment groups to vehicle control (II) and within each treatment (III), * indicates p < 0.05, ** indicates p < 0.001. Data represent mean + SEM of n = 4 mice.*

5.3.2 Histological evaluation of lung sections following treatments

The pathology of the lung exposed to the AgNW panel and controls were examined 24 hour after aspiration. The sections after exposure to VC, SFA and $AgNW_3$ showed normal histology of bronchioles, respiratory bronchioles, alveolar ducts and alveoli (Figure 5-3 I, II, IV). $AgNW_5$ and $AgNW_{10}$ produced minor granulomas and lymphocyte infiltrates and the majority of the lung histology appeared normal (Figure 5-3 V, VI). $AgNW_{14}$ and LFA caused more extensive granuloma and

lymphocyte infiltrates which is consistent with the amount of total granulocytes from the lavage fluid (Figure 5-3 III, VII). Accumulations of nanowires inside alveolar macrophages were common (Figure 5-3 V, VI white arrow). $AgNW_{14}$ produced the stronger response with more granulomatous areas compared to shorter fibres however this was still minor compared to the extensive interstitial thickening and remodelling of the alveolar spaces after LFA treatment (Figure 5-3 III, VII). Frustrated phagocytosis, classified as incomplete uptake of fibres by cells, was observed with $AgNW_{14}$ and LFA. Whole lung sections stained with H&E and higher magnification call-outs can be seen in Figure 5-4 to 5-10.

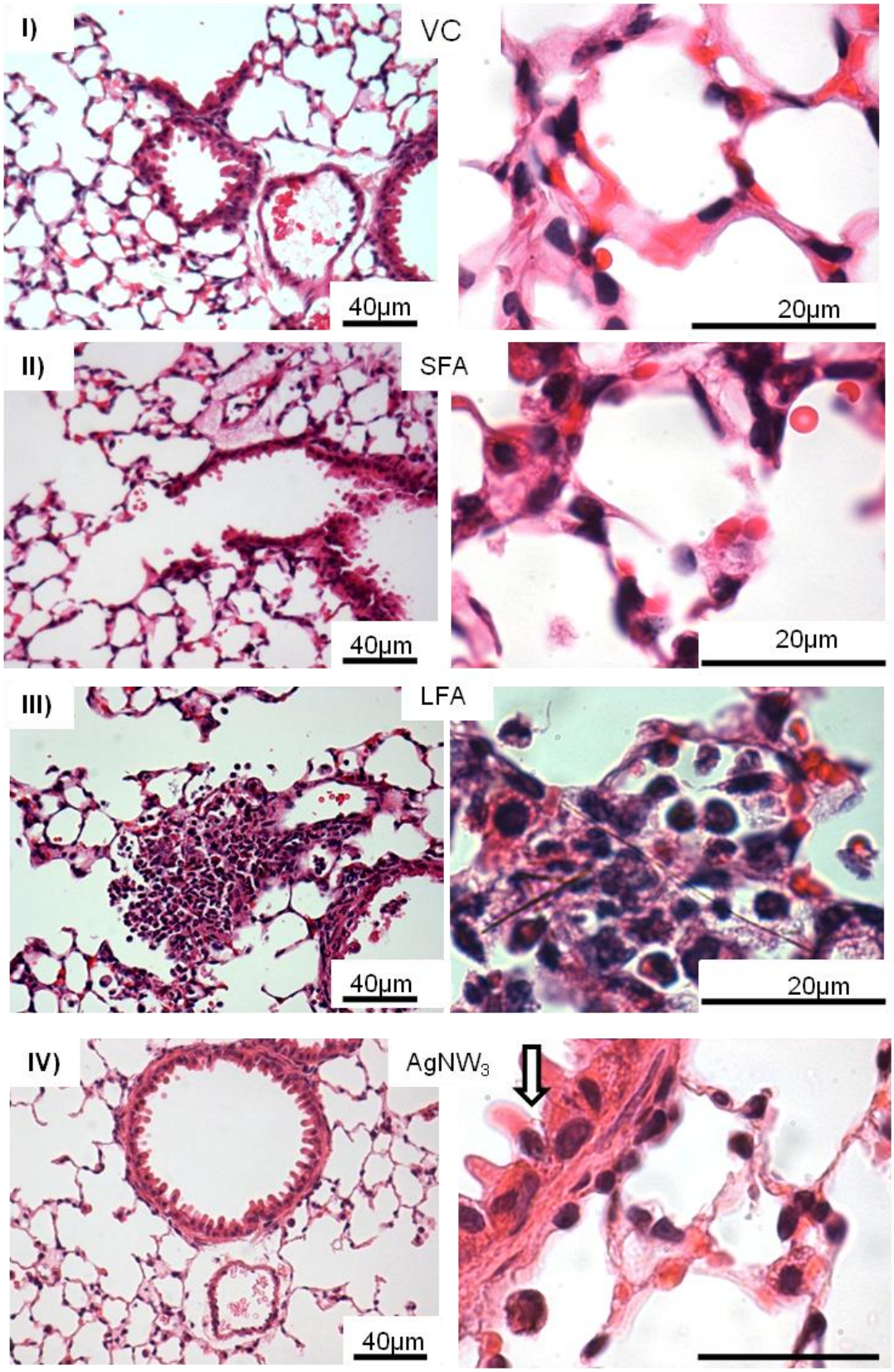
I)
VC
40µm
20µm
II)
SFA
40µm
20µm
III)
LFA
40µm
20µm
IV)
AgNW3
40µm

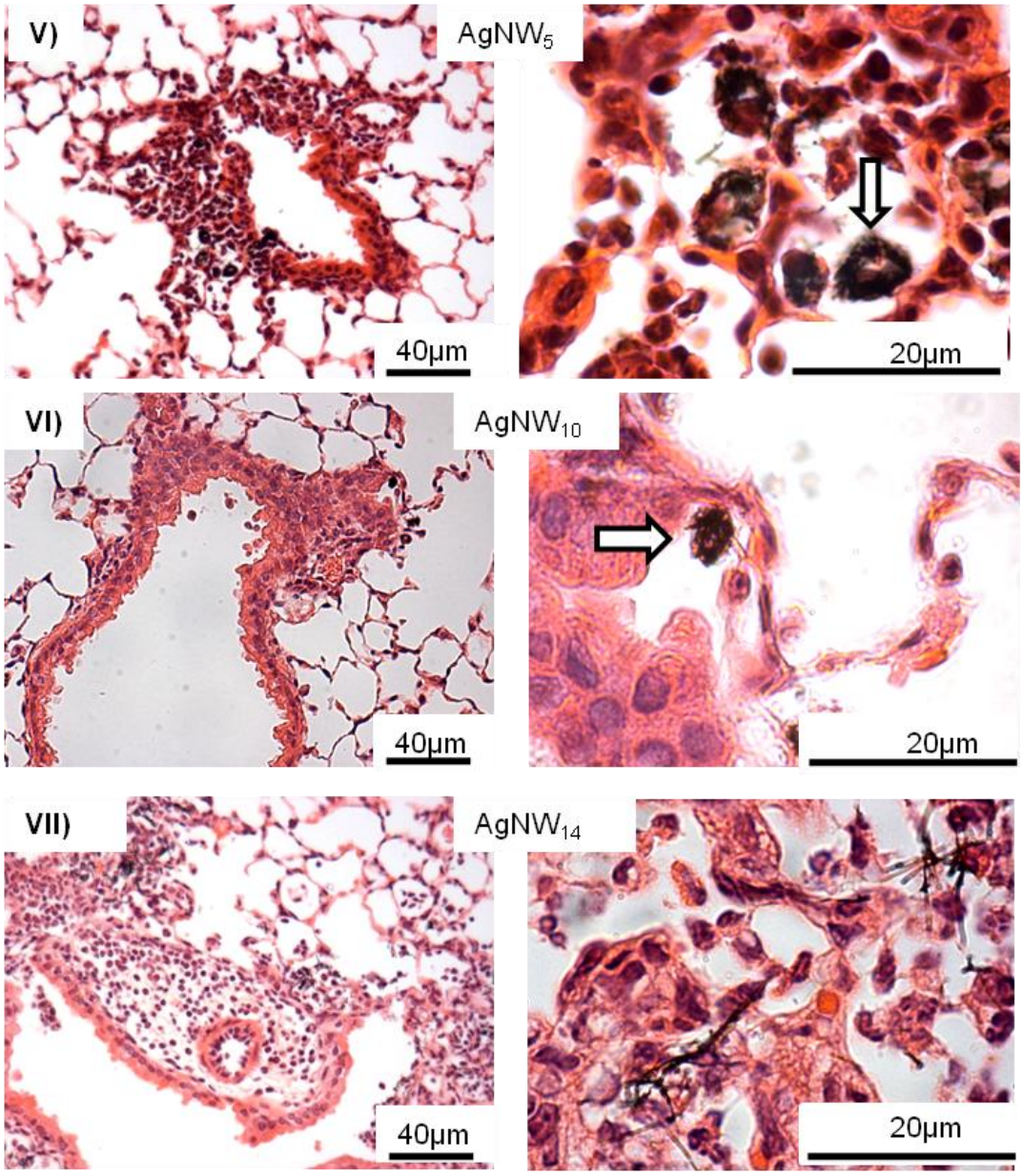

Figure 5-3: Lung histology 24 hour post aspiration to AgNW panel and controls. H&E stained lung sections at lower (left) and higher (right) magnification show normal alveolar structure in the vehicle control (I), SFA (II) and $AgNW_3$ (IV) sections. Small accumulations of inflammatory cells were seen after $AgNW_5$ (V) and $AgNW_{10}$ (VI) exposure whereas a greater amount of inflammatory cell infiltration in the alveoli, peribronchiolar and perivascular regions were observed after LFA (III) and $AgNW_{14}$ (VII). The white arrows indicate the areas of fibre accumulation. Abbreviations: al, alveolus; br, bronchiole; v, blood vessel. Representative images are shown, similar results are obtained from 2 mice.

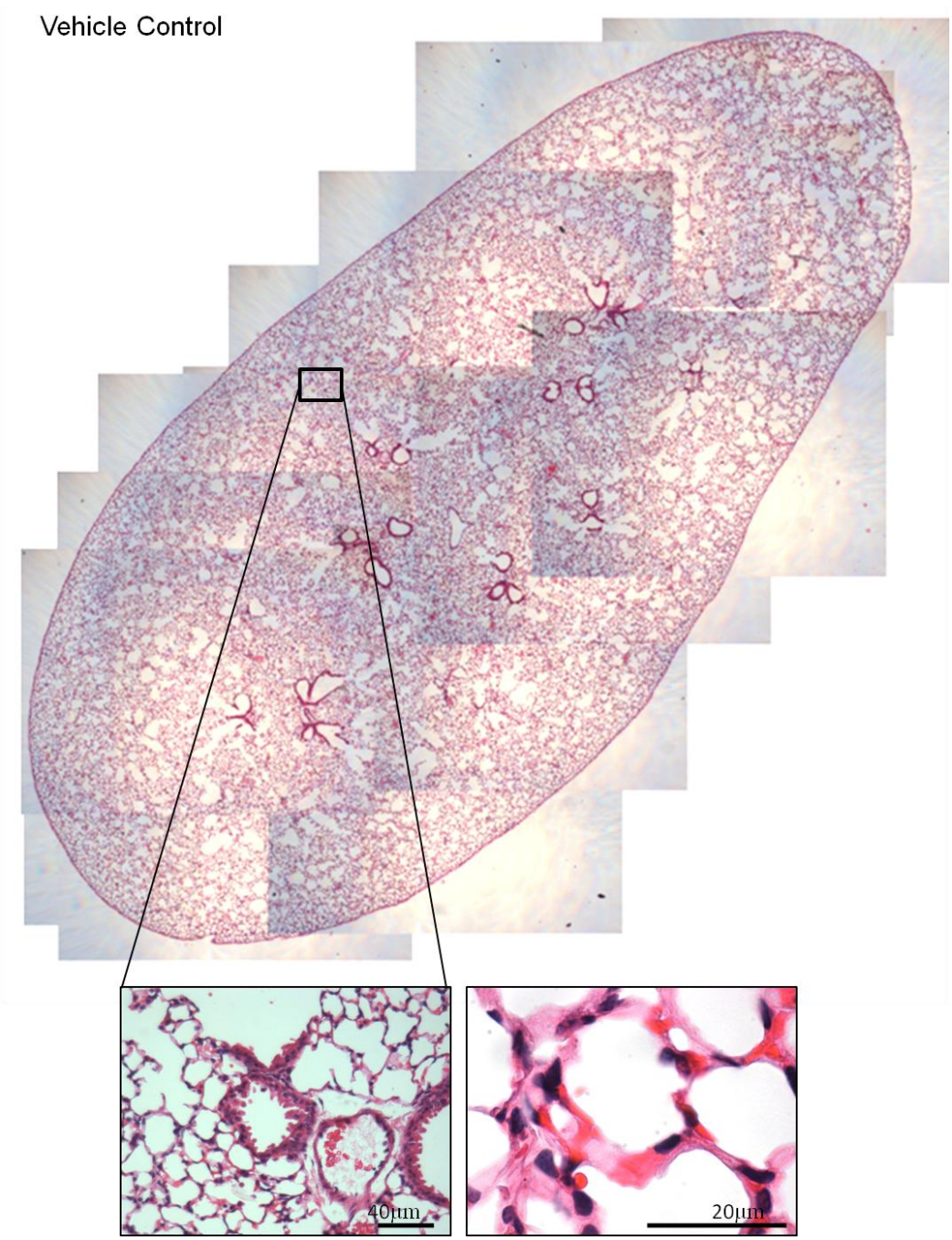

Figure 5-4: Lung pathology 24 hours post aspiration of vehicle control. Images of lung sections stained with H&E were realigned to show gross morphology of the lungs 24 hour post aspiration with vehicle control (0.5% BSA/saline). Call-outs stained with H&E show the normal structure of the terminal bronchioles, alveolar ducts, alveoli and alveolar septa.

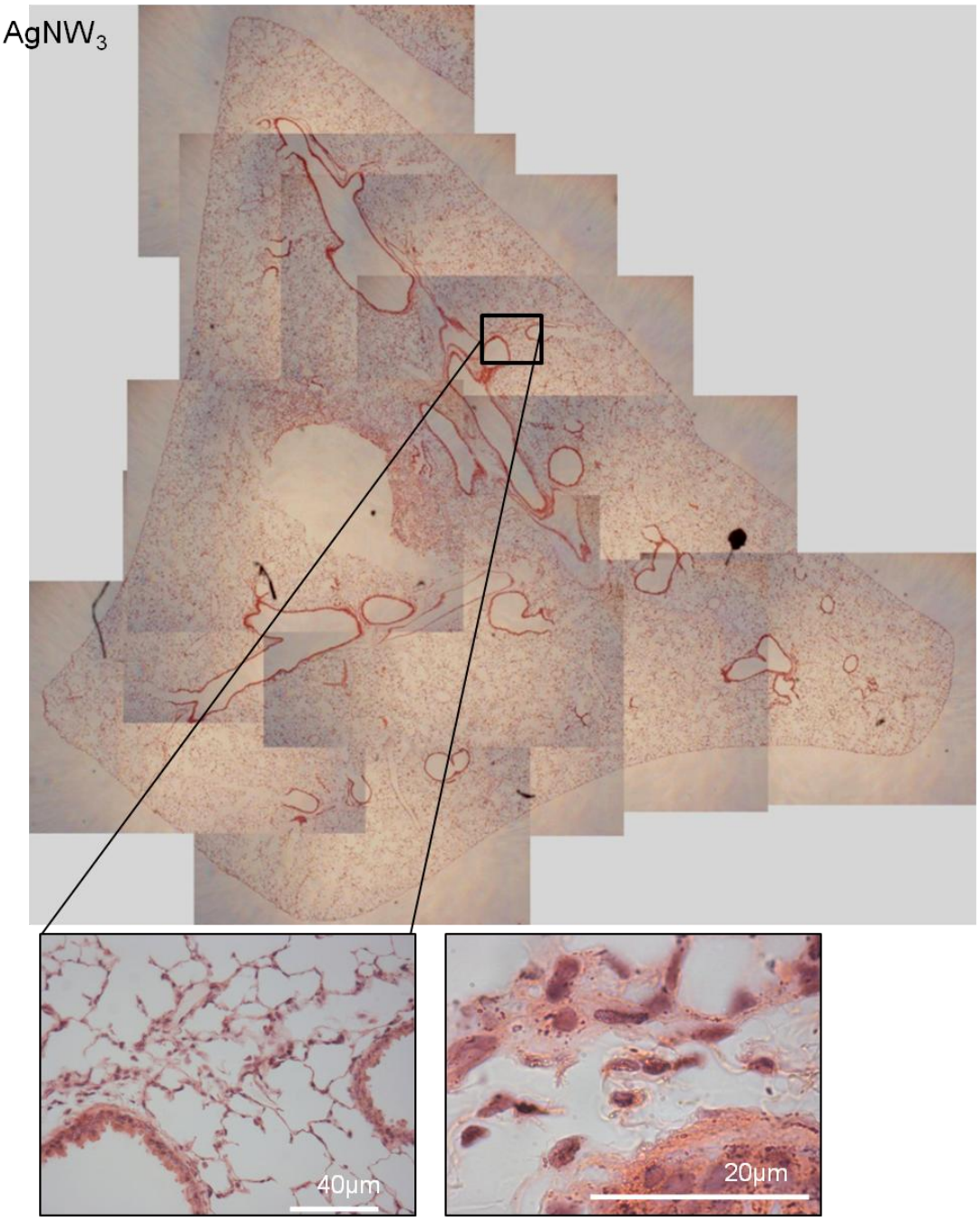

Figure 5-5: Lung pathology 24 hours post aspiration of $AgNW_3$. Images of lung sections stained with H&E were realigned to show gross morphology of the lungs 24 hour post aspiration with $AgNW_3$. Call-outs stained with H&E show the normal structure of the terminal bronchioles, alveolar ducts, alveoli and alveolar septa.

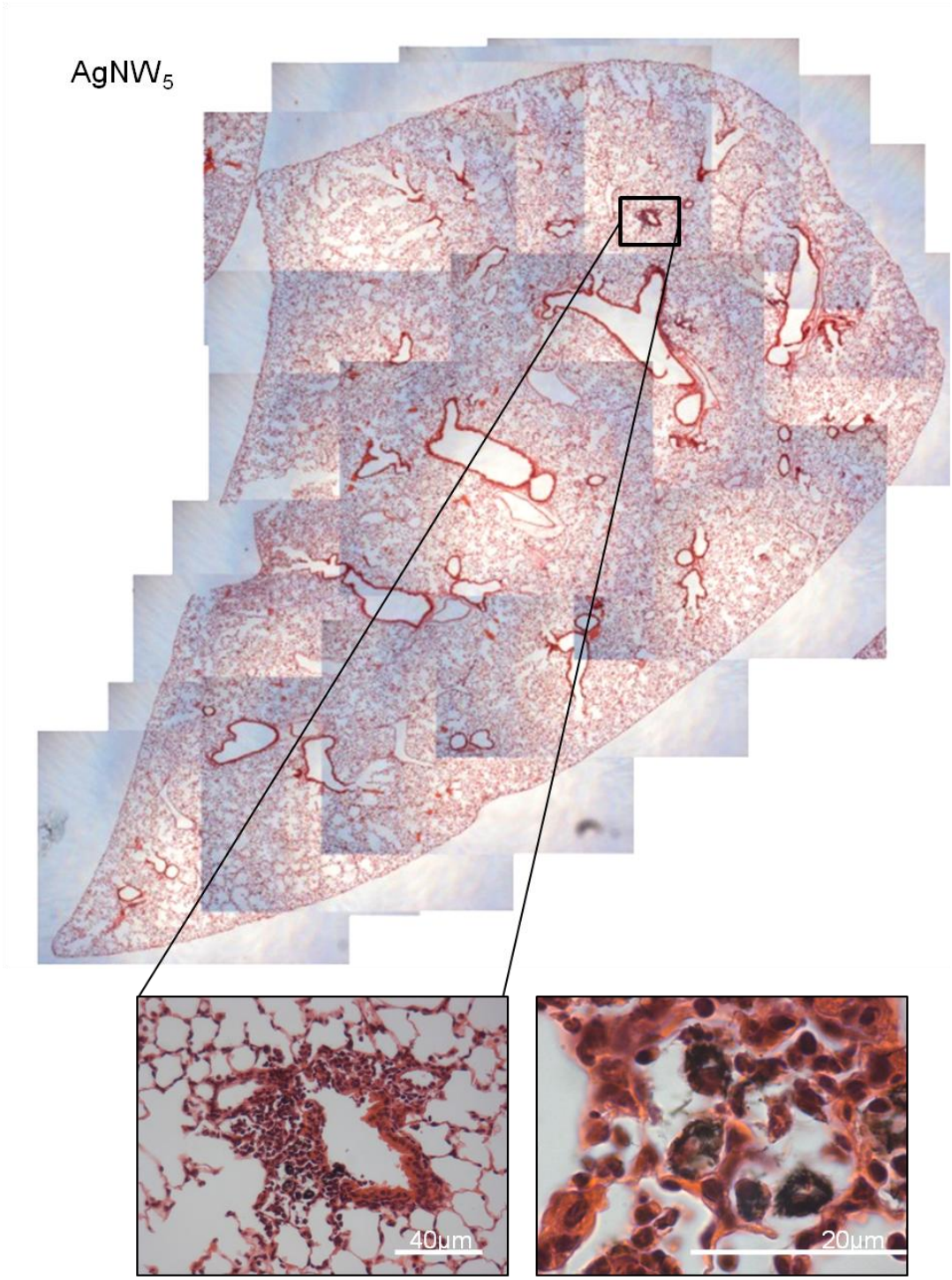

Figure 5-6: Lung pathology 24 hours post aspiration of $AgNW_5$. Images of lung sections stained with H&E were realigned to show gross morphology of the lungs 24 hour post aspiration with $AgNW_5$. Call-outs stained with H&E show mainly a normal structure of the terminal bronchioles, alveolar ducts, alveoli and alveolar septa with a few accumulations of AgNWs.

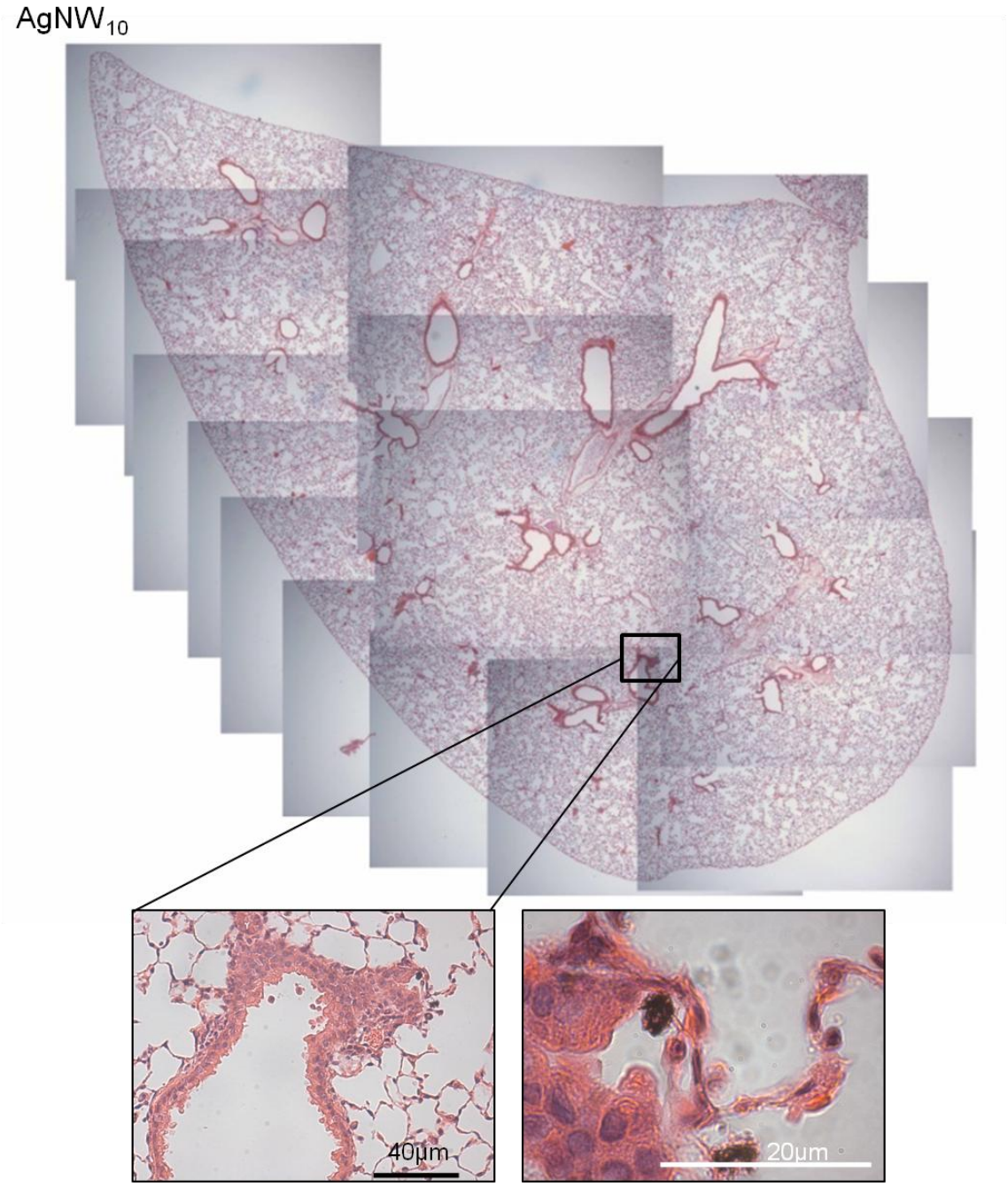

Figure 5-7: Lung pathology 24 hours post aspiration of $AgNW_{10}$. Images of lung sections stained with H&E were realigned to show gross morphology of the lungs 24 hour post aspiration with $AgNW_{10}$. Call-outs stained with H&E show normal structure of the terminal bronchioles, alveolar ducts, alveoli and alveolar septa with small accumulations of AgNW.

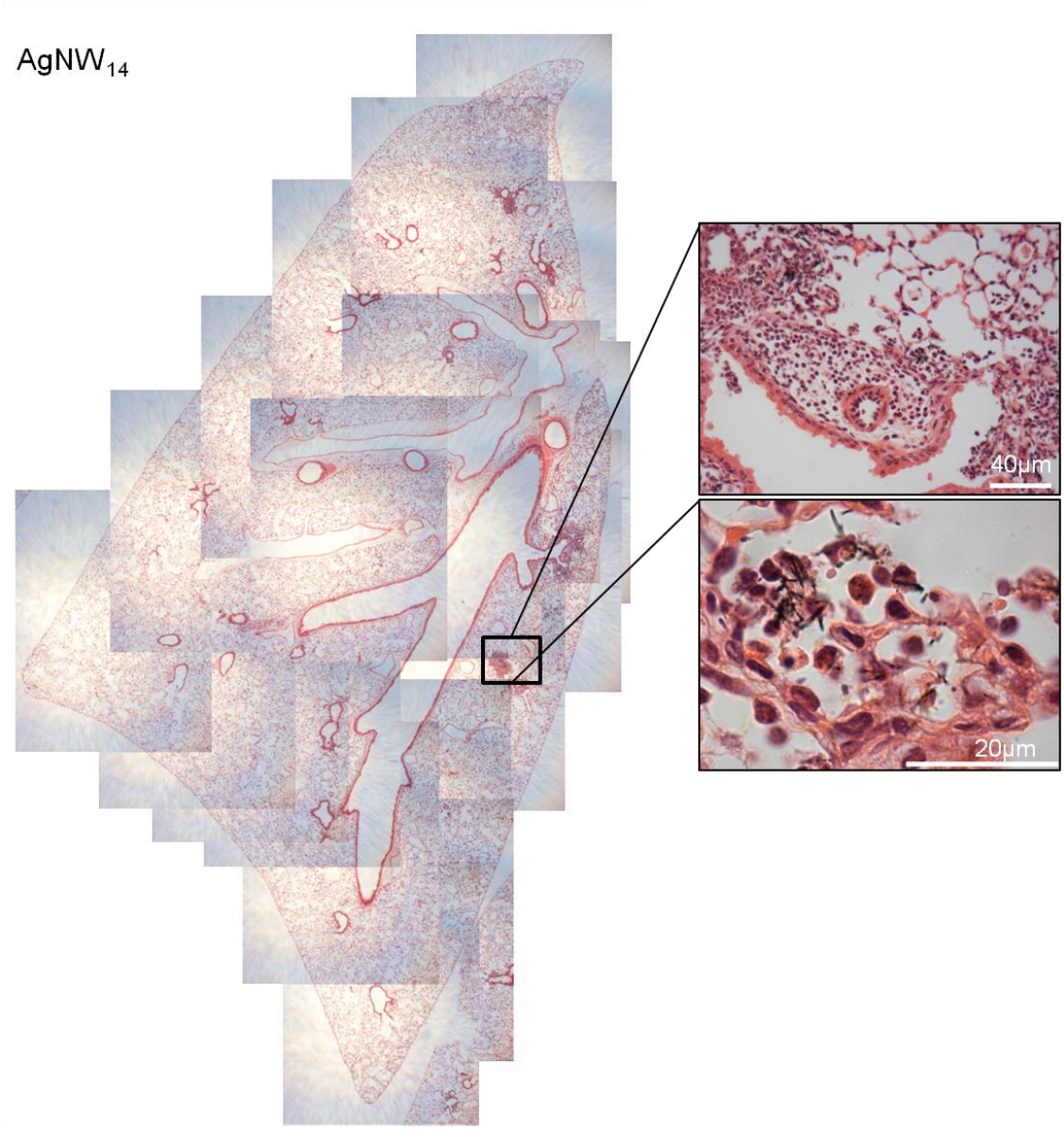

Figure 5-8: Lung pathology 24 hours post aspiration of $AgNW_{14}$. Images of lung sections stained with H&E were realigned to show gross morphology of the lungs 24 hour post aspiration with $AgNW_{14}$. Call-outs stained with H&E show small accumulations of cells and AgNW aggregates which are more frequent compared to shorter AgNWs but for the most part the lung resembled the vehicle control treated lungs.

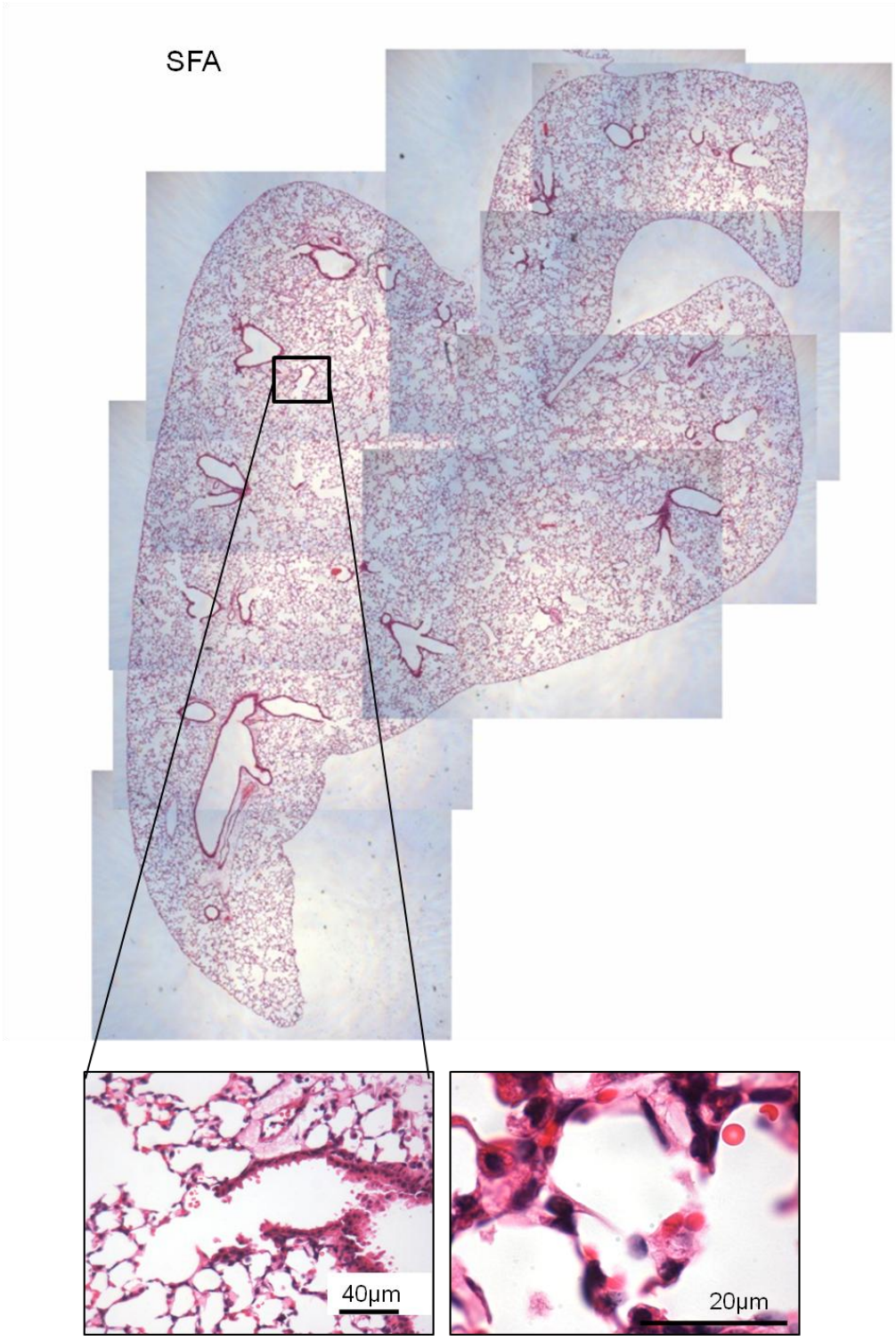

Figure 5-9: Lung pathology 24 hours post aspiration of SFA. Images of lung sections stained with H&E were realigned to show gross morphology of the lungs 24 hour post aspiration with SFA. Call-outs stained with H&E show a normal structure of the terminal bronchioles, alveolar ducts, alveoli and alveolar septa.

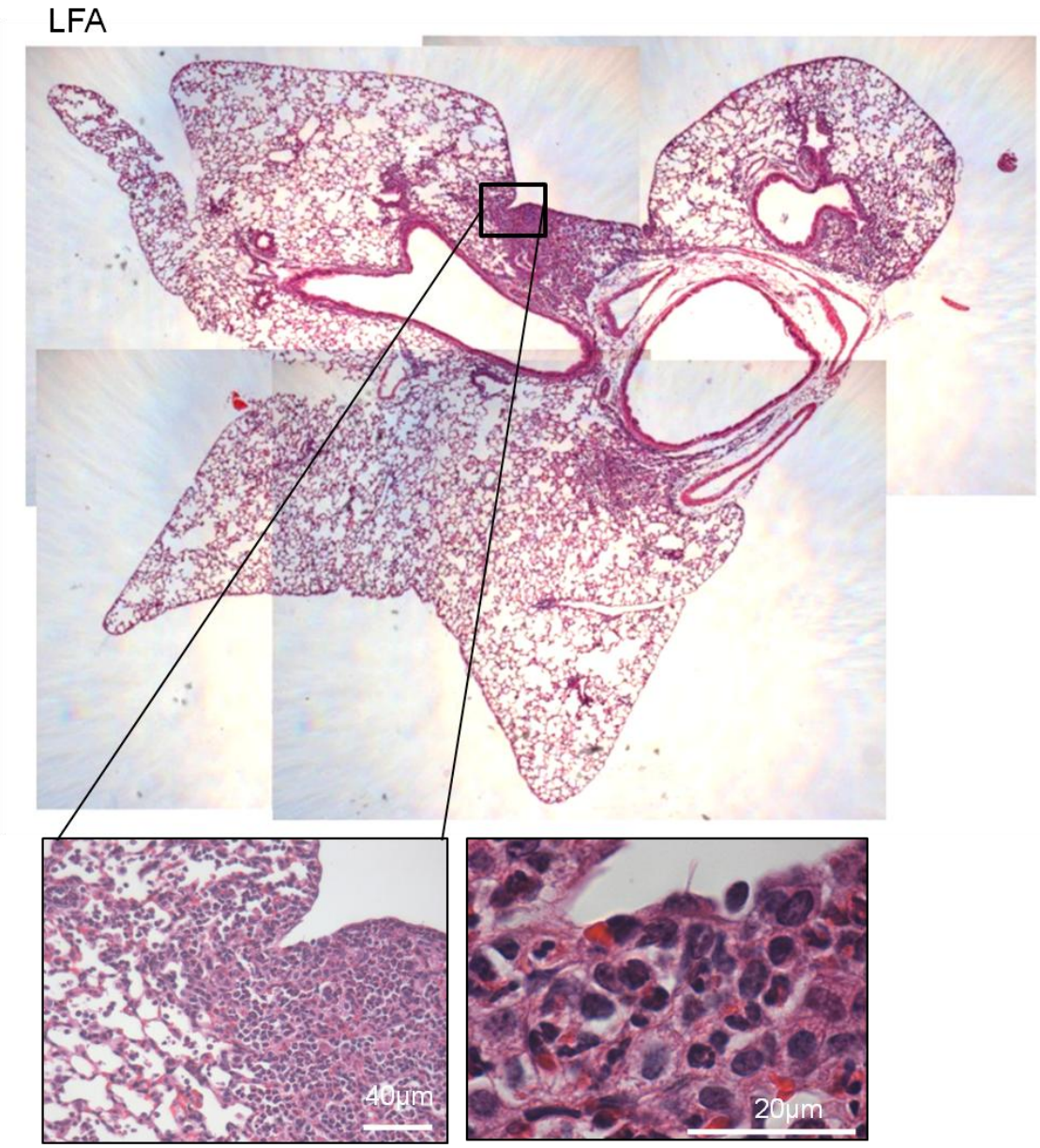

Figure 5-10: Lung pathology 24 hours post aspiration of LFA. Images of lung sections stained with H&E were realigned to show gross morphology of the lungs 24 hour post aspiration with LFA. Extensive granulomatous areas can be seen. Call-outs stained with H&E show lymphocyte infiltrates and extreme interstitial thickening.

5.3.3 Frustrated phagocytosis in alveolar macrophages

The link between the extent of frustrated phagocytosis and lung inflammation was examined in the lavage fluid. The uptake of different length of AgNW by alveolar macrophages was evident in cytospin images of the broncho-alveolar lavage fluid (Figure 5-11). Shorter fibres including SFA, $AgNW_3$, $AgNW_5$ and $AgNW_{10}$ could be completely phagocytosed by alveolar macrophages whereas LFA and $AgNW_{14}$ were undergoing frustrated phagocytosis indicated by the sharing of fibres between adjacent cells (Figure 5-11). This is in agreement with frustrated phagocytosis observed in histological sections and the extent of inflammation seen in the lavage fluid showing that frustrated phagocytosis of nanowires correlates with increased inflammation.

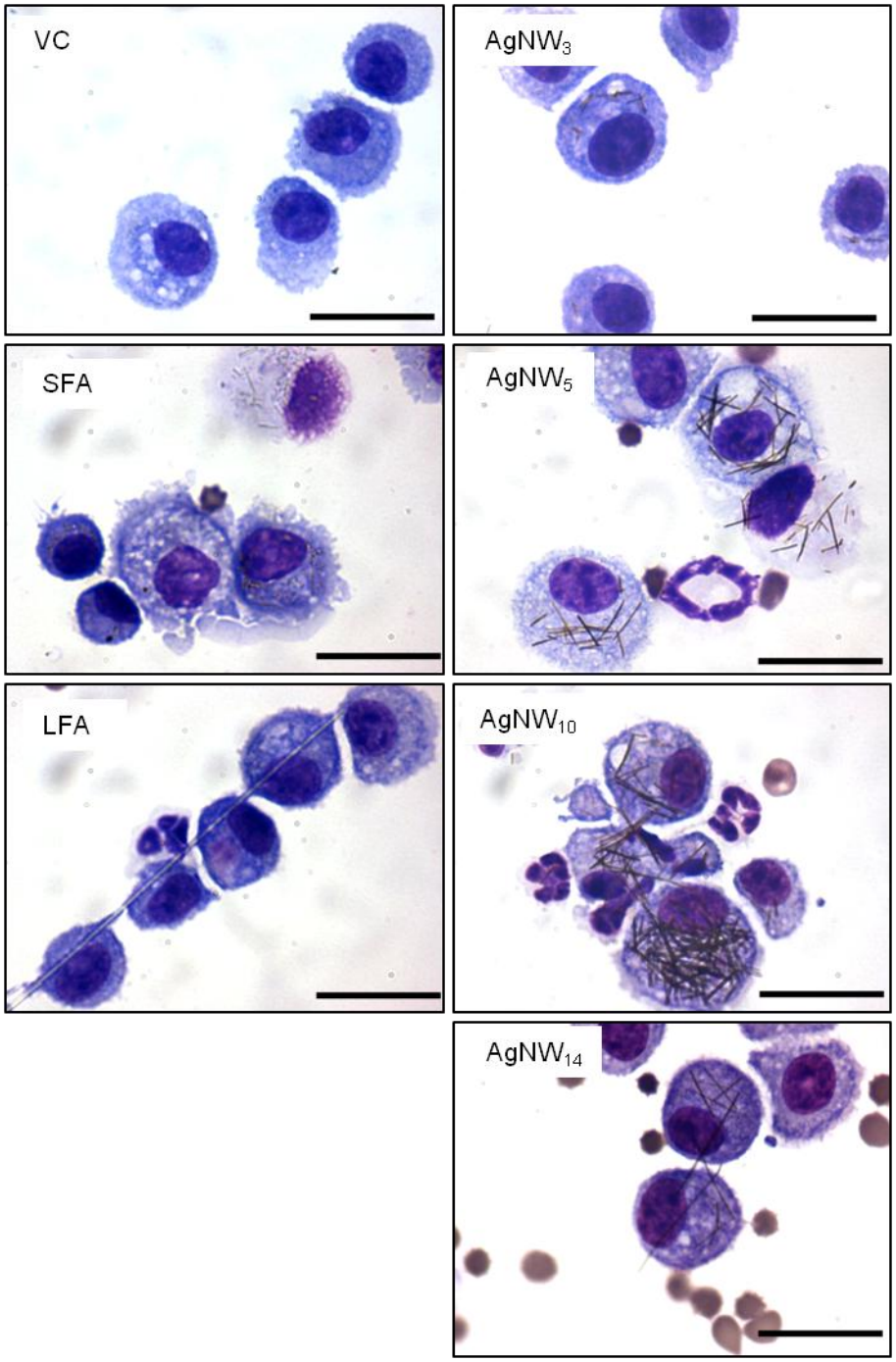

Figure 5-11: Uptake of AgNW and controls in alveolar macrophages. Cytospin images from the lavage fluid 24 hour post aspiration illustrates the complete uptake of shorter fibres including SFA, $AgNW_3$, $AgNW_5$ and $AgNW_{10}$ whereas LFA and $AgNW_{14}$ led to frustrated phagocytosis in alveolar macrophages. Scale bar 20 µm. Images are representative of n=4.

5.3.4 Fibre- length dependent inhibition of locomotion in BMMs

Fibres that deposit in the lower respiratory tract are cleared via macrophages, whereby the fibres are phagocytosed and transported to the foot of the mucociliary escalator for clearance. If this clearance mechanism is impaired, accumulation of the deposited fibre dose occurs over time. This study investigated the locomotion behavior of bone marrow derived mouse macrophages (BMMs) to treatment of the AgNW panel in an *in vitro* macrophage migration assay in order to aid the understanding of fibre-laden alveolar macrophage migration behaviour *in vivo*. In the macrophage migration assay, a wound was made into a confluent layer of cells and the migration of cells back into the wound was monitored. An initial dose response series with concentrations of 0.5, 1, 2.5 and 5 µg/cm^2 based on fibre number for $AgNW_{14}$ was performed to measure metabolic activity, membrane integrity and migratory behavior of the BMMs. The initial screening showed that a dose of 2.5 µg/cm^2 and below only a slight increase in membrane permeability and decrease in metabolic activity was measured, which was amplified at a dose of 5 µg/cm^2 (Figure 5-12).

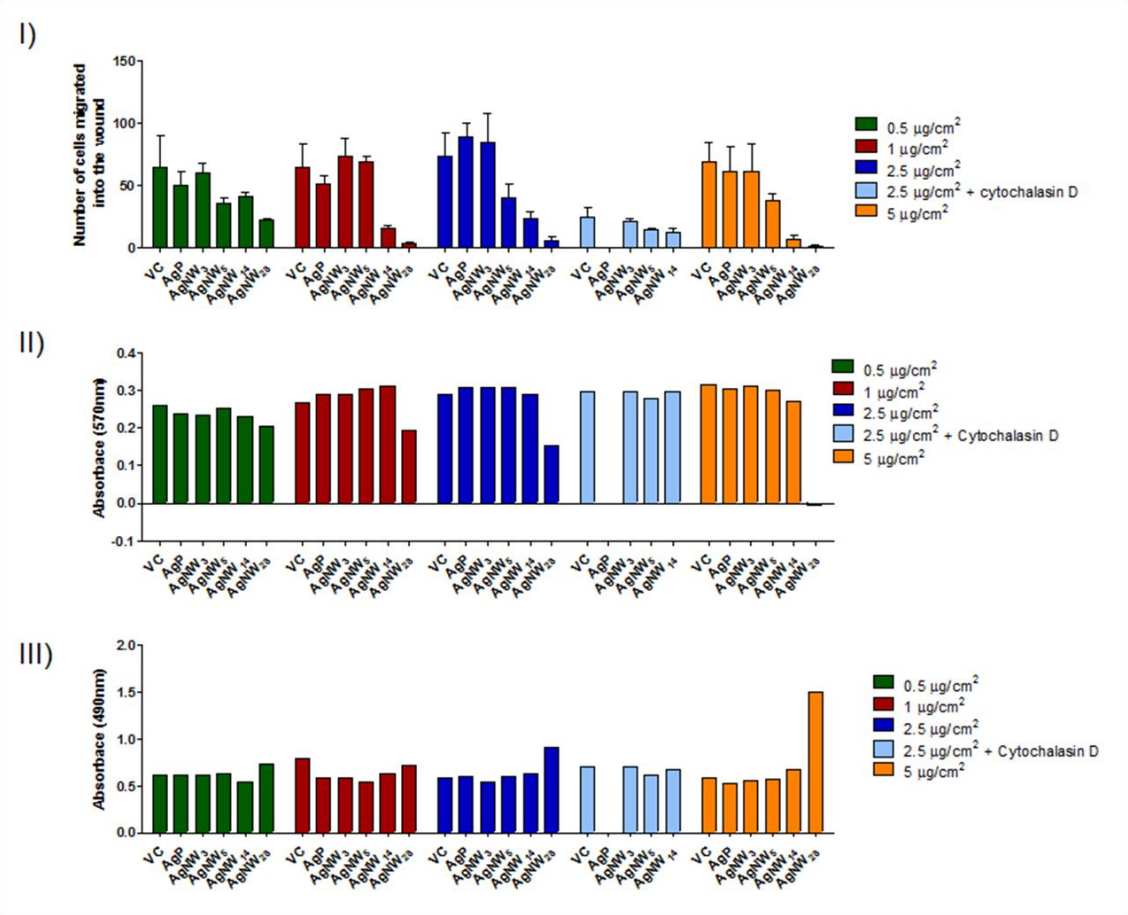

Figure 5-12: Dose response series for cell migration, membrane integrity and cell metabolism. I) A dose response series was performed to measure the number of cell migrated into the wound at concentrations of 0.5, 1, 2.5 and 5 µg/cm^2. Data represent mean + SEM of n = 3. II) Metabolic activity of BMMs was assessed via the reduction of AlamarBlue® at an absorbance of 570 nm. At a dose of 5 µg/cm^2 extensive reduction in metabolic activity was measured. III) The integrity of the BMM cell membrane after the different concentrations of AgNW and AgP was measured via the release of LDH into the cell supernatant and compared to VC. At a dose of 5 µg/cm^2 extensive increase in membrane permeability was measured. Initial screening of n=1.

For subsequent measurements a dose of 2.5 µg/cm^2 based on $AgNW_{14}$ was chosen (see Table 2-2). As shown in Figure 5-13 I, the untreated cells migrated into and repopulated wounds area within 30 hour. Similar wound closure was seen after treatment with AgP and $AgNW_3$ (Figure 5-13 I). A slight decrease in the

repopulation of the wound occurred during treatment with $AgNW_5$ whilst BMMs treated with $AgNW_{14}$ and $AgNW_{28}$ (Figure 5-13 II) demonstrate a substantial decrease in the ability to migrate into the wound compared to VC. In addition to light microscopy images, cells were fixed after 30 hours and images taken by SEM (Figure 5-14). The number of cells which migrated into the wound were counted and expressed as percentage of migrated cells normalised to VC and this revealed that locomotion was significantly decreased with $AgNW_5$, $AgNW_{14}$ and $AgNW_{28}$ (Figure 5-15 I). Cytochalasin D, a positive control which causes impaired migration due to disruption of the actin filaments produced a decrease in locomotion comparable to $AgNW_{14}$ (Figure 5-15 I). Differences in the rate of metabolic activity or cell death could not account for the inability of longer fibre-exposed macrophages to migrate into the wound as the treatment neither interfered with the metabolic activity measured via chemical reduction of Alamar Blue® (Figure 5-15 II) nor compromised cell membrane integrity measured as the release of lactate dehydrogenase into cell supernatant (Figure 5-15 III). Decrease in cell adhesion has been linked to a decrease in the ability of cell migration. Backscatter scanning electron microscopy (BSE) images confirm that treatment with AgNW did not impair the ability of cell adhesion and spreading (Figure 5-13 I, II bottom panel). To the contrary, extensive cell spreading is observed in cells treated with long fibres presumably a consequence of BMMs increasing the surface area involved in engulfing the fibres. Using BSE, nanowires and nanoparticles phagocytosed by BMMs could be visualised underneath the membrane as indicated by the arrow (Figure 5-13 I, II).

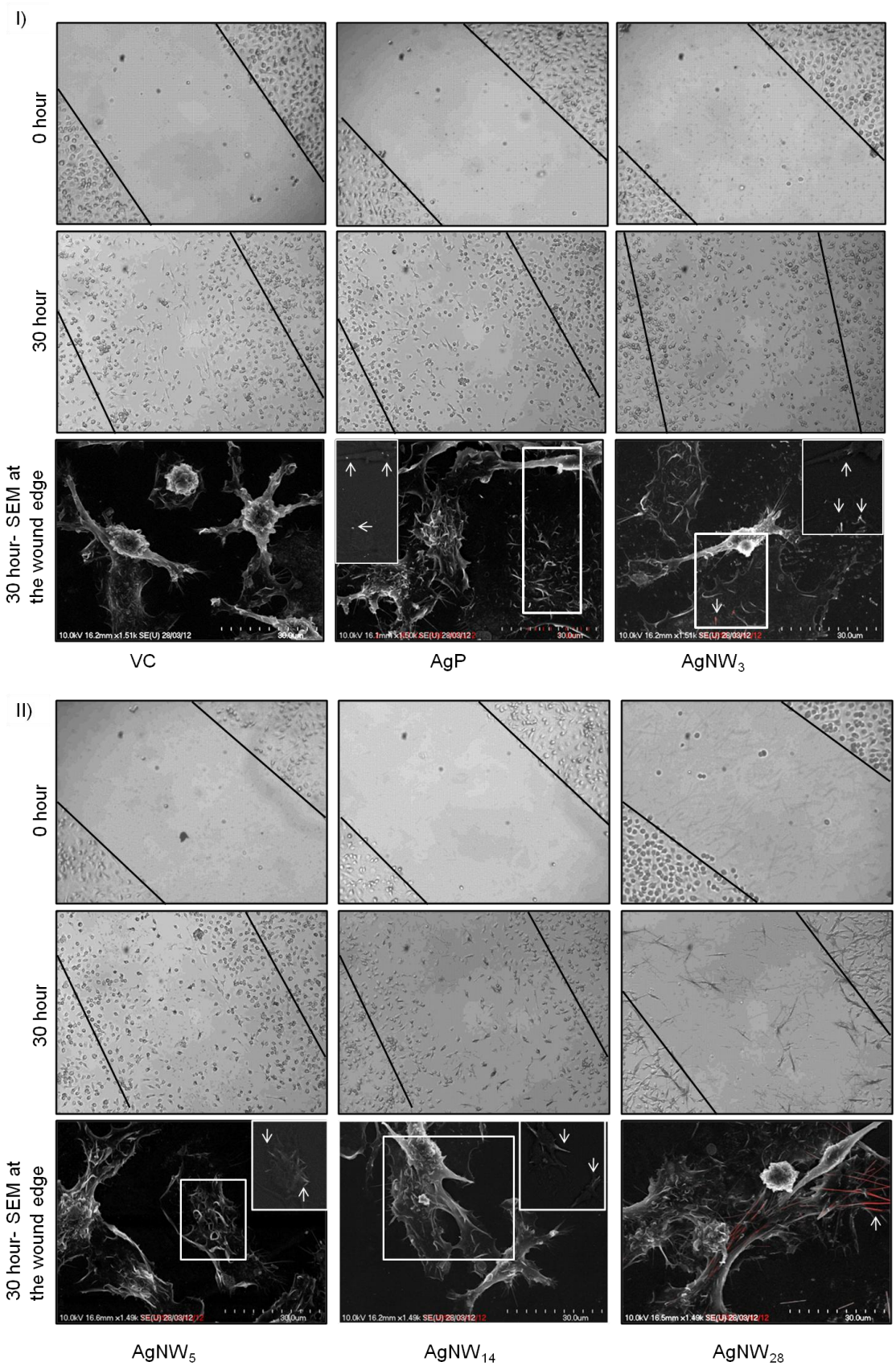
I)
0 hour
30 hour
30 hour- SEM at the wound edge
VC
AgP
AgNW3
II)
0 hour
30 hour
30 hour- SEM at the wound edge
AgNW5
AgNW14
AgNW28

Figure 5-13: Fibre-length dependent impaired migration of BMMs in a wound-healing assay. An artificial wound was created in the BMM monolayer using a pipette tip and the migration of BMMs into the wound was assessed after treatment with VC (I), AgP (I), $AgNW_3$ (I), $AgNW_5$ (II), $AgNW_{14}$ (II), $AgNW_{28}$ (II). The dose was adjusted to equal fibre number and based on 2.5 μg/cm^2 for $AgNW_{14}$. Photographs were taken immediately and at 30 hour after creating the wound. For BSE images were taken at the edge of the wound. No impairment of cell adhesion and spreading could be observed and in fact increased cell spreading due to uptake of longer fibres was observed. Nanoparticles and fibres could be visualised underneath the cell membrane as indicated by the white arrow in the inserts which are the non-overlayed BSE images. Representative images are shown; similar results are obtained in 3 independent experiments.

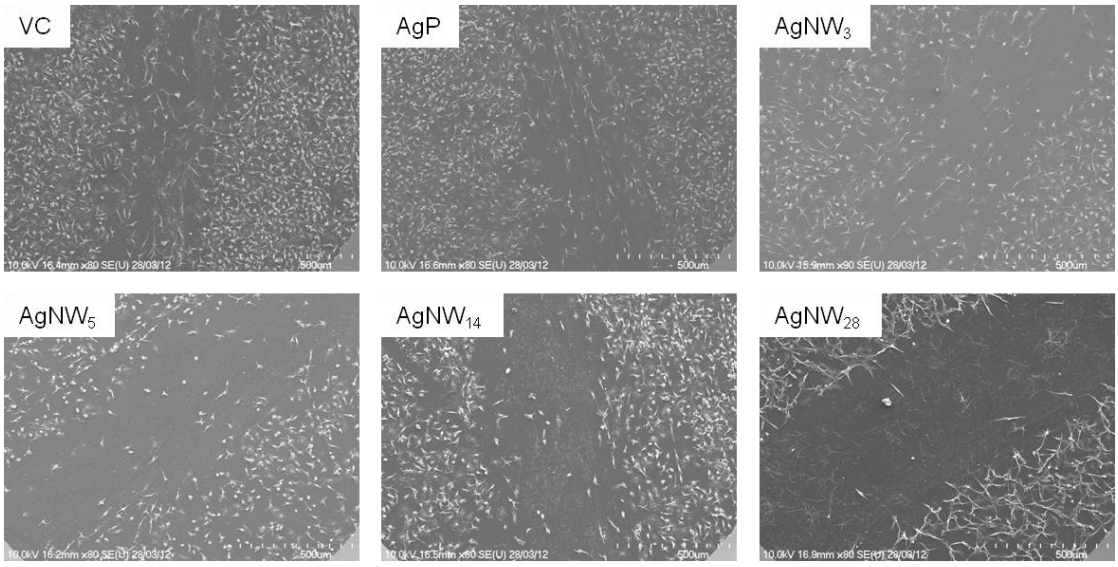

Figure 5-14: 30 hour macrophage migration assay in BMMs. SEM images showing the closer of the wound after 30 hour at different treatments with AgNW. Representative images are shown; similar results are obtained in 3 independent experiments.

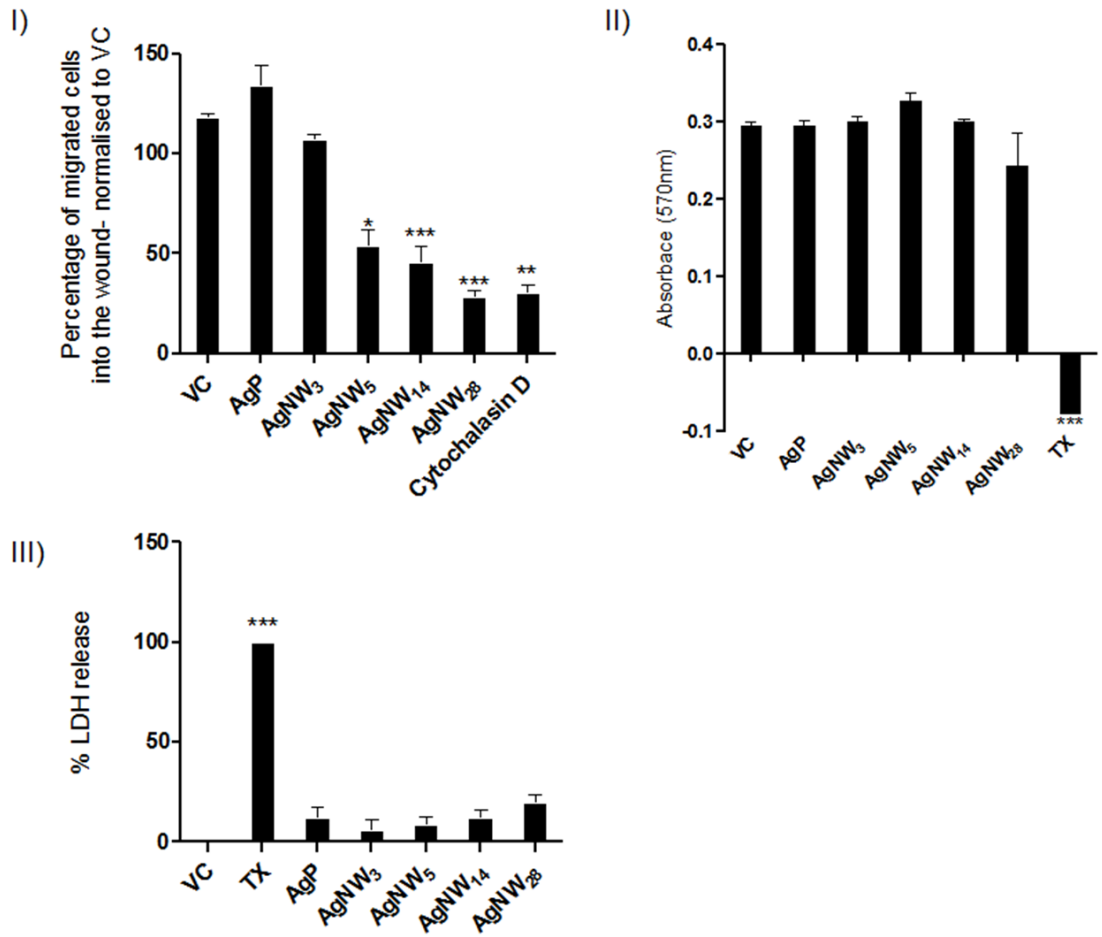

*Figure 5-15: Inhibition of BMMs migration in a macrophage migration assay and cell viability. I) The number of migrated cells in the 'wound' region was counted and expressed as percentage of cells migrated into the wound normalised to VC. Significant reduction of migration was seen with $AgNW_5$, $AgNW_{14}$, $AgNW_{28}$ and cytochalasin D, a positive control for actin cytoskeleton disruption. II) Metabolic activity of BMMs was assessed via the reduction of AlamarBlue® at an absorbance of 570 nm. At the dose used no significant reduction in metabolic activity was measured. III) The integrity of the cell membrane after the different treatments was measured via the release of LDH into the cell supernatant and compared to VC and TX, positive control. A sub-lethal dose was chosen at which none of the treatments led to a significant increase in cell permeability. Significance indicated compares treatment groups to vehicle control, * indicates $p < 0.05$, ** indicates $p < 0.001$, *** indicates $p < 0.0001$ ($n = 3$). Data represent mean + SEM of $n = 3$.*

5.3.5 Screening for kinase phosphorylation in BMMs after AgNW treatment

To reveal whether there was any fundamental change in the activation/metabolic state of the cells when they were impaired in their ability to migrate by phagocytosing long fibres, an initial screening of 46 kinase phosphorylation sites was performed.

The phospho- kinase array showed that kinases including GSK-3 α/β, Akt (S473), β-catenin and PLC-γ were activated on treatment with $AgNW_3$, $AgNW_5$ and $AgNW_{14}$ which can be explained via a general activation due to phagocytosis of particles (Figure 5-16 I, II). Kinases including STAT3, p53 (S392), p27 (T198), p27 (T157) and p70 S6 (T389) were more activated in $AgNW_5$ and $AgNW_{14}$ compared to $AgNW_3$ which correlate with the loss of locomotion (Figure 5-16 I, II). Interestingly, the highest level of activation of the cytoplasmic tyrosine kinase Src family members including Src, Lck, Hck and Frg was detected in the $AgNW_{14}$ treated BMM (Table 5-1). A summary of the relative pixel intensities of all kinases can be found in the Table 5-1 and Figure 5-17.

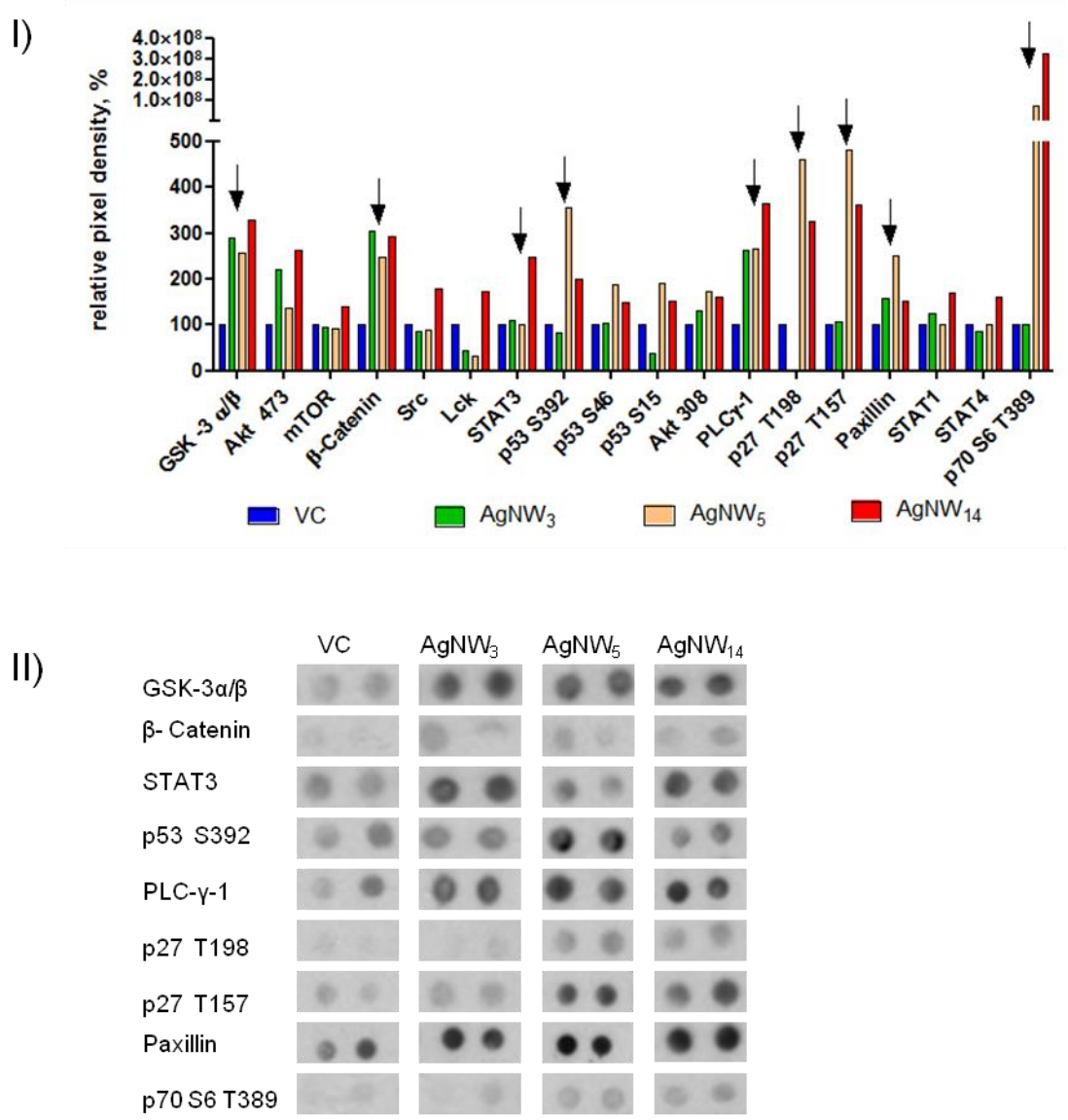

Figure 5-16: Phosphoproteomic analysis of BMMs exposed to AgNW. I) A phospho-kinase array (R&D) was performed to screen the phosphorylation state of 46 kinases in BMMs after treatments with $AgNW_3$, $AgNW_5$ and $AgNW_{14}$ whereby 15 kinases showed an increase in phosphorylation relative to VC. II) Immunoblot analysis extract of kinases involved in cell migration/mobility and adhesion. Results are based on an initial screening (n = 1). Phospho-kinase array and analysis was performed by Dr Tanya Chernova.

Table 5-1: Phosphoproteomic analysis of BMMs exposed to AgNWs. A phospho-kinase array (R&D) was performed to screen the phosphorylation state of 46 kinases in BMMs after treatments with AgNW. Relative pixel density in % compared to VC is shown for all kinases measured (n=1).

	VC	$AgNW_3$	$AgNW_5$	$AgNW_{14}$
p38 a	100	74.85	159.09	121.96
ERK 1/2	100	93.41	86.16	74.33
JNK pan	100	107.53	82.98	86.15
GSK -3 a/b	100	289.00	256.35	327.82
MEK1/2	100	115.86	97.57	129.87
MSK 1/2	100	77.77	96.81	79.48
Akt 473	100	221.51	137.80	261.48
mTOR	100	94.12	92.45	138.54
CREB	100	52.64	29.99	78.01
HPS27	100	128.64	131.60	141.17
AMPK a2	100	175.96	105.32	140.03
β-Catenin	100	306.22	249.12	293.51
Chk-2	100	54.89	97.63	103.00
Src	100	86.63	87.62	178.41
Lyn	100	52.63	45.04	67.14
Lck	100	43.72	32.90	171.80
Fyn	100	51.26	57.08	104.40

Yes	100	50.56	72.43	108.49
Frg	100	69.26	111.40	132.60
Hck	100	100.07	132.39	162.50
FAK	100	96.46	132.29	126.20
STAT2	100	126.91	97.21	120.56
STAT3	100	109.67	101.52	247.60
STAT 5a	100	115.59	122.06	135.43
STAT5 b	100	93.41	90.03	117.70
STAT5 A/B	100	121.44	116.31	154.23
STAT7	100	110.99	93.45	112.70
p53 S392	100	83.20	356.63	198.74
p53 S 46	100	105.01	189.05	147.20
p53 S15	100	38.12	190.13	152.74
Akt 308	100	131.34	172.40	161.11
p70 S6 T421/S424	100	134.21	104.95	134.33
p70S6 T229	100	93.99	142.35	136.85
cJun	100	107.21	141.34	160.83
PLC-γ1	100	263.56	266.54	363.68
Pyk -2	100	126.66	115.08	152.87
p27 T198	100	0.00	459.79	326.21
p27 T157	100	107.95	480.65	363.21

paxillin	100	159.08	250.35	152.23
RSK1/2/3	100	87.02	99.50	89.36
RSK1/2 S221 S227	100	78.24	111.36	104.93
STAT1	100	123.33	100.83	170.85
STAT4	100	85.95	101.54	160.66
eNOS S1177	100	156.19	173.36	94.30
p70 S6 kinase T389	100	100.00	74681710.00	325861181.50

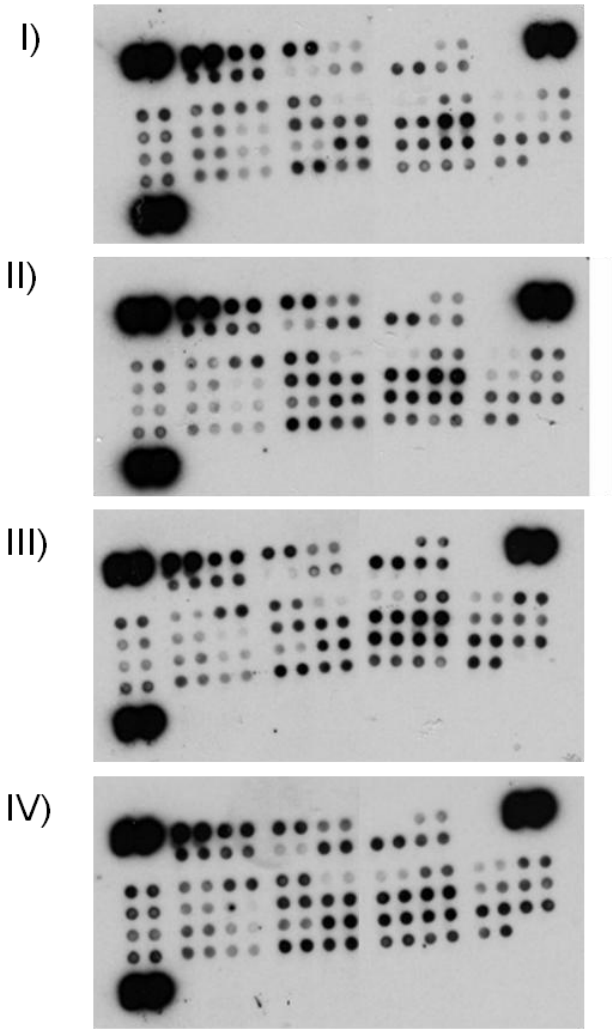

Figure 5-17: Phospho-kinase array immunoblots. I) VC, II) $AgNW_3$, III) $AgNW_5$, IV) $AgNW_{14}$.

5.4 Discussion

The aim of this study was to investigate length-dependent effects of AgNW in the lungs. To assess the role of fibre length in the initiation of inflammation the BAL profile was assessed after aspiration exposure. To assess the effect of length on macrophage clearance and retention of the long fibre dose we used an *in vitro* wound-healing assay. The latter study aimed to shed light onto the effects of fibre length on clearance of fibre-laden alveolar macrophages via migration from the alveolar region of the lung to the mucociliary escalator.

Fibre dimension is a critical factor for lung diseases after inhalation exposure of various forms of fibrous materials as demonstrated in a number of experimental studies, with long fibres being more pathogenic than short ones (Davis et al., 1987; Davis et al., 1986; VORWALD et al., 1951). Long term inhalation studies in rat have been performed with amosite asbestos preparations of short (1% > 5 µm), medium (UICC reference fibre) and long (30% > 5 µm, 11% > 10 µm). These studies showed that the short fibres and the slightly longer UICC sample were low in pathogenicity whilst the long fibres induced extensive fibrosis and pulmonary adenomas. This was in contrast to the studies performed using direct injection of the same samples of amosite asbestos into the peritoneal cavity which showed that UICC amosite was sufficiently long to cause mesothelioma in rats at the same frequency as long amosite fibres (Davis et al., 1986). This supports the findings of this study, that the length threshold for fibre effects in the lung is different to the length threshold for fibre effects at the mesothelial surface, the lung threshold being a higher value. Poland *et al.* demonstrated severe lung and peritoneal inflammation after aspiration exposure and direct intraperitoneal injection in mice of long (24 µm) nickel nanowire but only very mild diffuse alveolitis and mild peritoneal inflammation after exposure to short (4 µm) nickel nanowires (Poland et al., 2012). Similar results were obtained from studies on short (< 1 µm) and long (>13 µm) carbon nanotubes where a length-dependent inflammation in lung of mice after aspiration exposure was observed (Murphy et al., 2012a).

In the previous chapter the threshold length for pleural inflammation was reported. This data clearly showed that fibres below 5 µm in length were non-inflammatory

and that fibres 5 µm in length and longer caused extensive recruitment of inflammatory cells to the pleural space.

The current study addressed the lack of knowledge regarding the threshold length for acute pulmonary inflammation after deposition in the airspaces of the lungs. The pulmonary response to AgNW reported here showed a threshold length for the significant recruitment of inflammatory cells of 14 µm compared to the 5 µm fibre threshold length for pleural inflammation. The use of size categories means that the actual threshold could lie anywhere between 11- and 14 µm since the size category below, at which no inflammation was produced was 10 µm. This finding of a longer threshold in the lungs is consistent with previous reports implicating longer fibres in the development of lung carcinoma compared to mesothelioma (Davis et al., 1986). The different length thresholds for pulmonary versus pleural inflammation can be explained as a consequence of the different mechanisms of fibre clearance from the lung and the pleural space. Clearance of fibres from the pleural space is via lymphatic drainage to mediastinal lymph nodes through stomata, pores in the parietal pleura which are around 0.5-10 µm in diameter (Schinwald et al., 2012). Therefore a size-restricted clearance occurs in the pleural space leading to retention of fibres which cannot negotiate the stomata and subsequent recruitment of inflammatory cells (Murphy et al., 2011). The clearance mechanism in the lung relies on alveolar macrophage phagocytosis and migration to the foot of the mucociliary escalator and is discussed in more detail below.

While deposition of $AgNW_{14}$ in the airspaces led to a significant increase in inflammatory cells in the broncho-alveolar lavage fluid (BAL), shorter fibres including SFA, $AgNW_3$, $AgNW_5$ and $AgNW_{10}$ only produced a mild, non significant, increase in the total granulocyte number. It was noticeable that the length-dependent response was not linear and showed a marked step-increase in the inflammation between 10 and 14 µm. Histological examination of lung sections showed no recruitment of inflammatory cells after exposure to SFA or $AgNW_3$. Minor aggregations of inflammatory cells around terminal bronchioles and in alveolar airspaces were observed with $AgNW_5$ and $AgNW_{10}$ but these were more extensive in the $AgNW_{14}$ and LFA samples showing early stages of granuloma

development in the terminal airways/ proximal alveolar region. The histological response to LFA was strongest showing extensive aggregates of inflammatory cells. However, the BAL fluid from LFA-exposed mice, whilst showing an increase in the mean number of granulocyte that was almost 4 times the mean number in the mice exposed to SFA did not attain significance. Additionally, lavage from lungs exposed to LFA showed a smaller number of BAL granulocytes than $AgNW_{14}$ and this contrasted with the histology data that showed more lung inflammation with LFA than $AgNW_{14}$. The low PMN in the lavage from LFA-exposed lungs was possibly due to a poor return from the inflammation-congested areas of the lungs. The final scoring of LFA equal to $AgNW_{14}$ for BAL granulocytes (Table 5-2) therefore took into account both the histological and lavage data to provide the best assessment of their relative inflammogenicity. The lack of an inflammatory response with shorter AgNW, which can be considered to be equivalent to silver particles, is consistent with experimental studies demonstrating the minimal lung toxicity or inflammogenicity of nanosilver in a subacute murine and 28-day rat inhalation model (Stebounova et al., 2011; Ji et al., 2007). The study presented here focuses on short-time response due to the fact that the AgNW used in this study appear not to be biopersistent beyond a few days as reported in chapter 3.3.13. It is highly likely that the same length dependent effects would be shown by wholly biopersistent fibres and that the inflammation would be chronic. However, the determination of the threshold length for long term chronic inhalation studies is of utmost importance and biopersistence remains a key factor in the pathogenicity of long nanofibres.

The clearance efficiency of deposited fibres from the lower respiratory tract plays a major role in the development of pulmonary diseases since the retained dose, which is the dose accumulated in the alveolar region of the lungs after clearance accounts for the chronic pathogenic effects of inhaled fibres (Oberdorster, 1993).

Fibres deposited in the conducting airways are cleared rapidly via cilia in the mucociliary escalator and subsequently swallowed or expectorated. If fibres reach the respiratory bronchioles, alveolar ducts or alveolar sacs they are cleared slowly via alveolar macrophages (AM) phagocytosing the deposited fibres and transporting them upwards to the ciliated airways for mucociliary clearance. It has been noted in

many studies that there is selective retention of long biopersistent fibres of various sorts from the slow-clearing compartment with more effective clearance of the shorter fibres (Searl et al., 1999; Lippmann, 1990).

The mechanism by which fibre-laden alveolar macrophages are drawn to the terminal bronchioles at the foot of the ciliated airways is obscure. Possible explanations include the passive transport with alveolar fluid or amoeboid movement of AM either by random migration or directed migration along a chemotactic gradient (Lehnert, 1992). Other pathways of clearance, usually only important during high dust exposure or disease are intra- and transcellular pathways by which fibres can reach lung interstitium and lymph nodes from where they subsequently may reach the blood stream (Oberdorster, 1993; Holt, 1983; Miserocchi et al., 2008). A recent study investigated the effects of MWCNT on cell migration and adhesion of human dermal fibroblasts and murine fibroblasts, reporting a significant decrease in cell adhesion which was confirmed by the decrease of mRNA levels of important cell adhesion proteins FAK, fibronectin and laminin (Zhang et al., 2011). In addition fibroblast migration in a wound-healing assay was greatly impaired by MWCNT treatment and was accompanied by cytoskeletal derangement (Zhang et al., 2011), although it should be noted that the dose of MWCNT used in this study was cytotoxic to human fibroblast which could influence the adherence and migration properties of the cells.

This study investigated whether fibre length has an effect on the migration behaviour of BMMs *in vitro* after fibre exposure using a wound-healing assay, a surrogate for *in vivo* clearance of fibrous material to the mucociliary escalator by AM migration. We used a very low dose to study effects on BMM migration, based on 2.5 µg/cm^2 for $AgNW_{14}$ and all the other length classes were adjusted to provide the same fibre number. The dose used had no significant effect on cell metabolism or cell viability for any of the length classes, ensuring that the observed effects were not due to simply impaired cell viability. A clear length-dependent trend for inhibition of BMM cell migration was measured at fibre lengths of 5, 14 and 28 µm and at 28 µm there was more or less complete inhibition of motility. Presumably as a consequence of cell surface extension of AM during engulfment of long fibres, increased cell

spreading was observed and correlated with increased inhibition of migration. The BMMs in this study had an average diameter of 13 µm (Cannon and Swanson, 1992) whilst human alveolar macrophages have an average diameter of 21 µm (Krombach et al., 1997). Due to this difference the threshold length for clearance of fibres by alveolar macrophages in humans may be slightly higher.

An initial screening of 46 kinase phosphorylation sites was performed to get a snapshot of the kinase activation status of fibre-treated BMMs. The following discussion of the kinase phosphorylation is based on an n=1 and therefore has to be considered with caution.

We hypothesised that this might reveal whether there was any fundamental change in the activation/metabolic state of the cells when they were impaired in their ability to migrate by phagocytosing long fibres. The 3 µm long exposed cells act as a control for normal phagocytosis and when compared to the untreated kinase profile this showed most of the kinases (~32) remained unchanged. The kinases GSK-3 α/β, Akt 473, β-catenin and PLC-γ showed activation in all treatment groups suggesting a link to normal phagocytosis. Comparing the kinase phosphorylation profile of BMM exposed to 3 µm with those exposed to 5 and 14 µm should reveal differences associated with the long fibre-dependent loss of motility and 5 kinases out of 46 (STAT3, p53 (S392), p27 (T198), p27 (T157) and p70 S6 (T389)) exhibited increased phosporylation with $AgNW_{14}$ compared to $AgNW_3$. Tyrosine kinases of the Src family were noticeably induced by treatment with long fibres. These kinases have been implicated in intracellular signalling in macrophages influencing the amplitude of many pathways (Abram and Lowell, 2008). One of the Src downstream effectors is STAT3, a major modulator of inflammation, which is required for activation of macrophages (Lin and Bost, 2004). A marked induction of STAT3 following the $AgNW_{14}$ treatment is a likely result of Src activation. It's worth mentioning that a constitutive activation of STAT3 is a common feature in many solid tumours (Looyenga et al., 2012), therefore persisting activation of STAT3 in a chronic inflammation caused by long fibres may contribute to pro-oncogenic changes. Macrophage motility is known to be negatively regulated by p53 (Sablina et al., 2003) and the latter was induced in BMM treated with longer fibres, and might

have contributed to impairment of their migration. The role of p27 in regulation of cellular migration remains unclear, however, our finding would support the reports showing suppression of migration by induction of p27 (Berton et al., 2009). No kinases were down-regulated in the long fibre treated BMM compared to the controls confirming that there was no generalised loss of viability associated with failure to migrate. It is reported in the literature that a number of different kinase pathways are involved in the migration and adhesion processes. Among these are kinases that showed an increase in their phosphorylation state after long fibre treatment (Kobayashi et al., 2006; Ip and Wong, 2012; Roger et al., 2006; Huang et al., 2003; Lee et al., 2009; Yoon et al., 2012; Baruzzi et al., 2008). The results from the screening of the phosphorylation sites was mainly performed to see if crucial cellular signalling processes are impaired by the treatment of AgNW which might indicate that decreased cellular function, apoptosis/necrosis underlay the decrease in cell mobility. Our results showed that the long-fibre treatment did not negatively affect the cellular function of the BMMs as assessed by metabolic function, loss of membrane integrity or kinase profile. In fact long fibre treatment and inhibition of motility were associated with increased phosphorylation of some kinases involved in migration and adhesion. Clearly the interplay between adhesion and motility is complex since focal adhesion is required for motility and a more sophisticated analysis of mechanism underlying loss of motility with long fibre treatment is required. The results give an indication that cellular processes are intact in long fibre treated BMM and therefore that inhibition of locomotion can be best explained via a mechanical obstruction to motility. By this we suggest that the presence of long fibres inside the cells physically interferes with the necessary rearrangement of the cytoskeleton, membrane and other structures that are necessary for locomotion. This however has to be confirmed by an in depth investigation of the molecular mechanism involved in inhibition of migration.

Table 5-2: Summary of the length-dependent effects of fibres in the lungs.

Treatment	Endpoint				
	BAL Granulocytes*	Lung Histology**	Frustrated phagocytosis***	Impaired migration****	Δ kinase phosphorylation*****
Control	+	-	No	-	NA
SFA	+	-	No	NA	NA
LFA	+++	++++	Yes	NA	NA
$AgNW_3$	+	-	No	-	+
$AgNW_5$	++	+	No	+	+
$AgNW_{10}$	++	+	No	++	NA
$AgNW_{14}$	+++	+++	Yes	+++	++

* BAL granulocytes: <0.5 million (+); 0.5-1.0 million (++); 1–2 million (+++)
** Lung histology subjectively scored on the basis of the severity of lung inflammation (see results)
*** Frustrated phagocytosis on the basis of evaluation of cytospins for presence of frustrated phagocytosis
**** Impaired migration on the basis of degree of significant impairment compared to control (see Figure 6A)
***** Δ kinase phosphorylation based on subjective examination the levels of phosphorylation of the treated compared to the control levels of phosphorylation (see Figure 7). NA = not applicable.

In conclusion this study has shown that there are length-dependent effects on the lung and on BMM summarised in Table 5-2. These show length-dependent increases in inflammation by BAL and severity of lung injury by histology *in vivo* and evidence of accompanying impairment of macrophage migration by BMM *in vitro*. A threshold length for acute pulmonary inflammation after pharyngeal aspiration of AgNW was evident between 10 and 14 µm in length. This compares with the previous studies on the threshold length for pleural inflammation of 5 µm, determined using the same panel of AgNW. The difference in thresholds can be explained by the differences in clearance mechanism between the lung the pleural space. In the pleural space clearance is through stomata (Donaldson et al., 2010) whilst clearance of deposited fibres from beyond the ciliated airways is via uptake by AM and subsequent migration to the mucociliary escalator. Using an *in vitro* macrophage migration assay we showed that fibre length-dependent macrophage mobility, with a threshold for impairment at a length of 5 µm and increasing impairment with increasing length, until at 28 µm there was almost complete inhibition of motility. An explanation for the decrease in locomotion could be mechanical obstruction caused simply by the bulky long fibres interfering with the

movement process since there was no loss of viability or metabolism in the long fibre-treated cells and an initial screen of a number of 46 kinases showed only a change in 14 kinase phosphorylation sites. This study was a small-scale pilot study with acute inflammation and short term inhibition of migration *in vitro* as the endpoints. These results need to be confirmed in long term inhalation studies using a range of different nanofibres at plausible exposure concentrations before we can confidently utilize these thresholds for risk assessment and in benign-by-design for nanofibres.

Chapter 6: Pulmonary and pleural response to graphene nanoplatelets

Some of the following results have been published in

Schinwald A, Murphy FA, Jones A, MacNee W, Donaldson K. Graphene-based nanoplatelets: a new risk to the respiratory system as a consequence of their unusual aerodynamic properties. ACS Nano. 2012 Jan 24;6(1):736-46.

6.1 Acknowledgement

Calculation of the aerodynamic diameter for graphene nanoplatelets (GP) was performed by Dr Alan Jones, Institute of Occupational Medicine, Edinburgh. Carbon Black (Printex 90®) was provided by Evonik Degussa GmbH in Germany. It was used as an amorphous carbon particle control. I thank Steve Mitchell (University of Edinburgh) for sample preparation for SEM, TEM and BSEM technical.

6.2 Aims and Hypothesis

Graphene, a two dimensional (2D) crystalline material comprised of a single layer of carbon atoms tightly packed into a honeycomb lattice has recently been identified (Novoselov et al., 2004) and attracted substantial scientific interest due to its unique intrinsic properties of graphene. However, due to their nanoscale dimensions and thinness nanoplatelets could posseses a much lower aerodynamic diameter (D_{ae}) than would be expected from their maximum diameter (Sanchez et al., 2012) which would mean that this new, emerging material could pose unusual risks to the respiratory system after inhalation exposure. Unintentional occupational or enviromental exposure to graphene-based materials during manufacturing or intentional exposure via biomedical applications are likely with their increasing development and use. The aim of this study was to determine the respirability of commercially available graphene platelets (GP) from the basic principles of the aerodynamic behaviour of

plate-shaped particles which allowed us to calculate their aerodynamic diameter and to assess their inflammatory potential in the lungs and the pleural space after aspiration exposure and intrapleural injection. We hypothesised that it was the shape in which the graphene was presented that was driving the activity and that respirable nanoparticulate carbon black (CB) would be readily cleared via alveolar macrophages from the airspaces and via stomata from the pleural space to the mediastinal lymph nodes. In contrast GP, exceeding the size for complete phagocytosis would be retained in the lung and, after translocation to the pleural space, GP would be too large to negotiate the stomata in the parietal pleura and so would initiate inflammation.

6.3 Results

6.3.1 Characterisation of Graphene Nanoplatelets

For this study graphene nanoplatelet (GP) were purchased from a commercial source (cheaptubes.com) and characterised according to their size distribution, contaminating metals and generation of oxygen-centred free radicals. Nanoparticulate carbon black (Printex 90®) (CB) was provided by Evonik Degussa GmbH and used as an amorphous carbon particle control. Characteristics and specifications of CB and GP are summarised in Table 6-1. CB and layered (1-10 layer) graphene nanoplatelet morphology were examined using scanning electron microscopy (SEM) (Table 6-1). Electron paramagnetic resonance (EPR) measurements were performed to determine the generation of oxygen-centred free radicals of CB and GP. Results were compared to one-another and to a positive Pyrogallol control, a spontaneous superoxide anion generator with Tempone H used as a spin trap. Both CB and GP caused a significant increase in free radical generation with GP production increased by 2-fold compared to CB (Table 6-1). EPR signal is based on the surface are of the particle of interest since the surface are is driving the oxidative properties of the material. In this case GP have a smaller surface are compared to CB due to aggregation of multiple layers of single GP sheets, however if GP exists in a single layer it could possess a much greater

potential of generating oxygen-centred free radicals compared to CB. For quantification of contaminating metals the supernatant of 1 mg/ml of each sample in 0.5% BSA/saline was analysed using the technique of inductively-coupled mass spectrometry (ICP-MS). GP showed higher levels of ^{52}Cr, ^{63}Cu, ^{56}Fe, ^{55}Mn, ^{60}Ni and ^{64}Zn compared to CB, however all concentrations are negligible and not biologically relevant (Table 6-2).

Table 6-1: Characteristics and specifications of CB and GP. Morphology of materials by scanning electron microscopy (SEM). SEM of GP confirms morphology of the platelet shape. EPR measurement to determine generation of oxygen-centred free radicals. Surface area of CB from Donaldson et al. (Donaldson et al., 2000).

	CB	GP
Morphology	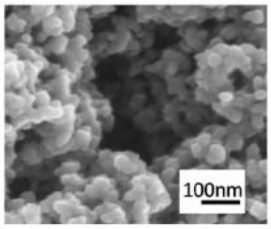	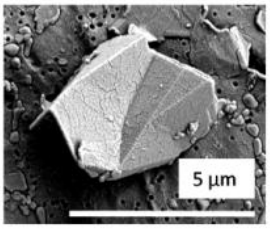
Projected diameter [µm] (mean ± s.e.m)	0.01 ± 0.01	5.64 ± 4.56
Layer number	0	1-10
Surface area [m²/g]	253.9	~100
Density [g/cm³]	~1.9	~2
EPR [Arbitrary Units]	451.3±52.2	867.3±77.5
Source	Evonik Degussa GmbH	Cheaptubes.com

Table 6-2: Concentration (ng/g) of soluble metal associated with CB and GP in the supernatant of a 1 mg/ml solution.

	Concentration (ng/g) of soluble metal associated with CB and GP										
	^{107}Ag	^{27}Al	^{111}Cd	^{59}Co	^{52}Cr	^{63}Cu	^{56}Fe	^{55}Mn	^{60}Ni	^{208}Pb	^{64}Zn
CB	0.1287	9.368	0.02333	0	0	1.161	0	0	0.07433	1.395	0
GP	0.3371	24.93	0.06652	2.799	29.98	15.39	437.8	52.19	121.8	1.563	22.1

6.3.2 Aerodynamics of platelet-shaped particles- calculation of the aerodynamic diameter

Calculation of the aerodynamic diameter of GP was performed to determine the deposition of these particles in the respiratory tract. Calculation was performed by Dr Alan Jones at the Institute of Occupational Medicine.

The gravitational settling speed of a particle is determined by the opposing effects of the gravitational force and the aerodynamic resistance. The aerodynamic drag force depends on the shape and orientation of the particle with respect to its direction of motion. A plate-like particle with uniform thickness may well settle under gravity with orientation perpendicular to its direction of motion. If it is not a uniform thickness, it might behave like a spear with a weighted tip (if one edge is relatively heavy) or it might be stable in the perpendicular orientation if the extra weight is central.

The gravitational force on a particle is determined by its volume and density. For a spherical particle with diameter d and density ρ, this is

$$F_g = \frac{\pi \cdot d^3 \cdot \rho}{6}.g \qquad (1)$$

where g is the gravitational acceleration.

For a platelet particle, with thickness t, and projected area diameter d_{proj} the equivalent gravitational force is;

$$F_g = \frac{\pi \cdot d_{proj}^{\ 2} \cdot t \cdot \rho}{4}.g \qquad (2)$$

The gravitational settling force is opposed by the aerodynamic resistance to the motion of the particle.

For a circular plate-like particle of diameter b that is infinitely thin, the aerodynamic resistance when the plate is perpendicular to the direction of motion at velocity V, the following expression can be obtained from Fuchs *et al*. (Fuchs N.A., 1964) for the resistance to motion

$$F_m = -8 \cdot \eta \cdot b \cdot V \qquad (3)$$

where η is the viscosity of air.

The above equation applies when the disc is perpendicular to the direction of motion.

When the infinitely thin circular plate-like particle is orientated parallel to the direction of motion, then the equation becomes:

$$F_m = -\frac{16}{3} \cdot \eta \cdot b \cdot V \qquad (4)$$

Fuchs(Fuchs N.A., 1964) also notes that the formula in equation 4 has given good agreement with data when Oseen's correction is introduced. For present purposes, the detail of Oseen's correction can be ignored.

When the particle reaches an equilibrium settling velocity (V_s,), then $F_m = F_g$, and by taking the projected area diameter d_{proj} as being approximately the same as the diameter of the circular plate, this leads to:

$$V_s = \frac{\pi \cdot d_{proj} \cdot t \cdot \rho \cdot g}{32\eta} \qquad (5)$$

The equivalent expression for a sphere of unit density (ρ_0) and diameter *d* is

$$V_{ss} = \frac{\pi \cdot d^2 \cdot \rho_0 \cdot g}{\eta} \qquad (6)$$

The definition of the aerodynamic equivalent diameter is the diameter of a unit density sphere with the same settling speed as particle; that is, if $V_{ss} = V_s$ then the d in equation 6 is the d_{ae} for the plate-like particle. This leads directly to an expression for the aerodynamic diameter of a plate-like particle as:

$$d_{ae} = \sqrt{\frac{9 \cdot \pi}{16} \cdot \frac{\rho}{\rho_0} . d_{proj} \cdot t} \qquad (7)$$

Using equation 7, we can estimate the aerodynamic diameter for plate-like-particles of given dimensions. Using this equation, we can estimate the aerodynamic diameter for plate-like-particles of given dimensions. The size of GP was measured using SEM and light microscopy images and plotted as percentage of GP per projected area diameter in the sample (Table 6-3). The GP consist of several sheets of graphene with a thickness of approximately 10 nm each, therefore their thickness increases to around 0.1 µm, depending on their dispersion. This information was used to calculate the D_{ae} of GP used in this study and shows that they are within the size range of the respirable fraction (Table 6-3).

Table 6-3: Size distribution of GP in the sample expressed as percentage of GP per projected area diameter. Aerodynamic diameter D_{ae} of GP at various projected diameters and a thickness (t) of 0.1 µm.

% of GP	Projected area diameter (d_{proj}) [µm]	Aerodynamic diameter (t= 0.1 µm)
57.4	5	1.33
32.9	10	1.88
6	15	2.30
2.8	20	2.66
0.6	25	2.97
0.3	30	3.26

6.3.3 Acute pulmonary inflammatory response to GP

To assess the hazard of GP to the lungs, GP were deposited in the lungs by pharyngeal aspiration at a dose of 50 µg per mouse. At 24 hour post exposure the total number of bronchoalveolar lavage (BAL) cells was increased significantly in GP exposed mice compared to vehicle control and mice aspirated with CB (Figure 6-1 I). This increase in cell number was mainly due to increase in polymorphonuclear leukocyteleukocytes (PMN), mainly neutrophils and eosinophils in the lavage fluid (Figure 6-1 I). The loss of membrane integrity of cells in the BAL, measured via the release of LDH was also significantly increased in GP treated mice (Figure 6-1 II). Concentration of the pro-inflammatory cytokines MCP-1, MIP-1α,

MIP-2 and IL-1β were measured in the BAL fluid using a quantikine kit. All cytokines measured were elevated after GP treatment compared to VC and CB, however only MIP-1α reached a significant difference (Figure 6-1 III).

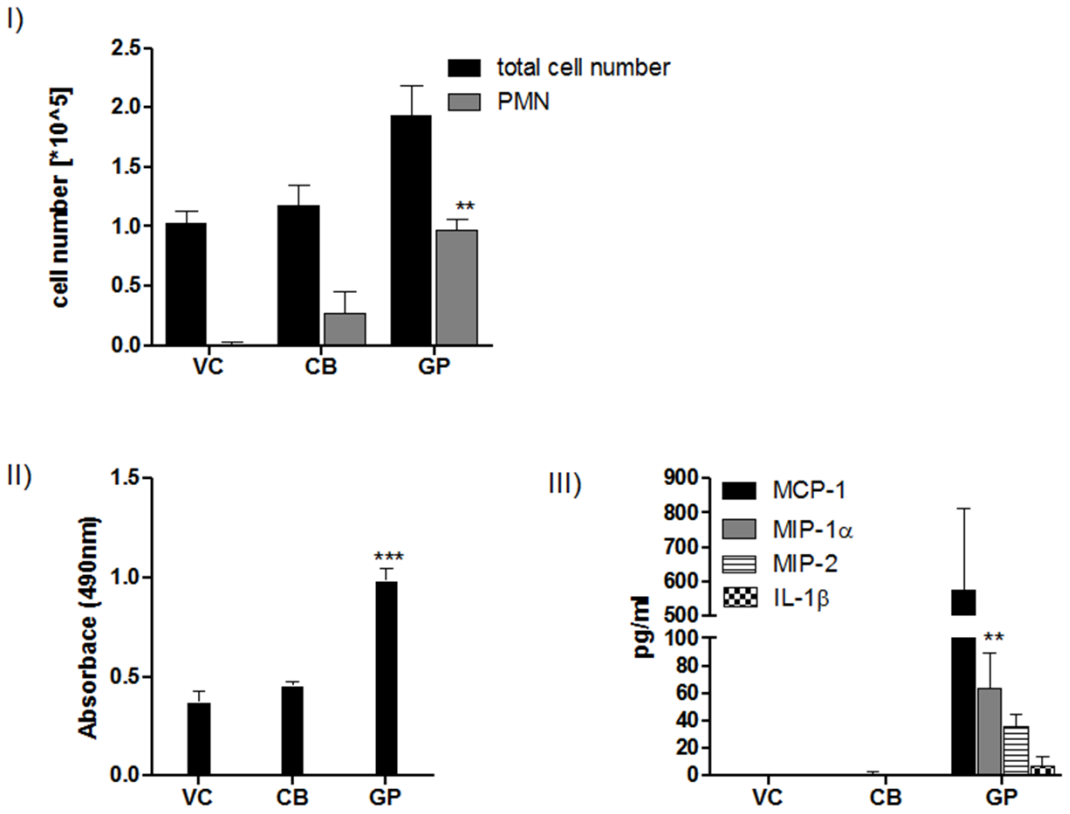

*Figure 6-1: Pulmonary inflammatory response to CB and GP 24 hour post aspiration. I) Total cell number and total granulocyte number to CB and GP in the lavage fluid. II) Measurement of the membrane integrity via LDH release in the lavage fluid. III) Concentration of the chemokines MCP-1 and MIP-1α as well as cytokines MIP-2 and IL-1β in BAL. Significance indicated compares treatment groups to vehicle control, ** indicates p < 0.001, *** indicates p < 0.0001 (n = 3). Data represent mean + SEM of n = 3.*

6.3.4 Histological examination of the lungs treated with GP and CB

Lung pathology 24 hour post aspiration was examined. Histological sections of lungs from mice treated with VC (Figure 6-2) and CB (Figure 6-3) had a normal histology. Histology sections of lungs from mice treated with GP showed granulomatous

lesions in the bronchiole lumen and in the vicinity of terminal bronchioles in the alveolar region (Figure 6-4).

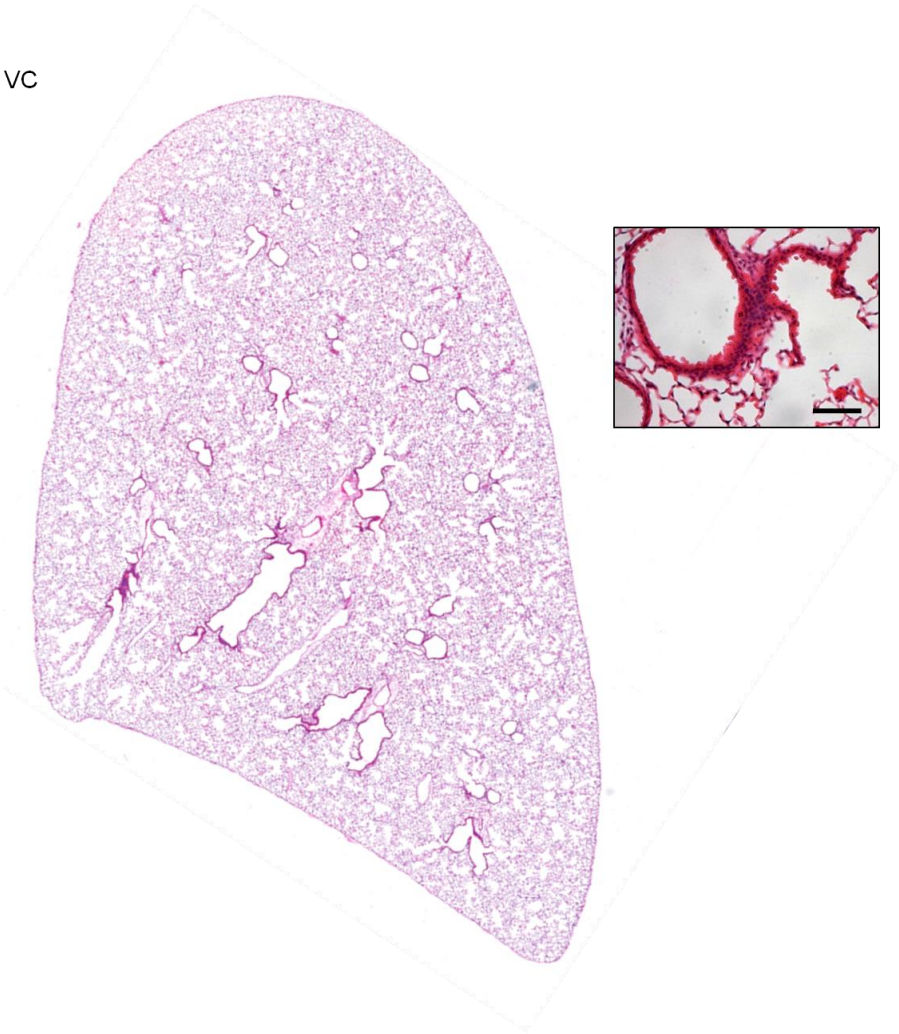

Figure 6-2: Lung pathology 24 hour post aspiration to VC. An entire lung section stained with Haematoxylin & Eosin (H&E) is shown to demonstrate gross pathology of a VC treated mouse (0.5% BSA/saline). Normal delicate structure of the lung including the terminal bronchioles and alveolar septa (callout) (representative image of an n=3). Scale bar insert 20 µm.

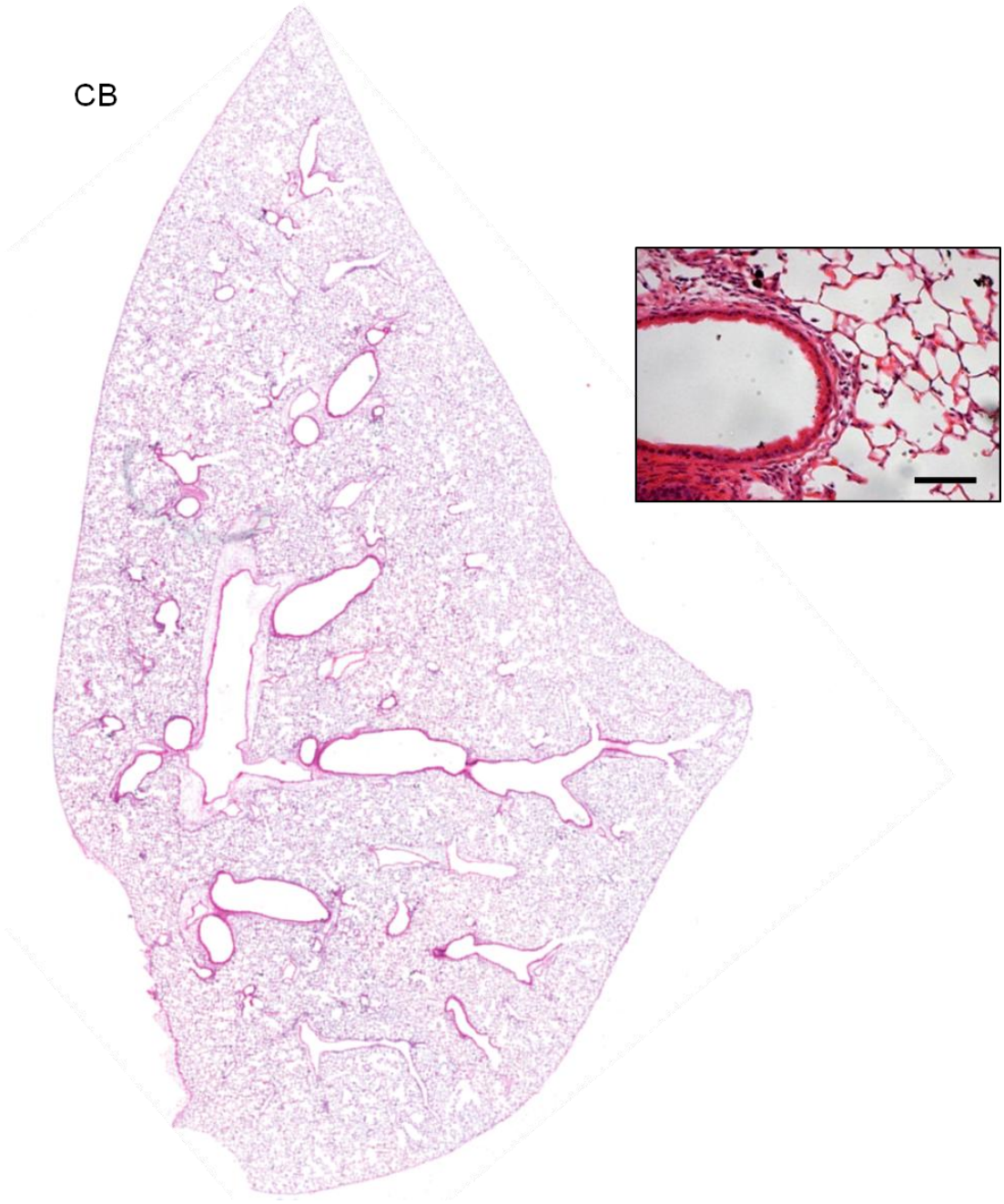

Figure 6-3: Lung pathology 24 hour post aspiration to carbon black (CB). An entire lung section stained with Haematoxylin & Eosin (H&E) is shown to demonstrate gross pathology of a CB treated mouse (50 µg/mouse). For the most part, the structure of the lung looks similar to the VC with minimal deposition of CB within the alveolar septa (callout) (representative image of an n=3). Scale bar insert 20 µm.

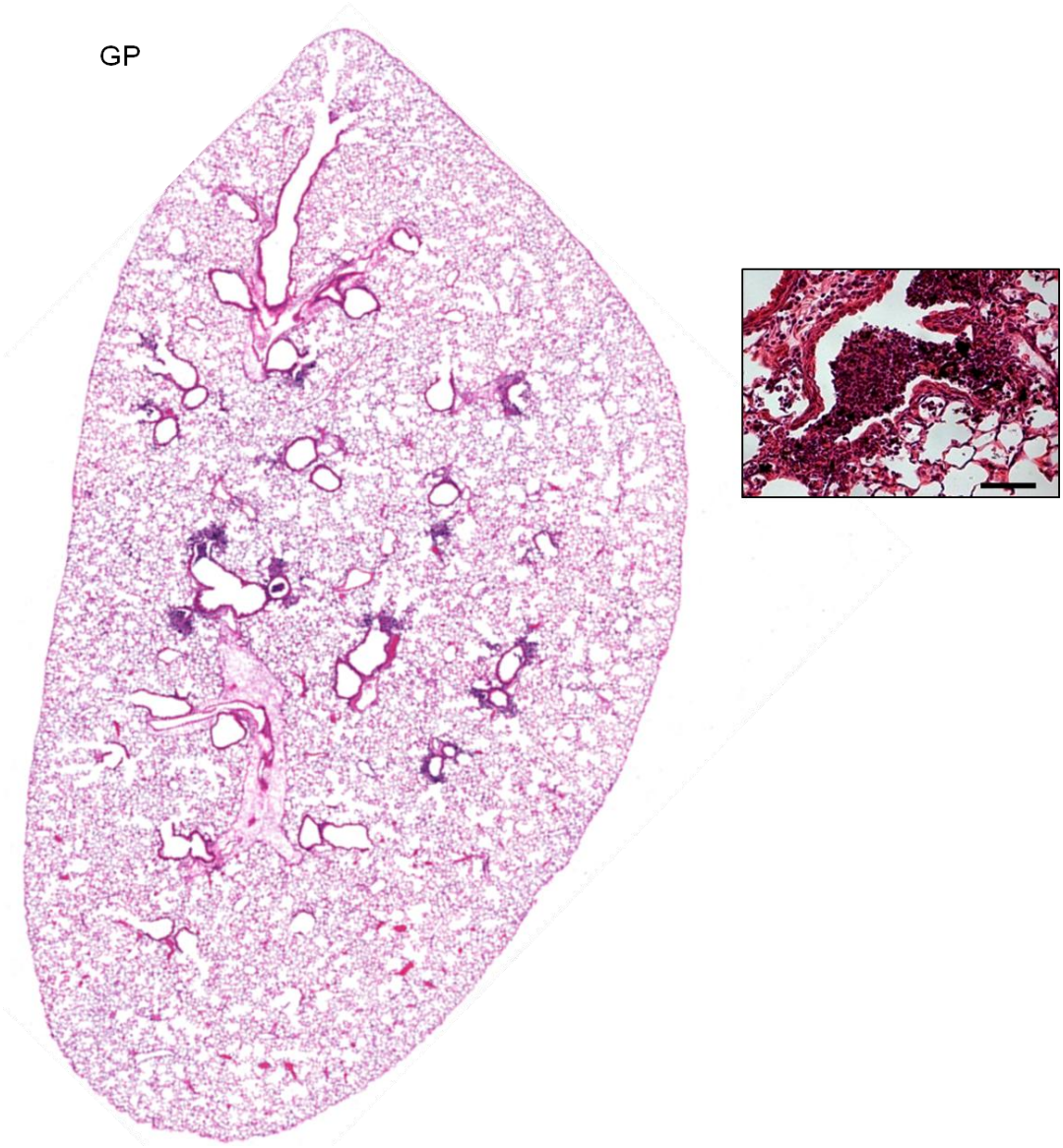

Figure 6-4: Lung pathology 24 hour post aspiration to graphene platelets (GP). An entire lung section stained with Haematoxylin & Eosin (H&E) is shown to demonstrate gross pathology of a GP treated mouse (50 µg/mouse). Extensive accumulations of inflammatory cells and GP aggregates are indentified (callout), mainly in the vicinity to terminal bronchioles. (representative image of an n=3). Scale bar insert 20 µm.

6.3.5 Medium term (1 week and 6 weeks) pulmonary inflammatory response to GP

The chronic response to CB/GP exposure was investigated 1 week and 6 weeks following a single exposure. The inflammatory response, measured in the number of total granulocytes decreased to a non-significant level from a 24 hour timepoint to 1 week and 6 weeks timepoint (Figure 6-5 II). The total cell number retrieved from the BAL was higher in all treatments at the 6 weeks timepoint compared to 24 hour and 1 week, however showed no significant increase (Figure 6-5 I).

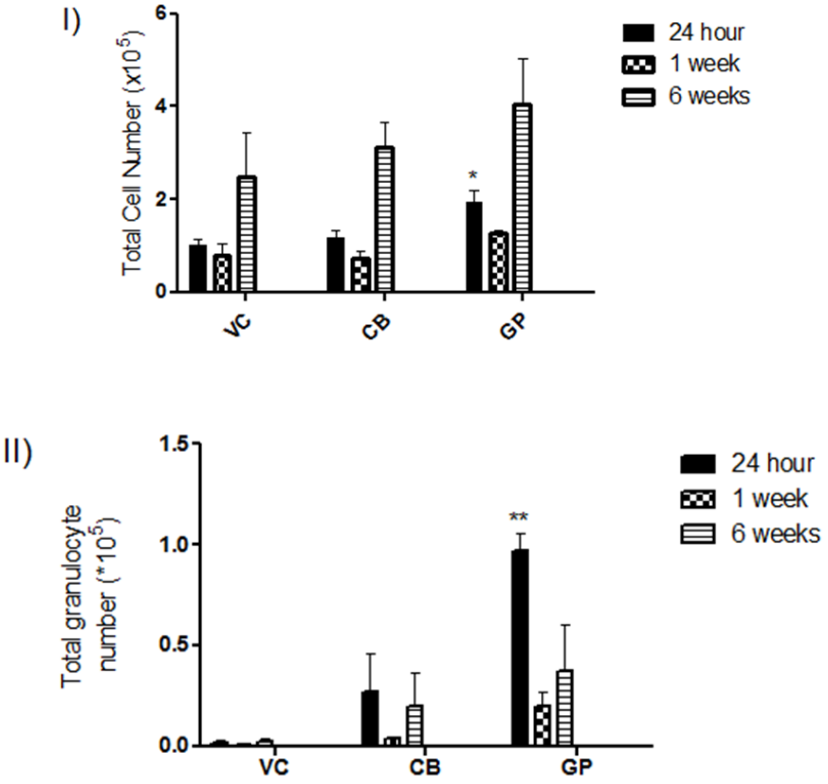

*Figure 6-5: Inflammatory response in the lungs after 24 hour, 1 week and 6 weeks exposure to CB and GP. Total cell number (I) and total granulocyte number (II) after pharyngeal aspiration of a single dose of 50 µg of CB and GP 1 week post treatment. Significance indicated compares treatment groups to vehicle control, * indicates $p < 0.05$, ** indicates $p < 0.001$ ($n = 3$). Data represent mean + SEM of $n = 3$.*

Histopathological changes in the lung sections 1 week and 6 weeks post aspiration were examined in lung sections stained with haematoxylin/Eosin (H&E) (left panel) and Picrosirius Red (PSR) (right panel) and compared to VC. One week post exposure, no granulomatous lesions could be observed in GP treated lung sections however an increased number of lymphocytes was present in the smooth muscle surrounding the bronchi and in the alveolar spaces (Figure 6-6 II). In CB treated lung sections only occasional areas of lymphocyte infiltrates could be observed (Figure 6-6 I). No granuloma formations, infiltration of inflammatory cells or epithelial hyperplasia was observed in lung section of GP exposed mice at a 6 week timepoint (Figure 6-6 III) which is indicative of a lack of immunogenicity. Assaying for lung fibrosis indicated by collagen deposition was determined using PSR staining but no increase in collagen deposition was observed (Figure III) in association with substantial accumulations of GP in the alveolar airspaces (see black arrow Figure 6-6 III).

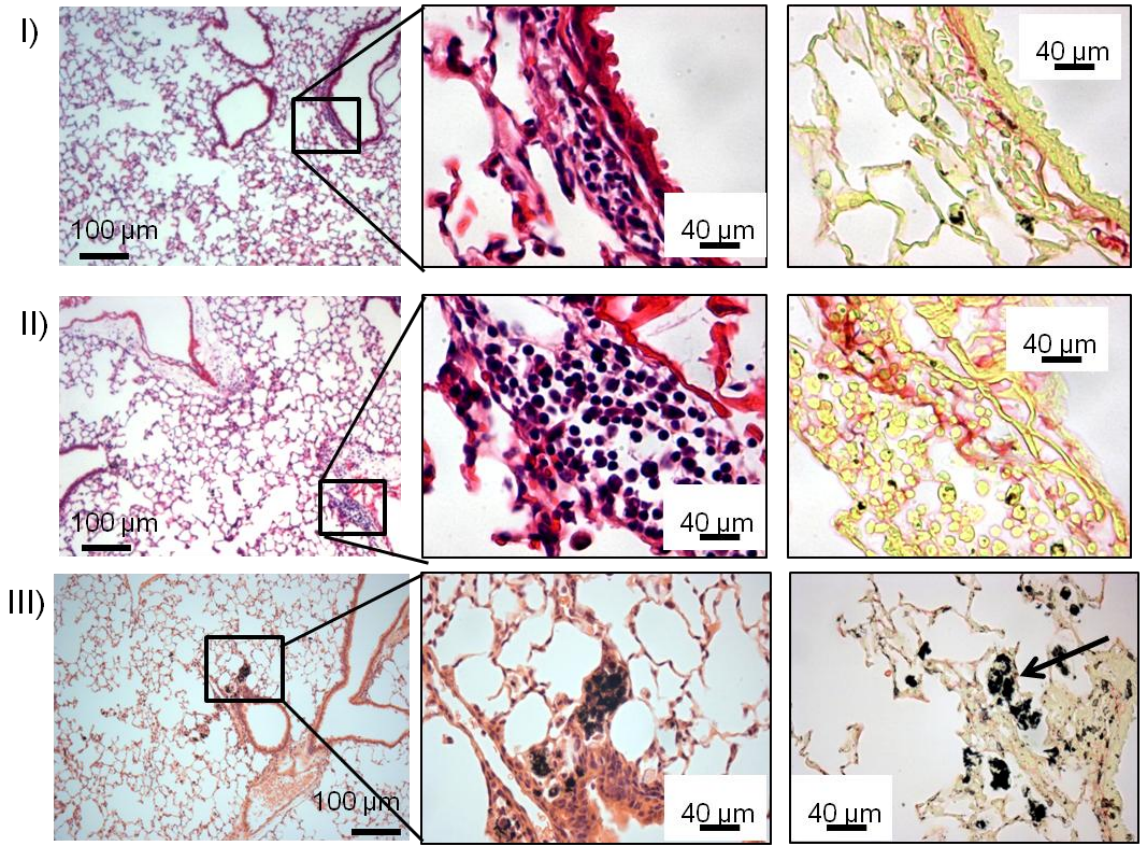

Figure 6-6: Lung pathology of CB treated mice at 1 week and GP treated mice at 1 week and 6 weeks. Histological examination showed minimal infiltration of lymphocytes in CB treated mice (I), which were seen in a greater extent in the GP treated mice after 1 week (II). At the 6 weeks timepoint minimal granulomatous areas were observed after GP exposure (III), even though GP aggregates were present in the lung sections. The right hand panel shows sections stained with Pico-Sirius Red to illustrate collagen deposition, which was comparative to VC in all treatments.Representative images of n=2.

6.3.6 Acute pleural response to GP after intrapleural injection

So far no information is available on the translocation of platelet shaped particles from the lung to the pleural space after inhalation exposure. If translocation to the pleural space occurs, platelet shaped particles could behave similar to fibrous materials in a way that they cannot negotiate stomata which would lead to accumulation of GP in the pleural space. Therefore, we set out to determine the inflammatory potential of GP after intrapleural injection.

The acute pleural inflammatory response was measured 24 hour after intrapleural injection of CB and GP. The pleural space was lavaged and a total and differential cell count was performed. Mice exposed to GP showed a significant increase in total cell number compared to vehicle control (Figure 6-7 I) with significant increases in the number of PMN which mainly comprised neutrophils. Chemokine and cytokine protein levels in the pleural lavage fluid were measured (MCP-1, MIP-1α, MIP-2 and IL-1β) using a quantikine array showing that MIP-1α was significantly increased, however only very low concentrations were detected due to the dilution of pleural fluid during the lavage process (Figure 6-7 II). Based on the very low concentration (5 pg/ml) detected, the statistically significant value can however not be considered as biologically significant. Cytospin preparation of lavaged cells showed complete uptake of CB into pleural macrophages (Figure 6-7 III); however GP, due to their shape and size could not be fully phagocytosed leading to frustrated phagocytosis. Rosette-like formations of macrophages around GP are a characteristic indicator of

frustrated phagocytosis where more than one macrophage surround a large nanoplatelet and share the attempt to phagocytose it (Figure 6-7 III). Histological examination of the parietal pleura showed areas of histiocytic aggregates in mice treated with GP (Figure 6-7 IV). The lesion area along the mesothelium was measured and was significantly increased compared to VC and CB at the 24 hour timepoint (VC/CB=0 $\mu m^2/\mu m$; GP= 19.5+ 11.6 $\mu m^2/\mu m$) (n=3). GP were associated with inflammatory cells along the parietal pleura as shown by SEM Figure 6-7 IV bottom line.

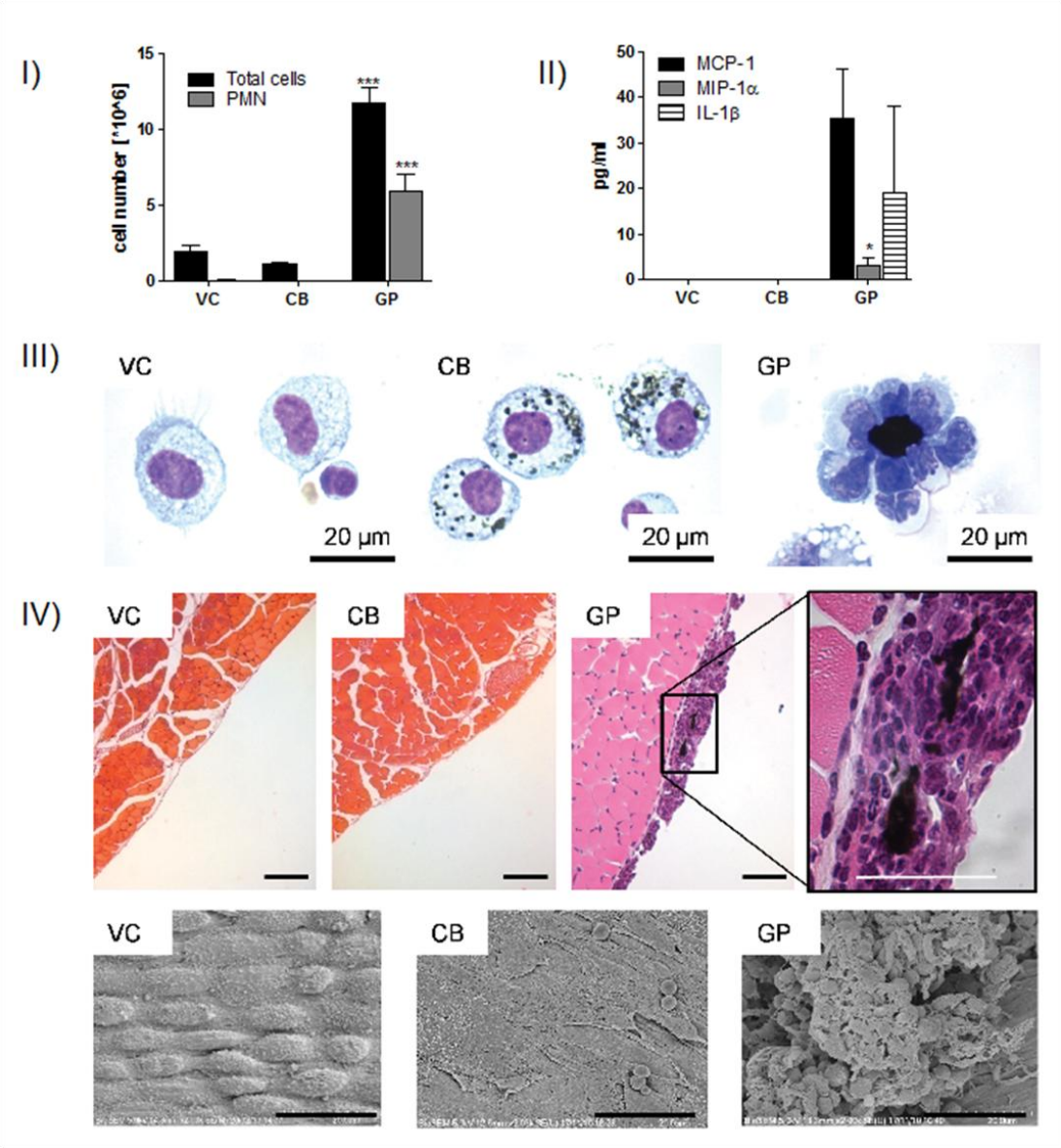

Figure 6-7: Pleural inflammatory response to CB and GP 24 hour post treatment. I) Total cell number and total granulocyte number after pleural injection of 5 µg of CB and GP. II) Concentration of the chemokines MCP-1 and MIP-1α as well as cytokines IL-1β in pleural lavage. (*) P < 0.05, (***) P < 0.001 compared to vehicle control. Data represent mean + S.E.M. of n = 4 for I and II.III) Representative images of pleural macrophages from untreated mice, CB and GP. Intrapleural injection of GP led to the formation of rosette-like cell/particle aggregations indicating frustrated phagocytosis (n=4). IV) Sections of chest wall were stained with both Haematoxylin & Eosin (H&E) at 24 hour post injection to identify a inflammatory response on the mesothelial cell layer of the parietal pleura (n=3). Pleural thickening can be seen after GP treatment, with an insert highlighting GP associated with inflammatory cells. Scale bar 100 µm, insert 20 µm. SEM micrographs show aggregations of inflammatory cells after GP treatment but normal mesothelial cell layer after VC and CB treatment (bottom panel). Scale bar 20µm.

6.3.7 Chronic pleural inflammatory response to GP after intrapleural injection

We further set out to determine the inflammatory response after 1 week in the pleural space to GP after intrapleural injection of a dose of 5 µg/mouse. The granulocyte response 1 week GP post exposure was decreased to a tenth compared to 24 hour exposure (Figure 6-8 I). The concentration of total protein in the lavage fluid was significantly increase in GP treated mice (Figure 6-8 II). Continuous thickening of the parietal pleura was present after 1 week exposure to GP (Figure 6-8 III). Inflammatory cells with associated GP were present along the parietal pleura (Figure 6-8 III insert). These areas of inflammatory cells appeared denser and granulomatous on SEM micrographs at a 1 week timepoint compared to 24 hour (n=3) (Figure 6-8 IV bottom panel). SEM was used to detect these more localised areas.

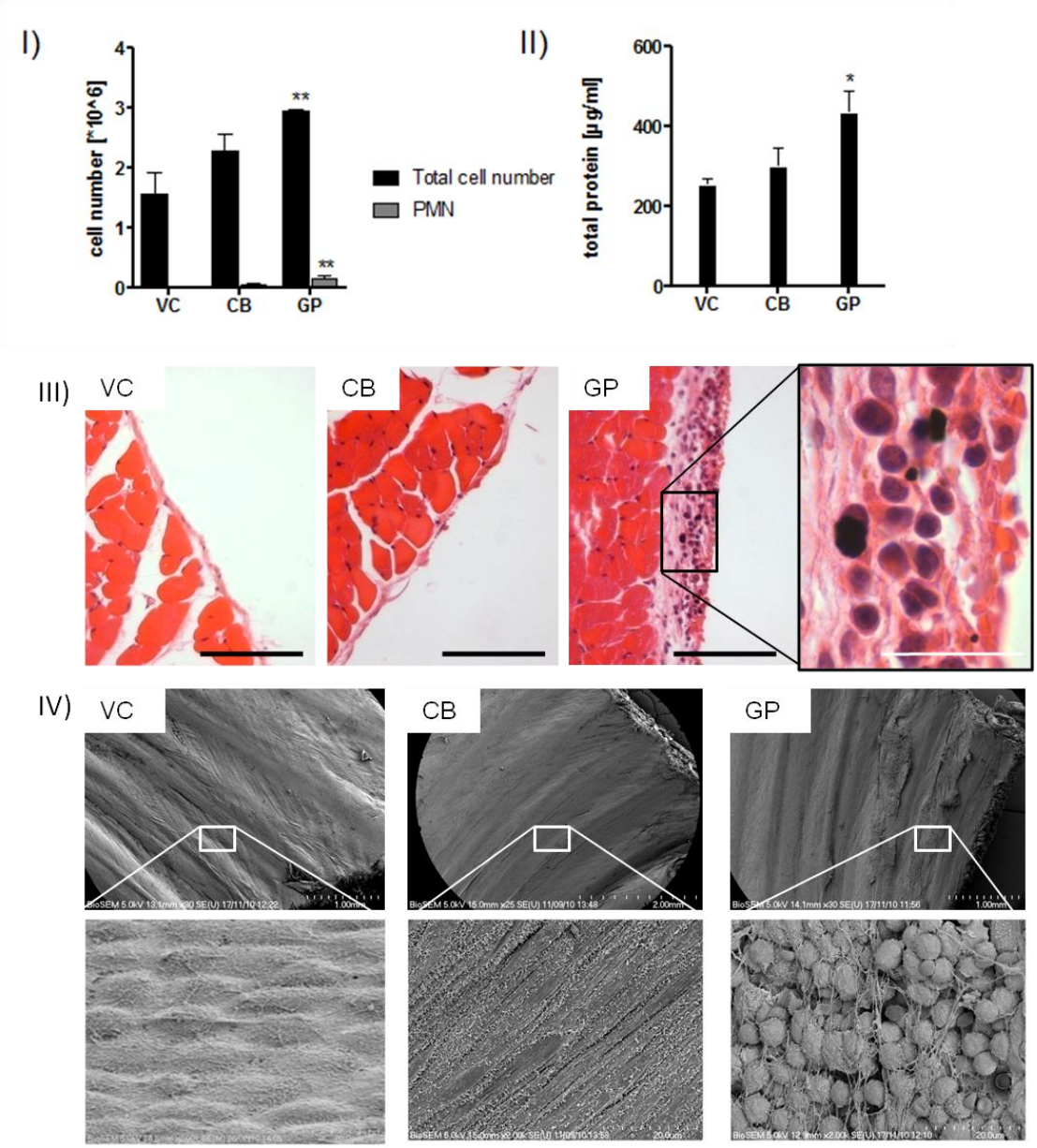

Figure 6-8: Inflammatory response in the pleural space after 1 week exposure to CB and GP. I) Total cell number and total granulocyte number after 1 week exposure to CB and GP in the lavage fluid. II) Measurement of the total protein concentration in the lavage fluid. (*) P < 0.05, (**) P < 0.01 compared to vehicle control. Data represent mean + S.E.M. of n = 4 for I and II.III) H&E stained parietal pleura section (n=1) (top panel) and SEM (n=3) (IV) in low and high magnification showing aggregations of inflammatory cells and granulomatous areas on parietal pleural 1 week post GP exposure.

6.3.8 Clearance of CB and GP from the pleural space in cranial mediastinal lymph nodes

To investigate the clearance of injected CB and GP from the pleural space via the lymphatic system, the mediastinal lymph nodes were sectioned and examined for particle deposition. CB particles were cleared from the pleural space after direct pleural injection via stomata to the cranial mediastinal lymph nodes as can be seen in histological lymph node sections after 24 hour and 1 week (Figure 6-9 I, II). 24 hour after GP exposure, few particles could be found in the lymph nodes which indicated prolonged retention in the pleural space (Figure 6-9 I). After 1 week GP have been cleared from the pleural space, however the amount of clearance appears much less compared to CB (Figure 6-9 II). Quantification of the GP size cleared to the lymph nodes could not be performed because of the difficulty to identifying individual platelets of GP in the sections.

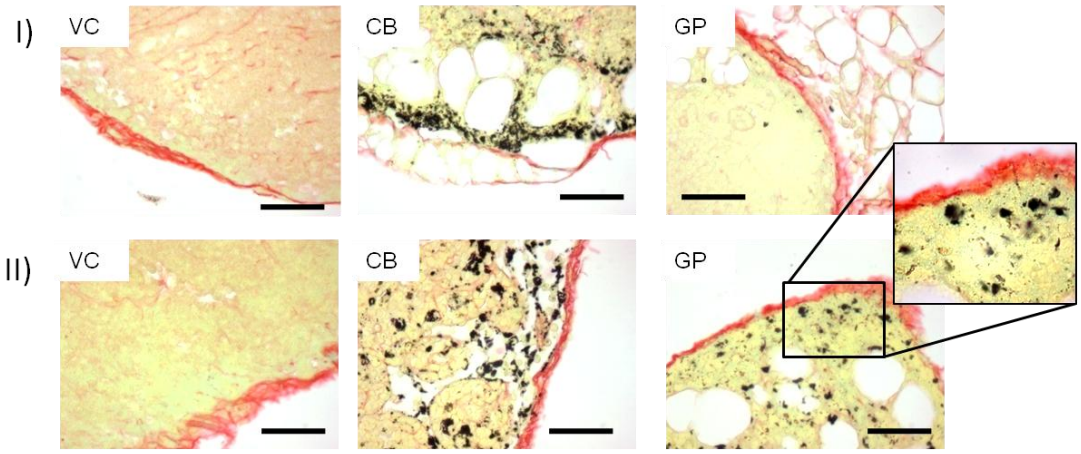

Figure 6-9: Clearance of CB to cranial mediastinal lymph nodes and prolonged retention of GP in the pleural space. Histological sections of lymph nodes stained with Picrosirius red 24 hour (I) and 1 week (II) post injection. CB could be cleared already after 24 hour, however GP was prolonged retained in the pleural space. Scale bar 40 µm, n=4 mice per treatment group with 2 sequential sections per lymph node.

6.3.9 Translocation of GP to the pleural space after aspiration exposure

Direct injection of GP into the pleural space doesn't give information about translocation of particles from the airspaceafter inhalation exposure since it bypasses the natural clearance mechanism of the lungs and process of moving from the airspaces to the pleural space. Therefore, to identify whether GP translocate to the pleura following pulmonary exposure, the tissue and alveolar macrophages lying immediately beneath the visceral pleura were examined in histological sections after aspiration exposure at a dose of 50 µg/mouse. No accumulations of GP were seen subjacent to the visceral pleura (data not shown). Additionally the pleural space was lavaged and the extent of inflammation measured at the timepoints 24 hour, 1 week and 6 weeks. At all timepoints no significant influx of inflammatory cells into the pleural space was measured after treatment with CB and GP compared to vehicle controls (Figure 6-10 I, II). This was verified by failure to detect aggregations of inflammatory cells or granuloma formation by SEM examination of the mesothelial surface of the parietal pleura (Figure 6-10 III, IV, V). The translocation of GP was compared to CNT at 24 hour, 1 week and 6 week timepoint (Figure 6-10 I, II, VI) (CNT data with permission from (Murphy et al., 2012a), these data were produced prior to the experiments presented in this chapter). Aspiration of CNT led to translocation to the pleural space at the 6 week timepoint as measured by increase in the total cell number and total granulocyte number and accumulation of inflammatory cells on the mesothelial surface of the parietal pleura as reported in Murphy *et al.* (Murphy et al., 2012a) (Figure 6-10 I, II, VI).

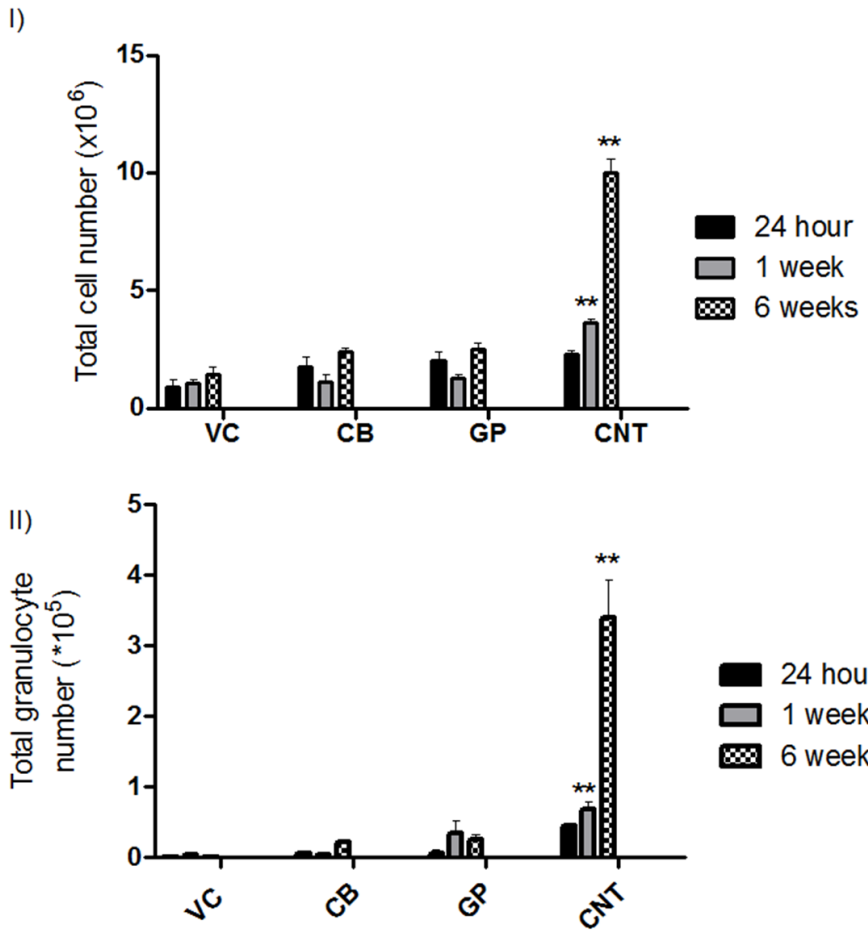
I)
Total cell number (x10^6)
15
10
5
0
**
**
VC
CB
GP
CNT
24 hour
1 week
6 weeks
II)
Total granulocyte number (*10^5)
5
4
3
2
1
0
**
**
VC
CB
GP
CNT
24 hour
1 week
6 weeks

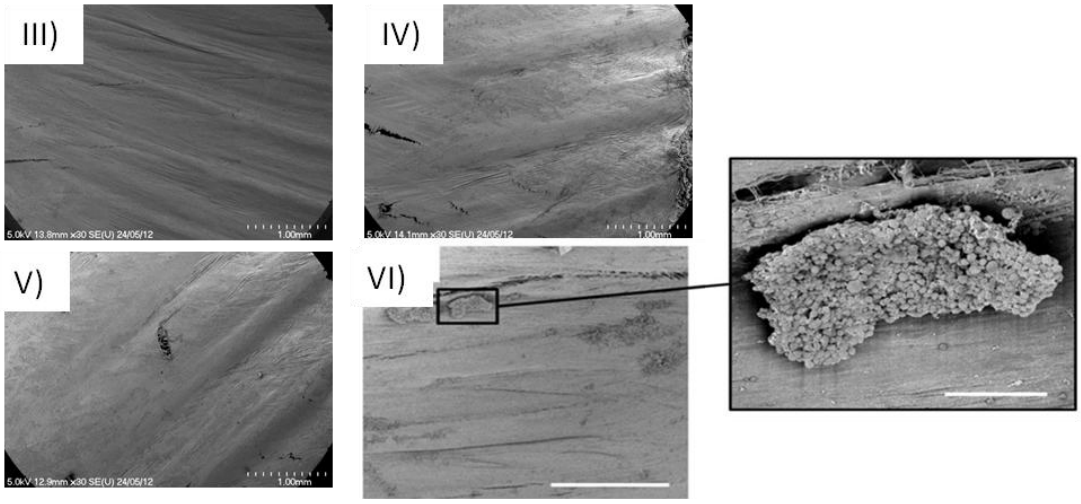
III)
IV)
V)
VI)

Figure 6-10: Inflammatory response in the pleural cavity after pulmonary exposure to CB, GP and CNT. The inflammatory response in the pleural cavity after CB, GP and CNT exposure via pharyngeal aspiration was examined. At 24 hour, 1 week and 6 weeks post exposure the pleural cavity was lavaged and total cell number (I) and total granulocyte number (II) were measured. Data represent mean + S.E.M. of n = 4. CNT data obtained with permission from Murphy et al. (Murphy et al., 2012a). The parietal pleura was examined by scanning electron microscopy (SEM) to identify lesion formation after pulmonary exposure to CB (IV) and GP (V). Normal mesothelium was observed in all treatments which was comparable to VC (III). VI) To illustrate an inflammatory response on the parietal pleura after aspiration exposure, SEM of parietal pleura after aspiration to 50 µg/mouse CNT at a 6 week timepoint is shown. Aggregates of inflammatory cells are present on the mesothelial surface indicating a translocation of CNT to the pleural space; this image was obtained with permission from Murphy et al. (Murphy et al., 2012a).

6.4 Discussion

In this study we addressed the public/occupational health hazard of GP in mouse lung from the point of view of aerodynamic deposition and the cellular responses in the lung. Although Duch *et al*. (Duch et al., 2011) have studied the biocompatibility of GP in the mouse lung from the point of view of biomedical/therapeutic application of GP, we believe that this study is the first to address pathogenicity of a nanoplatelet shaped particle. Nanoparticulate carbon black (CB) was used as a compact graphene nanoparticulate control and was aspirated at a mass dose found to be non-inflammatory in previous studies (Cho et al., 2010). Carbon nanoparticulate has also been reported by other groups not to cause oxidative stress or DNA damage in mice and rats after short-term nose-only inhalation (Wessels et al., 2011).

The atypical platelet-like shape of the GP particles attracted our attention as they may pose a new risk to the respiratory system after inhalation. Nanoplatelets exhibit specific material properties that could be important for biological interactions. Among these are surface area, surface chemistry and lateral dimensions. Due to their

platelet shape, they have an exceptionally high surface area per unit mass which is much greater than that of graphite and of carbon nanotubes (Pumera, 2009). The lateral dimensions of a material play an important role in biological interaction and determine the nature and consequences of cellular uptake and subsequent clearance.

Thus far, in the field of particle toxicology the fibre pathogenicity paradigm has been stated as the most robust structure-activity relationship, and it has frustrated phagocytosis of long fibres as the centre of the pathobiological mechanism (Donaldson and Tran, 2004). This structure-activity relationship focuses on fibres that are long, thin and biopersistent, having an aerodynamic diameter that makes them respirable (Donaldson et al., 2011). This structure-activity relationship however does not take sheet/platelet shape particles into account and therefore has to be reconsidered in the light of these new materials.

To be most harmful to the respiratory system, particles require an aerodynamic diameter small enough to penetrate beyond the ciliated airways i.e. they need to be respirable. Deposition occurs under the effects of gravitational force, aerodynamic resistance, interception and impaction which together determine the site of deposition in the lungs (Morgan and Seaton, 1984). The aerodynamic diameter is the index that is calculated from these parameters and determines the respirability of a particle and the site of deposition (Jones, 1993). Plate–shaped particles are not common in industry and so exposure is limited but does occur in the talc and nano-clay industries where there are plate-like particles (Cheng et al., 1988; Lordan et al., 2011). However these nanotechnologies have the potential to produce a range of different nanoplatelet-shaped particles. In this study we calculated the aerodynamics of commercially available nanoplatelets by taking into consideration gravitational settling force and aerodynamic resistance perpendicular and parallel to motion, and utilised an equation derived from the tenets of aerosol physics to estimate the aerodynamic diameter of platelet-like particles of the dimensions evident in our GP sample. This demonstrated that a platelet-shaped particle with a projected area diameter of 25 μm and a thickness of 0.1 μm has an aerodynamic diameter of about 3 μm, which is within the respirable size fraction of particles that deposit beyond the ciliated airways (Jones, 1993); These calculations are in line with the aerodynamic

sizes reported recently in Sanchez *et al.* (Sanchez et al., 2012) which also showed images suggesting that GP might lead to frustrated phagocytosis in macrophages.

Based on our determination that the GP sample used within these experiments were all respirable, we assessed the inflammatory potential of GP. Mice were exposed via pharyngeal aspiration to CB and GP for 24 hour, 1 week and 6 weeks. CB and GP are composed of the same material (graphene) and were both respirable but differed in their shape, which resulted in very different effects in the lung and the pleural space. CB did not cause any inflammatory response and was comparable to vehicle control in all assays, whereas GP caused extensive recruitment of inflammatory cells, including macrophages and granulocytes into the lung and pleural space after 24 hour exposure. Inflammation waned 1 week post exposure but continued to be significantly greater in total cells and granulocyte number than the vehicle control. The response to GP in the lung was similar to the response seen after aspiration exposure of long MWCNT using the same method (Murphy et al., 2011; Porter et al., 2010). Our previous study on fibre shaped HARN and recent studies on CNTs revealed that, due to their fibre like structure which similar to asbestos show an asbestos like pathogenicity and raised concern that exposure to fibre shaped HARN may lead to mesothelioma (Poland et al., 2008). Our result show that long fibres are not the only extended particles with low D_{ae} that are able to induce inflammation in the lung and the pleural space but that platelet like particles with a low D_{ae} have similar potency. The induction of acute and chronic inflammation is regulated by the release of cytokines and chemokines that invoke leukocyte recruitment. Analysis of BAL fluid revealed elevated levels of MCP-1, MIP-1α, MIP-1 and IL-1β after GP but not CB. MCP-1 and MIP-1α have been reported to contribute to the initiation and outcome of inflammation in the lung and in pulmonary alveolar macrophages after exposure to stone-wool and crocidolite asbestos (Tatrai et al., 2005). MCP-1 has further been identified to play a major role in lung leukocyte infiltration (Conti and DiGioacchino, 2001) and serves as a marker for the diagnosis of malignant pleural mesothelioma (Gueugnon et al., 2011).

In addition to short term inflammatory effects (24 hour and 1 week), the medium term inflammatory effects of pristine GP in the lung of mice after aspiration exposure

was investigated at a 6 weeks timepoint and showed no continuous inflammation, or granulomatous aggregations of inflammatory cells in the bronchial and alveolar regions, alveolar wall thickening or fibrosis. This contrasts with carbon nanotubes, which did show all of these types of effect at these timepoints in mice at the same dose (Murphy et al., 2012a). Even though little is known so far on the pulmonary toxicity of GP it has been shown that the *in vivo* toxicity of graphene- based materials is closely associated with their surface characteristics as summarized in Yang *et al*.(Yang et al., 2013). Duch *et al*. showed that graphene oxide and aggregated pristine GP caused sustained pulmonary inflammation *in vivo* compared to well-dispersed pristine GP (Duch et al., 2011). The lack of pulmonary inflammogenicity after exposure to GP in medium term studies is in contrast to recent studies on pulmonary effects of CNT, which reported that CNT have the potential to cause severe lung fibrosis and persistent inflammation after aspiration exposure at a 6 week timepoint (Wang et al., 2011b; Shvedova et al., 2005; Mercer et al., 2011; Murphy et al., 2012a). Both CNT and GP are composed of graphene yet show very different effects in the lungs and so further study is warranted to elucidate the underlying mechanisms for differences in the inflammatory response to CNT and GP.

We further went on to investigate the response of GP in the pleural space to identify if GP have a similar inflammatory potential compared to fibrous HARN. Significant pleural inflammation and accumulation of inflammatory cells along the parietal pleura mesothelium was measured after interapleural injection of GP at 24 hour, which however decreased to a tenth of the measured inflammation at a 1 week timepoint. The role of frustrated phagocytosis, a mechanism by which long fibres produce inflammation, has been examined in a number of studies (Brown et al., 2007; Dogra and Donaldson, 1995) and has been accepted as a contributing mechanism to the toxic effects of long fibres. Due to the extended shape of GP, we hypothesised that the uptake of GP by macrophages could be impaired leading to frustrated phagocytosis. Examination of pleural macrophages in the lavage fluid showed clear signs of frustrated phagocytosis after GP exposure whereas CB was fully taken up. This took the form of GP incompletely enclosed by macrophages and

‘rosettes‘ of up to 5 or 6 macrophages surrounding a single large platelet where all of the macrophages are in a state of frustrated phagocytosis.

The main mechanism by which long, fibre like particles cause harmful health effects in the pleura are failed clearance of longer fibres through stomata in the parietal pleura and subsequent retention in the pleural space and frustrated phagocytosis of pleural macrophages. We therefore investigated the retention of GP in the pleural space by examining the most caudal, posterior intercostal region of the parietal pleura, documented to have the highest abundance of stomata (Shinohara, 1997). Interstitial incorporation of asbestos fibres and coal dust occurs in these areas and so they are described as potential starting points for development of mesothelioma (Muller et al., 2002). In support of this hypothesis extensive accumulation of inflammatory cells in these areas on the parietal pleura where GP were retained was observed. In order to determine the clearance pathway of CB and GP, we examined the particle burden in cranial mediastinal lymph nodes (LN). Pleural fluid is drained through the parietal stomata via the lymphatic system to LN (Marco et al., 1992). CB was readily cleared to the mediastinal lymph nodes after 24 hour as could be seen in histological sections. In comparison, few GP had reached the LN after 24 hour, confirming retention of GP in the pleural space. After 1 week however, a higher number of GP could be identified in the mediastinal LN sections, which may explain the reduced inflammation seen 1 week after intrapleural exposure. Breakage of GP into smaller fragments after 1 week could explain the time- dependent clearance of GP to the LNs. We noted that the accumulation of GP in the LN seen at 1 week, whilst evident, was less than that seen 1 week after CB, suggesting that there is a substantial fraction of the GP dose that remains retained in the pleural space beyond one week.

The direct intrapleural injection study of GP allows to measure their pathogenicity with the assumption that GP translocate to the pleural space. It is however not shown yet if GP would translocate to the pleural space after inhalation exposure in enough quantity that would lead to adverse effects in the pleural space. It has been shown that fibre-shaped CNT can translocate to the pleural space after aspiration exposure leading to persistent inflammation and granuloma formation at the surface of the

parietal pleura, similar to that seen after asbestos fibre treatment (Murphy et al., 2012a; Mercer et al., 2010). We set out to determine if platelet shaped particles can translocate to the pleural space after aspiration exposure. The results showed that GP used in this study did not accumulate in the sub-visceral pleural tissue up to 6 weeks after aspiration exposure and no inflammatory response was measured in the pleural space up to 6 weeks post exposure. The absence of inflammation in the pleural space does not necessarily exclude the possibility of translocation of very small GP that are able to negotiate the parietal pleural stomata from reaching the pleural space but being cleared (Donaldson et al., 2010). It might be argued that GP had not reached the pleural space by 6 weeks but would get there eventually. However translocation of CNT from the airspaces of mice to the pleural space has been seen at 28 days (Mercer et al., 2010) and 6 weeks (Murphy et al., 2012a) and so we see no reason to conclude that GP translocation might only begin after 6 weeks. The difference in translocation behavior of CNT and GP could be explained by the structural morphology, whereby the fibrous structure of CNT could facilitate translocation as needles are more likely to penetrate cell layers (Mercer et al., 2010). In the case of GP, the platelet shape with its extended lateral dimension and no sharp, penetrating tip could inhibit translocation. However, one limitation of this study is the use of a single sample of GP with a wide distribution of lateral diameter up to 25 µm.

Collectively, our data show that large nano platelets can have a small enough D_{ae} to be respirable and to deposit beyond the ciliated airways where macrophages are the only mode of clearance, but are too large to be completely phagocytosed by macrophages. They, therefore are likely to cause an inflammatory response in the airspaces and be retained, similar to the response seen after long asbestos and other long fibre-like structures (Murphy et al., 2011). If, like long fibres, they are capable of reaching the pleural space they will be retained there as they will be too big to negotiate the stomata and, with sufficient dose, they will cause pleural inflammation and pleural pathology over time if they are sufficiently biopersistent. Our study showed however that no translocation of GP occurred up to 6 weeks post aspiration which could be explained by the shape of these particles. The fact that GP was not inflammogenic at a later timepoint, 6 weeks, has important implications for potential biomedical and technological applications of GP.

The decrease in the severity of inflammation after 1 week and 6 weeks treatment in the lung and the pleural space suggests degradation of GP into smaller fragments which could then be cleared via alveolar/pleural macrophages. In this study we focus on the morphology of the GP, rather than the graphene oxidation state, as regards pro-inflammatory effects especially frustrated phagocytosis. The argument of frustrated phagocytosis of GP is based on shape rather than chemistry, as does the argument of long fibres-elicited frustrated phagocytosis, which is an issue of fibre length, not composition (Donaldson et al., 2010; Donaldson, 2009). Future studies on different GP samples from different sources should examine the effect of surface chemistry/oxidation state, which might have an additional effect; however, we consider that any such effect will be in addition to the shape effect.

Chapter 7: Biopersistence of graphene nanoplatelets

7.1 Acknowledgement

Dr Colin Campbell was involved in the design of the GP biopersistence study, helped with Raman Spectroscopy of GP and provided input in interpreting the results. Dr Oleg Nerushev, Dr Andrei Gromov and Kate Fisher provided technical advice on the Raman spectrometer and chemical oxidation of GP.

7.2 Aims and hypothesis

The studies on the time course of GP inflammogenicity in the lung after pharyngeal aspiration showed a decrease in inflammation at a 6 week timepoint, even though GP were evidently resident in the lung tissue as was clear from the inspection of the sections of lung. The resistance of carbon nanomaterials to biological degradation is a major concern for their potential *in vivo* toxicity but recent investigations have shown that carbon nanomaterials, including graphene oxide and oxidized carbon nanotubes, can be degraded by oxidase enzymes including horseradish peroxidase and neutrophil myeloperoxidase (hMPO) *in vitro* and *in vivo* (Kagan et al., 2010; Graham et al., 1999; Kotchey et al., 2011; Shvedova et al., 2012) causing them to exhibit less inflammatory potential *in vivo*. This study aimed to investigate the *in vivo* oxidation and degradation of pristine GP in lung tissue at 24 hour, 1 week and 6 weeks after single aspiration exposure. The correlation between the biological effect study and the investigation of the material oxidation *in vivo* is based on the link between the decrease in biological effect with increased degradation of material due to oxidation. To aid in the interpretation of *in vivo* data, additional *in vitro* enzymatic degradation of pristine GP via horseradish peroxidase and chemical oxidation were also performed.

7.3 Results

7.3.1 Oxidation of GP in lung tissue

Degradation of GP via enzymatic oxidation in lung tissue was measured using Raman microspectroscopy. Section of lungs embedded in paraffin blocks from mice exposed to GP for 24 hour, 1 week and 6 week via pharyngeal aspiration were used. Characteristic graphene Raman spectra were recorded from GP within the sections enabling us to directly probe for oxidized graphitic material; data are presented as average spectra from 20 locations (Figure 7-1 I, III, IV, V). Oxidation is known to increase the ratio of the D (1360 cm^{-1}) band, which indicates disorder in sp^2-hybridized carbon systems to the G band (1580 cm^{-1}), evaluating the stretching of C-C bonds of graphene. Graphene spectra recorded in lung sections showed no significant difference between I_D/I_G at the different timepoints, indicating that no systematic oxidation had taken place over the period of 6 weeks (Figure 7-1 II). Spectra from lung sections also showed vibrations at 1300 cm^{-1} and 1440-1460 cm^{-1} characteristic of paraffin wax spectra at 20°C due to the CH_2 twisting band and overtones of the CH_2 bending, respectively (Zheng and Du, 2006). Background spectra from the paraffin block did not interfere with the specific Raman spectra for GP.

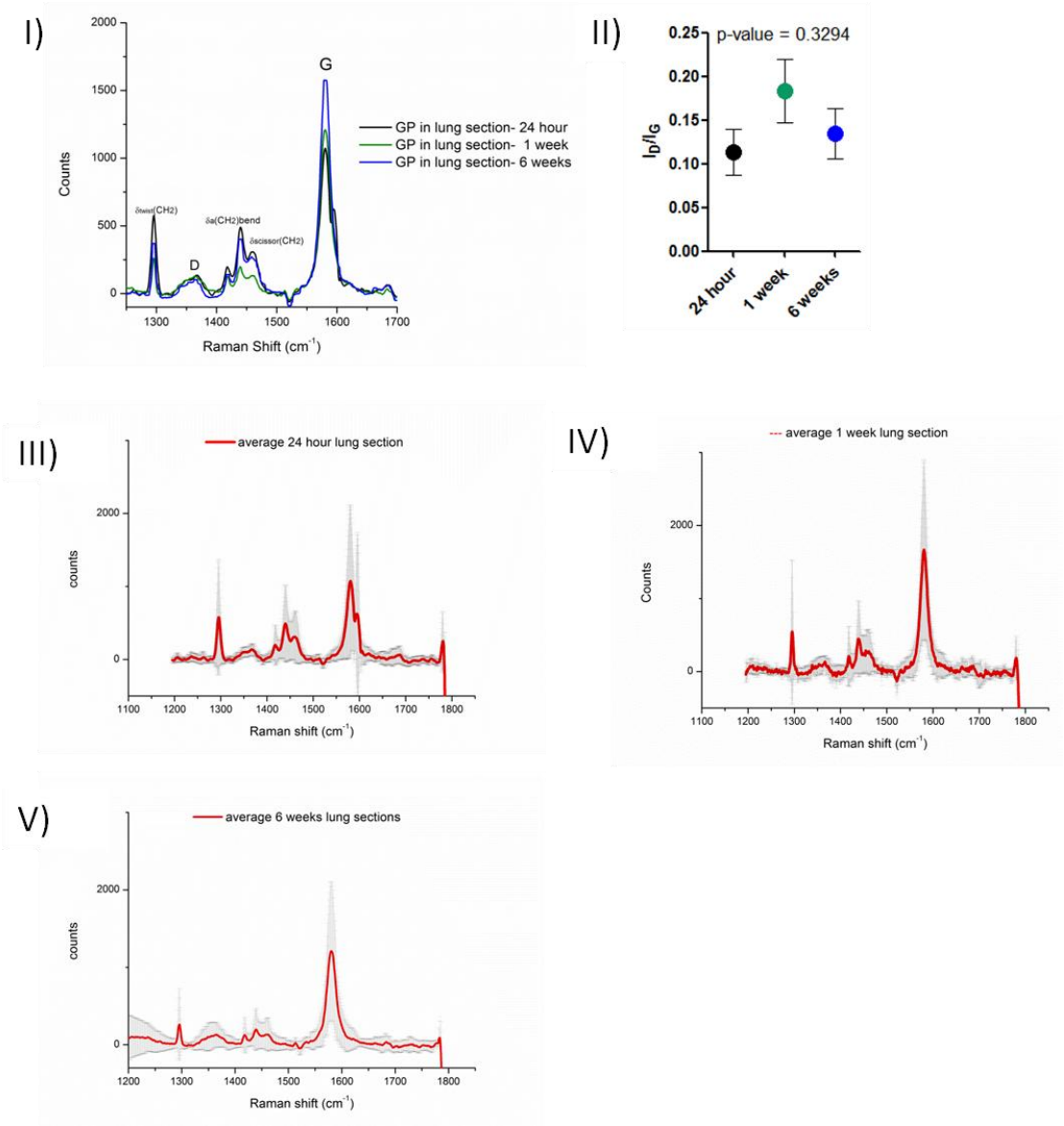

Figure 7-1: Raman spectroscopy of GP in lung sections. I) Raman spectra of GP in lung section embedded in paraffin from mice exposed for 24 hour, 1 week and 6 weeks to GP via pharyngeal aspiration. Characteristic D (1360 cm^{-1}) and the G band (1580 cm^{-1}) of graphene can be seen. Spectra at 1290 cm^{-1} and 1450 cm^{-1} is characteristic for paraffin wax. II) No statistically significant change in the ratio of I_D/I_G was measured as shown in the insert. Data represent mean of 20 spectra. Average and standard deviation of 20 locations from GP in lung tissue after 24 hour (III), 1 week (IV) and 6 weeks (V) post exposure.

7.3.2 Enzymatic oxidation of GP via Horseradish peroxidase

To determine the capability of peroxidases to oxidize GP, *in vitro* oxidation of GP was studied using the enzyme horseradish peroxidase (HRP). The active site of HRP, Fe(III) porphyrin IX has been reported to be analogous to leukocytic peroxidase in the oxidation of graphenic carbon (Kotchey et al., 2012). The suspensions with GP, HRP and H_2O_2 were left for 24 hour (H_2O_2 added every hour for 12 h) and 1 week (H_2O_2 added every day) at room temperature and Raman spectra were recorded to measure the change in the extent of oxidation of GP via the ratio I_D/I_G as well as a disorder induced Raman D'-band at 1620 cm^{-1}, indicating imperfect crystalline order (Malard et al., 2009). Control samples included GP without HRP and GP without H_2O_2. Between 0 hours and 24 hours the D:G ratio showed a modest increase from 0.12:1 to 0.22:1, however the disorder induced D'-band was recorded in three out of six spectra for HRP+ H_2O_2 treated samples and was not observed in untreated pristine samples (Figure 7-2 I, II, IV). The spectra recorded after 1 week incubation with HRP were similar to the spectra recorded after 24 hour with the exception of one spectrum, which showed an substantial increase in D:G ratio to 0.76:1 indicating extensive oxidation of GP (Figure 7-2 III, IV). Raman spectra from control samples were similar to those from pristine GP (data not shown). All averaged spectra with standard deviation are shown in Figure 7-2 I, II, III.

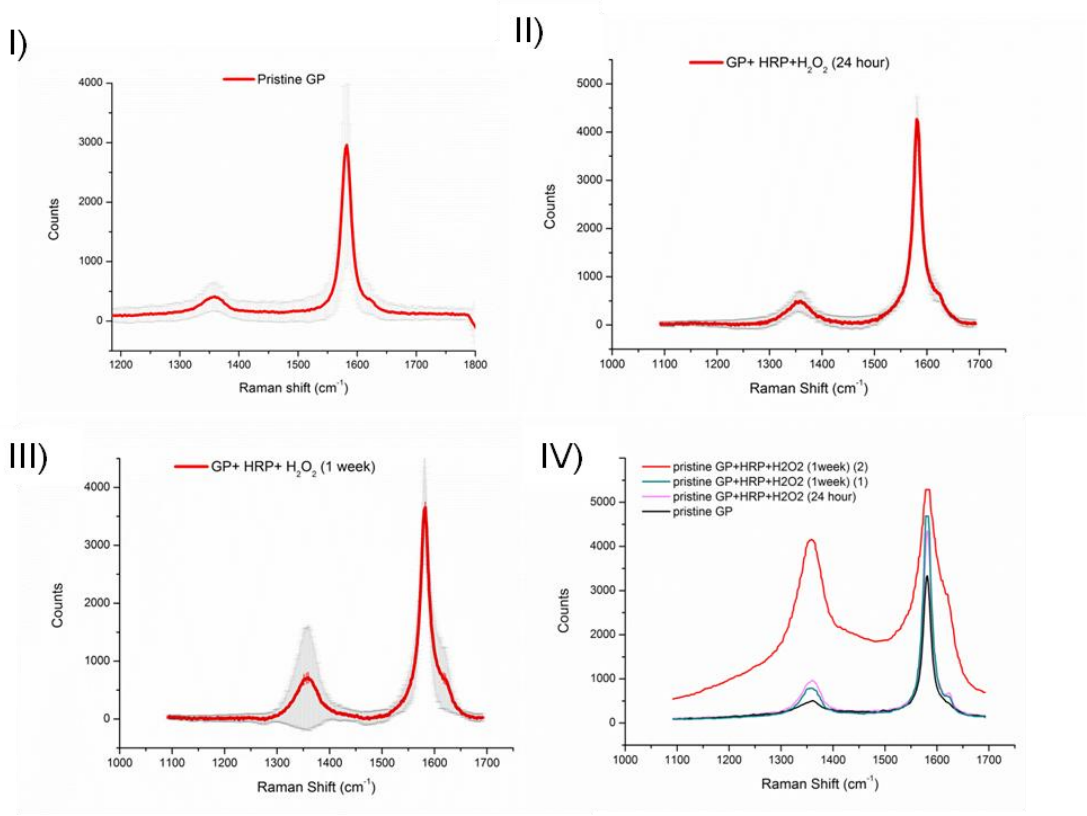

Figure 7-2: Raman Spectroscopy of GP after horse radish peroxidise (HRP) treatment. Raman spectra from pristine GP (I) and GP treated with HRP and H_2O_2 for 24 hours (II) and 1 week (III). Average and standard deviation of 20 locations (pristine) and 6 locations (HRP treatment) are shown. IV) Averaged raman spectra of pristine GP and GP incubated with HRP and H_2O_2 for 24 hour and 1 week. An increase in the D-band and D'-band at 1620 cm^{-1} was observed at 24 hour and 1 week compared to pristine spectra however no significant increase in I_D/I_G ratio was measured. For the 1 week timepoint one spectrum was recorded with an increase in D:G ratio to 0.76:1.

7.3.3 Chemical oxidation of GP via plasma ashing

To compare the spectroscopic data of enzymatic oxidation of GP to that of a chemical oxidation, O_2 plasma oxidation of the GP was performed. Raman spectra of chemical oxidized GP were recorded after 5, 10, 15, 40 and 60 min of plasma oxidation. An increase in the ratio of D:G band (0.12:1 (0 min), 0:22:1 (5 min),

0.24:1 (10 min), 0.27:1 (15 min), 0.19:1 (40 min) and 0:25:1 (60 min)) and a disorder induced Raman D'-band at 1620 cm^{-1} appeared indicating imperfect crystalline order and increase in the degree of oxidation of the GP (Figure 7-3 I) (Malard et al., 2009). All averaged spectra with standard deviation including plasma oxidation up to 60 min are shown in Figure 7-3 II-VII.

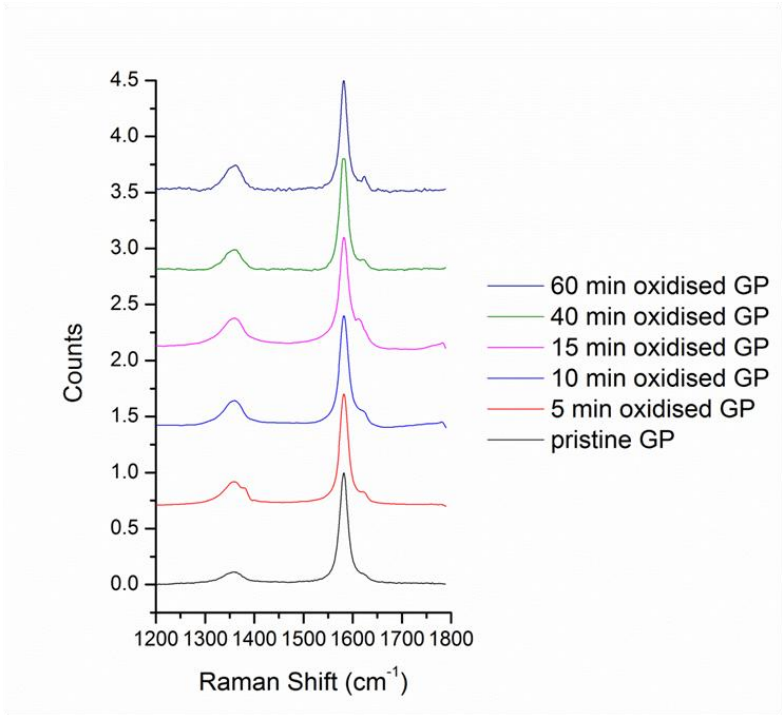
I)
Counts
Raman Shift (cm-1)
60 min oxidised GP
40 min oxidised GP
15 min oxidised GP
10 min oxidised GP
5 min oxidised GP
pristine GP

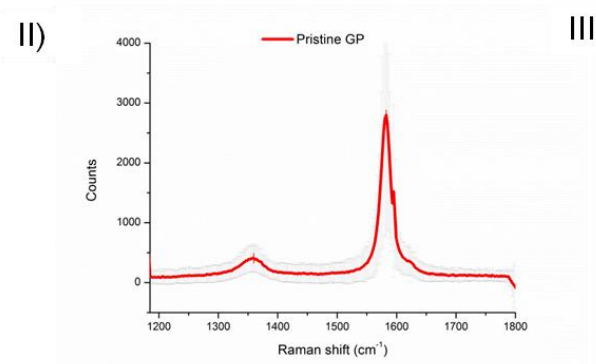
II)
Pristine GP
Counts
Raman shift (cm-1)

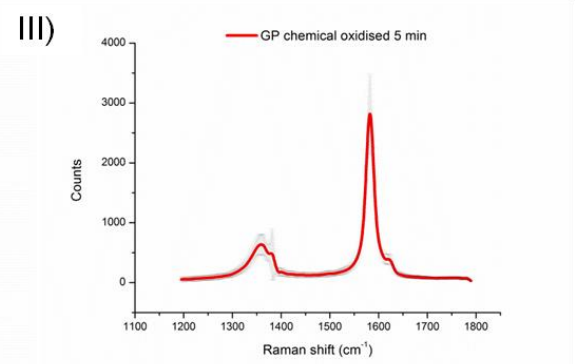
III)
GP chemical oxidised 5 min
Counts
Raman shift (cm-1)

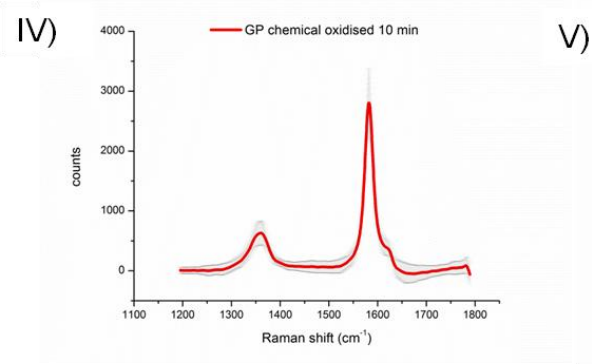
IV)
GP chemical oxidised 10 min
counts
Raman shift (cm-1)

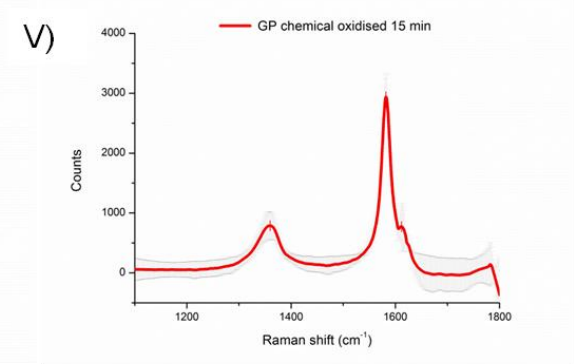
V)
GP chemical oxidised 15 min
Counts
Raman shift (cm-1)

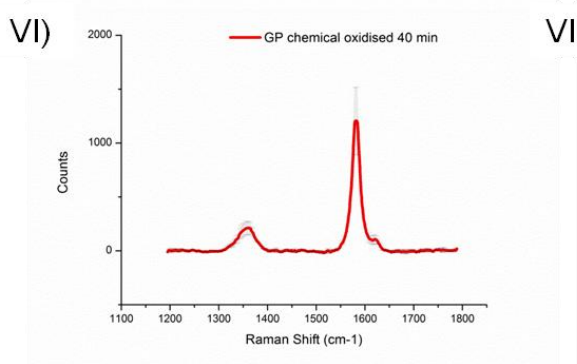
VI)
GP chemical oxidised 40 min
Counts
Raman Shift (cm-1)

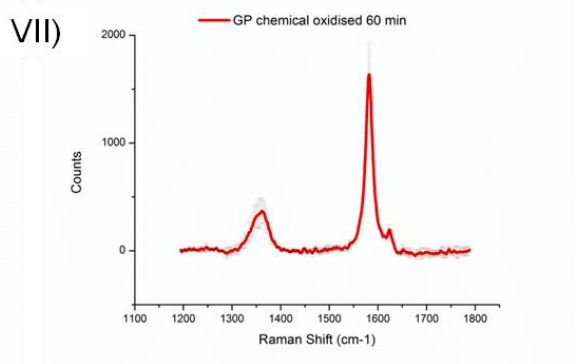
VII)
GP chemical oxidised 60 min
Counts
Raman Shift (cm-1)

Figure 7-3: Raman Spectroscopy of GP after plasma ashing. Summary of raman spectra (I) and individual raman spectra from pristine GP (II) and chemical oxidised GP using oxygen plasma for 5 min (III), 10 min (IV), 15 min (V), 40 min (VI) and 60 min (VII). Increase in D- band and disorder induced Raman D'-band at 1620 cm^{-1} indicating imperfect crystalline order. Average and standard deviation of 6 locations is shown.

7.4 Discussion

The aim of this study was to investigate the oxidation of GP in lung tissue up to 6 weeks after pharyngeal aspiration; parallel *in vitro* studies using intense enzymatic oxidation were also carried out.

Biopersistence is a major contributing factor to the toxicity of carbon-based materials and is dependent on the surface functionalization of these materials (Osmond-McLeod et al., 2011; Liu et al., 2010). Recent studies on the degradation of oxidized carbon nanomaterials by Kagan and coworkers have shown that enzymatic oxidation *in vivo* and *in vitro* leads to the disruption of the carbon structure in highly oxidized graphene as well as highly oxidized SWCNT and MWCNT (Kagan et al., 2010; Allen et al., 2008; Kotchey et al., 2011). In these studies of enzymatic degradation, the carbon nanomaterials were subjected to sever chemical oxidation prior to the enzymatic treatment in order to facilitate peroxidase mediated degradation via the interaction of positively charged residues of hMPO with the carboxyl surface of the nanotubes. Based on these studies our aim was to examine the degree of oxidation of non-oxidised pristine GP *in vivo* up to 6 weeks in lung tissue as well as *in vitro* using horseradish peroxidase which acts as a surrogate for leukocyte peroxidase as previously decribed (Kotchey et al., 2011). Raman spectroscopic evaluation of oxidative defects in pristine GP present in lung sections *in vivo* revealed that GP did not undergo oxidative change. This is in line with results published on the biopersistence of pristine CNT and reduced graphene oxide, showing less effective biodegradation by peroxidase compared to oxididized CNT (Kagan et al., 2010; Kotchey et al., 2011). A possible explanation between the degradation of pristine and

oxidized carbonaceous nanomaterials has been stated by Kotchey *et al*. as being a lack of binding sites for enzymes on the surface of pristine CNT and GP compared to oxidized surfaces with its covalently attached oxygen functional groups (epoxides, negative charged carboxyl groups) facilitating strong interaction with enzymes (Kagan et al., 2010; Kotchey et al., 2011). A recent study has shown that MPO-deficient mice show increased pulmonary inflammation and impaired clearance after pharyngeal aspiration of oxidized SWCNT due to impaired degradation compared to wild type mice (Shvedova et al., 2012). MPO is initially present in the local microenvironment after inhalation exposure and could also be present during long term inhalation exposure, however the importance of MPO in nanomaterial degradation is questionable since neutrophils play only a minor role in phagocytosis and clearance of deposited nanomaterials in the lungs, the bulk of particle clearance being mediated through alveolar macrophages (Lehnert and Morrow, 1985). The persistence of large accumulations of GP was very obvious at 6 weeks with no neutrophils in the lavage fluid and therefore MPO would be an unlikely factor in the applied experimental conditions. Therefore, a role for MPO in the dissolution, breakage and clearance of these particles seems most unlikely. Studies on the peroxidase activity of alveolar macrophage in rats during pulmonary inflammation have shown that alveolar macrophages acquire peroxidase activity from multiple sources during pulmonary inflammation but only 0.8% of all macrophages were positive for cytoplasmic peroxidase in normal rats (Shellito et al., 1987). Therefore future studies to clarify the impact of alveolar macrophages, if any, on biodegradation of graphenic nanomaterials are a priority.

In parallel with the studies on degradation of pristine GP *in vivo* we examined the potential enzymatic oxidation of GP *in vitro* using HRP and H_2O_2, as a surrogate for MPO as described in Kotchey *et al.* (Kotchey et al., 2011). No significant increase in I_D/I_G ratio was observed but another band, the D' band, located at 1620 cm^{-1} appeared, which is documented in literature to be linked to substantial defects in the graphene structure (Kudin et al., 2008; Malard et al., 2009). Additionally, the recording of one spectrum showing a substantial increase in the I_D/I_G ratio after 1 week HRP treatment leads to the conclusion that the oxidation process may be intrinsically non-linear and that this introduces a large variability to the process.

Minimal oxidation was seen in pristine GP treated *in vitro* with the peroxidase, but the extent of degradation was not comparable to complete dissolution of the graphene structure of oxidized GP after 20 days HRP H_2O_2 treatment reported in Kotchey *et al.* (Kotchey et al., 2011). Therefore, the timeframe for oxidation of pristine graphene appears to be much longer than for oxidized graphene. This is in line with the lack of oxidation we describe up to 6 weeks post exposure *in vivo* and the self-evident persistence of GP in lungs evident as large accumulations of particles in the histological section. However, from our study we cannot exclude the possibility that a small fraction of GP were being oxidized, comminuted and then cleared from the lungs and therefore not detected in our study. We showed that the absence of a biological effect of GP after a 6 weeks timepoint was not correlated with degradation via oxidation and subsequent clearance of the deposited GP.

Oxidative degradation of GP *in vivo* does not account for the lack of inflammation at a 6 weeks timepoint since no change in the I_D/I_G ratio in the Raman spectrum occurred, indicating no oxidation of pristine GP up to 6 weeks in lung tissue and in addition large accumulations were plainly seen in lung sections. *In vitro* oxidation of GP via HRP showed only minimal oxidation of GP indicating that pristine graphenic nanomaterials are more biopersistent and may behave differently *in vivo* to their oxidized counterpart. This study suggests that further research is warranted into biodegradation of pristine and oxidised carbonaceous nanomaterials via enzymatic oxidation, in particular by alveolar macrophages.

Chapter 8: Mechanism of graphene platelet inflammation *in vitro*

Some of the following results have been published in

Schinwald A, Murphy FA, Jones A, MacNee W, Donaldson K. Graphene-based nanoplatelets: a new risk to the respiratory system as a consequence of their unusual aerodynamic properties. ACS Nano. 2012 Jan 24;6(1):736-46.

8.1 Aims and hypothesis

Based on the study showing acute inflammation in the lung and the pleural space after GP exposure (chapter 6), the aim of this study was to elucidate the mechanism underlying the inflammatory response to GP *in vitro*. A number of endpoints were examined including oxidative stress, pro-inflammatory cytokine and chemokine up regulation and the involvement of the NALP3 inflammasome activation. IL-1β is known to be up regulated after asbestos, silica and CNT exposure (Dostert et al., 2008; Hornung et al., 2008) and has been implicated in frustrated phagocytosis and the NALP3 inflammasome activation (O'Neill, 2008). We hypothesised that the NALP3 inflammasome complex is an important component of the molecular pathway and underlying mechanism by which cells sense foreign bodies including GP.

8.2 Results

8.2.1 Characterisation of cell/particle interaction

Characterisation of differentiated THP-1 macrophage cells with GP was performed to identify if GP are readily internalised by the cells or led to frustrated phagocytosis. The interaction of differentiated THP-1 cells with graphene platelets was examined via SEM and TEM after a 4 hour exposure at a dose of 5 µg/cm². The SEM images revealed that GP exceeding the size of approximately 15 µm projected diameter could not be fully phagocytosed by THP-1 cells and therefore led to frustrated

phagocytosis (Figure 8-1 I). Complete uptake of smaller GP could be imaged using TEM as shown in Figure 8-1 II.

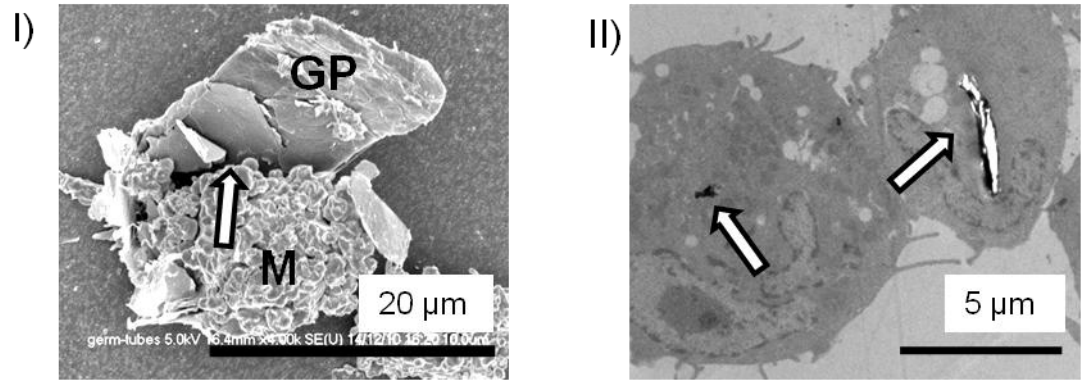

Figure 8-1: Cell/particle interactions to examine the uptake of GP on the surface using SEM and inside of the cells using TEM following 4 hour exposure to GP. I) SEM showing the attempted uptake of a GP by THP-1 macrophages (M). The arrow indicates the lip of the unclosed phagosome showing incomplete internalisation of the GP producing frustrated phagocytosis (n=3). II) TEM shows that small GP (≤ 5 µm) could be entirely internalised (arrows) (n=2).

8.2.2 GP-mediated loss of membrane integrity of THP-1 macrophages and depletion of reduced glutathione

Electron paramagnetic resonance (EPR) measurements were performed to determine the generation of oxygen-centred free radicals of CB and GP as described in chapter 6.3.1. Results were compared to one-another and to a positive Pyrogallol control, a spontaneous superoxide anion generator with Tempone H (without the addition of H_2O_2) used as a spin trap. Both CB and GP caused a significant increase in free radical generation with GP production increased by 2-fold compared to CB (Figure 8-2 I).

Release of LDH was used as an indicator of cell viability and measured after 24 hour exposure of THP-1 macrophages to CB and GP. A concentration range of 1 µg/cm², 5 µg/cm² and 10 µg/cm² for GP was used and concentrations of 5 µg/cm² and higher significantly increased LDH release whilst CB exposure at the same concentrations

did not (Figure 8-2 II). An explanation for the loss of membrane integrity could be the generation of reactive oxygen species and so the levels of free thiol groups, predominantly GSH, was measured as an indicator for oxidative stress, using the fluorescence probe, monobromobimane. After 4 hour of GP exposure the levels of free thiol groups was significantly lowered compared to the vehicle control (Figure 8-2 III, IV). CB did not cause a significant change in the levels of free thiol groups.

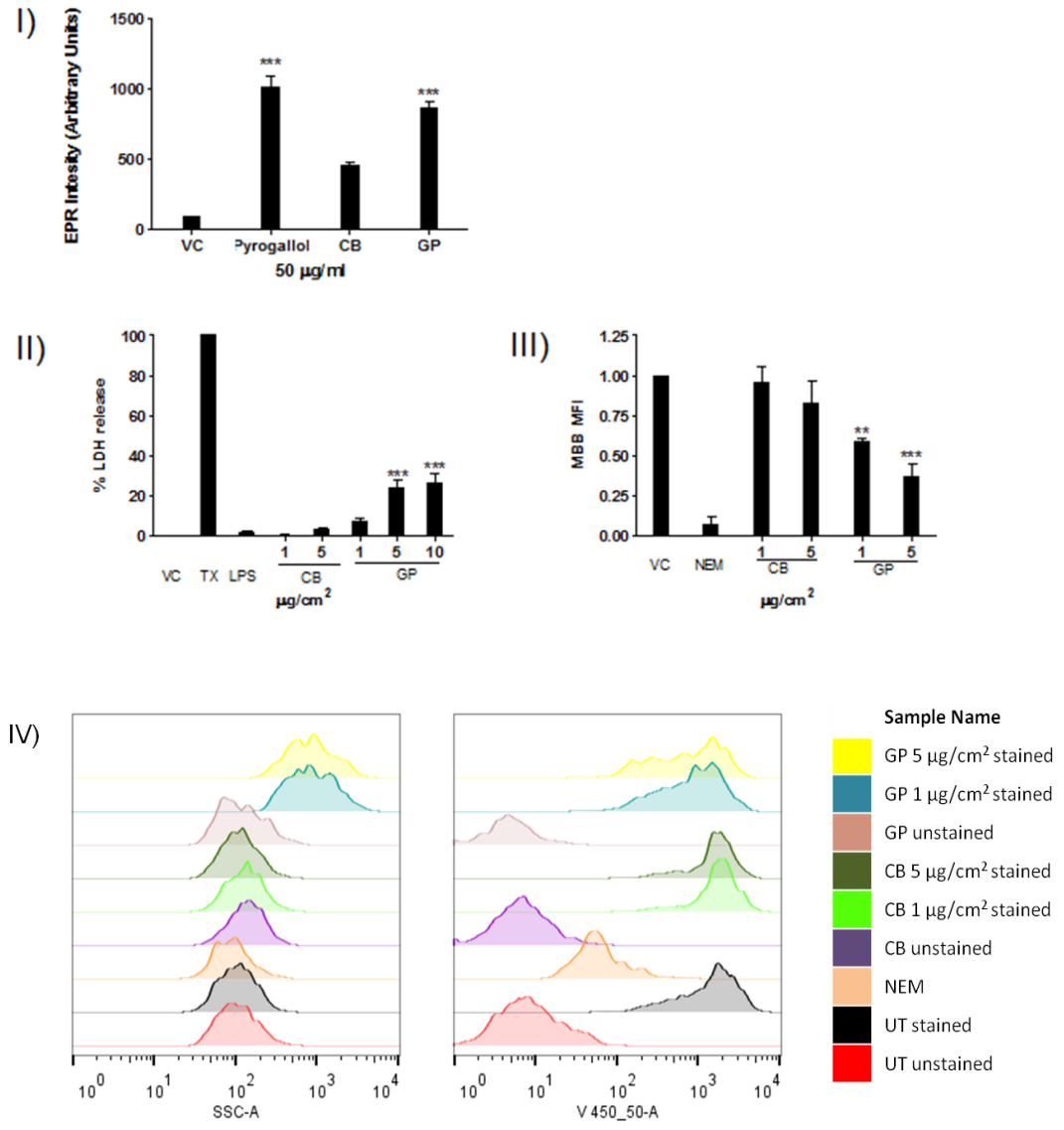

Figure 8-2: Determination of the generation of oxygen-centred free radicals, LDH release and the decrease in free thiol groups as indications of cell toxicity and oxidative stress. I) A significant increase in EPR intensity was measured in the GP sample which was comparable to the positive control Pyrogallol. Data expressed as

mean + s.e.m, n=3. II) Significant release of LDH after 24 hour exposure to GP at 5 and 10 µg/cm^2 while CB had no significant effect on LDH.Triton X (TX) was used as a positive control. Data expressed as mean + s.e.m, n=5. III) Mean fluorescence intensity (MFI) of monobromobimane (MBB) as indicator for levels of free thiol groups. GP exposure significantly reduced the MFI of MBB at all concentration measured. N-ethyl-maleimide (NEM) was used as a positive control Data expressed as mean + s.e.m, n=4. (**) p < 0.01, (***) p < 0.001 compared to vehicle control. FlowJo software (Tree Star Inc.) was used for analysing the data. Gating was based on FSC/SSC. IV) Left hand image shows a representative side-scatter plot to illustrate the change in 'granularity' after GP phagocytosis. Change in MBB fluorescence was detected through a 450/50 filter, showing the decrease in fluorescence intensity after GP treatment and NEM, the positive control.

8.2.3 Activation of the NALP3 inflammasome and pro-inflammatory cytokines after GP exposure *in vitro*

The cytokine IL-1β has been shown to be up regulated as a response to long fibre treatment in a number of studies. In this study we examined if IL-1β is also involved in the pro-inflammatory response to GP. We measured the concentration of IL-1β in the supernatant of THP-1 cells exposed for 24 hours to either LPS, CB (1 and 5 µg/cm²) or GP (1, 5 and 10 µg/cm²) by ELISA. LPS as well as all concentrations of GP led to a significant increase in IL-1β expression whereas CB treatment had no effect (Figure 8-3 I). To investigate if the attempt to phagocytose GP was involved in up regulating IL-1β expression, phagocytosis was inhibited via disruption of actin filaments using cytochalasin D at 0.2 µM. The inhibition of phagocytosis significantly reduced IL-1β expression at all concentrations of GP; however cytochalasin D had no effect on the level of IL-1β released by THP-1 cells exposed to LPS since its action is not dependent on phagocytic processes (Figure 8-3 I). Phagocytosis of large particle activators and subsequent release of IL-1β has been shown to be linked to the activation of the NALP3 inflammasome. Additional mechanisms involved in the activation of the NALP3 inflammasome are decreased intracellular K^+ linked to an efflux of K^+ and generation of ROS. By blocking the

efflux of K^+ via increasing extracellular K^+ concentration to 30 mM and the inhibition of generation of ROS via inhibition of NADPH oxidase using diphenylene iodonium (DPI) at 15 µM, the expression of IL-1β was significantly reduced in both LPS and GP exposed cells (Figure 8-3 I). An initial screening and a dose response series of the concentrations used for DPI, cytochalasin D and K^+ was previously performed in the lab by Dr Fiona Murphy on THP-1 cells and published in (Murphy et al., 2012b). To further assess which cytokines were involved in acute inflammation after particle exposure a cytokine bead array was performed. The selected panel of cytokines and chemokines was TNF, IL-6, IL-8, IL-1β, CCL-2 (MCP-1), CCL-5 (RANTES), CCL-3 (MIP-1α), basic FGF, IL-13 and TGF-β. Out of this range of cytokines, MCP-1, IL-8, MIP-1α and IL-1β were all significantly increased after GP exposure with no effect of CB exposure on these mediators (Figure 8-3 II).

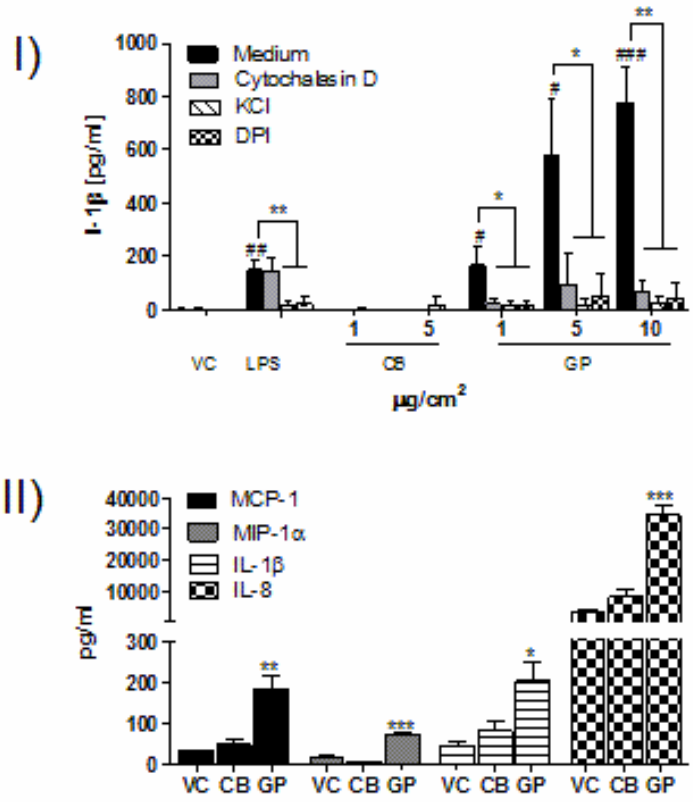

Figure 8-3: Data providing evidence consistent with the activation of the NALP3 inflammasome, and pro-inflammatory cytokine expression on GP, CB and LPS

treatment. I) IL-1β concentration in the supernatant of THP-1 cells exposed to LPS, CB and GP measured by ELISA. LPS (1 µg/ml) as well as GP at all concentrations led to a significant increase in IL-1β expression whereas CB treatment had no effect. Phagocytotic uptake of GP was inhibited by cytochalsin D at a concentration of 0.2 µM which led to a significant reduction of IL-1β expression in GP exposed cells. This effect was not observed in LPS treated cells. IL-1β expression after LPS and GP exposure was significantly reduced by inhibition of K^+ efflux (30 mM) and diphenylene iodonium (DPI) at 15 µM, an NADPH oxidase inhibitor. Data expressed as mean + s.e.m, n=4. II) Four cytokines (MCP-1, IL-8, IL-1β and MIP-1α) out of 11 tested were significantly upregulated after a 24 hour GP exposure. CB treatment did not lead to a significant increase in any of the cytokines measured. Data expressed as mean + s.e.m, n=3. (*) P < 0.05, (**) P < 0.01, (***) P < 0.001 compared to vehicle control. # p < 0.05, ## p < 0.01, ### p < 0.001 compared to vehicle control.

8.3 Discussion

The objective of this study was to examine the cellular interactions that are driving the acute inflammatory response to GP seen in the lung and the pleural space.

To elucidate the mechanism leading to GP-induced inflammation, cell-nanoparticle interaction was examined *in vitro* using a macrophage cell line and a number of pro-inflammatory cytokines and chemokines were measured and the expression of IL-1β put in relation to the activation of the NALP3 inflammasome.

To investigate the interaction of macrophages with GP, cells of a differentiated monocytic cell line, THP-1, were treated with GP and phagocytosis was examined using SEM and TEM. Frustrated phagocytosis could be observed in SEM images, showing GP only partly phagocytosed by macrophages. TEM revealed that only small GP (≤ 5 µm) were fully taken up. The membrane integrity of THP-1 cells after 24 hour GP exposure was also significantly impaired in a dose dependent manner. We also determined the generation of oxygen-centred free radicals by GP and CB using EPR. CB as well as GP generated a significant amount of free radicals, and GP generated approximately double that produced by CB. Therefore free radicals are

possibly involved in the pro-inflammatory effects seen *in vivo* and *in vitro* with GP compared to CB, although it is not likely that intrinsic free radical activity explains the extra potency of GP. We went on to determine the oxidative status of THP-1 cells by measuring the decrease in free thiol groups, mainly reduced glutathione after CB and GP treatment. Glutathione/glutathione disulfide is the major redox couple in cells and its tight regulation is critical in antioxidant defence and regulation of cellular events (Wu et al., 2004). Glutathione is the most abundant low-molecular-weight thiol and the loss of free thiol can be measured via loss of monobromobimane fluorescence (Wu et al., 2004). Exposure of THP-1 cells to GP led to a significant decrease in free thiol groups in a dose-dependent manner. Depletion of the antioxidant defence system by pollutants (Kelly et al., 1996) and respirable fibres (Brown et al., 2000) has been shown to result in oxidative stress and the activation of transcription factors including NF-κB (Brown et al., 1999). NF-κB regulates the transcription of inflammatory genes, including IL-1β, MIP-1α and MCP-1 (Rahman and MacNee, 1998). We measured a panel of acute phase cytokines involved in the inflammatory response after exposure of THP-1 cells to CB and GP. Four out of 11 different cytokines measured, MCP-1, IL-8, IL-1β and MIP-1α, were significantly elevated after GP exposure. The pro-inflammatory cytokine and neutrophil chemotaxin IL-8 has been shown to be elevated in airway epithelial cells and serum (Duncan et al., 2010) as well as alveolar macrophages (Broser et al., 1996) of asbestos exposed individuals (Duncan et al., 2010).

Since GP exposure led to an increased production of IL-1β, we explored the possibility that GP promote inflammation by activating the NALP3 inflammasome pathway. As described in chapter 4, the NALP3 inflammasome has been identified as an underlying mechanism for asbestos, silica, CNT and monosodium urate induced inflammation (O'Neill, 2008). We hypothesised that large particle activators like GP could have a similar effect as fibrous particles. In order to delineate the GP-induced signalling pathway leading to inflammasome activation, IL-1β production after GP exposure was compared to CB and LPS induced IL-1β release in cell culture medium and medium supplemented with inhibitors for phagocytosis, ROS generation and potassium efflux.CB was previously reported to activate the NALP3 inflammasome pathway leading to pyroptosis and IL-1β release (Reisetter et al., 2011). In this study

a dose of 30 µg/cm^2 was used, at which loss of cell membrane integrity was observed. In our study CB was used at a non-cytotoxic dose of 1 and 5 µg/cm^2 which did not lead to an increase in IL-1β expression.

We investigated whether phagocytosis is needed to trigger inflammasome activation by disrupting actin filaments via cytochalasin D (Dostert et al., 2008). Inhibition of phagocytosis significantly reduced IL-1β expression after GP treatment, but had no effect on LPS induced IL-1β production, which is not mediated via phagocytosis. We further provided evidence that GP activity is blocked by inhibiting efflux of K^+, which is necessary of NALP3 inflammasome activation. Reduction of IL-1β production was also achieved by inhibition of the NADPH oxidase supporting the hypothesis that ROS are generated via phagocytosis of GP through the activation of the reduced form of NADP. More detailed and extensive studies have to be performed to conclude that activation of the NALP3 inflammasome is involved in GP induced inflammation however the preliminary results from this study provide evidence leading to the conclusion that activation of the NALP3 inflammasome is involved in GP inflammation.

Chapter 9: Concluding remarks

This study focused on the shape/length of HARN as the Biologically Effective Dose, the key entity that drives pathophysiologically relevant forms of toxicity, inflammation being the one that was focused on here. Advances in nanotechnology allow the production of a range of different nanomaterials in various shapes, compositions, surface modifications, charges etc. to satisfy the production and industrial need for consumer end products. However, in regards to toxicological testing, this wide spectrum of new forms of materials make it difficult to deal with, since conventional toxicology can't be applied to all newly developed materials. Therefore, structure-toxicity relationships (STR) are urgently needed to describe the Biologically Effective Dose of new nanomaterials which would allow the identification of the toxicological potential of a nanomaterial based on the STR without the need of individual testing.

The development of STR, e.g. the fibre pathogenicity paradigm (FPP), has important implications on the risk assessment and exposure regulation. The current Health and Safety Executive standard on asbestos fibre sampling is based on the definition of 'fibres' developed by the British Occupational Hygiene Society in 1968, whereby countable fibres were defined as strutures visible by phase contrast optical microscopy with a length of 5-100 µm, an aspect ratio of 3:1 and a width of < 3 µm. In this study we showed that, fortuitously, this arbitrarily chosen fibre-definition coincides exactly with the threshold length for fibre induced pleural inflammation in mice. If the length set in the standard had been set higher then hazardous fibres would not have been counted and if it had been set lower an unnecessary penalty could have been applied to industries to comply with an overly-rigorous standard. The fact that synthetic nanofibres were used in the present studies to define the length threshold highlights the general relevance of the standard to the new generation of fibres made from novel materials by nanotechnological methods that are currently being synthesised or are under test for use in industry. There is a distinct possibility that workforces will be exposed to some of these nanofibres in workplace air and hygiene will be mandatory and our data suggest that the existing fibre–counting standard will be adequate for these new fibres

The present study also introduces a new high aspect material, namely nanoplatelets in the form of graphene as an exemplar, which pose an unusual risk to the lungs and possibly the pleural space, after inhalation exposure, due to their extended lateral dimensions. We showed that these sheet- or platelet shaped particles with nanoscale thickness but extended in their other two dimensions possess a low D_{ae} which allows them to be respirable and reach the lower respiratory tract. Thus they have the potential to cause adverse health effects and therefore warrant further investigation. We suggest that the extended lateral dimensions which produce the high aspect ratio are the driving properties in pathological response to GP. However it seems likely that layer thickness and the subsequent role that this plays in rigidity is a key factor in determining pathogenicity, and this was not investigated here. Our initial results showing inflammogenicity at an acute timepoint and non-inflammogenicity at medium timepoints have important implications in the hazard identification of GP following inhalation exposure and for their use in biomedical applications. Additionally, the biopersistence of pristine GP *in vivo* in lung tissue up to 6 weeks with no associated inflammation implies biocompatibility, which could open the way to applications in tissue engineering and drug delivery.

Our in vitro studies provide preliminary information regarding the mechanism by which the inflammatory response to HARN was initiated. As previously reported, activation of the NALP3 inflammasome complex and subsequent release of IL-1β may be an underlying mechanism of HARN induced inflammation - however more research is needed to confirm this.

The pathophysiological responses to HARN described here were based on single exposure via the routes of either pharyngeal aspiration or intrapleural injection at short and medium timepoints up to 6 weeks. Extrapolation of this data for the purpose of risk assessment is limited since the routes of exposure chosen are artificial and the data has to be confirmed by the use of more physiologically relevant exposure scenarios. Long term inhalation exposure studies with relevant concentration and repeated exposure as performed by Pauluhn *et al*. and Ma-Hock *et al*. (Pauluhn, 2010; Ma-Hock et al., 2009) are required to determine if the threshold length for pulmonary and pleural inflammation in response to fibrous HARN and the

observed loss of inflammation after GP exposure, continue over a prolonged time and repeated exposure.

Even though real-time exposure scenarios are necessary for the risk management of HARN, it has been shown that short term exposure studies via non-physiological routes can assist risk management as well as forming the basis for further investigations (Poland et al., 2008; Health and Safety Executive, 2009).

Based on the above understanding of the probable mechanisms, we suggest that potential risks to humans from fibrous and platelet shaped HARN exposure could be minimised by a safer-by-design approach for the manufacture of HARN. This would involve, where possible, producing only short fibres less than 5 μm and graphene platelets small enough to be phagocytosed by macrophages in order to minimise potential harmful effects. In addition to the 'safe-by design' approach, the new insights into the STR of HARN as presented in this study have important implications for nanofibre and nanoplatelet risk assessment.

However, the specific properties of these materials in a shape exceeding the 'safe-by-design' limitations may provide advantages compared to the particulate counterpart and HARN in the hazardous size ranges may therefore be produced. In this case strict criteria and counting methods should be defined to assess occupational exposure to HARN. Currently, to assess inhalation exposure to fibres, air is drawn through a filter onto which the airborne fibres fibres are deposited. The fibres are then counted using an optical microscopy according to a defined method; there are several variants of this method but the dominant approach is that published by the World Health Organisation. Only fibres with diameters less than 3 μm with a length greater than 5 μm and an aspect ratio of at least 3:1 are counted. In terms of exposure assessment of HARN, detection methods with higher magnification than optical microscopy have to be used such as TEM or SEM to overcome the resolution limitation. Currently there is no consensus on the most appropriate approach and much more work is needed to routinely detect and quantify HARN. The current regulations of nanomaterials in the European Union are covered by the 'substance' definition in REACH (Registration, Evaluation, Authorisation and Restriction of Chemicals).

When considering the interaction between toxicology and exposure science, it is evident that the development of a protective but not punitive fibre standard requires a strong synergy between the two disciplines allowing the identification of the most appropriate metric and assessment criteria. Wherever possible, such synergy should continue and this is more and more evident when considering the challenges of nanotechnology.

Chapter 10: Bibliography

Abram,C.L. and Lowell,C.A. (2008). The diverse functions of Src family kinases in macrophages. Frontiers in Bioscience *13*, 4426-4450.

Abu-Hijleh,M.F., Habbal,O.A., and Moqattash,S.T. (1995). The role of the diaphragm in lymphatic absorption from the peritoneal cavity. J. Anat. *186*, 453-467.

Adachi,Y., Aoki,C., Yoshio-Hoshino,N., Takayama,K., Curiel,D.T., and Nishimoto,N. (2006). Interleukin-6 induces both cell growth and VEGF production in malignant mesotheliomas. International Journal of Cancer *119*, 1303-1311.

Adamson,I.R. (1997). Early mesothelial cell proliferation after asbestos exposure: In vivo and in vitro studies. Environmental Health Perspectives *105*, 1205-1208.

Aitken,R.J., Chaudhry,M.Q., Boxall,A.B., and Hull,M. (2006). Manufacture and use of nanomaterials: current status in the UK and global trends. Occup. Med. (Lond). *56*, 300-306.

Akhavan,O. and Ghaderi,E. (2010). Toxicity of Graphene and Graphene Oxide Nanowalls Against Bacteria. ACS Nano *4*, 5731-5736.

Allen,B.L., Kichambare,P.D., Gou,P., Vlasova,I.I., Kapralov,A.A., Konduru,N., Kagan,V.E., and Star,A. (2008). Biodegradation of single-walled carbon nanotubes through enzymatic catalysis. Nano. Lett. *8*, 3899-3903.

Allen,I.C., Scull,M.A., Moore,C.B., Holl,E.K., McElvania-TeKippe,E., Taxman,D.J., Guthrie,E.H., Pickles,R.J., and Ting,J.P. (2009). The NLRP3 inflammasome mediates in vivo innate immunity to influenza A virus through recognition of viral RNA. Immunity. *30*, 556-565.

Antony,V.B., Hott,J.W., Kunkel,S.L., Godbey,S.W., Burdick,M.D., and Strieter,R.M. (1995). Pleural mesothelial cell expression of C-C (monocyte chemotactic peptide) and C-X-C (interleukin 8) chemokines. Am. J Respir. Cell Mol. Biol. *12*, 581-588.

Asbestosis Research Council (1968). The measurement of airborne asbestos dust by the membrane filter method. Technical note 1. Asbestosis Research Council.

Awasthi,K., Srivastava,A., and Srivastava,O.N. (2005). Synthesis of carbon nanotubes. J Nanosci. Nanotechnol. *5*, 1616-1636.

Azzali,G. (1999). The lymphatic vessels and the so-called "lymphatic stomata" of the diaphragm: a morphologic ultrastructural and three-dimensional study. Microvasc. Res. *57*, 30-43.

Balashazy,I., Hofmann,W., and Heistracher,T. (2003). Local particle deposition patterns may play a key role in the development of lung cancer. Journal of Applied Physiology *94*, 1719-1725.

Bartrip,P.W. (2004). History of asbestos related disease. Postgrad. Med J. *80*, 72-76.

Baruzzi,A., Caveggion,E., and Berton,G. (2008). Regulation of phagocyte migration and recruitment by Src-family kinases. Cellular and Molecular Life Sciences *65*, 2175-2190.

Bauernfeind,F., Ablasser,A., Bartok,E., Kim,S., Schmid-Burgk,J., Cavlar,T., and Hornung,V. (2011). Inflammasomes: current understanding and open questions. Cell Mol. Life Sci. *68*, 765-783.

bccresearch.com (2012). Nanotechnology: A Realistic Market Assessment. Online Source: http://www. bccresearch. com/report/nanotechnology-market-applications-products-nan031e. html (date accessed 30. 11. 2012).

Bellmann,B., Creutzenberg,O., Dasenbrock,C., Ernst,H., Pohlmann,G., and Muhle,H. (2000). Inhalation tolerance study for p-aramid respirable fiber-shaped particulates (RFP) in rats. Toxicological Sciences *54*, 237-250.

Bergstrand,H. (1990). The generation of reactive oxygen-derived species by phagocytes. Agents Actions Suppl. *30:199-211.*, 199-211.

Bernstein,D.M. and Hoskins,J.A. (2006). The health effects of chrysotile: Current perspective based upon recent data. Regulatory Toxicology and Pharmacology *45*, 252-264.

Bernstein,D.M., Rogers,R.A., Sepulveda,R., Donaldson,K., Schuler,D., Gaering,S., Kunzendorf,P., Chevalier,J., and Holm,S.E. (2010). The pathological response and fate in the lung and pleura of chrysotile in combination with fine particles compared to amosite asbestos following short-term inhalation exposure: interim results. Inhal. Toxicol. *22*, 937-962.

Berton,S., Belletti,B., Wolf,K., Canzonieri,V., Lovat,F., Vecchione,A., Colombatti,A., Friedl,P., and Baldassarre,G. (2009). The Tumor Suppressor Functions of p27(kip1) Include Control of the Mesenchymal/Amoeboid Transition. Molecular and Cellular Biology *29*, 5031-5045.

Bianchi,M.E. and Manfredi,A.A. (2007). High-mobility group box 1 (HMGB1) protein at the crossroads between innate and adaptive immunity. Immunological Reviews *220*, 35-46.

Bonner,J.C. (2010). Mesenchymal cell survival in airway and interstitial pulmonary fibrosis. Fibrogenesis. Tissue Repair. *3:15.*, 15.

Boutin,C., Dumortier,P., Rey,F., Viallat,J.R., and De,V.P. (1996). Black spots concentrate oncogenic asbestos fibers in the parietal pleura. Thoracoscopic and mineralogic study. Am J Respir. Crit Care Med. *153*, 444-449.

Broser,M., Zhang,Y., Aston,C., Harkin,T., and Rom,W.N. (1996). Elevated interleukin-8 in the alveolitis of individuals with asbestos exposure. Int. Arch. Occup. Environ. Health. *68*, 109-114.

Brown,D.M., Beswick,P.H., Bell,K.S., and Donaldson,K. (2000). Depletion of glutathione and ascorbate in lung lining fluid by respirable fibres. Ann Occup. Hyg. *44*, 101-108.

Brown,D.M., Beswick,P.H., and Donaldson,K. (1999). Induction of nuclear translocation of NF-kappaB in epithelial cells by respirable mineral fibres. J Pathol. *189*, 258-264.

Brown,D.M., Kinloch,I.A., Bangert,U., Windle,A.H., Walter,D.M., Walker,G.S., Scotchford,C.A., Donaldson,K., and Stone,V. (2007). An in vitro study of the potential of carbon nanotubes and nanofibres to induce inflammatory mediators and frustrated phagocytosis. Carbon *45*, 1743-1756.

Bryant,C. and Fitzgerald,K.A. (2009). Molecular mechanisms involved in inflammasome activation. Trends Cell Biol. *19*, 455-464.

Butler,J.P., Huang,J., Loring,S.H., Laifook,S.J., Wang,P.M., and Wilson,T.A. (1995). Model for A Pump That Drives Circulation of Pleural Fluid. Journal of Applied Physiology *78*, 23-29.

Byrne,F., Prina-Mello,A., Whelan,A., Mohamed,B.M., Davies,A., Gun'ko,Y.K., Coey,J.M.D., and Volkov,Y. (2009). High content analysis of the biocompatibility of nickel nanowires. Journal of Magnetism and Magnetic Materials *321*, 1341-1345.

Byrnes,R.W. (1996). Evidence for involvement of multiple iron species in DNA single-strand scission by H2O2 in HL-60 cells. Free Radical Biology and Medicine *20*, 399-406.

Cailhier,J.F.O., Sawatzky,D.A., Kipari,T., Houlberg,K., Walbaum,D., Watson,S., Lang,R.A., Clay,S., Kluth,D., Savill,J., and Hughes,J. (2006). Resident pleural macrophages are key orchestrators of neutrophil recruitment in pleural inflammation. American Journal of Respiratory and Critical Care Medicine *173*, 540-547.

Cannon,G.J. and Swanson,J.A. (1992). The macrophage capacity for phagocytosis. J Cell Sci. *101*, 907-913.

Cao,G. and Liu,D. (2008). Template-based synthesis of nanorod, nanowire, and nanotube arrays. Adv. Colloid Interface Sci. *136*, 45-64.

Chapman,H.A. (2011). Epithelial-Mesenchymal Interactions in Pulmonary Fibrosis. Annual Review of Physiology, Vol 73 *73*, 413-435.

Chen,X.C., Klingeler,R., Kath,M., El Gendy,A.A., Cendrowski,K., Kalenczuk,R.J., and Borowiak-Palen,E. (2012). Magnetic Silica Nanotubes: Synthesis, Drug Release, and Feasibility for Magnetic Hyperthermia. Acs Applied Materials & Interfaces *4*, 2303-2309.

Cheng,J.Q., Lee,W.C., Klein,M.A., Cheng,G.Z., Jhanwar,S.C., and Testa,J.R. (1999). Frequent mutations of NF2 and allelic loss from chromosome band 22q12 in

malignant mesothelioma: Evidence for a two-hit mechanism of NF2 inactivation. Genes Chromosomes & Cancer *24*, 238-242.

Cheng,Y., Yeh,H., and Allen,M.D. (1988). Dynamic Shape Factor of a Plate-Like Particle. Aerosol Science and Technology *8*, 109-123.

Cho,W.S., Duffin,R., Howie,S.E., Scotton,C.J., Wallace,W.A., MacNee,W., Bradley,M., Megson,I.L., and Donaldson,K. (2011). Progressive severe lung injury by zinc oxide nanoparticles; the role of Zn2+ dissolution inside lysosomes. Part Fibre Toxicol. *8:27.*, 27.

Cho,W.S., Duffin,R., Poland,C.A., Duschl,A., Oostingh,G.J., MacNee,W., Bradley,M., Megson,I.L., and Donaldson,K. (2012). Differential pro-inflammatory effects of metal oxide nanoparticles and their soluble ions in vitro and in vivo; zinc and copper nanoparticles, but not their ions, recruit eosinophils to the lungs. Nanotoxicology. *6*, 22-35.

Cho,W.S., Duffin,R., Poland,C.A., Howie,S.E., MacNee,W., Bradley,M., Megson,I.L., and Donaldson,K. (2010). Metal oxide nanoparticles induce unique inflammatory footprints in the lung: important implications for nanoparticle testing. Environ Health Perspect. *118*, 1699-1706.

Coin,P.G., Osornio-Vargas,A.R., Roggli,V.L., and Brody,A.R. (1996). Pulmonary fibrogenesis after three consecutive inhalation exposures to chrysotile asbestos. Am. J Respir. Crit Care Med. *154*, 1511-1519.

Coin,P.G., Roggli,V.L., and Brody,A.R. (1992). Deposition, Clearance, and Translocation of Chrysotile Asbestos from Peripheral and Central Regions of the Rat Lung. Environmental Research *58*, 97-116.

Coll,R.C. and O'Neill,L.A. (2011a). The cytokine release inhibitory drug CRID3 targets ASC oligomerisation in the NLRP3 and AIM2 inflammasomes. PLoS One. *6*, e29539.

Comar,M., Zanotta,N., Pesel,G., Visconti,P., Maestri,I., Rinaldi,R., Crovella,S., Cortale,M., De Zotti,R., and Bovenzi,M. (2012). Asbestos and SV40 in malignant pleural mesothelioma from a hyperendemic area of north-eastern Italy. Tumori *98*, 210-214.

Conti,P. and DiGioacchino,M. (2001). MCP-1 and RANTES are mediators of acute and chronic inflammation. Allergy Asthma Proc. *22*, 133-137.

Cooke,W. (1924). fibrosis of the lungs due to inhaltation of asbestos dust. British Medical Journal *2*, 147.

Crouch,E., Hartshorn,K., and Ofek,I. (2000). Collectins and pulmonary innate immunity. Immunol. Rev. *173:52-65.*, 52-65.

Cuzzocrea,S., Sautebin,L., De Sarro,G., Costantino,G., Rombola,L., Mazzon,E., Ialenti,A., De Sarro,A., Ciliberto,G., Di Rosa,M., Caputi,A.P., and Thiemermann,C.

(1999). Role of IL-6 in the pleurisy and lung injury caused by carrageenan. Journal of Immunology *163*, 5094-5104.

Dahm,M.M., Evans,D.E., Schubauer-Berigan,M.K., Birch,M.E., and Fernback,J.E. (2012). Occupational exposure assessment in carbon nanotube and nanofiber primary and secondary manufacturers. Ann Occup. Hyg. *56*, 542-556.

Dai,J. and Churg,A. (2001). Relationship of fiber surface iron and active oxygen species to expression of procollagen, PDGF-A, and TGF-beta(1) in tracheal explants exposed to amosite asbestos. Am. J Respir. Cell Mol. Biol. *24*, 427-435.

Davis,J.M., Addison,J., Bolton,R.E., Donaldson,K., Jones,A.D., and Smith,T. (1986). The pathogenicity of long versus short fibre samples of amosite asbestos administered to rats by inhalation and intraperitoneal injection. Br. J Exp. Pathol. *67*, 415-430.

Davis,J.M., Beckett,S.T., Bolton,R.E., Collings,P., and Middleton,A.P. (1987). Mass and number of fibres in the pathogenesis of asbestos-related lung disease in rats. Br. J Cancer *37*, 673-688.

Dikalov,S., Skatchkov,M., and Bassenge,E. (1997). Quantification of peroxynitrite, superoxide, and peroxyl radicals by a new spin trap hydroxylamine 1-hydroxy-2,2,6,6-tetramethyl-4-oxo-piperidine. Biochemical and Biophysical Research Communications *230*, 54-57.

Ditsworth,D., Zong,W.X., and Thompson,C.B. (2007). Activation of poly(ADP)-ribose polymerase (PARP-1) induces release of the pro-inflammatory mediator HMGB1 from the nucleus. Journal of Biological Chemistry *282*, 17845-17854.

Dogra,S. and Donaldson,K. (1995). Effect of long and short fibre amosite asbestos on in vitro TNF production by rat alveolar macrophages: the modifying effect of lipopolysaccharide. Ind. Health. *33*, 131-141.

Donaldson,K., Stone,V., Gilmour,P.S., Brown,D.M., and MacNee,W. (2000). Ultrafine particles: mechanisms of lung injury. Phil. Trans. R. Soc. Lond. A *358*, 2741-2749.

Donaldson,K. (2009). The inhalation toxicology of p-aramid fibrils. Critical Reviews in Toxicology *39*, 487-500.

Donaldson,K., Beswick,P.H., and Gilmour,P.S. (1996). Free radical activity associated with the surface of particles: a unifying factor in determining biological activity? Toxicol Lett. *88*, 293-298.

Donaldson,K., Murphy,F., Schinwald,A., Duffin,R., and Poland,C.A. (2011). Identifying the pulmonary hazard of high aspect ratio nanoparticles to enable their safety-by-design. Nanomedicine. (Lond). *6*, 143-156.

Donaldson,K., Murphy,F.A., Duffin,R., and Poland,C.A. (2010). Asbestos, carbon nanotubes and the pleural mesothelium: a review of the hypothesis regarding the role

of long fibre retention in the parietal pleura, inflammation and mesothelioma. Part Fibre. Toxicol. *7:5.*, 5.

Donaldson,K., Schinwald,A., Murphy,F., Cho,W.S., Duffin,R., Tran,L., and Poland,C. (2012). The Biologically Effective Dose in Inhalation Nanotoxicology. Acc. Chem. Res. [Epub ahead of print].

Donaldson,K. and Seaton,A. (2012). A short history of the toxicology of inhaled particles. Part Fibre Toxicol. *9:13.*, 13-19.

Donaldson,K., Stone,V., Tran,C.L., Kreyling,W., and Borm,P.J. (2004). Nanotoxicology. Occup. Environ. Med. *61*, 727-728.

Donaldson,K. and Tran,C.L. (2004). An introduction to the short-term toxicology of respirable industrial fibres. Mutat. Res *553*, 5-9.

Donaldson,K., Stone,V., Anthony, Lang, Robert, and Poland,C.A. (2008). Letter to the Editor. The Journal of Toxicological Sciences *33*, 385.

Dostert,C., Petrilli,V., Van,B.R., Steele,C., Mossman,B.T., and Tschopp,J. (2008). Innate immune activation through Nalp3 inflammasome sensing of asbestos and silica. Science. *320*, 674-677.

Driscoll,K.E., Hassenbein,D.G., Carter,J., Poynter,J., Asquith,T.N., Grant,R.A., Whitten,J., Purdon,M.P., and Takigiku,R. (1993). Macrophage Inflammatory Protein-1 and Protein-2 - Expression by Rat Alveolar Macrophages, Fibroblasts, and Epithelial-Cells and in Rat Lung After Mineral Dust Exposure. American Journal of Respiratory Cell and Molecular Biology *8*, 311-318.

Duch,M.C., Budinger,G.R., Liang,Y.T., Soberanes,S., Urich,D., Chiarella,S.E., Campochiaro,L.A., Gonzalez,A., Chandel,N.S., Hersam,M.C., and Mutlu,G.M. (2011). Minimizing oxidation and stable nanoscale dispersion improves the biocompatibility of graphene in the lung. Nano Lett. *11*, 5201-5207.

Duncan,K.E., Ghio,A.J., Dailey,L.A., Bern,A.M., Gibbs-Flournoy,E.A., Padilla-Carlin,D.J., Roggli,V.L., and Devlin,R.B. (2010). Effect of size fractionation on the toxicity of amosite and Libby amphibole asbestos. Toxicol. Sci. *118*, 420-434.

Ellison,M. (1993). The Annals of Occupational Hygiene. Volume 37, No. 2.

European Commission (2012). Nanomaterials. Online Source: http://ec. europa. eu/environment/chemicals/nanotech/index. htm#definition (date accessed 30. 11. 2012).

Fenoglio,I., Greco,G., Tornatis,M., Muller,J., Rayrnundo-Pinero,E., Beguin,F., Fonseca,A., Nagy,J.B., Lison,D., and Fubini,B. (2008). Structural defects play a major role in the acute lung toxicity of multiwall carbon nanotubes: Physicochemical aspects. Chemical Research in Toxicology *21*, 1690-1697.

Finkelstein,J.N. and Barrett,E.G. (2000). Alterations in Gene Expression in Pulmonary Cells Following Particles Interactions. In Particle-Lung Interactions, P.Gehr and J.Heyder, eds. (New York: Marcel Bekker, Inc), pp. 379-399.

Fleury-Feith,J., Lecomte,C., Renier,A., Matrat,M., Kheuang,L., Abramowski,V., Levy,F., Janin,A., Giovannini,M., and Jaurand,M.C. (2003). Hemizygosity of Nf2 is associated with increased susceptibility to asbestos-induced peritoneal tumours. Oncogene *22*, 3799-3805.

Frank,H. and Netter,M.D. (1979). The Ciba Collection of Medical Illustrations. The Respiratory System. 7th ed. West Caldwell, Ciba-Geigy Medical Education Division.

Frode,T.S., Souza,G.E.P., and Calixto,J.B. (2001). The modulatory role played by TNF-alpha and IL-1 beta in the inflammatory responses induced by carrageenan in the mouse model of pleurisy. Cytokine *13*, 162-168.

Fuchs N.A. (1964). The mechanics of Aerosols. 1st ed. Oxford, Pergamon Press and New York, The Macmillan Company.

futuremarketsinc.com (2012). Applications Chart for nanotubes companies: Nanomaterials Chart #9: Nanotubes. Online Source: http://www. futuremarketsinc. com/index. php?option=com_content&view=article&id=196:applications-chart-for-nanotubes-companies&catid=21&Itemid=58 (date accessed 21. 11. 2011).

Geim,A.K. and Novoselov,K.S. (2007). The rise of graphene. Nat. Mater. *6*, 183-191.

Geiser,M. (2010). Update on Macrophage Clearance of Inhaled Micro- and Nanoparticles. Journal of Aerosol Medicine and Pulmonary Drug Delivery *23*, 207-217.

Geiser,M. and Kreyling,W.G. (2010). Deposition and biokinetics of inhaled nanoparticles. Part Fibre Toxicol. *20;7:2.*, 2.

Geng,Y., Wang,S.J., and Kim,J.K. (2009). Preparation of graphite nanoplatelets and graphene sheets. Journal of Colloid and Interface Science *336*, 592-598.

Ghiazza,M., Scherbart,A.M., Fenoglio,I., Grendene,F., Turci,F., Martra,G., Albrecht,C., Schins,R.P., and Fubini,B. (2011). Surface iron inhibits quartz-induced cytotoxic and inflammatory responses in alveolar macrophages. Chem. Res. Toxicol. *24*, 99-110.

Goodglick,L.A. and Kane,A.B. (1990). Cytotoxicity of long and short crocidolite asbestos fibers in vitro and in vivo. Cancer Res. *50*, 5153-5163.

Graham,A., Higinbotham,J., Allan,D., Donaldson,K., and Beswick,P.H. (1999). Chemical differences between long and short amosite asbestos: differences in oxidation state and coordination sites of iron, detected by infrared spectroscopy. Occup. Environ. Med. *56*, 606-611.

Greillier,L. and Astoul,P. (2008). Mesothelioma and asbestos-related pleural diseases. Respiration. *76*, 1-15.

Gross,O., Poeck,H., Bscheider,M., Dostert,C., Hannesschlager,N., Endres,S., Hartmann,G., Tardivel,A., Schweighoffer,E., Tybulewicz,V., Mocsai,A., Tschopp,J., and Ruland,J. (2009). Syk kinase signalling couples to the Nlrp3 inflammasome for anti-fungal host defence. Nature. *459*, 433-436.

Gueugnon,F., Leclercq,S., Blanquart,C., Sagan,C., Cellerin,L., Padieu,M., Perigaud,C., Scherpereel,A., and Gregoire,M. (2011). Identification of novel markers for the diagnosis of malignant pleural mesothelioma. Am. J Pathol. *178*, 1033-1042.

Haas,A.R. and Sterman,D.H. (2012). Novel Intrapleural Therapies for Malignant Diseases. Respiration *83*, 277-292.

Hamilton,R.F., Wu,N., Porter,D., Buford,M., Wolfarth,M., and Holian,A. (2009). Particle length-dependent titanium dioxide nanomaterials toxicity and bioactivity. Part Fibre Toxicol. *6:35.*, 35.

Hassan,H. and Amer,A.O. (2011). Cell Intrinsic Roles of Apoptosis-Associated Speck-Like Protein in Regulating Innate and Adaptive Immune Responses. Thescientificworldjournal *11*, 2418-2423.

Health and Safety Executive (2009). Risk management of carbon nanotubes.

Heintz,N.H., Janssen,Y.M., and Mossman,B.T. (1993). Persistent induction of c-fos and c-jun expression by asbestos. Proc. Natl. Acad. Sci. U. S. A. *90*, 3299-3303.

Heintz,N.H., Janssen-Heininger,Y.M., and Mossman,B.T. (2010). Asbestos, lung cancers, and mesotheliomas: from molecular approaches to targeting tumor survival pathways. Am. J. Respir. Cell Mol. Biol. *42*, 133-139.

Hesterberg,T.W., Axten,C., McConnell,E.E., Oberdorster,G., Everitt,J., Miiller,W.C., Chevalier,J., Chase,G.R., and Thevenaz,P. (1997). Chronic inhalation study of fiber glass and amosite asbestos in hamsters: Twelve-month preliminary results. Environmental Health Perspectives *105*, 1223-1229.

Heyder,J. (2004). Deposition of inhaled particles in the human respiratory tract and consequences for regional targeting in respiratory drug delivery. Proc. Am. Thorac. Soc. *1*, 315-320.

Holt,P.F. (1957). Pneumococoniosis: Industrial Diseases od the Lung Caused by Dust. Pneumoconiosis 143-159.

Holt,P.F. (1983). Translocation of inhaled dust to the pleura. Environ. Res. *31*, 212-220.

Hornung,V., Bauernfeind,F., Halle,A., Samstad,E.O., Kono,H., Rock,K.L., Fitzgerald,K.A., and Latz,E. (2008). Silica crystals and aluminum salts activate the

NALP3 inflammasome through phagosomal destabilization. Nat. Immunol. *9*, 847-856.

Hornung,V. and Latz,E. (2010). Critical functions of priming and lysosomal damage for NLRP3 activation. Eur. J. Immunol. *40*, 620-623.

Huang,C., Rajfur,Z., Borchers,C., Schaller,M.D., and Jacobson,K. (2003). JNK phosphorylates paxillin and regulates cell migration. Nature. *424*, 219-223.

Hughes,J.M. and Weill,H. (1991). Asbestosis As A Precursor of Asbestos Related Lung-Cancer - Results of A Prospective Mortality Study. British Journal of Industrial Medicine *48*, 229-233.

Ip,C.K. and Wong,A.S. (2012). p70 S6 kinase and actin dynamics: A perspective. Spermatogenesis. *2*, 44-52.

ISO/TS 27687 (2008). Nanotechnologies- terminology and definitions for nano-objects - nanoparticle, nanofibre and nanoplate. ISO/TS 27687. ISO Standards.

Jamrozik,E., de,K.N., and Musk,A.W. (2011). Asbestos-related disease. Intern. Med J. *41*, 372-380.

Janssen,Y.M.W., Heintz,N.H., Marsh,J.P., Borm,P.J.A., and Mossman,B.T. (1994). Induction of C-Fos and C-Jun Protooncogenes in Target-Cells of the Lung and Pleura by Carcinogenic Fibers. American Journal of Respiratory Cell and Molecular Biology *11*, 522-530.

Jantz,M.A. and Antony,V.B. (2008). Pathophysiology of the pleura. Respiration. *75*, 121-133.

Jeffree,C.E., Rixon,H.W., Brown,G., Aitken,J., and Sugrue,R.J. (2003). Distribution of the attachment (G) glycoprotein and GM1 within the envelope of mature respiratory syncytial virus filaments revealed using field emission scanning electron microscopy. Virology. *306*, 254-267.

Ji,J.H., Jung,J.H., Kim,S.S., Yoon,J.U., Park,J.D., Choi,B.S., Chung,Y.H., Kwon,I.H., Jeong,J., Han,B.S., Shin,J.H., Sung,J.H., Song,K.S., and Yu,I.J. (2007). Twenty-eight-day inhalation toxicity study of silver nanoparticles in Sprague-Dawley rats. Inhal. Toxicol. *19*, 857-871.

Johnston,H.J., Hutchison,G., Christensen,F.M., Peters,S., Hankin,S., and Stone,V. (2010). A review of the in vivo and in vitro toxicity of silver and gold particulates: particle attributes and biological mechanisms responsible for the observed toxicity. Crit Rev. Toxicol. *40*, 328-346.

Jones,A.D. (1993). Respirable industrial fibres: deposition, clearence and dissolution in animal models. In The Annals of Occupational Hygiene., Ellison J.Mck., ed., pp. 211-226.

Kagan,V.E., Konduru,N.V., Feng,W., Allen,B.L., Conroy,J., Volkov,Y., Vlasova,I.I., Belikova,N.A., Yanamala,N., Kapralov,A., Tyurina,Y.Y., Shi,J., Kisin,E.R., Murray,A.R., Franks,J., Stolz,D., Gou,P., Klein-Seetharaman,J., Fadeel,B., Star,A., and Shvedova,A.A. (2010). Carbon nanotubes degraded by neutrophil myeloperoxidase induce less pulmonary inflammation. Nat. Nanotechnol. *5*, 354-359.

Kagedal,K., Zhao,M., Svensson,I., and Brunk,U.T. (2001). Sphingosine-induced apoptosis is dependent on lysosomal proteases. Biochem. J. *359*, 335-343.

Kamp,D.W., Graceffa,P., Pryor,W.A., and Weitzman,S.A. (1992). The Role of Free-Radicals in Asbestos-Induced Diseases. Free Radical Biology and Medicine *12*, 293-315.

Kamp,D.W. and Weitzman,S.A. (1999). The molecular basis of asbestos induced lung injury. Thorax. *54*, 638-652.

Kelly,D.P., Merriman,E.A., Kennedy,G.L., and Lee,K.P. (1993). Deposition, Clearance, and Shortening of Kevlar Para-Aramid Fibrils in Acute, Subchronic, and Chronic Inhalation Studies in Rats. Fundamental and Applied Toxicology *21*, 345-354.

Kelly,F.J., Blomberg,A., Frew,A., Holgate,S.T., and Sandstrom,T. (1996). Antioxidant kinetics in lung lavage fluid following exposure of humans to nitrogen dioxide. Am. J Respir. Crit Care Med. *154*, 1700-1705.

Kelly,F.J. and Mudway,I.S. (2006). Particle-Mediated Extracellular Oxidative Stress in the Lung. In Particle Toxicology, K.Donaldson and P.Borm, eds. Informa Healthcare), pp. 89-117.

Kindler,H.L. (2004). Moving beyond chemotherapy: novel cytostatic agents for malignant mesothelioma. Lung Cancer *45*, S125-S127.

Kishore,U., Greenhough,T.J., Waters,P., Shrive,A.K., Ghai,R., Kamran,M.F., Bernal,A.L., Reid,K.B.M., Madan,T., and Chakraborty,T. (2006). Surfactant proteins SP-A and SP-D: Structure, function and receptors. Molecular Immunology *43*, 1293-1315.

Knox,J.F. and Beattie,J. (1954). Distribution of mineral particles and fibers in the lung after exposure to asbestos dust. AMA. Arch. Ind. Hyg. Occup. Med. *10*, 30-36.

Kobayashi,T., Hino,S., Oue,N., Asahara,T., Zollo,M., Yasui,W., and Kikuchi,A. (2006). Glycogen synthase kinase 3 and h-prune regulate cell migration by modulating focal adhesions. Mol. Cell Biol. *26*, 898-911.

Kolosnjaj-Tabi,J., Hartman,K.B., Boudjemaa,S., Ananta,J.S., Morgant,G., Szwarc,H., Wilson,L.J., and Moussa,F. (2010). In vivo behavior of large doses of ultrashort and full-length single-walled carbon nanotubes after oral and intraperitoneal administration to Swiss mice. ACS Nano. *4*, 1481-1492.

Kotchey,G.P., Allen,B.L., Vedala,H., Yanamala,N., Kapralov,A.A., Tyurina,Y.Y., Klein-Seetharaman,J., Kagan,V.E., and Star,A. (2011). The Enzymatic Oxidation of Graphene Oxide. ACS Nano *5*, 2098-2108.

Kotchey,G.P., Hasan,S.A., Kapralov,A.A., Ha,S.H., Kim,K., Shvedova,A.A., Kagan,V.E., and Star,A. (2012). A natural vanishing act: the enzyme-catalyzed degradation of carbon nanomaterials. Acc. Chem. Res. *45*, 1770-1781.

Kreyling,W.G., Moeller,W., Semmler-Behnke,M., and Oberdorster,G. (2007). Particle Dosimetry: Deposition and Clearance from the Respiratory Tract and Translocation Towards Extra-Pulmonary Sites. In Particle Toxicology, K.Donaldson and P.Borm, eds. CRC Press, taylor and Francis Group), pp. 47-69.

Kreyling,W.G. and Scheuch,G. (2000). Clearance of particles deposited in the lungs. In Particle-Lung Interactions, P.Gehr and J.Heyder, eds. Marcel Dekker, In.), pp. 323-376.

Krinsley,D.H., Pye,K., Boggs,S., and Tovey,N.K. (1998). Backscattered Scanning Electron Microscopy and Image Analysis of Sediments and Sedimentary Rocks. 1st ed. London, Cambridge University Press.

Krombach,F., Munzing,S., Allmeling,A.M., Gerlach,J.T., Behr,J., and Dorger,M. (1997). Cell size of alveolar macrophages: An interspecies comparison. Environmental Health Perspectives *105*, 1261-1263.

Kubo,T., Toyooka,S., Tsukuda,K., Sakaguchi,M., Fukazawa,T., Soh,J., Asano,H., Ueno,T., Muraoka,T., Yamamoto,H., Nasu,Y., Kishimoto,T., Pass,H.I., Matsui,H., Huh,N., and Miyoshi,S. (2011). Epigenetic Silencing of MicroRNA-34b/c Plays an Important Role in the Pathogenesis of Malignant Pleural Mesothelioma. Clinical Cancer Research *17*, 4965-4974.

Kudin,K.N., Ozbas,B., Schniepp,H.C., Prud'homme,R.K., Aksay,I.A., and Car,R. (2008). Raman spectra of graphite oxide and functionalized graphene sheets. Nano Letters *8*, 36-41.

Kuempel,E.D., Geraci,C.L., and Schulte,P.A. (2012). Risk Assessment and Risk Management of Nanomaterials in the Workplace: Translating Research to Practice. Annals of Occupational Hygiene *56*, 491-505.

Kumar-Singh,S., Weyler,J., Martin,M.J.H., Vermeulen,P.B., and Van Marck,E. (1999). Angiogenic cytokines in mesothelioma: A study of VEGF, FGF-1 and-2, and TGF beta expression. Journal of Pathology *189*, 72-78.

Lai-Fook,S.J. (2004). Pleural mechanics and fluid exchange. Physiol Rev. *84*, 385-410.

Lai-Fook,S.J. and Kaplowitz,M.R. (1985). Pleural space thickness in situ by light microscopy in five mammalian species. J. Appl. Physiol. *59*, 603-610.

Lee,A.Y., Raz,D.J., He,B., and Jablons,D.M. (2007). Update on the molecular biology of malignant mesothelioma. Cancer *109*, 1454-1461.

Lee,M.H., Koria,P., Qu,J., and Andreadis,S.T. (2009). JNK phosphorylates beta-catenin and regulates adherens junctions. FASEB J. *23*, 3874-3883.

Lehnert,B.E. (1992). Pulmonary and thoracic macrophage subpopulations and clearance of particles from the lung. Environ. Health Perspect. *97:17-46.*, 17-46.

Lehnert,B.E. and Morrow,P.E. (1985). Characteristics of alveolar macrophages following the deposition of a low burden of iron oxide in the lung. J Toxicol Environ Health *16*, 855-868.

Li,J. (1993). Ultrastructural study on the pleural stomata in human. Funct. Dev. Morphol. *3*, 277-280.

Li,X.C. and Tay,B.K. (2011). Facile Fabrication of Si Nanowire Arrays for Solar Cell Application. Journal of Nanoscience and Nanotechnology *11*, 10539-10543.

Liang,F. and Chen,B. (2010). A review on biomedical applications of single-walled carbon nanotubes. Curr. Med Chem. *17*, 10-24.

Lin,T. and Bost,K.L. (2004). STAT3 activation in macrophages following infection with Salmonella. Biochemical and Biophysical Research Communications *321*, 828-834.

Lippmann,M. (1977). Regional deposition of particles in the human respiratory tract. In Handbook of Physiology, D.K.H.Lee, H.Falk, and S.D.Murphy, eds. American Physiological Society), pp. 213-232.

Lippmann,M. (1990). Effects of fiber characteristics on lung deposition, retention, and disease. Environ. Health Perspect. *88:311-7.*, 311-317.

Lippmann,M. (1993). Critical Fibre Parameters Affecting Disease Pathogenesis. In Fibre Toxicology, D.B.Warheit, ed. Academic Press, Inc), p. 288.

Liu,X.Y., Hurt,R.H., and Kane,A.B. (2010). Biodurability of single-walled carbon nanotubes depends on surface functionalization. Carbon *48*, 1961-1969.

Looyenga,B.D., Hutchings,D., Cherni,I., Kingsley,C., Weiss,G.J., and MacKeigan,J.P. (2012). STAT3 Is Activated by JAK2 Independent of Key Oncogenic Driver Mutations in Non-Small Cell Lung Carcinoma. Plos One *7*, e30820.

Lordan,S., Kennedy,J.E., and Higginbotham,C.L. (2011). Cytotoxic effects induced by unmodified and organically modified nanoclays in the human hepatic HepG2 cell line. J Appl. Toxicol. *31*, 27-35.

Lu,S., Duffin,R., Poland,C., Daly,P., Murphy,F., Drost,E., MacNee,W., Stone,V., and Donaldson,K. (2009). Efficacy of simple short-term in vitro assays for predicting

the potential of metal oxide nanoparticles to cause pulmonary inflammation. Environ. Health Perspect. *117*, 241-247.

Lu,Y.C., Yeh,W.C., and Ohashi,P.S. (2008). LPS/TLR4 signal transduction pathway. Cytokine. *42*, 145-151.

Lynch,I., Cedervall,T., Lundqvist,M., Cabaleiro-Lago,C., Linse,S., and Dawson,K.A. (2007). The nanoparticle-protein complex as a biological entity; a complex fluids and surface science challenge for the 21st century. Adv. Colloid Interface Sci. *134-135:167-74.*, 167-174.

Ma-Hock,L., Treumann,S., Strauss,V., Brill,S., Luizi,F., Mertler,M., Wiench,K., Gamer,A.O., van Ravenzwaay,B., and Landsiedel,R. (2009). Inhalation Toxicity of Multiwall Carbon Nanotubes in Rats Exposed for 3 Months. Toxicol. Sci. *112*, 468-481.

Malard,L.M., Pimenta,M.A., Dresselhaus,G., and Dresselhaus,M.S. (2009). Raman spectroscopy in graphene. Physics Reports-Review Section of Physics Letters *473*, 51-87.

Mankan,A.K., Dau,T., Jenne,D., and Hornung,V. (2012). The NLRP3/ASC/Caspase-1 axis regulates IL-1beta processing in neutrophils. Eur. J. Immunol. *42*, 710-715.

Marco,A.J., Domingo,M., Ruberte,J., Carretero,A., Briones,V., and Dominguez,L. (1992). Lymphatic drainage of Listeria monocytogenes and Indian ink inoculated in the peritoneal cavity of the mouse. Lab Anim. *26*, 200-205.

Mariathasan,S., Weiss,D.S., Newton,K., McBride,J., O'Rourke,K., Roose-Girma,M., Lee,W.P., Weinrauch,Y., Monack,D.M., and Dixit,V.M. (2006). Cryopyrin activates the inflammasome in response to toxins and ATP. Nature. *440*, 228-232.

Martinon,F. (2010). Signaling by ROS drives inflammasome activation. Eur. J. Immunol. *40*, 616-619.

Martinon,F., Petrilli,V., Mayor,A., Tardivel,A., and Tschopp,J. (2006). Gout-associated uric acid crystals activate the NALP3 inflammasome. Nature. *440*, 237-241.

Masters,S.L., Dunne,A., Subramanian,S.L., Hull,R.L., Tannahill,G.M., Sharp,F.A., Becker,C., Franchi,L., Yoshihara,E., Chen,Z., Mullooly,N., Mielke,L.A., Harris,J., Coll,R.C., Mills,K.H., Mok,K.H., Newsholme,P., Nunez,G., Yodoi,J., Kahn,S.E., Lavelle,E.C., and O'Neill,L.A. (2010). Activation of the NLRP3 inflammasome by islet amyloid polypeptide provides a mechanism for enhanced IL-1beta in type 2 diabetes. Nat. Immunol. *11*, 897-904.

Mercer,R.R., Hubbs,A.F., Scabilloni,J.F., Wang,L., Battelli,L.A., Friend,S., Castranova,V., and Porter,D.W. (2011). Pulmonary fibrotic response to aspiration of multi-walled carbon nanotubes. Part Fibre. Toxicol. *8:21.*, 21.

Mercer,R.R., Hubbs,A.F., Scabilloni,J.F., Wang,L., Battelli,L.A., Schwegler-Berry,D., Castranova,V., and Porter,D.W. (2010). Distribution and persistence of pleural penetrations by multi-walled carbon nanotubes. Part Fibre. Toxicol. *7:28.*, 28.

Metintas,M., Hillerdal,G., and Metintas,S. (1999). Malignant mesothelioma due to environmental exposure to erionite: follow-up of a Turkish emigrant cohort. European Respiratory Journal *13*, 523-526.

Michailova,K.N. (2004). The milky spots of the peritoneum and pleura: structure, development and pathology. Biomedical Reviews *15*, 47-66.

Miller,M.R., Borthwick,S.J., Shaw,C.A., McLean,S.G., McClure,D., Mills,N.L., Duffin,R., Donaldson,K., Megson,I.L., Hadoke,P.W., and Newby,D.E. (2009). Direct impairment of vascular function by diesel exhaust particulate through reduced bioavailability of endothelium-derived nitric oxide induced by superoxide free radicals. Environ. Health Perspect. *117*, 611-616.

Miserocchi,G., Negrini,D., and Mortola,J.P. (1984). Comparative features of Starling-lymphatic interaction at the pleural level in mammals. J Appl. Physiol. *56*, 1151-1156.

Miserocchi,G., Sancini,G., Mantegazza,F., and Chiappino,G. (2008). Translocation pathways for inhaled asbestos fibers. Environ. Health. *7:4.*, 4.

Mitchev,K., Dumortier,P., and De,V.P. (2002). 'Black Spots' and hyaline pleural plaques on the parietal pleura of 150 urban necropsy cases. Am. J. Surg. Pathol. *26*, 1198-1206.

Moalli,P.A., MacDonald,J.L., Goodglick,L.A., and Kane,A.B. (1987). Acute injury and regeneration of the mesothelium in response to asbestos fibers. Am. J. Pathol. *128*, 426-445.

Mohr,C., Gemsa,D., Graebner,C., Hemenway,D.R., Leslie,K.O., Absher,P.M., and Davis,G.S. (1991). Systemic Macrophage Stimulation in Rats with Silicosis - Enhanced Release of Tumor-Necrosis-Factor-Alpha from Alveolar and Peritoneal-Macrophages. American Journal of Respiratory Cell and Molecular Biology *5*, 395-402.

Morgan,W.K.C. and Seaton,A. (1984). Occupational lung disease. 2nd ed. Philadelphia, WB Saunders Co.

Mossman,B.T. and Churg,A. (1998). Mechanisms in the pathogenesis of asbestosis and silicosis. Am J Respir. Crit Care Med. *157*, 1666-1680.

Mueller,K.M. (2002). Principles of anatomy and pathology of the pleura. In Pleural Diseases, R.Loddenkemper and V.B.Antony, Chapter Nr. 1, 7th ed. London, European Respiratory Society Journals Ltd.

Muller,J., Delos,M., Panin,N., Rabolli,V., Huaux,F., and Lison,D. (2009). Absence of Carcinogenic Response to Multiwall Carbon Nanotubes in a 2-Year Bioassay in the Peritoneal Cavity of the Rat. Toxicol. Sci. *110*, 442-448.

Muller,J., Huaux,F., Moreau,N., Misson,P., Heilier,J.F., Delos,M., Arras,M., Fonseca,A., Nagy,J.B., and Lison,D. (2005). Respiratory toxicity of multi-wall carbon nanotubes. Toxicology and Applied Pharmacology *207*, 221-231.

Muller,K.M., Schmitz,I., and Konstantinidis,K. (2002). Black spots of the parietal pleura: morphology and formal pathogenesis. Respiration. *69*, 261-267.

Murphy,F.A., Poland,C.A., Duffin,R., Al-Jamal,K.T., Ali-Boucetta,H., Nunes,A., Byrne,F., Prina-Mello,A., Volkov,Y., Li,S.P., Mather,S.J., Bianco,A., Prato,M., MacNee,W., Wallace,W.A., Kostarelos,K., and Donaldson,K. (2011). Length-Dependent Retention of Carbon Nanotubes in the Pleural Space of Mice Initiates Sustained Inflammation and Progressive Fibrosis on the Parietal Pleura. American Journal of Pathology *178*, 2587-2600.

Murphy,F.A., Poland,C.A., Duffin,R., and Donaldson,K. (2012a). Length-dependent pleural inflammation and parietal pleural responses after deposition of carbon nanotubes in the pulmonary airspaces of mice. Nanotoxicology [Epub ahead of print].

Murphy,F.A., Schinwald,A., Poland,C.A., and Donaldson,K. (2012b). The mechanism of pleural inflammation by long carbon nanotubes: interaction of long fibres with macrophages stimulates them to amplify pro-inflammatory responses in mesothelial cells. Part Fibre Toxicol. *9*: 8.

Mutsaers,S.E. (2002). Mesothelial cells: their structure, function and role in serosal repair. Respirology. *7*, 171-191.

Mutsaers,S.E. (2004). The mesothelial cell. Int. J Biochem. Cell Biol. *36*, 9-16.

Nagai,H. and Toyokuni,S. (2010). Biopersistent fiber-induced inflammation and carcinogenesis: lessons learned from asbestos toward safety of fibrous nanomaterials. Arch. Biochem. Biophys. *502*, 1-7.

Nasreen,N., Hartman,D.L., Mohammed,K.A., and Antony,V.B. (1998). Talc-induced expression of C-C and C-X-C chemokines and intercellular adhesion molecule-1 in mesothelial cells. American Journal of Respiratory and Critical Care Medicine *158*, 971-978.

Negrini,D. and Moriondo,A. (2012). Pleural Function And Lymphatics. Acta Physiol (Oxf). 10.

Nel,A.E., Madler,L., Velegol,D., Xia,T., Hoek,E.M.V., Somasundaran,P., Klaessig,F., Castranova,V., and Thompson,M. (2009). Understanding biophysicochemical interactions at the nano-bio interface. Nature Materials *8*, 543-557.

NIOSH (2010). Draft Current Intelligence Bulletin on Occupational Exposure to Carbon Nanotubes and Nanofibres. National Institute for Occupational Safety and Health, Centre for Disease Control and Prevention.

Noppen,M., de Waele,M., Li,R., Vander Gucht,K., D'Haese,J., Gerlo,E., and Vincken,W. (2000). Volume and cellular content of normal pleural fluid in humans examined by pleural lavage. American Journal of Respiratory and Critical Care Medicine *162*, 1023-1026.

Novoselov,K.S., Geim,A.K., Morozov,S.V., Jiang,D., Zhang,Y., Dubonos,S.V., Grigorieva,I.V., and Firsov,A.A. (2004). Electric field effect in atomically thin carbon films. Science. *306*, 666-669.

Nurminen,M. and Tossavainen,A. (1994). Is There An Association Between Pleural Plaques and Lung-Cancer Without Asbestosis. Scandinavian Journal of Work Environment & Health *20*, 62-64.

O'Neill,L.A. (2008). Immunology. How frustration leads to inflammation. Science. *320*, 619-620.

Oberdorster,G. (1993). Lung Dosimetry: Pulmonary Clearance of Inhaled Particles. Aerosol Science and Technology *18*, 279-289.

Oberdorster,G., Ferin,J., Morse,P., Corson,N.M., and Morrow,P.E. (1988). Volumetric alveolar macrophage (AM) burden as a mechanism of impaired AM mediated particle clearance during chronic dust overloading of the lung. J. Aerosol Med. *1*, A207.

Oberdorster,G. (2010). Safety assessment for nanotechnology and nanomedicine: concepts of nanotoxicology. Journal of Internal Medicine *267*, 89-105.

Oberdorster,G., Oberdorster,E., and Oberdorster,J. (2005). Nanotoxicology: an emerging discipline evolving from studies of ultrafine particles. Environ. Health Perspect. *113*, 823-839.

Ogden,T.L. (2003). Commentary: the 1968 BOHS Chrysotile Asbestos Standard. Ann Occup. Hyg. *47*, 3-6.

Ohtsuka,Y., Munakata,M., Ukita,H., Takahashi,T., Satoh,A., Homma,Y., and Kawakami,Y. (1995). Increased Susceptibility to Silicosis and Tnf-Alpha Production in C57Bl/6J Mice. American Journal of Respiratory and Critical Care Medicine *152*, 2144-2149.

Osmond,M., Poland,C., Murphy,F., Waddington,L., Hawkins,S., Aitken,R., Clark,S., McCall,M., and Donaldson,K. (2010). Biodurability & Inflammogenicity of Carbon Nanotubes. CSIRO National Research Flagships. Safe Work Australia. Safe Work Australia.

Osmond-McLeod,M.J., Poland,C.A., Murphy,F., Waddington,L., Morris,H., Hawkins,S.C., Clark,S., Aitken,R., McCall,M.J., and Donaldson,K. (2011).

Durability and inflammogenic impact of carbon nanotubes compared with asbestos fibres. Part Fibre. Toxicol. *8:15.*, 15.

Owens,M.W. and Milligan,S.A. (1995). Pleuritis and pleural effusions. Curr. Opin. Pulm. Med. *1*, 318-323.

Oya,M., Shimada,T., Nakamura,M., and Uchida,Y. (1993). Functional morphology of the lymphatic system in the monkey diaphragm. Arch. Histol. Cytol. *56*, 37-47.

Pacurari,M., Yin,X.J., Zhao,J., Ding,M., Leonard,S.S., Schwegler-Berry,D., Ducatman,B.S., Sbarra,D., Hoover,M.D., Castranova,V., and Vallyathan,V. (2008). Raw single-wall carbon nanotubes induce oxidative stress and activate MAPKs, AP-1, NF-kappaB, and Akt in normal and malignant human mesothelial cells. Environ. Health Perspect. *116*, 1211-1217.

Palmen,N.G.M. and Evelo,C.T.A. (1996). Glutathione depletion in human erythrocytes and rat liver: A study on the interplay between bioactivation and inactivation functions of liver and blood. Toxicology in Vitro *10*, 273-281.

Palomaki,J., Valimaki,E., Sund,J., Vippola,M., Clausen,P.A., Jensen,K.A., Savolainen,K., Matikainen,S., and Alenius,H. (2011). Long, needle-like carbon nanotubes and asbestos activate the NLRP3 inflammasome through a similar mechanism. ACS Nano. *5*, 6861-6870.

Park,E.K., Jung,H.S., Yang,H.I., Yoo,M.C., Kim,C., and Kim,K.S. (2007). Optimized THP-1 differentiation is required for the detection of responses to weak stimuli. Inflammation Research *56*, 45-50.

Pascu,S.I., Arrowsmith,R.L., Bayly,S.R., Brayshaw,S., and Hu,Z. (2010). Towards nanomedicines: design protocols to assemble, visualize and test carbon nanotube probes for multi-modality biomedical imaging. Philos. Transact. A Math. Phys. Eng Sci. *368*, 3683-3712.

Pastva,A.M., Wright,J.R., and Williams,K.L. (2007). Immunomodulatory roles of surfactant proteins A and D: implications in lung disease. Proc. Am. Thorac. Soc. *4*, 252-257.

Pauluhn,J. (2010). Subchronic 13-week inhalation exposure of rats to multiwalled carbon nanotubes: toxic effects are determined by density of agglomerate structures, not fibrillar structures. Toxicol Sci. *113*, 226-242.

Peeters,P.M., Perkins,T.N., Wouters,E.F., Mossman,B.T., and Reynaert,N.L. (2013). Silica induces NLRP3 inflammasome activation in human lung epithelial cells. Part Fibre Toxicol. *10:3. doi: 10.1186/1743-8977-10-3.*, 3-10.

Peto,J., Hodgson,J.T., Matthews,F.E., and Jones,J.R. (1995). Continuing Increase in Mesothelioma Mortality in Britain. Lancet *345*, 535-539.

Petrilli,V., Papin,S., Dostert,C., Mayor,A., Martinon,F., and Tschopp,J. (2007). Activation of the NALP3 inflammasome is triggered by low intracellular potassium concentration. Cell Death. Differ. *14*, 1583-1589.

Piguet,P.F., Vesin,C., Grau,G.E., and Thompson,R.C. (1993). Interleukin 1 receptor antagonist (IL-1ra) prevents or cures pulmonary fibrosis elicited in mice by bleomycin or silica. Cytokine. *5*, 57-61.

Poland,C.A., Byrne,F., Cho,W.S., Prina-Mello,A., Murphy,F.A., Davies,G.L., Coey,J.M., Gounko,Y., Duffin,R., Volkov,Y., and Donaldson,K. (2012). Length-dependent pathogenic effects of nickel nanowires in the lungs and the peritoneal cavity. Nanotoxicology. *6*, 899-911.

Poland,C.A., Duffin,R., Kinloch,I., Maynard,A., Wallace,W.A., Seaton,A., Stone,V., Brown,S., MacNee,W., and Donaldson,K. (2008). Carbon nanotubes introduced into the abdominal cavity of mice show asbestos-like pathogenicity in a pilot study. Nat. Nanotechnol. *3*, 423-428.

Porter,D.W., Hubbs,A.F., Mercer,R.R., Wu,N., Wolfarth,M.G., Sriram,K., Leonard,S., Battelli,L., Schwegler-Berry,D., Friend,S., Andrew,M., Chen,B.T., Tsuruoka,S., Endo,M., and Castranova,V. (2010). Mouse pulmonary dose- and time course-responses induced by exposure to multi-walled carbon nanotubes. Toxicology. *269*, 136-147.

Prina-Mello,A., Diao,Z., and Coey,J.M. (2006). Internalization of ferromagnetic nanowires by different living cells. J Nanobiotechnology. *4:9.*, 9.

Prins,J.B., Williamson,K.A., Kamp,M.M.K., Van Hezik,E.J., Van der Kwast,T.H., Hagemeijer,A., and Versnel,M.A. (1998). The gene for the cyclin-dependent-kinase-4 inhibitor, CDKN2A, is preferentially deleted in malignant mesothelioma. International Journal of Cancer *75*, 649-653.

Pumera,M. (2009). Electrochemistry of graphene: new horizons for sensing and energy storage. Chem. Rec. *9*, 211-223.

Rahman,I. and MacNee,W. (1998). Role of transcription factors in inflammatory lung diseases. Thorax. *53*, 601-612.

Rajamaki,K., Lappalainen,J., Oorni,K., Valimaki,E., Matikainen,S., Kovanen,P.T., and Eklund,K.K. (2010). Cholesterol crystals activate the NLRP3 inflammasome in human macrophages: a novel link between cholesterol metabolism and inflammation. PLoS. One. *5*, e11765.

Rao,G.V., Tinkle,S., Weissman,D.N., Antonini,J.M., Kashon,M.L., Salmen,R., Battelli,L.A., Willard,P.A., Hoover,M.D., and Hubbs,A.F. (2003). Efficacy of a technique for exposing the mouse lung to particles aspirated from the pharynx. J Toxicol. Environ. Health A. *66*, 1441-1452.

Raphael,M.P., Christodoulides,J.A., Qadri,S.N., Simpkins,B.S., and Byers,J.M. (2010). Magnetic moment degradation of nanowires in biological media: real-time monitoring with SQUID magnetometry. Nanotechnology. *21*, 285101.

Rascoe,P.A., Jupiter,D., Cao,X.B., Littlejohn,J.E., and Smythe,W.R. (2012). Molecular pathogenesis of malignant mesothelioma. Expert Reviews in Molecular Medicine *14* [Epub ahead of print].

Reid,K.B. (1998). Functional roles of the lung surfactant proteins SP-A and SP-D in innate immunity. Immunobiology. *199*, 200-207.

Reisetter,A.C., Stebounova,L.V., Baltrusaitis,J., Powers,L., Gupta,A., Grassian,V.H., and Monick,M.M. (2011). Induction of inflammasome-dependent pyroptosis by carbon black nanoparticles. J. Biol. Chem. *286*, 21844-21852.

Rice,F. (2000). Crystalline Silica, Quartz. Geneva, World Health Organization.

Rimal,B., Greenberg,A.K., and Rom,W.N. (2005). Basic pathogenetic mechanisms in sificosis: current understanding. Current Opinion in Pulmonary Medicine *11*, 169-173.

Roger,A. (2005). Diagnositc Lung Cytology. In Thurlbeck's Pathology of the Lung, C.Andrew M., M.Jeffrey I., T.Henry D., and W.Joanne L., eds. Thieme Medical Publisher, Inc.), pp. 1041-1044.

Roger,L., Gadea,G., and Roux,P. (2006). Control of cell migration: a tumour suppressor function for p53? Biol. Cell. *98*, 141-152.

Romieu,I., Moreno-Macias,H., and London,S.J. (2010). Gene by environment interaction and ambient air pollution. Proc. Am. Thorac. Soc. *7*, 116-122.

Rosen,G.M., Finkelstein,E., and Rauckman,E.J. (1982). A Method for the Detection of Superoxide in Biological-Systems. Archives of Biochemistry and Biophysics *215*, 367-378.

Ruge,C.A., Kirch,J., Canadas,O., Schneider,M., Perez-Gil,J., Schaefer,U.F., Casals,C., and Lehr,C.M. (2011). Uptake of nanoparticles by alveolar macrophages is triggered by surfactant protein A. Nanomedicine-Nanotechnology Biology and Medicine *7*, 690-693.

Ruge,C.A., Schaefer,U.F., Herrmann,J., Kirch,J., Canadas,O., Echaide,M., Perez-Gil,J., Casals,C., Muller,R., and Lehr,C.M. (2012). The Interplay of Lung Surfactant Proteins and Lipids Assimilates the Macrophage Clearance of Nanoparticles. Plos One *7*, e40775.

Ryman-Rasmussen,J.P., Cesta,M.F., Brody,A.R., Shipley-Phillips,J.K., Everitt,J.I., Tewksbury,E.W., Moss,O.R., Wong,B.A., Dodd,D.E., Andersen,M.E., and Bonner,J.C. (2009). Inhaled carbon nanotubes reach the subpleural tissue in mice. Nature Nanotechnology *4*, 747-751.

Sablina,A.A., Chumakov,P.M., and Kopnin,B.P. (2003). Tumor suppressor p53 and its homologue p73 alpha affect cell migration. Journal of Biological Chemistry *278*, 27362-27371.

Sahithi,K., Swetha,M., Ramasamy,K., Srinivasan,N., and Selvamurugan,N. (2010). Polymeric composites containing carbon nanotubes for bone tissue engineering. Int. J Biol. Macromol. *46*, 281-283.

Sanchez,V.C., Jachak,A., Hurt,R.H., and Kane,A.B. (2012). Biological interactions of graphene-family nanomaterials: an interdisciplinary review. Chem. Res. Toxicol. *25*, 15-34.

Sanchez,V.C., Weston,P., Yan,A., Hurt,R.H., and Kane,A.B. (2011). A 3-dimensional in vitro model of epithelioid granulomas induced by high aspect ratio nanomaterials. Part Fibre. Toxicol. *8:17.*, 17.

Sandberg,W.J., Lag,M., Holme,J.A., Friede,B., Gualtieri,M., Kruszewski,M., Schwarze,P.E., Skuland,T., and Refsnes,M. (2012). Comparison of non-crystalline silica nanoparticles in IL-1beta release from macrophages. Part Fibre Toxicol. *9:32. doi: 10.1186/1743-8977-9-32.*, 32-39.

Schins,R.P., Duffin,R., Hohr,D., Knaapen,A.M., Shi,T., Weishaupt,C., Stone,V., Donaldson,K., and Borm,P.J. (2002). Surface modification of quartz inhibits toxicity, particle uptake, and oxidative DNA damage in human lung epithelial cells. Chem. Res. Toxicol. *15*, 1166-1173.

Schinwald,A., Murphy,F.A., Prina-Mello,A., Poland,C.A., Byrne,F., Movia,D., Glass,J.R., Dickerson,J.C., Schultz,D.A., Jeffree,C.E., MacNee,W., and Donaldson,K. (2012). The threshold length for fiber-induced acute pleural inflammation: shedding light on the early events in asbestos-induced mesothelioma. Toxicol. Sci. *128*, 461-470.

Schrand,A.M., Braydich-Stolle,L.K., Schlager,J.J., Dai,L., and Hussain,S.M. (2008). Can silver nanoparticles be useful as potential biological labels? Nanotechnology. *19*, 235104.

Schrand,A.M., Schlager,J.J., Dai,L., and Hussain,S.M. (2010). Preparation of cells for assessing ultrastructural localization of nanoparticles with transmission electron microscopy. Nat. Protoc. *5*, 744-757.

Schroder,K. and Tschopp,J. (2010). The inflammasomes. Cell. *19*, 821-832.

Schulz,H., Brand,P., and Heyder,J. (2000). Particle Deposition in the Respiratory Tract. In Particle-Lung Interactions, P.Gehr and J.Heyder, 2nd ed. New York, Informa Health Care USA, Inc., pp. 229-277.

Searl,A., Buchanan,D., Cullen,R.T., Jones,A.D., Miller,B.G., and Soutar,C.A. (1999). Biopersistence and durability of nine mineral fibre types in rat lungs over 12 months. Ann Occup. Hyg. *43*, 143-153.

Service,R.F. (2004). Nanotoxicology: Nanotechnology grows up. Science *304*, 1732-1734.

Sharma,H.S., Ali,S.F., Tian,Z.R., Patnaik,R., Patnaik,S., Sharma,A., Boman,A., Lek,P., Seifert,E., and Lundstedt,T. (2010). Nanowired-drug delivery enhances neuroprotective efficacy of compounds and reduces spinal cord edema formation and improves functional outcome following spinal cord injury in the rat. Acta Neurochir. Suppl. *106:343-50.*, 343-350.

Sharma,V., Park,K., and Srinivasarao,M. (2009). Shape separation of gold nanorods using centrifugation. Proc. Natl. Acad. Sci. U. S. A. *106*, 4981-4985.

Shellito,J., Sniezek,M., and Warnock,M. (1987). Acquisition of Peroxidase-Activity by Rat Alveolar Macrophages During Pulmonary Inflammation. American Journal of Pathology *129*, 567-577.

Shields,T.W., LoCicero III,J., Reed,C.E., and Feins,R.H. (2009). General Thoracic Surgery. 7th ed. Philadelphia, Lippincort Williams and Wilkins.

Shinohara,H. (1997). Distribution of lymphatic stomata on the pleural surface of the thoracic cavity and the surface topography of the pleural mesothelium in the golden hamster. Anat. Rec. *249*, 16-23.

Shukla,A., Gulumian,M., Hei,T.K., Kamp,D., Rahman,Q., and Mossman,B.T. (2003). Multiple roles of oxidants in the pathogenesis of asbestos-induced diseases. Free Radical Biology and Medicine *34*, 1117-1129.

Shvedova,A.A., Kapralov,A.A., Feng,W.H., Kisin,E.R., Murray,A.R., Mercer,R.R., St Croix,C.M., Lang,M.A., Watkins,S.C., Konduru,N.V., Allen,B.L., Conroy,J., Kotchey,G.P., Mohamed,B.M., Meade,A.D., Volkov,Y., Star,A., Fadeel,B., and Kagan,V.E. (2012). Impaired Clearance and Enhanced Pulmonary Inflammatory/Fibrotic Response to Carbon Nanotubes in Myeloperoxidase-Deficient Mice. Plos One *7*, e30923.

Shvedova,A.A., Kisin,E., Murray,A.R., Johnson,V.J., Gorelik,O., Arepalli,S., Hubbs,A.F., Mercer,R.R., Keohavong,P., Sussman,N., Jin,J., Yin,J., Stone,S., Chen,B.T., Deye,G., Maynard,A., Castranova,V., Baron,P.A., and Kagan,V.E. (2008). Inhalation vs. aspiration of single-walled carbon nanotubes in C57BL/6 mice: inflammation, fibrosis, oxidative stress, and mutagenesis. American Journal of Physiology-Lung Cellular and Molecular Physiology *295*, L552-L565.

Shvedova,A.A., Kisin,E.R., Mercer,R., Murray,A.R., Johnson,V.J., Potapovich,A.I., Tyurina,Y.Y., Gorelik,O., Arepalli,S., Schwegler-Berry,D., Hubbs,A.F., Antonini,J., Evans,D.E., Ku,B.K., Ramsey,D., Maynard,A., Kagan,V.E., Castranova,V., and Baron,P. (2005). Unusual inflammatory and fibrogenic pulmonary responses to single-walled carbon nanotubes in mice. American Journal of Physiology-Lung Cellular and Molecular Physiology *289*, L698-L708.

Sohaebuddin,S.K., Thevenot,P.T., Baker,D., Eaton,J.W., and Tang,L. (2010). Nanomaterial cytotoxicity is composition, size, and cell type dependent. Part Fibre. Toxicol. *7:22.*, 22.

Soligo,D., de Harven,E., Nava,M.T., and Lambertenghi-Deliliers,G. (1985). Immunocytochemistry with back-scattered electron. In The science of Biological specimen preparation for microscopy and microanalysis. In Scanning Microscopy, M.Müeller, R.P.Becker, A.Boyde, and J.J.Wolosewick, eds., pp. 289-297.

Son,S.J., Bai,X., Nan,A., Ghandehari,H., and Lee,S.B. (2006). Template synthesis of multifunctional nanotubes for controlled release. J. Control Release. *114*, 143-152.

Spurzem,J.R., Saltini,C., Rom,W., Winchester,R.J., and Crystal,R.G. (1987). Mechanisms of macrophage accumulation in the lungs of asbestos-exposed subjects. Am. Rev. Respir. Dis. *136*, 276-280.

Stanton,M.F. (1973). Some etiological considerations of fibre carcinogenesis. In Biological Effects of Asbestos, P.Bogovski, V.Timbrell, and J.Gilson, eds. World Health Organization, International Agency for Research on Cancer), p. 289.

Stanton,M.F. and Wrench,C. (1972). Mechanisms of Mesothelioma Induction with Asbestos and Fibrous Glass. Journal of the National Cancer Institute *48*, 797.

Stebounova,L.V., mcakova-Dodd,A., Kim,J.S., Park,H., O'Shaughnessy,P.T., Grassian,V.H., and Thorne,P.S. (2011). Nanosilver induces minimal lung toxicity or inflammation in a subacute murine inhalation model. Part Fibre. Toxicol. *8* (1): 5.

Stone,K.C., Mercer,R.R., Gehr,P., Stockstill,B., and Crapo,J.D. (1992). Allometric Relationships of Cell Numbers and Size in the Mammalian Lung. American Journal of Respiratory Cell and Molecular Biology *6*, 235-243.

Sulahian,T.H., Imrich,A., Deloid,G., Winkler,A.R., and Kobzik,L. (2008). Signaling pathways required for macrophage scavenger receptor-mediated phagocytosis: analysis by scanning cytometry. Respir. Res. *9:59*.

Suzuki,Y. and Yuen,S.R. (2002). Asbestos fibers contributing to the induction of human malignant mesothelioma. Ann N. Y. Acad. Sci. *982:160-76.*, 160-176.

Takagi,A., Hirose,A., Nishimura,T., Fukumori,N., Ogata,A., Ohashi,N., Kitajima,S., and Kanno,J. (2008). Induction of mesothelioma in p53+/- mouse by intraperitoneal application of multi-wall carbon nanotube. Journal of Toxicological Sciences *33*, 105-116.

Tamminen,J.A., Myllarniemi,M., Hyytiainen,M., Keski-Oja,J., and Koli,K. (2012). Asbestos exposure induces alveolar epithelial cell plasticity through MAPK/Erk signaling. Journal of Cellular Biochemistry *113*, 2234-2247.

Tanaka,S., Choe,N., Iwagaki,A., Hemenway,D.R., and Kagan,E. (2000). Asbestos exposure induces MCP-1 secretion by pleural mesothelial cells. Exp. Lung Res. *26*, 241-255.

Taniguchi,S. and Sagara,J. (2007). Regulatory molecules involved in inflammasome formation with special reference to a key mediator protein, ASC. Seminars in Immunopathology *29*, 231-238.

Tatrai,E., Brozik,M., Kovacikova,Z., and Horvath,M. (2005). The effect of asbestos and stone-wool fibres on some chemokines and redox system of pulmonary alveolar macrophages and pneumocytes type II. Biomed. Pap. Med. Fac. Univ Palacky. Olomouc. Czech. Repub. *149*, 357-361.

Temel,A. and Gundogdu,M.N. (1996). Zeolite occurrences and the erionite-mesothelioma relationship in Cappadocia, central anatolia, Turkey. Mineralium Deposita *31*, 539-547.

Thomas,E.D., Ramberg,R.E., Sale,G.E., Sparkes,R.S., and Golde,D.W. (1976). Direct evidence for a bone marrow origin of the alveolar macrophage in man. Science. *192*, 1016-1018.

Timbrell,V. (1983). Fibres and carcinogenesis. J. Occup. Health Soc. Aust. *3*, 3-12.

Tschopp,J. and Schroder,K. (2010). NLRP3 inflammasome activation: The convergence of multiple signalling pathways on ROS production? Nat. Rev. Immunol. *10*, 210-215.

Tsuchiya,S., Yamabe,M., Yamaguchi,Y., Kobayashi,Y., Konno,T., and Tada,K. (1980). Establishment and characterization of a human acute monocytic leukemia cell line (THP-1). Int. J Cancer. *26*, 171-176.

Turci,F., Tomatis,M., Lesci,I.G., Roveri,N., and Fubini,B. (2011). The iron-related molecular toxicity mechanism of synthetic asbestos nanofibres: a model study for high-aspect-ratio nanoparticles. Chemistry. *17*, 350-358.

Tweedale,G. (2002). Asbestos and its lethal legacy. Nature Reviews Cancer *2*, 311-315.

Unfried,K., Schurkes,C., and Abel,J. (2002). Distinct spectrum of mutations induced by crocidolite asbestos: clue for 8-hydroxydeoxyguanosine-dependent mutagenesis in vivo. Cancer Res. *62*, 99-104.

Uskokovic,V., Lee,K., Lee,P.P., Fischer,K.E., and Desai,T.A. (2012). Shape Effect in the Design of Nanowire-Coated Microparticles as Transepithelial Drug Delivery Devices. ACS Nano *6*, 7832-7841.

van oud Alblas,A.B. and van,F.R. (1979). Origin, Kinetics, and characteristics of pulmonary macrophages in the normal steady state. J Exp. Med. *149*, 1504-1518.

Van,N.R. (2011). Chemistry: The trials of new carbon. Nature. *469*, 14-16.

Virag,L. and Szabo,C. (2002). The therapeutic potential of poly(ADP-ribose) polymerase inhibitors. Pharmacological Reviews *54*, 375-429.

Virta,R. (2002). Asbestos: Geology, Mineralogy, Mining, and Uses. U. S. Dept. of the Interior, U. S. Geological Survey, Reston, VA (access date 06.06.2013).

Vorwald,A.J., Durkan,T.M., and Pratt,P.C. (1951). Experimental Studies of Asbestosis. Ama Archives of Industrial Hygiene and Occupational Medicine *3*, 1-43.

Wagner,J.C., Sleggs,C.A., and Marchand,P. (1960). Diffuse pleural mesothelioma and asbestos exposure in the North Western Cape Province. Br. J Ind. Med. *17:260-71.*, 260-271.

Walton,W.H. (1982). The nature,hazards and assessment of airborne dust: a review. Ann Ocucup. Hyg. *25*, 117-247.

Wang,L.Y., Luanpitpong,S., Castranova,V., Tse,W., Lu,Y.J., Pongrakhananon,V., and Rojanasakul,Y. (2011a). Carbon Nanotubes Induce Malignant Transformation and Tumorigenesis of Human Lung Epithelial Cells. Nano Letters *11*, 2796-2803.

Wang,N.S. (1974). The regional difference of pleural mesothelial cells in rabbits. Am. Rev. Respir. Dis. *110*, 623-633.

Wang,P.M. and Lai-Fook,S.J. (1992). Upward flow of pleural liquid near lobar margins due to cardiogenic motion. J Appl. Physiol. *73*, 2314-2319.

Wang,P.M. and Lai-Fook,S.J. (1993). Effect of ventilation frequency and tidal volume on pleural space thickness in rabbits. J Appl. Physiol. *75*, 1836-1841.

Wang,X., Xia,T., Ntim,S.A., Ji,Z.X., Lin,S.J., Meng,H., Chung,C.H., George,S., Zhang,H.Y., Wang,M.Y., Li,N., Yang,Y., Castranova,V., Mitra,S., Bonner,J.C., and Nel,A.E. (2011b). Dispersal State of Multiwalled Carbon Nanotubes Elicits Profibrogenic Cellular Responses That Correlate with Fibrogenesis Biomarkers and Fibrosis in the Murine Lung. ACS Nano *5*, 9772-9787.

Wang,Y. and Dickerson,J.C. (2011). Methods for the production of silver nanowires. Patent Number 7922787 (http://www. freepatentsonline. com/7922787. html).

Warheit,D.B., Hartsky,M.A., and Stefaniak,M.S. (1988). Comparative physiology of rodent pulmonary macrophages: in vitro functional responses. J Appl. Physiol. *64*, 1953-1959.

Weissenberg,A., Sydlik,U., Peuschel,H., Schroeder,P., Schneider,M., Schins,R.P., Abel,J., and Unfried,K. (2010). Reactive oxygen species as mediators of membrane-dependent signaling induced by ultrafine particles. Free Radic. Biol. Med. *49*, 597-605.

Wen,G.Y., Hong,M., Li,B.Y., Liao,W.P., Cheng,S.K., Hu,B.R., Calaf,G.M., Lu,P., Partridge,M.A., Tong,J., and Hei,T.K. (2011). Transforming growth factor-beta-induced protein (TGFBI) suppresses mesothelioma progression through the Akt/mTOR pathway. International Journal of Oncology *39*, 1001-1009.

Wessels,A., Van,B.D., Boots,A.W., Gerloff,K., Scherbart,A.M., Cassee,F.R., Gerlofs-Nijland,M.E., Van Schooten,F.J., Albrecht,C., and Schins,R.P. (2011). Oxidative stress and DNA damage responses in rat and mouse lung to inhaled carbon nanoparticles. Nanotoxicology. *5*, 66-78.

WHO (1997). Determination of airborne fiber number concentration: a recommended method by phase contrast microscopy. WHO, Geneva, Switzerland, ISBN: 924 1544961. WHO.

Wikeley,N.J. (1992). Asbestos and cancer: an early warning to the British TUC. Am. J Ind. Med. *22*, 449-454.

Winter,M., Beer,H.D., Hornung,V., Kramer,U., Schins,R.P., and Forster,I. (2011). Activation of the inflammasome by amorphous silica and TiO2 nanoparticles in murine dendritic cells. Nanotoxicology. *5*, 326-340.

Wu,G., Fang,Y.Z., Yang,S., Lupton,J.R., and Turner,N.D. (2004). Glutathione metabolism and its implications for health. J. Nutr. *134*, 489-492.

Yamashita,K., Yoshioka,Y., Higashisaka,K., Morishita,Y., Yoshida,T., Fujimura,M., Kayamuro,H., Nabeshi,H., Yamashita,T., Nagano,K., Abe,Y., Kamada,H., Kawai,Y., Mayumi,T., Yoshikawa,T., Itoh,N., Tsunoda,S., and Tsutsumi,Y. (2010). Carbon nanotubes elicit DNA damage and inflammatory response relative to their size and shape. Inflammation. *33*, 276-280.

Yang,H., Rivera,Z., Jube,S., Nasu,M., Bertino,P., Goparaju,C., Franzoso,G., Lotze,M.T., Krausz,T., Pass,H.I., Bianchi,M.E., and Carbone,M. (2010). Programmed necrosis induced by asbestos in human mesothelial cells causes high-mobility group box 1 protein release and resultant inflammation. Proc. Natl. Acad. Sci. U. S. A. *107*, 12611-12616.

Yang,K., Li,Y., Tan,X., Peng,R., and Liu,Z. (2013). Behavior and toxicity of graphene and its functionalized derivatives in biological systems. Small. *9*, 1492-1503.

Yang,K., Wan,J.M., Zhang,S.A., Zhang,Y.J., Lee,S.T., and Liu,Z.A. (2011). In Vivo Pharmacokinetics, Long-Term Biodistribution, and Toxicology of PEGylated Graphene in Mice. ACS Nano *5*, 516-522.

Ye,J., Shi,X., Jones,W., Rojanasakul,Y., Cheng,N., Schwegler-Berry,D., Baron,P., Deye,G.J., Li,C., and Castranova,V. (1999). Critical role of glass fiber length in TNF-alpha production and transcription factor activation in macrophages. Am. J. Physiol. *276*, L426-L434.

Yoon,J.H., Kim,H.E., Choi,J.Y., Bae,H.J., and Lee,S.G. (2012). Caffeoylserotonin suppresses THP-1 monocyte adhesion and migration via inhibition of the integrin beta1/FAK/Akt signalling pathway. Fitoterapia. *83*, 1364-1370.

Young,N.S., Levin,J., and Prendergast,R.A. (1972). An invertebrate coagulation system activated by endotoxin: evidence for enzymatic mediation. J. Clin. Invest. *51*, 1790-1797.

Zanella,C.L., Posada,J., Tritton,T.R., and Mossman,B.T. (1996). Asbestos causes stimulation of the extracellular signal-regulated kinase 1 mitogen-activated protein kinase cascade after phosphorylation of the epidermal growth factor receptor. Cancer Res. *56*, 5334-5338.

Zeillemaker,A.M., Mul,F.P.J., VanPapendrecht,A.A.G.M., Leguit,P., Verbrugh,H.A., and Roos,D. (1996). Neutrophil adherence to and migration across monolayers of human peritoneal mesothelial cells - The role of mesothelium in the influx of neutrophils during peritonitis. Journal of Laboratory and Clinical Medicine *127*, 279-286.

Zhang,Y., Wang,B., Meng,X., Sun,G., and Gao,C. (2011). Influences of acid-treated multiwalled carbon nanotubes on fibroblasts: proliferation, adhesion, migration, and wound healing. Ann Biomed. Eng. *39*, 414-426.

Zhang,Y.B., Ali,S.F., Dervishi,E., Xu,Y., Li,Z.R., Casciano,D., and Biris,A.S. (2010). Cytotoxicity Effects of Graphene and Single-Wall Carbon Nanotubes in Neural Phaeochromocytoma-Derived PC12 Cells. ACS Nano *4*, 3181-3186.

Zheng,M. and Du,W. (2006). Phase behavior, conformations, thermodynamic properties, and molecular motion of multicomponent paraffin waxes: A Raman spectroscopy study. Vibrational Spectroscopy *40*, 219-224.

Zhu,J.J., Kan,C.X., Wan,J.G., Han,M., and Wang,G.H. (2011). High-Yield Synthesis of Uniform Ag Nanowires with High Aspect Ratios by Introducing the Long-Chain PVP in an Improved Polyol Process. Journal of Nanomaterials.

Zucali,P.A., Ceresoli,G.L., De Vincenzo,F., Simonelli,M., Lorenzi,E., Gianoncelli,L., and Santoro,A. (2011). Advances in the biology of malignant pleural mesothelioma. Cancer Treatment Reviews *37*, 543-558.

Appendix 1: Publications

1. Donaldson K, Murphy F, **Schinwald A**, Duffin R, Poland CA. 2011. **Identifying the pulmonary hazard of high aspect ratio nanoparticles to enable their safety-by-design**. *Nanomedicine* (Lond). Jan;6(1):143-56.

2. **Schinwald A**, Murphy FA, Jones A, MacNee W, Donaldson K. **Graphene-based nanoplatelets: a new risk to the respiratory system as a consequence of their unusual aerodynamic properties**. ACS Nano. 2012 Jan 24;6(1):736-46.

3. Murphy FA, **Schinwald A**, Poland CA, Donaldson K. **The mechanism of pleural inflammation by long carbon nanotubes: interaction of long fibres with macrophages stimulates them to amplify pro-inflammatory responses in mesothelial cells**. Part Fibre Toxicol. 2012 Apr 3;9:8.

4. **Schinwald A**, Murphy F, Prina-Mello A, Poland C, Byrne F, Glass J, Dickerson J, Schultz D, Movia D, Jeffree C, Macnee W, Donaldson K. **The threshold length for fibre-induced acute pleural inflammation: shedding light on the early events in asbestos-induced mesothelioma**. Toxicological Sciences. 2012 May 12; 128(2):461-70.

5. **Schinwald A** & Donaldson K. **Use of back-scatter electron signals to visualise cell/nanowires interactions *in vitro* and *in vivo*; frustrated phagocytosis of long fibres and compartmentalisation in mesothelial cells**. Particle and Fibre Toxicology. 2012 Aug 28; 9(1):34.

6. Donaldson K, **Schinwald A**, Murphy F, Cho WS, Duffin R, Tran L, Poland C. **The biologically effective dose in inhalation nanotoxicology**. Accounts of Chemical Research. 2012 Sep 24. [Epub ahead of print].

7. **Schinwald A**, Chernova T, Donaldson K. **Use of silver nanowires to determine thresholds for fibre length-dependent pulmonary inflammation and inhibition of macrophage migration *in vitro***. Particle and Fibre Toxicology. 2012 Dec 2;9:47

Research article under revision:

- **Schinwald A**, Murphy F, Askounis A, Koutsos V, Sefiane K, Donaldson K, Campbell C. **Minimal Oxidation and Inflammogenicity of Pristine Graphene with Residence in the Lung.** Submitted to Nanotoxicology.

Review article under submission:

- **Schinwald A**, Cherrie JW, Poland CA, Donaldson K. **Fibre length and mesothelioma – new science illuminates an old question and highlights new risks**. Submitted to Environmental International.

- Donaldson K, Poland CA, Murphy FA, MacFarlane M, Chernova T, **Schinwald A**. **Pulmonary toxicity of carbon nanotubes and asbestos – similarities and differences**. Submitted to Advanced Drug Delivery Reviews.

1. Donaldson K, Murphy F, **Schinwald A**, Duffin R, Poland CA. 2011. **Identifying the pulmonary hazard of high aspect ratio nanoparticles to enable their safety-by-design**. *Nanomedicine* (Lond). Jan;6(1):143-56.

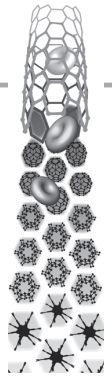

Identifying the pulmonary hazard of high aspect ratio nanoparticles to enable their safety-by-design

High aspect ratio, or fiber-shaped, nanoparticles (HARNs) represent a growth area in nanotechnology as their useful properties become more apparent. Carbon nanotubes, the best known and studied of the HARNs are handled on an increasingly large scale, with subsequent potential for human inhalation exposure. Their resemblance to asbestos fibers precipitated fears that they might show the same type of pathology as that caused by asbestos and there is emerging evidence to support this possibility. The large number of other HARNs, including nanorods, nanowires and other nanofibers, require similar toxicological scrutiny. In this article we describe the unusual hazard associated with fibers, with special reference to asbestos, and address the features of fibers that dictate their pathogenicity as developed in the fiber pathogenicity paradigm. This paradigm is a robust structure:toxicity model that identifies thin, long, biopersistent fibers as the effective dose for fiber-type pathogenic effects. It is likely that HARNs will in general conform to the paradigm and such an understanding of the features that make fibers pathogenic should enable us to design safer HARNs.

KEYWORDS: carbon nanotubes ▪ fibers ▪ high aspect ratio ▪ mesothelioma ▪ nanotoxicology

Ken Donaldson[†1,2], Fiona Murphy[1], Anja Schinwald[1], Rodger Duffin[1] & Craig A Poland[2]

[1]MRC/University of Edinburgh Centre for Inflammation Research, ELEGI Colt Laboratory, Queen's Medical Research Institute, 47 Little France Crescent, Edinburgh, EH16 4TJ, UK
[2]Institute of Occupational Medicine, Research Avenue, North Riccarton, Edinburgh, UK
[†]Author for correspondence:
Tel.: +44 131 242 6580
ken.donaldson@ed.ac.uk

High aspect ratio nanoparticles: definitions & volume of production

Owing to the unique properties of matter in the nanosize scale, nanomaterials are being incorporated into a wide variety of consumer products, and research in developing new nanomaterials is proceeding remarkably fast. A material is defined as a nano-object (used here to define a nanoparticle as nano-object) as having one, two or three external dimensions in the nanoscale [1], (i.e., a nanoparticle is a particle with at least one dimension less than 100 nm). According to the structure and nanoscale dimension of the material it can be further split into three different categories. 1D nanoscale materials are referred to as nano-layers, -films or -surfaces, whereas 2D nanoscale materials are categorized as nanotubes, nanowires and nanorods; the third category consists of nanoparticles, which are nanoscale in all three dimensions.

This article focuses on nanomaterials, which are nanoscale in 2D, particularly high aspect ratio (aspect ratio [AR] = length:width ratio) nanomaterials for which the acronym HARNs, signifying high aspect ratio nanoparticles, has been used [2]. The reason for focusing on HARNs in this article are:

- Their useful and novel electrophysical properties and their increasing production compared with other nanoscale materials, as a consequence of which there is increasing potential for inhalation exposure;
- Concern that, if HARNs are inhaled into the lungs they may behave similar to asbestos, some of which can be classified as HARNs, albeit natural in origin;
- Exposure to asbestos fibers caused a worldwide epidemic of disease, although not all fibers that can be breathed into the lungs are as pathogenic as asbestos and the different forms of asbestos are not equally pathogenic. Therefore, if we can fully understand what features render a fiber pathogenic then we have the potential to develop HARNs that are safe by design.

As the name implies, HARNs have a high ratio of length-to-diameter, with a high surface area and can be composed of a variety of elements and compounds; at present, HARNs include nanotubes, nanowires and nanorods (Figure 1). The terms nanowire and nanorod are used interchangeably in literature and the definition of these terms is still somewhat vague. The distinguishing feature between nanowires and nanorods is their length. Nanowires can be up to millimeters in length whereas each dimension of nanorods is within 100 nm. Therefore, the standard AR of nanorods is 3–5 in comparison with the AR of nanowires, which can

future medicine part of fsg

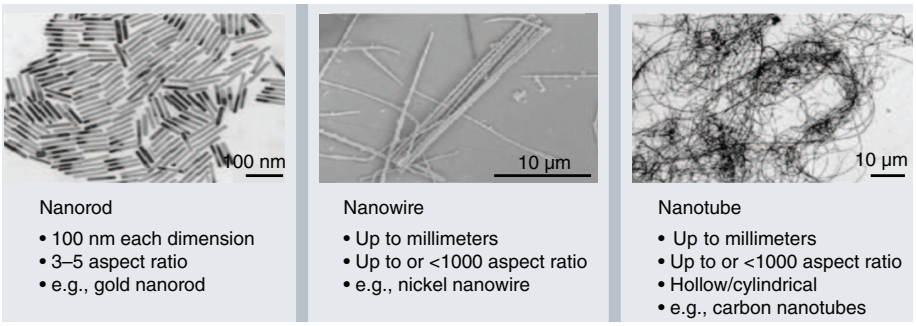

Figure 1. Images and characteristics of the different types of high aspect ratio nanoparticles.
Gold nanorod image used with permission from [11].

be greater than 1000. Another term used in the literature for HARNs is nanofibers, which are occasionally used as an umbrella term for nanowires and nanotubes. According to the WHO a fiber is a particle that has a maximum diameter of 3 µm, a minimum length of 5 µm and an AR greater than 3:1 [3]. Best known of all HARNs are carbon nanotubes (CNTs), which are long, thin cylindrical structures comprising single or multiple layers of concentric graphene sheets. CNTs have been optimized for a huge range of applications by derivatization of the surface with a range of chemical moieties. Carbon, packed in the graphenic structure of CNTs exhibits exceptional properties from electrical and thermal conductivity to tensile strength and rigidity. The development and optimization of CNTs for a huge range of applications, from use in electronics to structural engineering, has been a feature of the developing nanotechnologies industry [4].

The advantages in the production of nanowires, nonCNTs and nanorods over CNTs could include controllability of length, diameter, geometry, surface functionality and purity during the production process. Various techniques have been developed to synthesize nanowires and nanorods based on different methods (e.g., evaporation–condensation, dissolution–condensation and vapor–liquid–solid), but the template-based approaches have proved the most versatile. Dependent on the material under use, different template-based synthesis methods can be utilized [5]. For electrically conductive materials, the electrochemical deposition method is used and various nanowires and nanorods have been synthesized using this method, including metals such as Au, Ni, Co, Fe and Pb, as well as semiconductors, conductive polymers and oxides. Their applications range from electronic devices to tools for biology and medicine [6]. With regard to nanomedicine applications, CNTs in particular have been identified for a number of potential uses, including imaging, enhancement of bone growth and targeting and delivery of drugs [7–9]. Prina-Mello *et al.* produced ferromagnetic nickel nanowires with various ARs for manipulating, identification and counting of living cells [10]. Sharma *et al.* studied the neuroprotective efficacy of compounds attached to nanowires in comparison with normal compound delivery and reported an enhanced beneficial effect of the nanowire–drug delivered compound [11]. Other template-based synthesis methods are electrophoretic deposition from colloidal dispersion and template filling. A wide range of HARNs has been produced using the electrophoretic deposition method including polycrystalline oxides such as ZnO, TiO_2 and SiO_2 [5]. Amongst these, ceramic nanoparticles have drawn special attention in the fields of drug delivery, imaging, sensing and thermotherapy due to their biocompatibility, simple preparation and ease of surface modification. In addition, silica nanotubes combined with iron oxide seem to be a promising tool for image-guided drug delivery. The tubular shape permits loading of large amounts of the desired molecule, whereas the outer surface can be modified using, for example, polyethylenglycol or targeting moieties [12].

Year by year there is a near exponential increase in publications based on nanomaterials as well as a considerable expansion in market potential (Table 1) [13]. According to the data summarized in a recent report by the Federal Ministry of Education and Science in Germany, the compound annual growth rate of HARNs (excluding CNTs) is 30%. Even more outstanding is the annual growth rate of single-walled CNTs, which is 200% [101]. These figures correlate with the number of HARN-related publications, which rose from 86 in the year 2000 to 1822 in the year 2009 (Figure 2).

Table 1. Estimated market for nanoparticles.

Market segment	World market volume [M$]/base year			CAGR (%)
	Past	*Present*	*Future*	
MWCNT	290/2006	650/2010		80
SWCNT	78/2006	5000/2010		200
Nanofibers (excluding CNTs)	48/2007	176/2012	825/2017	30
Metallic nanopowders (e.g., Ag)	89/2005	770/2010		53
Ceramic nanopowder (US market)	220/2006	580/2011		21
Nanotechnology in the healthcare market (US market)	23,000/2006	53,000/2011		18
Nanomedicine	18,000/2006	39,000/2011		17

Market growth trends and forecasts are based on information derived from relevant financial and market information, amongst others.
CAGR: Compound annual growth rate; CNT: Carbon nanotube; MWCNT: Multiwalled carbon nanotube; SWCNT: Single-walled carbon nanotube.
Data from [13,101].

Comparing this number with the amount of publications on nanoparticles, which was 3231 in the year 2009, the increasing importance of HARNs in nanotechnology industry becomes obvious. The increasing growth of the HARN industry suggests considerable potential for human exposure to airborne HARNs as these materials are handled in the workplace during industrial preparation and use. However, despite rapid growth in the publications reporting the development, optimization and potential applications of various HARNs, the number of publications based on toxicity studies of HARNs makes up only 6% of all publications, whereas the proportion of toxicity studies on nanoparticles is 19% out of all nanoparticle publications. These data illustrate quite clearly the worrying mismatch between the increases in research focused on the development and use of HARNs versus research concerned with potential health effects of exposure to HARNs.

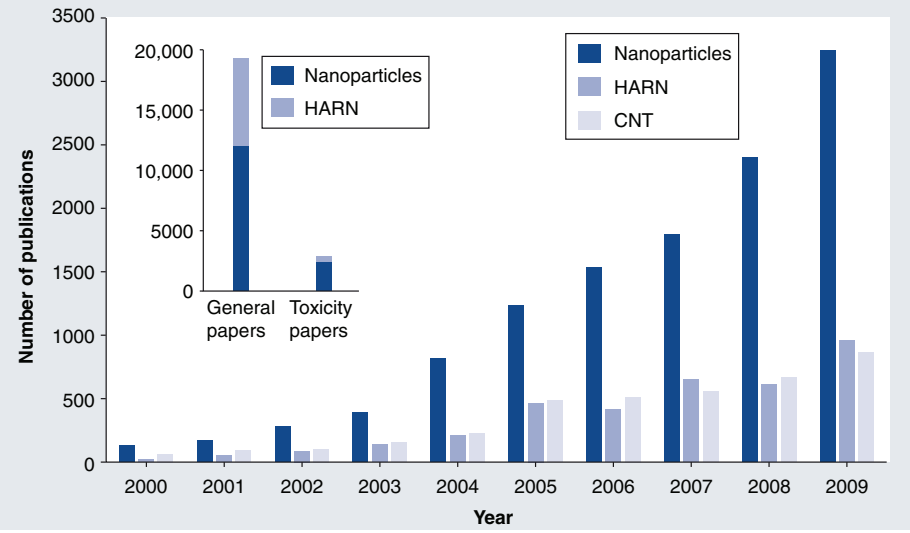

Figure 2. Number of publications on the topics of nanoparticles, high aspect ratio nanoparticles, excluding carbon nanotubes, and carbon nanotubes. Shows the increase in the number of publications on the main three categories of nanomaterials from 2000 to 2009. HARN in this graph include nanofibers, nanowires, nanorods and nanotubes made of materials other than carbon. These data are based on publications in the PubMed database. The search in the database was performed using the 'advanced search option' and 'limits' to specify the date range of publications in each field. Number of publication was revealed using the search terms 'carbon nanotubes' and 'nanoparticles'. HARN data was obtain by summing the number of hits from 'nanofibers', 'nanowires', 'nanorods' and 'nanotubes' using the 'Search Builder option NOT' to exclude CNTs.
CNT: Carbon nanotube; HARN: High aspect ratio nanoparticle.

Asbestos

Consideration of the likely adverse health effects arising from inhalation exposure associated with the use of HARNs is inevitably viewed in the context of the asbestos experience. Asbestos comprises a number of crystalline silicate minerals found ubiquitously in the earth's crust, which was discovered to be industrially useful in the late nineteenth century. The subsequent mining, working and incorporation of asbestos fibers into a vast range of consumer products gave rise to exposure of workers and end-users. Asbestos occurs as six minerals – one of the serpentine class (chrysotile) and five of the amphibole class (amosite, crocidolite, tremolite, anthophyllite and actinolite). Of these, only chrysotile, amosite and crocidolite have proved to be of significant industrial importance, with concomitant human exposure, although tremolite exposure occurs as a contaminant of chrysotile.

Annual world production of asbestos is currently approximately 2,000,000 tons worldwide with Russia as the leading producer, followed by China, Kazakhstan, Brazil, Canada, Zimbabwe, and Colombia, which together accounted for 96% of the world production of asbestos in 2007.

There is an important distinction to be made between chrysotile and the amphibole asbestos types in terms of chemical composition and chemical stability, which is reflected in the differences in their pathogenic potency (discussed in the following paragraphs). This highlights an important point – namely, that not all respirable fibers are equally pathogenic – there is a structure:toxicity model termed the 'fiber pathogenicity paradigm' that predicts whether a fiber is or is not pathogenic (described later). Notwithstanding these differences, all commercial forms of asbestos, including chrysotile, are classified as human carcinogens by the International Agency for Research on Cancer [14] and there have been calls for them to be banned on a global scale [15]. The asbestos minerals are crystalline, and contain fracture planes, or weaknesses, in the crystal structure meaning that when the rock is stressed (e.g., by crushing of the ore or during mining) the crystal fractures into long thin fibers that can be released into the air. These high AR fibers, which can be, in the case of chrysotile fibrils, less than 100 nm in diameter but very long, are normally termed fibers, but they can be seen as naturally occurring HARNs. Owing to their lightness and shape, asbestos fibers can readily become airborne and remain there for a protracted time. If they are inhaled and are thin enough, they can deposit in various parts of the respiratory tree, depending on their aerodynamic size. Once deposited in the lungs the accumulation of fibers can lead to a number of diseases principal amongst which are fibrosis or scarring of the lung parenchyma and bronchogenic carcinoma. In addition, asbestos exposure also causes a number of diseases in the pleura, including mesothelioma, pleural effusion and pleural fibrosis.

The fiber pathogenicity paradigm

Most important for the HARN issue is the question – what are the properties of fibers that imbue them with pathogenicity? If we understand the properties that render fibers pathogenic or not then we can use this information to test or benchmark HARNs as to their likelihood of showing asbestos-like pathogenic behavior. We can also potentially utilize the paradigm to design safe HARNs.

Several decades of fiber toxicology studies, on both asbestos and synthetic vitreous fibers (SVF) have resulted in the fiber pathogenicity paradigm, which highlighted the fiber parameters that dictate whether or not a fiber will be pathogenic when inhaled from an airborne respirable cloud (Figure 3).

These factors are width, length and biopersistence (Figure 3). It should be noted that the pathogenicity paradigm pertains only to the fiber hazard of HARNs. It does not describe the potential hazard that might occur from inhalation exposure to any HARNs that is not long enough (see following paragraphs), in which case it is effectively a particle whose toxicology is understood in terms of an entirely different paradigm.

Width

Width or diameter is the main factor that determines aerodynamic diameter, which is the property that controls whether, or where, in the respiratory tract any particle deposits. Deposition in the lungs is complex, resulting from the size and aerodynamic behavior of the fibers as they negotiate the complex branching structure of the pulmonary airways in the airstream. Aerodynamic diameter (D_{ae}) is the measure that defines where in the respiratory tree any fiber deposits with the extra role of interception, which is a mode of deposition specific to fibers that results from the center of gravity of a fiber following the airstream at a bifurcation while the tip makes contact with the surface of the lung causing immediate deposition. D_{ae} is determined predominantly by the width of the fiber, the aerodynamic diameter of any conventional fiber, composed of material of around unit density, being approximately

three-times its width [16]. The lung has fast and effective clearance in the larger airways, where the mucociliary escalator traps the particles in mucus, which is then swept up to the mouth for swallowing to the gut. Beyond the ciliated airways in the gas exchange regions, clearance is by macrophages that move around on the lung surface and phagocytose or engulf the particles. The particle or short fiber-loaded macrophages then move upwards onto the mucociliary escalator for upward clearance to the mouth and the gut leading to effective clearance of particles [17] and short fibers [18]. This more fragile and slow clearing alveolar and terminal bronchiolar compartment beyond the ciliated airways where blood is very close to the body surface for gas exchange is considered to be much more sensitive to particle effects. This region is termed the respiratory zone and the aerodynamic size fraction of fibers that reaches this zone is termed the respirable fraction, and is generally considered to be the fraction of greatest health concern. Alveolar macrophage clearance from this region is highly effective for micron-sized particles, which are sconfined to the air space and can be collected by the alveolar macrophages [17]. However, Semmler Behnke *et al.* have shown very different clearance/retention kinetics for nanoparticles [19]. These show 80% interstitialization of Ir nanoparticles, which are re-entrained over 6 months back on to the epithelial surface where they are cleared, probably in macrophages, resulting in only 10% retention after 6 months.

Length

Once deposited, length is the factor that determines whether a fiber can be effectively cleared from beyond the ciliated airways by macrophages and whether the attempt of macrophages to phagocytose the fibers leads to inflammation [20,21]. Long fibers (>~15 µm) cannot be engulfed and effectively phagocytosed by macrophages while short fibers are effectively cleared [18]. For some HARNs, the rigidity or ability to coil up into a bundle could be an important factor in modifying the length. In the process of attempting phagocytosis, the macrophage extends along the fiber, but cannot close the phagosome owing to the length of the fiber. This situation of frustrated phagocytosis (Figure 4) leads to lysosomal instability, activation of the NALP inflammasome; a multiprotein complex that modulates innate immune function, and chronic stimulation of the cell resulting in the macrophage releasing a range of proinflammatory molecules [22].

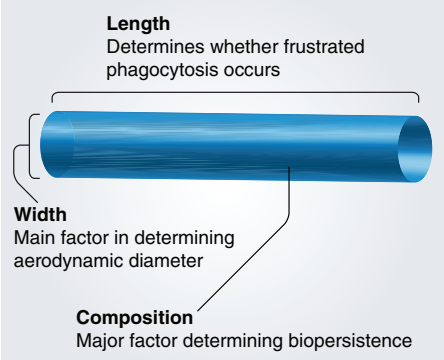

Figure 3. Important parameters governing the pathogenicity of any respirable fiber.

Biopersistence

The property of retaining structural integrity during residence in lung tissue is known a biopersistence. The concept of biopersistence arises from the observation that different natural and man-made fibers with the same length distribution had very different lung retention times following deposition in the lungs and those which were most biopersistent in the lungs had the highest fibrogenic and carcinogenic potential [23]. Within the lung, the less biopersistent components of the fiber may wholly, or partially, dissolve causing them to split longitudinally, as seen with fibrils of chrysotile asbestos, or break transversely as in the case of glass fibers. This arises as a result of the fluid milieu of the lung leaching certain structural components or to the acidic environment of

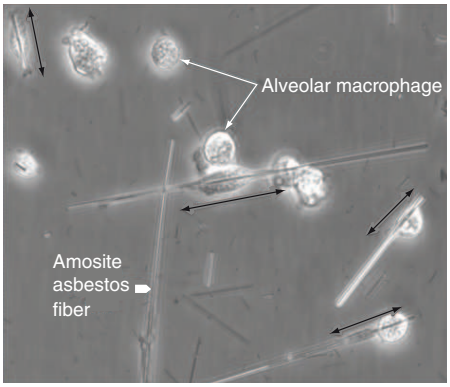

Figure 4. Frustrated phagocytosis in alveolar macrophages by amosite asbestos fibers. Image of macrophages of the NR8383 cell line; white arrow, attempting to phagocytose long amosite asbestos fibers (white chevron). The resultant elongation of the cells along the fibers as they attempt, but fail, to completely enclose the long fiber (black arrows) is termed frustrated phagocytosis.

macrophage phagolysosomes acting in the same way to weaken the fiber.

The effect that dissolution may have on a fiber can be varied, causing surface modification or weakening of the structure leading to breaks with subsequent formation of short fibers, more easily cleared by macrophages (Figure 5). The influence of characteristics, such as susceptibility to dissolution and breakage, was shown by Miller *et al.* using rat exposure data from the Colt Fiber Research Program in the UK and studies from the program of the Thermal Insulation Manufacturers Association in Switzerland and the USA [24]. The role of biopersistence was more directly shown by Searl *et al.* by comparing the length fraction of biopersistent amosite asbestos against nonbiopersistent man-made vitreous fiber (MMVF)-10 between 3 days and 12 months postinhalation in rats. In the case of the MMVF-10 sample, the number of short fibers increased after 12 months indicating breakage of the long fibers supplementing the population of short fibers [18]. Even within the asbestos family of minerals there are differences in biopersistence. Chrysotile asbestos has been shown to be less biopersistent than the amphibole forms of asbestos, such as crocidolite and tremolite. This has been attributed to the layer of a magnesium hydroxide or brucite between the silicate sheets of chrysotile, which is more prone to dissolution causing the layers to unravel and break. The importance of this was shown by McDonald and colleagues who analyzed post-mortem lung tissue from Quebec chrysotile miners by electron microscopy for levels of different forms of asbestos. They found that despite the main exposure being to chrysotile asbestos with only tremolite as a minor contaminant, chrysotile and tremolite were found in approximately equal quantities in the lungs [25]. This suggests that exposure to low levels of biopersistent tremolite lead to a cumulative build up of dose, while the dissolution of chrysotile led to a reduction in retained dose over time. As a concept, exposure to a fiber with a dimension that allows penetration of the lung but does not allow clearance by macrophages leaves only one route of clearance, namely dissolution or breakage. Therefore, exposure to a biopersistent fiber that will not dissolve or break means that it shall persist in the lung environment where it may trigger pathological effects.

Biopersistence studies with HARNs

The only HARN that has been investigated from the point of view of biopersistence is the CNT. It would be anticipated that single-walled CNTs (SWCNTs) are more amenable to degradation than multiwalled CNTs (MWCNTs) and that treatments that disrupted the graphene structure of SWCNTs introducing defects, would also render the CNTs more easily degradable. This has been confirmed in recent studies by Kane and colleagues, who concluded that greater biosolubility would be seen in any SWCNTs following any treatment 'that causes collateral damage to the tubular graphenic backbone in the form of neighboring active sites that provide points of attack for further oxidative degradation' [26]. Similar results were found when SWCNTs that have been highly oxidized by acid treatment and then exposed to neutrophil peroxidase underwent dissolution [27]. It seems unlikely that unoxidized/unmodified SWCNTs or MWCNTs that have undergone mild oxidation would be rendered soluble by the general

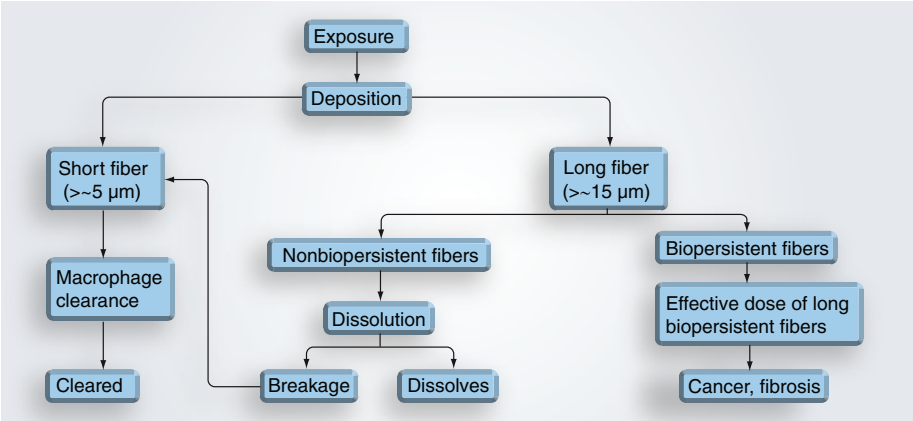

Figure 5. The relationship between biopersistence, clearance and the biologically effective dose of long fibers.

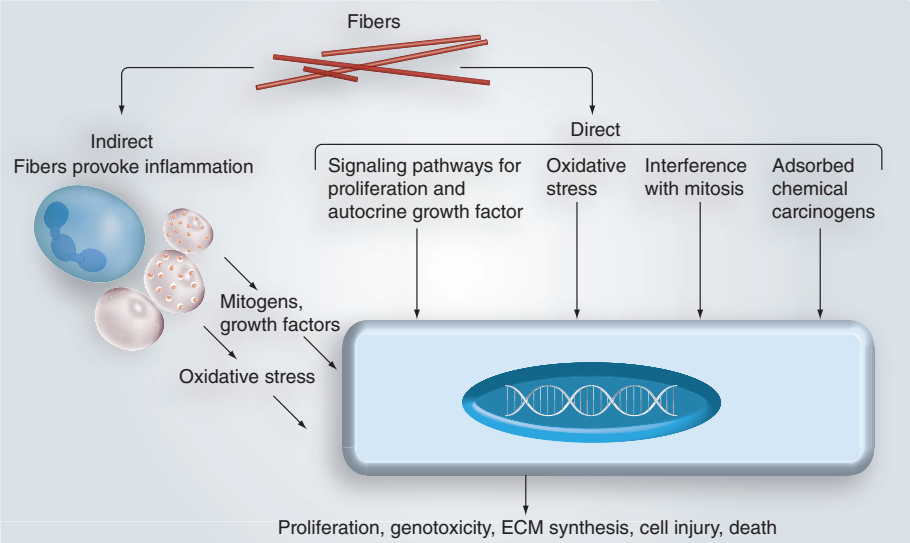

Figure 6. The target cell shown could be an epithelial cell in the lining of the bronchial tree (bronchogenic carcinoma) or a mesothelial cell in the parietal pleura (pleural mesothelioma) and the diagram illustrates the direct and indirect pathways by which fibers may cause procarcinogenic effects.
Adapted from [57].

oxidizing environment of the lungs. This is borne out by numerous studies where CNTs have been introduced into the lungs and have been readily visible in sections months later.

The general issue of CNT biopersistence should be addressed using conventional durability (measuring solubility *in vitro*) or biopersistence (measuring change in lung burden over time) protocols that are available [28,29].

Mechanism of lung disease caused by long fibers

The process of inflammation is the initial cellular response to cell death and oxidative stress arising as a direct result of the accumulation of long fibers in tissue above a threshold dose. Inflammation in turn gives rise to cell injury, gene expression of proinflammatory molecules and further oxidative stress, as amply demonstrated in cells and lungs exposed to asbestos and other fibers (Figure 6). Thus, there are at least two ways that oxidative stress can arise in tissue where fibers have deposited – directly by interaction between the fibers and target cell such as epithelial cells, and indirectly when inflammatory leukocytes release oxidants that affect the target cells. The milieu in the lung tissue containing long fibers, with cell injury genotoxicity, oxidative stress and proliferation, is a fertile one for genetic injury, mutation, fibrosis and cancer. A proportion of the fibers that deposit peripherally in the lungs translocate to the pleural tissues [2] (see following sections) where they cause a similar sequence of events leading to a number of unusual fiber-specific pleural diseases, including fibrosis, pleural effusion and mesothelioma. Mesothelioma is a tumor arising on the parietal pleura of the chest wall, which is almost exclusively linked to asbestos exposure, although there are other agents that may occasionally cause this effect. Mesothelioma has become a major concern from exposure to respirable fibers since it occurs at low exposure when the other effects are not apparent and because of its insidious and uniformly fatal course.

Mesothelioma & the pleural mesothelium as a unique target for fibers including HARNs

Translocation to the pleural space

The pleural space is the space between the chest wall and the lungs. The entire surface of the pleural cavity is lined with a single layer of mesothelial cells, with the mesothelial layer covering the lungs known as the visceral pleural, whereas the mesothelial layer attached to the chest wall and diaphragm is referred to as the parietal pleura. The development of pleural pathologies due to inhalation of asbestos fibers would suggest a biologically effective dose of fibers is delivered to this extrapulmonary tissue. Although the exact mechanism of fiber translocation from the lungs to the pleural space is unknown, there is a body of literature that suggests a proportion of all

particles that deposit in the distal regions of the lung translocate to the pleural space. A study carried out by Mitchev *et al.* on healthy individuals showed the presence of 'black spots', benign areas of particle accumulation, on the parietal pleura in 92.7% of a cohort of 150 urban dwellers examined at autopsy [30]. A greater accumulation of black spots has been noted on the parietal pleural surface of miners reflecting their higher exposure levels to coal dust [31]. Black spots represent areas of particle accumulation where a proportion of inhaled particles reaching the pleural space become interstitialized in the parietal pleura of the chest wall as they are in the process of being cleared. Studies investigating the link between asbestos exposure and the development of pleural pathologies have also detected asbestos fibers retained along the parietal pleura. Dodson *et al.* reported that short (<5 µm) chrysotile fibers were predominantly translocated into the pleura in the lungs of ex-shipyard workers exposed to both chrysotile and amphibole asbestos fiber types [32]. Kohyama and Suzuki also reported an apparent predilection for short fiber movement into the pleural space after finding large amounts of short chrysotile fibers in pleural tissue even though the fiber burden in the lung contained a greater percentage of amosite fibers [33]. A study by Boutin *et al.* [34], however, which compared the fiber burden in areas containing black spots to normal areas of parietal pleura, found a high number of long fibers particularly associated with the black spots, with 22% of all fibers found in these areas greater than 5 µm in length. They also showed a clear-cut concordance between the long amphibole asbestos fiber burden in the lung and the black spots of the parietal pleura, but not the areas of normal pleura. Heterogeneity of distribution of fibers within the pleural space can most likely account for the conflicting results from previous studies, which reported a preponderance of short chrysotile fibers in the pleura. These studies suggest that both short and long fibers deposited in the distal alveolar regions of the lung follow an incompletely elucidated route of particle clearance from the lung to the pleural space.

No published study has as yet reported the translocation of HARN fibers to the pleural space after administration into the lung; however, recently a study by Ryman-Rasmussen *et al.* [35] reported the deposition of inhaled short CNTs throughout the lungs and directly adjacent to the visceral pleura, wholly consistent with the notion that CNTs can reach the distal lung and the pleura. From the current understanding of particle/fiber movement from the lungs it is entirely probable that subpleurally deposited CNTs, as reported by Ryman-Rasmussen, and other forms of HARNs will translocate into the pleural space. This suggests the more pertinent question to be asked regarding the toxicity of these new materials and their potential to cause a fiber-like hazard is not whether they reach the pleural space but how they are dealt with once they are there.

Clearance from the pleural space

As mentioned previously, length is a controlling factor governing the macrophage-mediated clearance of fibers from the distal alveolar regions of the lungs. Similarly, clearance of particles and fibers from the pleural space appears to also be length dependent. The primary mechanism of clearance from the pleural space is to remove the particles passively in the flow of pleural fluid out of the pleural space where it joins the lymphatic system [36]. Stomata or pores, approximately 3–10 µm in diameter, act as a sieve for drainage from the pleural space and are found in highest abundance in the most caudal, posterior intercostal spaces and to a lesser extent in the ventral, parasternal region [36,37]. Normally, the elutriating effects of the lungs serve to allow only particles smaller than approximately 5 µm, and therefore smaller than the diameter of the stomata, to reach the distal lung and pleural space. These particles are easily cleared in the flow of pleural fluid where they drain to the mediastinal, parasternal and hilar lymph nodes [38]. However, this clearance mechanism appears to fail when high AR fibers are encountered (Figure 7). In contrast to the movement of fibers in the lung, where it is the diameter of the fibers rather than the length that is the ruling factor in fiber deposition, in the pleural space when the length of a fiber is greater than the diameter of the stomata, interception of the fiber ends with the mesothelial cells surrounding the stomata will occur [2]. This results in blockage of the stomata, accumulation of fibers at these drainage points and potential damage to the mesothelial cells. The presence of fibers in the pleural space will attract resident pleural macrophages, which will accumulate at these areas of deposition. Similar to the attempts of alveolar macrophages to clear long fibers from the lung, pleural macrophages may be unable to fully engulf the fibers leading to a state of frustrated phagocytosis causing further inflammation, fibrosis and genotoxicity in the adjacent mesothelial cells in the areas of congestion around the stomatal entrances.

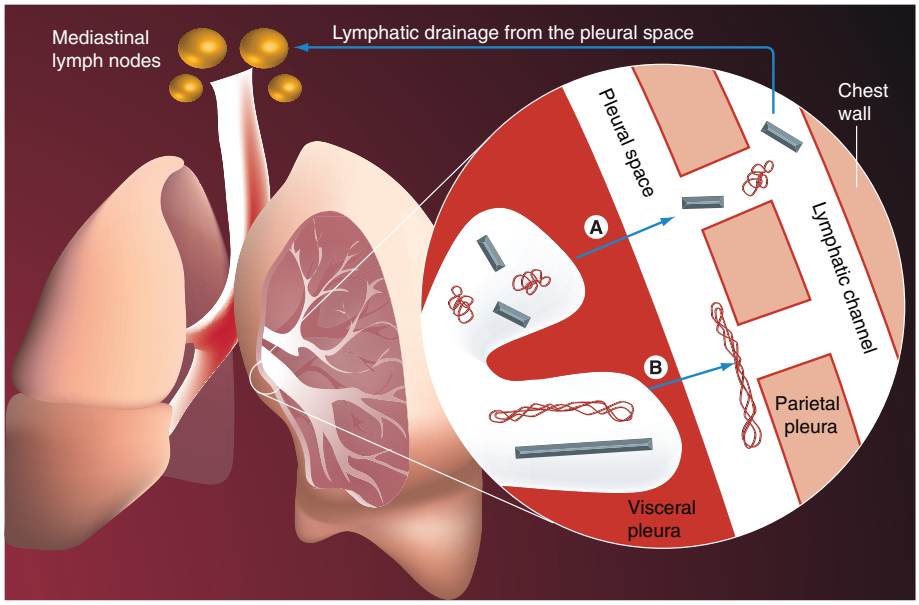

Figure 7. Size-dependent clearance from the pleural space. (A) Short fibers and small carbon nanotube tangles that deposit subpleurally migrate to the pleural space and exit in the flow of pleural fluid through the stomata where they follow the lymphatic drainage to the mediastinal lymph nodes. **(B)** Long fibers and long carbon nanotubes also reach the pleural space but cannot negotiate the stomata and so they are retained where they cause inflammation and potentially long-term disease.

HARNs in the pleural space

The role of length-dependent retention in the pleural space in the pathogenesis of disease needs to be considered when testing the potential of new types of HARNs to cause pleural disease. A study carried out recently in our laboratory investigated the potential adverse reaction to fiber-like MWCNTs in the pleural space, focusing on the response at the parietal pleura of the chest wall and diaphragm [Murphy *et al.*, Manuscript in Preparation]. A method of injection into the pleural space was developed to ensure that the dose of particles was delivered into the pleural cavity without injection into the lung. A panel of both long and short MWCNTs were injected directly into the pleural cavity and the inflammatory response in the pleural space and at the parietal pleura was examined at a number of time points up to 6 months postinjection. Acute inflammation followed by progressive fibrosis and granuloma development was found only in response to the long MWCNT samples and the long amosite asbestos control with long MWCNTs visible in association with the granulomas at each time point. Short MWCNTs failed to cause a sustained response with only a mild thickening of the mesothelium visible at day one, which had completely resolved by day 7.

The sustained response to the long but not short MWCNTs fully supports the hypothesis that length-dependent retention is the driving force behind the pathogenesis of long fibers in the pleural space. In particular, the retention of long fibers at the parietal pleura provides an explanation of the enhanced ability of long asbestos fibers to cause mesothelioma after inhalation compared with short fibers [39,40]. The operation of a similar length-dependent mechanism of clearance from the peritoneal cavity (see following sections) also explains the markedly greater potential of long fibers instilled into the peritoneal cavity to cause mesothelioma at that site compared with short fibers [39].

Diameter of fibers determines whether a fiber will reach the distal regions of the lung and therefore translocate to the pleural space, whereas length of the fiber is the limiting factor controlling clearance from the pleural space. This suggests that any HARNs with sufficiently small diameter and long length could pose a mesothelioma hazard.

Using the peritoneal cavity as a model of direct mesothelial exposure

When assessing the biological activity of various forms of fibers, the peritoneal cavity of rodents has often been used as a surrogate for the thoracic mesothelium due to the similarity of the

two cavities in terms of the mesothelial lining and the ease of access to the peritoneal cavity [41–44]. The peritoneal or abdominal cavity is the largest body cavity and contains the abdominal organs covered with a mesothelium, which is easily accessible for the introduction of fibers. In surface area, the peritoneal mesothelium is equal to that of the skin [45] and in many ways the peritoneal cavity is analogous to the pleural cavity, which is not surprising considering its shared origin, in the primitive mesoderm during embryonic development. The pleural and peritoneal cavities differ in that the two main roles of the pleural cavity are to lubricate the movement of the lungs and provide a fluid-filled tight coupling between the lung surface and thoracic cage. There is no such coupling role for the peritoneal cavity, instead its primary role is to lubricate the motion of the organs contained within the abdomen and as such whilst the cavity is lubricated, it is not fluid filled. The peritoneal cavity is lined with a mesothelium with a structure identical to that of the pleural, and indeed all mesothelial layers [46]. It also contains stomata that overlie lymphatic lacunae (similar to those seen in the pleural cavity) linking the cavity to the underlying diaphragmatic lymphatics. The diaphragm is considered the principle route of drainage from the peritoneal cavity [47–49] via the parasternal lymph trunks to the parasternal and mediastinal lymph nodes [48]. The physiological nature of the peritoneal cavity means that particles which enter the cavity can be rapidly removed in the liquid flow from the cavity through the diaphragm, or taken up by resident phagocytic cells. Particles that cannot negotiate the narrow (3–12 µm) stomatal openings [50] are retained causing an inflammatory and fibrotic response as demonstrated with asbestos and CNTs [51].

Despite the fact that the peritoneal cavity is a dynamic environment, with size-dependent routes of clearance via the stomata to outlying lymph nodes [52] and lined with a highly responsive mesothelium capable of mediating an inflammatory response [50], the rodent peritoneal assay is not without its critics. The main criticism relates to the lack of physiological relevance as a route of exposure. Indeed, the peritoneal model is not a model of inhalation exposure, it is simply a surrogate for the thoracic mesothelium, as a specific cellular target for asbestos carcinogenicity. Fiber length-dependent retention occurs in both the pleural space and the peritoneal cavity, making the latter an appropriate model for clearance/retention of particulates in the mesothelial space. It is notable that a proportion of the mesotheliomas that arise in asbestos-exposed individuals occur in the peritoneal cavity and so there is exposure of the peritoneal mesothelium to fibers following inhalation and translocation, and a response that mimics mesothelioma formation in the pleural space [53].

Recently, there have been several studies using the peritoneal assay to investigate the *in vivo* response to CNTs. One of the first was a study by our own group in which the role of length in inflammogenicity and fibrosis was examined using a 50 µg intraperitoneal injection of CNTs of differing length and appropriate asbestos controls [51]. We found that long, fiber-like CNTs generated a strong and persistent inflammatory response similar to that seen with long amosite asbestos fibers. Short CNTs, compact carbon particles and short lengths (<5 µm) of amosite asbestos generated no such inflammation and there was no evidence of retention in the peritoneal space suggesting rapid clearance [54]. Over an extended period, the long CNT and asbestos samples generated substantial fibrosis and the presence of foreign body giant cells typical of a foreign body reaction, again not seen with the compact particle controls. This led us to the conclusion that the length of the CNT and asbestos, in line with the structure:toxicity relationship, was causing length-dependent retention in the peritoneal cavity and subsequent response. This work has more recently been supported by a study by Yamashita and colleagues. They found that MWCNTs injected into the peritoneal cavity of mice generated inflammation and genetic damage, which was related to the length and thickness of the CNTs, although interestingly they did not find this the case for SWCNTs [55]. Again, it was this key length of approximately 15 µm that they found to be most inflammogenic in this fiber-sensitive model. The importance of fiber length in a model based on clearance and retention was demonstrated in a paper by Muller and colleagues [56]. They utilized the peritoneal model to investigate the potential carcinogenicity of MWCNTs, using crocidolite as a positive control particle. Over a period of 2 years they were unable to demonstrate a carcinogenic response to the CNTs for which, among other reasons, they cited the length of the CNTs as a contributing factor behind their negative findings. This was because the CNTs used were all less than 0.7 µm and so if singlet fibers were present then they very likely were rapidly cleared leaving only large, nonfibrous agglomerates.

Conclusion: future research and designing safe HARNs

The fiber pathogenicity paradigm is independent of specific chemical composition and therefore embraces asbestos, glass fibers and one organic fiber [16]. Our studies with CNTs [51] and as yet unpublished studies with NiO nanowires point towards the likelihood that all HARNs will conform to the general fiber pathogenicity paradigm, although further research is needed. This future research should address the general utility of the paradigm for a range of HARNs, including nanorods, nanowires and nanotubes of various compositions. Such studies would entail examining a wide range of HARNs for ability to cause length-dependent proinflammatory effects *in vitro* and studies on length-dependent retention at the parietal pleural stomata. Another major aim would be to provide quantitative data on biopersistence, the key attribute of the paradigm, for each HARN and to be able to relate the biopersistence data to pathogenic potential. Nanotechnology methodology could be used to address the key question regarding the true cut-off of length for a 'long' fiber, which is not answerable using naturally occurring fibers that always exist in a broad length distribution. The types of methodologies used to make HARNs are such that the HARNs can be manufactured in tight length distributions. By making HARNs in 3-µm length categories (e.g., -9, -12, -15, -18 and -20 µm long) these could be used to answer the big question – what is the length beyond which long fiber effects occur? This may amount to more than one value since the length beyond which frustrated phagocytosis occurs leading to effect in the lungs might be different from the length beyond which retention in the pleural space occurs, leading to pleural effects, since the length-dependent processes involved are quite different.

The three properties identified by the fiber pathogenicity paradigm as those that determine the likelihood that any fiber sample will pose a fiber-type (asbestos-type) hazard – long, thin and biopersistent – form the biologically effective dose for fiber-type effects. Therefore, the safe design of HARNs from the point of view of the paradigm is relatively straightforward and making HARNs short, thick or nonbiopersistent will reduce their hazard. In particular, designing in time-dependent programmed biodegradeability would be a very desirable approach to safe HARN design. Table 2 shows the best current assessment of the quantiative values that would be used to attain safe HARNs. Of course, the advantages of HARNs in any industrial setting may well rely upon properties that accompany length, thinness or biopersistence, and the intrinsic properties of the material may also dictate fiber dimensions and biopersistence. There may well be a contradiction in the production of safe HARNs, if safety stipulates short, low AR particles or biodegradable ones, which will conflict with the technical requirements of these new materials. Therefore, management of the risks from these materials, by safe handling to minimize exposure, needs to be mandatory. Where HARNs cannot be made safe-by-design, as in any industrial setting, due regard must therefore be paid to the size distribution and quantity of the airborne fibers in the workplace air.

Hygiene precautions to reduce inhalation exposure should be set in motion concomitant with the extent of the hazard identified by these size data and knowledge of the biopersistence derived empirically from biopersistence/durability studies or from knowledge of the inherent properties of the material of which the fibers are composed. Many workplaces handle hazardous materials, they simply handle them in safe ways that minimize exposure and HARNs are no different. However, it is difficult at the moment to measure dimensions of very thin fibers in the air and there needs to be more research in this direction so that real-time monitoring of airborne nanofibers can occur in workplaces.

Table 2. Safe values for the three factors in the fiber pathogenicity paradigm.

Characteristic of the FPP	'Safe' value	Rationale/comment
Width	>3 µm	Too thick to be respirable/cut-off for respirability in humans is 5 µm aerodynamic diameter; for fibers, the aerodynamics is approximately three-times the actual diameter
Length	<5 µm	Too short to cause frustrated phagocytosis/the actual value is unknown, but is somewhere between 10 and 20 µm
Biopersistent	Undergoes rapid dissolution in the lungs	Long fibers dissolve and break so are shortened and long fiber dose does not build-up/the actual soluble components lost will depend on the composition of the HARN

HARN: High aspect ratio nanoparticle; FPP: Fiber pathogenicity paradigm.

Financial & competing interests disclosure

The authors acknowledge financial assitance from The Colt Foundation and the UK Department of Health. The authors have no other relevant affiliations or financial involvement with any organization or entity with a financial interest in or financial conflict with the subject matter or materials discussed in the manuscript apart from those disclosed.

No writing assistance was utilized in the production of this manuscript.

Executive summary

High aspect ratio nanomaterials: definitions & volume of production

- High aspect ratio nanomaterials (HARNs) are a new class of material that are nanoscale and have a high length-to-width ratio (e.g., nanotubes, nanowires and nanorods).
- HARNs are increasingly being incorporated into a wide variety of products with a consequent increase in potential for inhalation exposure.
- There is a need to match the increases in research into the development and applications of HARNs versus HARN-related safety research.

Asbestos & the fiber pathogenicity paradigm

- Inhalation exposure to asbestos and naturally occurring high aspect ratio fibers can lead to a number of diseases that affect the lungs (e.g., fibrosis and bronchogenic carcinoma) or the pleura (e.g., mesothelioma, pleural effusion and pleural fibrosis).
- The fiber pathogenicity paradigm is a structure/toxicity model for fibers that highlights width, length and biopersistence in dictating whether or not a fiber will be pathogenic upon inhalation.

Mechanism of lung disease caused by long fibers

- Long fibers can interact directly with target cells (e.g., epithelial or mesothelial cells) causing cell death and oxidative stress or by provoking an inflammatory response recruiting leukocytes that will then release oxidants, cytokines and growth factors, creating a fertile environment for genetic injury, mutation, fibrosis and cancer.

Clearance from the pleural space

- The development of pleural pathologies is a particle response unique to fibrous particles.
- A proportion of all particles deposited in the distal lung will translocate to the pleural space but subsequent clearance from the pleural space is size dependent.
- Small particles and short fibers are easily cleared in fluid flow through stomata in the parietal pleural into the lymphatic system; however, fibers longer than the calibre of the stomatal openings cannot pass through and are retained where they may cause inflammation, fibrosis and genotoxicity in the adjacent mesothelial cells. This suggests that any biopersistent HARN with sufficiently small diameter and long length could pose a mesothelioma hazard.
- The peritoneal cavity is often used as a surrogate for the thoracic cavity when investigating the pathogenicity of fibers owing to the similarity of the mesothelial lining of the two cavities and the greater ease of access to the peritoneal cavity. Clearance from the peritoneal cavity, similar to the pleural cavity is via stomata in the diaphragm, which drain to the lymphatics.

Conclusion: future research & designing safe high aspect ratio nanomaterials

- HARNs have the potential to conform to the fiber pathogenicity paradigm and, therefore, may pose an occupational inhalation hazard.
- Identification of the link between structure and toxicity of HARNs can be exploited to design HARNs that are safer (i.e., short, thick and nonbiopersistent fibers). However, if these properties conflict with the technical requirements of the HARN, sufficient management of the risks to exposure needs to be mandatory.

Bibliography

Papers of special note have been highlighted as:
- ▪ of interest
- ▪▪ of considerable interest

1 Nanotechnologies – terminology and definitions for nano-objects – nanoparticle, nanofibre and nanoplate. ISO/TS 27687 (2008).

2 Donaldson K, Murphy F, Duffin R, Poland C: Asbestos, carbon nanotubes and the pleural mesothelium: a review of the hypothesis regarding the role of long fiber retention in the parietal pleura, inflammation and mesothelioma. *Part. Fiber Toxicol.* 7, 5 (2010).

▪▪ **A comprehensive review detailing the hypothesis that selective retention of long fibers in the pleural space leads to inflammation and disease.**

3 WHO: Determination of airborne fiber number concentrations: a recommended method by phase constrast optical microscopy. WHO, Geneva, Switzerland, ISBN: 924 1544961 (1997).

4 Aitken RJ, Chaudhry MQ, Boxall AB, Hull M: Manufacture and use of nanomaterials: current status in the UK and global trends. *Occup. Med. (Lond.)* 56(5), 300–306 (2006).

5 Cao G, Liu D: Template-based synthesis of nanorod, nanowire, and nanotube arrays. *Adv. Colloid Interface Sci.* 136(1–2), 45–64 (2008).

6 Corr SA, O'Byrne A, Gun'ko YK *et al.:* Magnetic-fluorescent nanocomposites for biomedical multitasking. *Chem. Commun. (Camb.)* (43), 4474–4476 (2006).

7 Pascu SI, Arrowsmith RL, Bayly SR, Brayshaw S, Hu Z: Towards nanomedicines: design protocols to assemble, visualize and test carbon nanotube probes for multi-modality biomedical imaging. *Philos. Transact. A Math. Phys. Eng. Sci.* 368(1924), 3683–3712 (2010).

8 Sahithi K, Swetha M, Ramasamy K, Srinivasan N, Selvamurugan N: Polymeric composites containing carbon nanotubes for bone tissue engineering. *Int. J. Biol. Macromol.* 46(3), 281–283 (2010).

9 Liang F, Chen B: A review on biomedical applications of single-walled carbon nanotubes. *Curr. Med. Chem.* 17(1), 10–24 (2010).

10 Prina-Mello A, Diao Z, Coey JM: Internalization of ferromagnetic nanowires by different living cells. *J. Nanobiotechnology* 4, 9 (2006).

11 Sharma HS, Ali SF, Tian ZR *et al.*: Nanowired-drug delivery enhances neuroprotective efficacy of compounds and reduces spinal cord edema formation and improves functional outcome following spinal cord injury in the rat. *Acta Neurochir. Suppl.* 106, 343–350 (2010).

12 Son SJ, Bai X, Nan A, Ghandehari H, Lee SB: Template synthesis of multifunctional nanotubes for controlled release. *J. Control. Release* 114(2), 143–152 (2006).

13 nano.DE-Report 2009. Status quo der Nanotechnologie in Deutschland. Bundesministerium für Bildung und Forschung, Bonn, Berlin, Germany, 2009.

14 IARC: *Asbestos: IARC Monographs. Supplement 7*. IARC France, World Health Organization, France (1987).

15 LaDou J: The asbestos cancer epidemic. *Environ. Health Perspect.* 112(3), 285–290 (2004).

16 Donaldson K: The inhalation toxicology of p-aramid fibrils. *Crit. Rev. Toxicol.* 39(6), 487–500 (2009).

17 Langenback EG, Bergofsky EH, Halpern JG, Foster WM: Supramicron-sized particle clearance from alveoli: route and kinetics. *J. Appl. Physiol.* 69(4), 1302–1308 (1990).

18 Searl A, Buchanan D, Cullen RT, Jones AD, Miller BG, Soutar CA: Biopersistence and durability of nine mineral fiber types in rat lungs over 12 months. *Ann. Occup. Hyg.* 43(3), 143–153 (1999).

19 Semmler-Behnke M, Takenaka S, Fertsch S *et al.*: Efficient elimination of inhaled nanoparticles from the alveolar region: evidence for interstitial uptake and subsequent reentrainment onto airways epithelium. *Environ. Health Perspect.* 115(5), 728–733 (2007).

20 Ye J, Shi X, Jones W *et al.*: Critical role of glass fiber length in TNF-α production and transcription factor activation in macrophages. *Am. J. Physiol.* 276(3 Pt 1), L426–L434 (1999).

21 Donaldson K, Li XY, Dogra S, Miller BG, Brown GM: Asbestos-stimulated tumor-necrosis-factor release from alveolar macrophages depends on fiber length and opsonization. *J. Pathol.* 168, 243–248 (1992).

22 Hamilton RF, Wu N, Porter D, Buford M, Wolfarth M, Holian A: Particle length-dependent titanium dioxide nanomaterials toxicity and bioactivity. *Part. Fiber Toxicol.* 6, 35 (2009).

▪ **Demonstrates that alteration of anatase TiO_2 nanomaterial into a long fiber structure creates a highly toxic particle that initiates an inflammatory response in alveolar macrophages.**

23 Bignon J, Saracci R, Touray JC: Introduction: INSERM-IARC-CNRS workshop on biopersistence of respirable synthetic fibers and minerals. *Environ. Health Perspect.* 102(Suppl. 5) 3–5 (1994).

24 Miller BG, Jones AD, Searl A *et al.*: Influence of characteristics of inhaled fibers on development of tumours in the rat lung. *Ann. Occup. Hyg.* 43(3), 167–179 (1999).

25 McDonald JC: Mineral fiber persistence and carcinogenicity. *Ind. Health* 36(4), 372–375 (1998).

26 Liu X, Hurt RH, Kane AB: Biodurability of single-walled carbon nanotubes depends on surface functionalization. *Carbon NY.* 48(7), 1961–1969 (2010).

27 Kagan VE, Konduru NV, Feng W *et al.*: Carbon nanotubes degraded by neutrophil myeloperoxidase induce less pulmonary inflammation. *Nat. Nanotechnol.* 5(5), 354–359 (2010).

28 Bernstein DM and Riego Sintes JM: Methods for the determination of the hazardous properties for human health of man made mineral fibers (MMMF). European Commission Joint Research Centre. Institute for Health and Consumer Protection, Unit: Toxicology and Chemical Substances. European Chemicals Bureau April 1999. ECB/TM/26 rev 7 ISPRA Italy (1999).

29 Maxim LD, Hadley JG, Potter RM, Niebo R: The role of fiber durability/biopersistence of silica-based synthetic vitreous fibers and their influence on toxicology. *Regul. Toxicol. Pharmacol.* 46(1), 42–62 (2006).

30 Mitchev K, Dumortier P, De Vuyst P: 'Black spots' and hyaline pleural plaques on the parietal pleura of 150 urban necropsy cases. *Am. J. Surg. Pathol.* 26(9), 1198–1206 (2002).

31 Muller KM, Schmitz I, Konstantinidis K: Black spots of the parietal pleura: morphology and formal pathogenesis. *Respiration* 69(3), 261–267 (2002).

32 Dodson RF, Williams MG, Jr, Corn CJ, Brollo A, Bianchi C: Asbestos content of lung tissue, lymph nodes, and pleural plaques from former shipyard workers. *Am. Rev. Respir. Dis.* 142(4), 843–847 (1990).

33 Kohyama N, Suzuki Y: Analysis of asbestos fibers in lung parenchyma, pleural plaques, and mesothelioma tissues of North American insulation workers. *Ann N Y Acad. Sci.* 643, 27–52 (1991).

34 Boutin C, Dumortier P, Rey F, Viallat JR, De Vuyst P: Black spots concentrate oncogenic asbestos fibers in the parietal pleura. Thoracoscopic and mineralogic study. *Am. J. Respir. Crit. Care Med.* 153(1), 444–449 (1996).

35 Ryman-Rasmussen JP, Cesta MF, Brody AR *et al.*: Inhaled carbon nanotubes reach the subpleural tissue in mice. *Nat. Nanotechnol.* 4(11), 747–751 (2009).

▪ **Reports the distal and subpleural deposition of carbon nanotubes in the lungs of mice after a single inhalation exposure; suggests the ability of carbon nanotubes to migrate to the pleural space.**

36 Ryman-Rasmussen JP, Cesta MF, Brody AR *et al.*: Inhaled carbon nanotubes reach the subpleural tissue in mice. *Nat. Nanotech.* 4, 747–751 (2009).

37 Shinohara H: Distribution of lymphatic stomata on the pleural surface of the thoracic cavity and the surface topography of the pleural mesothelium in the golden hamster. *Anat. Rec.* 249(1), 16–23 (1997).

38 Parungo CP, Colson YL, Kim SW *et al.*: Sentinel lymph node mapping of the pleural space. *Chest* 127(5), 1799–1804 (2005).

39 Davis JG, Addison J, Bolton RE, Donaldson K, Jones AD, Smith T: The pathogenicity of long versus short fiber samples of amosite asbestos administered to rats by inhalation and intraperitoneal injection. *Br. J. Exp. Pathol.* 67, 415–430 (1986).

▪ **Landmark study comparing the pathogenicity of long and short asbestos using two routes of exposure – inhalation and intraperitoneal injection – and demonstrating the markedly greater potential of long fibers to cause fibrosis, pulmonary tumors and mesothelioma.**

40 Berman DW, Crump KS, Chatfield EJ, Davis JM, Jones AD: The sizes, shapes, and mineralogy of asbestos structures that induce lung tumors or mesothelioma in AF/HAN rats following inhalation. *Risk Anal.* 15(2), 181–195 (1995).

41 Cullen RT, Searl A, Miller BG, Davis JM, Jones AD: Pulmonary and intraperitoneal inflammation induced by cellulose fibers. *J. Appl. Toxicol.* 20(1), 49–60 (2000).

42 Kane AB, Macdonald JL, Moalli PA: Acute injury and regeneration of mesothelial cells produced by crocidolite asbestos fibers. *Am. Rev. Respir. Dis.* 133, A198–A198 (1986).

43 Moalli PA, Macdonald JL, Goodglick LA, Kane AB: Acute injury and regeneration of the mesothelium in response to asbestos fibers. *Am. J. Pathol.* 128, 426–445 (1987).

▪▪ **Examined the mesothelial response to intraperitoneal injection of asbestos fibers and advanced the hypothesis that it is the size of the lymphatic stomata on the peritoneal surface of the diaphragm that accounts for the selective accumulation of long fibers and the subsequent inflammatory response.**

44 Donaldson K, Addison J, Miller BG, Cullen RT, Davis JG: Use of the short-term inflammatory response in the mouse peritoneal- cavity to assess the biological-activity of leached vitreous fibers. *Environ. Health Perspect.* 102, 159–162 (1994).

45 Wegner G: Chirurgische Bemerkungen uber die Peritonealhohle, mit besonderer Berucksichtigung der Ovariotomie. *Arch Klin Chir* 20, 51–145 (1877)

46 Whitaker D, Papadimitriou JM, Walters MN: The mesothelium: a histochemical study of resting mesothelial cells. *J. Pathol.* 132(3), 273–284 (1980).

47 Tsilibary EC, Wissig SL: Absorption from the peritoneal cavity: SEM study of the mesothelium covering the peritoneal surface of the muscular portion of the diaphragm. *Am. J. Anat.* 149(1), 127–133 (1977).

48 bu-Hijleh MF, Habbal OA, Moqattash ST: The role of the diaphragm in lymphatic absorption from the peritoneal cavity. *J. Anat.* 186(Pt 3), 453–467 (1995).

49 Ettarh RR, Carr KE: Ultrastructural observations on the peritoneum in the mouse. *J. Anat.* 188(Pt 1), 211–215 (1996).

50 Mutsaers SE, Prele CM, Brody AR, Idell S: Pathogenesis of pleural fibrosis. *Respirology* 9(4), 428–440 (2004).

51 Poland CA, Duffin R, Kinloch I *et al.*: Carbon nanotubes introduced into the abdominal cavity of mice show asbestos-like pathogenicity in a pilot study. *Nat. Nanotechnol.* 3(7), 423–428 (2008).

▪▪ **Used the peritoneal model of mesothelium exposure and showed for the first time that multiwalled carbon nanotubes can produce asbestos-like, length-dependent inflammogenic and fibrotic responses.**

52 Sureshkumar V, Paul B, Uthirappan M *et al.*: Proinflammatory and anti-inflammatory cytokine balance in gasoline exhaust induced pulmonary injury in mice. *Inhal. Toxicol.* 17(3), 161–168 (2005).

53 Donaldson K, Borm PJ, Castranova V, Gulumian M: The limits of testing particle-mediated oxidative stress *in vitro* in predicting diverse pathologies; relevance for testing of nanoparticles. *Part. Fiber Toxicol.* 6(1), 13 (2009).

54 Donaldson K, Stone V, Seaton A, Tran L, Aitken R, Poland C: Induction of mesothelioma in $p53^{+/-}$ mouse by intraperitoneal application of multi-wall carbon nanotube. *J. Toxicol. Sci.* 33(3), 385–388 (2008).

55 Yamashita K, Yoshioka Y, Higashisaka K *et al.*: Carbon nanotubes elicit DNA damage and inflammatory response relative to their size and shape. *Inflammation* 33(4), 276–280 (2010).

56 Muller J, Delos M, Panin N, Rabolli V, Huaux F, Lison D: Absence of carcinogenic response to multiwall carbon nanotubes in a 2-year bioassay in the peritoneal cavity of the rat. *Toxicol. Sci.* 110(2), 442–448 (2009).

57 Kane AB: Mechanisms of mineral fiber carcinogenesis. *IARC Sci. Publ.* (140), 11–34 (1996).

Website

101 Nanotechnology: Nanofibers: Technologies and Developing Markets www.bccresearch.com/report/NAN043A.html

2. **Schinwald A**, Murphy FA, Jones A, MacNee W, Donaldson K. **Graphene-based nanoplatelets: a new risk to the respiratory system as a consequence of their unusual aerodynamic properties**. ACS Nano. 2012 Jan 24;6(1):736-46.

Graphene-Based Nanoplatelets: A New Risk to the Respiratory System as a Consequence of Their Unusual Aerodynamic Properties

Anja Schinwald,[†] Fiona A. Murphy,[†] Alan Jones,[‡] William MacNee,[†] and Ken Donaldson[†,*]

[†]Centre for Inflammation Research, Queen's Medical Research Institute, MRC/University of Edinburgh, 47 Little France Crescent, Edinburgh EH16 4TJ U.K. and [‡]Institute of Occupational Medicine, Research Avenue North, Riccarton, Edinburgh EH14 4AP U.K.

ABSTRACT

Graphene is a new nanomaterial with unusual and useful physical and chemical properties. However, in the form of nanoplatelets this new, emerging material could pose unusual risks to the respiratory system after inhalation exposure. The graphene-based nanoplatelets used in this study are commercially available and consist of several sheets of graphene (few-layer graphene). We first derived the respirability of graphene nanoplatelets (GP) from the basic principles of the aerodynamic behavior of plate-shaped particles which allowed us to calculate their aerodynamic diameter. This showed that the nanoplatelets, which were up to 25 μm in diameter, were respirable and so would deposit beyond the ciliated airways following inhalation. We therefore utilized models of pharyngeal aspiration and direct intrapleural installation of GP, as well as an *in vitro* model, to assess their inflammatory potential. These large but respirable GP were inflammogenic in both the lung and the pleural space. MIP-1α, MCP-1, MIP-2, IL-8, and IL-1β expression in the BAL, the pleural lavage, and cell culture supernatant from THP-1 macrophages were increased with GP exposure compared to controls but not with nanoparticulate carbon black (CB). *In vitro*, macrophages exposed to GP showed expression of IL-1β. This study highlights the importance of nanoplatelet form as a driver for *in vivo* and *in vitro* inflammogenicity by virtue of their respirable aerodynamic diameter, despite a considerable 2-dimensional size which leads to frustrated phagocytosis when they deposit in the distal lungs and macrophages attempt to phagocytose them. Our data suggest that nanoplatelets pose a novel nanohazard and structure-toxicity relationship in nanoparticle toxicology.

KEYWORDS: graphene nanoplatelets · aerodynamic diameter · lung · pleura · inflammation · phagocytosis · cytokine activation · inflammasome · ROS

Graphene, a two-dimensional (2D) crystalline material comprising a single layer of carbon atoms tightly packed into a honeycomb lattice has recently been identified[1] and has attracted substantial scientific interest due to its unique intrinsic properties. However, the novel platelet-like shape has drawn our attention to the toxicology of these emerging materials. Unintentional occupational or environmental exposure to graphene-based materials during manufacturing or intentional exposure *via* biomedical applications are likely with their increasing development and use. Thus far, the information on the inhalation toxicity of graphene nanoplatelets (GP) or platelet-shaped particles in general is very limited.[2] Nanoplatelets may pose an unusual risk to the lungs and the pleural space because of their aerodynamic properties. Deposition in the respiratory tract is determined by the aerodynamic diameter (Dae) which is defined as the diameter of a sphere of unit density with the same terminal settling velocity as the particle itself.[3] The respiratory or pulmonary fraction denotes the size fraction of particles, <5 μm Dae, that deposit beyond the ciliated airways where alveolar macrophages are the main clearance mechanism, and is considered to pose the highest risk in health terms. Sanchez *et al.* recently calculated the deposition fraction of graphene nanoplatelets with different lateral dimensions ranging from 0.001 to 100 μm in the nasopharyngeal, tracheobronchial, and alveolar region either moving along or perpendicular to the polar axis.[2] This theoretical calculation revealed that there would be substantial deposition of such nanoplatelets throughout the respiratory tract. Normally alveolar macrophages only encounter compact particles elutriated by transit through the ever-narrowing airways of the lung, which they can fully ingest. Fibres are a case where an "accident of aerodynamics" means that very long fibers, if they are thin, can penetrate to the distal lung where macrophages fail to fully engulf the long fibers leading to frustrated phagocytosis and inflammation.[4] Because of their

* Address correspondence to ken.donaldson@ed.ac.uk.

Received for review November 2, 2011 and accepted December 23, 2011.

Published online December 23, 2011
10.1021/nn204229f

nanoscale dimensions and thinness, nanoplatelets have a much lower Dae than would be expected from their maximum diameter.[2] Attempted uptake of platelet-shaped particles by macrophages in the alveolar region could result in frustrated phagocytosis, inflammation, failed clearance (leading to retention and accumulation of an od dose) and translocation of nanoplatelets to the pleural space.

The lung and the pleural space are key target tissues for diseases related to fiber-shaped particles, for example, asbestos. Exposure to asbestos fibers in poorly regulated workplaces caused a worldwide epidemic of a range of lung and pleural pathologies which include lung fibrosis, lung cancer, pleural plaques, pleural effusion, and pleural mesothelioma.[5] The pleural mesothelium has proven to be uniquely sensitive to fibers. The exact mechanism by which long, biopersistent fiber-shaped particles cause their harmful effects is partially understood and involves a sequence of events including retention of long fibers in the lung due to failed clearance by alveolar macrophages, frustrated phagocytosis, and recruitment of inflammatory cells to the site of fiber retention. Following translocation to the pleura there is retention of longer fibers at stomata at the parietal pleura, inducing inflammation and prolonged interaction between fibers and mesothelial cells. These events culminate in the development of lung and pleural diseases after exposure to long biopersistent fibers.[6,7]

We used a model of pharyngeal aspiration and direct intrapleural injection[7] of the GP to assess the acute and sustained inflammatory response of the lung and the pleural space, respectively. The approach of direct intrapleural injection is justified on the basis that a fraction of all inhaled particles and fibers that deposit in the peripheral lung translocate into the pleural space.[8−10] We do note however that translocation of GP from the distal lung region to the pleural space has yet to be shown. As a compact nanoparticle control for comparison with GP, we used nanoparticulate carbon black (CB) which is also composed of graphene sheets that are present as disjointed layers.[11] We hypothesized that it was the shape in which the graphene was presented that was driving the activity, and that respirable CB would be readily cleared *via* alveolar macrophages from the airspaces and *via* stomata from the pleural space to the mediastinal lymph nodes. In contrast, GP, exceeding the size for complete phagocytosis, would be retained in the lung and, after translocation to the pleural space, would be too large to negotiate the stomata in the parietal pleura and so would initiate inflammation. *In vitro* models were used to elucidate the mechanism leading to inflammation after interactions between GP and macrophages. We assessed the inflammatory potential of GP *via* indicators such as frustrated phagocytosis, cytokine release, and the involvement of the NALP3 inflammasome.

TABLE 1. Characteristics and Specifications of CB and GP[a]

	CB	GP
Morphology	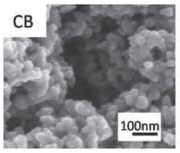	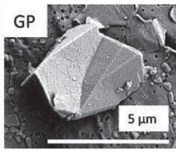
Projected diameter [µm] (mean ± s.e.m)	0.01 ± 0.01	5.64 ± 4.56
Layer number	0	1-10
Surface area [m^2/g]	253.9	~100
Density [g/cm^3]	~1.9	~2
EPR [Arbitrary Units]	451.3±52.2	867.3±77.5
Source	Evonik Degussa GmbH	Cheaptubes.com

[a] Morphology of materials by scanning electron microscopy (SEM). SEM of GP confirms morphology of the platelet shape. EPR measurement to determine generation of oxygen-centred free radicals. Surface area of CB from Donaldson *et al.*[12]

RESULTS

Characterization of Graphene Nanoplatelets. Characteristics and specifications of CB and GP are summarized in Table 1. Nanoparticulate carbon black (CB) and layered (1−10 layer) graphene nanoplatelet (GP) morphology were examined using scanning electron microscopy (SEM) (Table 1). Electron paramagnetic resonance (EPR) measurements were performed to determine the generation of oxygen-centered free radicals of CB and GP. Results were compared to one another and to a positive Pyrogallol (benzene-1,2,3-triol) control, a spontaneous superoxide anion generator with Tempone H used as a spin trap. Both CB and GP caused a significant increase in free radical generation with GP production increased by 2-fold compared to CB (Table 1). The concentration of soluble metals was measured for CB and GP and showed that both samples possess negligible amounts of soluble contaminating metals that would not be biologically active (Supporting Information Table 1).

Aerodynamics of Nanoplatelets—Calculation of the Aerodynamic Diameter. The gravitational settling speed of a particle is determined by the opposing effects of the gravitational force and the aerodynamic resistance. The aerodynamic drag force depends on the shape and orientation of the particle with respect to its direction of motion. A plate-like particle with uniform

thickness settles under gravity with orientation perpendicular to its direction of motion. If it is not a uniform thickness, it might behave like a spear with a weighted tip (if one edge is relatively heavy) or it might be stable in the perpendicular orientation if the extra weight is central. By taking the gravitational force, the aerodynamic resistance and the circular plate-like shape of a particle into account we derived an expression for the aerodynamic diameter of a plate-like particle as

$$d_{ae} = \sqrt{\frac{9\pi}{16}\frac{\rho}{\rho_0} d_{proj} t}$$

d_{ae} = aerodynamic diameter t = platelet thickness d_{proj} = projected diameter ρ_0 = unit density ρ = density

Using this equation, we can estimate the aerodynamic diameter for plate-like-particles of given dimensions. The size of GP was measured using SEM and light microscopy images and plotted as percentage of GP per projected area diameter in the sample (Tables 1 and 2). The GP consist of several sheets of graphene with a thickness of approximately 10 nm each, therefore their thickness increases to around 0.1 μm, depending on their dispersion. This information was used to calculate the Dae of GP used in this study and shows that they are within the size range of the respirable fraction (Table 2). Full derivation of the Dae equation can be found in the Supporting Information.

In Vivo. *Acute Pulmonary Inflammatory Response to GP.* To assess the hazard of GP to the lungs, GP were deposited in the lungs by pharyngeal aspiration at a dose of 50 μg per mouse. At 24 h postexposure the total number of bronchoalveolar lavage (BAL) cells was increased significantly in GP-exposed mice compared to vehicle control and mice aspirated with CB (Figure 1A). This increase in cell number was mainly due to an increase in polymorphonuclear leucocytes (PMN), mainly neutrophils and eosinophils in the lavage fluid (Figure 1A). The membrane leakage from cells in BAL was also significantly increased in GP-treated mice (Figure 1B). Concentration of the pro-inflammatory cytokines MCP-1, MIP-1α, MIP-1, and IL-1β were measured in the BAL fluid. All cytokines were elevated after GP treatment compared to VC and CB, however only MIP-2 reached a significant difference (Figure 1C). Histological sections of lungs from mice treated with GP showed granulomatous lesions in the bronchiole lumen and near the alveolar region. VC and CB had a normal histology (Figure 1D) (see Supporting Information for gross pathology of the entire lung section Figure I). The response to CB/GP exposure was investigated one week following exposure and continued to show an increased inflammatory response to GP compared to CB and VC treated animals which was, however, significantly less compared with response at 24 h postaspiration (Supporting Information, Figure II).

TABLE 2. Size Distribution of GP in the Sample Expressed as Percentage of GP per Projected Area Diameter, Aerodynamic Diameter Dae of GP at Various Projected Diameters and a Thickness (t) of 0.1 μm

	projected area	aerodynamic
% of GP	diameter (d_{proj}) [μm]	diameter [μm] (t = 0.1 μm)
57.4	5	1.33
32.9	10	1.88
6	15	2.30
2.8	20	2.66
0.6	25	2.97
0.3	30	3.26

Acute Pleural Response to GP. The acute pleural inflammatory response was measured 24 h after intrapleural injection of CB and GP. The pleural space was lavaged and a total and differential cell count was performed. Mice exposed to GP showed a significant increase in total cell number compared to vehicle control (Figure 2A) with significant increases in the number of PMN which mainly comprised eosinophils and neutrophils (Figure 2A). Chemokine and cytokine protein levels in the pleural lavage fluid were measured (MCP-1, MIP-1α, MIP-1, and IL-1β) showing that MIP-1α was significantly increased (Figure 2B). Cytospin preparation of lavaged cells showed complete uptake of CB into pleural macrophages (Figure 2C); however, GP, due to their shape and size, could not be fully phagocytosed leading to frustrated phagocytosis. Rosette-like formations of macrophages around GP are a characteristic indicator of frustrated phagocytosis where more than one macrophage surround a large nanoplatelet and share the attempt to phagocytose it (Figure 2C). Histological examination of the parietal pleura showed areas of histiocytic aggregates in mice treated with GP (Figure 2D). The lesion area along the mesothelium was measured and was significantly increased compared to VC and CB at the 24 h time point (VC/CB = 0 $\mu m^2/\mu m$; GP = 19.5 $\pm$ 11.6 $\mu m^2/\mu m$) (n = 3). GP were associated with inflammatory cells along the parietal pleura. The acute inflammatory response has largely resolved 1 week after exposure as can be seen by the decrease in total cell number to a quarter of the number found at 24 h (Supporting Information, Figure III).

Clearance of CB and GP from the Pleural Space to Cranial Mediastinal Lymph Nodes. CB particles were cleared from the pleural space after direct pleural injection *via* stomata to the cranial mediastinal lymph nodes as can be seen in histological lymph node sections after 24 h and 1 week (Figure 3A,B). Twenty-four hours after GP exposure, a few particles could be found in the lymph nodes which indicates prolonged retention in the pleural space (Figure 3A). After 1 week GP have been cleared from the pleural space; however, the amount of clearance appears to be much less compared to that of CB (Figure 3B). Quantification of

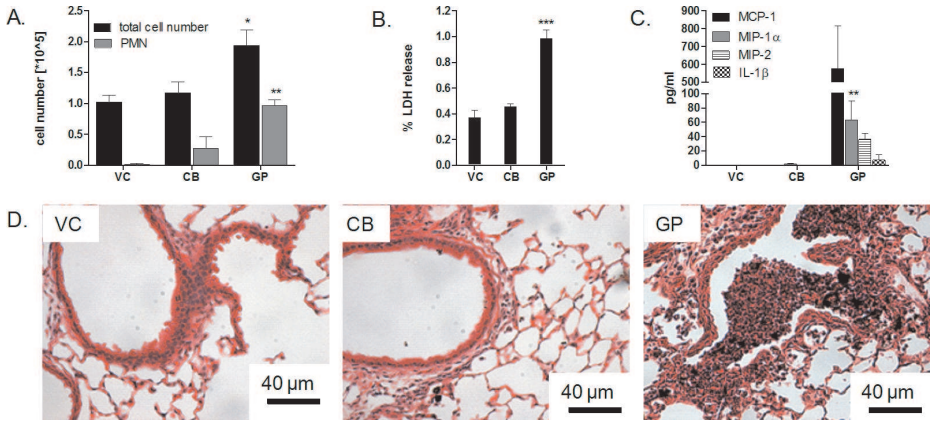

Figure 1. Pulmonary inflammatory response to CB and GP 24 h postaspiration. (A) Total cell number and total granulocyte number in the lavage fluid following exposure to CB and GP. (B) Measurement of the membrane leakage as LDH levels in the lavage fluid. (C) Concentration of the chemokines MCP-1 and MIP-1α as well as cytokines MIP-1 and IL-1β in BAL. (∗) $P < 0.05$, (∗∗) $P < 0.01$, (∗∗∗) $P < 0.001$ compared to vehicle control. (D) Lung histology 24 h postaspiration. Ganulomatous lesion was present in the bronchiolar lumen after GP exposure but normal lung pathology was seen in the CB treated mice which is comparable to VC.

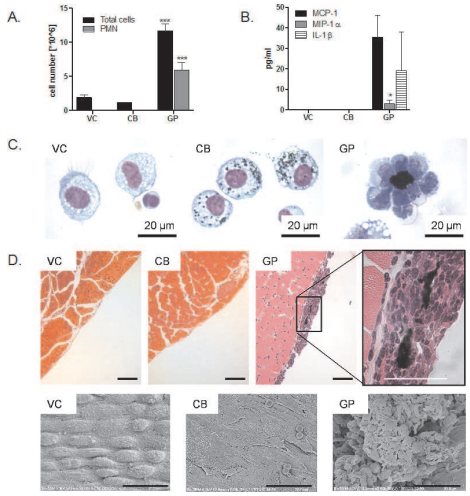

Figure 2. Pleural inflammatory response to CB and GP 24 h post-treatment. (A) Total cell number and total granulocyte number after pleural injection of 5 µg of CB and GP. (B) Concentration of the chemokines MCP-1 and MIP-1α as well as cytokines IL-1β in pleural lavage. (∗) $P < 0.05$, (∗∗∗) $P < 0.001$ compared to vehicle control. (C) Representative images of pleural macrophages from untreated mice and mice treated with CB and GP. Intrapleural injection of GP led to the formation of rosette-like cell/particle aggregations indicating frustrated phagocytosis. (D) Sections of chest wall were stained with both haematoxylin and eosin (H&E) at 24 h postinjection to identify an inflammatory response on the mesothelial cell layer of the parietal pleura ($n = 3$). Pleural thickening can be seen after GP treatment, with an insert highlighting GP associated with inflammatory cells. Scale bar = 100 µm, insert = 20 µm. SEM micrographs show aggregations of inflammatory cells after GP treatment but normal mesothelial cell layer after VC and CB treatment (Figure 2 bottom panels). Scale bar = 20 µm.

the GP size cleared to the lymph nodes could not be performed because of the difficulty of identifying individual platelets of GP in the section.

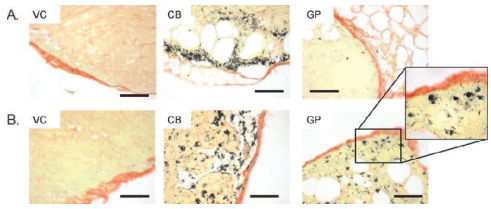

Figure 3. Clearance of CB to cranial mediastinal lymph nodes and prolonged retention of GP in the pleural space. Histological sections of lymph nodes stained with Picrosirius red 24 h (A) and 1 week (B) postinjection. CB was cleared to the nodes after 24 h, however GP was retained longer in the pleural space. Scale bar = 40 µm, $n = 4$ mice per treatment group with 2 sequential sections per lymph node.

In Vitro. *Characterization of Cell/Particle Interaction.* The interaction of differentiated THP-1 cells with graphene platelets was examined *via* scanning electron microscopy (SEM) and transmission electron microscopy (TEM). The SEM images revealed that GP exceeding a size of approximately 15 µm projected diameter could not be fully phagocytosed by THP-1 cells and therefore led to frustrated phagocytosis (Figure 4A,B). Complete uptake of smaller GP could be imaged using TEM as shown in Figure 4B.

GP-Mediated Loss of Membrane Integrity of THP-1 Macrophages and Depletion of Reduced Glutathione. Release of LDH was used as an indicator of cell viability and measured after 24 h exposure of THP-1 macrophages to CB and GP. A concentration range of 1 µg/cm^2, 5 µg/cm^2, and 10 µg/cm^2 of GP was used, and concentrations of 5 µg/cm^2 and higher significantly increased LDH release while CB exposure at the same concentrations did not (Figure 5A). An explanation for loss of membrane integrity could be the generation of reactive oxygen species and so the levels of free thiol groups, predominantly GSH, were measured as an

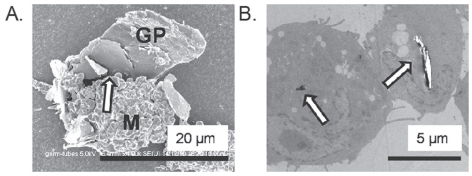

Figure 4. Cell/particle interactions to examine the uptake of GP on the surface using SEM and inside of the cells using TEM following 4 h exposure to GP. (A) SEM and (B) TEM of GP-exposed THP-1 cells. (A) SEM showing the attempted uptake of a GP by THP-1 macrophages (M). The arrow indicates the lip of the unclosed phagosome showing incomplete internalization of the GP producing frustrated phagocytosis. (B) TEM shows that small GP (≤5 μm) could be entirely internalized (arrows).

indicator for oxidative stress, using the fluorescence probe, monobromobimane. After 4 h of GP exposure the levels of free thiol groups were significantly lowered compared to the vehicle control (Figure 5B). CB did cause a significant change in the levels of free thiol groups.

Activation of the NALP3 Inflammasome and Pro-inflammatory Cytokines after GP Exposure in Vitro. We measured the concentration of IL-1β in the supernatant of THP-1 cells exposed for 24 h to either LPS, CB (1 and 5 μg/cm^2), or GP (1, 5, and 10 μg/cm^2). LPS as well as all concentrations of GP lead to a significant increase in IL-1β expression, whereas CB treatment had no effect (Figure 6A). To investigate if the attempt to phagocytose GP was involved in upregulating IL-1β expression, phagocytosis was inhibited *via* disruption of actin filaments using cytochalasin D. The inhibition of phagocytosis significantly reduced IL-1 β expression at all concentrations of GP; however, cytochalasin D had no effect on the level of IL-1 β released by THP-1 cells exposed to LPS since its action is not dependent on phagocytic processes (Figure 6A). Additional mechanisms involved in the activation of the NALP3 inflammasome are decreased intracellular K+ linked to an efflux of K+ and generation of ROS. By blocking the efflux of K+ *via* increasing extracellular K+ concentration and the inhibition of generation of ROS *via* inhibition of NADPH oxidase using DPI, the expression of IL-1β was significantly reduced in both LPS and GP exposed cells (Figure 6A). To further assess which cytokines were involved in acute inflammation after particle exposure, a cytokine bead array was performed. The selected panel of cytokines was TNF, IL-6, IL-8, IL-1β, MCP-1, RANTES, MIP-1α, basic FGF, IL-13 and TGF-β. MCP-1, IL-1, MIP-1α, and IL-1β were all significantly increased after GP exposure with no effect of CB exposure on these cytokines (Figure 6B).

DISCUSSION

Although Duch *et al.*[12] have studied the biocompatibility of GP in the mouse lung from the point of view of biomedical/therapeutic application of GP, we believe that ours is the first peer-reviewed publication to address the public/occupational health hazard of GP in

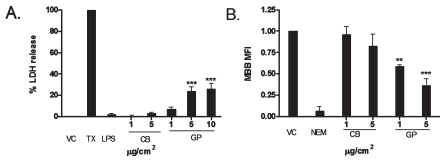

Figure 5. Determination of LDH release and the decrease in free thiol groups as indications of cell toxicity and oxidative stress. (A) Significant release of LDH after 24 h exposure to GP while CB had no significant effect on LDH. Data were expressed as mean ± s.e.m, n = 5. (B) Mean fluorescence intensity (MFI) of monobromobimane (MBB) as indicator for levels of free thiol groups. GP exposure significantly reduced the MFI of MBB at all concentrations measured. Data were expressed as mean ± s.e.m, n = 4. (**) P < 0.01, (***) P < 0.001 compared to vehicle control.

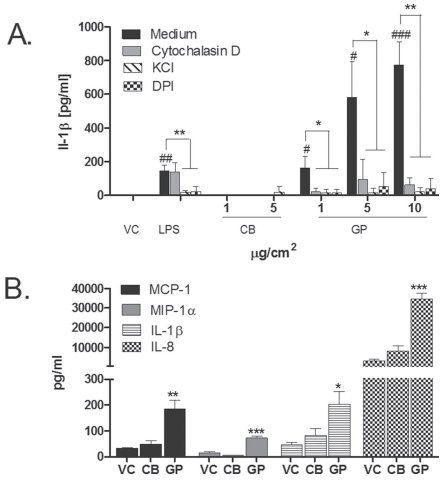

Figure 6. Data providing evidence consistent with activation of the Nalp3 inflammasome, and pro-inflammatory cytokine expression on GP, CB, and LPS treatment. (A) IL-1β concentration in the supernatant of THP-1 cells exposed to LPS, CB, and GP. LPS (1 μg/mL) as well as GP at all concentrations led to a significant increase in IL-1β expression, whereas CB treatment had no effect. Phagocytotic uptake of GP was inhibited by cytochalsin D which led to a significant reduction of IL-1β expression in GP exposed cells. This effect was not observed in LPS treated cells. IL-1β expression after LPS and GP exposure was significantly reduced by inhibition of K+ efflux and diphenylene iodonium (DPI), an NADPH oxidase inhibitor. Data were expressed as mean ± s.e.m, n = 4. (B) Four cytokines (MCP-1, IL-8, IL-1β and MIP-1α) out of 11 tested were significantly upregulated after a 24 h GP exposure. CB treatment did not lead to a significant increase in any of the cytokines measured. Data were expressed as mean ± s.e.m, n = 3. (*) P < 0.05, (**) P < 0.01, (***) P < 0.001 compared to vehicle control. (#) p < 0.05, (##) p < 0.01, (###) p < 0.001 compared to vehicle control.

rat lung from the point of view of aerodynamic deposition and the cellular responses in lung. We further elucidate the mechanism leading to GP-induced inflammation, using *in vitro* methods and a macrophage cell line. Nanoparticulate carbon black (CB) was used as a compact graphene nanoparticulate control and was aspirated at a mass dose found to be noninflammatory in previous studies.[13]

The atypical platelet-like shape of the GP particles attracted our attention as they may pose a new risk to the respiratory system after inhalation. Nanoplatelets exhibit specific material properties that could be important for biological interactions. Among these are surface area, surface chemistry, and lateral dimensions. Owing to their platelet shape, they have an exceptionally high surface area per unit mass which is much greater than that of graphite and of carbon nanotubes.[14] The lateral dimensions of a material play an important role in biological interaction and determine the nature and consequences of cellular uptake and subsequent clearance.

Thus far, in the field of particle toxicology, the fiber pathogenicity paradigm has been stated as the most robust structure–activity relationship, and it has frustrated phagocytosis of long fibers as the center of the pathobiological mechanism.[15] This structure–activity relationship focuses on fibers that are long, thin, and biopersistent, having an aerodynamic diameter that makes them respirable.[16] This structure–activity relationship however does not take sheet/platelet shape particles into account and therefore has to be reconsidered in the light of these new materials.

To be most harmful to the respiratory system, particles require an aerodynamic diameter small enough to penetrate beyond the ciliated airways, that is, they need to be respirable. Deposition occurs under the effects of gravitational force, aerodynamic resistance, interception, and impaction which together determine the site of deposition in the lungs.[17] The aerodynamic diameter is the index that is calculated from these parameters and determines the respirability of a particle and the site of deposition.[3] Plate-shaped particles are not common in industry, and so exposure is limited, but does occur in the talc and nanoclay industries where there are plate-like particles.[18,19] However the nanotechnologies have the potential to produce a range of different nanoplatelet-shaped particles. In this study we calculated the aerodynamics of commercially available nanoplatelets by taking into consideration the gravitational settling force and aerodynamic resistance perpendicular and parallel to motion, and utilized an equation derived from the tenets of aerosol physics to estimate the aerodynamic diameter of platelet-like particles of the dimensions evident in our GP sample. This demonstrated that a platelet-shaped particle with a projected area diameter of 25 μm and a thickness of 0.1 μm has an aerodynamic diameter of about 3 μm, which is within the respirable size fraction of particles that deposit beyond the ciliated airways. These calculations are in line with the aerodynamic sizes reported recently in Sanchez *et al.*[2] which also showed images suggesting that GP might lead to frustrated phagocytosis in macrophages.

On the basis of our determination that the GP samples used within these experiments were all respirable, we assessed the inflammatory potential of GP. Mice were exposed *via* pharyngeal aspiration and pleural injection to CB and GP for 24 h and 1 week. CB and GP are composed of the same material, graphene, and were both respirable but differed in their shape, which resulted in very different effects in the lung and the pleural space. CB did not cause any inflammatory response and was comparable to vehicle control in all assays, whereas GP caused extensive recruitment of inflammatory cells, including macrophages and granulocytes into the lung and pleural space after 24 h exposure. Inflammation waned 1 week post-exposure but continued to be significantly greater in total cells and granulocyte number than the vehicle control. The response to GP in the lung and the pleural space was similar to the response seen after aspiration exposure and intrapleural injection of long MWCNT using the same method.[7,20] Recent studies revealed that long CNT, due to their fiber-like structure similar to asbestos show an asbestos like pathogenicity and raised concern that exposure to CNT may lead to mesothelioma.[21] Our results show that long fibers are not the only extended particles with low Dae that are able to induce inflammation in the lung and the pleural space, but that platelet like particles with a low Dae have similar potency. The induction of acute and chronic inflammation is regulated by the release of cytokines and chemokines that invoke leukocyte recruitment. Analysis of BAL and pleural lavage fluid revealed elevated levels of MCP-1, MIP-1α, IL-8, and IL-1β after GP but not CB. MCP-1 and MIP-1α have been reported to contribute to the initiation and outcome of inflammation in the lung and in pulmonary alveolar macrophages after exposure to stone-wool and crocidolite asbestos.[22] MCP-1 has further been identified to play a major role in lung leukocyte infiltration[23] and serves as a marker for the diagnosis of malignant pleural mesothelioma.[24]

The main mechanisms by which long, fiberlike particles cause harmful health effects in the pleura are the failed clearance of longer fibers through stomata in the parietal pleura and subsequent retention in the pleural space, frustrated phagocytosis of pleural macrophages, and the involvement of the NALP3 inflammasome.[25] We therefore investigated the retention of GP in the pleural space by examining the most caudal, posterior intercostal region of the parietal pleura, documented to have the highest abundance of stomata.[7,26] Interstitial incorporation of asbestos fibers and coal dust occurs in these areas and so they are described as potential starting points for the development of mesothelioma.[11] In support of this hypothesis we observed extensive accumulation of inflammatory cells in these areas on the parietal pleura where GP were retained. To determine the clearance pathway of CB and GP, we examined the particle burden in cranial mediastinal lymph nodes (LN). Pleural fluid is drained

through the parietal stomata *via* the lymphatic system to LN.[7,27] CB was readily cleared to the mediastinal lymph nodes after 24 h as could be seen in histological sections. In comparison, few GP had reached the LN after 24 h, confirming retention of GP in the pleural space. After 1 week however, a higher number of GP could be identified in the mediastinal LN sections, which may explain the reduced inflammation seen 1 week after intrapleural exposure. Brakeage of GP into smaller fragments after 1 week could explain the time-dependent clearance of GP to the LNs. We noted that the accumulation of GP in the LN seen at 1 week, while evident, was less than that seen 1 week after CB, suggesting that there is a substantial fraction of the GP dose that remains retained in the pleural space beyond one week.

The role of frustrated phagocytosis, a mechanism by which long fibers produce inflammation, has been examined in a number of studies[28,29] and has been accepted as a contributing mechanism to the toxic effects of long fibers. Due to the extended shape of GP, we hypothesized that the uptake of GP by macrophages could be impaired leading to frustrated phagocytosis. Examination of pleural macrophages in the lavage fluid showed clear signs of frustrated phagocytosis after GP exposure, whereas CB was fully taken up. This took the form of GP incompletely enclosed by macrophages and "rosettes" of up to five or six macrophages surrounding a single large platelet where all of the macrophages are in a state of frustrated phagocytosis.

To further investigate the interaction of macrophages with GP, we treated cells of a differentiated monocytic cell line, THP-1, with GP and examined phagocytosis using scanning electron microscopy (SEM) and transmission electron microscopy (TEM). Frustrated phagocytosis could be observed in SEM images, showing GP only partly phagocytosed by macrophages. TEM revealed that only small GP ($\leq 5\ \mu$m) were fully taken up. The membrane integrity of THP-1 cells after 24 h GP exposure was also significantly impaired in a dose-dependent manner. We also determined the generation of oxygen-centered free radicals by GP and CB using EPR. CB as well as GP generated a significant amount of free radicals, and GP generated approximately double that produced by CB. Therefore free radicals are possibly involved in the pro-inflammatory effects seen *in vivo* and *in vitro* with GP compared to CB, although it is not likely that intrinsic free radical activity explains the extra potency of GP. We went on to determine the oxidative status of THP-1 cells by measuring the decrease in free thiol groups, mainly reduced glutathione after CB and GP treatment. Glutathione/glutathione disulfide is the major redox couple in cells, and its tight regulation is critical in antioxidant defense and regulation of cellular events.[30] Glutathione is the most abundant low-molecular-weight thiol, and the loss of free thiol can be measured *via* loss of monobromobimane fluorescence.[30] Exposure of THP-1 cells to GP lead to a significant decrease in free thiol groups in a dose-dependent manner. Depletion of the antioxidant defense system by pollutants[31] and respirable fibers[32] has been shown to result in oxidative stress and the activation of transcription factors including NF-κB.[33] NF-κB regulates the transcription of inflammatory genes, including IL-1β, MIP-1α, and MCP-1.[34] We measured a panel of acute-phase cytokines involved in the inflammatory response after exposure of THP-1 cells to CB and GP; 4 out of 11 different cytokines measured, MCP-1, IL-8, IL-1β and MIP-1α, were significantly elevated after GP exposure. The pro-inflammatory cytokine and neutrophil chemotaxin IL-8 has been shown to be elevated in airway epithelial cells and serum[35] as well as alveolar macrophages[36] of asbestos-exposed individuals.[35] IL-1β is known to be upregulated after asbestos, silica, and CNT exposure[37,38] and has been implicated in frustrated phagocytosis and the NALP3 inflammasome activation.[39] The underlying mechanism by which frustrated phagocytosis of long fibers induces acute and chronic inflammation is poorly understood. Recent studies however identified the NALP3 inflammasome complex as an important component of the molecular pathway by which cells sense foreign bodies like asbestos fibers and initiate an inflammatory response. The inflammasome is a multiprotein complex consisting of nucleotide-binding oligomerization domain (NOD)-like receptors (NLR) which is activated *via* damage-associated molecular patterns (DAMPs) and forms a complex with apoptosis-associated speck-like protein containing a caspase-recruiting domain (CARD) and pro-caspase 1. Activation of caspase 1 leads to expression of IL-1β and IL-18, which mediate pro-inflammatory effects.[40] The inflammasome can be activated *via* different pathways including low intracellular potassium concentration[41], reactive oxygen species produced by NALP3 activators *via* NADPH oxidase,[42] frustrated phagocytosis[39] and phagosomal destabilization.[38] Since GP exposure led to an increased production of IL-1β, we explored the possibility that GP promote inflammation by activating the inflammasome pathway. To delineate the GP-induced signaling pathway leading to inflammasome activation, IL-1β production after GP exposure was compared to CB and LPS induced IL-1β release in cell culture medium and medium supplemented with inhibitors for phagocytosis, ROS generation, and potassium efflux. We investigated whether phagocytosis is needed to trigger inflammasome activation by disrupting actin filaments *via* cytochalasin D.[37] Inhibition of phagocytosis significantly reduced IL-1β expression after GP treatment, but had no effect on LPS induced IL-1β production, which is not mediated *via* phagocytosis. We further provided evidence that GP activity is

blocked by inhibiting efflux of K+, which is necessary for NALP3 inflammasome activation. Reduction of IL-1β production was also achieved by inhibition of the NADPH oxidase supporting the hypothesis that ROS are generated *via* phagocytosis of GP through the activation of the reduced form of NADP. We therefore carried out limited studies which, while providing data consistent with activation of the NALP3 inflammasome by GP, require more detailed and extensive studies to confirm this impression.

Collectively, our data show that large nanoplatelets can have a small enough Dae to be respirable and to deposit beyond the ciliated airways where macrophages are the only mode of clearance, but are too large to be completely phagocytosed by macrophages. They, therefore are likely to cause an inflammatory response in the airspaces and be retained, similar to the response seen after long asbestos and other long fiber-like structures[7] (Schinwald *et al*., manuscript under submission). If, like long fibers they are capable of reaching the pleural space, they will be retained there as they will be too big to negotiate the stomata and, with sufficient dose, they will cause pleural inflammation and pleural pathology over time if they are sufficiently biopersistent.

Our study also provides information regarding the mechanism by which the inflammatory response to GP was initiated using *in vitro* models. Four cytokines have been detected to be involved in the onset of inflammation after GP exposure (MIP-1α, MCP-1, IL-8, and IL-1β). While IL-1β may have been activated *via* the NALP3 inflammasome complex, more research is needed to confirm this. We further emphasized the importance of phagocytosis and subsequent ROS generation in the activation of IL-1β release.

We mainly focused on the acute inflammatory reaction in the lung and the pleural space up to 7 days and the data showed a decrease in the severity of inflammation after 7 day treatment which suggests degradation of GP into smaller fragments which could then be cleared *via* alveolar/pleural macrophages. A study of the chronic effects of GP exposure, preferably after inhalation exposure is warranted to investigate biopersistence and effects after inhalation compared to the instillation models used here. In this study we focus on the morphology of the GP, rather than the graphene oxidation state, in regards to pro-inflammatory effects especially frustrated phagocytosis. The argument of frustrated phagocytosis of GP is based on shape rather than chemistry, as is the argument of long fibers-elicited frustrated phagocytosis, which is an issue of fiber length, not composition[6,43] Future studies on different GP samples from different sources should examine the effect of the surface chemistry/oxidation state, which might have an additional effect; however, we consider that any such effect will be in addition to the shape effect.

CONCLUSION

This study highlights the importance of particle shape as a driver for *in vivo* and *in vitro* toxicity and introduces a new shape that may pose an unusual risk to the lungs and the pleural space after inhalation exposure. We suggest that sheet/platelet-shaped particles with nanoscale thickness can be very large in two dimensions but possess a low Dae. Thus they have the potential to cause adverse health effects and therefore warrant further investigation. We further suggest that lateral dimensions are the driving properties in pathological response to GP and that these also require more research. It also seems likely that layer thickness and the subsequent role that this plays in rigidity is a key factor but was not investigated here. On the basis of the above understanding of the probable mechanisms, we suggest that potential risks to humans from graphene platelet exposure could be minimized by manufacturing graphene platelets small enough to be phagocytosed by macrophages. Our initial data also suggest that the GP are not fully biopersistent, and clear slowly to the mediastinal lymph nodes. Further work is needed to determine the extent of GP biopersistence and its impact on pathogenicity.

MATERIAL AND METHODS

Characterization of Nanoparticle Carbon Black (CB) and Graphene Nanoplatelets (GP). Carbon Black (Printex 90) was provided by Evonik Degussa GmbH in Germany. It was used as an amorphous carbon particle control. Graphene nanoplatelets grade 2 (GP) produced by chemical exfoliation were purchased from cheaptubes.com. GP have a surface area of about 100 m^2/g, a density of $\sim$2.0 g/cm^3, an average thickness of approximately 10 nm and an average diameter of 5 μm based on manufacturers description. One of the GP consists of several sheets of graphene, and GP are therefore classified as few-layer graphene. Physical characteristics were determined using light microscopy and scanning electron microscopy (SEM). The levels of endotoxin in the sample suspension were evaluated by the Limuluss Amoebocyte Lysate assay (Lonza) according to manufacturer's description using supernatant of CB and GP suspension to avoid interference of particles with the assay. No endotoxin level were detected in the samples. CB and GP stock solution was prepared at 1 mg/mL in 0.5% BSA/saline for *in vivo* work or cell culture medium without FBS for *in vitro* work and dispersed by sonication in an ultrasonicating water bath at 230 V, 50 Hz, 350W (FB11002, Fisherbrand, Thermo Fisher Scientific, Inc., MA, USA) for 6 h to break up aggregates.

Scanning Electron Microscopy of CB and GP. CB and GP were dispersed in 0.1% BSA (heat-shocked fractionate) (Sigma-Aldrich, Poole, UK)/saline at a concentration 50 μg/mL by ultrsonication. The suspension was filtered onto an Isopore membrane filter (Millipore), dried, and gold sputter coated. Scanning electron microscopy was carried out using a Hitachi S-2600N digital scanning electron microscope (Oxford Instruments, Oxfordshire, UK).

Light Microscopy of CB and GP. For light microscopy images a concentration of 50 μg/mL was used to demonstrate the dispersion of the materials. A 10 μL aliquot of CB or GP solution were mixed with 10 μL of glycerol (Sigma-Aldrich, Poole, UK) to reduce the motion of the GP. The suspension was placed on glass slide and covered with a glass coverslip and sealed.[7] Images were captured at 100× magnification using QCapture Pro software (Media Cybernetics). A total of 300 GP/GP-aggregates were measured according to their projected area diameter by using a graticule. The size was plotted per length category.

Electron Paramagnetic Resonance. CB and GP were diluted to a final concentration of 50 μg/mL in Hanks Balanced Salt Solution (HBSS) (Sigma-Aldrich, Poole, UK) and sonicated for 1 h. HBSS and 1 mM Pyrogallol (Sigma), a known superoxide generator were diluted in Hanks buffer and used as negative and positive controls, respectively. Peroxynitrite, superoxide, and peroxyl radical release were detected using spin trap Tempone-H (Alexis Biochemicals, San Diego, CA). Tempone-H was added to the samples and controls to give a final concentration of 1 mM. EPR spectra were measured after 60 min incubation at 37 °C using the following instrumental conditions: Microwave frequency, 9.39 GHz, magnetic field, 3355 G; sweep width, 55 G; sweep time, 30 s; number of passes, 1; modulation amplitude, 1500 mG; receiver gain, 1E1; phase, 180; microwave frequency, 9.30−9.55 GHz. Intensity values of the highest spectra peak were recorded and graphed against each other (arbitrary units).

ICP−MS Analysis. For quantification of contaminating metals, the supernatant of 1 mg/mL of each sample were analyzed using the technique of inductively coupled mass spectrometry (ICP−MS). The CB and GP suspension was made up in 0.5% BSA/saline to be consistent with experimental conditions. Supernatant was collected from a 1 mg/mL solution of each sample, after overnight mixing, by centrifugation at 13 000 rpm for 30 min. Samples were analyzed by ICP−MS using an Agilent 7500ce (with octopole reaction system), employing an rf forward power of 1540 W and reflected power of 1 W, with argon gas flows of 0.82 L min^{-1} and 0.2 L min^{-1} for carrier and makeup flows, respectively. Sample solutions were taken up into the micromist nebulizer by peristaltic pump at a rate of 0.06 rps (approximately 1.2 mL min^{-1}). The gas flow for the helium mode was 6.5 mL min^{-1}. Skimmer and sample cones were made of nickel. The instrument was operated in spectrum multitune acquisition mode, and five replicate runs per sample were employed. Each mass was analyzed in fully quant mode (three points per unit mass). ^{107}Ag, ^{27}Al, ^{111}Cd, ^{59}Co, ^{52}Cr, ^{63}Cu, ^{56}Fe, ^{55}Mn, ^{60}Ni, ^{208}Pb, and ^{64}Zn were analyzed in "nogas" mode then ^{56}Fe, ^{60}Ni, ^{52}Cr, ^{63}Cu, and ^{66}Zn were further analyzed in helium mode to remove any polyatomic interferences.

In Vivo. *Experimental Animals.* Nine week old female C57BL/6 strain mice (Harlan, UK) were used in this study. Mice were kept in a group size of five in standard caging with sawdust bedding within a pathogen-free Home Office approved facility. Mice were maintained on a normal 12 h light and dark cycle. Prior to the treatment mice were kept for 7 days in the facility to acclimatize. The work was carried out by staff holding a valid UK Home Office personal license under a Home Office approved project license.

Pharyngeal Aspiration and Broncho-Alveolar Lavage. The given particle dose for pharyngeal aspiration was 50 μg per mouse of CB and GP in 0.5% BSA/saline. Vehicle control was 0.5% BSA/saline. Mice were anesthetized with isoflurane and the tongue was gently held in full extension while 50 μL of particle suspension was pipet onto the base of the tongue.[44] The tongue was held extended until at least two breaths were complete. To stimulate inhalation and to induce a gasp reflex the nasal cavities of the mice were covered. Mice were observed until full recovery.

Mice were sacrificed 24 h and 1 week postexposure of a single dose by terminal anesthesia by injection of 0.5 mL of pentobarbitone (200 mg/mL) into the peritoneal cavity followed by exsanguinations *via* the abdominal aorta. After the pleural cavity was lavaged (see Intrapleural Injection and Pleural Lavage section) the thoracic cavity was exposed and the trachea cannulated using a 23 gauge needle and ligated. The lungs were lavaged three times with 800 μL of ice-cold sterile saline. The first lavage was retained separately and the subsequent lavages were pooled.

Intrapleural Injection and Pleural Lavage. Samples were prepared by ultrasonication as described and injected into the pleural cavity of female C57Bl/6 mice (aged 8 weeks) using a sleeve over the tip of a 27G to prevent the needle to pass through the pleural space into the lung. The concentration of each treatment was 50 μg/mL which equates to a single dose of 5 μg per mouse and an injected volume of 100 μL per mouse. Mice were euthanized after 24 h (n = 6) and 7 days (n = 4) by asphyxiation in 100% CO_2. The pleural space was lavaged with three 1 mL washes of sterile saline and kept on ice.

Differential Cell Count/Total Protein and Lactate Dehydrogenase Measurement. To separate the cellular fraction from the supernatant the lavage fluid from BAL and pleural lavage was centrifuged for 5 min at 2000*g* at 4 °C in a Mistral 3000i centrifuge (Thermo Fisher Scientific, Inc., MA, USA). Total cell count was performed using a NucleoCounter (ChemoMetec, 7 A/S, Allerød, Denmark) and cyto-centrifugation with following Diff-Quik staining using Diff-Quik stainset (Dade Behring Gmbh, Marburg, Germany) were prepared for differential cell counts. In the supernatant, membrane integrity using the Cytotoxicity Detection Lactate Dehydrogenase kit (Roche Diagnostics Ltd., Burgess Hill, UK) and protein content using the bicinchoninic acid (BCA) protein assay (Sigma-Aldrich, Poole, UK) were measured following the manufacturer's instructions.

Dissection of Lung, Diaphragm and Chest Wall. For histological examination the lungs and heart were removed on-block and fixed by installation of 10% ice-cold formalin without foregoing lavage and submerged in fixative for a period of 4 h prior to processing. The heart was removed and the lung separated into individual lobes and transferred to 70% ethanol for 24 h. The tissue was embedded in paraffin, sectioned and stained with H&E to show gross pathology and Pico-Sirius Red (PSR) to show collagen deposition. Serial images were taken at 2.5× magnification using QCaputre Pro software (Media Cybernetics, Inc., MD, USA) and seamlessly realigned using Adobe Phtotoshop CS3, version 10.0.1 (Adobe Systems Inc.) to show the entire section of the lungs. Images at 20× magnification were taken to show higher maginification areas of the lung sections.

The diaphragm and the lower right posterior portion of the chest wall, approximately an area of 1 cm × 0.5 cm along the spine was cut out from the mice after lavage, washed in ice-cold saline, and fixed for 4 h in 30% formalin. The tissue was excised from the surrounding tissue and either embedded in paraffin, sectioned, and stained with haematoxylin and eosin (H&E) for gross pathology or prepared for scanning electron microscopy (SEM).

Methodology for Lesion Quantification. Images from chest wall section were taken at 10× magnification using QCapture Pro software (media Cybernetics Inc., MD, USA). Photoshop CS3 (Adobe systems Inc., CA, USA) was used to seamlessly realign the images to give a high resolution image of the large sections of chest wall. To quantify the lesion area per unit chest wall length (mm^2/mm), the length of the each section along the mesothelium and the lesion area was measured using calibrated Image-Pro Plus software (Media Cybernetics Inc., MD, USA).

Scanning Electron Microscopy. Scanning electron microscopy was carried out using a Hitachi S-2600N digital scanning electron microscope (Oxford Instruments, Oxfordshire, UK). Tissue was prepared using tetroxide staining, critical-point dried, and gold sputter coated.

Chemokine and Cytokine Measurement. Chemokines MCP-1 and MIP-1α and cytokines MIP-2 and IL-1β were measured in nondiluted BAL and pleural lavage fluid following the manufacturers' instructions (Quantikine kit of R&D systems).

In Vitro. *Cell Culture.* The immortalized human monocytic cell line THP-1 was used for *in vitro* studies. THP-1 cells were cultured in RPMI media supplemented with 10% heat inactivated FBS, 1% penicillin/streptomycin and 1% L-glutamine (PAA, Austria). Prior to each treatment the cells were differentiated to macrophages using 10 ng/mL phorbol 12-myristate

13-acetate (PMA) (Sigma) for 2 days at 37 °C in 5% CO_2 atm as previously described.[45]

Measurement of Membrane Integrity. The conversion of lactate to pyruvate was detected using the Cytotoxicity Detection Lactate Dehydrogenase kit (Roche Diagnostics Ltd., Burgess Hill, UK) following the manufacturer's instructions. THP-1 cells were seeded in 24-well plates at a density of 1 × 106/mL in 500 μL medium containing 10% FBS and differentiated as described above. Prior to treatment the cells were washed with PBS and 500 μL of 1% FBS RPMI medium was added to each well. Cells were treated for 24 h with either lipopolysaccharide at a final concentration of 1 μg/mL, NPCB at 1 μg/cm^2 or 5 μg/cm^2 and GP at a concentration range of 1 μg/cm^2, 5 μg/cm^2, and 10 μg/cm^2 in cell media and media supplemented with either cytochalasin D at a concentration of 0.2 μM (Enzo Life Sciences), potassium chloride at 30 mM (Sigma), and diphenyleneiodonium chloride at 15 μM (Sigma). Triton X (0.1%, Sigma) was used as a positive control, and the cells were incubated with Triton X for 30 min. After the treatment the supernatant was centrifuged for 5 min at 2000*g*, transferred, centrifuged again for 5 min at 13000*g* and used for activity assay according to manufacturer's instructions. A microplate reader (BioTek SynergyHT) was used to measure the optical density at 490 nm. Results are given as the mean ± sem of five independent experiments.

Cytokine Bead Array. The supernatant of untreated cells and cells treated with 5 μg/cm^2 CB and GP in medium was used to screen for 11 cytokines important in acute inflammation and apoptosis to identify cytokines unregulated after treatment. The cytokine levels were measured using a BD Cytometric Bead Array Flex Set. The flex set included the human soluble protein buffer master kit and bead numbers D9, A7, A9, B4, D8, D4, B9, C5, E6, B6 representing the cytokines TNF, IL-6, IL-8, IL-1, MCP-1, Rantes, MIP-1α, basic FGF, IL-13 and TGF-β.

Twenty-five microliters of mixed capture antibodies were added to 50 μL of each supernatant or standard in a 96 well plate and incubated for 1 h at room temperature. Detection reagent was added to each well and incubated for 2 h at room temperature. After centrifugation at 1500*g* for 5 min the supernatant was removed and wash buffer was added to each well and agitated for 5 min for resuspension of the beads. BD FACSArray Bioanalyzer was used to measure the fluorescence intensity and FACP array software was used for analysis. The concentration of each cytokine was calculated using the standard curve and expressed as pg/mL. Results are given as the mean ± sem of three independent experiments.

ELISA. The supernatant of all treatment groups (including supplemented media) was further used to measure the expression of IL1-β using human IL1-β/IL-1F2 DuoSet (R&D Systems Europe Ltd., Abingdon, UK) according to manufacturer's description. Results are given as the mean ± sem of five independent experiments.

Detection of Reduced Glutathione (GSH) as Indicator of the Oxidative Status of Cells. The oxidative status of glutathione can be detected *via* monobromobimane (MBB), which becomes fluorescence after binding nonenzymatically free thiol group of GSH. THP-1 cells were seeded in 12- well plates at a density of 0.5 × 105/mL in 2.5 mL medium containing 10% FBS and differentiated as described above. Prior to treatment the cells were washed with PBS, and 2.5 mL of 1% FBS RPMI medium was added to each well. Cells were treated for 4 h with either NPCB or GP at 1 μg/cm^2 or 5 μg/cm^2 in cell media. *N*-Ethyl-maleimide (NEM) (100 μM, Sigma-Aldrich) was used as a negative, depletion of reduced glutathione. Supernatant and cells were transferred into falcon tubes and centrifuged for 3 min at 1500*g*. PBS was added to the pellet and centrifuged for 3 min at 1500*g* and repeated twice. A 150 μL portion of 50 μM monobromobimane (MBB) (Sigma-Aldrich) was added to the pellets and incubated for 10 min at 37 °C. Controls were included in all measurements and comprised untreated/unstained and untreated/stained samples as well as treated/unstained samples. The dye was detected using a BD LSRFortessa flow cytometer. MBB was excited by a violet laser (405 nm, 50 mW) and the emission was detected through a 455/40 filter. FlowJo software (Tree Star Inc.) was used for analyzing the data. Gating was based on FCS/SCS and the data is expressed as mean fluorescence intensity. The mean value of the blank sample was subtracted from the stained samples. Results are given as the mean ± sem of four independent experiments.

Scanning/Transmission Electron Microscopy. THP-1 cells were differentiated as described above and seeded in 24 well plates on Thermanox Plastic Coverslips (NUNC, Rochester, NY USA) at a density of 1 × 106/mL. The cells were treated with 1 μg/cm^2 and 5 μg/cm^2 NPCB and GP for 4 days at 37 °C in 5% CO_2 atm and washed 5× with 0.1 M sodium cacodylate (pH 7.2) buffer. Overnight fixation was done in 3% glutaraldehyde/0.1 M sodium cacodylate (pH 7.2) buffer. After fixation the cells adherent to the coverslips were washed in sodium cacodylate buffer, postfixed in 1% osmium tetroxide in 0.1 M sodium cacodylate buffer for 45 min, critical-point dried, and gold sputter coated.

Samples for TEM were embedded in Araldite resin. Sections 1 μm thick were cut on a Reichert OMU4 ultramicrotome (Leica Microsystems (UK) Ltd., Milton Keynes), stained with Toluidine Blue and viewed in a light microscope to select suitable areas for investigation. Ultrathin sections, 60 nm thick were cut from selected areas, stained in uranyl acetate and lead citrate then viewed in a Phillips CM120 transmission electron microscope (FEI UK Ltd., Cambridge, England). Images were taken on a Gatan Orius CCD camera (Gatan UK, Oxon, England). Samples for SEM were gold sputter coated and viewed using a Hitachi S-2600N digital scanning electron microscope (Oxford Instruments, Oxfordshire, UK).

Statistical Analysis. All data are shown as the mean ± sem, and these were analyzed using one-way analysis of variance (ANOVA). Multiple comparison were analyzed using the Tukey-HSD method and in all cases, values of $P < 0.05$ were consider significant. (GraphPad InStat Software Inc., CA, USA).

Acknowledgment. The authors declare they have no conflict of interests. We thank S. Mitchell (University of Edinburgh) for sample preparation for SEM and technical assistance, Bob Morris for histology sample preparation, and the Colt Foundation (A.S., K.D) for financial support.

Supporting Information Available: ICP−MS analysis of soluble metals in supernatant of CB and GP (Table 1); calculation of the aerodynamic diameter of nanoplatelet shaped particles; gross pathology of lung section after 24 h exposure, (Figure I); response to CB and GP treated mice after 1 week, including cell count and histology of lung and pleura (Figures II and III). This material is available free of charge *via* the Internet at http://pubs.acs.org.

REFERENCES AND NOTES

1. Novoselov, K. S.; Geim, A. K.; Morozov, S. V.; Jiang, D.; Zhang, Y.; Dubonos, S. V.; Grigorieva, I. V.; Firsov, A. A. Electric Field Effect in Atomically Thin Carbon Films. *Science* **2004**, *306*, 666–669.
2. Sanchez, V. C.; Jachak, A.; Hurt, R. H.; Kane, A. B. Biological Interactions of Graphene-Family Nanomaterials—An Interdisciplinary Review. *Chem. Res. Toxicol.* **2011**.
3. Jones, A. D.; Ellison, J. M. Respirable Industrial Fibres: Deposition, Clearence and Dissolution in Animal Models. *Ann Occup. Hyg.* **1993**, *37*, 211–226.
4. Donaldson, K. The Inhalation Toxicology of p-Aramid Fibrils. *Crit. Rev. Toxicol.* **2009**, *39*, 487–500.
5. Heintz, N. H.; Janssen-Heininger, Y. M.; Mossman, B. T. Asbestos, Lung Cancers, and Mesotheliomas: from Molecular Approaches to Targeting Tumor Survival Pathways. *Am. J. Respir. Cell Mol. Biol.* **2010**, *42*, 133–139.
6. Donaldson, K.; Murphy, F. A.; Duffin, R.; Poland, C. A. Asbestos, Carbon Nanotubes and The Pleural Mesothelium: A Review of the Hypothesis Regarding the Role of Long Fibre Retention in The Parietal Pleura, Inflammation and Mesothelioma. *Part Fibre. Toxicol.* **2010**, *7:5*, 5.
7. Murphy, F. A.; Poland, C. A.; Duffin, R.; Al-Jamal, K. T.; Ali-Boucetta, H; Nunes, A; Byrne, F; Prina-Mello; Volkov, Y; Li, S.; *et al.* Length-Dependent Retention of Carbon Nanotubes in the Pleural Space of Mice Initiates Sustained Inflammation and Progressive Fibrosis on The Parietal Pleura. *Am. J. Pathol.* **2011**, *178*, 2587–2600.

8. Miserocchi, G.; Sancini, G.; Mantegazza, F.; Chiappino, G. Translocation Pathways for Inhaled Asbestos Fibers. *Environ. Health.* **2008**, *7:4*, 4.
9. Ryman-Rasmussen, J. P.; Cesta, M. F.; Brody, A. R.; Shipley-Phillips, J. K.; Everitt, J. I.; Tewksbury, E. W.; Moss, O. R.; Wong, B. A.; Dodd, D. E.; Andersen, M. E.; *et al.* Inhaled Carbon Nanotubes Reach the Subpleural Tissue in Mice. *Nat. Nanotechnol.* **2009**, *4*, 747–751.
10. Mercer, R. R.; Hubbs, A. F.; Scabilloni, J. F.; Wang, L.; Battelli, L. A.; Schwegler-Berry, D.; Castranova, V.; Porter, D. W. Distribution and Persistence of Pleural Penetrations by Multiwalled Carbon Nanotubes. *Part Fibre. Toxicol.* **2010**, *7:28*, 28.
11. Muller, K. M.; Schmitz, I.; Konstantinidis, K. Black Spots of the Parietal Pleura: Morphology and Formal Pathogenesis. *Respiration* **2002**, *69*, 261–267.
12. Duch, M. C.; Budinger, G. R.; Liang, Y. T.; Soberanes, S.; Urich, D.; Chiarella, S. E.; Campochiaro, L. A.; Gonzalez, A.; Chandel, N. S.; Hersam, M. C.; *et al*. Minimizing Oxidation and Stable Nanoscale Dispersion Improves the Biocompatibility of Graphene in the Lung. *Nano Lett.* **2011**, *11*, 5201–5207.
13. Cho, W. S.; Duffin, R.; Poland, C. A.; Howie, S. E.; MacNee, W.; Bradley, M.; Megson, I. L.; Donaldson, K. Metal Oxide Nanoparticles Induce Unique Inflammatory Footprints in The Lung: Important Implications for Nanoparticle Testing. *Environ. Health Perspect.* **2010**, *118*, 1699–1706.
14. Pumera, M. Electrochemistry Of Graphene: New Horizons for Sensing and Energy Storage. *Chem. Rec.* **2009**, *9*, 211–223.
15. Donaldson, K.; Tran, C. L. An Introduction to the Short-Term Toxicology of Respirable Industrial Fibres. *Mutat. Res.* **2004**, *553*, 5–9.
16. Donaldson, K.; Murphy, F.; Schinwald, A.; Duffin, R.; Poland, C. A. Identifying the Pulmonary Hazard of High Aspect Ratio Nanoparticles to Enable Their Safety-By-Design. *Nanomedicine. (London)* **2011**, *6*, 143–156.
17. Morgan, W. K. C.; Seaton, A. *Occupational Lung Disease*; 2nd ed.; WB Saunders Co.: Philadelphia, PA; 1984.
18. Cheng, Y.; Yeh, H.; Allen, M. D. Dynamic Shape Factor of a Plate-like Particle. *Aerosol Sci. Technol.* **1988**, *8*, 109–123.
19. Lordan, S.; Kennedy, J. E.; Higginbotham, C. L. Cytotoxic Effects Induced by Unmodified and Organically Modified Nanoclays in the Human Hepatic Hepg2 Cell Line. *J Appl. Toxicol.* **2011**, *31*, 27–35.
20. Porter, D. W.; Hubbs, A. F.; Mercer, R. R.; Wu, N.; Wolfarth, M. G.; Sriram, K.; Leonard, S.; Battelli, L.; Schwegler-Berry, D.; Friend, S.; *et al*. Mouse Pulmonary Dose- and Time Course-Responses Induced by Exposure to Multi-Walled Carbon Nanotubes. *Toxicology* **2010**, *269*, 136–147.
21. Poland, C. A.; Duffin, R.; Kinloch, I.; Maynard, A.; Wallace, W. A.; Seaton, A.; Stone, V.; Brown, S.; MacNee, W.; Donaldson, K. Carbon Nanotubes Introduced into the Abdominal Cavity of Mice Show Asbestos-like Pathogenicity in a Pilot Study. *Nat. Nanotechnol.* **2008**, *3*, 423–428.
22. Tatrai, E.; Brozik, M.; Kovacikova, Z.; Horvath, M. The Effect of Asbestos and Stone-Wool Fibres on some Chemokines and Redox System of Pulmonary Alveolar Macrophages and Pneumocytes Type II. *Biomed. Pap. Med. Fac. Univ. Palacky. Olomouc. Czech. Repub.* **2005**, *149*, 357–361.
23. Conti, P.; DiGioacchino, M. MCP-1 and RANTES are Mediators of Acute and Chronic Inflammation. *Allergy Asthma Proc.* **2001**, *22*, 133–137.
24. Gueugnon, F.; Leclercq, S.; Blanquart, C.; Sagan, C.; Cellerin, L.; Padieu, M.; Perigaud, C.; Scherpereel, A.; Gregoire, M. Identification of Novel Markers for the Diagnosis of Malignant Pleural Mesothelioma. *Am. J. Pathol.* **2011**, *178*, 1033–1042.
25. Palomaki, J.; Valimaki, E.; Sund, J.; Vippola, M.; Clausen, P. A.; Jensen, K. A.; Savolainen, K.; Matikainen, S.; Alenius, H. Long, Needle-like Carbon Nanotubes and Asbestos Activate the NLRP3 Inflammasome through a Similar Mechanism. *ACS Nano* **2011**, *5*, 6861–6870.
26. Shinohara, H. Distribution of Lymphatic Stomata on the Pleural Surface of the Thoracic Cavity and the Surface Topography of the Pleural Mesothelium in the Golden Hamster. *Anat. Rec.* **1997**, *249*, 16–23.
27. Marco, A. J.; Domingo, M.; Ruberte, J.; Carretero, A.; Briones, V.; Dominguez, L. Lymphatic Drainage of Listeria Monocytogenes and Indian Ink Inoculated in the Peritoneal Cavity of the Mouse. *Lab. Anim.* **1992**, *26*, 200–205.
28. Brown, D. M.; Kinloch, I. A.; Bangert, U.; Windle, A. H.; Walter, D. M.; Walker, G. S.; Scotchford, C. A.; Donaldson, K.; Stone, V. An *In Vitro* Study of the Potential of Carbon Nanotubes and Nanofibers to Induce Inflammatory Mediators and Frustrated Phagocytosis. *Carbon* **2007**, *45*, 1743–1756.
29. Dogra, S.; Donaldson, K. Effect of Long and Short Fibre Amosite Asbestos on *in Vitro* TNF Production by Rat Alveolar Macrophages: The Modifying Effect of Lipopolysaccharide. *Ind. Health.* **1995**, *33*, 131–141.
30. Wu, G.; Fang, Y. Z.; Yang, S.; Lupton, J. R.; Turner, N. D. Glutathione Metabolism and Its Implications for Health. *J. Nutr.* **2004**, *134*, 489–492.
31. Kelly, F. J.; Blomberg, A.; Frew, A.; Holgate, S. T.; Sandstrom, T. Antioxidant Kinetics in Lung Lavage Fluid Following Exposure of Humans to Nitrogen Dioxide. *Am. J Respir. Crit. Care Med.* **1996**, *154*, 1700–1705.
32. Brown, D. M.; Beswick, P. H.; Bell, K. S.; Donaldson, K. Depletion of Glutathione and Ascorbate in Lung Lining Fluid by Respirable Fibres. *Ann. Occup. Hyg.* **2000**, *44*, 101–108.
33. Brown, D. M.; Beswick, P. H.; Donaldson, K. Induction of Nuclear Translocation of NF-Kappa B in Epithelial Cells by Respirable Mineral Fibres. *J Pathol.* **1999**, *189*, 258–264.
34. Rahman, I.; MacNee, W. Role of Transcription Factors in Inflammatory Lung Diseases. *Thorax.* **1998**, *53*, 601–612.
35. Duncan, K. E.; Ghio, A. J.; Dailey, L. A.; Bern, A. M.; Gibbs-Flournoy, E. A.; Padilla-Carlin, D. J.; Roggli, V. L.; Devlin, R. B. Effect of Size Fractionation on the Toxicity of Amosite and Libby Amphibole Asbestos. *Toxicol. Sci.* **2010**, *118*, 420–434.
36. Broser, M.; Zhang, Y.; Aston, C.; Harkin, T.; Rom, W. N. Elevated Interleukin-8 in the Alveolitis of Individuals with Asbestos Exposure. *Int. Arch. Occup. Environ. Health.* **1996**, *68*, 109–114.
37. Dostert, C.; Petrilli, V.; Van, B. R.; Steele, C.; Mossman, B. T.; Tschopp, J. Innate Immune Activation Through Nalp3 Inflammasome Sensing of Asbestos and Silica. *Science* **2008**, *320*, 674–677.
38. Hornung, V.; Bauernfeind, F.; Halle, A.; Samstad, E. O.; Kono, H.; Rock, K. L.; Fitzgerald, K. A.; Latz, E. Silica Crystals and Aluminum Salts Activate the NALP3 Inflammasome through Phagosomal Destabilization. *Nat. Immunol.* **2008**, *9*, 847–856.
39. O'Neill, L. A. Immunology. How Frustration Leads to Inflammation. *Science* **2008**, *320*, 619–620.
40. Tschopp, J.; Schroder, K. NLRP3 Inflammasome Activation: The Convergence of Multiple Signalling Pathways on ROS Production? *Nat. Rev. Immunol.* **2010**, *10*, 210–215.
41. Petrilli, V.; Papin, S.; Dostert, C.; Mayor, A.; Martinon, F.; Tschopp, J. Activation of The NALP3 Inflammasome Is Triggered by Low Intracellular Potassium Concentration. *Cell Death. Differ.* **2007**, *14*, 1583–1589.
42. Martinon, F. Signaling by ROS Drives Inflammasome Activation. *Eur. J. Immunol.* **2010**, *40*, 616–619.
43. Donaldson, K. The Inhalation Toxicology of *p*-Aramid Fibrils. *Crit Rev. Toxicol.* **2009**, *39*, 487–500.
44. Rao, G. V.; Tinkle, S.; Weissman, D. N.; Antonini, J. M.; Kashon, M. L.; Salmen, R.; Battelli, L. A.; Willard, P. A.; Hoover, M. D.; Hubbs, A. F. Efficacy of a Technique for Exposing the Mouse Lung to Particles Aspirated from the Pharynx. *J Toxicol. Environ. Health A.* **2003**, *66*, 1441–1452.
45. Park, E. K.; Jung, H. S.; Yang, H. I.; Yoo, M. C.; Kim, C.; Kim, K. S. Optimized THP-1 Differentiation Is Required for the Detection of Responses to Weak Stimuli. *Inflammation Res.* **2007**, *56*, 45–50.

Supplementary information

ICP-MS analysis

For quantification of contaminating metals the supernatant of 1 mg/ml of each sample in 0.5% BSA/saline were analysed using the technique of inductively-coupled mass spectrometry (ICP-MS). GP showed higher levels of ^{52}Cr, ^{63}Cu, ^{56}Fe, ^{55}Mn, ^{60}Ni and ^{64}Zn compared to CB, however all concentrations are negligible and not biologically relevant (Table I).

Concentration (ng/g) of soluble metal associated with CB and GP											
	^{107}Ag	^{27}Al	^{111}Cd	^{59}Co	^{52}Cr	^{63}Cu	^{56}Fe	^{55}Mn	^{60}Ni	^{208}Pb	^{64}Zn
CB	0.1287	9.368	0.02333	0	0	1.161	0	0	0.07433	1.395	0
GP	0.3371	24.93	0.06652	2.799	29.98	15.39	437.8	52.19	121.8	1.563	22.1

Table I. Concentration (ng/g) of soluble metal associated with CB and GP in the supernatant of a 1 mg/ml solution.

Aerodynamics of platelet-shaped particles

The gravitational settling speed of a particle is determined by the opposing effects of the gravitational force and the aerodynamic resistance. The aerodynamic drag force depends on the shape and orientation of the particle with respect to its direction of motion. A plate-like particle with uniform thickness may well settle under gravity with orientation perpendicular to its direction of motion. If it is not a uniform thickness, it might behave like a spear with a weighted tip (if one edge is relatively heavy) or it might be stable in the perpendicular orientation if the extra weight is central.

The gravitational force on a particle is determined by its volume and density. For a spherical particle with diameter d and density ρ, this is

$$F_g = \frac{\pi \cdot d^3 \cdot \rho}{6} . g \qquad (1)$$

Where *g* is the gravitational acceleration.

For a platelet particle, with thickness *t,* and projected area diameter d_{proj} the equivalent gravitational force is;

$$F_g = \frac{\pi \cdot d_{proj}^{\ 2} \cdot t \cdot \rho}{4} . g \qquad (2)$$

The gravitational settling force is opposed by the aerodynamic resistance to the motion of the particle.

For a circular plate-like particle of diameter *b* that is infinitely thin, the aerodynamic resistance when the plate is perpendicular to the direction of motion at velocity *V*, the following expression can be obtained from Fuchs *et al*. [1] for the resistance to motion

$$F_m = -8 \cdot \eta \cdot b \cdot V \qquad (3)$$

Where η is the viscosity of air.

The above equation applies when the disc is perpendicular to the direction of motion.

When the infinitely thin circular plate-like particle is orientated parallel to the direction of motion, then the equation becomes:

$$F_m = -\frac{16}{3} \cdot \eta \cdot b \cdot V \qquad (4)$$

Fuchs[1] also notes that the formula in equation 4 has given good agreement with data when Oseen's correction is introduced. For present purposes, the detail of Oseen's correction can be ignored.

When the particle reaches an equilibrium settling velocity (V_s,), then $F_m = F_g$, and by taking the projected area diameter d_{proj} as being approximately the same as the diameter of the circular plate, this leads to:

$$V_s = \frac{\pi \cdot d_{proj} \cdot t \cdot \rho \cdot g}{32\eta} \qquad (5)$$

The equivalent expression for a sphere of unit density (ρ_0) and diameter *d* is

$$V_{ss} = \frac{\pi \cdot d^2 \cdot \rho_0 \cdot g}{\eta} \qquad (6)$$

The definition of the aerodynamic equivalent diameter is the diameter of a unit density sphere with the same settling speed as particle; that is, if $V_{ss} = V_s$ then the d in equation 6 is the d_{ae} for the plate-like particle. This leads directly to an expression for the aerodynamic diameter of a plate-like particle as:

$$d_{ae} = \sqrt{\frac{9 \cdot \pi}{16} \cdot \frac{\rho}{\rho_0} . d_{proj} \cdot t} \qquad (7)$$

Using equation 7, we can estimate the aerodynamic diameter for plate-like-particles of given dimensions as shown in the Table 1 of our paper.

In vivo

Acute pulmonary inflammatory response to GP

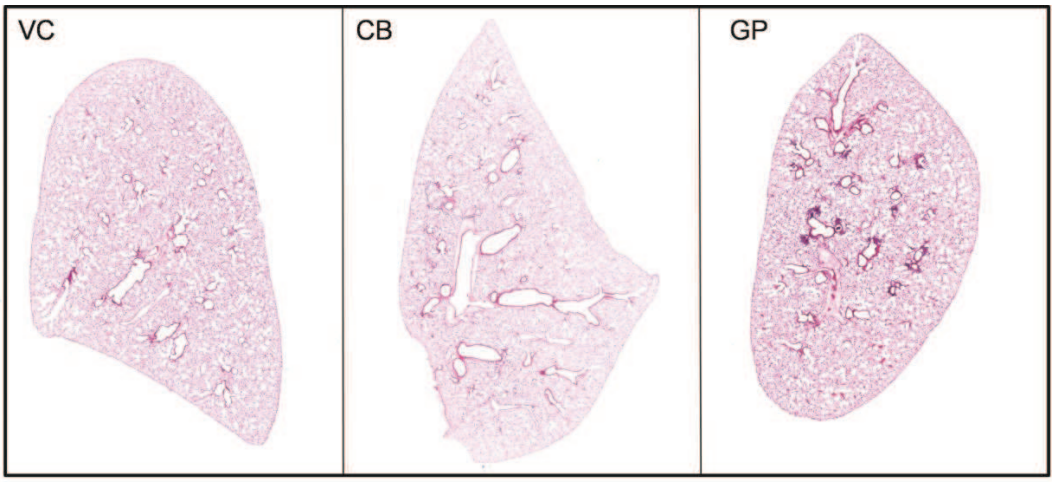

Figure I. Lung pathology 24 hour post aspiration. The effect of 50 µg CB and GP aspiration is demonstrated 24 hour post aspiration. Each panel shows an entire lung section stained with Haematoxylin & Eosin (H&E) to demonstrate gross pathology. CB lung has normal pathology however in the lung of GP treated mice granulomatous areas are present (n=3).

Chronic pulmonary inflammatory response to GP

To assess the chronic inflammation to the lungs, CB and GP were aspirated into the lungs at a single dose of 50 µg per mouse. After 1 week post GP exposure, the granulocyte number continued to be significantly elevated (Fig. IIA) but was decreased compared to the 24 hour response. CB did not lead to an significant increase in total cell number or PMN (Fig. IIA). No granulomatous lesions could be observed in GP treated lung sections however an increased number of lymphocytes was present in the smooth muscle surrounding the bronchi and in the alveolar spaces (Fig. IIB). In CB treated lung sections only occasional areas of lymphocyte infiltrates could be observed (Fig. IIB).

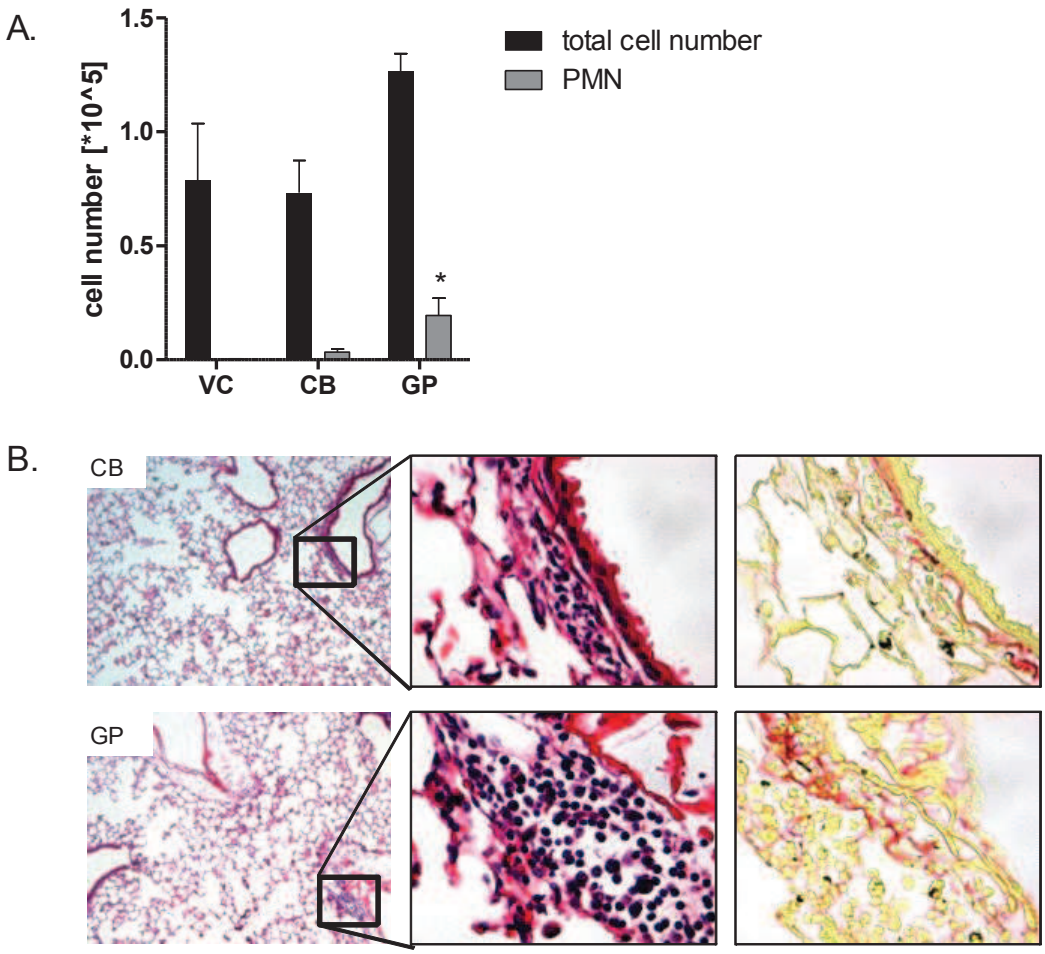

Figure II Inflammatory response in the lungs after 1 week exposure to CB and GP. A. Total cell number and total granulocyte number after pharyngeal aspiration of a single dose of 50 µg of CB and GP 1 week post treatment. B. Histological examination showed infiltration of lymphocytes in CB and GP treated mice, with a greater extent in the GP. Sections were stained with Pico-Sirius Red to show collagen deposition (right panel).

Chronic pleural inflammatory response to GP

The granulocyte response to 1 week GP exposure after intrapleural injection was decreased to a tenth compared to 24 hour exposure (Fig. IIIA). The concentration of total protein in the lavage fluid was significantly increase in GP treated mice (Fig. IIIB). Continuous thickening of the parietal pleura was present after 1 week exposure to GP (Fig. IIIC). Inflammatory cells with associated GP were present along the parietal pleura. These areas of inflammatory cells appeared denser and granulomatous on SEM micrographs (n=3) (Fig. IIIC bottom panel). SEM was used to detect these more localised areas.

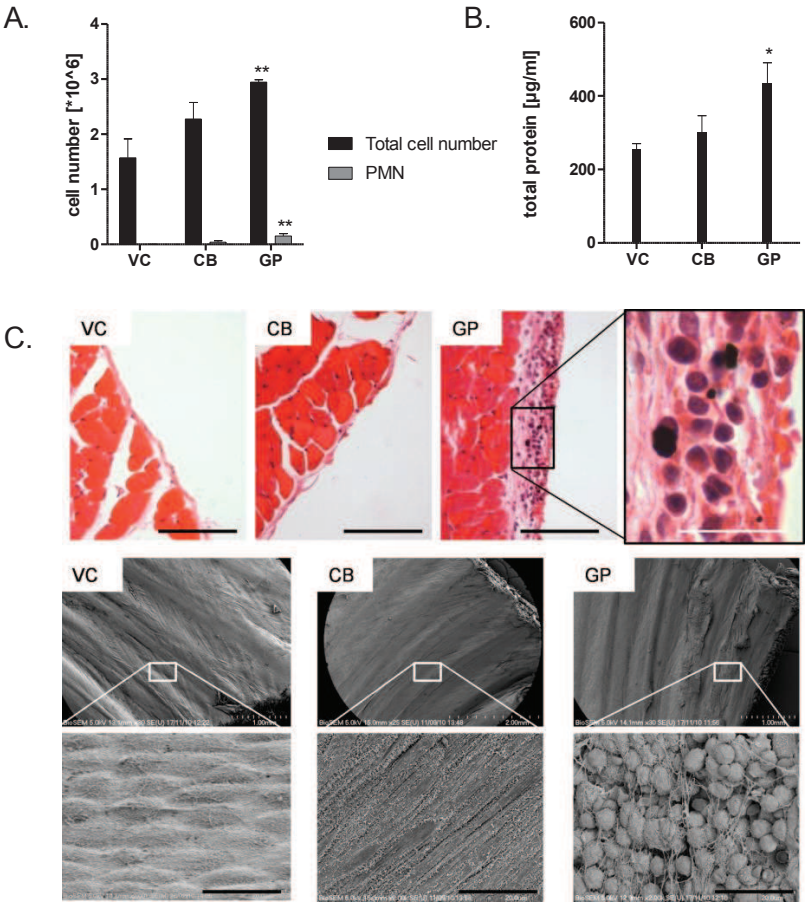

Figure III Inflammatory response in the pleural space after 1 week exposure to CB and GP. A. Total cell number and total granulocyte number after 1 week exposure to CB and GP in the lavage fluid. B. Measurement of the total protein concentration in the lavage fluid. Single asterisk (*) indicates $p < 0.05$, double asterisk (**) indicates $p < 0.01$ compared to vehicle control. C. H&E stained parietal pleura section (n=1) (top panel) and SEM (n=3) (bottom panel) in low and high magnification showing aggregations of inflammatory cells and granulomatous areas on parietal pleural 1 week post GP exposure.

Reference List

1. Fuchs N.A. *The mechanics of Aerosols;* Pergamon Press, Oxford, England, and The Macmillan Company, New York: 1964.

1. Murphy FA, **Schinwald A**, Poland CA, Donaldson K. **The mechanism of pleural inflammation by long carbon nanotubes: interaction of long fibres with macrophages stimulates them to amplify pro-inflammatory responses in mesothelial cells**. Part Fibre Toxicol. 2012 Apr 3;9:8.

Murphy et al. Particle and Fibre Toxicology 2012, 9:8
http://www.particleandfibretoxicology.com/content/9/1/8

PARTICLE AND FIBRE TOXICOLOGY

RESEARCH Open Access

The mechanism of pleural inflammation by long carbon nanotubes: interaction of long fibres with macrophages stimulates them to amplify pro-inflammatory responses in mesothelial cells

Fiona A Murphy[1], Anja Schinwald[1], Craig A Poland[2] and Ken Donaldson[1*]

Abstract

Carbon nanotubes (CNT) are high aspect ratio nanoparticles with diameters in the nanometre range but lengths extending up to hundreds of microns. The structural similarities between CNT and asbestos have raised concern that they may pose a similar inhalation hazard. Recently CNT have been shown to elicit a length-dependent, asbestos-like inflammatory response in the pleural cavity of mice, where long fibres caused inflammation but short fibres did not. However the cellular mechanisms governing this response have yet to be elucidated. This study examined the in vitro effects of a range of CNT for their ability to stimulate the release of the acute phase cytokines; IL-1β, TNFα, IL-6 and the chemokine, IL-8 from both Met5a mesothelial cells and THP-1 macrophages. Results showed that direct exposure to CNT resulted in significant cytokine release from the macrophages but not mesothelial cells. This pro-inflammatory response was length dependent but modest and was shown to be a result of frustrated phagocytosis. Furthermore the indirect actions of the CNT were examined by treating the mesothelial cells with conditioned media from CNT-treated macrophages. This resulted in a dramatic amplification of the cytokine release from the mesothelial cells, a response which could be attenuated by inhibition of phagocytosis during the initial macrophage CNT treatments. We therefore hypothesise that long fibres elicit an inflammatory response in the pleural cavity via frustrated phagocytosis in pleural macrophages. The activated macrophages then stimulate an amplified pro-inflammatory cytokine response from the adjacent pleural mesothelial cells. This mechanism for producing a pro-inflammatory environment in the pleural space exposed to long CNT has implications for the general understanding of fibre-related pleural disease and design of safe nanofibres.

Keywords: Carbon nanotubes, Pleura, Mesothelioma, Asbestos, Inflammation

Background

Carbon nanotubes (CNT) are high aspect ratio nanoparticles comprising single (SWCNT) or concentrically stacked multiwalled (MWCNT) graphene sheets rolled seamlessly into a cylinder. Their high aspect-ratio and novel properties make CNT a useful industrial material and has led to their incorporation into a wide variety of consumer products. However, as the applications of CNT continue to grow, so too does the potential for occupational inhalation exposure with obvious potential hazards for worker health [1]. The structural similarities between CNT and asbestos have raised particular concern regarding the potential pathogenicity of CNT in the lung and serosal cavities, specifically the pleural and peritoneal spaces, which are key target tissues for asbestos-related disease [2].

Carbon nanotubes have been found to cause a range of pathogenic effects, oxidative stress [3] inflammation and NLRP3 inflammasome activation [4], fibrosis [5,6] and genotoxicity [7].

The mesothelial lining of the pleural cavity has long been known to be particularly sensitive to asbestos exposure producing pleural effusion, pleural plaques and

* Correspondence: ken.donaldson@ed.ac.uk
[1]MRC/University of Edinburgh Centre for Inflammation Research, ELEGI Colt Laboratory, Queen's Medical Research Institute, 47 Little France Crescent, Edinburgh EH16 4TJ, UK
Full list of author information is available at the end of the article

fibrosis [8]. Cancer arising in the mesothelial cells lining both the peritoneal and pleural cavities, mesothelioma, is a response almost unique to fibrous particles. The exact mechanisms leading to fibre-induced mesothelioma formation are unknown although fibre dimensions [9-11], biopersistence [12], the generation of reactive oxygen species (ROS) [13] and inflammation [14] have all been implicated. Due to its uniformly poor prognosis, mesothelioma is the disease of most concern when contemplating the potential toxicity of new high aspect ratio nanoparticles; pleural plaques and effusion are also a consequence of long fibre dose in the pleural space. The ability of fibres to induce an inflammatory response in the pleura has been considered to be a key mechanism in the production of mesothelioma and other pleural pathology[15,16]. A length dependent inflammatory response, similar to that seen with asbestos, has been reported for CNT and other high aspect ratio nanomaterials (HARN) in a number of studies using the peritoneal cavity as a model of mesothelium exposure [17,18] and more recently in a study conducted by the present authors investigating the response to CNT instilled into the pleural cavity [19]. The length-dependent response in the pleural cavity was characterised by an initial acute inflammatory reaction as indicated by an influx of granulocytes and an increase in protein concentration in the lavage fluid [19]. The length-dependent response to CNT in vivo was attributed to the fibre length-restricted clearance mechanisms from the pleural space through stomata in the parietal pleura leading to specific retention of long fibres while short fibres are efficiently cleared [19]. Nevertheless the detailed interactions between the CNT and pleural mesothelial cells and macrophages at these points of retention are unknown and are the focus of the present study.

Inhaled fibres that reach the pleural space will encounter mesothelial cells lining the pleural cavity and also resident pleural macrophages. Mesothelial cells, historically thought of as barrier cells that provide a lubricated surface that locks the parietal pleura to the visceral pleura allowing for lung movements, are now also known to play a prominent role in the initiation, perpetuation and resolution of inflammation in the pleural cavity [20]. During injury or infection, mesothelial cells can respond by producing a spectrum of pro- and anti-inflammatory cytokines and chemokines, growth factors, oxidants, extracellular matrix molecules and mediators of the complement cascade [20]. Macrophages are also present in the pleural space and can play a role in host defence and immuno-inflammatory responses [21]. The primary function of professional phagocytes such as pleural macrophages is to ingest foreign material that may pose a threat to the body and so pleural macrophages are likely to play a key role in the removal of inhaled particles and fibres that are retained in the pleural space. We therefore hypothesised that the response of the mesothelial cells and macrophages upon exposure to CNT or other fibres will be crucial in the pathogenesis of fibre-related pleural inflammation and therefore in subsequent pleural disease.

Here, we aim to use in vitro methods to elucidate the relative roles of the macrophages and mesothelial cells in driving the inflammatory response to long fibres. Long and short CNT samples were examined in an effort to infer whether the response to the CNT was length-dependent, as is the case in the inflammatory response in the pleural space in vivo [19]. Using the same panel of CNT as described by Murphy et al. [19] we examined the ability of long and short CNT to elicit pro-inflammatory responses in both a human non-transformed mesothelial cell line (Met5A), and macrophages derived from the human monocyte cell line (THP-1) as a surrogate for pleural macrophages, by direct exposure to CNT. The release of TNFα, IL-6, IL-8 and IL-1β; acute phase pro-inflammatory cytokines was measured as an indicator of the pro-inflammatory potential of the CNT panel. In addition we hypothesized that the inflammatory response could be driven by cross-talk between the macrophages and mesothelial cells and so we also examined the effect of conditioned media from CNT-treated macrophages on the mesothelial pro-inflammatory response.

Results

Effect of direct exposure to CNT panel on mesothelial cell and macrophage viability

Mesothelial cell viability, as measured by trypan blue exclusion assay, was examined after 24 hour exposure to the CNT panel over a dose range from 5 to 50 μg/cm^2. A significant loss of cell viability was seen only in response to NT_{long1} (20 μg/cm^2) and NT_{long2} (20 ug/cm^2, 50 μg/cm^2) (Figure 1A). This loss of cell viability coincided with an increase in supernatant LDH levels in Met5A cultures treated with NT_{long1} and NT_{long2} at the two highest doses only (Figure 1B). Exposure of macrophages (THP-1) to all the members of the CNT panel caused a significant increase in supernatant LDH only at the higher doses (Figure 1C). Trypan blue exclusion assay could not be carried out on THP-1 cells exposed to CNT as macrophages clumped together during the treatments making accurate assessment of the cellular viability by this method impossible. Based on these data a sub-lethal dose of 5 μg/cm^2 was selected for treatments of both Met5A and THP-1 cells for the subsequent activation studies.

Effects of direct exposure to the CNT panel on pro-inflammatory cytokine release from mesothelial cells

In order to investigate the effect CNT might have on mesothelial cell activation we assayed, using a cytometric bead array system, the concentration of a number of

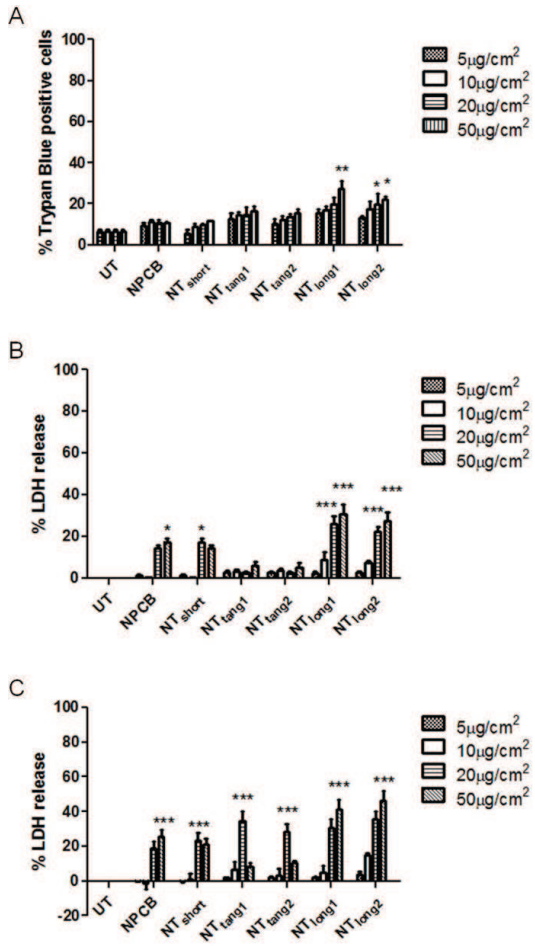

Figure 1 The effect of the CNT panel on cell viability. The viability of mesothelial cells was measured by trypan blue exclusion (A) and LDH release (B) after a 24 hour exposure to the CNT panel, UT indicates untreated control. LDH release was also used as an indicator of cell viability of macrophages at 24 hours after CNT treatment (C). Data expressed as a mean ± sem, n = 3. Significance versus vehicle control *** indicates $p < 0.001$.

pro-inflammatory cytokines present in Met5A cell supernatants following direct exposure to the CNT panel for 24 hours (Figure 2A). No member of the CNT panel had an effect on the supernatant concentrations of IL-1β, IL-6, IL-8 or TNFα in Met5A cultures compared to LPS, a positive control to activate cells, which caused a significant increase in the concentration of all four cytokines.

Effects of direct exposure to the CNT panel on pro-inflammatory cytokine release from macrophages

In order to investigate the impact of CNT phagocytosis on macrophage activation, we measured the concentration of IL-1β, IL-6, IL-8 and TNFα present in the THP-1 cells supernatants following exposure to the CNT panel (Figure 2B). Only the CNT samples containing long fibres- NT_{long1} and NT_{long2} caused a significant increase in IL-1β and IL-6 concentrations compared to untreated cells. NT_{long1} also induced a significant increase in IL-8 concentration; however no increase was seen with NT_{long2}. NT_{long2} did appear to elevate the concentration of TNFα, but this elevation was not statistically significant. No increase in cytokine concentration was seen after exposure to NPCB, NT_{short}, NT_{tang1} or NT_{tang2}.

Role of frustrated phagocytosis in length-dependent IL-1β release from macrophage

The appearance of the THP-1 cells after 24 hour treatment with the CNT panel at a dose of 5 μg/cm^2 is shown in Figure 3 as Diffquik stained light micrograph images (A-G) or as scanning electron micrograph figures (H - K). Normal cells are shown in Figure 3D and 3H. NPCB and the short CNT samples; NT_{short}, NT_{tang1} and NT_{tang2} appear to be easily taken up by the macrophages as they are seen as accumulations of black particles within the cells (Figure 3A, B, E and 3F) but were not visible on the cell surface in SEM images confirming that they had been effectively phagocytosed (Figure 3I and 3J). NT_{long1} and NT_{long2} were not completely taken up by the cells which showed the classic features of frustrated phagocytosis with fibrous CNT extended from the cell surfaces (Figure 3G and 3K) or a single long fibre could be shared by more than one cell (Figure C). This state of frustrated phagocytosis appeared more extensive in cells treated with the longer NT_{long2} sample. We selected one cytokine, IL-1β, to test the hypothesis that the length-dependent pro-inflammatory effects were due to frustrated phagocytosis of long fibres. THP-1 cells were co-incubated with the NT_{long1} and NT_{long2} samples and an inhibitor of phagocytosis (cytochalasin D) and the release of IL-1β was measured by ELISA (Figure 4). Cytochalasin D, a potent inhibitor of actin polymerisation, prevented the uptake of the long CNT by the THP-1 cells (Figure 4A) and inhibited the increase in IL-1β concentration caused by exposure to NT_{long1} and NT_{long2} in a dose-dependent pattern. However it had no effect on the IL-1β concentrations caused by LPS, which does not require phagocytosis to elicit a pro-inflammatory response. Measurements of supernatant LDH levels showed there was no loss of cell viability due to cytochalasin D treatments (Figure 4B).

Effect of conditioned media from CNT-exposed macrophages on mesothelial cell viability

In order to test the hypothesis that CNT that reach the pleural space stimulate mesothelial cells indirectly via the release of cytokines from particle-activated macrophages, we used conditioned media from CNT-exposed THP-1

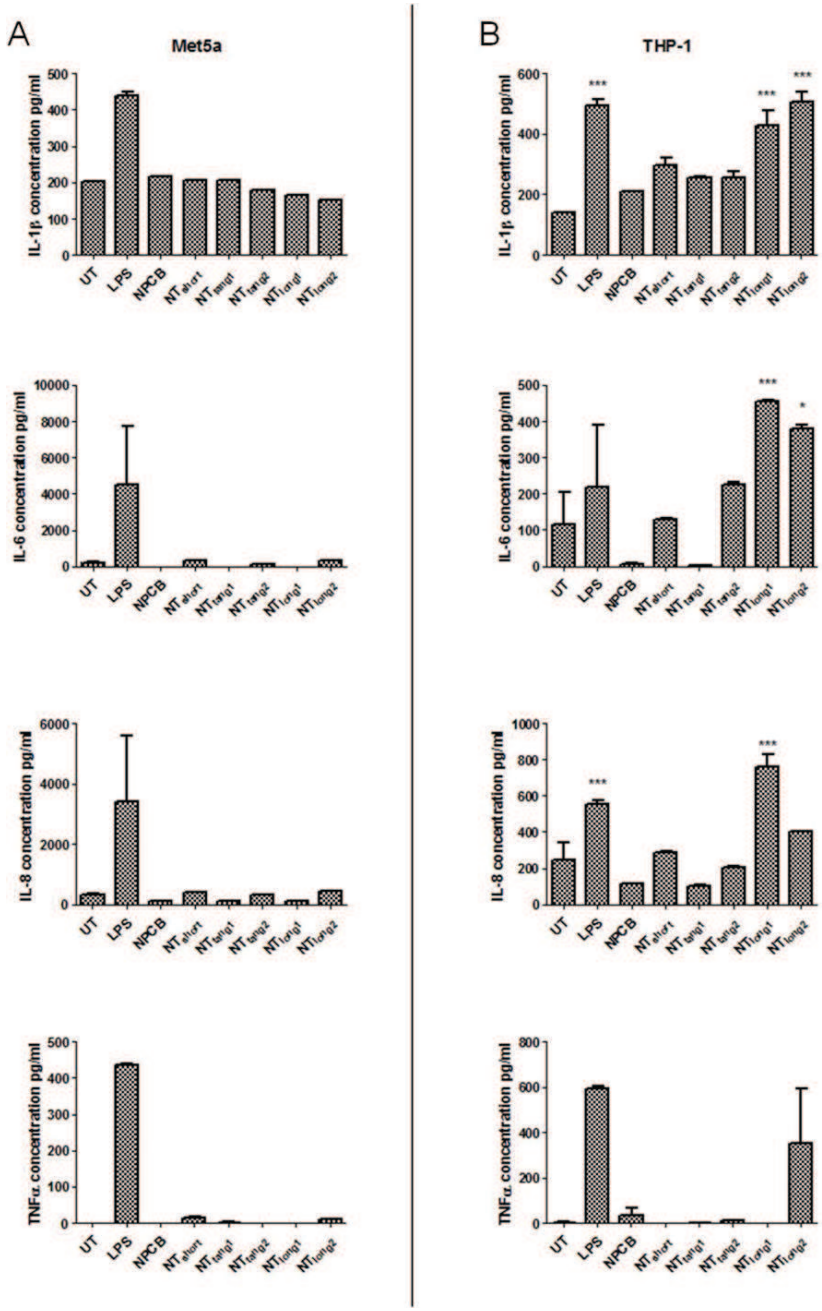

Figure 2 The effect of the direct exposure to the CNT panel on cytokine release from mesothelial cells and macrophages. No increase in the levels of IL-1β, IL-6, IL-8 or TNFα was detected after mesothelial cells were exposed to the CNT panel. However significant increases in IL-1β and IL-6 and IL-8 were seen in macrophages treated to long CNT samples only. UT indicates untreated control Data expressed as a mean ± sem, n = 3.

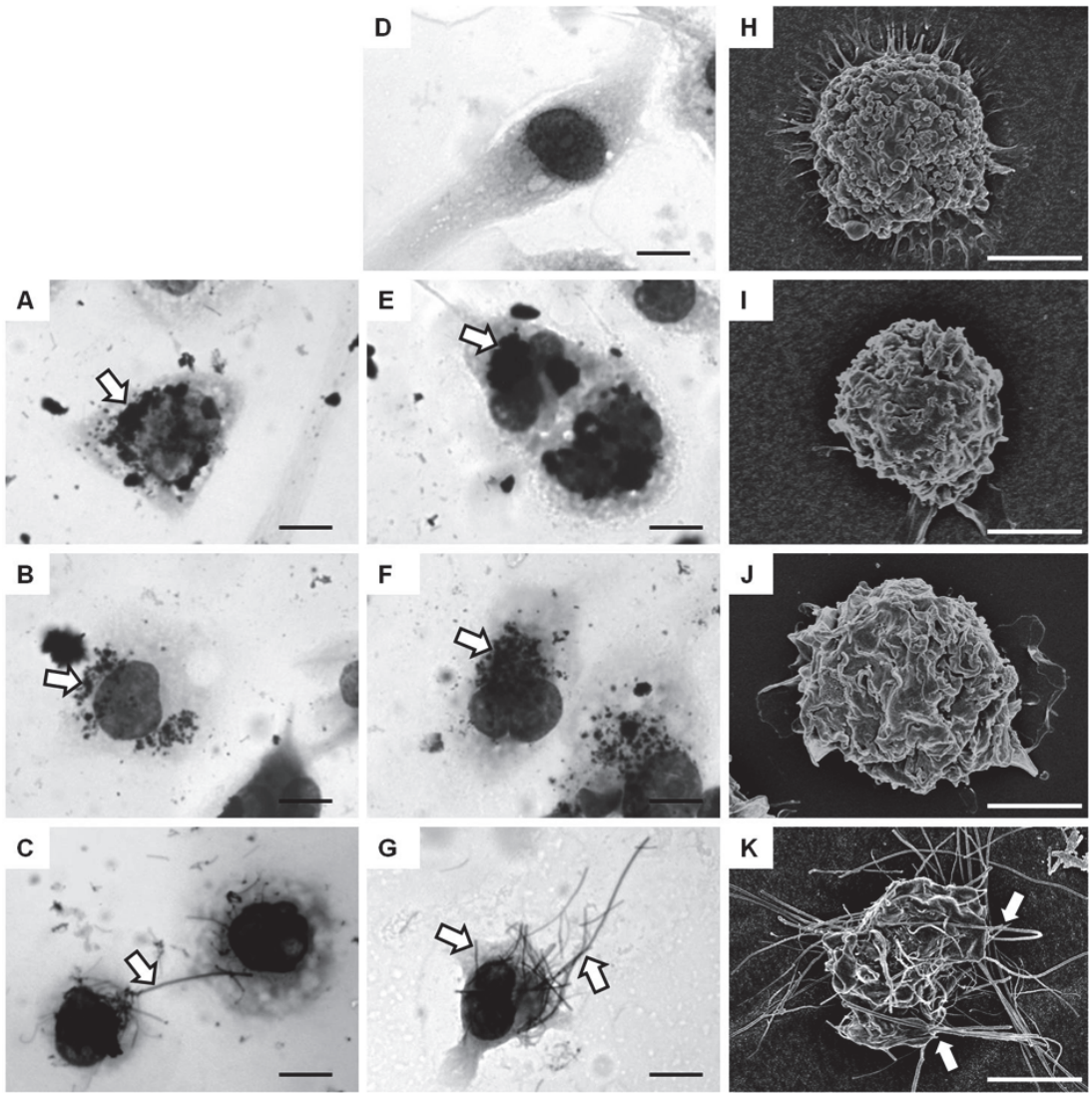

Figure 3 Uptake of CNT by macrophages. Light micrographs (A-G) of THP-1 cells untreated (D) or treated with the CNT panel. NPCB (A), NT_{short} (E), NT_{tang1} (B) and NT_{tang2} (F) appear as aggregates within the cells (white arrows). However NT_{long1} (C) and NT_{long2} (G) appear to be protruding from the cells (white arrows). Scale bar indicates 20 μm. SEM images (H-K) show an untreated THP-1 cell (H) and THP-1 cells treated with NPCB (I), NT_{short} (J) and NT_{long2} (K). No particles can be seen associated with the cell surface or protruding from the cells in I or J however the fibre from the NT_{long2} (K) sample appear on the surface of the cells and also protruding from the cell. Scale bar indicates 10 μm.

cells to treat Met5A cells and measured the concentrations of pro-inflammatory cytokines in the Met5A supernatant (Figure 5A).

No increase in LDH release from the Met5A cells treated with the conditioned media confirm the treatments did not caused a loss of membrane integrity and therefore cell viability (Figure 5B).

Effect of conditioned media from CNT-exposed macrophages on mesothelial cell production of pro-inflammatory cytokines

Whilst direct exposure of Met5A cells to the CNT panel had not caused any increases in IL-1β, treatment with conditioned media from THP-1 cells exposed to LPS, NT_{long1} or NT_{long2} resulted in approximately two-fold

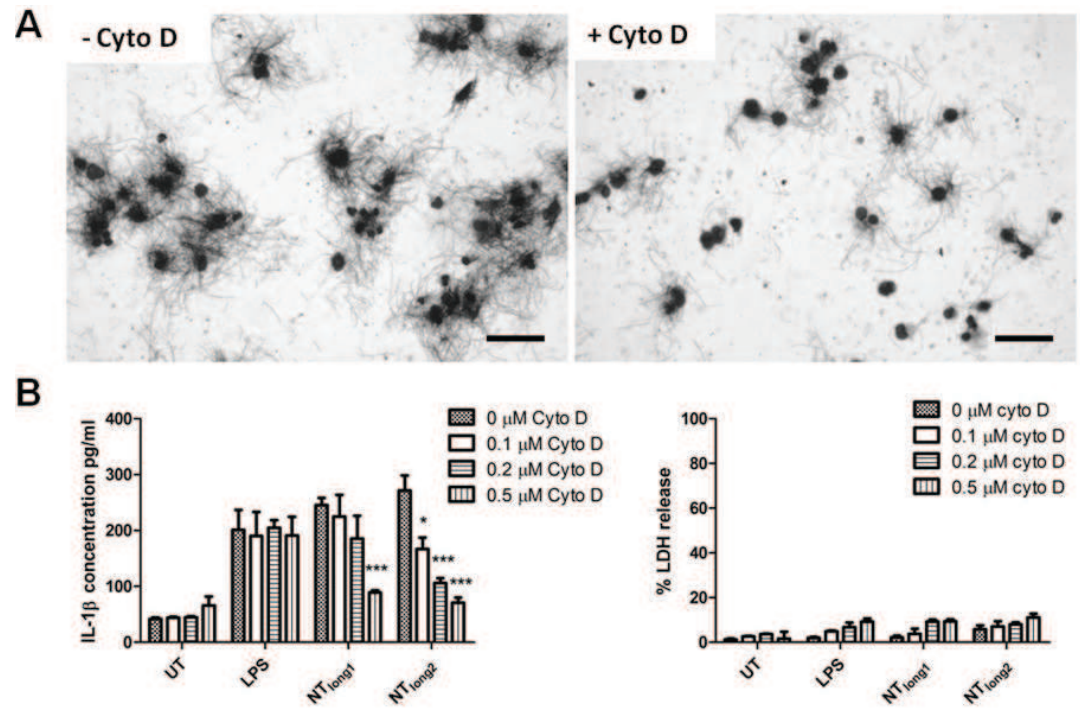

Figure 4 Inhibition of IL-1β release from long CNT-treated macrophages. (A) Example images of macrophages treated with NT_{long2} with or without cytochalasin D. Cytochalasin D inhibits the attempted uptake of long fibres by the macrophages. (B) Cytochalasin D caused a dose-dependent inhibition of IL-1β release from macrophages treated with NT_{long1} and NT_{long2} but not LPS. Significance versus 0 μM cytochalasin D within each treatment group *** indicates $p < 0.001$. A loss of cell viability in the presence of cytochalasin D was not detected by LDH release. Data expressed as mean ± sem, n = 3.

increase in IL-1β concentration compared with the combined total from both cell types exposed directly as shown by the horizontal lines on the bars (Figure 6A).

Media from THP-1 cells exposed to the NT_{long1} and NT_{long2} samples also had a significant effect on the production of IL-6, IL-8 and TNFα by Met5A (Figure 6B-D). The potentiation of Met5A activation was most pronounced when Met5A had been exposed to NT_{long2}-exposed THP-1 media which resulted in a 20-fold, 30-fold and 6-fold increase in the concentrations of IL-6, IL-8 and TNFα respectively, when compared with the combined total from each cell type exposed directly. Conditioned media from NT_{long1} treated THP-1 cells also caused a significant increase in the production of IL-6, IL-8 and TNFα from Met5A cells albeit to a lesser extent. Exposure to media from THP-1 cells treated with NPCB, NT_{short}, NT_{tang1} or NT_{tang2} did not have any effect on the production of the pro-inflammatory cytokines; IL-1β, IL-6, IL-8 or TNFα, by Met5A cells.

The levels of IL-1β and IL-6 released from Met5A cells treated with the conditioned media from THP-1 cells treated with NT_{long2} was attenuated when the THP-1 cells were co-exposed to NT_{long2} and cytochalasin D to prevent phagocytosis (Figure 7).

Iron content

The iron content of the CNT samples is given in the Additional file 1.

Interference of CNT in the assays

We precluded interference of CNT in the assays used here and the evidence is present in the Additional file 1.

Discussion

We previously reported that long CNT but not short CNT were capable of causing inflammation in the peritoneal [17] and pleural spaces [19]. Whilst retention of the long fibres at stomata represent the key initiating step the cellular mechanism, especially the interaction between macrophages and mesothelial cells, leading to inflammation was not elucidated. The present study addressed three hypotheses as to the mechanism by which CNT cause pro-inflammatory effects in the pleural cavity. These three hypotheses centred on the major cells of the pleural cavity, mesothelial cells and macrophages, are outlined in diagrammatic form in Figure 8. The refractoriness of the

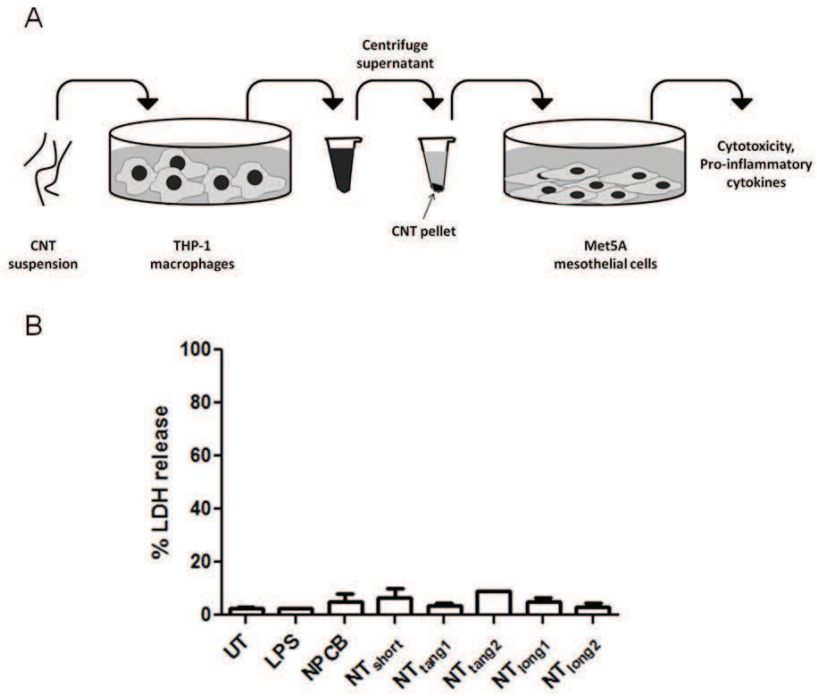

Figure 5 The effect of conditioned media from CNT-exposed macrophages on mesothelial cell viability. (A) Schematic diagram representing the conditioned media experimental procedure. THP-1 cells were treated with CNT suspensions for 24 hours, supernatant was removed and centrifuged to remove any suspended CNT, conditioned media was added to the Met5A cells for 24 hours after which cell viability and production of cytokines was measured. Cell viability of mesothelial cells was measured by LDH release (B) but no cell death was detected.

mesothelial cells to long CNT effects and the existing literature describing how conditioned media from macrophages treated with particles greatly amplify the pro-inflammatory responses of epithelial cells [22] and endothelial cells [23] led us to discount the alternative hypothesis, that products released by mesothelial cells could stimulate amplifying pro-inflammatory responses in the macrophages. Whilst mesothelial cells did prove refractory, in terms of cytokine release, to direct exposure to long and short CNT, macrophages exposed to long fibre CNT samples did release significant quantities of pro-inflammatory cytokines. When the supernatant from the long fibre-exposed macrophages was added to mesothelial cells it stimulated the mesothelial cells to release substantial quantities of cytokines that were much greater than those produced by the macrophages in response to long CNT or the mesothelial cells exposed to long CNT (Summarised in Table 1) or the sum of these two. Therefore the pro-inflammatory milieu generated by macrophages in response to long fibre CNT samples was a potent activator of mesothelial cells and caused a dramatic amplification of cytokine production by the mesothelial cells. Supernatants were centrifuged at 13,000 rpm for 5 minutes to remove any CNT and this procedure produced a black pellet and a clear supernatant. When the clear supernatant was added to the target mesothelial cells, in contrast to the direct treatment with CNT where black CNT were readily visible inside the cells, no particles were visible in or on the cells. It is not possible to preclude the presence of very small amounts of CNT but these would be trace amounts well below the threshold of effect.

The mechanism and outcome of phagocytosis of long CNT differs from that of short CNT or NPCB, in that phagocytosis proceeds initially but the macrophage cannot effectively enclose the extended structure of a long fibre culminating in the phenomenon of 'frustrated phagocytosis' [24]. The uptake of long fibres by macrophages and the subsequent pro-inflammatory response from the mesothelial cells exposed to their supernatant could be attenuated by inhibiting the phagocytosis of the long fibres by macrophages during the initial treatments using the microfilament poison Cytochalasin D; this confirms that the process of frustrated phagocytosis is is the key one that leads to inflammation in the case of the long fibre CNT. The macrophage response to LPS, which does not require microfilament-mediated

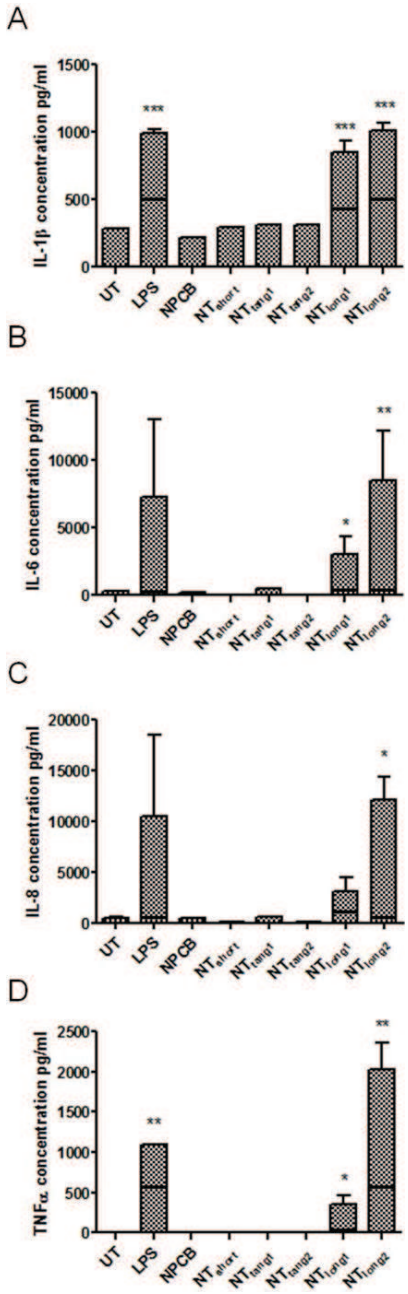

Figure 6 The effect of conditioned media on cytokine release from cells. IL-1β, IL-6, IL-8 and TNFα supernatant levels were measured 24 hours after mesothelial cells were exposed to media from CNT-treated macrophages. A length-dependent increase in concentration was observed for each of the cytokines. The black horizontal lines on the graph indicate the level of cytokine expressed by the THP-1 cells which is still present in the conditioned media. Data expressed as mean ± sem, n = 3. Significance versus vehicle control *** indicates $p < 0.001$.

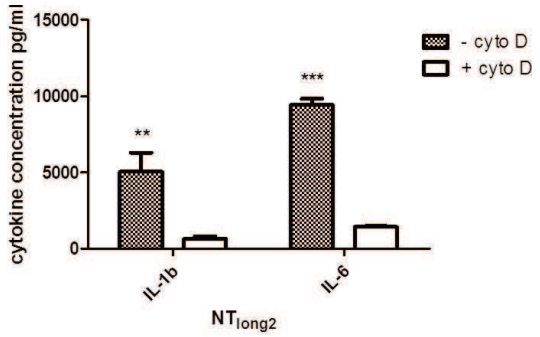

Figure 7 The effect of conditioned media from macrophages co-exposed to NT_{long2} and cytochalasin D on mesothelial production of IL-1β and IL-6. A significant reduction in the levels of IL-1β and IL-6 release from mesothelial cells exposed to conditioned media from macrophages treated with NT_{long2} and cytochalasin D was observed compared to mesothelial cells treated with conditioned media from macrophages treated with NT_{long2} alone. Data expressed as mean ± sem, n = 3. Significance versus vehicle control *** indicates $p < 0.001$.

uptake into cells by phagocytosis, was not attenuated by the addition of cytochalasin D highlighting the necessity of particle uptake and the role of frustrated phagocytosis in the pro-inflammatory reaction produced in response to CNT exposure. Our results suggest that indirect activation of mesothelial cells by pro-inflammatory cytokines elaborated from longCNT-exposed macrophages is a key initiating event in the development of pleural inflammation and disease.

Previous studies have described that long, needle-like CNT and asbestos activated the NLRP3 inflammasome

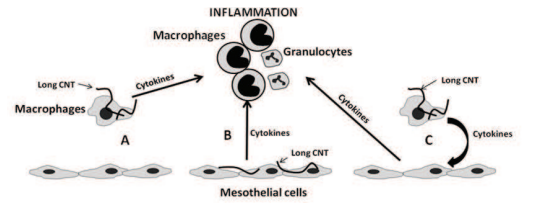

Figure 8 Potential mechanisms of the long fibre-mediated inflammatory response. The following three potential mechanisms by which CNT cause inflammation in the pleural space were explored in this study. (A) Long fibres interact with the pleural macrophages producing cytokines that directly elicit an inflammatory response. (B) Long fibres interact directly with mesothelial cells with the subsequent factors released leading to granulocyte influx. (C) Long fibres interact with macrophages inducing the release of cytokines which stimulate the mesothelial cells, amplifying the inflammatory response. As initial results showed no response from the mesothelial cells to direct exposure to CNT, the effect of factors released from CNT-exposed mesothelial cells on macrophages was not examined.

Table 1 Summary of cytokine release from cells

	IL-1β		IL-6		IL-8		TNFα	
	NT_{short}	NT_{long2}	NT_{short}	NT_{long2}	NT_{short}	NT_{long2}	NT_{short}	NT_{long2}
Mesothelial cells (pg/m)	205 ± 26	153 ± 17	340 ± 11	347 + 2	392 ± 15	458 ± 16	15 ± 2	10 ± 3
Macrophages (pg/ml)	296 ± 23	506 ± 34	128 ± 39	380 + 8	286 ± 8	403 ± 4	6 ± 2	350 ± 200
Mesothelial cells + conditioned media (pg/ml)	293 ± 2	1012 ± 59	214 ± 8	8479 + 3640	121 ± 29	12130 ± 2254	14 ± 4	2029 ± 328

The cytokine release for the three treatment groups are compared side by side using one short CNT (NT_{short}) and one long CNT (NT_{long2}) as exemplars

and secretion of IL-1β from LPS-primed human macrophages [25] whilst our macrophages were not primed with LPS. In our study the THP-1 cells had been differentiated with PMA [26]which gives then a phenotype similar to resting monocyte-derived macrophages.

A proportion of all particles and fibres that deposit in the distal regions of the lung will translocate into the pleural cavity thereby facilitating direct interactions between them and the patrolling macrophages of the pleural space and the mesothelial cells lining it [24]. According to Mercer et al. [34]CNT that reach the distal lung are likely to be predominantly present inside alveolar macrophages. However CNT in the immediate subpleural site, whilst a low proportion of all CNT, were all in tissue i.e. not in macrophages [27]. Therefore the CNT in the pleural space may be taken there inside alveolar macrophages, whilst the non-phagocytosed CNT that reach the pleural space from the sub-pleural tissue may be taken up by pleural macrophages. Research is needed to better understand the secretory profile of pleural macrophages or alveolar macrophages containing CNT in the pleural space. Mesothelial cells are reported to be uniquely sensitive to asbestos fibres with direct exposure in vitro inducing death [28,29], inflammatory mediator production [28], oxidative stress [30] and genotoxicity [39,40]. Although the potential pathogenicity of CNT has been tested in a variety of lung-derived cell types with responses including inflammation [33] and oxidative stress [34] reported, there is a paucity of data concerning the direct effects of CNT on mesothelial cells. Pacurari et al. examined the direct effects of SWCNT and MWCNT on normal and malignant mesothelial cells and reported a decrease in cell viability, activation of pro-inflammatory transcription factors and pro-inflammatory MAPK pathway activation [35,36]. However these effects were very modest and seen at 5-10 times the dose used in the present paper. There was also ongoing PARP activation suggesting that the cells were also undergoing apoptosis, making this data difficult to interpret as to the true role of direct pro-inflammatory effects of CNT on mesothelial cells at plausible doses. In contrast, within the present study we found mesothelial cell cytotoxicity only at the highest exposures used in preliminary studies but no evidence of pro-inflammatory responses after exposure of mesothelial cells to a low sub-lethal dose (5 $\mu g/cm^2$) of the panel of CNT. The inflammatory response to CNT after direct injection into the pleural space in vivo, characterised by an influx of inflammatory granulocytes [19], would undoubtedly require the actions of acute phase cytokines such as IL-1β, TNFα, IL-6 and IL-8. The inability of CNT to directly stimulate the production of such cytokines in mesothelial cells in vitro would suggest the interactions between CNT and mesothelial cells are not directly responsible for the initiation of inflammation.

In contrast to the findings with mesothelial cells, exposure of macrophages to the CNT panel resulted in the induction of modest length-dependent pro-inflammatory responses. This was evident when only the long fibre-containing samples (NT_{long1} and NT_{long2}) induced the production of the acute phase cytokines IL-1β and IL-6. The lack of response to the short CNT samples and particulate graphite in the form of NPCB suggest that the pro-inflammatory response to CNT in the pleural space is solely dependent on length. Length is a controlling factor in the clearance of fibres from the pleura where only long fibres are selectively retained for sufficient time to actually become involved in interactions with macrophages at stomatal openings [19]. Any fibre that exceeds a maximum length for macrophage uptake will result in frustrated phagocytosis, a state where the macrophages are unable to fully engulf long fibres resulting in the release of oxidants and pro-inflammatory signals [24]. Frustrated phagocytosis has long been known to play an important role in asbestos effects [24,37] and has also been implicated more recently in the inflammatory responses to long CNT elicited from macrophages in vitro [38] and in vivo [17] and long TiO_2 nanofibres [39]. Brown et al. reported an increase in the production of TNFα and a concurrent increase of ROS by macrophages in response to CNT and showed that this response was specifically related to the length of the CNT fibres [38]. The presence of macrophages undergoing frustrated phagocytosis in the peritoneal lavage fluid of mice exposed to long CNT was noted by Poland et al. who suggested that this macrophage-mediated response may be playing a role in the inflammation [17]. Here, using a panel of CNT similarly defined by length we showed the length-dependent release of a number of pro-inflammatory

cytokines from macrophages exposed to the long fibre CNT samples only. Frustrated phagocytosis of TiO_2 nanobelts longer than 15 μm was demonstrated by Hamilton et al. who also described the mechanism by which the inability of macrophages to completely enclose long fibres lead to pro-inflammatory responses via lysosomal destabilisation and NALP3 inflammasome activation [39]. The NALP3 inflammasome controls the maturation and release of IL-1β from activated cells [40] and activation of the NALP3 inflammasome via lysosomal destabilisation and the release of the lysosomal enzyme cathepsin B was reported in response to macrophage uptake of crystalline silica particles [41]. The activation of the NALP3 inflammasome by long CNT has also recently been demonstrated by Palomaki et al. in primary macrophages primed with LPS who, also reported a role for the $P2X_7$ receptor and its downstream tyrosine kinases, Src and Syk, in the activation of the NALP3 inflammasome in response to 'rigid, needle-like material' [42]. The induction of NALP3 via frustrated phagocytosis of long CNT is in keeping with studies examining the inflammatory response to asbestos and other fibrous particles which have also demonstrated the importance of the NALP3-mediated inflammatory response to particles and fibres in vivo. Inhibition or knock-out studies of key components of the NALP3 inflammasome prior to administration of asbestos fibres [43], silica [41,43,44] or MSU [41] crystals into the lungs of mice have all shown an attenuated inflammatory response compared to wild-type controls. The role for NALP3 in the activation of an inflammatory response suggests that direct interaction between macrophages and long fibres is the initiating mechanism for the development of long fibre-related inflammation and subsequent disease. Mesothelial cells are well equipped to participate in the initiation and resolution of inflammation. Secretion of chemokines by stimulated mesothelial cells promotes directed migration of granulocytes which can lead to influx of inflammatory cells from the vasculature into the serosal space [45]. Mesothelial cells have been shown to be directly stimulated to produce a range of pro-inflammatory mediators including cytokines, chemokines, growth factors and oxidants in response to bacterial endotoxin and asbestos but have also been shown to be highly responsive to factors secreted by macrophages [20]. Previous studies with PM10 and diesel soot have also shown that fixed cells-epithelial cells and endothelial cells respectively, show much greater responses to particle-free conditioned media from macrophages treated with particles than to direct treatment with the particles [22,23]. Similarly, in the present study a greatly amplified mesothelial pro-inflammatory response was conferred by the particle-free conditioned medium of long CNT-exposed macrophages. The role of cross-talk between macrophages and mesothelial cells in amplifying inflammation has been demonstrated previously by Betjes et al. when peritoneal mesothelial cells were shown to produce high levels of IL-8 in response to conditioned media from macrophages treated with the bacteria *Staphylococcus epidermidis*, but not to the bacteria themselves [46]. IL-1β and TNFα also mimicked induction of the mesothelial IL-8 response and the response to the conditioned media was blocked by the addition of anti-IL-1β and anti-TNFα antibodies [46]. The pro-inflammatory effect of the supernatant from macrophages exposed to the long CNT samples described here was similarly attenuated by inhibiting release of IL-1β by blocking phagocytosis with cytochalasin D highlighting the importance of phagocytosis in eliciting secretion of cytokines that drive the pro-inflammatory effects on the mesothelial cells. The acute inflammatory response seen in the pleural space after the injection of long CNT is characterised by the rapid influx of granulocytes into the pleural cavity [19]. The data suggest that it is a release of high levels of mesothelial IL-8 or KC, the mouse analogue of IL-8 in response to stimulatory factors released from macrophages attempting to phagocytose long CNT fibres that explains the inflammatory cell influx in vivo. Taking these 3 studies together [22,23,46] TNFα and IL-1β are the most likely candidate cytokines released by macrophages undergoing frustrated phagocytosis of long CNT that drive the pro-inflammatory effects in the mesothelial cells seen in our studies.

The mesothelial response to macrophage stimulation is also important in tissue repair. Macrophages were recruited in large numbers to the pleural space following long CNT deposition there [19]. Macrophages have been shown to stimulate mesothelial cell proliferation in response to injury in vivo with the rate of serosal healing dependent on the number of macrophages present [47] and also the macrophage-mediated release of cytokines such as TNFα [48]. Our data suggest that macrophages exposed to long CNT in the pleural space will have similar mitogenic effects on mesothelial cells which may lead to disregulated growth patterns.

The cross-talk between macrophages and mesothelial cells is known to be important in the normal inflammatory processes in the serosal cavities but, if disregulated, may also help to promote the development of mesothelioma. The precise mechanism that leads to mesothelioma development in the presence of fibres is unknown but a role for chronic inflammation in response to retained biopersistent fibres has been postulated [15]. Exposure of normal human mesothelial cells to asbestos fibres in vitro has not been shown to lead to cell transformation even though phenotypic changes such as chromosomal changes and extended lifespan were observed [31,32]. However Wang et al. [49] carried out a study examining the effect on mesothelial cells of erionite, a

naturally occurring long biopersistent fibre which causes mesothelioma in man and rodents following inhalation [50-52]. In this study, treatment of mesothelial cells with erionite in combination with pro-inflammatory cytokines highlighted a potential role for an inflammatory environment in the transformation of mesothelial cells [49]. While erionite alone had no effect on cell transformation, both IL-1β and TNFα could stimulate formation of transformed cells as identified by their anchorage-independent growth in soft agar. While the cytokines could induce the formation of tumorigenic colonies alone the effect was more potent in the presence of the erionite fibres [49]. TNFα has also been shown by Yang et al. to inhibit asbestos-induced cell death by activating the NF-κB signalling pathway in mesothelial cells [53]. The TNFα-mediated resistance to the cytotoxicity may promote tumour formation by increasing the pool of mesothelial cells with fibre-mediated genomic damage in the inflammogenic environment which evade normal cell death. This suggests that inflammation and inflammatory cytokines may play an important role in mesothelioma. Here we showed that mesothelial cells exposed to a cocktail of cytokines and other mediators produced by macrophages treated with long CNT amplify and propagate the inflammatory response thereby likely contributing to disease development in the pleural space.

A recent paper [54] has focused on the diameter of CNT and claimed that MWCNTs ~50 nm diameter showed mesothelial cell membrane piercing and cytotoxicity in vitro and subsequent inflammogenicity; in contrast CNT with a diameter of ~150 nm or ~2-20 nm were less inflammogenic. We found no support for this diameter hypothesis - the samples with least activity (short or tangled CNT) had diameters of 14.8, 10.4 and 84.9 nm respectively whilst the most active (the long CNT) was 165 nm diameter, quite close to the 150 nm diameter found to have no activity in the Nagai study [54].

Iron has been implicated in CNT activity via it's ability to cause oxidative stress [55,56]. However the levels of iron in our sample showed no relationship with activity in any of the assays; in particular the long CNT which had the most activity, had least iron.

Although we deal here solely with inflammation as a factor in fibre pathogenicity and mesothelioma production there are other effects of long fibres on mesothelial cells such as clastogenic and genotoxic ones that are important in themselves and possibly in concert with inflammation in leading to mesothelioma [54,57].

Conclusion

In summary, the data presented in this study describe a mechanism for the initiation of a long fibre mediated inflammatory response in the pleural space via frustrated phagocytosis. Only long fibres are retained in the pleural space and we have shown firstly that the incomplete phagocytosis of long CNT by macrophages, but not mesothelial cells, elicits a modest pro-inflammatory cytokine response. Secondly we show that the supernatant from macrophages exposed to long fibres produces a much-amplified pro-inflammatory response in target mesothelial cells. This amplified mesothelial cell response to macrophage products was attenuated by inhibition of macrophage phagocytosis, of long fibres confirming a role for frustrated phagocytosis. This study furthers our understanding of the role of macrophage/mesothelial cross-talk as a mechanism underlying the generation of a length-dependent inflammatory response to CNT in the pleural space. In addition, this in vitro model may prove useful for in vitro toxicity screening of the large number of new high aspect ratio nanofibres currently being developed, thereby reducing the need for animal testing.

Methods

CNT panel

The panel of particles investigated consisted of 5 different samples of multiwalled CNT and nano-particle carbon black (NPCB) as was used previously in Murphy et al. [19] (Table 2). The NT_{long1} sample (Mitsui & Co. Ltd., Japan) was produced by catalytic chemical vapour synthesis using the floating reaction method. The NT_{long2} sample was produced in an academic research laboratory (Dr Ian Kinloch, University of Manchester) using catalytic vapour discharge (CVD) method using a ferrocene-toluene feedstock to grow nanotubes from iron catalysts held on a silica plate. These nanotubes grew aligned as mats, meaning they were straight and un-entangled. The nanotubes were harvested from the mats using a razor blade, with some residual iron remaining within the nanotubes. We also included one commercially available short straight CNT ($NT_{short;}$ Nanoamor Inc., TX, USA) and two curled and tangled nanotubes of different lengths (NT_{tang1} which was cut to form predominantly short NT fibres and the original length NT sample (NT_{tang2}); NanoLab, Inc., MA, USA). These were produced by CVD with an iron and ceramic oxide (aluminosilicate) catalyst support which was removed using HCl and Hydrofluoric acid treatment. Trace metals and endotoxin levels previously tested and reported in Poland et al. [17] were low and thus not considered to play a role in these studies.

CNT suspensions

CNT were suspended in RPMI-1640 media (PAA Laboratories Ltd., UK) containing 0.5% bovine serum albumin (BSA; Sigma-Aldrich, Poole, UK) at a concentration of 500 μg/ml and dispersed by sonication at 230 V, 50 Hz, 350 W for 2 hours in an ultrasonic bath

Table 2 Characteristics of the particle panel

	NPCB	NT_{short}	NT_{tang1}	NT_{tang2}	NT_{long1}	NT_{long2}
Source	**Degussa Printex 90**	**Nanostructured & Amorphous Materials, Inc.**	**NanoLab, Inc.**	**NanoLab, Inc.**	**Mitsui & Co.**	**University of Manchester [Dr. I. Kinloch]**
Diameter (nm)	14	25.7 ± 1.6	14.84 ± 0.05	10.40 ± 0.32	84.89 ± 1.9	165.02 ± 4.68
Length (μm)	-	1-2	1-5	5-20	Mean 13	Mean 36
% fibre greater than 15 μm	‡	‡	‡	‡	24.04	84.26

(FB11002, Fisherbrand, Thermo Fisher Scientific, Inc., MA, USA). Suspensions were prepared freshly each day and used immediately upon removal from the ultrasonic bath.

Cell culture and treatment

The immortalised human mesothelial cell lineMet5A, and the monocytic cell line THP-1 were obtained from the American Type Culture Collection (ATCC) and maintained at sub-culture in RPMI-1640 supplemented with 10% foetal calf serum (PAA Laboratories Ltd., UK) at 37°C and 4% CO_2. Prior to experimentation Met5A cells were seeded in 24-well plates (Corning, Amsterdam, The Netherlands) at a concentration of 2.5×10^5 cells/well and allowed to adhere for 24 hours. THP-1 monocytic cells (2.5×10^5 cells/well) were differentiated into macrophages with 10 ng/ml phorbol 12-myristate 13-acetate (PMA; Sigma-Aldrich, Poole, UK) in 24-well plates for 48 hours. Prior to the treatment of both cell types the media was replaced with RPMI media containing 0% FCS, 1% penicillin/streptomycin and 1% L-Glutamate. Cells were treated with the CNT panel for 24 hours using a range of doses to determine cell viability, 5 μg/cm^2 was chosen as a sub-lethal dose for subsequent activation studies. Cytochalasin D (Enzo Life Science) was used to co-treat THP-1 cells along with NT_{long1}, NT_{long2}, or LPS. Light microscopy images of THP-1 cells treated with the panel of CNT were captured at ×40 magnification using QCapture Pro software (Media Cybernetics, MD, USA). For the conditioned media treatments THP-1 cells were treated with the CNT panel (5 μg/cm2) for 24 hours, supernatant was removed and centrifuged at 13,000 rpm for 5 minutes to remove any CNT. Conditioned media was added to the Met5A cells for 24 hours.

Scanning electron microscopy

THP-1 cells were grown on Thermonox coverslips (Nunc, Roskilde, Denmark) and treated with NPCB, NT_{short} or NT_{long2} for 24 hours. Cells were fixed with 10% Formalin and were stained with osmium tetroxide prior to critical point drying, mounted and gold sputter coated before examination by scanning electron microscopy (SEM) using an Hitachi S-2600 N digital scanning electron microscope (Oxford Instruments, Oxfordshire, UK).

Trypan blue exclusion assay

Met5A cells were plated as above before treatment with the particle panel for 24 hours at doses ranging from 5-50 μg/cm^2. The cell supernatant was removed and kept for LDH measurements, cells were washed once with PBS and incubated with 0.4% trypan blue (Sigma-Aldrich, Poole, UK) for 5 minutes. Excess trypan blue was removed and cells washed with PBS. Dead cells, as indicated by incorporation of the trypan blue dye, were counted and calculated as a percentage of total cells.

Lactate dehydrogenase assay

One hundred microlitres of cell supernatant from Met5A and THP-1 cells exposed to the CNT panel at doses ranging from 5-50 μg/cm^2 or LPS (1 μg/ml) was added in triplicate to a 96 well plate (Corning, Amsterdam, The Netherlands) and 100 μl of the LDH test reagent (diaphorase/NAD + mixed with iodotetrazolium chloride and sodium lactate at a ratio of 1:45) added to each well. Cells treated with 0.1% Triton-X were used as a positive control for 100% cell lysis. Following a 30 minute incubation period the absorbance of each well at 490 nm wavelength was established using a Synergy HT microplate reader (BioTek Instruments, Inc. VT, USA).

Cytokine bead array

The media levels of IL-1β, IL-6, IL-8 and TNFα were measured after direct exposure of the mesothelial cells and macrophages to the CNT panel and exposure of the mesothelial cells to the conditioned media from CNT-treated macrophages by cytokine bead array (BD CBA Flex Set, BD Biosciences, San Jose, CA). Briefly, 25 μl of the mixed capture antibodies were added along with 50 μl of the supernatant samples and standards to each well of a 96-well plate and incubated at room temperature for one hour. Twenty-five microlitres of the mixed PE detection reagent was added to each well and incubated at room temperature for two hours. The plate was centrifuged at 1500 rpm for 5 minutes and the supernatant completely

removed. One hundred and fifty microlitres of the wash buffer was added to each well. The plate was agitated for 5 minutes to resuspend the beads before the samples were analyzed using the BD FACSArray Bioanalyzer (BD Biosciences, San Jose, CA). Results were analysed using FCAP array software and sample concentrations of each cytokine were established via extrapolation from the appropriate recombinant protein standard curve.

ELISA

The media levels of IL-1β and IL-6 after macrophage inhibition studies was established using ELISA DuoSet kits (R&D systems, Abingdon, UK) specific to each analyte of interest. Ninety-six well microtitre plates were incubated overnight at 4°C with 100 μl of coating antibody raised against IL-1β or IL-6. The plates were washed 3 times with 0.05% Tween-20 in phosphate buffered saline (PBS; pH 7.2) and blocked using reagent diluent (1% BSA in PBS; R&D systems, Abingdon, UK) for 1 hour (room temperature) prior to further washing and addition of test samples/standards in triplicate. After 2 hrs the plates were washed and a biotinylated detection antibody added to each well followed by a further 2 hr incubation, followed by washing and the addition of HRP conjugated Streptavidin. The plates were washed and developed using a TMB substrate solution (Sigma-Aldrich, Poole, UK). The subsequent reaction was stopped with 0.5 M H_2SO_4, resulting in a yellow colour, and read at 450 nm. Sample concentrations of IL-1β, IL-6 were established via extrapolation from the appropriate recombinant protein standard curve.

Statistical analysis

All data are shown as the mean + s.e.m. and these were analysed using one-way analysis of variance (ANOVA). Multiple comparisons were analysed using the Tukey-HSD method, with values of $P < 0.05$ considered statistically significant (Instat, Graphpad Software Inc., CA, USA).

Additional material

Additional file 1: Supplementary information.

Abbreviations

CNT: carbon nanotubes; THP-1: macrophage cell line; Met5A: mesothelial cell line; NPCB: nanoparticulate carbon black; PARP: Poly (ADP-ribose) polymerase; TiO2: titanium dioxide; NALP3: NACHT: LRR and PYD domains-containing protein 3; P2X7: purinergic receptor; MSU: monosoium urate; IL-8: Interleukin 8; KC: keratinocyte -derived chemokine; TNFα: tumour necrosis factor α; NF-κB: Nuclear factor-κB; CVD: catalytic vapour discharge; ATCC: American Type Culture Collection; RPMI: Roswell Park Memorial Institute Medium; FCS: foetal calf serum; SEM: scanning electron microscopy; PBS: phosphate buffered saline; LDH: lactate dehydrogenase; FACS: fluorescence activated cell sorter.

Acknowledgements

We gratefully acknowledge Mitsui & Co. and Dr. Ian Kinloch (University of Manchester) for the provision of multiwalled carbon nanotube samples. We thank S. Mitchell (University of Edinburgh) for sample preparation for SEM and technical assistance. We thank the UK Department of Health (F.A.M.) and The Colt Foundation for the financial support (A. S., K.D.). This is an independent report commissioned and funded by the Policy Research Programme in the Department of Health and the views expressed are not necessarily those of the Department.

Author details

[1]MRC/University of Edinburgh Centre for Inflammation Research, ELEGI Colt Laboratory, Queen's Medical Research Institute, 47 Little France Crescent, Edinburgh EH16 4TJ, UK. [2]Institute of Occupational Medicine, Research Avenue North, Riccarton, Edinburgh EH14 4AP, UK.

Authors' contributions

All authors have made substantial contributions to conception and design and interpretation of data; FAM acquired the data with the assistance of AS. All authors were involved drafting or revising the manuscript and all authors have given final approval of the version to be published. All authors take public responsibility for the content. All authors read and approved the final manuscript.

Competing interests

KD has carried out consultancy for the nanotechnology industry not related to the scientific content of this manuscript.

Received: 20 December 2011 Accepted: 3 April 2012
Published: 3 April 2012

References

1. Donaldson K, Aitken R, Tran L, Stone V, Duffin R, Forrest G, *et al*: **Carbon nanotubes: a review of their properties in relation to pulmonary toxicology and workplace safety.** *Toxicol Sci* 2006, **92**:5-22.
2. Donaldson K, Murphy F, Schinwald A, Duffin R, Poland CA: **Identifying the pulmonary hazard of high aspect ratio nanoparticles to enable their safety-by-design.** *Nanomedicine* 2011, **6**:143-156.
3. Ye S, Wang Y, Jiao F, Zhang H, Lin C, Wu Y, *et al*: **The role of NADPH oxidase in multi-walled carbon nanotubes-induced oxidative stress and cytotoxicity in human macrophages.** *J Nanosci Nanotechnol* 2011, **11**:3773-3781.
4. Meunier E, Coste A, Olagnier D, Authier H, Lefevre L, Dardenne C, *et al*: **Double-walled carbon nanotubes trigger IL-1beta release in human monocytes through Nlrp3 inflammasome activation.** *Nanomedicine* 2011.
5. Shvedova AA, Kisin ER, Mercer R, Murray AR, Johnson VJ, Potapovich AI, *et al*: **Unusual inflammatory and fibrogenic pulmonary responses to single-walled carbon nanotubes in mice.** *Am J Physiol Lung Cell Mol Physiol* 2005, **289**:L698-L708.
6. He X, Young SH, Schwegler-Berry D, Chisholm WP, Fernback JE, Ma Q: **Multiwalled carbon nanotubes induce a fibrogenic response by stimulating reactive oxygen species production, activating NF-kappaB signaling, and promoting fibroblast-to-myofibroblast transformation.** *Chem Res Toxicol* 2011, **24**:2237-2248.
7. Donaldson K, Poland CA, Schins RP: **Possible genotoxic mechanisms of nanoparticles: criteria for improved test strategies.** *Nanotoxicology* 2010, **4**:414-420.
8. Donaldson K, Brown RC, Brown GM: **New perspectives on basic mechanisms in lung-disease .5. Respirable industrial fibers - mechanisms of pathogenicity.** *Thorax* 1993, **48**:390-395.
9. Stanton MF, Wrench C: **Mechanisms of mesothelioma induction with asbestos and fibrous glass.** *Journal of the National Cancer Institute* 1972, **48**:797-821.
10. Walker C, Everitt J, Barrett JC: **Possible cellular and molecular mechanisms for asbestos carcinogenicity.** *American Journal Of Industrial Medicine* 1992, **21**:253-273.
11. Miller BG, Searl A, Davis JM, Donaldson K, Cullen RT, Bolton RE, *et al*: **Influence of fibre length, dissolution and biopersistence on the production of mesothelioma in the rat peritoneal cavity.** *Ann Occup Hyg* 1999, **43**:155-166.

12. Barrett JC: **Cellular and Molecular Mechanisms of Asbestos Carcinogenicity - Implications for Biopersistence.** *Environmental Health Perspectives* 1994, **102**:19-23.
13. Okada F: **Beyond foreign-body-induced carcinogenesis: Impact of reactive oxygen species derived from inflammatory cells in tumorigenic conversion and tumor progression.** *International Journal Of Cancer* 2007, **121**:2364-2372.
14. Yang HN, Testa JR, Carbone M: **Mesothelioma Epidemiology, Carcinogenesis, and Pathogenesis.** *Current Treatment Options in Oncology* 2008, **9**:147-157.
15. Okada F, Fujii J: **Molecular mechanisms of inflammation-induced carcinogenesis.** *Journal of Clinical Biochemistry and Nutrition* 2006, **39**:103-111.
16. Nagai H, Toyokuni S: **Biopersistent fiber-induced inflammation and carcinogenesis: lessons learned from asbestos toward safety of fibrous nanomaterials.** *Arch Biochem Biophys* 2010, **502**:1-7.
17. Poland CA, Duffin R, Kinloch I, Maynard A, Wallace WA, Seaton A, *et al*: **Carbon nanotubes introduced into the abdominal cavity of mice show asbestos-like pathogenicity in a pilot study.** *Nat Nanotechnol* 2008, **3**:423-428.
18. Takagi A, Hirose A, Nishimura T, Fukumori N, Ogata A, Ohashi N, *et al*: **Induction of mesothelioma in p53+/- mouse by intraperitoneal application of multi-wall carbon nanotube.** *J Toxicol Sci* 2008, **33**:105-116.
19. Murphy FA, Poland CA, Duffin R, Al Jamal KT, Ali-Boucetta H, Nunes A, *et al*: **Length-dependent retention of carbon nanotubes in the pleural space of mice initiates sustained inflammation and progressive fibrosis on the parietal pleura.** *Am J Pathol* 2011, **178**:2587-2600.
20. Mutsaers SE: **Mesothelial cells: Their structure, function and role in serosal repair.** *Respirology* 2002, **7**:171-191.
21. Jantz MA, Antony VB: **Pathophysiology of the pleura.** *Respiration* 2008, **75**:121-133.
22. Jimenez LA, Drost EM, Gilmour PS, Rahman I, Antonicelli F, Ritchie H, *et al*: **PM(10)-exposed macrophages stimulate a proinflammatory response in lung epithelial cells via TNF-alpha.** *Am J Physiol Lung Cell Mol Physiol* 2002, **282**:L237-L248.
23. Shaw CA, Robertson S, Miller MR, Duffin R, Tabor CM, Donaldson K, *et al*: **Diesel exhaust particulate–exposed macrophages cause marked endothelial cell activation.** *Am J Respir Cell Mol Biol* 2011, **44**:840-851.
24. Donaldson K, Murphy FA, Duffin R, Poland CA: **Asbestos, carbon nanotubes and the pleural mesothelium: a review of the hypothesis regarding the role of long fibre retention in the parietal pleura, inflammation and mesothelioma.** *Part Fibre Toxicol* 2010, **7**:5.
25. Palomaki J, Valimaki E, Sund J, Vippola M, Clausen PA, Jensen KA, *et al*: **Long, needle-like carbon nanotubes and asbestos activate the NLRP3 inflammasome through a similar mechanism.** *ACS Nano* 2011, **5**:6861-6870.
26. Daigneault M, Preston JA, Marriott HM, Whyte MK, Dockrell DH: **The identification of markers of macrophage differentiation in PMA-stimulated THP-1 cells and monocyte-derived macrophages.** *PLoS One* 2010, **5**:e8668.
27. Mercer RR, Hubbs AF, Scabilloni JF, Wang L, Battelli LA, Schwegler-Berry D, *et al*: **Distribution and persistence of pleural penetrations by multi-walled carbon nanotubes.** *Part Fibre Toxicol* 2010, **7**:28.
28. Yang H, Rivera Z, Jube S, Nasu M, Bertino P, Goparaju C, *et al*: **Programmed necrosis induced by asbestos in human mesothelial cells causes high-mobility group box 1 protein release and resultant inflammation.** *Proc Natl Acad Sci USA* 2010, **107**:12611-12616.
29. Broaddus VC, Yang L, Scavo LM, Ernst JD, Boylan AM: **Asbestos induces apoptosis of human and rabbit pleural mesothelial cells via reactive oxygen species.** *Journal of Clinical Investigation* 1996, **98**:2050-2059.
30. Swain WA, Faux SP: **Activation of p38 MAP Kinase by Crocidolite in Mesothelial Cells is Dependent upon Oxidative Stress.** *Ann Occup Hyg* 2002, **46(Suppl 1)**:136-139.
31. Xu LX, Flynn BJ, Ungar S, Pass HI, Linnainmaa K, Mattson K, *et al*: **Asbestos induction of extended lifespan in normal human mesothelial cells: interindividual susceptibility and SV40 T antigen.** *Carcinogenesis* 1999, **20**:773-783.
32. Lechner JF, Tokiwa T, LaVeck M, Benedict WF, Banks-Schlegel S, Yeager H Jr, *et al*: **Asbestos-associated chromosomal changes in human mesothelial cells.** *Proc Natl Acad Sci USA* 1985, **82**:3884-3888.
33. Ye SF, Wen W, Wang YF, Lin CL, Wu YH, Zhang QQ: **Multi-walled Carbon Nanotubes Induces Nuclear Factor-kappa B Activation in A549 Cells.** *Chemical Journal of Chinese Universities-Chinese* 2010, **31**:497-501.
34. Pulskamp K, Diabate S, Krug HF: **Carbon nanotubes show no sign of acute toxicity but induce intracellular reactive oxygen species in dependence on contaminants.** *Toxicology Letters* 2007, **168**:58-74.
35. Pacurari M, Yin XJ, Zhao J, Ding M, Leonard SS, Schwegler-Berry D, *et al*: **Raw single-wall carbon nanotubes induce oxidative stress and activate MAPKs, AP-1, NF-kappaB, and Akt in normal and malignant human mesothelial cells.** *Environ Health Perspect* 2008, **116**:1211-1217.
36. Pacurari M, Yin XJ, Ding M, Leonard SS, Schwegler-Berry D, Ducatman BS, *et al*: **Oxidative and molecular interactions of multi-wall carbon nanotubes (MWCNT) in normal and malignant human mesothelial cells.** *Nanotoxicology* 2008, **2**:155-170.
37. Mossman BT, Churg A: **Mechanisms in the pathogenesis of asbestosis and silicosis.** *Am J Respir Crit Care Med* 1998, **157**:1666-1680.
38. Brown DM, Kinloch IA, Bangert U, Windle AH, Walter DM, Walker GS, *et al*: **An in vitro study of the potential of carbon nanotubes and nanofibres to induce inflammatory mediators and frustrated phagocytosis.** *Carbon* 2007, **45**:1743-1756.
39. Hamilton RF, Wu NQ, Porter D, Buford M, Wolfarth M, Holian A: **Particle length-dependent titanium dioxide nanomaterials toxicity and bioactivity.** *Particle and Fibre Toxicology* 2009, **6**:35.
40. Tschopp J, Schroder K: **NLRP3 inflammasome activation: the convergence of multiple signalling pathways on ROS production?** *Nature Reviews Immunology* 2010, **10**:210-215.
41. Hornung V, Bauernfeind F, Halle A, Samstad EO, Kono H, Rock KL, *et al*: **Silica crystals and aluminum salts activate the NALP3 inflammasome through phagosomal destabilization.** *Nature Immunology* 2008, **9**:847-856.
42. Palomaki J, Valimaki E, Sund J, Vippola M, Clausen PA, Jensen KA, *et al*: **Long, Needle-like Carbon Nanotubes and Asbestos Activate the NLRP3 Inflammasome through a Similar Mechanism.** *ACS Nano* 2011.
43. Dostert C, Petrilli V, Van Bruggen R, Steele C, Mossman BT, Tschopp J: **Innate immune activation through Nalp3 inflammasome sensing of asbestos and silica.** *Science* 2008, **320**:674-677.
44. Cassel SL, Eisenbarth SC, Iyer SS, Sadler JJ, Colegio OR, Tephly LA, *et al*: **The Nalp3 inflammasome is essential for the development of silicosis.** *Proceedings Of The National Academy Of Sciences Of The United States Of America* 2008, **105**:9035-9040.
45. Visser CE, Steenbergen JJE, Betjes MGH, Meijer S, Arisz L, Hoefsmit ECM, *et al*: **Interleukin-8 Production by Human Mesothelial Cells After Direct Stimulation with Staphylococci.** *Infection and Immunity* 1995, **63**:4206-4209.
46. Betjes MGH, Tuk CW, Struijk DG, Krediet RT, Arisz L, Hart M, *et al*: **Interleukin-8 Production by Human Peritoneal Mesothelial Cells in Response to Tumor-Necrosis-Factor-Alpha, Interleukin-1, and Medium Conditioned by Macrophages Cocultured with Staphylococcus-Epidermidis.** *Journal Of Infectious Diseases* 1993, **168**:1202-1210.
47. Mutsaers SE, Whitaker D, Papadimitriou JM: **Stimulation of mesothelial cell proliferation by exudate macrophages enhances serosal wound healing in a murine model.** *American Journal Of Pathology* 2002, **160**:681-692.
48. Mutsaers SE, McAnulty RJ, Laurent GJ, Versnel MA, Whitaker D, Papadimitriou JM: **Cytokine regulation of mesothelial cell proliferation in vitro and in vivo.** *European Journal of Cell Biology* 1997, **72**:24-29.
49. Wang YH, Faux SP, Hallden G, Kirn DH, Houghton CE, Lemoine NR, *et al*: **Interleukin-1 beta and tumour necrosis factor-alpha promote the transformation of human immortalised mesothelial cells by erionite.** *International Journal of Oncology* 2004, **25**:173-178.
50. Wagner JC, Skidmore JW, Hill RJ, Griffiths DM: **Erionite exposure and mesotheliomas in rats.** *Br J Cancer* 1985, **51**:727-730.
51. Maltoni C, Minardi F, Morisi L: **Pleural mesotheliomas in Sprague-Dawley rats by erionite: first experimental evidence.** *ENVIRONMENTAL RESEARCH* 1982, **29**:238-244.
52. Dikensoy O: **Mesothelioma due to environmental exposure to erionite in Turkey.** *Current Opinion in Pulmonary Medicine* 2008, **14**:322-325.
53. Yang HN, Bocchetta M, Kroczynska B, Elmishad AG, Chen YB, Liu ZM, *et al*: **TNF-alpha inhibits asbestos-induced cytotoxicity via a NF-kappa B-dependent pathway, a possible mechanism for asbestos-induced oncogenesis.** *Proceedings Of The National Academy Of Sciences Of The United States Of America* 2006, **103**:10397-10402.

54. Nagai H, Okazaki Y, Chew SH, Misawa N, Yamashita Y, Akatsuka S, *et al*: **Diameter and rigidity of multiwalled carbon nanotubes are critical factors in mesothelial injury and carcinogenesis.** *Proc Natl Acad Sci USA* 2011, **108**:E1330-E1338.
55. Kagan VE, Tyurina YY, Tyurin VA, Konduru NV, Potapovich AI, Osipov AN, *et al*: **Direct and indirect effects of single walled carbon nanotubes on RAW 264.7 macrophages: role of iron.** *Toxicol Lett* 2006, **165**:88-100.
56. Johnston HJ, Hutchison GR, Christensen FM, Peters S, Hankin S, Aschberger K, *et al*: **A critical review of the biological mechanisms underlying the in vivo and in vitro toxicity of carbon nanotubes: The contribution of physico-chemical characteristics.** *Nanotoxicology* 2010, **4**:207-246.
57. Kane AB: **Mechanisms of mineral fibre carcinogenesis.** In *Mechanisms of Fibre Carcinogenesis*. Edited by: Kane AB, Boffetta P, Saracci R, Wilbourn JD. IARC Publications, Lyon; 1996:11-34.

doi:10.1186/1743-8977-9-8
Cite this article as: Murphy *et al.*: The mechanism of pleural inflammation by long carbon nanotubes: interaction of long fibres with macrophages stimulates them to amplify pro-inflammatory responses in mesothelial cells. *Particle and Fibre Toxicology* 2012 **9**:8.

Murphy et al
Supplementary material

Excluding CNT interference in the assay

We checked the potential of the CNT samples used here to interfere with assays where elements of the assay might adsorb to the particle surface. To test for an effect in the LDH assay Met5A cells were lysed (100% LDH release) and incubated with 50μg/cm^2 long/short CNT or media control and LDH assessed.. No difference was seen between the LDH levels in samples incubated with the media control or the CNT samples (Supplementary Figure 1). The Trypan blue assay is not amenable to adsorption artefact since the blueness of cell is estimated by eye and, cells were not sufficiently highly loaded that the blue staining was obscured. In addition, the similarity in results between the Trypan Blue assay and the LDH assay with only the long CNT proving to have statistically significant cytotoxicity supports the contention that the cytotoxicity assays are not affected by adsorption. In order for adsorption artefact to explain the difference between NT long and NTshort in cytokine assays the NTshort would need to adsorb 3 - 6 times more cytokine per unit mass than the NTlong. We chose IL-8 as an examplar cytokine and diluted it to 500 pg/ml and dispersed NT long and NT short at 5μg/ml, the only dose used in these studies; these were then incubated overnight and IL-8 measured. There was no significant difference in the levels of IL-8 between untreated IL-8 and IL-8 treated with either long or short CNT (Supplementary Figure 2).
We conclude that interference of CNT in assays cannot explain any of the differential effects seen between long and short CNT in this study.

Iron content
The soluble iron content of the samples here has been previously published [1] and were as follows :- (units μg/g) CNT_{short} 24.3 , CNT_{tang} 7.9 , CNT_{long} <0.1.

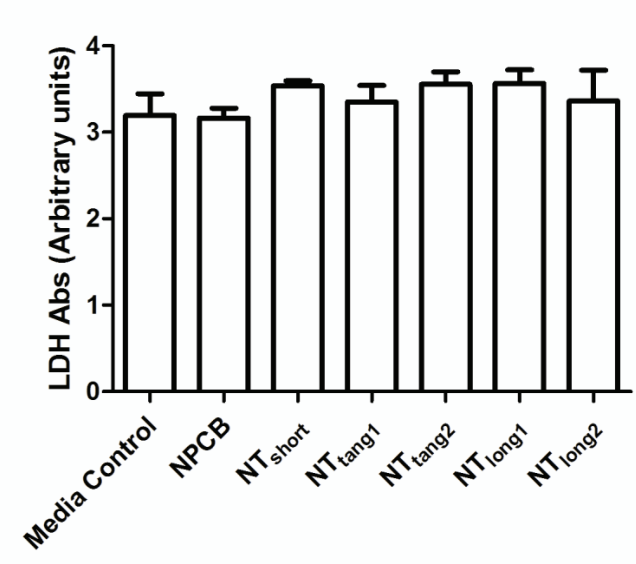

Supplementary Figure 1 Effect of CNT on measurement of LDH in the LDH assay.

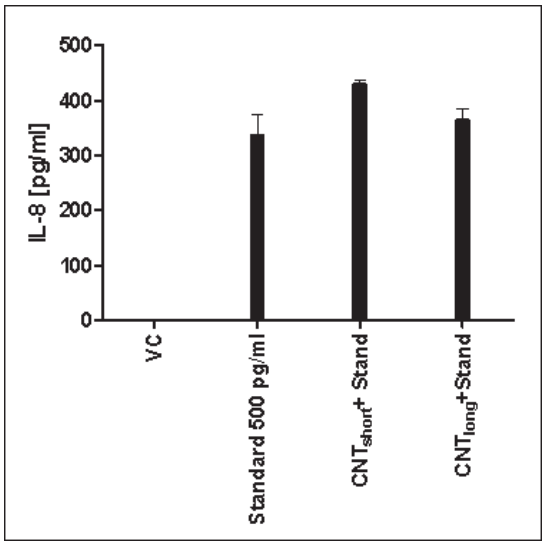

Supplementary Figure 2 Effect of CNT on levels of IL-8

Reference List

1. Murphy FA, Poland CA, Duffin R, Al Jamal KT, Ali-Boucetta H, Nunes A *et al*.: **Length-dependent retention of carbon nanotubes in the pleural space of mice initiates sustained inflammation and progressive fibrosis on the parietal pleura.** *Am J Pathol* 2011, **178:** 2587-2600.

4. **Schinwald A,** Murphy F, Prina-Mello A, Poland C, Byrne F, Glass J, Dickerson J, Schultz D, Movia D, Jeffree C, Macnee W, Donaldson K. **The threshold length for fibre-induced acute pleural inflammation: shedding light on the early events in asbestos-induced mesothelioma.** Toxicological Sciences. 2012 May 12; 128(2):461-70.

TOXICOLOGICAL SCIENCES **128(2)**, 461–470 (2012)
doi:10.1093/toxsci/kfs171
Advance Access publication May 12, 2012

The Threshold Length for Fiber-Induced Acute Pleural Inflammation: Shedding Light on the Early Events in Asbestos-Induced Mesothelioma

Anja Schinwald,* Fiona A. Murphy,* Adriele Prina-Mello,† Craig A. Poland,‡ Fiona Byrne,§ Dania Movia,† James R. Glass,¶ Janet C. Dickerson,¶ David A. Schultz,¶ Chris E. Jeffree,‖ William MacNee,* and Ken Donaldson*,‡,[1]

**MRC/University of Edinburgh, Centre for Inflammation Research, Queen's Medical Research Institute, 47 Little France Crescent, Edinburgh EH16 4TJ, United Kingdom; †School of Medicine and Centre for Research on Adaptive Nanostructures and Nanodevices (CRANN), Trinity College Dublin, Dublin 2, Ireland; ‡Institute of Occupational Medicine, Research Avenue North, Riccarton, Edinburgh EH14 4AP, United Kingdom; §School of Physics and CRANN, Trinity College Dublin, Dublin 2, Ireland; ¶Seashell Technology, LLC,3252 Holiday Court, Suite 115, La Jolla, California 92037; and ‖University of Edinburgh, Institute of Molecular Plant Sciences, Daniel Rutherford Building, King's Buildings, Edinburgh EH9 3JH, United Kingdom*

[1]To whom correspondence should be addressed. Fax: 0131 651 1558. E-mail: ken.donaldson@ed.ac.uk.

Received February 10, 2012; accepted May 01, 2012

Suspicion has been raised that high aspect ratio nanoparticles or nanofibers might possess asbestos-like pathogenicity. The pleural space is a specific target for disease in individuals exposed to asbestos and by implication of nanofibers. Pleural effects of fibers depends on fiber length, but the key threshold length beyond which adverse effects occur has never been identified till now because all asbestos and vitreous fiber samples are heterogeneously distributed in their length. Nanotechnology advantageously allows for highly defined length distribution of synthetically engineered fibers that enable for in-depth investigation of this threshold length. We utilized the ability to prepare silver nanofibers of five defined length classes to demonstrate a threshold fiber length for acute pleural inflammation. Nickel nanofibers and carbon nanotubes were then used to strengthen the relationship between fiber length and pleural inflammation. A method of intrapleural injection of nanofibers in female C57Bl/6 strain mice was used to deliver the fiber dose, and we then assessed the acute pleural inflammatory response. Chest wall sections were examined by light and scanning electron microscopy to identify areas of lesion; furthermore, cell–nanowires interaction on the mesothelial surface of the parietal pleura *in vivo* was investigated. Our results showed a clear threshold effect, demonstrating that fibers beyond 4 μm in length are pathogenic to the pleura. The identification of the threshold length for nanofiber-induced pathogenicity in the pleura has important implications for understanding the structure–toxicity relationship for asbestos-induced mesothelioma and consequent risk assessment with the aim to contribute to the engineering of synthetic nanofibers by the adoption of a benign-by-design approach.

Key Words: **silver nanowires; asbestos; pleural inflammation; HARN; fiber threshold; risk assessment.**

Asbestos caused and continues to cause a pandemic of lung and pleural disease due to inhalation of airborne respirable fibers, which reach the most peripheral parts of the lungs producing fibrosis and lung cancer and enter the pleura causing fibrosis and mesothelioma (Delgermaa *et al.*, 2011; Heintz *et al.*, 2010; Mossman *et al.*, 2011). Because of these risks, asbestos has been banned in most Western countries but, due to exposure in the past and the long lag time to diagnosis, there is a substantial number of ongoing deaths from mesothelioma per year in countries that used asbestos industrially. High aspect ratio nanomaterials (HARN) are characterized by their high ratio of length to width, are nanoscale in two dimensions, may be made from a wide range of elements and compounds, and fall either into the category of nanotubes, nanowires, or nanorods (Donaldson *et al.*, 2011). Chrysotile asbestos fibrils, which are commonly less than 100 nm in diameter, fulfill the criteria for a HARN, albeit a naturally occurring example. The fibrous shape brings advantages over compact nanoparticulate counterparts for certain industrial applications, and the intrinsic size, shape, and properties of metal nanoparticles can be tailored and fine tuned with great precision (Wiley *et al.*, 2005). The increasing use of HARN in the nanotechnology industries inevitably implies increased risk of exposure of workers during manufacturing processes. This has attracted the attention of risk assessors and toxicologists due to the similarities between asbestos and HARN, with mesothelioma being a major focus of concern.

We previously recorded that direct exposure of the peritoneal (Poland *et al.*, 2008) and the pleural mesothelial surfaces (Murphy *et al.*, 2011) produced inflammatory and fibrotic effects only with long (>10 μm) samples of carbon nanotubes (CNTs), a manufactured nanofiber that is in ever-higher production. Crucially, this length-dependent effect is also seen with asbestos fibers in the induction of mesothelioma, lung cancer, and fibrosis in rats (Davis *et al.*, 1986). These studies clearly imply that long, straight CNT should be risk managed like asbestos (British Standards Institution, 2007).

A fiber pathogenicity paradigm has been developed based on toxicology studies with asbestos and other natural and man-made fibers (Donaldson *et al.*, 2009, 2011). In 1996, Kane summarized parameters that render a fibrous material pathogenic, that is, biopersistence, dimensions (length, width), chemical composition, and surface reactivity. The parietal pleura is the key site of retention of long, biopersistent fibers, and the pleura is a site where fiber-specific pathology, including pleural effusion and the mesothelioma, is initiated (Donaldson *et al.*, 1989, 2010). Studies investigating the role of the length of asbestos and other fibers *in vitro* and *in vivo* in the development of pleural disease led to the overwhelming conclusion that longer fibers (> approximately 8 µm) are more pathogenic than shorter fibers (Davis *et al.*, 1986; Davis and Jones, 1988; Dodson *et al.*, 2003; Heintz *et al.*, 2010). Although fiber length is accepted as the major contributing factor to fiber pathogenicity, the length threshold value at which long-fiber effects occur in the pleura is unknown.

In the present study, we utilized the technical advances of nanotechnology to produce nanofibrous structures in tightly defined length categories to investigate the threshold length for fiber effects in the pleural space.

MATERIALS AND METHODS

Particle panel. The panel of nanowires consisted of five different lengths of silver nanowires (AgNWs) (www.seashelltech.com), abbreviated in the text as $AgNW_3$, $AgNW_5$, $AgNW_{10}$, $AgNW_{14}$, and $AgNW_{28}$ according to their mean length in micrometer (µm). The AgNW panel was provided in isopropanol at a concentration of 30 mg/ml. They were synthesized using a polyol process as described in U.S. patent number 7,922,787 B2 issued to Seashell Technology, San Diego, CA. Synthesis of AgNW and reaction conditions to obtain different lengths did not affect the chemical composition of the different nanowires. Sizing of the nanowire length was performed by light microscopy (100× magnification using QCaptur objective) (n = 100) (Table 1 and Supplementary figs. 1A–C). Mixed length amosite asbestos enriched for long fibers (100% fibers ≥ 5 µm, 50.3% fibers > 15 µm, and 35.2% fibers > 20 µm), hereafter referred to as long fiber asbestos (LFA), and shortened amosite asbestos (SFA; 3.1% fibers ≥ 5 µm) (Donaldson *et al.*, 1989) were used to link the response to asbestos pathogenicity. Both LFA and SFA were created from the same batch of South African amosite (Davis *et al.*, 1986) obtained from the Manville Corporation, United States. SFA was prepared by grinding long fibers in a ceramic ball mill, and the resulting fiber preparation sedimented in water. The process of ball milling used to shorten the LFA to make the SFA was associated with small changes in the iron chemistry (Graham *et al.* 1999; Tomatis *et al.* 2010). SFA contained a consistent fraction of nonfibrous particles based on the definition of a fiber by the WHO (1997) (i.e., longer than 5 µm, thinner than 3 µm, and with an aspect ratio greater than 3:1). Additionally short (4 µm/$NiNW_4$) and long (20 µm/$NiNW_{20}$) nickel nanowires (NiNWs) and short (2 µm/NT_2) and long (13 µm/NT_{13} and 36 µm/NT_{36}) multiwalled CNTs (MWCNTs) were used (see Supplementary table 1 and Supplementary fig. 2) as alternative forms of HARN. (NiNWs) were fabricated by electrochemical template synthesis at Trinity College (TCD, Ireland) as previously reported by Byrne *et al.* (2009) and Poland *et al*. (forthcoming) (see Supplementary table 1). The surface of these wires is coated with a layer of nickel oxide, which is approximately of 3–4 nm thickness, which act as protective layer against the chemical dissolution (Prina-Mello *et al.*, 2006). Material particulate control panel consisted of Ag-nanoparticle (Ag-P), Ni-nanoparticle (Ni-P), nanoparticle carbon black (NPCB) as reported in Supplementary table 1. Nanowires were tested for the presence of bacterial endotoxins using a Limulus Amebocyte Lysate test (Lonza Group, Switzerland), but no endotoxin was detectable (detection limit < 10pg/ml). To test the endotoxin levels, supernatant of the AgNW and NiNW solutions were used to avoid interference of AgNW or NiNW with the assay.

Experimental animals. Nine-week-old female C57Bl/6 strain mice (Harlan, U.K.) were used in this study. Mice were kept in a group size of five in standard caging with sawdust bedding within a pathogen-free Home Office approved facility. Mice were maintained on a normal 12-h light and dark cycle. Prior to the treatment, mice were kept for 7 days in the facility to acclimatize. The work was carried out by staff holding a valid U.K. Home Office personal licence under a Home Office approved project licence.

TABLE 1
Characterization of Silver Nanowire Length (AgNW)

	$AgNW_3$	$AgNW_5$	$AgNW_{10}$	$AgNW_{14}$	$AgNW_{28}$
Mean length (µm)	3	5	10	14	28
% fiber per length category (µm)					
0.5–1.5	6	2	0	0	0
1.5–2.5	39	7	0	2	0
2.5–3.5	53	22	2	2	0
3.5–4.5	2	14	0	0	0
4.5–5.5		12	3	0	0
5.5–6.5		40	9	0	0
6.5–7.5		2	4	2	0
7.5–8.5		1	4	2	0
8.5–9.5			24	23	0
9.5–10.5			14	14	0
10.5–15.5			34	17	22
15.5–20.5			6	26	13
20.5–30.5				12	20
30.5–40.5					31
40.5–50.5					9
50.5–60.5					5
Diameter (nm, mean ± SEM)	115 ± 3	118 ± 3	128 ± 2	121 ± 3	120 ± 4

Intrapleural injection and lavage. Samples were prepared in 0.5% bovine serum albumin (BSA; Sigma-Aldrich, Poole, U.K.)/saline and injected into the pleural cavity of unanesthetized female C57BI/6 mice at a dose of 5 µg per mouse and an injection volume of 100 µl per mouse. The site of injection was the right upper quadrant of the thorax. Mice were euthanized after 24 h and 1 week ($n = 4$) by asphyxiation in 100% CO_2. The pleural space was lavaged with three 1-ml washes of sterile saline. Cellular fraction and lavage fluid were separated by centrifugation. Total cell count was performed using a NucleoCounter (ChemoMetec, 7 A/S, Allerød, Denmark), and cyto-centrifugation followed by Diff-Quik staining using Diff-Quik stainset (Dade Behring GmbH, Marburg, Germany) were performed for differential cell counts. Images of lavaged cells were taken using QCapture Pro (Media Cybernetics Inc., Bethesda, MD).

Dissection. After 24-h and 1-week exposure, the lower right posterior portion of the chest wall was resected from the mice after lavage, washed in ice-cold saline, and fixed for 4 h in 30% formalin. The resected chest wall was an area of approximately 10 mm × 10 mm adjacent to the spine including the lower six ribs and intercostal space and, according to Shinohara *et al.* (1997), resulted to be rich in stomata. The chest wall was excised from the surrounding tissue, embedded on edge in paraffin, sectioned, and stained with hematoxylin and eosin for gross pathology ($n = 2$ per treatment for chest wall). Representative images of chest wall samples and lesion area were obtained by taking serial images at 10× magnification using QCapture Pro software (Media Cybernetics Inc.).

Scanning electron microscopy and backscatter secondary electron microscopy. Specimens were fixed and dehydrated as above, mounted on scanning electron microscopy (SEM) aluminum stubs, and rotary coated with about 8 nm of carbon in an Edwards 306A vacuum coating system (Edwards High Vacuum, Crawley, U.K.).

SEM of carbon-coated specimens was carried out using a Hitachi 4700 II field emission SEM (Hitachi High-Tech, Maidenhead, U.K.) at a beam accelerating voltage of 10 kV and a working distance of about 8 mm. Secondary electron (SE) and backscatter secondary electron (BSE) images were taken simultaneously using an annular YAG crystal BSE detector and the upper SE detector to produce perfectly synchronized image pairs. The two images were superimposed using Adobe Photoshop (Adobe Systems Incorporated, San Jose, CA) by layering the BSE image with the grayscale SE image using the Lighten function and pasting this image into the red channel of the SE image after conversion to RGB, thus color coding in red the strong BSE signal from the nanowires and the SE image appearing in gray.

Statistics. All data are shown as the mean ± SEM and these were analyzed using one-way analysis of variance. Multiple comparisons were analyzed using Tukey's honestly significant difference method and in all cases, values of $p < 0.05$ were considerably significant (GraphPad InStat Software Inc., La Jolla, CA).

RESULTS

Characteristics of the Particle Panel

AgNWs were characterized by SEM and light microscopy and showed a uniform dispersion in diameter and tight length distribution for each class (Table 1 and Supplementary fig. 1). Dissolution of AgNW was measured via change in pH compared with that of vehicle control across the 24-h exposure. No significant change in dissolution of AgNW occurred as shown by the almost flat slope of the curve across the 24-h exposure, and no difference in dissolution was observed between all AgNW lengths (Supplementary fig. S3A).

In addition to the AgNW panel, a range of nanofiber controls were used in this study including short (2 µm/NT_2) (mean length/acronym) and long (13 µm/NT_{13}, 36 µm/NT_{36}) MWCNTs (Murphy *et al.*, 2011) and short (4 µm/$NiNW_4$) and long (20 µm/$NiNW_{20}$) NiNWs. The CNT samples have been previously characterized by Murphy *et al.* (2011), whereas NiNWs were characterized according to their length distribution and diameter as previously described by Poland *et al.* (forthcoming) and Byrne *et al.* (2009), respectively. A modest extent of NiNW dissolution over 24 h was detected using pH change measurement; this is possible due to the saline solution degradation as shown by its reference curve (Supplementary fig. 3B).

Silver nanoparticulate (35 nm/Ag-P), NPCB, and Ni-P were included as material nanoparticulate controls. Well-characterized mixed length amosite asbestos enriched for long fibers and SFA (see Supplementary Information) were used as long (> 10 µm) and short pathogenic fiber control.

Acute Inflammatory Response to Intrapleural Injection of Silver Nanofibers and Controls

The pleural cavity was lavaged 24 h after intrapleural injection, and the acute inflammatory reaction measured as the total cell number and total granulocytes (predominantly neutrophils plus a low proportion of eosinophils) in the lavage. There was a clear length-dependent inflammatory response to AgNW, with significant increases in both total cell and total granulocyte number after treatment with AgNW that were 5 µm and longer (Figs. 1B and 1C) and LFA (Fig. 1D). In contrast, neither the very short fibers ($AgNW_3$ and SFA) nor the compact nanoparticles (Ag-P) elicited a significant inflammation (Figs. 1B–D). The length-dependent response reveals that the total granulocyte number induced was significantly increased ($p < 0.01$) with $AgNW_5$ compared with $AgNW_3$ (Fig. 1C). Moreover, there was no significant difference in inflammatory response (granulocytes) as length increased among $AgNW_5$, $AgNW_{10}$ and $AgNW_{14}$, demonstrating an all-or-nothing type of response beyond the 5 µm length. For $AgNW_{28}$, there was a significant increase in total cell number and granulocyte cell number compared with $AgNW_5$ (Figs. 1B and 1C). This all-or-nothing response was confirmed by a dose effect series for $AgNW_3$ and $AgNW_5$ (see Supplementary figs. 4A and 4B). $AgNW_3$ did not lead to a significant increase in inflammatory cells up to a tested dose of 10 µg per mouse.

The general design of this study used equal fiber mass; therefore, many more short fibers than long fibers were injected, yet still this greater number of short fibers in the dose of $AgNW_3$ was much less inflammogenic than the fewer long fibers in the dose of $AgNW_5$. Because fiber exposure is regulated in workplaces on the basis of the fiber number, we calculated the number of fibers per treatment for $AgNW_3$ and $AgNW_5$, the key lengths spanning the threshold value (see Supplementary materials and methods). Based on fiber number calculations, we reexpressed the inflammatory response 'per fiber,' and this

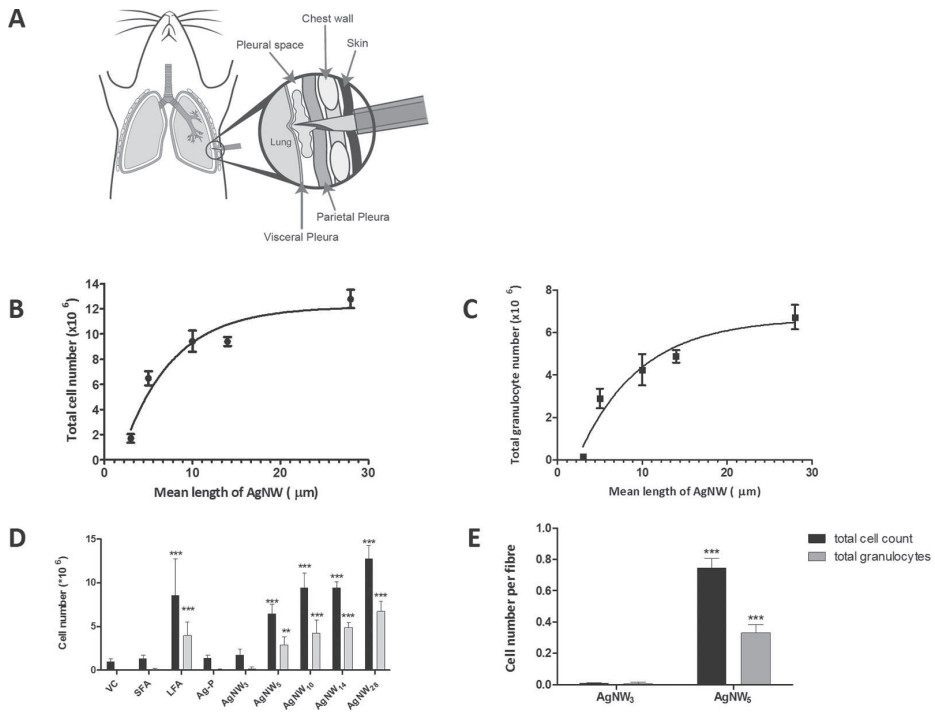

FIG. 1. Illustration of pleural injection and length-dependent response to AgNW in the pleural space 24 h postinjection. (A) Illustration of pleural injection showing a modified needle with a sleeve penetrating the chest wall into the pleural space to deliver the dose of nanofibers (Murphy *et al.*, 2011). (B) Count of total cell number in relation to fiber length of AgNW after 24-h treatment in female C57Bl/6 mice. All lengths were significantly greater than $AgNW_3$ ($p < 0.001$). Significant difference of $AgNW_5$ versus $AgNW_{10}$ ($p < 0.05$), $AgNW_5$ versus $AgNW_{14}$ ($p < 0.05$) and $AgNW_5$ versus $AgNW_{28}$ ($p < 0.001$) is observed. Data represent mean ± SEM of $n = 4$ mice. (C) Total granulocyte count from pleural lavage 24 h postinjection of AgNW in female C57Bl/6 mice. The influx of total granulocytes (neutrophil and eosinophil) is dependent on fiber length of AgNW. All lengths were significantly greater then $AgNW_3$ ($p < 0.01$–0.001). No significant difference of $AgNW_5$ versus $AgNW_{10}$ and $AgNW_5$ versus $AgNW_{14}$ is observed, whereas there is a significant difference of $AgNW_5$ versus $AgNW_{28}$ ($p < 0.001$). (D) Total cells and total granulocytes were counted in lavage fluid of mice treated with SFA, LFA, and AgNW panel. (E) Acute inflammatory response expressed per fiber. Equalization to fiber number reinforced the identified threshold value. Data represent mean ± SEM of $n = 4$ mice.

clearly showed that the fiber-specific inflammatory potency of the $AgNW_3$ fibers is negligible compared with the marked specific inflammogenicity of $AgNW_5$ fibers (Fig. 1E).

Light Microscopy and SEM of Parietal Pleura Surface

The pathogenic response to AgNW by the surface of the parietal pleura was examined by light microscopy and by SEM at 24-h postexposure. The pleural surface layer was a continuous normal mesothelium after intrapleural injection of vehicle control, SFA, Ag-P, and $AgNW_3$ (Figs. 2A–D). In contrast, sections of the parietal pleura from mice injected with LFA and $AgNW_{5/10/14/28}$ showed large lesions comprising macrophages and granulocytes at the pleural surface (Figs. 2E–I and Supplementary fig. 5).

Inflammatory Response After 7-Day Exposure

To address the course of the response, a 7-day time point was assessed at the 5-µg dose. The acute inflammatory response had largely resolved at this time point, although there was still a length-dependent effect detectable at $AgNW_{14/28}$ (Supplementary fig. 6A). Histological sections of the chest wall at 7 days continued to show thickening of the submesothelial cell layer in the same length-dependent pattern as the acute inflammation, that is, with a threshold at 5 µm (see Supplementary fig. 6B). BSE microscopy of *in vivo* biopersistence and light microscopy of *in vitro* durability showed that AgNWs retain their structural integrity over the 1-day time point but are not biopersistent over a protracted time (Fig. 3 and Supplementary fig. 7).

Phagocytosis of AgNW in Pleural Lavage Fluid and in Lesions on the Parietal Pleura

The degree of phagocytosis of different lengths of AgNW in pleural macrophages was assessed by light microscopy in cytospin preparations and by BSE in lesions on the parietal pleura. $AgNW_3$ and $AgNW_5$ could, for the most part, be fully phagocytosed inside pleural macrophages recovered in the lavage fluid (Fig. 3B) and in lesions on the parietal pleura imaged by BSE (Fig. 3F) at 1 day. In contrast, $AgNW_{10/14/28}$ lead to frustrated phagocytosis in the pleural macrophages (Figs. 3C–E and 3G, Supplementary fig. 8).

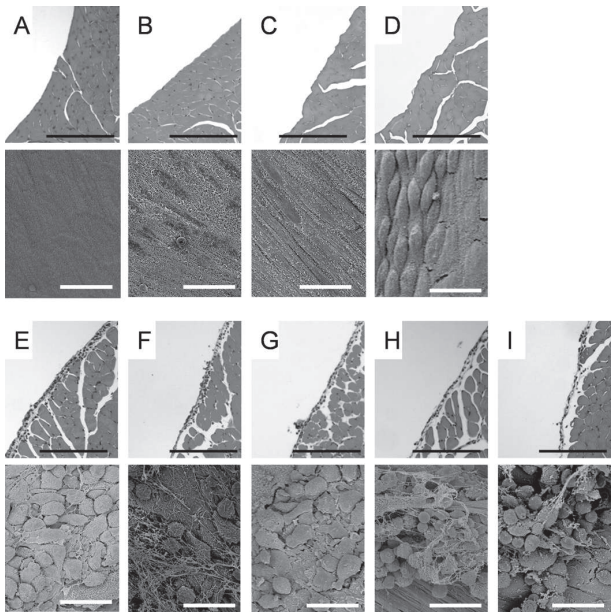

FIG. 2. Length-dependent response of AgNW on the parietal mesothelial surface 24 h postinjection. Hematoxylin and eosin histology sections and SEM images of VC (A), mice treated with Ag-P (B), $AgNW_3$ (C), SFA (D), $AgNW_5$ (E), $AgNW_{10}$ (F), $AgNW_{14}$ (G), $AgNW_{28}$ (H), and LFA (I). No alteration on the mesothelial surface can be seen in the mice treated with Ag-P, $AgNW_3$, and SFA. Normal mesothelial cells on the parietal pleura appear either flat as seen in the image of VC-exposed mesothelium or in a more rounded or raised form in areas called the lacunar regions, such as that seen in the image of SFA-exposed mesothelium (Donaldson *et al.*, 2010). Accumulation of inflammatory cells was observed on the mesothelial lining in mice treated with long AgNW (≥ 5 µm) and LFA. Scale bar: black 100 µm; white 20 µm.

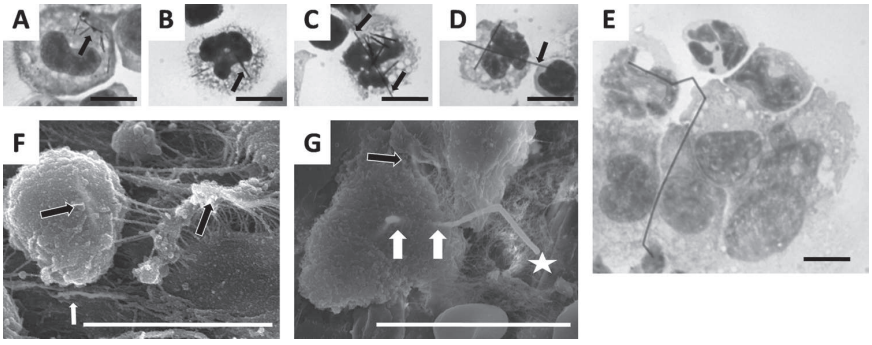

FIG. 3. Phagocytosis of AgNW in pleural lavage fluid and in inflammatory cells in lesions on the parietal pleura. Cytospin preparation of the pleural lavage fluid from mice treated with $AgNW_3$ (A) and $AgNW_5$ (B) shows complete phagocytosis of nanowires in pleural macrophages (nanowires indicated by the arrow). (C) $AgNW_{10}$ is not entirely phagocytosed, showing the ends of a nanowire protruding from a cell (indicated by two arrows). Frustrated phagocytosis of macrophages was observed after $AgNW_{14/28}$ treatment (D and E). A number of macrophages can be seen sharing a single fiber indicated by the arrow (F). All cytospin images are 100 magnification. Merged secondary electron and backscatter electron SEM images of the lesion's surface on the parietal pleura from mice treated with $AgNW_5$ (F) and $AgNW_{10}$ (G). (F) Two fibers are shown, which are fully phagocytosed by pleural macrophages (black arrows). The white arrow shows a fiber on the surface in the lesion area. (G) The star indicates frustrated phagocytosis of macrophages with $AgNW_{10}$. The loci where unclosed phagosomes must be present are indicated by the white arrows. The black arrow shows a fiber that is shared by two cells each of which must have an unclosed phagosome. Scale bar for all images 10 µm.

In addition, the presence of AgNW on the chest wall of mice treated with $AgNW_3$ was assessed, and no $AgNW_3$ could be found on the parietal pleura using BSE; hence, we assume that they were readily cleared from the pleural space after 24 h.

Role of Silver Ion Toxicity and Soluble Metals

We determined the release of soluble silver into saline for the different fiber lengths using inductively coupled plasma mass spectrometry, but these data are confounded by the formation

of insoluble silver chloride. We also collected the soluble products from the AgNWs of long and short lengths into saline and assessed the ability to cause pleural inflammation. Although we found no difference between soluble extracts of short and long AgNWs, this also may have been confounded by the formation of silver chloride and so these data are not included in this paper. The issue of the potential formation of silver chloride from silver ions and chloride ions raises an important question as to whether silver ions could ever be toxic *in vivo* because of their rapid removal by the formation of insoluble silver chloride following reaction with chloride ions, which are ubiquitous in biological systems. Furthermore, it seems to be impossible to measure silver ion release from Ag-P into biological media because chloride ions would always be present in biological media with the formation of silver chloride.

Acute Inflammatory Response to Intrapleural Injection of Nickel Nanofibers, CNTs and Controls

The acute inflammatory response to AgNW and SFA/LFA in the pleural space after intrapleural injection was compared with other forms of HARN NT_2, NT_{13}, and NT_{36} (Murphy *et al.*, 2011) and $NiNW_4$ and $NiNW_{20}$ using the same method. NPCB and Ni-P were included as material nanoparticulate controls (Supplementary table S1). Particulates and short fibers (NPCB, Ni-P, Ag-P, SFA, NT_2, $AgNW_3$, $NiNW_4$) produced no significant increase in total cell number and granulocytes 24 h after intrapleural injection (Fig. 4). In contrast, all fiber samples that were 5 µm and longer produced an inflammatory response (LFA, NT_{13}, NT_{36}, $AgNW_{5/10/14/28}$, $NiNW_{20}$) (Fig. 4 and Supplementary fig. 9). The data clearly show that the threshold length for long fiber effects in the pleural space is 5 µm. The difference in response to $NiNW_4$ and $AgNW_5$ is dramatic but can be explained by their size distribution curves, which are illustrated in Figure 4B. Hardly any $NiNW_4$ are longer than 5 µm; however, ~40% $AgNW_5$ are ≥ 5 µm (see Supplementary figs. 1C and 2). Further information excluding a role for soluble Ni ions can be found in Supplementary Information.

Size of Stomata Across Mammalian Species

To link the outcome from the mouse study to the human risk relating to fiber length, the size of human parietal pleural stomata and the site of long fiber retention are most relevant. We performed a literature search on the size range of stomata on the diaphragm or the parietal pleura of various species, which shows a remarkable constancy (Table 2). From mouse to human, the size ranges from 0.8 to 10 µm. This is in agreement with allometric scaling for lung cells in mammals ranging in size from shrews to horses (Stone *et al.*, 1992), which showed no mean difference in size for cells such as epithelial cells across this large range of body mass.

DISCUSSION

In this study, the use of defined length classes of nanofibers allowed us to quantify the threshold length for inflammatory effects in the pleural space, the key site for fiber pathogenicity. A method of intrapleural injection of particles, previously described by Murphy *et al*. (2011), was used to measure acute inflammation in the pleural space. This method is justified on the basis that a fraction of all inhaled particles and fibers that deposit in the peripheral lung translocate into the pleural space (Mercer *et al.*, 2010; Miserocchi *et al.*, 2008; Mitchev *et al.*, 2002; Walton, 1982). A dose of 5 µg was selected to allow comparison of the results with previously published data investigating the length-dependent effect of CNT in the pleural space (Murphy *et al.*, 2011).

We used a very specific panel of AgNW in different length classes, otherwise identical in composition, diameter, and solubility. This demonstrated a clear length threshold value for fiber pathogenicity in the pleural space of 5 µm. Significant increase in total cell number and granulocytes in the pleural space was observed after exposure to fibers of a length including 5 µm and longer, which could be confirmed via histological and SEM examination of the parietal pleura of the chest wall. Injecting a single dose into the pleural space, as we have done here, massively overrepresents the number of fibers that reach the stomata compared with inhalation, yet there was no inflammatory effect of any of the short nanofibers. The fact that the huge dose and high dose rate of short fibers produced by instillation into the pleura proved noninflammatory argues that the short fibers would be noninflammatory to the pleura following inhalation, when the dose reaching the pleura and the dose rate to the pleura would be vastly less than used here.

In our previous study (Poland *et al.*, 2008), we emphasized the role of long fiber frustrated phagocytosis but had no data on the exact cutoff length. Here nanofibers in tight size ranges enabled us to show that true frustrated phagocytosis, where fibers actually protrude from the surface of the cell, is not necessary for long fiber-induced inflammation in the pleural space. This is argued on the basis that $AgNW_5$ caused inflammation in the pleural space but was for the most part phagocytosed by pleural macrophages.

The role of Ag ion in mediating the toxic effects of compact Ag-P has been discussed extensively. Information about the role of Ag ion release in observed toxicity of silver particulates is mainly based on *in vitro* experiments at extremely high doses and cannot be correlated with *in vivo* observations (Johnston *et al.*, 2010). Recent studies could not identify a significant health effect after nanosilver exposure in *in vivo* studies (Stebounova *et al.*, 2011). This is consistent with the primary role for fiber length in the pleural pathogenicity of the AgNW panel used here. If soluble silver was the explanatory factor for the pattern of inflammation after intrapleural AgNW injection, a greater amount of soluble Ag release from longer AgNW should be observed. This was shown not to be the case and in

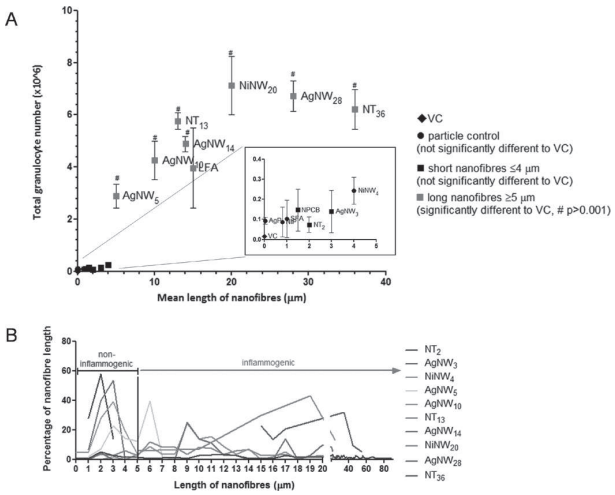

FIG. 4. The acute pleural response to CNT, NiNW, AgNW, SFA, and LFA in various lengths. (A) Female C57Bl/6 mice were intrapleurally instilled with 5 µg/mouse of NPCB (14 nm), NT_2, NT_{13}, NT_{36}, Ni-P, $NiNW_4$, $NiNW_{20}$, Ag-P (35 nm), $AgNW_3$, $AgNW_5$, $AgNW_{10}$, $AgNW_{14}$, $AgNW_{28}$, SFA, and LFA. Total granulocyte number is shown from pleural lavage 24-hour postexposure. A clear length-dependent threshold response in the pleural space to different sources and compositions of high aspect ratio nanomaterials from 5 µm in length is evident; NPCB/NT_2/NT_{36} data are obtained from Murphy *et al.* (2011). Length is shown as mean. Data represent mean ± SEM of $n = 4$ mice. (B) The percentage of nanofibers per length is plotted to illustrate their length distribution in relation to the cutoff length for fiber-induced pleural inflammation.

TABLE 2
Size of Stomata Across Mammalian Species

Species	Stomatal size (µm)	Reference
Bat	0.8–2	Azzali (1999)
Hedgehog, gerbil, bat, mouse	1.8–6	Azzali (1999)
Monkey	3–8	Oya *et al.* (1993)
Sheep	1–3	Lai-Fook (2004)
Human	6.2	Li (1993)
Rat, mouse, rabbit, hamster, human	4–10	Abu-Hijleh *et al.* (1995)
Human	2–8	Muller *et al.* (2002)

fact all samples give off negligible amounts of silver ions or other contaminating metals in femto- to picogram dilutions that would not be biologically active.

We set out to determine whether length was a unifying factor in pleural toxicity across a range of HARN in addition to AgNW to rule out material-specific effects and to further determine the length threshold for pleural inflammation. We obtained good support for the contention that, for acute pleural inflammation, length is the predominant structural explanatory variable across a range of fibrous nanomaterials and asbestos.

The greater pathogenic potency of long asbestos fibers in asbestos-induced pathology was identified in animal studies in the first half of the 20th century and with special reference to mesothelioma in the later studies of Stanton and Wrench (1972) and Davis *et al.* (1986). A mechanistic basis for the extra pathogenic effect of long asbestos fibers is evident in the greater retention of long fibers in the lungs compared with short fibers and the greater potency of long fibers in general at eliciting proinflammogenic effects *in vivo* (Poland *et al.*, 2008) and *in vitro* (Poland *et al.*, forthcoming). With special reference to the translocation of fibers to the pleural space and the occurrence of pleural pathology, we have noted that a fraction of all deposited particles translocate to the pleural space (Mercer *et al.*, 2010; Ryman-Rasmussen *et al.*, 2009). By using the model of direct pleural instillation, we bypassed various mechanisms of fiber clearance throughout the respiratory tract. However, recently, rodent pharyngeal aspiration and inhalation models using CNT (Mercer *et al.*, 2011; Ryman-Rasmussen *et al.*, 2009) verified the translocation of inhaled CNT to subpleural region where they caused pleural inflammation. However, so far the length threshold for fibers to reach the pleural space after inhalation exposure in rodent model is not known. Studies investigating the dimensions of asbestos fibers in mesothelial tissue from mesothelioma patients revealed that fibers up to a length of 62 µm were found in tumor tissue, with an average of 4.55 µm (Suzuki and Yuen, 2002). These data show that even the longest AgNW used in this study could potentially reach the subpleural tissue in humans after inhalation exposure. Nanofibers could reach the pleural space freely or in macrophages. In the study by Ryman-Rasmussen *et al.* (2009), MWCNTs were found subpleurally in macrophages, in subpleural mesenchymal cells, and free in the collagen matrix of the subpleura. In the study by Mercer *et al.* (2011), the "pleural penetrations" of CNT could be free fiber or fibers in macrophages. Long fibers translocated to the pleural space, both free or inside macrophages, are retained because they cannot negotiate the stomata in the parietal pleura, through which the efferent flow

of pleural fluid passes (Donaldson *et al.*, 2010). We believe that this explains the propensity of long fibers to cause pleural effects including mesothelioma when compact particles and short fibers do not. However, till this point, there has been no quantitative data on the threshold length for retention at the parietal stomata. The data here suggest that fibers of 5 µm, and above in length, are likely to be retained at the stomata where they can elicit inflammation. However, we do not doubt that a high enough dose of the shorter fibers would be inflammogenic in the pleural cavity due to artifactual aggregation into mats and clog in the stomata. This was shown previously by Kane (1996) in the peritoneal cavity, which possesses identical stomatal mechanism for fiber clearance (Goodglick and Kane, 1990).

Naturally, for purposes of extrapolating to the human risk relating to fiber length, the size of human parietal pleural stomata and the site of long fiber retention are most relevant. Across mammalian species, there is a remarkable consistency in the reported size of stomata on the diaphragm or parietal pleura. Therefore, we suggest that our findings of a general threshold for fiber retention that is applicable to humans are well served by the mouse model described here. We can only speculate on the events that follow from the first retention of a long fiber at a stoma, but the lodging of a long fiber at a stoma and recruitment of inflammatory cells to it may enhance the likelihood of further retention of long fibers and lead eventually to effective blockage of the stoma.

It has not escaped our notice that the global regulation of fibers is based on a standard definition of a fiber as an object that has a length greater than 5 µm, a width less than 3 µm, and an aspect ratio of greater than 3:1 (WHO, 1997). The 5-µm length regulatory standard was defined in the middle of the last century, and its origin was described in 1982 by Walton (Walton, 1982). It is fortuitous that the length of 5 µm was chosen, albeit without recourse to any scientific knowledge on length-dependent parietal pleural retention, as a margin of safety from long fibers (10–20 µm) that were known, even then, to be the most pathogenic fraction (Walton, 1982).

Ours is of course a study of a short-term response, but we contend that it is rationally related to long-term pathology in the pleural space and the argument for this is twofold. The first is the argument of dose, by which we mean that the model we put forward relies on acute inflammation as both a marker of, and a response to, retention in the pleural space and we confirm here that short fibers transit out of the pleural space. So long fibers must represent the only dose that could be related to the acute, but importantly also the chronic, responses seen in the pleural space to fibers. The second argument is based on the endpoint studied: inflammation is known to be directly related to fibrosis and cancer caused by asbestos through well-understood pathways and mechanisms (Dai and Churg, 2001; Dostert *et al.*, 2008; Nagai and Toyokuni, 2010; Unfried *et al.*, 2002).

The fact that the AgNWs used here were not biopersistent beyond a few days and does not detract from the relevance of the length-dependent effects demonstrated here. Biopersistent fibers of the same dimensions would have the same acute effect as AgNWs but, in contrast, would evoke an ongoing chronic inflammatory response that would lead to pathological change as we have reported for long, biopersistent MWCNTs (Murphy *et al.*, 2011). A clear link therefore exists between fiber length and the potential to cause acute inflammation; additionally, there is a link between fiber biopersistence and the ability for acute inflammation to become chronic and a link between chronic pleural inflammation and the common pleural pathologies associated with asbestos exposure, such as pleural fibrosis and mesothelioma.

Biopersistence therefore remains a key factor in determining the pathogenic effects of long nanofibers and warrants further elucidation, if the biopersistent nanofibers in narrowly defined length classes similar to the AgNW can be obtained. Our data suggest that any long, biopersistent fiber will be retained on the parietal pleura and is likely to engender chronic inflammation.

The conclusion of the threshold length of this study is mainly based on linear, straight, single fibers. However, long fibers that are tangled and agglomerated in their overall morphology, as is often the case with tangled CNT, have been shown to cause less inflammation due to their tightly packed spherical agglomerated state (Murphy *et al.*, 2011; Poland *et al.*, 2008). Therefore, the aggregation state of the nanofibers has to be considered to assess their toxicity.

In summary, our data provide for the first time a quantitative threshold for respirable fiber length in inducing pleural inflammation using a range of nanofibers. The threshold length for inducing pleural inflammogenicity in a range of fibers including amosite asbestos is 5 µm in the mouse, which we suggest can be extrapolated to humans. This knowledge is a valuable addition to our understanding of the mechanism of asbestos-related pleural disease, especially for mesothelioma and its relationship to fiber length. We recognize that this research was carried out in a mouse model and with a necessarily restricted range of nanofibers and that extrapolation to humans is not straightforward. Therefore, for regulatory purposes, we urge further research on the important issue of the threshold length for safe fibers with regard to the mesothelioma hazard to the pleura and the role of biopersistence. From the present data, however, we may conclude that, for acute inflammation, there is good evidence that short fibers less than 5 µm in length form the basis of safer-by-design nanofibers, and this has an important implication for fiber and nanofiber risk assessment.

SUPPLEMENTARY DATA

Supplementary data are available online at http://toxsci.oxfordjournals.org/.

FUNDING

Colt Foundation (A.S., K.D.); the Department of Health (F.A.M.); NAMDIATREAM (EU-FP7 project ref 246479

to A.P.-M., F.B.); CRANN Pathfinder (Science Foundation Ireland CSET programme to D.M.).

ACKNOWLEDGMENTS

We thank S. Mitchell (University of Edinburgh) for sample preparation for SEM and technical assistance.

REFERENCES

Abu-Hijleh, M. F., Habbal, O. A., and Moqattash, S. T. (1995). The role of the diaphragm in lymphatic absorption from the peritoneal cavity. *J. Anat.* **186**(Pt 3)**,** 453–467.

Azzali, G. (1999). The lymphatic vessels and the so-called "lymphatic stomata" of the diaphragm: A morphologic ultrastructural and three-dimensional study. *Microvasc. Res.* **57,** 30–43.

British Standards Institution. (2007). *PD 6699-2:2007 Guide to safe handling and disposal of manufactured nanomaterials*. Available at http://www.bsigroup.com/en/sectorsandservices/Forms/PD-6699-2/Download-PD6699-2-2007/. Accessed June 20, 2012.

Byrne, F., Prina-Mello, A., Whelan, A., Mohamed, B. M., Davies, A., Gun'ko, Y. K., Coey, J. M. D., and Volkov, Y. (2009). High content analysis of the biocompatibility of nickel nanowires. *J. Magn. Magn. Mater.* **321,** 1341–1345.

Dai, J., and Churg, A. (2001). Relationship of fiber surface iron and active oxygen species to expression of procollagen, PDGF-A, and TGF-beta(1) in tracheal explants exposed to amosite asbestos. *Am. J. Respir. Cell Mol. Biol.* **24,** 427–435.

Davis, J. M., Addison, J., Bolton, R. E., Donaldson, K., Jones, A. D., and Smith, T. (1986). The pathogenicity of long versus short fibre samples of amosite asbestos administered to rats by inhalation and intraperitoneal injection. *Br. J. Exp. Pathol.* **67,** 415–430.

Davis, J. M., and Jones, A. D. (1988). Comparisons of the pathogenicity of long and short fibres of chrysotile asbestos in rats. *Br. J. Exp. Pathol.* **69,** 717–737.

Delgermaa, V., Takahashi, K., Park, E. K., Le, G. V., Hara, T., and Sorahan, T. (2011). Global mesothelioma deaths reported to the World Health Organization between 1994 and 2008. *Bull. World Health Organ.* **89,** 716–724C.

Dodson, R. F., Atkinson, M. A., and Levin, J. L. (2003). Asbestos fiber length as related to potential pathogenicity: A critical review. *Am. J. Ind. Med.* **44,** 291–297.

Donaldson, K., Brown, G. M., Brown, D. M., Bolton, R. E., and Davis, J. M. (1989). Inflammation generating potential of long and short fibre amosite asbestos samples. *Br. J. Ind. Med.* **46,** 271–276.

Donaldson, K., Murphy, F., Schinwald, A., Duffin, R., and Poland, C. A. (2011). Identifying the pulmonary hazard of high aspect ratio nanoparticles to enable their safety-by-design. *Nanomedicine (Lond).* **6,** 143–156.

Donaldson, K., Murphy, F. A., Duffin, R., and Poland, C. A. (2010). Asbestos, carbon nanotubes and the pleural mesothelium: A review of the hypothesis regarding the role of long fibre retention in the parietal pleura, inflammation and mesothelioma. *Part. Fibre Toxicol.* **7,** 5

Dostert, C., Petrilli, V., Van, B. R., Steele, C., Mossman, B. T., and Tschopp, J. (2008). Innate immune activation through Nalp3 inflammasome sensing of asbestos and silica. *Science* **320,** 674–677.

Goodglick, L. A., and Kane, A. B. (1990). Cytotoxicity of long and short crocidolite asbestos fibers in vitro and in vivo. *Cancer Res.* **50,** 5153–5163.

Graham, A., Higinbotham, J., Allan, D., Donaldson, K., and Beswick, P. H. (1999). Chemical differences between long and short amosite asbestos: Differences in oxidation state and coordination sites of iron, detected by infrared spectroscopy. *Occup. Environ. Med.* **56,** 606–611.

Heintz, N. H., Janssen-Heininger, Y. M., and Mossman, B. T. (2010). Asbestos, lung cancers, and mesotheliomas: From molecular approaches to targeting tumor survival pathways. *Am. J. Respir. Cell Mol. Biol.***42,** 133–139.

Johnston, H. J., Hutchison, G., Christensen, F. M., Peters, S., Hankin, S., and Stone, V. (2010). A review of the in vivo and in vitro toxicity of silver and gold particulates: Particle attributes and biological mechanisms responsible for the observed toxicity. *Crit. Rev. Toxicol.* **40,** 328–346.

Kane, A. B. (1996). Mechanisms of mineral fibre carcinogenesis. *IARC Sci. Publ.* **140**, 11–34.

Lai-Fook, S. J. (2004). Pleural mechanics and fluid exchange. *Physiol. Rev.* **84,** 385–410.

Li, J. (1993). Ultrastructural study on the pleural stomata in human. *Funct. Dev. Morphol.* **3,** 277–280.

Mercer, R. R., Hubbs, A. F., Scabilloni, J. F., Wang, L., Battelli, L. A., Friend, S., Castranova, V., and Porter, D. W. (2011). Pulmonary fibrotic response to aspiration of multi-walled carbon nanotubes. *Part. Fibre Toxicol.* **8,** 21.

Mercer, R. R., Hubbs, A. F., Scabilloni, J. F., Wang, L., Battelli, L. A., Schwegler-Berry, D., Castranova, V., and Porter, D. W. (2010). Distribution and persistence of pleural penetrations by multi-walled carbon nanotubes. *Part. Fibre Toxicol.* **7,** 28.

Miserocchi, G., Sancini, G., Mantegazza, F., and Chiappino, G. (2008). Translocation pathways for inhaled asbestos fibers. *Environ. Health* **7,** 4.

Mitchev, K., Dumortier, P., and De, V. P. (2002). 'Black Spots' and hyaline pleural plaques on the parietal pleura of 150 urban necropsy cases. *Am. J. Surg. Pathol.* **26,** 1198–1206.

Mossman, B. T., Lippmann, M., Hesterberg, T. W., Kelsey, K. T., Barchowsky, A., and Bonner, J. C. (2011). Pulmonary endpoints (lung carcinomas and asbestosis) following inhalation exposure to asbestos. *J. Toxicol. Environ. Health B Crit. Rev.* **14,** 76–121.

Muller, K. M., Schmitz, I., and Konstantinidis, K. (2002). Black spots of the parietal pleura: Morphology and formal pathogenesis. *Respiration* **69,** 261–267.

Murphy, F. A., Poland, C. A., Duffin, R., Al-Jamal, K. T., Ali-Boucetta, H., Nunes, A., Byrne, F., Prina-Mello, A., Volkov, Y., Li, S., *et al.* (2011). Length-dependent retention of carbon nanotubes in the pleural space of mice initiates sustained inflammation and progressive fibrosis on the parietal pleura. *Am. J. Pathol.* **178,** 2587–2600.

Nagai, H., and Toyokuni, S. (2010). Biopersistent fiber-induced inflammation and carcinogenesis: Lessons learned from asbestos toward safety of fibrous nanomaterials. *Arch. Biochem. Biophys.* **502,** 1–7.

Oya, M., Shimada, T., Nakamura, M., and Uchida, Y. (1993). Functional morphology of the lymphatic system in the monkey diaphragm. *Arch. Histol. Cytol.* **56,** 37–47.

Poland, C. A., Byrne, F., Cho, W. S., Prina-Mello, A., Murphy, F. A., Davies, G. L., Coey, J. M., Gounko, Y., Duffin, R., Volkov, Y., *et al.* (Forthcoming). Length-dependent pathogenic effects of nickel nanowires in the lungs and the peritoneal cavity. *Nanotoxicology*.

Poland, C. A., Duffin, R., Kinloch, I., Maynard, A., Wallace, W. A., Seaton, A., Stone, V., Brown, S., MacNee, W., and Donaldson, K. (2008). Carbon nanotubes introduced into the abdominal cavity of mice show asbestos-like pathogenicity in a pilot study. *Nat. Nanotechnol.* **3,** 423–428.

Prina-Mello, A., Diao, Z., and Coey, J. M. (2006). Internalization of ferromagnetic nanowires by different living cells. *J. Nanobiotechnol.* **4,** 9.

Ryman-Rasmussen, J. P., Cesta, M. F., Brody, A. R., Shipley-Phillips, J. K., Everitt, J. I., Tewksbury, E. W., Moss, O. R., Wong, B. A., Dodd, D. E., Andersen, M. E., *et al.* (2009). Inhaled carbon nanotubes reach the subpleural tissue in mice. *Nat. Nanotechnol.* **4,** 747–751.

Shinohara, H. (1997). Distribution of lymphatic stomata on the pleural surface of the thoracic cavity and the surface topography of the pleural mesothelium in the golden hamster. *Anat. Rec.* **249,** 16–23.

Stanton, M. F., and Wrench, C. (1972). Mechanisms of mesothelioma induction with asbestos and fibrous glass. *J. Natl. Cancer Inst.* **48,** 797–821.

Stebounova, L. V., Mcakova-Dodd, A., Kim, J. S., Park, H., O'Shaughnessy, P. T., Grassian, V. H., and Thorne, P. S. (2011). Nanosilver induces minimal lung toxicity or inflammation in a subacute murine inhalation model. *Part. Fibre Toxicol.* **8**, 5.

Stone, K. C., Mercer, R. R., Gehr, P., Stockstill, B., and Crapo, J. D. (1992). Allometric relationships of cell numbers and size in the mammalian lung. *Am. J. Respir. Cell Mol. Biol.* **6,** 235–243.

Suzuki, Y., and Yuen, S. R. (2002). Asbestos fibers contributing to the induction of human malignant mesothelioma. *Ann. N.Y. Acad. Sci.* **982,** 160–176.

Tomatis, M., Turci, F., Ceschino, R., Riganti, C., Gazzano, E., Martra, G., Ghigo, D., and Fubini, B. (2010). High aspect ratio materials: Role of surface chemistry vs. length in the historical "long and short amosite asbestos fibers". *Inhal. Toxicol.* **22,** 984–998.

Unfried, K., Schürkes, C., and Abel, J. (2002). Distinct spectrum of mutations induced by crocidolite asbestos: Clue for 8-hydroxydeoxyguanosine-dependent mutagenesis in vivo. *Cancer Res.* **62,** 99–104.

Walton, W. H. (1982). The nature, hazards and assessment of airborne dust: A review. *Ann. Occup. Hyg.* **25,** 117–247.

Wiley, B., Sun, Y. G., Mayers, B., and Xia, Y. N. (2005). Shape-controlled synthesis of metal nanostructures: The case of silver. *Chem.-A Eur. J.* **11,** 454–463.

WHO. (1997). *Determination of Airborne Fiber Number Concentration: A Recommended Method by Phase Contrast Microscopy.* WHO, Geneva, Switzerland.

Supporting Online Material for

The threshold length for fibre-induced acute pleural inflammation: shedding light on the early events in asbestos-induced mesothelioma.

Anja Schinwald, Fiona A. Murphy, Adriele Prina-Mello, Craig A. Poland, Fiona Byrne, James R. Glass, Janet C. Dickerson, David A. Schultz, Dania Movia, Chris E. Jeffree, William MacNee, Ken Donaldson

correspondence to: ken.donaldson@ed.ac.uk

Materials and Methods

Light microscopy/Backscatter SEM of AgNW and fibre length count

Whilst the limit of resolution of light microscopy would normally preclude the visualisation of 120 nm diameter nanowires, the surface plasmon resonance properties of silver NP mean that they have a strong scattering cross section allowing for sub 100 nm nanoparticles to be easily visualized with a conventional microscope (Schrand *et al.* 2010). For light microscopy images a concentration of 50 µg/ml of AgNW was used to demonstrate the dispersion of the materials at the concentration used for pleural injection (Table 1 and Fig. S1a) and to confirm the durability over 1 day of AgP and AgNW after rotation for 24 hour in pH 5.0 saline solution (Fig. S7c). Ten µl of AgNW (50 µg/ml) suspended in 0.5 % bovine serum albumin (BSA; Sigma-Aldrich, Poole, UK)/saline were mixed with 10 µl of glycerol (Sigma-Aldrich, Poole, UK) to reduce the flow of AgNW. The suspension was placed on glass slide and covered with a glass coverslip and sealed (Murphy *et al.* 2011). Images were captured at x100 magnification using QCapture Pro software (Media Cybernetics). From each batch 100 fibres were measured according to their length by using a graticule and by using measurement software (Image-Pro Plus; Media Cybernetics Inc., MD, USA). The length distribution was plotted as percentage fibre per length category and percentage of fibre greater than length (Table 1, Fig. S1c).

For BSEM (Fig. S1b) AgNW/saline suspension was filtered onto an Isopore™ membrane filter (Millipore), dried and rotary-coated with about 8 nm of carbon in an Edwards 306A vacuum coating system (Edwards High Vacuum, Crawley, UK). Backscatter SEM of carbon-coated specimens was carried out using a Hitachi 4700 II field emission SEM (Hitachi High-

Tech, Maidenhead, UK) at a beam accelerating voltage of 10 kV and a working distance of about 8 mm.

Calculation for equalised fibre length

Since fibre exposure is regulated on the basis of the fibre number we calculated the number of fibres per treatment for $AgNW_3$ and $AgNW_5$, the key lengths spanning the threshold value.

Length of NW (average) [µm] = 5.00
Diameter of NW [µm] = 0.118
Density of NW [µg/ml] = 1.05×10^7
Volume of NW [ml] = $5 * \prod * \left(\frac{0.118}{2}\right)^2$
$= 5.468 \times 10^{-14}$
Weight of NW [µg] = $5.468 \times 10^{-14} \times 1.05 \times 10^7$
$= 5.741 \times 10^{-7}$
Dose [µg] per mouse = 5.00
Number of NW = $\frac{5.00}{5.741 \times 10^{-7}}$
$= 8708836 = \cong 8.7\ mln\ wires$

Length of NW (average) [µm] = 3.00
Diameter of NW [µm] = 0.115
Density of NW [µg/ml] = 1.05×10^7
Volume of NW [ml] = $3 * \prod * \left(\frac{0.115}{2}\right)^2$
$= 3.116 \times 10^{-14}$
Weight of NW [µg] = $3.116 \times 10^{-14} \times 1.05 \times 10^7$
$= 3.272 \times 10^{-7}$
Dose [µg] per mouse = 5.00
Number of NW = $\frac{5.00}{3.272 \times 10^{-7}}$
$= 15282107 = \cong 15.2\ mln\ wires$

pH measurements for dissolution of NWs

Russell RL060P Portable pH Meter (Thermo Electron Corporation, USA) + Semi-micro with a Pellon junction microelectrode (VWR, Ireland) was used for pH measurements. Sodium chloride topical irrigation sterile solution (sodium chloride 0.9 % w/w) (Johnson & Johnson, UK) was used as a control and of nanowires (NW) dilutions. NW solution was prepared by adding stock NWs solution to saline (final NWs concentration: 50 µg/mL) into a clean, dry eppendorf (1.5 mL). pH measurements were repeated every 2 hours for 24 hours (n=3). Measurements were carried out under the same environmental conditions (21 degree Celsius, RH =64 %). A linear fitting on the averaged data of each NW and solution measured were applied. The linear fitting associated to the saline pH variations was compared to those of the NWs solutions. This data allowed to identify time-dependent pH variations that are significant. Statistical analysis is measured as difference in the slope of the linear fitting of each measurement (Student's t-test).

Discussion:

Role of Ni ion release and size distribution curve

Soluble Ni ions from the NiNW are unlikely to play a role since previous studies have shown that degradation of NiNW in biological media is minimal (Raphael *et al.* 2010).

Additionally, the NiNW used in this study are covered by a 3-4 nm layer of nickel oxide (Prina-Mello *et al.* 2006) which is insoluble and so would prevent dissolution of the underlying nickel metal surface (Raphael *et al.* 2010); we also previously showed that the soluble products from NiO NP were not inflammogenic (Cho *et al.* 2011) in the lung. Following injection into the peritoneal cavity of NiNW from the same source as those used in

the present study, only long NiNW produced a significant inflammatory response and not Ni nanoparticles or short NiNW (Poland *et al.* 2011).

Furthermore, as stated in the manuscript to preclude a role of the soluble, ionic fraction of NiNWs in the assay, the amount of Ni released was measured by ICP-MS. Thus, $NiNW_{4/20}$ and Ni-P were incubated with BSA/saline for 24 h and measured. These were found to be in the picogram region or not quantifiable since below the BSA/saline threshold level (see Table S3A,B).

To completely rule out the effect of soluble Ni an aqueous extract of long NiNW was instilled into the peritoneal cavity and did not cause inflammation. We have previously shown that the response of the pleura and peritoneal cavities are identical in terms of the response to fibre length (Poland *et al.* 2011) (Murphy *et al.* 2011), since the response is based on retention at stomata in the mesothelial lining in both cases. Therefore the release of Ni ions from long NiNW does not explain greater pleural mesothelial inflammation caused by long NiNW in the present study.

Reference List

1. Cho, W. S., Duffin, R., Poland, C. A., Duschl, A., Oostingh, G. J., MacNee, W., Bradley, M., Megson, I. L., and Donaldson, K. (2011). Differential pro-inflammatory effects of metal oxide nanoparticles and their soluble ions in vitro and in vivo; zinc and copper nanoparticles, but not their ions, recruit eosinophils to the lungs. *Nanotoxicology.*

2. Murphy, F. A., Craig A.Poland, Rodger Duffin, Khuloud T.Al-Jamal, Hanene Ali-Boucetta, Antonio Nunes, Fiona Byrne, Adriele Prina-Mello, Yuri Volkov, Shouping Li, Stephen J.Mathe, Alberto Bianco, Maurizio Prato, William MacNee, William A.Wallace, Kostas Kostarelos, and Ken Donaldson (2011). Length-dependent retention of carbon nanotubes in the pleural space of mice initiates sustained inflammation and progressive fibrosis on the parietal pleura. *Am J Pathol* **178**(6), 2587-2600.

3. Poland, C. A., Byrne, F., Cho, W. S., Prina-Mello, A., Murphy, F. A., Davies, G. L., Coey, J. M., Gounko, Y., Duffin, R., Volkov, Y., and Donaldson, K. (2011). Length-dependent pathogenic effects of nickel nanowires in the lungs and the peritoneal cavity. *Nanotoxicology.*

4. Prina-Mello, A., Diao, Z., and Coey, J. M. (2006). Internalization of ferromagnetic nanowires by different living cells. *J Nanobiotechnology.* **4:9.**, 9.

5. Raphael, M. P., Christodoulides, J. A., Qadri, S. N., Simpkins, B. S., and Byers, J. M. (2010). Magnetic moment degradation of nanowires in biological media: real-time monitoring with SQUID magnetometry. *Nanotechnology.* **21**(28), 285101.

6. Schrand, A. M., Schlager, J. J., Dai, L., and Hussain, S. M. (2010). Preparation of cells for assessing ultrastructural localization of nanoparticles with transmission electron microscopy. *Nat. Protoc.* **5**(4), 744-757.

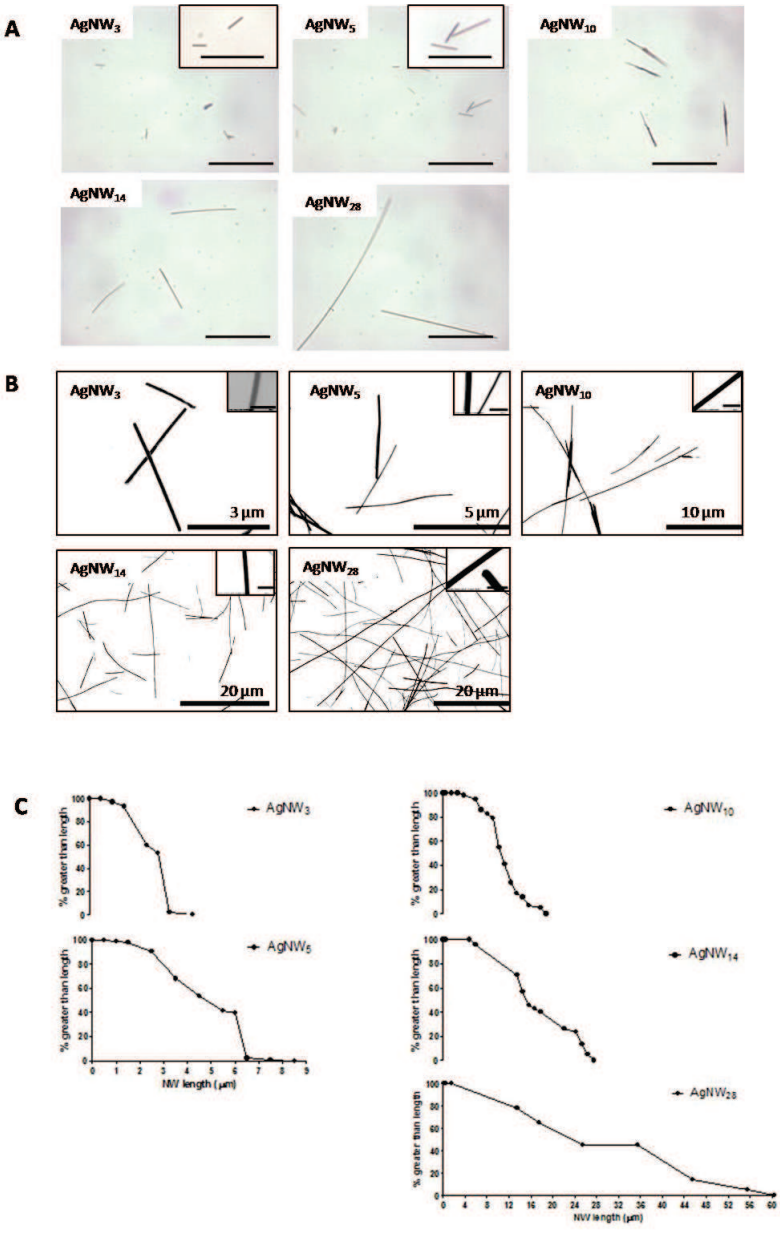
A
AgNW3
AgNW5
AgNW10
AgNW14
AgNW28
B
AgNW3
AgNW5
AgNW10
3 µm
5 µm
10 µm
AgNW14
AgNW28
20 µm
20 µm
C
% greater than length
AgNW3
AgNW5
AgNW10
AgNW14
AgNW28
NW length (µm)

Fig. 1. Light microscope and BSEM images of AgNW panel and size distribution. A) Light microscopy images of AgNW panel in 0.5% BSA/saline at a concentration of 50 µg/ml. Scale bar 20 µm, insert 10 µm. B) BSEM of 5 µg/ml AgNW in saline. Insert shows the diameter of each AgNW sample (scale bar 500nm). C) Size distribution of AgNWs plotted as % greater than any length. 100 fibres were calculated for each group.

Table 1. Mean length ± s.e.m. and source of additional nanofibres and controls.
*Courtesy of Murphy *et al*.(Murphy *et al.* 2011).

	Length (mean, µm ± s.e.m.)	Diameter (nm, mean ± s.e.m.)	Source
AgP	0.035±0.01		Nanostructured & Amorphous Materials, Inc.
NPCB (Printex 90®)*	0.01 ± 0.005		Evonik Degussa GmbH
NT_2*	2.0 ± 0.2	20-30	Nanostructured & Amorphous Materials, Inc.
NT_{13}*	13.0 ± 6.1	84.9 ± 1.9	Mitsui & Co. Ltd., Japan
NT_{36}*	36.0 ± 3.4	165.0 ± 4.7	University of Manchester [Dr. I. Kinloch]
Ni-P	0.8 ± 0.2		Nanostructured & Amorphous Materials, Inc.
$NiNW_4$	4.2 ± 0.9	200 ± 10	CRANN - Trinity College Dublin [Drs Byrne F., and Prina-Mello A.]
$NiNW_{20}$	20.3 ± 5.5	200 ± 10	CRANN - Trinity College Dublin [Drs Byrne F., and Prina-Mello A.]

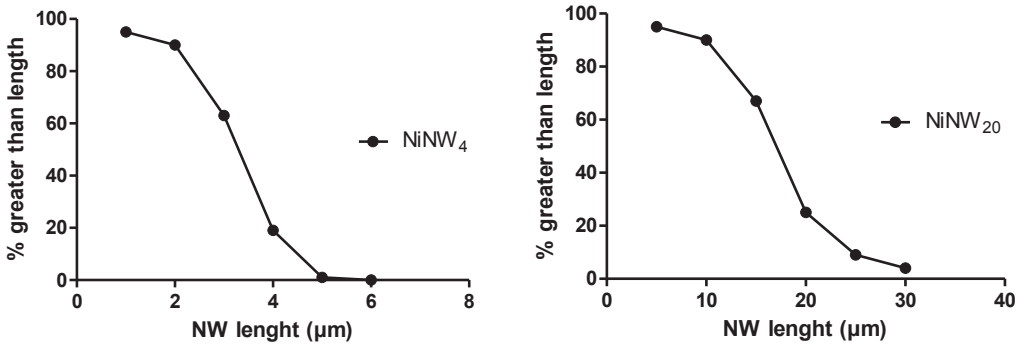

Fig. 2. Nickel nanowire size distribution. Size distributions of nickel nanowire were carried out by measuring the lengths of at least 100 fibres under scanning eletron microscope. Average length for short NiNW is 4.2 ± 0.9µm, average of long NiNW is 20.3 ± 5.5µm.

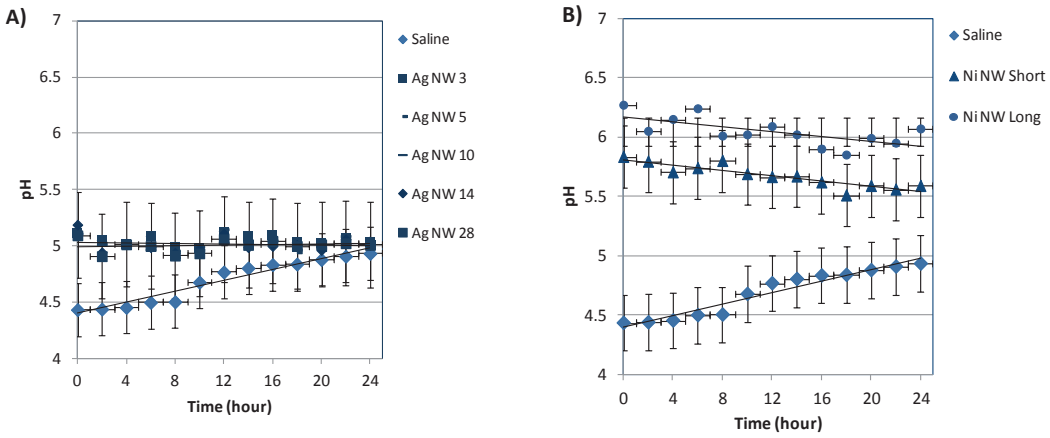

Fig. 3. Dissolution measurement of NW. A) Comparison between sterile saline solution (as baseline) and $AgNW_{3,\ 5,\ 10,\ 14,\ 28}$ dispersed in sterile saline solution. Average value of pH and standard deviation calculated for every time point up to 24h (interval 2 h) (n = 3). No statistical difference between Ag samples. Statistical significance AgNWs vs saline ($p<0.01$). B) Comparison between sterile saline solution (as baseline) and nickel nanowires long and short dispersed in sterile saline solution. Average value of pH and standard deviation calculated for every time point up to 24h (interval 2 h) (n = 3). Statistical significance saline vs Ni NW $p<0.01$, NiNW long VS short (>0.05).

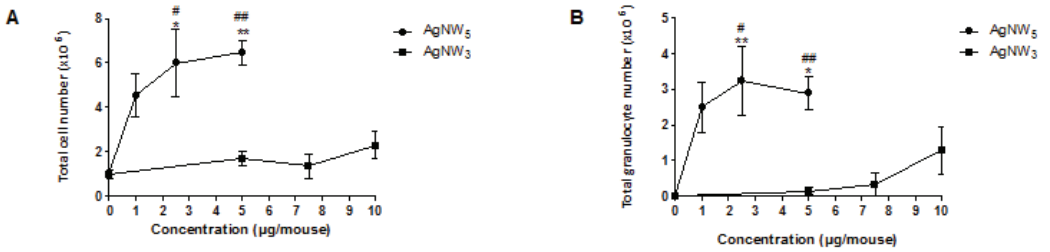

Fig. 4. Dose effect series for $AgNW_3$ and $AgNW_5$ measuring the acute 24 hour inflammatory response. Total cell number (A) and total granulocyte number (B) of $AgNW_5$ at a dose of 1.0, 2.5 and 5.0 µg/mouse and $AgNW_3$ at a dose of 5.0, 7.5 and 10.0 µg/mouse. Significance versus vehicle control (0 µg/mouse), * indicates $p<0.05$, ** indicates $p<0.01$. A) # indicates $p<0.05$, significance of $AgNW_5$ (2.5 µg/mouse) vs $AgNW_3$ (7.5 µg/mouse), ## indicates $p<0.05$, significance of $AgNW_5$ (5 µg/mouse) vs $AgNW_3$ (5.0, 7.5 µg/mouse); B) # indicates $p<0.05$, significance of $AgNW_5$ (2.5 µg/mouse) vs $AgNW_3$ (5.0, 7.5 µg/mouse), ## indicates $p<0.05$, significance of $AgNW_5$ (5.0 µg/mouse) vs $AgNW_3$ (5.0 µg/mouse). Data represent mean ± s.e.m. of n=4 mice.

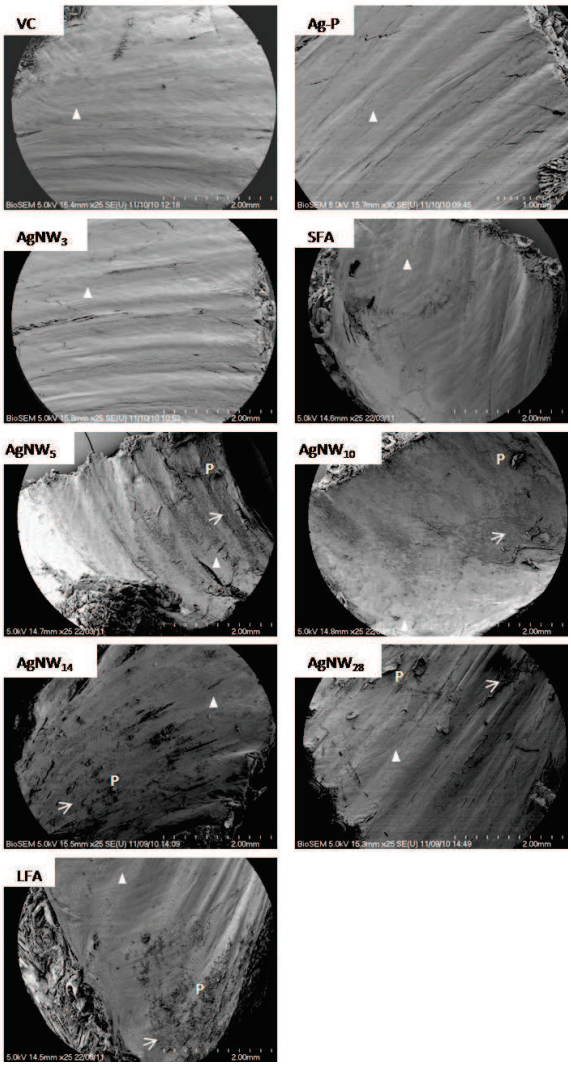

Fig. 5. Length dependent response of AgNW on the parietal mesothelial surface 1 week post injection. Overview of whole chestwall section at low magnification. Triangle indicates normal mesothelial cell layer, arrow indicates lesion areas of accumulated inflammatory cells and P indicates papillae or tongue-like structures made up of cell aggregates, which extend from the surface of the mesothelium.

A

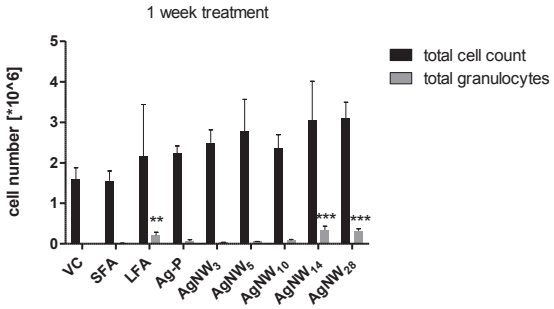
1 week treatment
total cell count
total granulocytes
cell number [*10^6]
5
4
3
2
1
0
**
***
***
VC
SFA
LFA
Ag-P
AgNW3
AgNW5
AgNW10
AgNW14
AgNW28

B

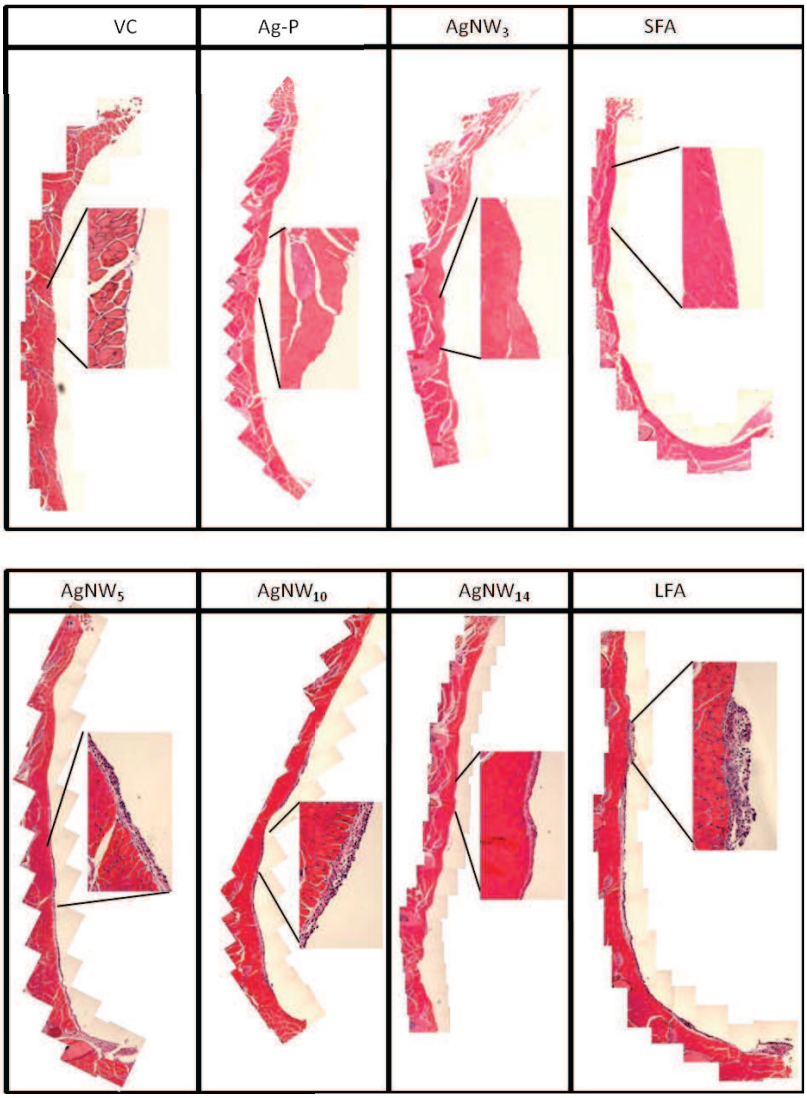
VC
Ag-P
AgNW3
SFA
AgNW5
AgNW10
AgNW14
LFA

Figure 6. Total cell number and total granulocyte number from pleural lavage fluid and H&E stained histology section of parietal pleura 1 week post exposure. A) Total cell number and total granulocyte number 1 week post exposure to 5 µg/mouse of SFA, LFA, Ag-P and AgNW panel. Significance versus Vehicle control * indicates $p<0.05$, ** indicates $p<0.01$, *** indicates $p<0.001$. Data represent mean ± s.e.m. of n=4 mice. B) Normal appearance of mesothelial lining after VC, Ag-P, $AgNW_3$ and SFA exposure but thickening of the pleural sub-mesothelial layer can be seen in mice exposed to $AgNW_{5\text{-}14}$ and LFA. No thickening of the mesothelial cell layer could be seen after $AgNW_{28}$ exposure at 1 week. This was most likely due to retention of these very long fibres at the site of injection.

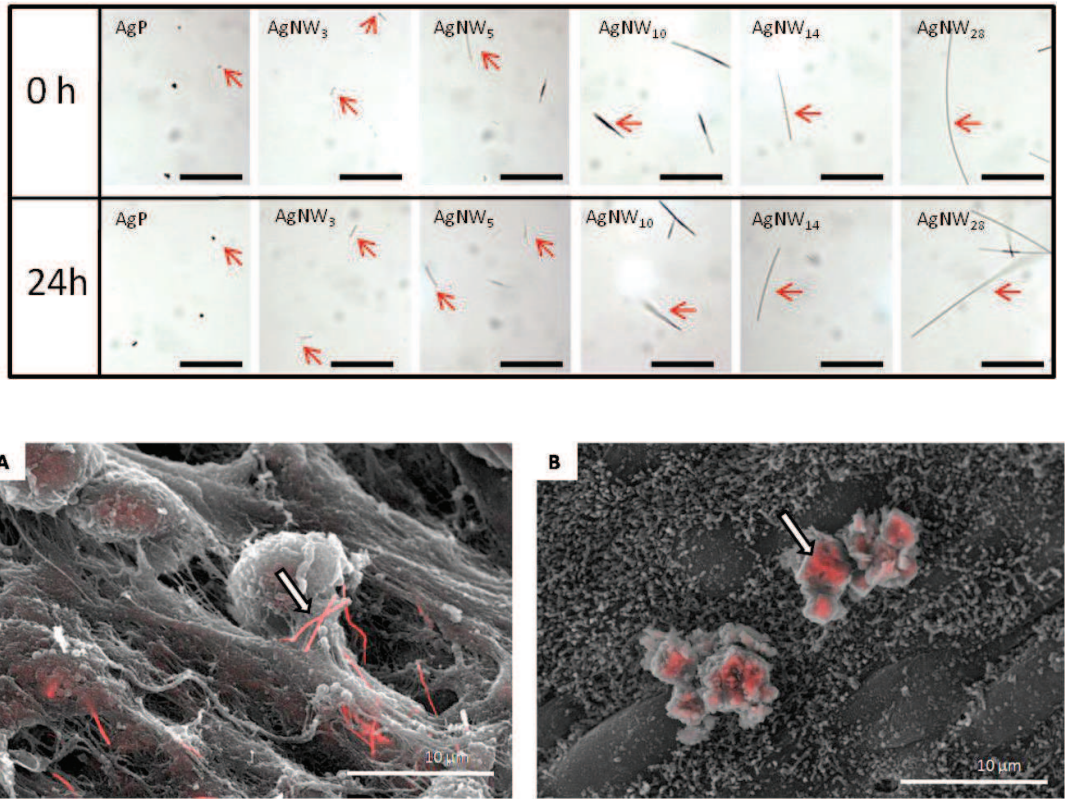

Figure 7. Biopersistence/durability of AgP and AgNW. Merged secondary electron and backscatter electron SEM images of the parietal pleura from mice treated with $AgNW_5$. A) AgNWs appear intact in their morphology inside pleural macrophages 24 hour post-exposure, however after 1 week (B) dissolution can be seen, evident as a more diffuse and 'ghost-like appearance of the AgNW (arrows) inside macrophages. C) Light micrograph images of AgP and AgNW at 0 hour and 24 hour after rotation in pH 5.0 saline solution. No dissolution or change in morphology was observed after 24 hour. Red arrows indicate AgP and AgNW. Scale bar 10 µm.

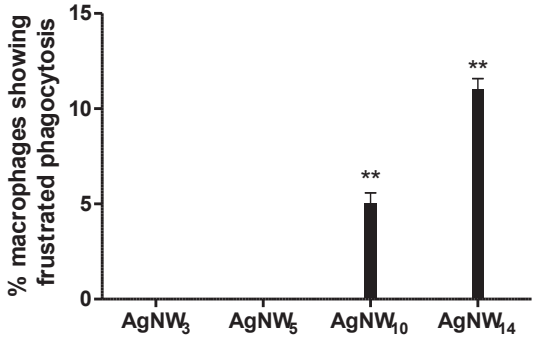

Fig. S. Percentage of frustrated phagocytosis of pleural macrophages. 50 fibre-containing macrophages were counted in the lavage fluid from $AgNW_3$, $AgNW_5$, $AgNW_{10}$, $AgNW_{14}$ treatment. The percentage of macrophages showing frustrated phagocytosis (not fully enclosed fibres) was calculated by comparing to the number of macrophages with completely enclosed fibres. Macrophages from $AgNW_{10}$ and $AgNW_{14}$ treatment show a significant increase in frustrated phagocytosis compared to $AgNW_3$ (** indicates $p<0.01$). Data represent mean ± s.e.m. of n=4 mice. $AgNW_{28}$ was not counted since too few very long fibres could be seen on the cytospin preparation.

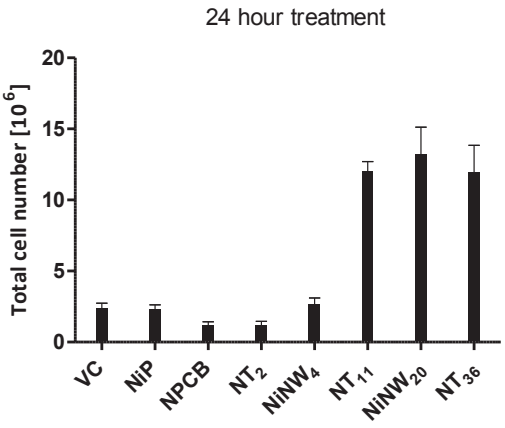

Fig. 9. Total cell number from pleural lavage fluid after 24 hour. A) Total cell number in lavage fluid of mice treated at a concentration of 5 μg/mouse with the material control panel NiP, NiNWs, NPCB and NTs at 24 hour post-injection. Significance versus Vehicle control * indicates $p<0.05$, ** indicates $p<0.01$, *** indicates $p<0.001$. Data represent mean ± s.e.m. of n=4 mice.

5. **Schinwald A** & Donaldson K. **Use of back-scatter electron signals to visualise cell/nanowires interactions *in vitro* and *in vivo*; frustrated phagocytosis of long fibres and compartmentalisation in mesothelial cells**. Particle and Fibre Toxicology. 2012 Aug 28; 9(1):34.

PARTICLE AND
FIBRE TOXICOLOGY

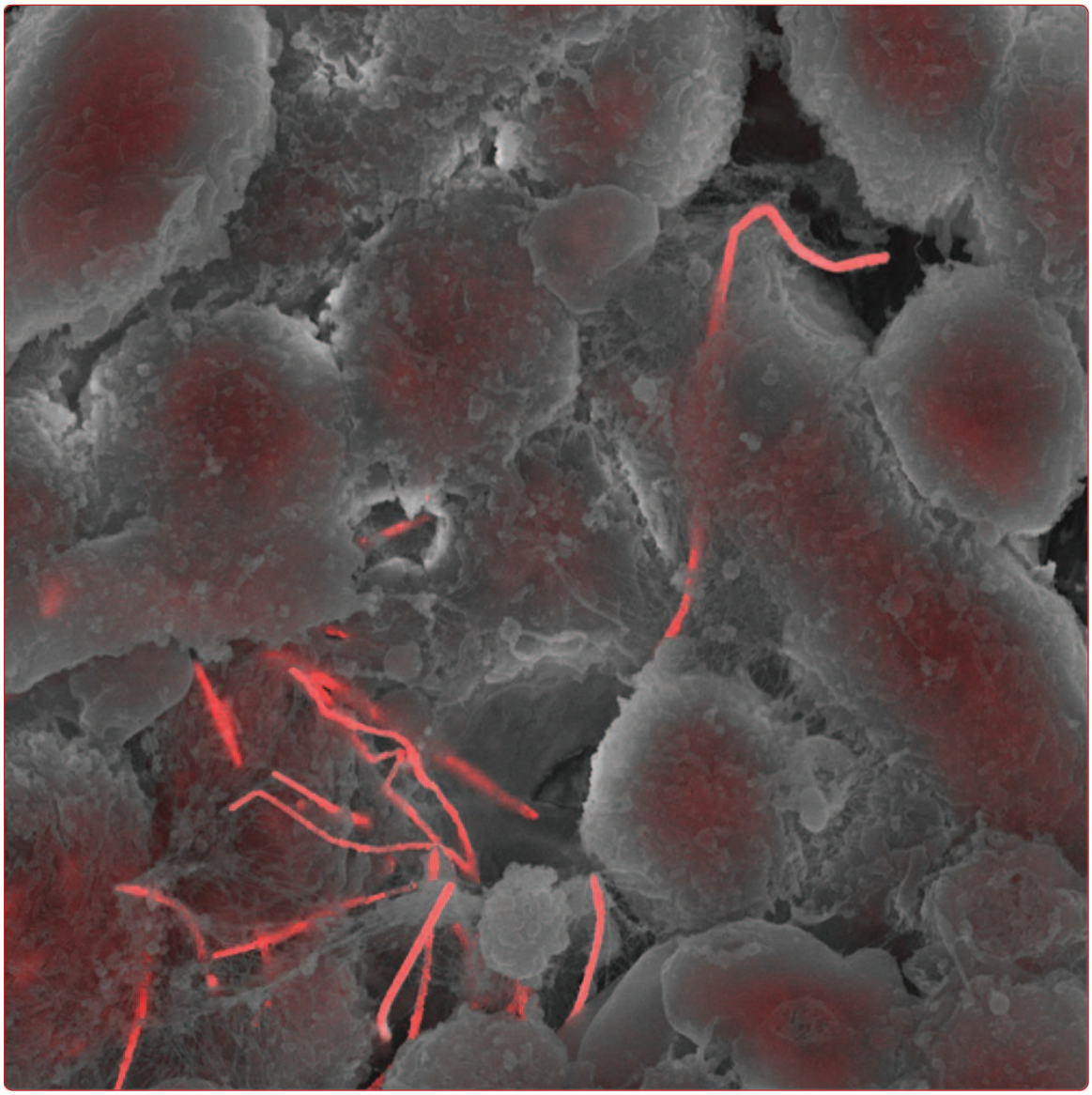

Use of back-scatter electron signals to visualise cell/nanowires interactions *in vitro* and *in vivo*; frustrated phagocytosis of long fibres in macrophages and compartmentalisation in mesothelial cells in vivo

Schinwald and Donaldson

BioMed Central

Schinwald and Donaldson *Particle and Fibre Toxicology* 2012, **9**:34
http://www.particleandfibretoxicology.com/content/9/1/34

Schinwald and Donaldson *Particle and Fibre Toxicology* 2012, **9**:34
http://www.particleandfibretoxicology.com/content/9/1/34

PARTICLE AND FIBRE TOXICOLOGY

METHODOLOGY Open Access

Use of back-scatter electron signals to visualise cell/nanowires interactions *in vitro* and *in vivo*; frustrated phagocytosis of long fibres in macrophages and compartmentalisation in mesothelial cells in vivo

Anja Schinwald and Ken Donaldson*

Abstract

Background: Frustrated phagocytosis has been stated as an important factor in the initiation of an inflammatory response after fibre exposure. The length of fibrous structures has been linked to the potential of fibres to induce adverse health effects for at least 40 years. However, we only recently reported for the first time the threshold length for fibre-induced inflammation in the pleural space and we implicated frustrated phagocytosis in the pro-inflammatory effects of long fibres. This study extends the examination of the threshold value for frustrated phagocytosis using well-defined length classes of silver nanowires (AgNW) ranging from 3–28 μm and describes in detail the morphology of frustrated phagocytosis using a novel technique and also describes compartmentalisation of fibres in the pleural space.

Methods: A novel technique, backscatter scanning electron microscopy (BSE) was used to study frustrated phagocytosis since it provides high-contrast detection of nanowires, allowing clear discrimination between the nanofibres and other cellular features. A human monocyte-derived macrophage cell line THP-1 was used to investigate cell-nanowire interaction *in vitro* and the parietal pleura, the site of fibre retention after inhalation exposure was chosen to visualise the cell- fibre interaction *in vivo* after direct pleural installation of AgNWs.

Results: The length cut-off value for frustrated phagocytosis differs *in vitro* and *in vivo*. While *in vitro* frustrated phagocytosis could be observed with fibres ≥14 μm, *in vivo* studies showed incomplete uptake at a fibre length of ≥10 μm. Recently we showed that inflammation in the pleural space after intrapleural injection of the same nanofibre panel occurs at a length of ≥5 μm. This onset of inflammation does not correlate with the onset of frustrated phagocytosis as shown in this study, leading to the conclusion that intermediate length fibres fully enclosed within macrophages as well as frustrated phagocytosis are associated with a pro-inflammatory state in the pleural space. We further showed that fibres compartmentalise in the mesothelial cells at the parietal pleura as well as in inflammatory cells in the pleural space.

(Continued on next page)

* Correspondence: ken.donaldson@ed.ac.uk
Centre for Inflammation Research, Queen's Medical Research Institute, MRC/University of Edinburgh, 47 Little France Crescent, Edinburgh EH16 4TJ, UK

(Continued from previous page)

Conclusion: BSE is a useful way to clearly distinguish between fibres that are, or are not, membrane-bounded. Using this method we were able to show differences in the threshold length at which frustrated phagocytosis occurred between *in vitro* and *in vivo models*. Visualising nanowires in the pleura demonstrated at least 2 compartments – in leukocyte aggregations and in the mesothelium - which may have consequences for long term pathology in the pleural space including mesothelioma.

Keywords: Backscatter scanning electron microscopy (BSE), Frustrated phagocytosis, THP-1 macrophages, Pleural macrophages, Parietal pleura mesothelium

Background

The toxicology of fibres is a sub-specialty of particle toxicology developed in response to the asbestos experience [1] but whose tenets have been used to quantify the hazards from vitreous fibres [2] organic fibres such as p-aramid [3] and most recently nanofibres [4,5]. Current understanding of the fibre hazard is based on the 'fibre pathogenicity paradigm' which has predictive power and is the most robust structure/ toxicity relationship in particle toxicology. The paradigm identifies thinness, length and biopersistence as the 3 features that determine the pathogenic potential of any fibre sample [5]. Thinness determines respirability, that is the likelihood that a fibre penetrates the respiratory tract beyond the ciliated airways [3] where most damage is likely to occur, whilst biopersistence determines whether the fibre will retain its structure integrity i.e. fibrous shape, during residence in the lung. If the fibre is composed of soluble components that are leached from the fibre under the conditions it encounters *in vivo*, then the fibre is likely to become weakened, break and become part of the short fibre pool. Short fibres are not pathogenic in the fibre sense, although they may have harmful effects as particles, whilst long fibres do cause fibre-type pathogenicity; this length-dependent pathogenicity has been demonstrated in numerous studies *in vivo* [6-8] and *in vitro* [9-11].

One major arbiter of length-dependent pathogenic effect is the alveolar macrophage and pleural macrophage whose normal function is to phagocytose fibres and clear them. Because of the unusual aerodynamics of fibres, extremely long fibres penetrate and deposit beyond the ciliated airways [3]. Macrophages that attempt to phagocytose long fibres cannot enclose them leading to 'frustrated phagocytosis' as shown diagrammatically in Figure 1; in contrast short fibres are fully enclosed in the phagosomes (Figure 1).

We recently reported length-dependent effects of a range of fibres including asbestos [8], carbon nanotubes [12,13], silver nanowires (AgNW) [14] and nickel nanowires (NiNW) [11] at the peritoneal and pleural mesothelial surfaces. All of these fibre types appear to comply with the fibre pathogenicity paradigm with length-dependent effects in the pleural space as a result of retention at stomata (3–10 μm in diameter) on the parietal pleura and frustrated phagocytosis. These data show persuasively that the length threshold for pleural retention of any fibres is 5 μm and that fibre shorter than this threshold are not retained and do not cause inflammation [14].

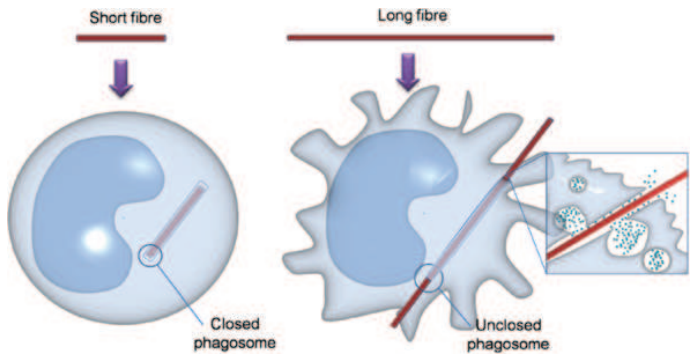

Figure 1 Diagrammatic representation of short fibre complete phagocytosis and long fibre –mediated frustrated phagocytosis. Short fibres can be fully phagocytosed by macrophages whereas long fibres are too long to be fully taken up leading to an unclosed membrane and leakage of cell content.

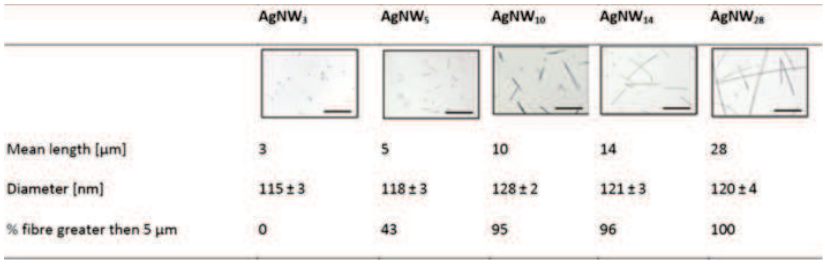

Figure 2 Characteristics of AgNW panel. Light microscopy images of AgNW panel in 0.5% BSA/saline. Scale bar 20 µm.

Whilst we evoked frustrated phagocytosis in the pro-inflammatory effects, we also noted that intermediate 5 µm length fibres, were fully enclosed by macrophages but were pro-inflammatory, as previously recorded [14]. Due to restrictions on space we could not fully explore the morphological basis of this new effect and here we extend these findings to fully characterise fibre length effects particularly frustrated phagocytosis *in vitro* and *in vivo*. We utilised the technique of backscatter electron microscopy in particular to investigate this phenomenon. We also describe the retention of fibres in the parietal mesothelial layer, an anatomical region not hitherto identified a retention compartment for fibres.

Results

AgNW panel

Characteristic of the AgNW panel are summarised in Figure 2. The images illustrate the uniform distribution of the AgNWs with no aggregation being present. Complete characterisation of the AgNW panel was described previously by Schinwald *et al*. [14].

Membrane integrity and metabolic activity in the *in vitro* model

The *in vitro* experiments were based on a treatment dose which was non/low-toxicity to THP-1 cells in culture adjusted for each fibre length to produce approximately the same fibre number (Table 1). The 2 µg/cm^2 dose based on $AgNW_{14}$ was determined by measuring the membrane integrity via the release of lactate dehydrogenase (LDH) into the supernatant and cell proliferation of the THP-1 cells after 24 hour treatment; however, $AgNW_{28}$ caused a significant decrease in membrane integrity and loss of proliferation and metabolic activity (Figure 3A,B).

Table 1 Calculation for the mass adjustments for equalisation of number

Length class [µm]	Calculation to equalise for the same fibre number	Dose (µg/cm^2)
3	3/14 × 2	0.4
5	5/14 × 2	0.6
10	10/14 × 2	1.4
14	standard	2.0
28	28/14 × 2	4.0

Bright field microscopy of THP-1 cells after 4 hour exposure *in vitro*

THP-1 cells were exposed to the panel of AgNWs for 4 hours and bright field images were taken using a 60× magnification. THP-1 cells completely phagocytose $AgNW_3$ (Figure 4A) and $AgNW_5$ (Figure 4B). The fibres were fully taken up as indicated by the yellow circle. $AgNW_{10}$ were mostly phagocytosed with only a small percentage of fibre-ends protruding out of the cells as indicated by the red arrow (Figure 4C). Frustrated phagocytosis was observed after treatment with $AgNW_{14}$ and $AgNW_{28}$. In Figure 5d the black arrow indicates a fibre shared by two cells and another fibre only partly enclosed by the cell (red arrow Figure 4D and E).

Characterisation of Cell/Nanowire interaction in vitro using BSE

Backscatter electron microscopy (BSE) enabled us to visualise the interaction of THP-1 macrophage cells with AgNW. We mainly focused on the uptake/phagocytosis of the five different size categories of AgNW to identify the cut-off value, at which frustrated phagocytosis occurs *in vitro*. Figure 5A-E show differentiated THP-1 macrophages after 4 hour treatment with $AgNW_3$ (A), $AgNW_5$ (B), $AgNW_{10}$ (C), $AgNW_{14}$ (D) and $AgNW_{28}$ (E). In Figure 5A one external $AgNW_3$ can be seen (white arrow) and a few $AgNW_3$ can be seen just underneath the surface of a macrophage as indicated by the black arrow (Figure 5A insert). After treatment with $AgNW_5$, nanowires were fully taken up by macrophages as indicated by the white arrow (Figure 5B insert). A small proportion of cells showing incomplete uptake of $AgNW_{10}$ fibres could be observed as indicated by the white arrow

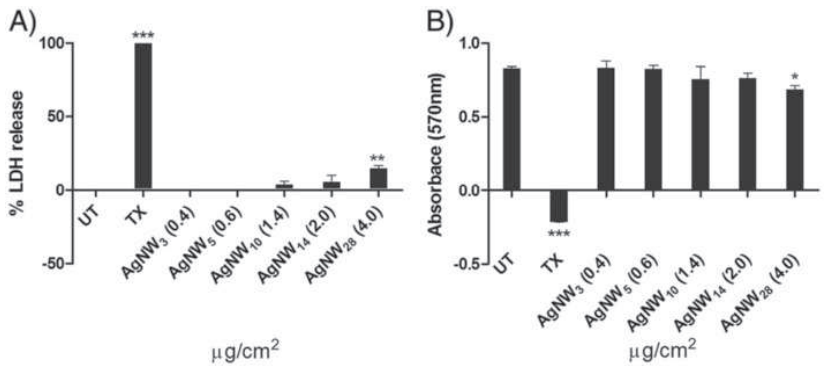

Figure 3 THP-1 membrane integrity and proliferation/metabolic activity. A) Measurement of membrane integrity plotted as % LDH release based and positive and negative control. Only $AgNW_{28}$ lead to a significant release of LDH into the supernantant. **B**) Proliferation and metabolic activity was measured using alamarBlue®. Cell treated with $AgNW_{28}$ showed decreased proliferation. Significance versus vehicle control *P <0.05, **P <0.01. Data represent mean ± s.e.m. of n = 5.

(Figure 5C) however most of the fibres were membrane bound (black/white arrow) and therefore phagocytosed by the cells. Obvious frustrated phagocytosis could be observed from a nanowire length of 14 μm (Figure 5D) and 28 μm (Figure 5E). A much greater amount of AgNW was observed protruding through cells or shared between adjacent cells indicating frustrated phagocytosis (white arrow). The number of unphagocytosed fibres per cell was quantified and significantly increased with $AgNW_{14}$ ($p > 0.05$) and $AgNW_{28}$ ($p > 0.001$).

In vivo

Uptake of AgNWs in pleural macrophages from pleural lavage

In Figure 6A a macrophage is shown from a pleural lavage after treatment with $AgNW_3$. The macrophage could readily phagocytose a number of short (3 μm) AgNWs (Figure 6A). After treatment with $AgNW_5$ (Figure 6B), again the nanowires were fully taken up by the pleural macrophages in the lavage fluid. However, $AgNW_{10}$ (C), $AgNW_{14}$ (D) and $AgNW_{28}$ (E) could not

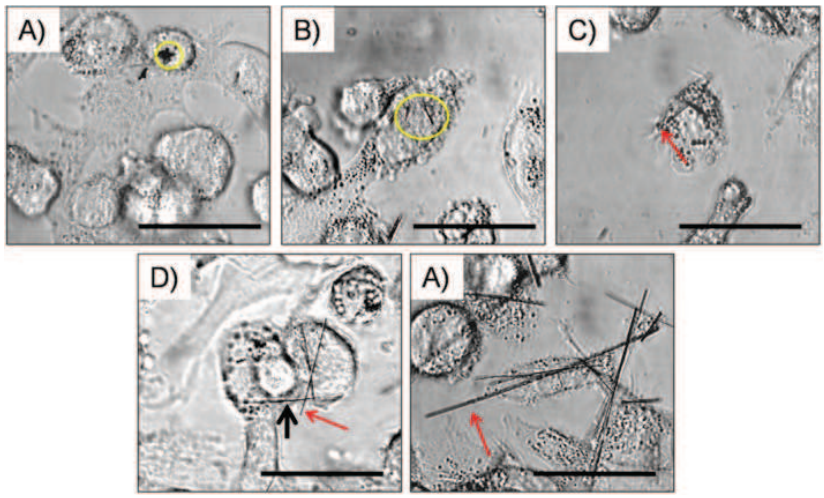

Figure 4 Bright-field microscope image of THP-1 cells treated with AgNWs. A) $AgNW_3$ and B) $AgNW_5$ were fully enclosed by the cell as indicated by the yellow circle. **C**) $AgNW_{10}$ were mostly taken up, however a small number of fibres were not fully enclosed and fibre ends were protruding out of the cells as indicated by the red arrow. **D**) $AgNW_{14}$ and **C**) $AgNW_{28}$ caused frustrated phagocytosis. Red arrows indicate fibres partly taken up by THP-1 cells and the black arrow indicates sharing of a fibre between two adjacent cells. Scale bar = 20 μm.

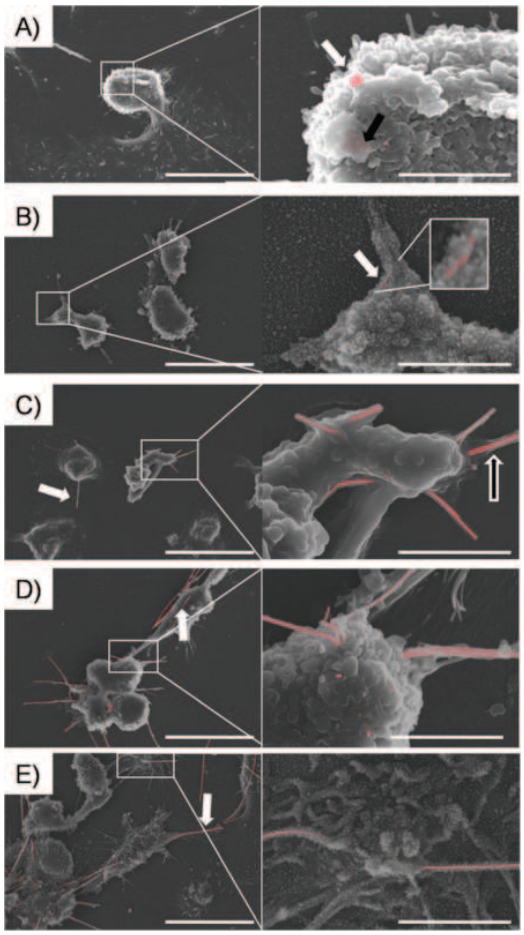

Figure 5 BSE images of differentiated THP-1 cells treated for 4 hours with AgNW. A) $AgNW_3$ treated macrophages showed full phagocytosis of the nanowires. Only one nanowire could be visualised outside a cell (white arrow) and a few underneath the surface indicated by the black arrow. **B**) After $AgNW_5$ treatment all nanowires were phagocytosed by cells after 4 hours (white arrow). **C**) A big proportion of $AgNW_{10}$ appear membrane bound and therefore phagocytosed by cells (black/white arrow), however a few fibres could be seen protruding out of cells (white arrow). Frustrated phagocytosis was observed after $AgNW_{14}$ (**D**) and $AgNW_{28}$ (**E**) treatments, since most of fibres can be seen protruding out of the cells or shared between cells (white arrow and insert). BSE merged image with a scale bar of 10 μm and 5 μm for the inserts.

be fully phagocytosed by the cells anymore, leading to frustrated phagocytosis. Enlargement of the pleural macrophages (Figure 6D) could be observed. Data from the same animals as described here were utilised in Schinwald *et al*. [14] where details of the inflammatory effects accompanying these cellular changes can be obtained.

Phagocytosis/frustrated phagocytosis *in vivo* on the parietal pleura surface 24 hour post exposure

Backscatter scanning electron microscopy examination was carried out on the macrophage accumulations on the parietal pleura samples from mice injected with $AgNW_3$, $AgNW_5$ and $AgNW_{10}$ at 24 hour post intrapleural instillation in order to examine the development of interaction between the mesothelial cell layer/inflammatory cells on the surface. The dose of 5 μg per mouse used in this study lead to a significant increase in inflammation after treatment with $AgNW_5$, $AgNW_{10}$, $AgNW_{14}$ and $AgNW_{28}$ as previously reported [14]. A dose response was performed by increasing the dose of $AgNW_3$ up to 10 μg which resulted in no significant increase in inflammation. The dose of $AgNW_5$ was decreased to 1 μg and 2.5 μg whereby 2.5 μg continuously showed significant inflammation [14]. $AgNW_3$ treatment was chosen to investigate if any short fibre were retained in the pleural space after intrapleural injection even though no inflammatory response was observed. $AgNW_5$ and $AgNW_{10}$ treatments were chosen since both treatments lead to a significant increase in pleural inflammation however differ in their interactions with pleural macrophages [14]. No $AgNW_3$ could be observed on the parietal pleura surface 24 hour post treatments confirming that short fibres are readily cleared from the pleural space. In contrast to $AgNW_3$, both $AgNW_5$ and $AgNW_{10}$ lead to an aggregation of inflammatory cells on the surface of the parietal pleura with accumulation of nanowires within the lesion area (Figure 7A,C). Most $AgNW_5$ were fully phagocytosed by pleural macrophages (Figure 7A, B and insert, stars). In comparison, $AgNW_{10}$ showed a number of fibres only partly phagocytosed and therefore leading to frustrated phagocytosis (Figure 7C,D white arrow). Some $AgNW_5$ and $AgNW_{10}$ were not taken up by macrophages as indicated by the yellow arrows (Figure 7A,C). By looking at the surface with higher magnification unclosed membrane could be visualised in pleural macrophages phagocytosing $AgNW_{10}$ (Figure 7D and insert, black arrows).

Phagocytosis/frustrated phagocytosis *in vivo* on the parietal pleura surface 1 week post exposure

BSEM of parietal pleura after 1 week treatment with $AgNW_5$ are shown in Figure 8A,B,C and $AgNW_{10}$ in Figure 8D,E,F. By 1 week, $AgNW_5$ started to lose their integrity, presumably in the acidic conditions within a phagosome as seen in Figure 8A,B indicated by the black arrow. Non-dissolved fibres overlying the mesothelial cell layer appear intact in their morphology (Figure 8B, white arrow). Ghost-like structures of nanofibres which are covered by microvilli (Figure 8B,C star) could be seen. $AgNW_{10}$ could be found either in accumulations of inflammatory cells which appeared denser and more

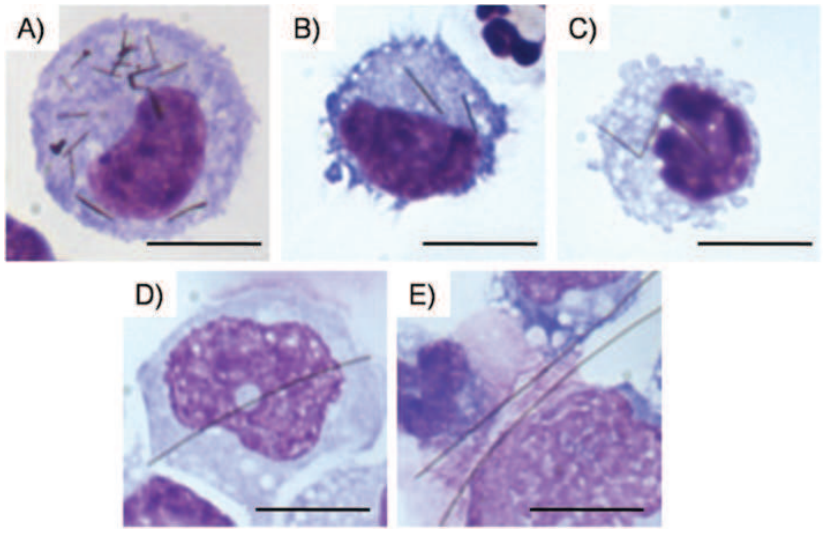

Figure 6 Representative cytospin images of lavaged cells from the pleural space after 24 hour treatment with AgNWs. A) $AgNW_3$ inside a pleural macrophage showing complete phagocytosis. **B**) Pleural macrophage with a fully phagocytosed $AgNW_5$ (**B**) and $AgNW_{10}$ (**C**). **D**) A pleural macrophage with increased cell size to phagocytose $AgNW_{14}$. **E**) Frustrated phagocytosis after $AgNW_{28}$ exposure. 3 macrophages sharing 2 long fibres. All images are shown at 100x magnification with a 10 μm scale bar.

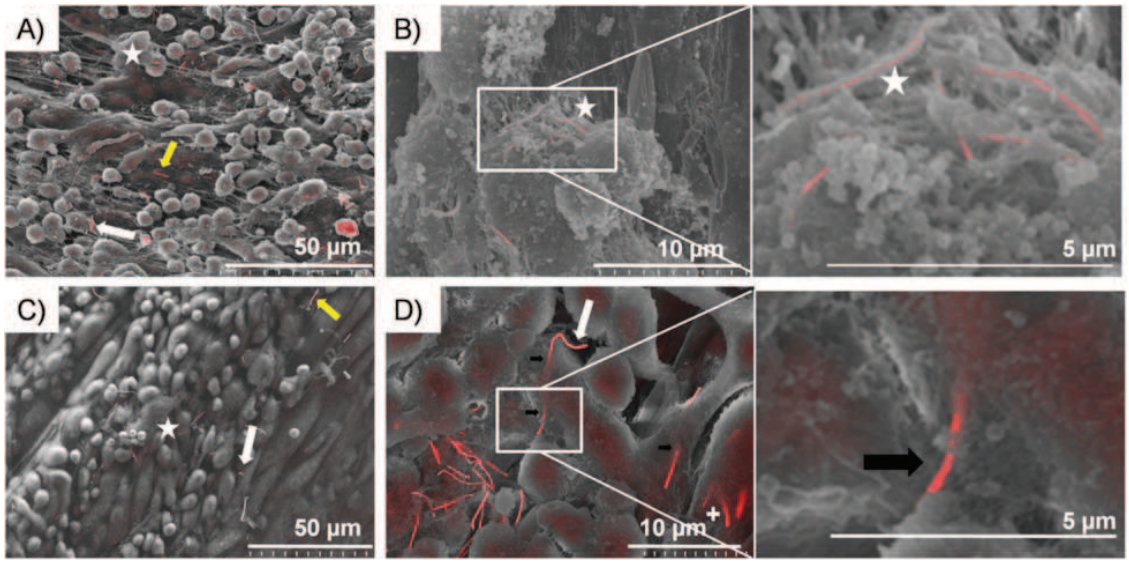

Figure 7 Images of the parietal pleura surface 24 hour post pleural instillation of $AgNW_5$ and $AgNW_{10}$. Overview of the lesion area on the surface of the parietal pleura with $AgNW_5$ (**A**) and $AgNW_{10}$ (**C**). The yellow arrow indicates a nanowire which is not taken up by inflammatory cells whereas the star indicates a fibre that is fully phagocytosed but can be visualised underneath the surface of the cell. The white arrow indicates nanowires which are protruding out of cells. **B**) This figure shows $AgNW_5$ that are fully phagocytosed by pleural macrophages but can be visualised underneath the surface as indicated by the star. **D**) $AgNW_{10}$ is causing frustrated phagocytosis in a macrophage in the centre of the image. The unclosed cell membrane is indicated by the black arrows and exposed fibre surface is indicated by the white arrow. The cross on the lower right of the image indicates fibres which are largely internalised but whose tips rise vertically to penetrate the cell surface adjacent to the other long fibre.

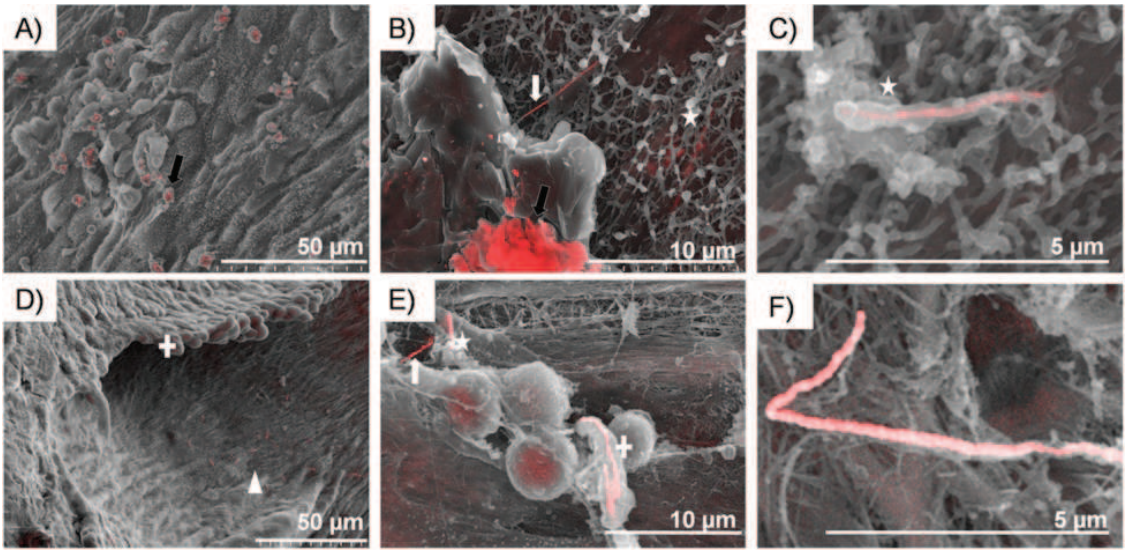

Figure 8 Images of macrophages on the parietal pleura 1 week post pleural instillation of $AgNW_5$ and $AgNW_{10}$. Lesion area showing $AgNW_5$ (**A**) dissolving inside macrophages, as can be seen by the loss of fibre structure (black arrow) (**B**). Intact nanofibres on the mesothelial cell layer as indicated by the white arrow (**B**) and membrane bound as indicated by the star (**B**,**C**). **D**) Lesion area appears denser and more granulomatous after 1 week treatment $AgNW_{10}$ and occasional nanowires can be seen in these granulomatous areas as indicated by the white cross. Surprisingly, a large part of the nanowires were seen on and within the mesothelial cell layer indicated by the triangle. These nanowires appeared structurally intact whereas nanowires fully phagocytosed by macrophages as seen in **E**) indicated by the cross on the right side start to dissolve under the acidic condition within a macrophage. On the top left of this image, a fibre is partly internalised (star) and partly exposed (white arrow). **F**) $AgNW_{10}$ which is partly membrane bound on the mesothelial cell layer.

granulomatous after 1 week (Figure 8D cross), or in the mesothelial cell layer (Figure 8D triangle). $AgNW_{10}$ also started to lose integrity inside the phagocytic compartments of pleural macrophages (Figure 8E cross). Figure 8F shows $AgNW_{10}$ partly membrane bound on the mesothelial cell layer. Data from the same animals as described here were utilised in Schinwald *et al*. [14].

Compartmentalisation of nanowires into mesothelial cells

So far, we hypothesised that after a prolonged exposure to fibres in general up to 7 days, the instilled fibres in the pleural space would either be cleared from the pleural space and enter the lymphatic drainage system or be accumulated in a granulomatous lesion on the parietal pleura at stomata [15]. By using backscatter imaging, for the first time it was possible to visualise nanowires in the mesothelial cell layer of the parietal pleura. Both treatments, $AgNW_5$ and $AgNW_{10}$ (but not $AgNW_3$ which were not observed as they had been cleared) showed nanofibres either on the surface of the mesothelial cells (black arrow Figure 9B) or taken up by these cells (white arrow Figure 9A,B). This is especially surprising for $AgNW_5$, since pleural macrophages are able to phagocytose these fibres completely as shown in Figure 7B. By comparing the structure/shape of the nanowires associated with the mesothelial layer (Figure 9) and within macrophages (Figure 8B,E), it can quite clearly be seen that the nanowires are still intact after 1 week in the mesothelial layer whereas within the phago-lysosome of a macrophage the fibres start to degrade and lose integrity. These images show evidence that not all fibres longer than 5 µm are internalised by macrophages during the early inflammatory reaction, and that some are compartmentalised into the mesothelial layer which could lead to direct effects on the mesothelial cells and pleural diseases in a later stage if they are biopersistent.

Discussion

The capacity of alveolar macrophages for phagocytosis and clearance of particles and fibres from the lung is of major relevance in pulmonary defence and development of lung and pleural diseases. In this study we addressed the length cut-off value at which frustrated phagocytosis occurs *in vitro* and *in vivo*. We recently defined the threshold length for inflammogenicity in the pleural space for a range of fibres including those used here [14]. However in that paper we were unable, due to restrictions on space, to fully explore the role of frustrated phagocytosis nor fully describe the disposition of fibres in the pleural space. In the present paper we were able to quantitatively

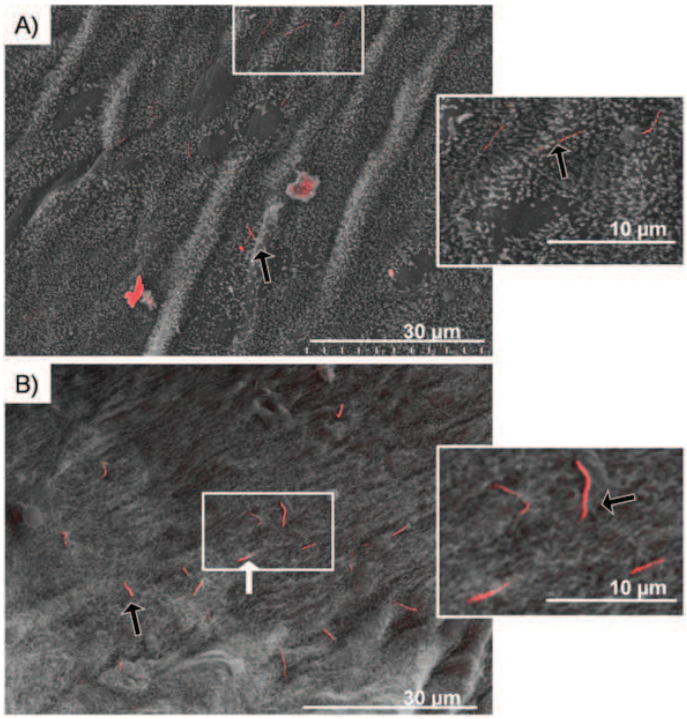

Figure 9 Mesothelial surfaces of the parietal pleura 1 week post injection of $AgNW_5$ and $AgNW_{10}$. Mesothelial cell layer of the parietal pleura after $AgNW_5$ (**A**) and $AgNW_{10}$ (**B**) exposure. AgNWs can be seen on the surface of the mesothelial layer as indicated by the black arrow. These AgNW are also partly taken up by mesothelial cells as indicated by the white arrow. The morphology of the nanofibres on the mesothelial layer appears intact.

compare phagocytosis/ frustrated phagocytosis of 5 different lengths of silver nanofibres ranging from 3–28 μm where inflammogenicity was determined in a previous study [14]. Thus far, the polydispersity of fibre length in samples including naturally occurring fibres and synthetic vitreous fibres prohibited the accurate investigation of the toxicity of various fibre lengths. The tight length classes of nanofibres used in this study, produced using nanotechnological methods, allowed us to perform a quantitative and qualitative comparison of the role of fibre length and frustrated phagocytosis *in vitro* and *in vivo*.

The use of a novel technique, backscatter electron microscopy allowed us to distinguish between membrane bound fibres and unphagocytosed fibres and to visualise the interaction of inflammatory cells with different length of nanofibres on the parietal pleura, the site of fibre retention *in vivo*.

The need for macrophages to internalise and therefore clear fibres from the lung and the pleural space has long been accepted [16] but the cut-off length below which complete internalisation of particles/fibres occurs is unknown. An extensive study has investigated the phagocytic capacity of murine bone marrow-derived macrophages to engulf various sizes of latex beads in a range of 13 μm to >30 μm in diameter [17]. By measuring the bead diameter they calculated a phagocytosis capacity of 19.8 μm, which is 1.44 times the actual diameter of the cell. In regard to the phagocytosis of fibres by macrophages, Ye *et al*. investigated the role of glass fibre length in TNF-α production and NF-κB activation in a mouse macrophage cell line and correlated and increase in both cytokine level and transcription factor to incomplete phagocytosis of long fibres (17 μm) whereas short fibres (7 μm) were fully phagocytosed and therefore had less expression of the measured endpoints [9]. These data correlate with our identified threshold length for frustrated phagocytosis *in vitro*, which is ≥ 14 μm.

An *in vivo* study performed by Oberdorster *et al.* assessed the clearance of small (~3 μm in diameter) and large (~10 μm in diameter) polystyrene microspheres in rat and identified minimal clearance of larger spheres after a 200 days post position period [18]. This was considered to be due to impaired clearance of particles when the macrophage particle load is 60% of its normal volume.

Frustrated phagocytosis has been implicated to play a major role in the development of an inflammatory milieu after exposure to fibres *in vitro* [19,20]. We recently demonstrated that frustrated phagocytosis is a major factor in the genesis of inflammation in the pleural space after deposition of long fibres whereby macrophages undergoing frustrated phagocytosis of the long fibres release factors that promote a potent pro-inflammatory cytokine response from adjacent mesothelial cells [20]. In addition we have demonstrated that 5 μm is the threshold for pro-inflammatory effects of fibre in the pleural space for a wide range of fibers [14]. However, so far frustrated phagocytosis has not been fully visualised *in vivo* in the pleura and the fibre length threshold for frustrated phagocytosis *in vivo* is unknown. Here we showed that the length cut off value at which long fibres can be fully phagocytosed by macrophages differs *in vitro* and *in vivo*. Whereas *in vitro* fibres of 10 μm could be completely phagocytosed, *in vivo* inflammatory cells on the parietal pleura showed incomplete uptake and frustrated phagocytosis of 10 μm fibres. There are a number of potential explanations for this anomalous difference between *in vivo* and *in vitro* length-dependent effect. The *in vivo* model is a pleural granuloma in mice and this is very different from the *in vitro* situation. Firstly the cells used *in vitro* are human cells, secondly they are a cell line and thirdly they are not in the granulomatous milieu but are spread out singly on plastic, submerged in medium with 10% serum, a very abnormal environment. We conclude that investigations on frustrated phagocytosis and its relation to the pathological effects of fibres need to be carried out *in vivo* although future work could be focussed on trying different cell lines and culture conditions with the aim of finding a better *in vitro* model that mimics the *in vivo* findings.

Interestingly, pleural injection of $AgNW_5$ lead to significant inflammation in the pleural space [14] but was not associated with frustrated phagocytosis *in vivo*. These results show that frustrated phagocytosis is not solely responsible for the onset of an inflammatory reaction in the pleural space after exposure to fibrous particles and that fibres around 5 μm can be fully phagocytosed but nonetheless cause sufficient cellular stress to induce pro-inflammatory effects (Figure 10).

In this study we focused on the interaction of macrophages with nanofibres, however, our investigations of the parietal pleura revealed that intact nanofibres can also be found on the normal mesothelial cell layer after 1 week exposure. So far, we hypothesised that fibres, which are retained in the pleural space would be accumulated in lesions on the parietal pleura. In our study the mesothelial cells do not seem to be pro-inflammatory in this position as they have not attracted leukocytes to their vicinity and so their main effect may be by direct

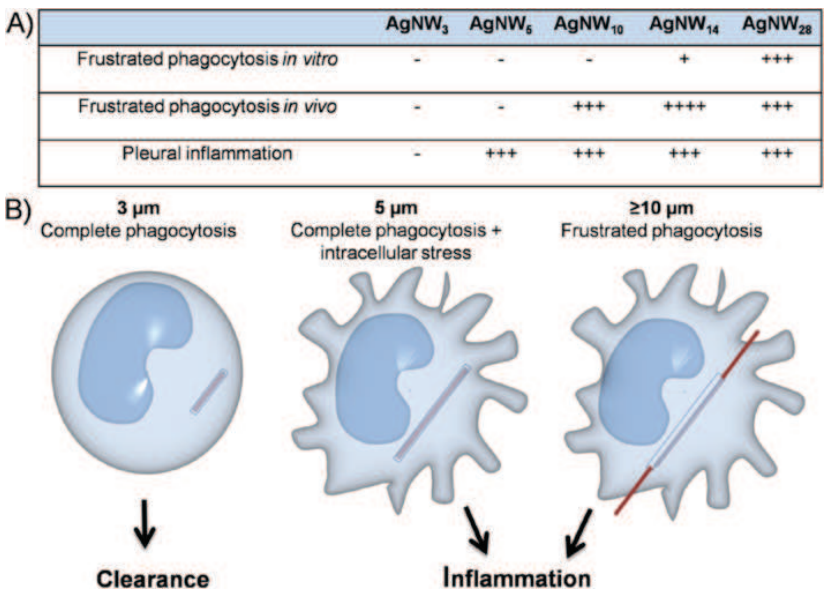

Figure 10 Length categories of frustrated phagocytosis and pleural inflammation and diagrammatic representation of frustrated phagocytosis. A) Summary of frustrated phagocytosis and pleural inflammation *in vitro* and *in vivo*. **B**) Diagrammatic representations of the length-dependent effects seen at the level of the macrophage in granulomas on the parietal pleura after instillation of fibres. These suggest that fibres 3 μm and shorter can be phagocytosed with no inflammation and cleared from the pleural space. Fibres 5 μm long can be entirely enclosed but are associated with inflammation whilst 10 μm fibres clearly cause frustrated phagocytosis and inflammation.

genotoxic or cytotoxic effects on the mesothelial cells. A lack of direct pro-inflammatory effect of the nanowires on the mesothelial cells would be consistent with our recent study on the interactions between long carbon nanotubes, macrophages and mesothelial cells in the genesis of inflammation. Work with long carbon nanotubes show that fibres interacting with macrophages cause the macrophages to release factors that evoke large scale production of inflammatory mediators by adjacent mesothelial cells [20]. Activated mesothelial cells produce a number of pro-inflammatory mediators including prostaglandins, nitric oxide, reactive oxygen species, cytokines and growth factors. Prolonged release of these pro-inflammatory mediators due to retention of fibres on the mesothelial surface may play a role in stimulation of tumour growth [21]. In contrast direct interaction between carbon nanotubes and mesothelial cells *in vitro* produced very little pro-inflammatory cytokine release by the mesothelial cells but did lead to significant membrane damage at higher carbon nanotube concentrations at a similar extent to that seen in macrophages [20]. A study by Adamson reported that exposure to long (≤20 μm) crocidolite asbestos fibres lead to increased pleural mesothelial cell proliferation in mice but no uptake of fibres in mesothelial cells was observed and again an indirect effect of mitogens released by cells in the sub-pleural lung tissues was implicated [22].

Therefore nanofibres that escape macrophage phagocytosis and take up residence in the mesothelium may be relatively non-inflammatory but represent a direct genotoxic threat. The interaction of AgNW with mesothelial cells changed their biopersistent characteristics, since AgNW appeared intact in their shape compared to compartmentalisation in macrophages where dissolution is observed. Silver ion measurements may not be helpful in clarifying AgNW persistence either *in vivo* or *in vitro* to the complexity of interpreting the data due to silver chloride formation as discussed in Schinwald *et al*. [14].

Our findings suggest therefore the threshold length of 5 μm is a threshold for retention of fibres that has at least 2 sequels:- 1) inflammation in the pleural space ; 2) compartmentalisation and localisation of such fibres to the mesothelial layer.

Conclusion

The use of backscatter scanning electron microscopy enabled us to identifying frustrated phagocytosis *in vitro* and *in vivo* using metal-based nanofibre samples without the further need of nanofibre modification including radio labelling or fluorescence labelling to visualise their interaction with cells and tissue. The images and data provided in this study show a clear cut-off value for frustrated phagocytosis *in vitro* and *in vivo* (Figure 10). We could visualise the interaction of nanowires with pleural inflammatory cells *in vivo* and revealed that frustrated phagocytosis is not the only factor for the onset of pleural inflammation and 5 μm fibres can be fully enclosed but are still associated with inflammation as previously described [14]. The contrast between the *in vitro* and *in vivo* finding for the length threshold for frustrated phagocytosis suggest that THP-1 macrophages do not provide a good model for the length dependent phagocytic events that occur *in vivo* in the murine pleural space. More research may provide a better *in vitro* model that mimics the *in vivo* effects. We also visualised the interaction of mesothelial cells with nanofibres and described a novel compartmentalisation of them in mesothelial cells which appeared to show different biopersistence characteristics compared to compartmentalisation in macrophages. However this needs to be confirmed by more quantitative studies rather than the merely descriptive data that are presented here.

Materials and methods

Backscatter electron signals by scanning electron microscopy

Elements with high atomic number (*Z*) such as silver reflect or back-scatter electrons more strongly than the lower *Z* light elements (predominantly H, C, N, O, P) of which cells are composed. Back-scattered electron imaging (BSE) is therefore a useful way to study frustrated phagocytosis since it provides high-contrast detection of nanowires, allowing clear discrimination between the nanofibres and other cellular features. Since the BSE signal from the fibres is attenuated by overlying cellular material, the method allows a clear distinction to be made between fibres that are, or are not, membrane-bounded, and can allow detection of fully phagocytosed fibres, which would not otherwise be detected in an SE image, provided they are at shallow depth within the cell.

This principle has been used widely for detection of colloidal gold markers in immunocytochemistry [23,24].

Fibre panel and size distribution

The fibre panel consisted of five distinct length classes of silver nanowires, hereafter referred to as $AgNW_3$, $AgNW_5$, $AgNW_{10}$, $AgNW_{14}$ and $AgNW_{28}$ whereby the subscript numbers indicate the average length of the nanowires. AgNW length diameter, contamination, soluble metal content, endotoxin level and dispertion was characterised as described previously by Schinwald *et al.* [14] (Figure 2). The samples were kindly provided by Seashell Technology, San Diego and synthesised using a polyol process as decribed in the US patent number 7,922,787 B2.

For light microscopy images 1 mg/ml of AgNWs were dispersed in 0.5% bovine serum albumin (BSA; Sigma-Aldrich, Poole, UK) and 10 μl of suspension was mixed in equal

volume of glycerol (Sigma-Aldrich, Poole, UK) to reduce the flow of AgNW. The suspension was placed on a glass slide, covered with coverslip and images taken using QCapture Pro software (Media Cybernetics).

In vitro study

In vitro macrophages exposed to fibres of different lengths

Cell culture The immortalised human monocytic cell line THP1 was used for *in vitro* studies. Cells were cultured in RPMI media supplemented with 10% heat inactivated FBS, 1% penicillin/streptomycin and 1% L-Glutamine (PAA, Austria). Prior to each treatment the cells were seeded in 24-well plates at a density of $0.5*10^6$/ml in 500 μl medium containing 10% FBS and 10 ng/ml phorbol 12-myristate 13-acetate (PMA) (Sigma) for 2 days at 37°C in 5% CO_2 atmosphere [25]. Fibres were uniformly dispersed in cell culture medium (RPMI 1640) supplemented with 1% penicillin/streptomycin and 1% L-Glutamine (PAA, Austria) and 0.5% bovine serum albumin (BSA; Sigma-Aldrich, Poole, UK) and briefly vortexed. Cells were treated with AgNW equalised to fibre number since fibre exposure is regulated on the basis of the fibre number and so relative potency needs to be determined on a per-fibre basis. To equalise for fibre number a dose of 2 μg/cm^2 for $AgNW_{14}$ was chosen as the standard in vitro dose based on previous measurement of membrane integrity and proliferation. Based on 2 μg/cm^2 for $AgNW_{14}$, concentrations for the other length classes AgNW panel were calculated assuming that fibres thickness was constant in the different length classes (Table 1).

Measurement of membrane integrity and proliferation of THP-1

Cells were seeded at a concentration of $0.5*10^6$ cells/ml and treated for 24 hours as described above. TritonX (Sigma) was used as a positive control for cell death and was added at a final concentration of 0.1% for 30 mins. After the treatment supernatant was centrifuged for 5 mins at 2000 rpm, transferred and centrifuged again for 5 mins at 13000 rpm**.** The conversion of lactate to pyruvate was detected using the Cytotoxicity Detection Lactate Dehydrogenase kit (Roche Diagnostics Ltd., Burgess Hill, UK) following the manufacturer's instructions. A microplate reader (BioTek® SynergyHT) was used to measure the optical density at 490 nm. Results are given as the mean ± SEM of 5 independent experiments.

Cells in the culture dish were used to measure their proliferation and metabolic activity via a chemical reduction of AlamarBlue® (Invitrogen). 150 μl of PBS and 15 μl of AlamarBlue® was added to each well and incubated for 3 hours at 37°C in 5% CO_2 atmosphere. Absorbance was monitored at 570 nm and 600 nm as a reference wavelength. Data are normalized to 600 nm value. Results are given as the mean ± SEM of 5 independent experiments.

Preparation for BSE

THP-1 cells were differentiated as described above and seeded into 24 well plates on Thermanox® Plastic Coverslips (NUNC™, Rochester, NY USA) at a density of $0.5*10^6$/ml. The cells were treated for 4 hours using concentration as described above at 37°C in 5% CO_2 atmosphere. After the treatment they were washed 5× with 0.1 M sodium cacodylate (pH 7.2) buffer. Overnight fixation was done in 3% glutaraldehyde/ 0.1 M sodium cacodylate (pH 7.2) buffer. After fixation the cells adherent to the coverslips were washed three times in sodium cacodylate buffer.

Bright field microscopy

THP-1 cells were differentiated as described above in a μ-dish (35 mm) (ibidi, Germany) and treated for 4 hours as described above. Brightfield microscope images were taken using Leica confocal laser scanning microscope SP5 at a 60× oil immersion objective lens.

In vivo study

Intra pleural injection of fibres

Fibres were uniformly dispersed in 0.5% bovine serum albumin (BSA; Sigma-Aldrich, Poole, UK)/saline at a concentration of 50 μg/ml which equates a dose of 5 μg per mouse and injected into the pleural cavity of female C57BI/6 mice (aged 8 weeks) at a volume of 100 μl per mouse as described previously by Schinwald *et al.* [14]. We used a sleeve close to the tip of a 27 G needle to prevent it penetrating beyond the pleural space into the lung [13]. Mice were euthanized after 24 hours (n = 4) and 7 days (n = 4) by asphyxiation in 100% CO_2.

Lavage of pleural space

The pleural space was lavaged with three 1 ml washes of sterile saline and kept on ice. To separate the cellular fraction from the supernatant the lavage fluid was centrifuged for 5 minutes at 2000 rpm at 4°C in a Mistral 3000i centrifuge (Thermo Fisher Scientific, Inc., MA, USA). Cyto-centrifugation with following Diff-Quik staining using Diff-Quik stainset (Dade Behring Gmbh, Marburg, Germany) were prepared for visualising uptake of fibres in pleural macrophages.

Preparation parietal pleura for BSE

Tissue dissection

The lower right posterior portion of the chest wall, approximately an area of 1 cm × 0.5 cm along the spine was cut out from the mice after lavage, washed in ice-cold saline and fixed for 4 hours in 30% formalin. The

tissue was excised from the surrounding tissue and fixed with 3% glutaraldehyde in 0.1 M Sodium Cacodylate buffer (pH 7.3) for 3 hours then washed in three 10 minute changes of 0.1 M Sodium Cacodylate buffer.

Cell and tissue preparation for BSE

Fixed samples were dehydrated in 50%, 70%, 90% and 100% normal grade acetones for 10 minutes each, then for a further two 10-minute changes in analar acetone. Dehydrated samples were critical point dried and mounted on SEM aliminium stubs and rotary-coated with about 8 nm of carbon in an Edwards 306A vacuum coating system (Edwards High Vacuum, Crawley, UK).

BSE

SEM of carbon-coated specimens was carried out using a Hitachi 4700 II field emission SEM (Hitachi High-Tech, Maidenhead, UK) at a beam accelerating voltage of 10 kV and a working distance of about 8 mm. Secondary electron (SE) and BSE images were taken simultaneously using an annular YAG crystal BSE detector and the upper SE detector to produce perfectly-synchronised image pairs. The two images were superimposed using Adobe Photoshop. The SE and BSE image were converted to grayscale, the BSE image was pasted into the SE image by using the layer function "lighten". This newly merged image and the SE image were converted to RGB mode, and overlayed by pasting the red channel of the BSE image into the red channel of the greyscale SE image, thus colour coding in red the strong BSE signal from the nanowires, the SE image appearing in grey.

Methodology for quantifying unphagocytosed fibres

Image-Pro plus software (Media Cybernetics Inc., MD, USA) was used to measure the amount AgNW outside macrophages. The intensity of red pixels of the nanofibres differs if the fibre is taken up by a cell and therefore covered by a cell layer (lower intensity) or if the fibres is unphagocytosed (higher intensity). Using Image-Pro software, it was possible to specifically select the red pixel intensity of unphagocytosed cells which was expressed as object and area count. The number of objects (unphagocytosed fibres) was divided by the number of cells per image and expressed as unphagocytosed fibres per cell. Approximately 100 cells per image were counted (n = 3).

Statistical analysis

All data are shown as the mean ± s.e.m. and these were analysed using one-way analysis of variance (ANOVA). Multiple comparison were analysed using Tukey-HSD method and in all cases (GraphPad InStat Software Inc., CA, USA).

Abbreviations

AgNW: Silver Nanowires; NiNW: Nickel nanowires; BSM: Backscatter scanning electron microscopy; LDH: Lactate dehydrogenase.

Competing interests

The authors declare that they have no competing interests.

Authors' contributions

A.S. conceived and designed the experiments, analysed the data and wrote the manuscript. K.D. initiated the study, oversaw all experimental work and contributed to manuscript preparation. All authors read and approved the final manuscript.

Acknowledgements

We thank Chris Jeffree for specialist input in BSM and S. Mitchell (University of Edinburgh) for sample preparation for SEM and technical assistance and the Colt Foundation (A.S., K.D) for financial support. We also thank James R. Glass, Janet C. Dickerson and David A. Schultz from Seashell Technology for providing the AgNW samples.

Received: 14 May 2012 Accepted: 15 August 2012
Published: 28 August 2012

References

1. Kamp DW: **Asbestos-induced lung diseases: an update.** *Transl Res* 2009, **153:**143–152.
2. Warheit DB, Driscoll KE, Oberdoerster G, Walker C, Kuschner M, Hesterberg TW: **Contemporary issues in fiber toxicology.** *Fundam Appl Toxicol* 1995, **25:**171–183.
3. Donaldson K: **The inhalation toxicology of p-aramid fibrils.** *Crit Rev Toxicol* 2009, **39:**487–500.
4. Donaldson K, Murphy FA, Duffin R, Poland CA: **Asbestos, carbon nanotubes and the pleural mesothelium: a review of the hypothesis regarding the role of long fibre retention in the parietal pleura, inflammation and mesothelioma.** *Particle and Fibre Toxicology* 2010, **7:**5.
5. Donaldson K, Murphy F, Schinwald A, Duffin R, Poland CA: **Identifying the pulmonary hazard of high aspect ratio nanoparticles to enable their safety-by-design.** *Nanomedicine (Lond)* 2011, **6:**143–156.
6. Wright GW, Kuschner M: **The influence of varying lengths of glass and asbestos fibres on tissue response in guinea pigs.** *Inhaled Part* 1975, **4**(Pt 2):455–744. 455–474.
7. Davis JM, Addison J, Bolton RE, Donaldson K, Jones AD, Smith T: **The pathogenicity of long versus short fibre samples of amosite asbestos administered to rats by inhalation and intraperitoneal injection.** *Br J Exp Pathol* 1986, **67:**415–430.
8. Donaldson K, Brown GM, Brown DM, Bolton RE, Davis JM: **Inflammation generating potential of long and short fibre amosite asbestos samples.** *Br J Ind Med* 1989, **46:**271–276.
9. Ye J, Shi X, Jones W, Rojanasakul Y, Cheng N, Schwegler-Berry D, *et al*: **Critical role of glass fiber length in TNF-alpha production and transcription factor activation in macrophages.** *Am J Physiol* 1999, **276:**L426–L434.
10. Donaldson K, Li XY, Dogra S, Miller BG, Brown GM: **Asbestos-stimulated tumour necrosis factor release from alveolar macrophages depends on fibre length and opsonization.** *J Pathol* 1992, **168:**243–248.
11. Poland CA, Byrne F, Cho WS, Prina-Mello A, Murphy FA, Davies GL, *et al*: **Length-dependent pathogenic effects of nickel nanowires in the lungs and the peritoneal cavity.** *Nanotoxicology* 2011, [Epub ahead of print].
12. Poland CA, Duffin R, Kinloch I, Maynard A, Wallace WA, Seaton A, *et al*: **Carbon nanotubes introduced into the abdominal cavity of mice show asbestos-like pathogenicity in a pilot study.** *Nat Nanotechnol* 2008, **3:**423–428.
13. Murphy FA, Poland CA, Rodger D, Al-Jamal KT, Hanene A-B, Antonio N, *et al*: **Length-dependent retention of carbon nanotubes in the pleural space of mice initiates sustained inflammation and progressive fibrosis on the parietal pleura.** *Am J Pathol* 2011, **178:**2587–2600.
14. Schinwald A, Murphy F, Prina-Mello A, Poland CA, Byrne F, Glass JR, *et al*: **The threshold length for fibre-induced acute pleural inflammation: shedding light on the early events in asbestos-induced mesothelioma.** *Toxicol Sci* 2012, Ref Type: In Press.

15. Boutin C, Dumortier P, Rey F, Viallat JR, De Vuyst P: **Black spots concentrate oncogenic asbestos fibers in the parietal pleura. Thoracoscopic and mineralogic study.** *Am J Respir Crit Care Med* 1996, **153:**444–449.
16. Lehnert BE: **Pulmonary and thoracic macrophage subpopulations and clearance of particles from the lung.** *Environ Health Perspect* 1992, **97:**17–46.
17. Cannon GJ, Swanson JA: **The macrophage capacity for phagocytosis.** *J Cell Sci* 1992, **101:**907–913.
18. Oberdorster G, Ferin J, Morse P, Corson NM, Morrow PE: **Volumetric alveolar macrophage (AM) burden as a mechanism of impaired AM mediated particle clearance during chronic dust overloading of the lung.** *J Aerosol Med* 1988, **1:**A207.
19. Brown DM, Kinloch IA, Bangert U, Windle AH, Walter DM, Walker GS, *et al*: **An in vitro study of the potential of carbon nanotubes and nanofibres to induce inflammatory mediators and frustrated phagocytosis.** *Carbon* 2007, **45:**1743–1756.
20. Murphy FA, Schinwald A, Poland CA, Donaldson K: **The mechanism of pleural inflammation by long carbon nanotubes: interaction of long fibres with macrophages stimulates them to amplify pro-inflammatory responses in mesothelial cells.** *Part Fibre Toxicol* 2012, **9:**8.
21. Mutsaers SE: **Mesothelial cells: their structure, function and role in serosal repair.** *Respirology* 2002, **7:**171–191.
22. Adamson IR: **Early mesothelial cell proliferation after asbestos exposure: In vivo and in vitro studies.** *Environ Health Perspect* 1997, **105:**1205–1208.
23. Soligo D, de Harven E, Nava MT, Lambertenghi-Deliliers G, Müeller M, Becker RP, Boyde A, Wolosewick JJ: **Immunocytochemistry with back-scattered electron. In The science of Biological specimen preparation for microscopy and microanalysis**. In *Scanning Microscopy*; 1985:289–297.
24. Jeffree CE, Rixon HW, Brown G, Aitken J, Sugrue RJ: **Distribution of the attachment (G) glycoprotein and GM1 within the envelope of mature respiratory syncytial virus filaments revealed using field emission scanning electron microscopy.** *Virology* 2003, **306:**254–267.
25. Park EK, Jung HS, Yang HI, Yoo MC, Kim C, Kim KS: **Optimized THP-1 differentiation is required for the detection of responses to weak stimuli.** *Inflamm Res* 2007, **56:**45–50.

doi:10.1186/1743-8977-9-34
Cite this article as: Schinwald and Donaldson: Use of back-scatter electron signals to visualise cell/nanowires interactions *in vitro* and *in vivo*; frustrated phagocytosis of long fibres in macrophages and compartmentalisation in mesothelial cells in vivo. *Particle and Fibre Toxicology* 2012 **9**:34.

6. Donaldson K, **Schinwald A**, Murphy F, Cho WS, Duffin R, Tran L, Poland C. **The biologically effective dose in inhalation nanotoxicology**. Accounts of Chemical Research. 2012 Sep 24.

ACCOUNTS
of chemical research

The Biologically Effective Dose in Inhalation Nanotoxicology

KEN DONALDSON,[*,†] ANJA SCHINWALD,[†] FIONA MURPHY,[‡] WAN-SEOB CHO,[§] RODGER DUFFIN,[⊥] LANG TRAN,[∥] AND CRAIG POLAND[∥]

[†]*University of Edinburgh, Edinburgh, U.K.,* [‡]*Dong-A University, Busan, South Korea,* [§]*MRC Toxicology Unit, Leicester, U.K.,* [⊥]*CXR Biosciences, Dundee, U.K., and* [∥]*Institute of Occupational Medicine, Edinburgh, U.K.*

RECEIVED ON MARCH 23, 2012

CONSPECTUS

In all branches of toxicology, the biologically effective dose (BED) is the fraction of the total dose of a toxin that actually drives any toxic effect. Knowledge of the BED has a number of applications including in building structure—activity relationships, the selection of metrics, the design of safe particles, and the determination of when a nanoparticle (NP) can be considered to be "new" for regulatory purposes. In particle toxicology, we define the BED as "the entity within any dose of particles in tissue that drives a critical pathophysiogically relevant form of toxicity (e.g., oxidative stress, inflammation, genotoxicity, or proliferation) or a process that leads to it."

In conventional chemical toxicology, researchers generally use the mass as the metric to describe dose (such as mass per unit tissue or cells in culture) because of its convenience. Concentration, calculated from mass, may also figure in any description of dose. In the case of a nanoparticle dose, researchers use either the mass or the surface area. The mass of nanoparticles is not the only driver of their activity: the surfaces of insoluble particles interact with biological systems, and soluble nanoparticles can release factors that interact with these systems. Nanoparticle shape can modify activity.

In this Account, we describe the current knowledge of the BED as it pertains to different NP types. Soluble toxins released by NPs represent one potential indicator of BED for wholly or partially soluble NPs composed of copper or zinc. Rapid dissolution of these NPs into their toxic ions in the acidic environment of the macrophage phagolysosome causes those ions to accumulate, which leads to lysosome destabilization and inflammation. In contrast, soluble NPs that release low toxicity ions, such as magnesium oxide NPs, are not inflammogenic. For insoluble NPs, ζ potential can serve as a BED measurement because the exposure of the particle surface to the acidic milieu of the phagolysosome and interactions with the lysosomal membrane can compromise the integrity of the NPs. Researchers have explored oxidative potential of NPs most extensively as an indicator of the BED: the ability of an NP to cause oxidative stress in cells is a key factor in determining cell toxicity, inflammogenicity, and oxidative DNA adduct formation. Finally we discuss BEDs for high aspect ratio nanoparticles because long fibers or nanoplatelets can cause inflammation and further effects. These consequences arise from the paradoxically small aerodynamic diameter of fibers or thin platelets. As a result, these NPs can deposit beyond the ciliated airways where their extended dimensions prevent them from being fully phagocytosed by macrophages, leading to frustrated phagocytosis. Although knowledge is accumulating on the BED for NPs, many questions and challenges remain in understanding and utilizing this important nanotoxicological parameter.

In conventional chemical toxicology, the mass is the metric generally used to describe dose (e.g., mass per unit tissue or cells in culture) because of its convenience, although concentration, calculated from mass, may also figure in any description of dose. In the case of nanoparticles, the mass or the surface area dose is used. However, nanoparticles are unlikely to have their effect as a consequence simply of their mass since the quantity that interacts with the biological system is the surface for insoluble particles or any soluble factors released in the case of soluble particles

Published on the Web 09/24/2012 www.pubs.acs.org/accounts
10.1021/ar300092y

and may be modified by shape. Our aim here is to describe current knowledge on the biologically effective dose (BED) as it pertains to different nanoparticle (NP) types. Soluble toxins released by NPs represent a potential BED for wholly or partially soluble NPs such as copper or zinc NPs. Rapid dissolution into ions in the acidic milieu of the macrophage phagolysosome leads to accumulation of the toxic ions, which causes lysosome destabilization leading to inflammation. In contrast, soluble NPs that release low toxicity ions, such as magnesium oxide NPs, are not inflammogenic because the ions that are released are low in toxicity. The ζ potential is a BED for insoluble NPs because the charge on the surface of the particle can be exposed in the acidic milieu of the phagolysosome, interacting with the lysosomal membrane leading to loss of integrity. The oxidative potential of NPs remains one of the BED that has been most explored, and the ability of NPs to cause oxidative stress in cells is a key factor in determining cell toxicity, inflammogenicity, and oxidative DNA adduct formation. The final BED discussed here is high aspect ratio, where long fibers or nanoplatelets cause inflammation and its consequences. This arises as a consequence of the paradoxically small aerodynamic diameter of fibers or thin platelets, enabling them to deposit beyond the ciliated airways where their extended dimensions prevents them being fully phagocytosed by macrophages, leading to frustrated phagocytosis. While knowledge is accumulating on the BED, there is still a great deal of research yet to be done and challenges faced in utilizing this important parameter, possibly the most important one for nanotoxicology.

The Biologically Effective Dose (BED) in Toxicology

Dose is central to toxicology, and the concept of dose for particles can actually be considered more deeply in terms of what is driving the response. Specifically, particles while often measured in terms of mass do not exert their effect as a consequence simply of their mass. The term used to describe the actual component of the total dose that drives adverse effects is the biologically effective dose (BED). We here define the particle BED as "the entity within any mass dose of particles that drives a critical pathophysiogically relevant form of toxicity in tissue", for example, inflammation, genotoxicity, or cellular proliferation. The BED is useful concept for several reasons (Figure 1 and Table 1). Any given particle sample might have more than one BED such as the presence of polyaromatic hydrocarbons (PAHs) as well as reactive transition metals in PM_{10}, and indeed, the BED might drive more than one response, for example, a local

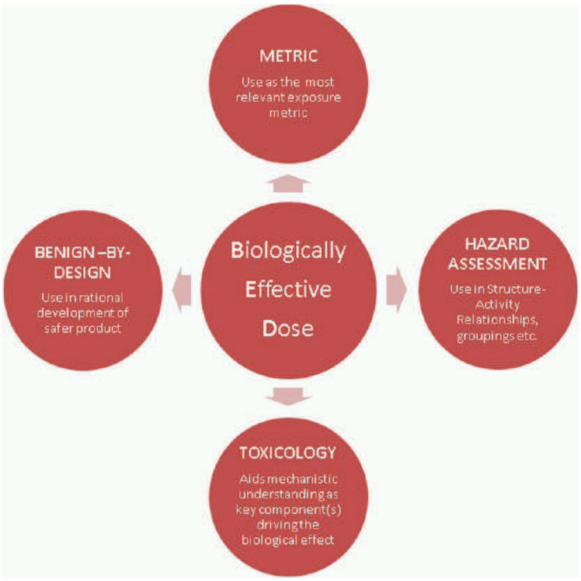

FIGURE 1. The uses and importance of the biologically effective dose.

response at the portal of entry and a more distal response in a target organ that it affects directly by translocation or indirectly by release of mediators at the portal of entry. Therefore in considering any BED, we need to define the response of interest and in terms of this Account, we confine ourselves to inflammation as the response of interest since it has multiple roles to play in particle-induced health effects and pathology.

It is notable that, despite knowledge of the BED and the obvious benefit of measuring the BED as a better guide for risk management, neither the quartz nor fiber BED, which are known, is the metric used in exposure measurement/risk assessment; the mass and fiber number are the metrics used for quartz and fibers respectively. The reason behind this simply reflects the challenges in measurement of particle exposure other than mass, particularly using real-time measurement systems. While there are improvements in this area, such as being able to measure surface area (often based on algorithms rather than direct measurement), certain factors such as particle reactivity or biopersistence are unlikely to ever be integrated into real-time exposure metrics.

At the level of individual cells, the BED of various nanoparticles (NP) is becoming better understood as discussed below. The BED is synonymous with particle physicochemical characteristics that are relevant for structure/toxicity (activity) relationships (STR). This is because structures defined in STRs drive the response and therefore are ideally the

TABLE 1. Details on How the BED Can Be Used for Hazard Identification, Risk Management, Predictive Toxicology, and Benign-by-Design

use of BED	rationale
hazard identification	the BED allows prediction of the types of hazard outcome, for example, a highly oxidative particle is likely to cause oxidative DNA adducts; a fiber-shaped nanoparticle may pose a mesothelioma hazard
risk management	since the BED drives the adverse effect, measuring the BED as the exposure metric most closely measures the harmful exposure and so would allow the most effective risk management
predictive toxicology	determining the BED and its potency using toxicological approaches allows prediction of the type of hazard (hazard identification) and likely potency in causing pathogenic effects
benign-by-design	knowledge of the BED allows particles designers a structural target that they may address to produce a safer, less harmful particle

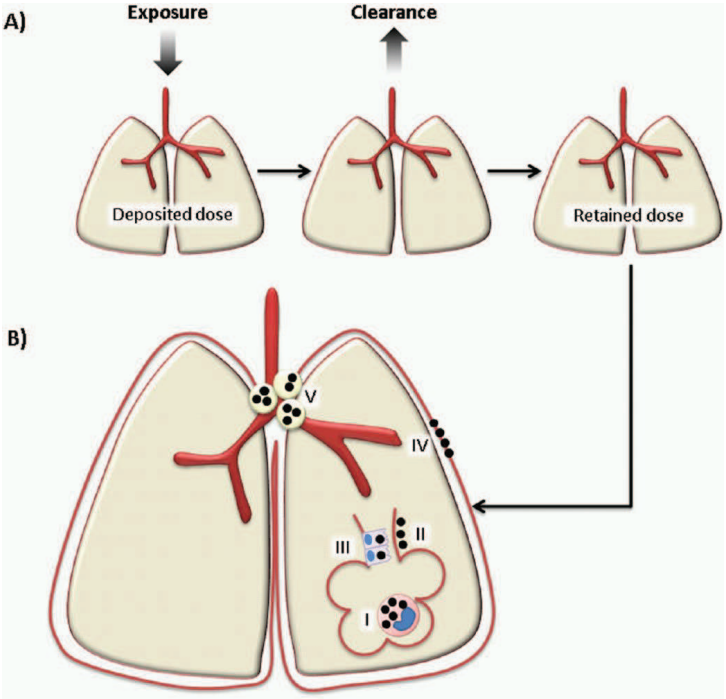

FIGURE 2. (A) The retained dose shown as the deposited dose minus the dose that is mechanically cleared and (B) the sequestration compartments in the lungs where the retained particle dose (black dots) can be found:-(I) alveolar macrophages; (II) interstitium in terminal airways; (III) epithelial cells; (IV) the parietal pleura; (V) mediastinal lymph nodes. In addition, if lesions arise, particles can be trapped in the developing lesions.

BED for a specific pathophysiologically relevant response(s). The BED therefore is crucial and can be useful in a number of ways (Figure 1) that aid hazard identification, risk management, predictive toxicology (i.e., *in silico* approaches), and benign-by-design to allow the informed development of safer nanomaterials. More detailed examples of these uses are given in Table 1.

Retention Compartments Where the BED Is Applied

It is informative to consider where the BED is applied. The lung is a complex organ, and the delivery of a particle dose is a complex interplay related to the anatomy of the lung, the flow of air, and the aerodynamic size and composition of the particles, all of which govern how much and where an inhaled dose of particles deposits in the lung. A major part of the "ineffective" dose is the fraction that is cleared by mechanical clearance (Figure 2A) to leave the retained dose. The retained dose distributes into various compartments over time where residence can be transient or more long-lived. Classically the clearance from the airways, propelled by the mucociliary escalator, is much faster than clearance from beyond the ciliated airways, which depends on macrophage action. Depending on the particle in question and its BED, there can be an effect in these compartments that contributes to pathogenicity. While low toxicity particles generally cause minimal effects at plausible doses, pathogenic particles can have various pro-inflammatory, mitogenic, genotoxic, or other pathophysiogically relevant effects. The compartments are shown in Figure 2B, and the

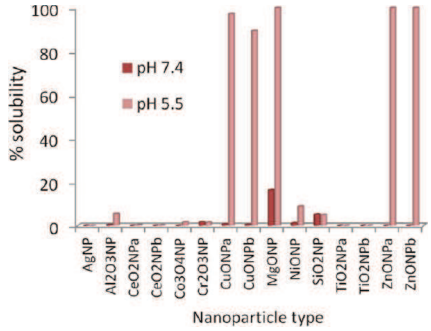

FIGURE 3. Solubility (%) of a panel of metal/metal-oxide NPs in Gamble's solution at pH 7.4 and 5.5; data are shown as mean; all SEM were <10% of the mean. Same composition NPs from different sources are labeled with a and b subscripts such as CeO_2NP_a and CeO_2NP_b. Solubility test was carried out three times. Data were redrawn from ref 1.

effects of the particle BED in these compartments give responses that provide the pathological nuances that are seen with different particles and that we would anticipate with different NPs.

Biologically Effective Doses of Nanoparticles

The BED, as discussed above, gets to the heart of how any particle dose drives response. Within any mass dose of particles that elicits a toxic response, there must be one or more entities that are the actual drivers, and these, by definition, are the BED(s). They can take the form of one or more physicochemical characteristics associated with the particles and can be soluble or ionic species released from the particle or characteristics integral to the particle surface or the particle shape. Below we outline exemplar BEDs that have been described for various nanoparticle types.

Soluble Toxins Released from NPs. Some NPs will undergo a degree of solubility (ionization) in biological fluids. Using metal oxide NPs, we have seen measurable but limited solubility in water or neutral conditions[1] (Figure 3). However, in the acidic conditions typical of phagolysosomes and lysosomes, NPs show variable solubility (Figure 3); copper oxide NPs, magnesium oxide NPs, and zinc oxide NPs showed rapid, complete dissolution in acid conditions (pH 5.5), while other NPs showed minimal dissolution (Figure 3).

The neutral-soluble fraction may be important for particles bathed in lung-lining fluid or the fluid of the interstitium, which have a pH around neutrality. For example, the concentration of soluble ions from the nickel oxide NP, zinc oxide NP, and copper oxide NP suspensions in neutral saline ranged from 5 to 12 ppm.

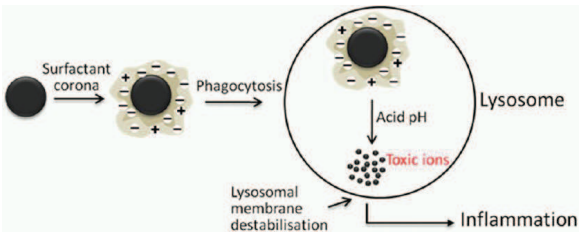

FIGURE 4. The mode of action of high-solubility NPs composed of material that ionizes to toxic ions in causing inflammation. High-solubility NPs deposit in the neutral environment of the lung lining and first develop a corona from the lung surfactant into which they deposit. They are then taken up into macrophage phagolysosomes, which have an acidic pH. In the acidic phagolysosomal milieu, dissolution to toxic ions is greatly accelerated compared with dissolution rate at neutrality and the toxic ions accumulate to a high concentration. This causes lysosomal membrane destabilization and inflammation. See ref 1 for more details.

Treatment of the alveolar type II epithelial cell line, A549 with the neutral-soluble fraction of zinc oxide NPs and copper oxide NPs increased interleukin (IL)-8 via activator protein (AP)-1 or nuclear factor κB (NF-κB) activation while that with nickel oxide NPs did not. Chelation of ions in the neutral-soluble fraction of zinc oxide NPs and copper oxide NPs abolished the effect demonstrating the role of the ions as the BED for the inflammatory reaction in these cells, and in a rat lung instillation model, low concentrations of neutral-soluble fractions had a role in recruiting neutrophils to the lung.[2]

The acid-soluble fraction is relevant because of the compartmentation of particles into macrophage phagolysosomes, which typically have a pH of around 5.5 and dissolution commonly occurs much faster in this acidic environment. For example, zinc oxide NPs produced an acute eosinophilic inflammation in a rat instillation model,[2] and instillation of the relevant concentration of soluble zinc ions produced the same magnitude of eosinophilic inflammation as the whole NP, suggesting that the BED for eosinophil recruitment was zinc ions and not the NP *per se*. On the other hand, despite being highly soluble at pH 5.5, magnesium oxide NPs did not elicit inflammation in the rat instillation model.[1] This is because Mg^{2+} is a nontoxic ion and may even protect against cell injury.[3] Therefore, the relative toxicity of the compositional ions of high-solubility NPs is the principal parameter dictating the toxicity of these NPs and its toxic ions can be the BED (Figure 4).

In addition to degree of solubility impacting on the BED, solubility also is a factor in biopersistence. Dissolution to *harmless ions* is likely to be nonharmful since there is no

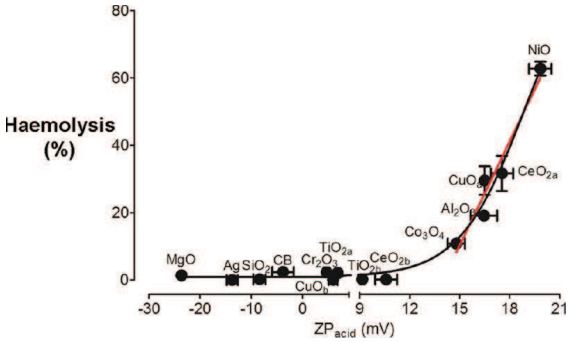

FIGURE 5. Effect of the ζP_{acid} value on the ability of any NP sample to cause lysis of erythrocyte membranes. Redrawn from ref 4.

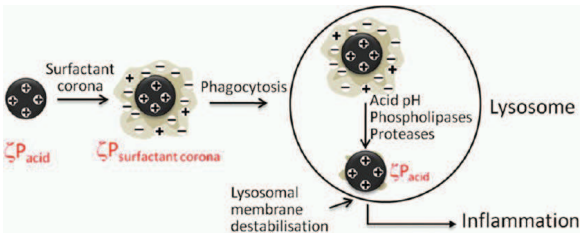

FIGURE 6. The hypothesized mechanism of inflammation caused by low solubility, high ζP_{acid} NPs. The high ζP_{acid} of NP is changed to $\zeta P_{surfactant\text{-}corona}$. This corona, however, can be digested by the enzymes and the acidic conditions of lysosomal fluid, which can restore the high ζP_{acid}, which is inflammogenic via destabilization of lysosomal membrane. Redrawn from ref 4.

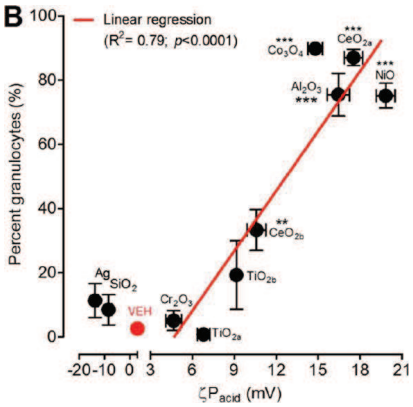

FIGURE 7. Relationship between ζP_{acid} and lung inflammogenicity. Plot of ζP_{acid} versus percentage of total granulocytes in the BAL. NPs having negative ζP_{acid} were not associated with inflammation but NPs having positive ζP_{acid} had a significant linear correlation with the percentage of total granulocytes in the BAL (Pearson correlation test, $R^2 = 0.86$, $p = 0.0009$, 95% confidence interval = 0.64−0.99. Used with permission from ref 4. Copyright 2012 Society of Toxicology.

build-up of particles; however, dissolution to *harmful ions* would lead to pathogenic effects. The consequences of slow or partial dissolution are more difficult to predict and would depend on the toxicity of the ions and of the residuum of the particle that is retained.

ζ-Potential. The electric potential created between the charged groups associated with the surface of a particle and the suspension medium is the ζ potential (ζP) and provides information concerning the surface charge of particles. The ζP, as might be anticipated, shows dynamic changes depending on the pH of the medium and the adsorption of protein to form the corona.[4] Subsequently most metal oxide NPs have a negative ζP in PBS (pH 7.4), a predominantly positive ζP in acidic physiological saline (pH 5.6) (ζP_{acid}), and a slightly negative ζP when there is a corona of proteins ($\zeta P_{surfactant\text{-}corona}$) or lung lining fluid. The basis for advancing ζP as a BED is that when NPs are phagocytosed by alveolar macrophages the proteolytic enzymes and acidic pH (pH 5.6)[5] found in the phagolysosome may strip off the corona and reveal the naked surface of the particle[4] restoring the precoronal ζP_{acid}. If the restored ζP_{acid} of the NP has a high positive value, it has the potential to bind to and damage membranes, as shown by ability to lyse erythrocyte membranes as a model membrane target (Figure 5).

We suggest that the same type of enhanced interaction between NPs with a high positive ζP_{acid} and the internal face of the lysosomal membrane could cause destabilization of the lysosomes, which can trigger inflammation or cell death (Figure 6).

Thus the ζP_{acid} represents a BED for some NPs, and this is supported by the finding that the ζP_{acid} of metal/metal-oxide NPs showed a linear correlation with the ability of a range of NP samples to cause acute lung inflammation. This was shown by instilling a panel of metal/metal oxide NPs into rat lungs at equal surface area dose and plotting the ζP_{acid} with the extent of the inflammation.[4] There was a clear threshold ζP_{acid} level triggering both inflammation (Figure 7) and the membranolytic effect (Figure 6) that was around +12 mV[4] (Figure 7). Therefore for some NPs the ζP_{acid} represents the BED, but this may be quite site-specific since it requires an acidic and hydrolytic environment such as the macrophage phagolysosome for its full expression.

Oxidative Potential. Throughout the particle toxicology literature, there are numerous instances where pathogenic particles possess oxidative potential and cause their effects via the final common pathway of oxidative stress. For example, in the case of quartz, the elicitation of oxidative stress and the formation of damaging hydrogen bonds between the silanol groups at the quartz surface and the cell membrane is a key driver of oxidative stress and ensuing

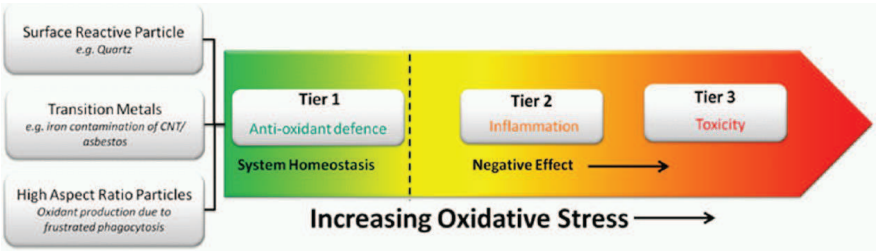

FIGURE 8. The relationship of biologically effective dose to the driving of oxidative stress and graded cellular responses. Adapted from ref 22.

inflammation.[6] It should however be noted that in some cells nonoxidative pro-inflammatory mechanisms also prevail.[7] In some studies, NP oxidative activity measured directly by chemical methods can be related to their ability to cause inflammation,[8] but other studies have not found this simple relationship[9]

Taking another example of a different NP, the generation of oxidative stress in cells by exposure to carbon nanotubes has been described by several research groups.[10] The oxidative potential of carbon nanotubes has been ascribed to the transition metal catalysts remaining after production, which can be a source of free radicals.[11] {However for longer fibers of carbon nanotubes, the length of the fibers and not iron is the BED (see below).}

Nel and co-workers[12]suggested a hierarchy of response to particle-induced oxidative stress. Within this model, the normal physiological levels of oxidative stress are dealt with by the cell by gene expression for antioxidants but intermediate levels of oxidative stress may cause a more severe responses such as inflammation (e.g., via activation of NF-κB), while high levels of oxidative stress cause cell death (Figure 8).

As shown in Figure 8, several BEDs can have oxidative potential and so exert their effect through oxidative stress. Examples include phagocytosis of long fibers driving the release of superoxide radicals due to activation of the NADPH oxidase system.[13] Another example of BED driving oxidative stress is the photocatalytic activity of titanium dioxide under UV light.

High Aspect Ratio Particles. Nanofibers. The geometric shape/structure of particles has long been accepted as a crucial factor in enhancing toxicity. The role of fiber length/aspect ratio first became apparent because of asbestos, which caused a worldwide epidemic of lung cancer and fibrosis, as well as pleural diseases such as mesothelioma, pleural fibrosis, and pleural plaques. The correlation of adverse health effects and fiber structure is a robust structure–toxicity relationship encapsulated in the fiber pathogenicity paradigm (FPP), which defines the features that define the fiber BED[14] (Figure 9).

Particles/fibers that deposit beyond the ciliated airways are cleared via alveolar macrophages, and this relies on complete phagocytic uptake. However longer fibers cannot readily be completely taken up by macrophages, which results in frustrated phagocytosis (Figure 10). This incomplete or frustrated phagocytosis is pro-inflammatory[14] as shown in Figure 11.

As well as being pro-inflammatory, the sheer bulk of a long fiber(s) inside a macrophage is likely to be an obstacle to the normal process of motility leading to accumulation of longer fibers in the lower respiratory tract,[15] recruitment of inflammatory cells, secretion of pro-inflammatory mediators, and generation of reactive oxygen species (see below)[14] The clearance rate of longer fibers is also impacted by the biopersistence of the deposited fibers. Nonbiopersistent long fibers can break into smaller fragments and be cleared via macrophages whereas biopersistent long fibers remain in the lower respiratory tract, and some may translocate to the pleural space surrounding the lungs.[14] The generality of the translocation of particles and fibers from the lungs to the pleural space has been demonstrated, and liquid and particles in the pleural space drain to mediastinal lymph nodes by drainage through stomata on the parietal pleura.[14] With a diameter $<10\ \mu$m,[16] the parietal pleura therefore acts like a sieve, retaining longer fibers at the parietal pleura where they can cause pathogenic responses. There is therefore a good mechanistic basis for biopersistent long fibers as the BED of long fibers for pleural responses.

The similarities between asbestos and manufactured nanofibers, including nanotubes, -rods, and -wires, has engendered concern as to their potential to cause similar hazards. Following initial data supporting the hypothesis that nanofibers conformed to the FPP in the peritoneal cavity,[17] we went on to test for length-dependent fiber pathogenicity after direct exposure of the mesothelial lining of the pleural space using a panel of high aspect ratio

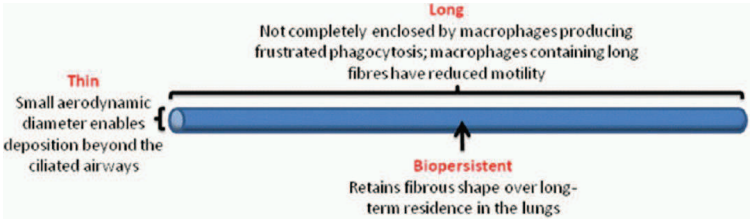

FIGURE 9. The three structural elements that determine the toxicity of fibers; see text for details.

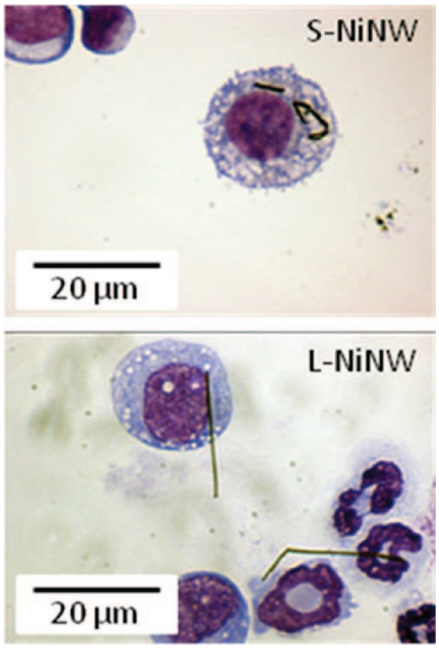

FIGURE 10. Macrophages that have phagocytosed short nickel nanowires (S-NiNW, upper image) and long nickel nanowires (L-NiNW, lower image). With short nanowires, the fibers can be clearly seen completely enclosed within the cell (upper image, white arrow) while the phagocytosis of long fibers produces the classical picture of frustrated phagocytosis with the fiber protruding from the cell surface (lower image, black arrow). Image modified from ref 23.

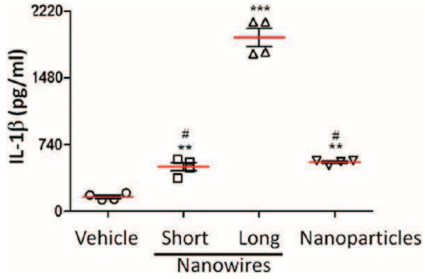

FIGURE 11. Pro-inflammatory effects, as production of the cytokine IL-1β by THP-1 macrophages exposed to vehicle, long or short nickel nanowires, or nickel nanoparticles. Note the clear specific effect of the long nanowires in stimulating IL-1β release.

nanoparticles (HARN) samples.[18] Only long nanofibers and long asbestos fibers elicited sustained inflammation in the pleural space and extensive lesion formation and fibrosis along the parietal pleura. These studies support the contention that long, biopersistent nanofibers represent the BED for this type of nanomaterial. Most recently, we have addressed the threshold fiber length for the onset of fiber pathogenicity in the pleural space using silver nanowires and nickel oxide nanowires with tightly sized length categories. After direct intrapleural injection, we were able to identify a clear cutoff value of 5 μm for acute long fiber effects in the pleural space.[19] We are therefore able to further delineate the nanofiber BED as biopersistent fibers longer then 5 μm.[18]

Nanoplatelets. Recently high aspect ratio materials made of graphene in the form of nanoplatelets are attracting substantial scientific interest. Like fibers, the platelet shape could pose unusual risk to the lungs and the pleural space after inhalation due to their aerodynamic properties. Very thin sheets with a high aspect can have a low aerodynamic diameter (D_{ae}) compared with their geometric size. The respirable size for humans cuts off at around an D_{ae} of 5 μm.[20] We calculated the aerodynamic diameter of a commercial form of graphene nanoplatelets (GNPs), which could be up to 30 μm across, and we found the 30 μm diameter nanoplatelets to possess an D_{ae} of 3.3 μm, well inside the respirable range (Table 2). Such a particle can therefore deposit beyond the ciliated airways where the macrophages will fail to fully engulf them, producing frustrated phagocytosis[21] and inflammation. We reported that respirable-sized but physically large and extended graphene nanoplatelets were able to cause inflammation in the lung and the pleural space after pharyngeal aspiration and direct intrapleural injection.[21] The inflammatory response was accompanied by frustrated phagocytosis of pulmonary and pleural macrophage observeable in vitro (Figure 12), and macrophage cells treated with respirable GNPs in vitro produced increased cytokine levels compared with a

TABLE 2. Range of Sizes of Nanoplatelets in the GNP Sample as Their Projected Diameter[a] and the Calculated Aerodynamic Diameter, Clearly Showing That the Nanoplatelets Having a Very Large Projected Diameter even up to 30μm Are Still Respirable

projected diameter [μm]	aerodynamic diameter (μm)
5	1.3
10	1.9
15	2.3
20	2.7
25	3
30	3.3

[a]The diameter of a circle having the same area as the particle.

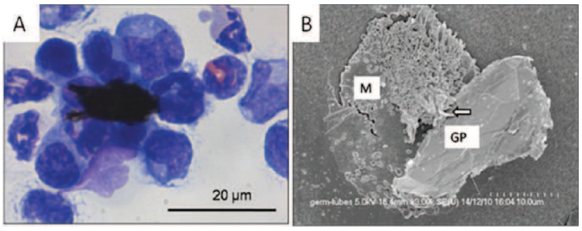

FIGURE 12. (A) Light micrograph of macrophages lavaged from the pleural space following instillation of graphene nanoplatelets. Note accumulation of cells around a large but respirable nanoplatelet with several cells showing frustrated phagocytosis as they attempt to enclose the same nanoplatelet. (B) Scanning electron microscope image of a macrophage (M) in culture failing to fully enclose a large yet respirable graphene nanoplatelet (GP) producing classical frustrated phagocytosis; arrow shows the attempt of the macrophage membrane to enclose the nanoplatelet.

nanoparticle carbon black control (Figure 13). Thus, for nanoplatelets, large extended thin particles with D_{ae} are a BED.

Collectively our data with nanofibers and nanoplatelets highlights the shape of high aspect nanomaterials as a BED, the driver for in vivo toxicity. Both nanofibers and nanoplatelets with nanoscale diameter or thickness can be very large in one or two dimensions but possess a low D_{ae}, which allows them to deposit in the lower respiratory tract. Therefore the fibrous and platelet habit can be seen as key BEDs if the material of which they are composed is biopersistent.

Benefits and Challenges of the BED. Despite the accumulated knowledge regarding the various BEDs that NPs possess and their roles in driving pathological processes, their remain major gaps and challenges in their use. In any single type of NP numerous factors may contribute to the BED making for a compound BED that could be the sum of particle shape, composition, soluble toxins, etc. Furthermore different BEDs may also impact on different pathways with differing potencies and may also be affected by aggregation in air and potential disaggregation in the lungs. As a hypothetical example, a long thin nanofiber may have a

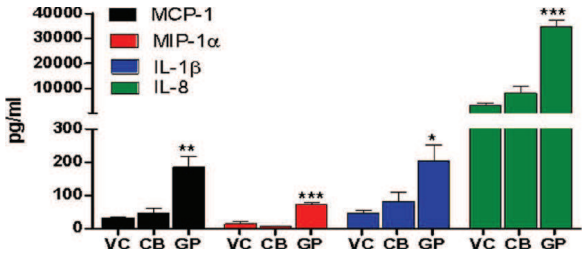

FIGURE 13. Release of four cytokines from THP-1 cells treated with vehicle (VC), carbon black (CB), and graphene nanoplatelets (GP) Adapted from ref 21. Note that GP produces a consistent and significant increase in release of the four cytokines compared with vehicle or nanoparticulate carbon black, a compact nanoform of graphene.

BED as a consequence of high aspect, but if it is composed of a reactive material, it may have ζ potential type BED and may also release soluble ions that have a soluble ion type of BED. Adoption of a metric based on such a complex BED seems to pose almost insuperable difficulties and so merely knowing the BED, if the BED is compound and complex, does not necessarily offer a solution to the issue of basing the metric on the BED. However some particles are likely to have a single BED, for example, surface area in the low-toxicity, low-solubility materials, and these pose a clearer target.

Conclusion

Knowledge of the BED is of great value for a variety of reasons in considering the hazard of any nanoparticle (Figure 1). By considering a particle not just as a single entity, but as a sum or sums of the attributes that drive toxicological response in a biological systems, one can understand the root drivers of toxicity, which opens the way to a number of key applications (Figure 1). Data is continuing to accumulate on the nanoparticle hazard and with increased knowledge of the toxicological profile/biological interactions of nanoparticles and the physicochemical properties, nanoparticles may be grouped into categories with a similar BED for hazard evaluation purposes. Other potential BEDs have been listed,[21] but firm evidence for their role in toxicological processes and the development of adverse effects and disease remain to be demonstrated. Other BEDs no doubt will become apparent as more data accumulates, but we do not consider that there will be a very large number, just as the variety of BEDs for conventional pathological particles is quite limited.

BIOGRAPHICAL INFORMATION

Ken Donaldson was born 1950 in St Andrews, Scotland, and attended the University of Stirling, obtaining a B.Sc. Hons. (First Class) in Biology (1978), and University of Edinburgh, obtaining a

Ph.D. (1982) and D.Sc. (1994). He was Head of the Cell Biology Unit of the Institute of Occupational Medicine, Edinburgh (1984−1992) and Professor of Pathobiology at Edinburgh Napier University (1992−2002) and is presently Professor of Respiratory Toxicology in the University of Edinburgh. He has published over 330 peer-reviewed papers, reviews, and book chapters on the toxicology of all the major types of pathogenic particles.

Anja Schinwald was born in 1987 in Hallein, Austria. She received a BA.rer.nat and a MA.rer.nat (First class) from Paris Lodron University of Salzburg/Johannes Kepler University of Linz in Molecular Biosciences (2010). Currently she is in her third year of a Ph.D. program at the University of Edinburgh focusing on high aspect ratio nanomaterials in relation to the asbestos pathogenicity paradigm.

Fiona Murphy was born in 1984 in Galway, Ireland, and attended the National University of Ireland, Galway, obtaining a B.Sc. (Hons) in Biotechnology (2007), and University of Edinburgh, obtaining an M.Sc. in Life Sciences (2008). She carried out her Ph.D. studies in the University of Edinburgh assessing the potential pathogenicity of carbon nanotubes in the pleural cavity. She is currently employed as Career Development Fellow by the MRC Toxicology Unit in Leicester, U.K., where her interests are focused on the molecular mechanisms involved in the development and progression of malignant mesothelioma.

Wan-Seob Cho was born in 1977 in Korea and attended the Seoul National University obtaining a B.Sc. in Veterinary Medicine (2000), M.Sc. (2002), and Ph.D. (2004) in Veterinary Pathology. He was a Scientific Officer in the Korea Food and Drug Administration (2002−2008) and a postdoctoral fellow at the University of Edinburgh (2008−2011). He took up the post of Assistant Professor of Toxicology in Dong-A University, Korea, in 2011. He has published over 50 peer-reviewed papers and book chapters on toxicology and his current interests are structure−toxicity relationships of metal/metal-oxide nanoparticles.

Rodger Duffin was born 1975 in County Antrim, Northern Ireland, and attended Edinburgh Napier University, obtaining a B.Sc. Hons (First Class) in Biomedicine with Toxicology (1997), and University of Edinburgh, obtaining a Ph.D. (2001). After postdoctoral training abroad, he returned to the University of Edinburgh Centre for Inflammation Research and became an MRC Senior Fellow in Respiratory Medicine. In 2012, he became Deputy Director of Research in CXR Biosciences, Dundee. He has published over 90 peer-reviewed papers, reviews, and book chapters on the toxicology of pathogenic particles. His current research interests are focused on nanotoxicology and investigative and mechanistic toxicology towards drug development.

Lang Tran was born in 1958 in Saigon. He has worked as a Mathematical Modeller and Toxicologist at the Institute of Occupational Medicine in Edinburgh since 1990. He has published extensively in Nanotoxicology and is currently the coordinator of a number of large EU FP7 projects.

Craig Poland was born in Aberdeen, Scotland, in 1980 and undertook a B.Sc. (Hons) degree in cell biology and pathology at the University of St Andrews (2002) followed by an M.Sc. in Biomedical Sciences at Edinburgh Napier University (2005) and Ph.D. in the toxicology of nanoparticles (2009) at the University of Edinburgh. In 2010, he moved to the Institute of Occupational Medicine as a research toxicologist where his focus is on assessment of nanomaterial hazard and risk. His overall research interest lies in understanding particle/biological interactions and how this can better inform safe particle design and inform risk assessment to protect worker and consumer health.

FOOTNOTES

The authors declare no competing financial interest.

REFERENCES

1 Cho, W. S.; Duffin, R.; Poland, C. A.; Duschl, A.; Oostingh, G. J.; MacNee, W.; Bradley, M.; Megson, I. L.; Donaldson, K. Differential Pro-Inflammatory Effects of Metal Oxide Nanoparticles and Their Soluble Ions in Vitro and in Vivo; Zinc and Copper Nanoparticles, but Not Their Ions, Recruit Eosinophils to the Lungs. *Nanotoxicology* **2012**, *6*, 22–35.

2 Cho, W. S.; Duffin, R.; Howie, S. E.; Scotton, C. J.; Wallace, W. A.; MacNee, W.; Bradley, M.; Megson, I. L.; Donaldson, K. Progressive Severe Lung Injury by Zinc Oxide Nanoparticles; the Role of Zn2+ Dissolution inside Lysosomes. *Part Fibre Toxicol.* **2011**, *8*, No. 27.

3 Flink, E. B.; Dedhia, H. V.; Dinsmore, J.; Doshi, H. M.; Banks, D.; Hshieh, P. High-Dose Magnesium Sulfate Attenuates Pulmonary Oxygen Toxicity. *Crit. Care Med.* **1992**, *20*, 1692–1698.

4 Cho, W. S.; Duffin, R.; Thielbeer, F.; Bradley, M.; Megson, I. L.; MacNee, W.; Poland, C. A.; Tran, C. L.; Donaldson, K. Zeta Potential and Solubility to Toxic Ions as Mechanisms of Lung Inflammation Caused by Metal/Metal Oxide Nanoparticles. *Toxicol. Sci.* **2012**, *126*, 469–477.

5 Nyberg, K.; Johansson, U.; Rundquist, I.; Camner, P. Estimation of pH in Individual Alveolar Macrophage Phagolysosomes. *Exp. Lung Res.* **1989**, *15*, 499–510.

6 Borm, P. J.; Tran, L.; Donaldson, K. The Carcinogenic Action of Crystalline Silica: A Review of the Evidence Supporting Secondary Inflammation-Driven Genotoxicity as a Principal Mechanism. *Crit. Rev. Toxicol.* **2011**, *41*, 756–770.

7 Ovrevik, J.; Refsnes, M.; Schwarze, P.; Lag, M. The Ability of Oxidative Stress to Mimic Quartz-Induced Chemokine Responses Is Lung Cell Line-Dependent. *Toxicol. Lett.* **2008**, *181*, 75–80.

8 Rushton, E. K.; Jiang, J.; Leonard, S. S.; Eberly, S.; Castranova, V.; Biswas, P.; Elder, A.; Han, X.; Gelein, R.; Finkelstein, J.; Oberdorster, G. Concept of Assessing Nanoparticle Hazards Considering Nanoparticle Dosemetric and Chemical/Biological Response Metrics. *J. Toxicol. Environ. Health, Part A* **2010**, *73*, 445–461.

9 Lu, S.; Duffin, R.; Poland, C.; Daly, P.; Murphy, F.; Drost, E.; MacNee, W.; Stone, V.; Donaldson, K. Efficacy of Simple Short-Term in Vitro Assays for Predicting the Potential of Metal Oxide Nanoparticles to Cause Pulmonary Inflammation. *Environ. Health Perspect.* **2009**, *117*, 241–247.

10 Srivastava, R. K.; Pant, A. B.; Kashyap, M. P.; Kumar, V.; Lohani, M.; Jonas, L.; Rahman, Q. Multi-Walled Carbon Nanotubes Induce Oxidative Stress and Apoptosis in Human Lung Cancer Cell Line-A549. *Nanotoxicology* **2011**, *5*, 195–207.

11 Kagan, V. E.; Tyurina, Y. Y.; Tyurin, V. A.; Konduru, N. V.; Potapovich, A. I.; Osipov, A. N.; Kisin, E. R.; Schwegler-Berry, D.; Mercer, R.; Castranova, V.; Shvedova, A. A. Direct and Indirect Effects of Single Walled Carbon Nanotubes on RAW 264.7 Macrophages: Role of Iron 3. *Toxicol. Lett.* **2006**, *165*, 88–100.

12 Nel, A.; Xia, T.; Madler, L.; Li, N. Toxic Potential of Materials at the Nanolevel. *Science* **2006**, *311*, 622–627.

13 Ye, S.; Wang, Y.; Jiao, F.; Zhang, H.; Lin, C.; Wu, Y.; Zhang, Q. The Role of NADPH Oxidase in Multi-Walled Carbon Nanotubes-Induced Oxidative Stress and Cytotoxicity in Human Macrophages. *J Nanosci. Nanotechnol.* **2011**, *11*, 3773–3781.

14 Donaldson, K.; Murphy, F. A.; Duffin, R.; Poland, C. A. Asbestos, Carbon Nanotubes and the Pleural Mesothelium: A Review of the Hypothesis Regarding the Role of Long Fibre Retention in the Parietal Pleura, Inflammation and Mesothelioma. *Part Fibre Toxicol.* **2010**, *7*, No. 5.

15 Coin, P. G.; Roggli, V. L.; Brody, A. R. Persistence of Long, Thin Chrysotile Asbestos Fibers in the Lungs of Rats. [Review] [24 Refs]. *Environ. Health Perspect.* **1994**, *102* (Suppl 5), 197–199.

16 Schinwald, A.; Murphy, F.; Prina-Mello, A.; Poland, C.; Byrne, F.; Glass, J.; Dickerson, J.; Schultz, D.; Movia, D.; Jeffree, C.; MacNee, W.; Donaldson, K. The Threshold Length for Fibre-Induced Acute Pleural Inflammation: Shedding Light on the Early Events in Asbestos-Induced Mesothelioma. *Toxicol. Sci.* **2012,** DOI: 10.1093/toxsci/kfs171.

17 Poland, C. A.; Duffin, R.; Kinloch, I.; Maynard, A.; Wallace, W. A.; Seaton, A.; Stone, V.; Brown, S.; MacNee, W.; Donaldson, K. Carbon Nanotubes Introduced into the Abdominal Cavity of Mice Show Asbestos-Like Pathogenicity in a Pilot Study. *Nat. Nanotechnol.* **2008**, *3*, 423–428.

18 Murphy, F. A.; Poland, C. A.; Duffin, R.; Al Jamal, K. T.; Ali-Boucetta, H.; Nunes, A.; Byrne, F.; Prina-Mello, A.; Volkov, Y.; Li, S.; Mather, S. J.; Bianco, A.; Prato, M.; MacNee, W.; Wallace, W. A.; Kostarelos, K.; Donaldson, K. Length-Dependent Retention of Carbon Nanotubes in the Pleural Space of Mice Initiates Sustained Inflammation and Progressive Fibrosis on the Parietal Pleura. *Am. J. Pathol.* **2011**, *178*, 2587–2600.

19 Schinwald, A.; Murphy, F. A.; Prina-Mellon, A.; Poland, C. A.; Byrne, F.; Movia, D.; Glass, J. R.; Dickerson, J. C.; Schultz, D. A.; Jeffree, C. E.; Macnee, W.; Donaldson, K. The threshold length for fiber-induced acute pleural inflammation: shedding light on the early events in asbestos-induced mesothelioma. *Toxicol Sci.* **2012**, *128* (2), 461–470.

20 Moller, W.; Kreyling, W. G.; Schmid, O.; Semmler-Behnke, M.; Schulz, H. Deposition, retention and clearance and translocation of inhaled fine and nano-sized particles in the respiratory tract. In *Particle-lung cell interactions*, 2nd ed.; Gehr,P., Muhlfeld, C., Rothen-Rutishauser, B., Blank, F., Eds; Informa Healthcare: New York, 2010, 79—107.

21 Schinwald, A.; Murphy, F. A.; Jones, A.; MacNee, W.; Donaldson, K. Graphene-Based Nanoplatelets: A New Risk to the Respiratory System as a Consequence of Their Unusual Aerodynamic Properties. *ACS Nano* **2012**, *6*, 736–746.

22 Nel, A. E.; Madler, L.; Velegol, D.; Xia, T.; Hoek, E. M.; Somasundaran, P.; Klaessig, F.; Castranova, V.; Thompson, M. Understanding Biophysicochemical Interactions at the Nano-Bio Interface. *Nat. Mater.* **2009**, *8*, 543–557.

23 Poland, C. A.; Byrne, F.; Cho, W. S.; Prina-Mello, A.; Murphy, F. A.; Davies, G. L.; Coey, J. M.; Gounko, Y.; Duffin, R.; Volkov, Y.; Donaldson, K. Length-Dependent Pathogenic Effects of Nickel Nanowires in the Lungs and the Peritoneal Cavity. *Nanotoxicology* **2011**, DOI: 10.3109/17435390.2011.626535.

7. **Schinwald A**, Chernova T, Donaldson K. **Use of silver nanowires to determine thresholds for fibre length-dependent pulmonary inflammation and inhibition of macrophage migration *in vitro***. Particle and Fibre Toxicology. 2012 Dec 2;9:47

Schinwald et al. Particle and Fibre Toxicology 2012, 9:47
http://www.particleandfibretoxicology.com/content/9/1/47

PARTICLE AND FIBRE TOXICOLOGY

RESEARCH Open Access

Use of silver nanowires to determine thresholds for fibre length-dependent pulmonary inflammation and inhibition of macrophage migration *in vitro*

Anja Schinwald[1], Tanya Chernova[2] and Ken Donaldson[1*]

Abstract

Background: The objective of this study was to examine the threshold fibre length for the onset of pulmonary inflammation after aspiration exposure in mice to four different lengths of silver nanowires (AgNW). We further examined the effect of fibre length on macrophage locomotion in an *in vitro* wound healing assay. We hypothesised that exposure to longer fibres causes both increased inflammation and restricted mobility leading to impaired clearance of long fibres from the lower respiratory tract to the mucociliary escalator *in vivo*.

Methods: Nine week old female C57BL/6 strain mice were exposed to AgNW and controls via pharyngeal aspiration. The dose used in this study was equalised to fibre number and based on 50 μg/ mouse for $AgNW_{14}$. To examine macrophage migration *in vitro* a wound healing assay was used. An artificial wound was created in a confluent layer of bone marrow derived macrophages by scraping with a pipette tip and the number of cells migrating into the wound was monitored microscopically. The dose was equalised for fibre number and based on 2.5 $\mu g/cm^2$ for $AgNW_{14}$.

Results: Aspiration of AgNW resulted in a length dependent inflammatory response in the lungs with threshold at a fibre length of 14 μm. Shorter fibres including 3, 5 and 10 μm elicited no significant inflammation. Macrophage locomotion was also restricted in a length dependent manner whereby AgNW in the length of ≥5 μm resulted in impaired motility in the wound closure assay.

Conclusion: We demonstrated a 14 μm cut-off length for fibre-induced pulmonary inflammation after aspiration exposure and an *in vitro* threshold for inhibition of macrophage locomotion of 5 μm. We previously reported a threshold length of 5 μm for fibre-induced pleural inflammation. This difference in pulmonary and pleural fibre- induced inflammation may be explained by differences in clearance mechanism of deposited fibres from the airspaces compared to the pleural space. Inhibition of macrophage migration at long fibre lengths could account for their well-documented long term retention in the lungs compared to short fibres. Knowledge of the threshold length for acute pulmonary inflammation contributes to hazard identification of nanofibres.

Keywords: Asbestos fibre, Silver nanofibres, Aspiration, Clearance, Migration

* Correspondence: ken.donaldson@ed.ac.uk
[1]MRC/University of Edinburgh, Centre for Inflammation Research, Queen's Medical Research Institute, 47 Little France Crescent, Edinburgh EH16 4TJ, UK
Full list of author information is available at the end of the article

Background

The determinants of the pathogenicity of fibrous materials include fibre diameter, length and biopersistence which form the basis of the fibre pathogenicity paradigm (FPP) [1]. Studies on asbestos fibres, synthetic vitreous fibres and nanofibres have shown that they all may pose a significant health hazard when inhaled during their manufacture and/or use [2-5]. These various different fibrous materials possess considerable differences in their pathogenicity in keeping with the FPP [6]. It has been accepted for many years that fibre length plays a crucial role in the development of asbestos related diseases. For example Davis *et al.* performed a number of experiments investigating the pathogenicity of various length and compositions of asbestos fibres via the routes of inhalation and intraperitoneal injection [7,8]. The inhalation studies showed that fibres with a significant proportion (~11%) of fibres > 10 μm caused widespread pulmonary fibrosis and cancer whereas shorter fibres (less than 5 μm) and UICC amosite (intermediate length) caused less fibrosis or carcinogenesis. However, the UICC amosite fibres and long asbestos fibres had similar potency in causing mesothelioma whilst virtually no carcinogenicity was seen with short fibres [8]. This study showed for the first time a difference in the fibre lengths required for the induction of lung diseases and the lengths for peritoneal mesothelioma and by analogy pleural mesothelioma. However, the precise threshold lengths for both lung and peritoneal pathology after fibre exposure were unknown at the time. In a recent study we determined the threshold length for fibre-induced pathogenicity in the pleura [9] as being 5 μm, using distinct length classes of silver nanowires (AgNW). The aim of the current study was to determine the threshold length for fibre-induced lung inflammation by comparing the pulmonary inflammatory response to the same panel of different length classes of AgNW after their deposition in the airspaces of the lungs.

The normal lung clearance mechanisms provide a defence mechanism for removing fibre dose and yet selective retention of longer fibres is well-documented [10,11]. For the key fraction of fibres that deposit beyond the ciliated airways and are slowly cleared, macrophage are the central cells involved in phagocytosing and transporting the fibres to the foot of the mucociliary escalator for clearance. We therefore hypothesised that the uptake of long fibres impairs the ability of macrophages to migrate whilst short fibres do not, providing a mechanism for selective retention of long fibres. We addressed this hypothesis using the samples with different fibre length classes and assessed their effects on macrophage migration in an *in vitro* wound closure assay.

Results

Length dependent inflammatory response to AgNW in lung at 24 hour

The panel of AgNW used for pharyngeal aspiration is represented in Figure 1. The inflammatory response to the panel of AgNW and control fibres as assessed by the bronchoalveolar lavage fluid (BAL) profile was measured 24 hour post aspiration. An initial dose response series was performed with $AgNW_{14}$ at a dose of 5, 10, 25 and

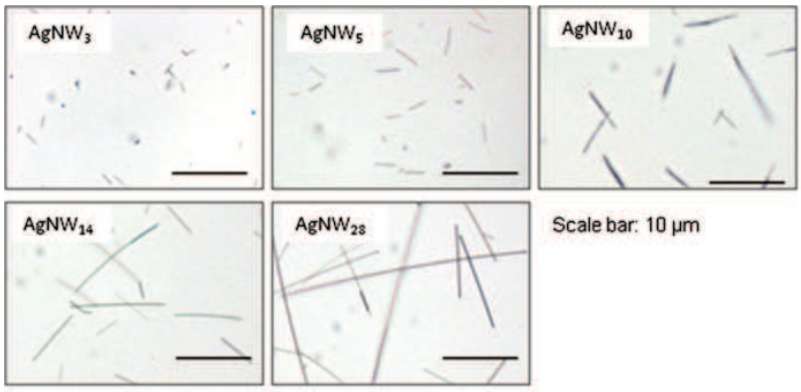

	AgNW$_3$	AgNW$_5$	AgNW$_{10}$	AgNW$_{14}$	AgNW$_{28}$
Mean length (μm)	3	5	10	14	28
% fibre ≥5μm	0	55	98	96	100
Diameter (nm, mean±s.e.m.)	115±3	118±3	128±2	121±3	120±4

Figure 1 Characteristics of AgNW panel. Representative images of the AgNW (1 mg/ml) and their mean length (μm), percentage of fibre ≥ 5 μm and average diameter (nm). Scale bar: 10 μm.

Table 1 Calculation for the mass adjustments for equalisation of fibre number *in vivo*

Particle	Calculation to equalise for the same fibre number	Dose (μg/mouse)	Total fibre number
SFA	Short fibre control	10.7	$50.48*10^6$
$AgNW_3$	3/14 × 50	10.7	$32.71*10^6$
$AgNW_5$	5/14 × 50	17.9	$31.19*10^6$
$AgNW_{10}$	10/14 × 50	35.7	$28.17*10^6$
$AgNW_{14}$	standard	50.0	$32.76*10^6$
LFA*	Long fibre control	50.0	$8.24*10^6$

*LFA fibre counting 164,705 fibres/μg on the basis of WHO counting criteria.

50 μg/mouse (n = 2) and SFA and LFA at a dose of 10 and 50 μg/mouse (n = 2) (data not shown). The dose of 50 μg/mouse was chosen since it gave a persistent inflammatory response with $AgNW_{14}$ and LFA. The dose was adjusted so that each of the different treatments (Table 1) comprised the similar fibre number. No change in total bronchoalveolar cell number was measured after exposure to equal numbers of the different fibre lengths compared to vehicle control (Figure 2A). However the total number of granulocytes was significantly increased after exposure to $AgNW_{14}$ (Figure 2B). A length dependent trend towards an increase in granulocyte number with $AgNW_5$, $AgNW_{10}$ and LFA was observed, although this was not significant (Figure 2B). $AgNW_3$ and SFA produced no increase in granulocyte number compared to VC (Figure 2B).

The effect of length on inflammation was demonstrated by plotting AgNW length against inflammation and it is clear that the relationship is not linear and that there is a discernible step–increase in granulocyte recruitment at a length between 10 and 14 μm. (Figure 2C). Total amount of protein and increase in membrane permeability by the release of LDH was measured but showed no significant difference between the treatments (data not shown).

Histological evaluation of lung sections following treatments

The pathology of the lung exposed to the AgNW panel and controls were examined 24 hour after aspiration. The sections after exposure to VC, SFA and $AgNW_3$ showed normal histology of bronchioles, respiratory bronchioles, alveolar ducts and alveoli (Figures 3A, B, D and Additional file 1: Figure S1). $AgNW_5$ and $AgNW_{10}$ produced minor granulomas and lymphocyte infiltrates and the majority of the lung histology appeared normal. $AgNW_{14}$ and LFA caused more extensive granuloma and lymphocyte infiltrates which is consistent with the amount of total granulocytes from the lavage fluid (Figure 3E, F, and Additional file 1: Figure S1). Accumulations of nanowires inside alveolar macrophages were common (Figure 3E, F white arrow and Additional file 1: Figure S1). $AgNW_{14}$ produced the strongest response with more granulomatous areas compared to shorter

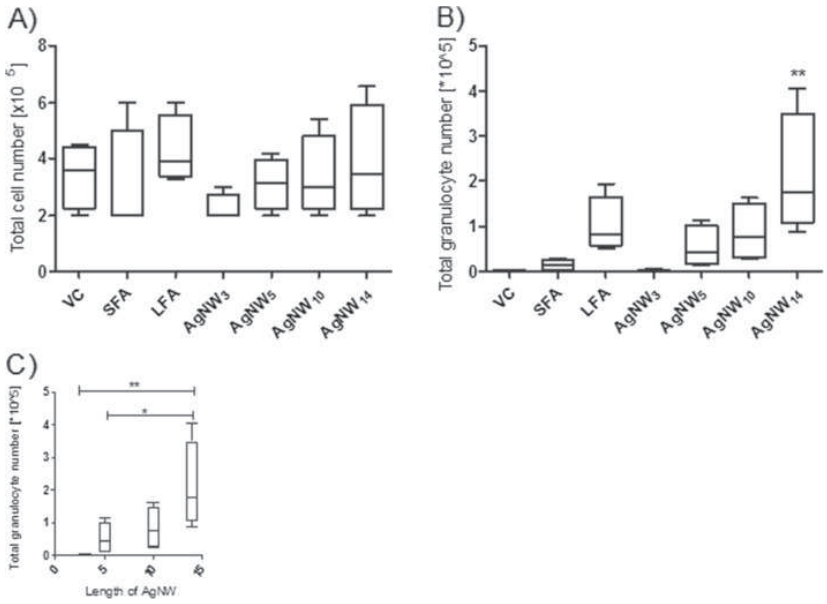

Figure 2 Length dependent inflammatory response to AgNW in the lungs at 24 hour. C57/Bl6 mice were exposed to AgNW and control panel by pharyngeal aspiration. At 24 hour post exposure the lungs were lavaged and total cell number (**A**) and total granulocyte number (**B**) were measured. **C**) The acute inflammatory increase was plotted against length of AgNW. Significance indicated compares treatment groups to vehicle control (**B**) and within each treatment (**C**), * indicates $p < 0.05$, ** indicates $p < 0.001$. Data represent mean ± SEM of n = 4 mice.

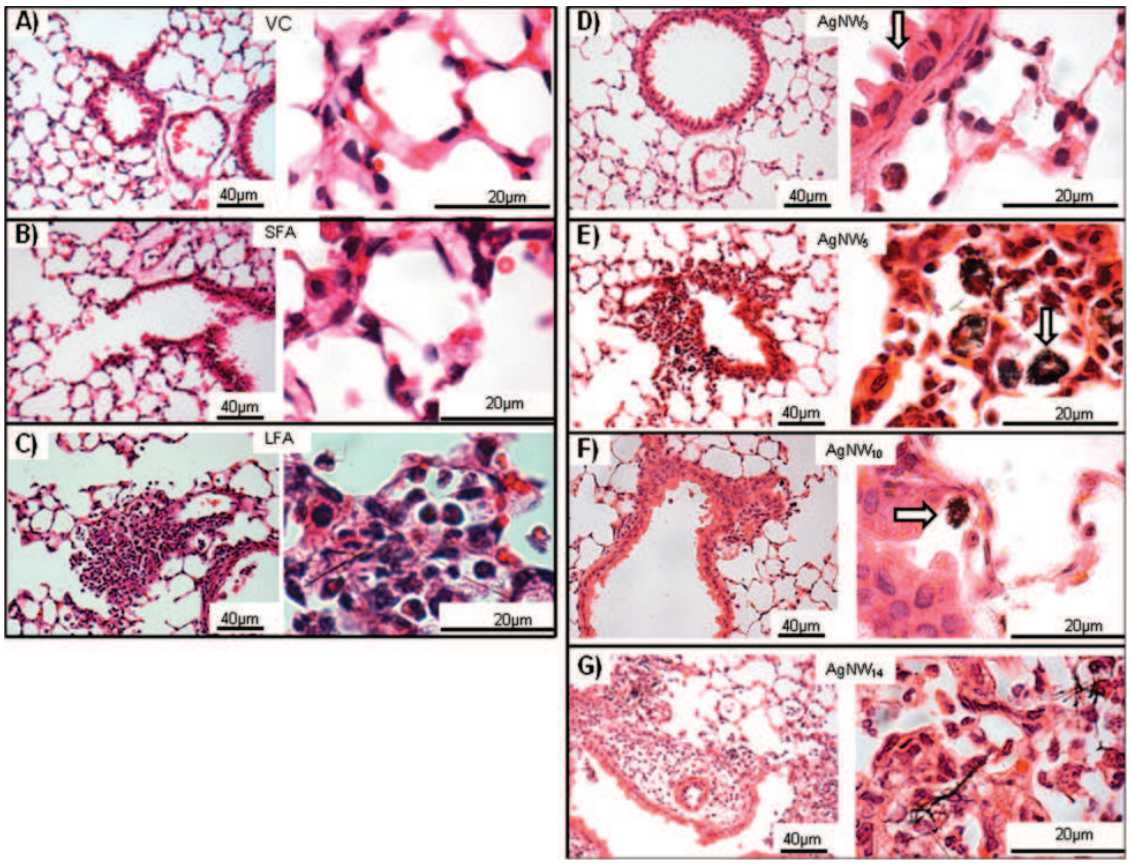

Figure 3 Lung histology 24 hour post aspiration to AgNW panel and controls. H&E stained lung sections at lower (left) and higher (right) magnification show normal alveolar structure in the vehicle control (**A**), SFA (**B**) and $AgNW_3$ (**D**) sections. Small accumulations of inflammatory cells were seen after $AgNW_5$ (**E**) and $AgNW_{10}$ (**F**) exposure whereas a greater amount of inflammatory cell infiltration in the alveoli, peribronchiolar and perivascular regionswere observed after LFA (**C**) and $AgNW_{14}$ (**G**). The white arrows are indicating the areas of fibre accumulation. Abbreviations: al, alveolus; br, bronchiole; v, blood vessel. Representative images are shown, similar results are obtained from 2 mice.

fibres however this was still minor compared to the extensive interstitial thickening and remodelling of the alveolar spaces after LFA treatment (Figure 3C, G, and Additional file 1: Figure S1). Frustrated phagocytosis, classified as incomplete uptake of fibres by cells [12], was observed with $AgNW_{14}$ and LFA.

Frustrated phagocytosis in alveolar macrophages

The uptake of different length of AgNW by alveolar macrophages was evident in cytospin images of the broncho-alveolar lavage fluid (Figure 4). Shorter fibres including SFA, $AgNW_3$, $AgNW_5$ and $AgNW_{10}$ could be completely phagocytosed by alveolar macrophages (Figure 4B, D, E) whereas LFA, and $AgNW_{14}$ were undergoing frustrated phagocytosis indicated by the sharing of fibres between adjacent cells (Figure 4C, G). This is in agreement with frustrated phagocytosis observed in histological sections and the extent of inflammation seen in the lavage fluid showing that frustrated phagocytosis of nanowires correlates with increased inflammation.

Fibre-length dependent inhibition of locomotion in bone marrow derived macrophages

As shown in Figure 5A and Additional file 1: Figure S2, the untreated cells migrated into and repopulated wounds area within 30 hour. Similar wound closure was seen after treatment with silver nanoparticles (AgP) and $AgNW_3$ (Figure 5A). A slight decrease in the closure of the wound occurred during treatment with $AgNW_5$ whilst BMMs treated with $AgNW_{14}$ and $AgNW_{28}$ (Figure 5B) demonstrate a substantial decrease in the ability to migrate into the wound compared to VC. The number of cells which

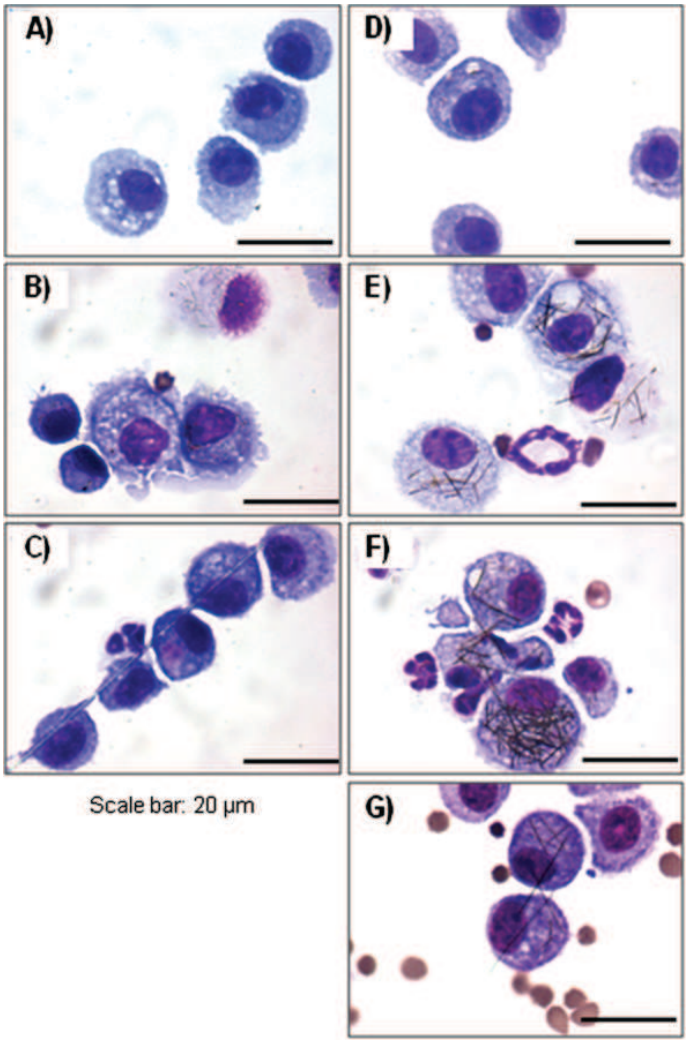

Figure 4 Uptake of AgNW and controls in alveolar macrophages. Cytospin images from the lavage fluid 24 hour post aspiration illustrates the complete uptake of shorter fibres including SFA (**B**), $AgNW_3$ (**D**), $AgNW_5$ (**E**) and $AgNW_{10}$ (**F**) whereas LFA (**C**) and $AgNW_{14}$ (**G**) lead to frustrated phagocytosis in alveolar macrophages. Scale bar 20 µm.

migrated into the wound were counted and expressed as percentage of migrated cells normalised to VC and this revealed that locomotion was significantly decreased with $AgNW_5$, $AgNW_{14}$ and $AgNW_{28}$ (Figure 6A). Cytochalasin D, a positive control which causes impaired migration due to disruption of the actin filaments produced a decrease in locomotion comparable to $AgNW_{14}$ (Figure 6A). Differences in the rate of metabolic activity or cell death could not account for the inability of macrophages to migrate into the wound as the treatment did not interfere with the metabolic activity measured via chemical reduction of Alamar Blue® (Figure 6B) and had no effect on cell membrane integrity measured as the release of lactate dehydrogenase into cell supernatant (Figure 6C). Decrease in cell adhesion has been linked to a decrease in the ability of cell migration. Backscatter scanning electron microscopy (BSE) images confirm that treatment with AgNW did not impair the ability of cell adhesion and spreading (Figure 5A,B). To the contrary, extensive cell spreading is observed in cells treated with long fibres presumably a consequence of BMMs increasing the surface area involved in engulfing the fibres (Figure 5A, B). Using BSE, nanowires and nanoparticles phagocytosed by BMMs could be visualised underneath the membrane as indicated by the arrow (Figure 5A, B).

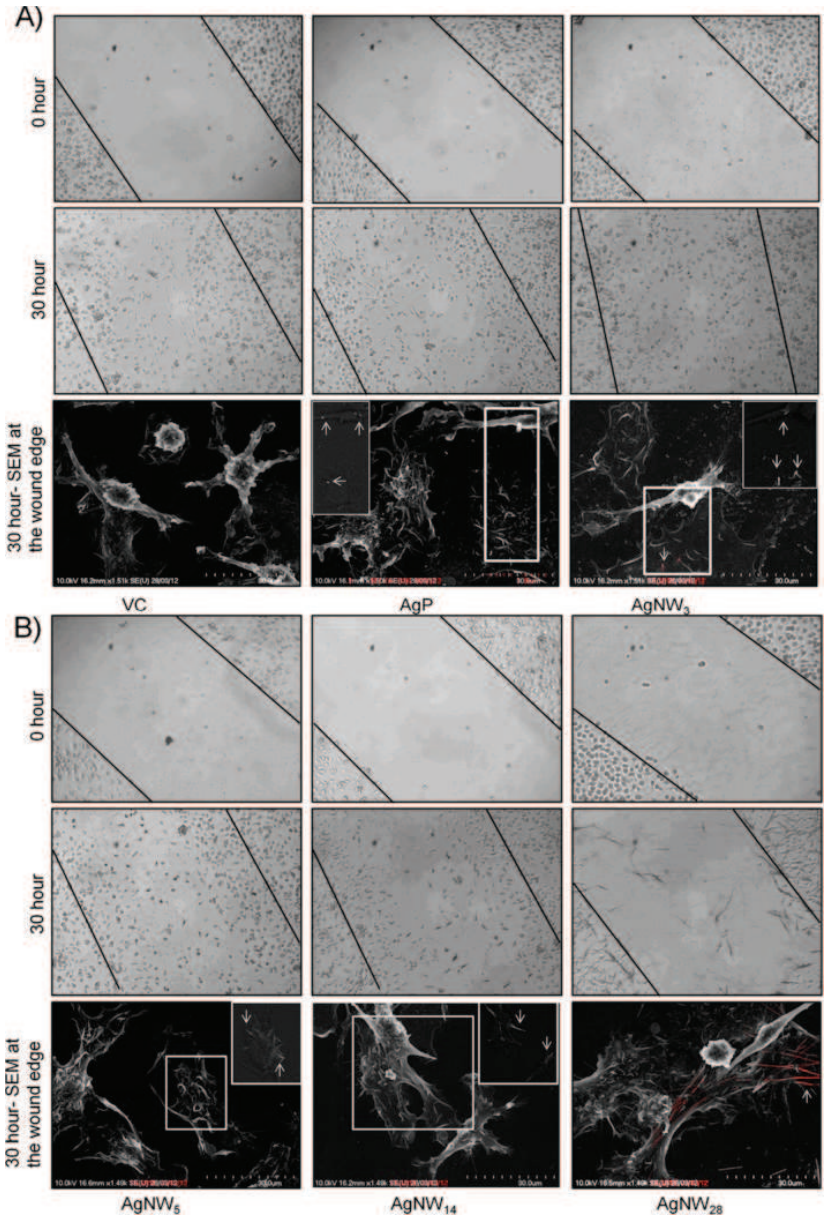

Figure 5 Fibre-length dependent impaired migration of BMMs in a wound-healing assay. A,**B**) An artificial wound was created in the BMM monolayer using a pipette tip and the migration of BMMs into the wound was assessed after treatment with VC, AgP, $AgNW_3$, $AgNW_5$, $AgNW_{14}$, $AgNW_{28}$. The dose was adjusted to fibre number and based on 2.5 μg/cm^2 for $AgNW_{14}$. Photographs were taken immediately and at 30 hour after creating the wound. For BSE images were taken at the edge of the wound. No impairment of cell adhesion and spreading could be observed and in fact increased cell spreading due to uptake of longer fibres was observed. Nanoparticles and fibres could be visualised underneath the cell membrane as indicated by the white arrow in the inserts which are the non-overlayed BSE images. Representative images are shown; similar results are obtained in 3 independent experiments.

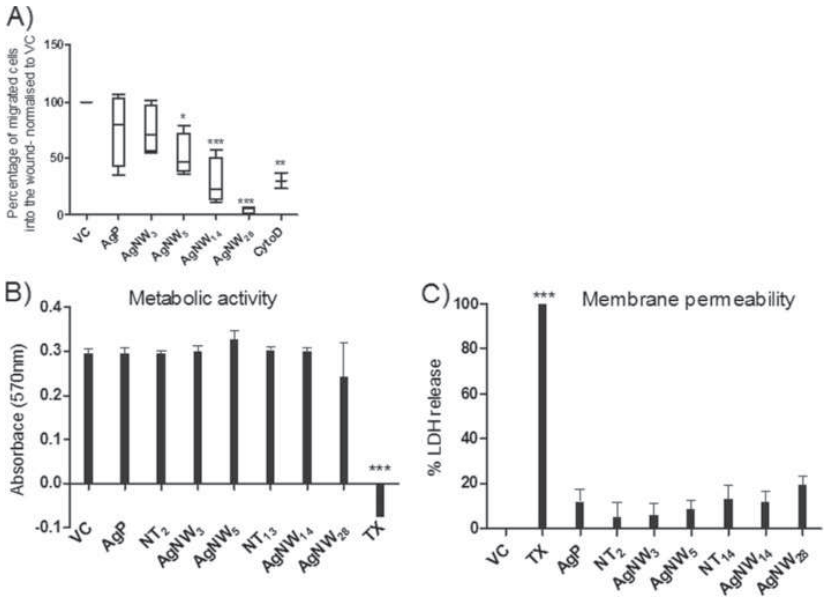

Figure 6 Inhibition of BMMs migration in a wound-healing assay and cell viability. A) The number of cell migrated was counted and expressed as percentage of cells migrated into the wound normalised to VC. Significant reduction of migration was seen with $AgNW_5$, $AgNW_{14}$, $AgNW_{28}$ and cytochalasin D, a positive control for actin cytoskeleton disruption. **B**) Metabolic activity of BMMs was assessed via the reduction of AlamarBlue® at an absorbance of 570 nm. At the dose used no significant reduction in metabolic activity was measured. **C**) The integrity of the cell membrane after the different treatments was measured via the release of LDH into the cell supernatant and compared to VC and TX, positive control. A sub-lethal dose was chosen at which none of the treatments lead to a significant increase in cell permeability. Significance indicated compares treatment groups to vehicle control, * indicates $p < 0.05$, ** indicates $p < 0.001$, *** indicates $p < 0.0001$ ($n = 3$). Data represent mean ± SEM of $n = 3$.

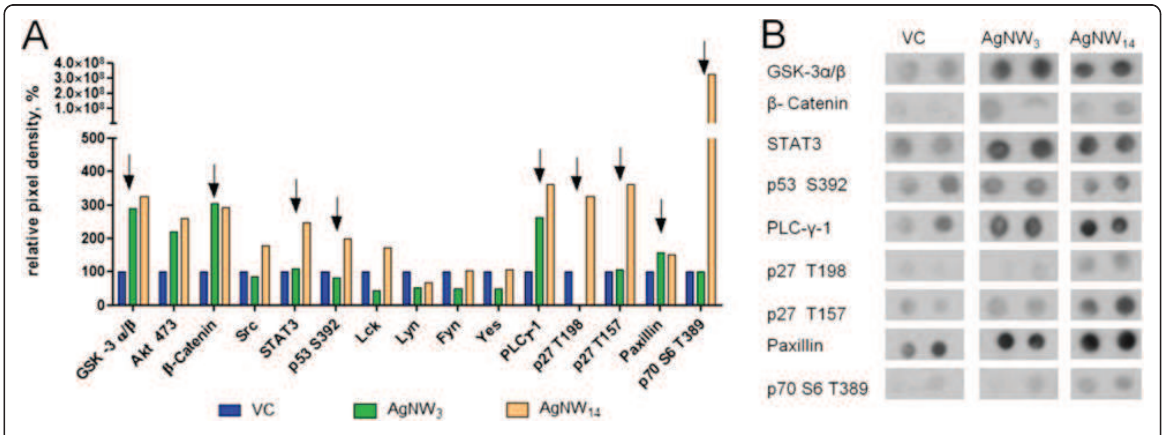

Figure 7 Phosphoproteomic analysis of BMMs exposed to AgNW. A) A phospho- kinase array (R&D) was performed to screen the phosphorylation state of 46 kinases in BMMs after treatments with $AgNW_3$ and $AgNW_{14}$ whereby 15 kinases showed an increase in phosphorylation relative to VC. **B**) Immunoplot analysis extract of kinases involved in cell migration/mobility and adhesion. Results are based on an initial screening ($n = 1$).

Screening for kinase phosphorylation in BMMs after AgNW treatment

The phospho- kinase array showed that kinases including GSK-3 α/β, Akt (S473), β-catenin and PLC-γ were activated on treatment with both the $AgNW_3$ and the $AgNW_{14}$ which can be explained via a general activation due to phagocytosis of particles (Figure 7A, B). Kinases including STAT3, p53 (S392), p27 (T198), p27 (T157) and p70 S6 (T389) were more activated in $AgNW_{14}$ compared to $AgNW_3$ which correlate with the loss of locomotion (Figure 7A, B). Interestingly, the highest level of activation of the cytoplasmic tyrosine kinase Src family members including Src, Lck, Hck and Frg was detected in the $AgNW_{14}$-treated BMM (Figure 7A, Additional file 1: Table S1). A summary of the relative pixel intensities of all kinases can be found in the Additional file 1: Table S1, Figure S3.

Discussion

The aim of this study was to investigate length-dependent effects of AgNW in the lungs. To assess the role of fibre length in the initiation of inflammation the BAL profile was assessed after aspiration exposure. To assess the effect of length on macrophage clearance and retention of the long fibre dose we used an *in vitro* wound-healing assay. The latter study aimed to shed light onto the effects of fibre length on clearance of fibre-laden alveolar macrophages via migration from the alveolar region of the lung to the mucociliary escalator.

Fibre dimension is a critical factor for lung diseases after inhalation exposure of various forms of fibrous materials as demonstrated in a number of experimental studies, with long fibres being more pathogenic than short ones [7,8,13,14]. We recently reported a length threshold of 5 μm for inflammation in the pleural cavity using the same range of tightly length –defined silver nanowires used here [9].

Long term inhalation studies in rat have been performed with amosite asbestos preparations of short (1% > 5 μm), medium (UICC reference fibre) and long (30% > 5 μm, 11% > 10 μm). These studies showed that the short fibres and the slightly longer UICC sample were low in pathogenicity whilst the long fibres induced extensive fibrosis and pulmonary adenomas. This was in contrast to the studies performed using direct injection of the same samples of amosite asbestos into the peritoneal cavity which showed that UICC amosite was sufficiently long to cause mesothelioma in rats at the same frequency as long amosite fibres [8]. This supports findings of the present study, that the length threshold for fibre effects in the lung is different to the length threshold for fibre effects at the mesothelial surface, the lung threshold being a higher value. More recent studies on adverse effects of nanofibres have shown a positive correlation between increasing fibre length and greater lung and pleural/peritoneal inflammation [4,15,16]. Poland *et al.* showed severe lung and peritoneal inflammation after aspiration exposure and direct intraperitoneal injection in mice of long (24 μm) nickel nanowire but only very mild diffuse alveolitis and mild peritoneal inflammation after exposure to short (4 μm) nickel nanowires [4]. Similar results were obtained from studies on short (<1 μm) and long (>13 μm) carbon nanotubes where the resultant pathophysiological response was compared to short and long amosite asbestos fibres [15-17]. These studies have shown that carbon nanotubes (CNT) induce a length- dependent inflammation in the peritoneal and pleural space of mice [15-17].

We recently investigated the threshold length for pleural inflammation and reported that various forms of high aspect ratio nanomaterials including amosite asbestos fibres, carbon nanotubes, nickel nanowires and the silver nanowires used here, showed a clear length threshold of 5 μm for initiation of an inflammatory response in the pleural space after direct intrapleural injection [9]. The data clearly showed that fibres below 5 μm in length were non-inflammatory and that fibres 5 μm in length and longer caused extensive recruitment of inflammatory cells [9,18] to the pleural space.

The current study addressed the lack of knowledge regarding the threshold length for acute pulmonary inflammation after deposition in the airspaces of the lungs. The pulmonary response to AgNW reported here showed a threshold length for the significant recruitment of inflammatory cells of 14 μm compared to the 5 μm fibre threshold length for pleural inflammation [9,18]. The use of size categories means that the actual threshold could lie anywhere between 11- and 14 μm since the size category below, at which no inflammation was produced was 10 μm. Our finding of a longer threshold in the lungs is consistent with previous reports implicating longer fibres in the development of lung carcinoma compared to mesothelioma [8,9]. The different length thresholds for pulmonary versus pleural inflammation can be explained as a consequence of the different mechanisms of fibre clearance from the lung and the pleural/ space. Clearance of fibres from the pleural space is via lymphatic drainage to mediastinal lymph nodes through stomata, pores in the parietal pleura which are around 0.5–10 μm in diameter [9]. Therefore a size-restricted clearance occurs in the pleural space leading to a retention of fibres which cannot negotiate the stomata and subsequent recruitment of inflammatory cells [15]. The clearance mechanism in the lung relies on alveolar macrophage phagocytosis and migration to the foot of the mucociliary escalator and is discussed in more detail below.

While deposition of $AgNW_{14}$ in the airspaces lead to a significant increase in inflammatory cells in the broncho-alveolar lavage fluid (BAL), shorter fibres including SFA, $AgNW_3$, $AgNW_5$ and $AgNW_{10}$ only produced a mild, non significant, increase in the total granulocyte number. It was noticeable that the length-dependent response was not linear and showed a marked step-increase in the inflammation between 10 and 14 μm. Histological examination of lung sections showed no recruitment of inflammatory cells after exposure to SFA or $AgNW_3$. Minor aggregations of inflammatory cells around terminal bronchioles and in alveolar airspaces were observed with $AgNW_5$ and $AgNW_{10}$ but these were more extensive in the $AgNW_{14}$ and LFA samples showing early stages of granuloma development in the terminal airways/ proximal alveolar region. The histological response to LFA was strongest showing extensive aggregates of inflammatory cells. However, the BAL fluid from LFA-exposed mice, whilst showing an increase in the mean number of granulocyte that was almost 4 times the mean number in the mice exposed to SFA did not attain significance. Additionally, lavage from lungs exposed to LFA resulted in a smaller number of BAL granulocytes than $AgNW_{14}$ and this contrasted with the histology data that showed more lung inflammation with LFA than $AgNW_{14}$. The low PMN in the lavage from LFA-exposed lungs was possibly due to a poor return from the inflammation-congested areas of the lungs. The final scoring of LFA equal to $AgNW_{14}$ for BAL granulocytes (Table 2) therefore took into account both the histological and lavage data to provide the best assessment of their relative inflammogenicity. The lack of an inflammatory response with shorter AgNW, which can be considered to be equivalent to silver particles, is consistent with experimental studies demonstrating the minimal lung toxicity or inflammogenicity of nanosilver in a subacute murine and 28-day rat inhalation model [19,20]. The role of silver ion release and its impact on silver nanoparticle toxicity is a controversial topic and experimental situations where soluble silver has been shown to play a role is mainly based on extremely high doses [21]. There is no reason to believe that silver ions played any role here as discussed extensively in our recent paper using the same panel [9] due to the low toxicity of silver nanoparticles and their proclivity to form silver chloride in biological systems. The study presented here focuses on short-time response due to the fact that the AgNW used in this study appear not to be biopersistent beyond a few days [9]. It is highly likely that the same length dependent effects would be shown by wholly biopersistent fibres and that the inflammation would be chronic. However, the determination of the threshold length for long term chronic inhalation studies is of utmost importance and biopersistence remains a key factor in the pathogenicity of long nanofibres.

The clearance efficiency of deposited fibres from the lower respiratory tract plays a major role in the development of pulmonary diseases since the retained dose, which is the dose accumulated in the alveolar region of the lungs after clearance mechanism accounts for the chronic pathogenic effects of inhaled fibres [22].

Fibres deposited in the conducting airways are cleared rapidly via cilia in the mucociliary escalator and subsequently swallowed or expectorated. If fibres reach the respiratory bronchioles, alveolar ducts or alveolar sacs they are cleared slowly via alveolar macrophages (AM) phagocytosing the deposited fibres and transporting them upwards to the ciliated airways for mucociliary clearance. It has been noted in many studies that there is selective retention of long biopersistent fibres of various sorts from the slow-clearing compartment with more effective clearance of the shorter fibres [11,23].

The mechanism by which fibre-laden alveolar macrophages are drawn to the terminal bronchioles at the foot

Table 2 Summary of the length-dependent effects of fibres in the lungs

		Endpoint				
		BAL Granulocytes*	Lung Histology**	Frustrated phagocytosis***	Impaired migration****	Δ kinase phosphorylation*****
Treatment	**Control**	+	-	No	-	NA
	SFA	+	-	No	NA	NA
	LFA	+++	++++	Yes	NA	NA
	$AgNW_3$	+	-	No	-	+
	$AgNW_5$	++	+	No	+	+
	$AgNW_{10}$	++	+	No	++	NA
	$AgNW_{14}$	+++	+++	Yes	+++	++

* BAL granulocytes: <0.5 million (+); 0.5-1.0 million (++); 1–2 million (+++).
** Lung histology subjectively scored on the basis of the severity of lung inflammation (see results).
*** Frustrated phagocytosis on the basis of evaluation of cytospins for presence of frustrated phagocytosis.
**** Impaired migration on the basis of degree of significant impairment compared to control (see Figure 6A).
***** Δ kinase phosphorylation based on subjective examination the levels of phosphorylation of the treated compared to the control levels of phosphorylation (see Figure 7). *NA* = not applicable.

of the ciliated airways is obscure. Possible explanations include the passive transport with alveolar fluid or amoeboid movement of AM either by random migration or directed migration along a chemotactic gradient [24]. Other pathways of clearance, usually only important during high dust exposure or disease are intra- and transcellular pathways by which fibres can reach lung interstitium and lymph nodes from where they subsequently may reach the blood stream [22,25,26]. A recent study investigated the effects of MWCNT on cell migration and adhesion of human dermal fibroblasts and murine fibroblasts, reporting a significant decrease in cell adhesion which was confirmed by the decrease of mRNA levels of important cell adhesion proteins FAK, fibronectin and laminin [27]. In addition fibroblast migration in a wound- healing assay was greatly impaired by MWCNT treatment and was accompanied by cytoskeletal derangement [27], although it should be noted that the dose of MWCNT used in this study was cytotoxic to human fibroblast which could influence the adherence and migration properties of the cells.

We set out to investigate whether fibre length has an effect on the migration behaviour of BMMs *in vitro* after fibre exposure using a wound-healing assay, a surrogate for *in vivo* clearance of fibrous material to the mucociliary escalator by AM migration. We used a very low dose to study effects on BMM migration, based on 2.5 $\mu g/cm^2$ for $AgNW_{14}$ and all the other length classes were adjusted to provide the same fibre number. The dose used had no significant effect on cell metabolism or cell viability for any of the length classes, ensuring that the observed effects were not due to simply impaired cell viability. A clear length-dependent trend for inhibition of BMM cell migration was measured at fibre lengths of 5, 14 and 28 μm and at 28 μm there was more-or less complete inhibition of motility. Presumably as a consequence of cell surface extension of AM during engulfment of long fibres, increased cell spreading was observed and correlated with increased inhibition of migration. The BMMs in this study had an average diameter of 13 μm [28] whilst human alveolar macrophages have an average diameter of 21 μm [29]. Due to this difference the threshold length for clearance of fibres by alveolar macrophages in humans may be slightly higher.

An initial screening of 46 kinase phosphorylation sites was performed to get a snapshot of the kinase activation status of fibre- treated BMMs. We hypothesised that this might reveal whether there was any fundamental change in the activation/metabolic state of the cells when they were impaired in their ability to migrate by phagocytosing long fibres. The 3 μm long exposed cells act as a control for normal phagocytosis and when compared to the untreated kinase profile this showed most of the kinases (~32) remained unchanged. The kinases GSK-3 α/β, Akt 473, β-catenin and PLC-γ showed activation in all treatment groups suggesting a link to normal phagocytosis. Comparing the kinase phosphorylation profile of BMM exposed to 3 μm with those exposed to 14 μm should reveal differences associated with the long fibre-dependent loss of motility and 5 kinases out of 46 (STAT3, p53 (S392), p27 (T198), p27 (T157) and p70 S6 (T389)) exhibited increased phosporylation with $AgNW_{14}$ compared to $AgNW_3$. Tyrosine kinases of the Src family were noticeably induced by treatment with long fibres. These kinases have been implicated in intracellular signalling in macrophages influencing the amplitude of many pathways [30]. One of the Src downstream effectors is STAT3, a major modulator of inflammation, which is required for activation of macrophages [31]. A marked Induction of STAT3 following the $AgNW_{14}$ treatment is a likely result of Src activation. It's worth mentioning that a constitutive activation of STAT3 is a common feature in many solid tumours [32], therefore persisting activation of STAT3 in a chronic inflammation caused by long fibres may contribute to pro-oncogenic changes. Macrophage motility is known to be negatively regulated by p53 [33] and the latter was induced in BMM treated with longer fibres, and might have contributed to impairment of their migration. The role of p27 in regulation of cellular migration remains unclear, however, our finding would support the reports showing suppression of migration by induction of p27 [34]. No kinases were down-regulated in the long fibre treated BMM compared to the controls confirming that there was no generalised loss of viability associated with failure to migrate. It is reported in the literature that a number of different kinase pathways are involved in the migration and adhesion processes among these are kinases that showed an increase in their phosphorylation state after long fibre treatment [35-41]. The results from the screening of the phosphorylation sites was mainly performed to see if crucial cellular signalling processes are impaired by the treatment of AgNW which might indicate that decreased cellular function, apoptosis/necrosis underlay the decrease in cell mobility. Our results showed that the long-fibre treatment did not negatively affect the cellular function of the BMMs as assessed by metabolic function, loss of membrane integrity or kinase profile. In fact long fibre treatment and inhibition of motility were associated with increased phosphorylation of some kinases involved in migration and adhesion. Clearly the interplay between adhesion and motility is complex since focal adhesion is required for motility and a more sophisticated analysis of mechanism underlying loss of motility with long fiber treatment is required but is outwith the scope of the present paper. The results give an indication that cellular processes are intact in long fiber treated BMM and therefore that inhibition of locomotion

can be best explained via a mechanical obstruction to motility. By this we suggest that the presence of long fibres inside the cells physically interferes with the necessary rearrangement of the cytoskeleton, membrane and other structures that are necessary for locomotion. This however has to be confirmed by an in depth investigation of the molecular mechanism involved in inhibition of migration which is beyond the scope of the present manuscript.

Conclusion

In conclusion we have shown that there are length-dependent effects on the lung and on BMM summarised in Table 2. These show length-dependent increases in inflammation by BAL and severity of lung injury by histology in vivo and evidence of accompanying impairment of macrophage migration by BMM in vitro; frustrated phagocytosis was only evident at the longest fibre lengths indicating that complete uptake of longer fibres still causes cell impairment, in the absence of classical frustrated phagocytosis as we previously reported [9,12]. A threshold length for acute pulmonary inflammation after pharyngeal aspiration of AgNW was evident between 10 and 14 μm in length. This compares with our previous studies on the threshold length for pleural inflammation of 5 μm, determined using a panel that utilised the AgNW used here [9]. No previous study has used tight length- restricted fibre populations to demonstrate thresholds as shown here and in our previous study in the pleural space [9]. The present study showing that the threshold length for induction of pulmonary inflammation is longer than the threshold length for pleura inflammation is in accordance with extrapolations using asbestos fibres [8]. The difference in thresholds can be explained by the differences in clearance mechanism between the lung the pleural space. In the pleural space clearance is through stomata [6] whilst clearance of deposited fibres from beyond the ciliated airways is via uptake by AM and subsequent migration to the mucociliary escalator. Using an *in vitro* wound healing assay we showed that fibre length-dependent macrophage mobility, with a threshold for impairment at a length of 5 μm and increasing impairment with increasing length, until at 28 μm there was almost complete inhibition of motility. An explanation for the decrease in locomotion could be mechanical obstruction caused simply by the bulky long fibres interfering with the movement process since there was no loss of viability or respiration in the long fibre-treated cells and an initial screen of a number of 46 kinases showed no decrease kinase phosphorylations. We note however that this is a small-scale aspiration study with acute inflammation and short term inhibition of migration *in vitro* as the endpoints. Our results need to be confirmed in long term inhalation studies using a range of different nanofibres at plausible exposure before we can confidently utilize these thresholds for risk assessment and in benign-by-design for nanofibres.

Methods

Particle panel

The panel of particles investigated here consisted of four silver nanowires (AgNW) samples (Figure 1), a silver nanoparticle control (AgP) and two amosite asbestos samples, long amosite asbestos (LFA) and short amosite asbestos (SFA) as previously described in Schinwald *et al.* [9]. AgP was purchased from Nanostructured & Amorphous Materials, Inc. with a diameter of 35 nm, a purity of 99,5% and a specific surface area of 30–50 m^2/g. The AgNW samples were kindly provided by Seashell Technology, San Diego (www.seashelltech.com). The polyol process was used for the synthesis of the AgNW which is described in patent number 7,922,787 B2. Detailed description of particle panel characteristics including concentration of soluble metal and dissolution can be found in Schinwald *et al.* [9]. AgNW synthesis and reaction conditions to obtain different lengths did not affect the chemical composition of the different nanowires and no coating of the nanowires was performed. The panel was dispersed in isopropanol and diluted to a working concentration of 1 mg/ml in 0.5% bovine serum albumin (BSA; Sigma-Aldrich, Poole, UK)/saline. For light microscope images the AgNW (1 mg/ml) were were mixed with 10 μl of glycerol (Sigma-Aldrich, Poole, UK) to reduce the flow of AgNW. The suspension was placed on glass slide and covered with a glass coverslip and sealed [15]. Images were captured at x40 magnification using QCapture Pro software (Media Cybernetics). As a control panel mixed length amosite asbestos enriched for long fibres (100% fibres ≥5 μm, 50.3% fibres >15 μm, 35.2% fibres >20 μm), hereafter referred to as long fibre asbestos (LFA), and shortened amosite asbestos (SFA; 3.1% fibres ≥5 μm, mean length 1 μm, mean diameter 300 nm) [42] were used.

In vivo

Experimental animals

Nine week old female C57BL/6 strain mice (Harlan, UK) were used in this study. Mice were kept in a group size of five in standard caging with sawdust bedding within a pathogen-free Home Office approved facility. Mice were maintained on a normal 12 hour light and dark cycle. Prior to the treatment mice were kept for 7 days in the facility to acclimatise. The work was carried out by staff holding a valid UK Home Office personal licence under a Home Office approved project licence.

Pharyngeal aspiration and bronchoalveolar lavage

The dose of AgNW panel for pharyngeal aspiration was equalised to fibre number since fibre exposure is regulated on the basis of the fibre number and so relative potency needs to be determined on a per-fibre basis. To equalise for fibre number a dose of 50 μg/mouse for $AgNW_{14}$ was chosen as the standard *in vivo* dose based on previous measurement of membrane integrity and proliferation. Based on 50 μg/mouse for $AgNW_{14}$, concentrations for the other length classes AgNW panel were calculated assuming that fibres thickness was constant in the different length classes (Table 1). Particle panel was dispersed in 0.5% bovine serum albumin (BSA; Sigma-Aldrich, Poole, U.K.)/saline and briefly vortexed to assist dispersion. Vehicle control (VC) consisted of 0.5% BSA/saline.

Mice were anesthetized with isoflurane (2-chloro-2-(difluoromethoxy)-1,1,1 trifluoroethane) and the tongue was gently held in full extension while 50 μl of particle suspension was pipette onto the base of the tongue [43]. The tongue was held extended until at least two breaths were complete. To stimulate inhalation and to induce a gasp reflex the nasal cavities of the mice were covered. Mice were observed until full recovery.

Mice were sacrificed at 24 hour by terminal anaesthesia. 0.5 ml of pentobarbitone (200 mg/ml) (2, 2, 2-Tribromomethanol) was injected in the peritoneal cavity followed by exsanguinations via the abdominal aorta. The thoracic cavity was exposed and the trachea cannulated using a 23 gauge needle and legated. The lungs were lavaged three times with 800 μl of ice-cold sterile saline. The first lavage was retained separately for LDH and total protein measurements and the subsequent lavages were pooled.

Calculation for total fibre number: e.g. $AgNW_3$
Length of NW (average) [μm] =3.00
Diameter of NW [μm] =0.115
Density of NW [μg/ml] =1.05 x 10^{-7}

$$\text{Volume of NW [ml]} = 3 * \prod * \left(\frac{0.115}{2}\right)^2 = 0.03116 \times 10^{-14}$$

$$\text{Weight of NW [μg]} = 3.116 \times 10^{-14} \times 1.05 \times 10^{-7} = 3.272 \times 10^{-7}$$

Dose [μg] per mouse = 10.70

$$\text{Number of NW} = \frac{10.70}{3.272 \times 10^{-7}} = 32719592.52 \cong 32.71 \times 106 \text{ fibers}$$

Lung dissection

For histological examination of lung pathology no forgoing BAL was performed and n = 2 for each treatment was used. 10% formalin was instilled into the lungs to fix the lung tissue and removed 'en block' with the heart. The lung and heart were kept for 4 hours in fixative prior to processing. The heart was removed and the lung was dissected into individual lobes and placed flat in a tissue cassette. The tissue was dehydrated through graded alcohol (ethanol) and embedded in paraffin. 4 μm sections were cut from the block covering all lobes of the lung and stained with H&E to show gross pathology.

Differential cell count/ total protein and lactate dehydrogenase measurement

The cellular fraction was separated from the supernatant of lavage fluid from BAL by centrifugation for 5 minutes at 2000 g at 4°C in a Mistral 3000i centrifuge (Thermo Fisher Scientific, Inc., MA, USA). Total cell count was performed using a NucleoCounter (ChemoMetec, 7 A/S, Allerød, Denmark) and cyto-centrifugation with following Diff-Quik staining using Diff-Quik stainset (Dade Behring Gmbh, Marburg, Germany) were prepared for differential cell counts.

In the supernatant, membrane integrity using the Cytotoxicity Detection Lactate Dehydrogenase kit (Roche 25 Diagnostics Ltd., Burgess Hill, UK) and protein content using the bicinchoninic acid (BCA) protein assay (Sigma-Aldrich, Poole, UK) were measured following the manufacturer's instructions.

In vitro

Generation of bone marrow derived macrophages

Bone marrow-derived macrophages (BMMs) were generated from 8 week old wild-type C57/Bl6 mouse femurs and tibias. In brief, the bone marrow was flushed with PBS using a 24 gauge needle, resuspended, passed through a cell strainer and centrifuged at 15000 rpm for 3 min. Cells were resuspended in red blood cell lysis buffer Hybrid Max™ (Sigma- Aldrich, UK) for 5 min at room temperature. Cells were centrifuged, resuspended in DMEM (Dulbecco's Modified Eagle Medium, Life Technologies) containing 10% FCS, 1% penicillin/ streptomycin and 20% L929 cell media and plated in a 10-cm^2 non tissue coated dish and cultured for 7 days.

Wound healing assay

After 7 day differentiation BMMs were seeded in 24 well plates at a density of 0.5x10^6/ml in DMEM containing 10% FCS, 1% penicillin/ streptomycin and 20% L929 cell media and culture for 2 days as a confluent monolayer. The medium was replaced with DMEM containing 0% FCS and 1% penicillin/ streptomycin. Cells were treated with AgNW equalised to fibre number. To equalise for fibre number a dose of 2.5 μg/cm^2 for $AgNW_{14}$ was chosen as the standard *in vitro* dose based on previous measurement of membrane integrity and proliferation.

Based on 2.5 μg/cm^2 for $AgNW_{14}$, concentrations for the other length classes AgNW panel were calculated assuming that fibres thickness was constant in the different length classes (Table 3). For the control particle, AgP, a dose of 0.5 μg/cm^2 was used, equal to the shortest fibre ($AgNW_3$). The panel was dispersed in 0.5% BSA/cell culture medium (DMEM, 0% FCS) and added to the cells. An artificial wound was created by scraping with a pipette tip and the number of cells migrating into the wound was monitored microscopically and photographs were taken immediately and after 30 hour. Images were acquired through a Zeiss Axiovert S100 microscope equipped with a 30x objective lens and were captured using RS Photometrics CoolSnap. The number of cells migrated into the wound was counted and expressed as percentage compared to vehicle control. Results are given as the mean ± SEM of 3 independent experiments.

Backscatter scanning electron microscopy

Backscatter scanning electron microscopy is based on elastic scattering of high energy electron further inside the sample. Elements with high atomic numbers (Z) such as silver give a stronger signal then lower Z elements. The signal is in general weak and can therefore only provide a contrast between regions with a larger difference in atomic number [12].

BMM cells were prepared as described above and seeded into 24 well plates on ThermanoxR Plastic Coverslips (NUNC™, Rochester, NY USA) at a density of 0.5*10^6/ml. The cells were treated for 30 hours using concentration as described above at 37°C in 5% CO2 atmosphere. After the treatment they were washed 5x with 0.1 M sodium cacodylate (pH 7.2) buffer. Cells were fixed overnight in 3% glutaraldehyde/ 0.1 M sodium cacodylate (pH 7.2) buffer and subsequently washed three times in sodium cacodylate buffer.

BSE of carbon-coated specimens was carried out using a Hitachi 4700 II field emission SEM (Hitachi High-Tech, Maidenhead, UK) at a beam accelerating voltage of 10 kV and a working distance of about 8 mm. Secondary electron (SE) and BSE images were taken simultaneously using an annular YAG crystal BSE detector and the upper SE detector to produce perfectly-synchronised image pairs. Both images were superimposed using Adobe Photoshop. The SE and BSE image were converted to grayscale, the BSE image was pasted into the SE image by using the layer function "lighten". This newly merged image and the SE image were converted to RGB mode, and overlayed by pasting the red channel of the BSE image into the red channel of the greyscale SE image, thus colour coding in red the strong BSE signal from the nanowires, the SE image appearing in grey.

Table 3 Calculation for the mass adjustments for equalisation of fibre number *in vitro*

Length class [μm]	Calculation to equalise for the same fibre number	Dose (μg/cm^2)	Total fibre number
3	3/14 × 2.5	0.5	1528953
5	5/14 × 2.5	0.9	1568374
14	standard	2.5	1638164
28	28/14 × 2.5	5	1638164

Measurement of membrane integrity and proliferation of BMMs

Supernatant of the wound healing assay was collected and analysed for membrane integrity using using the Cytotoxicity Detection Lactate Dehydrogenase kit (Roche Diagnostics Ltd., Burgess Hill, UK) following the manufacturer's instructions. TritonX (Sigma) was used as a positive control for cell death and was added at a final concentration of 0.1% for 30mins. The supernatant was centrifuged for 5 mins at 2000 rpm, transferred and centrifuged again for 5 mins at 13000 rpm. The conversion of lactate to pyruvate was detected using a microplate reader (BioTek® SynergyHT) to measure the optical density at 490 nm. Results are given as the mean ± SEM of 3 independent experiments.

Cells in the culture dish were used to measure their proliferation and metabolic activity via a chemical reduction of AlamarBlue® (Invitrogen). 150 μl of PBS and 15 μl of AlamarBlue® was added to each well and incubated for 3 hours at 37°C in 5% CO2 atmosphere. Absorbance was monitored at 570 nm and 600 nm as a reference wavelength. Data are normalized to 600 nm value. Results are given as the mean ± SEM of 3 independent experiments.

Proteome profiler array

BMMs were differentiated as described above and seeded at 0.5x10^6/ml in DMEM containing 10% FCS, 1% penicillin/ streptomycin and 20% L929 cell media and culture for 2 days as a confluent monolayer in a 60 mm tissue culture dish. The medium was replaced with DMEM containing 0% FCS and 1% penicillin/streptomycin and the particle panel was added at the concentrations described above and treated for 30 h. The cells were rinsed with cold phosphate-buffered saline (PBS) and immediately solubilised in lysis buffer by pippeting up and down and rocking the cell lysate at 4°C for 30 min. The lysate was centrifuged at 14,000 x g for 5 min, the supernatant was transferred into new test tubes and the protein concentration was measured using the bicinchoninic acid (BCA) protein assay (Sigma-Aldrich, Poole, UK) following the manufacturer's instructions. 500 μg of lysates were diluted and incubated with the Human-Phospho – MAPK Array Kit (Proteome Profiler™, R&D Systems) as per manufacturer's instructions. Plots were

developed on X-ray films following exposure to chemi-luminescent reagents.

Statistical analysis

All data are shown as the mean ± s.e.m. and these were analysed using one-way analysis of variance (ANOVA). Multiple comparison were analysed using Tukey-HSD method and in all cases, values of $P < 0.05$ were consider significant. (GraphPad InStat Software Inc., CA, USA).

Additional file

Additional file 1: Figure S1. 24 hour wound healing assay in BMMs. SEM images showing the closer of the wound after 24 hour at different treatments with AgNW. **Table S1:** Phosphoproteomic analysis of BMMs exposed to AgNW. A phospho- kinase array (R&D) was performed to screen the phosphorylation state of 46 kinases in BMMs after treatments with AgNW. Relative pixel density in % compared to VC is shown for all kinases measured (n=1). **Figure S2:** Phospho-kinase array immunoplots. A) VC, B) AgNW3, C)AgNW5, D) AgNW14.

Abbreviations

BSE: Backscatter scanning electron microscopy; BMM: Bone marrow derived macrophages; FPP: Fibre pathogenicity paradigm; LDH: Lactate deydrogenase; LFA: Long fibre amosite asbestos; SEM: Scanning electron microscopy; SFA: Short fibre amosite asbestos; AgNW: Silver nanowire; AgP: Silver nanoparticle; VC: Vehicle control.

Competing interests

The authors declare that they have no competing interests.

Authors' contributions

AS conceived and designed the experiments, analysed the data and wrote the manuscript. KD initiated the study, oversaw all experimental work and contributed to manuscript preparation. TC performed the proteome kinase array and contributed to the manuscript preparation. All authors read and approved the final manuscript.

Acknowledgements

We thank S. Mitchell (University of Edinburgh) for sample preparation for SEM and technical assistance. We also thank James R. Glass, Janet C. Dickerson and David A. Schultz from Seashell Technology for providing the AgNW samples. This research was funded by the Colt Foundation (A.S., K.D.) and MRC (T.C).

Author details

[1]MRC/University of Edinburgh, Centre for Inflammation Research, Queen's Medical Research Institute, 47 Little France Crescent, Edinburgh EH16 4TJ, UK. [2]MRC Toxicology Unit, Hodgkin Building, Lancaster Road, Leicester LE1 9HN, UK.

Received: 17 October 2012 Accepted: 26 November 2012
Published: 2 December 2012

References

1. Donaldson K: **The inhalation toxicology of p-aramid fibrils.** *Crit Rev Toxicol* 2009, **39:**487–500.
2. Mossman BT, Lippmann M, Hesterberg TW, Kelsey KT, Barchowsky A, Bonner JC: **Pulmonary endpoints (lung carcinomas and asbestosis) following inhalation exposure to asbestos.** *J Toxicol Environ Health B Crit Rev* 2011, **14:**76–121.
3. Oberdorster G: **Determinants of the pathogenicity of man-made vitreous fibers (MMVF).** *Int Arch Occup Environ Health* 2000, **73**(Suppl:S60-8):S60–S68.
4. Poland CA, Byrne F, Cho WS, Prina-Mello A, Murphy FA, Davies GL, *et al*: **Length-dependent pathogenic effects of nickel nanowires in the lungs and the peritoneal cavity.** *Nanotoxicology* 2011, **6:**899–911.
5. Mercer RR, Hubbs AF, Scabilloni JF, Wang L, Battelli LA, Friend S, *et al*: **Pulmonary fibrotic response to aspiration of multi-walled carbon nanotubes.** *Part Fibre Toxicol* 2011, **8:**21.
6. Donaldson K, Murphy FA, Duffin R, Poland CA: **Asbestos, carbon nanotubes and the pleural mesothelium: a review of the hypothesis regarding the role of long fibre retention in the parietal pleura, inflammation and mesothelioma.** *Part Fibre Toxicol* 2010, **7**(5):5.
7. Davis JM, Beckett ST, Bolton RE, Collings P, Middleton AP: **Mass and number of fibres in the pathogenesis of asbestos-related lung disease in rats.** *Br J Cancer* 1987, **37:**673–688.
8. Davis JM, Addison J, Bolton RE, Donaldson K, Jones AD, Smith T: **The pathogenicity of long versus short fibre samples of amosite asbestos administered to rats by inhalation and intraperitoneal injection.** *Br J Exp Pathol* 1986, **67:**415–430.
9. Schinwald A, Murphy FA, Prina-Mello A, Poland CA, Byrne F, Movia D, *et al*: **The threshold length for fiber-induced acute pleural inflammation: shedding light on the early events in asbestos-induced mesothelioma.** *Toxicol Sci* 2012, **128:**461–470.
10. Coin PG, Osornio-Vargas AR, Roggli VL, Brody AR: **Pulmonary fibrogenesis after three consecutive inhalation exposures to chrysotile asbestos.** *Am J Respir Crit Care Med* 1996, **154:**1511–1519.
11. Searl A, Buchanan D, Cullen RT, Jones AD, Miller BG, Soutar CA: **Biopersistence and durability of nine mineral fibre types in rat lungs over 12 months.** *Ann Occup Hyg* 1999, **43:**143–153.
12. Schinwald A, Donaldson K: **Use of back-scatter electron signals to visualise cell/nanowires interactions in vitro and in vivo; frustrated phagocytosis of long fibres in macrophages and compartmentalisation in mesothelial cells in vivo.** *Part Fibre Toxicol* 2012, **9:**34.
13. Stanton MF, Layard M, Tegeris A, Miller E, May M, Morgan E, *et al*: **Relation of particle dimension to carcinogenicity in amphibole asbestoses and other fibrous minerals.** *JNCI* 1981, **67:**965–975.
14. Vorwald AJ, Durkan TM, Pratt PC: **Experimental studies of asbestosis.** *AMA Arch Ind Hyg Occup Med* 1951, **3:**1–43.
15. Murphy FA, Poland CA, Duffin R, Al-Jamal KT, Ali-Boucetta H, Nunes A, *et al*: **Length-dependent retention of carbon nanotubes in the pleural space of mice initiates sustained inflammation and progressive fibrosis on the parietal pleura.** *Am J Pathol* 2011, **178:**2587–2600.
16. Murphy FA, Poland CA, Duffin R, Donaldson K: **Length-dependent pleural inflammation and parietal pleural responses after deposition of carbon nanotubes in the pulmonary airspaces of mice.** *Nanotoxicology* 2012, **6:**2587–2600.
17. Poland CA, Duffin R, Kinloch I, Maynard A, Wallace WA, Seaton A, *et al*: **Carbon nanotubes introduced into the abdominal cavity of mice show asbestos-like pathogenicity in a pilot study.** *Nat Nanotechnol* 2008, **3:**423–428.
18. Schinwald A, Murphy F, Prina-Mello A, Poland CA, Byrne F, Glass JR, *et al*: **The threshold length for fibre-induced acute pleural inflammation: shedding light on the early events in asbestos-induced mesothelioma.** *Toxicol Sci*, . in press.
19. Stebounova LV, mcakova-Dodd A, Kim JS, Park H, O'Shaughnessy PT, Grassian VH, *et al*: **Nanosilver induces minimal lung toxicity or inflammation in a subacute murine inhalation model.** *Part Fibre Toxicol* 2011, **8:**5.
20. Ji JH, Jung JH, Kim SS, Yoon JU, Park JD, Choi BS, *et al*: **Twenty-eight-day inhalation toxicity study of silver nanoparticles in Sprague–Dawley rats.** *Inhal Toxicol* 2007, **19:**857–871.
21. Johnston HJ, Hutchison G, Christensen FM, Peters S, Hankin S, Stone V: **A review of the in vivo and in vitro toxicity of silver and gold particulates: particle attributes and biological mechanisms responsible for the observed toxicity.** *Crit Rev Toxicol* 2010, **40:**328–346.
22. Oberdorster G: **Lung dosimetry: pulmonary clearance of inhaled particles.** *Aerosol Sci Tech* 1993, **18:**279–289.
23. Lippmann M: **Effects of fiber characteristics on lung deposition, retention, and disease.** *Environ Health Perspect* 1990, **88:**311–317.
24. Lehnert BE: **Pulmonary and thoracic macrophage subpopulations and clearance of particles from the lung.** *Environ Health Perspect* 1992, **97:**17–46.
25. Holt PF: **Translocation of inhaled dust to the pleura.** *Environ Res* 1983, **31:**212–220.
26. Miserocchi G, Sancini G, Mantegazza F, Chiappino G: **Translocation pathways for inhaled asbestos fibers.** *Environ Health* 2008, **7:**4.

27. Zhang Y, Wang B, Meng X, Sun G, Gao C: **Influences of acid-treated multiwalled carbon nanotubes on fibroblasts: proliferation, adhesion, migration, and wound healing.** *Ann Biomed Eng* 2011, **39:**414–426.
28. Cannon GJ, Swanson JA: **The macrophage capacity for phagocytosis.** *J Cell Sci* 1992, **101:**907–913.
29. Krombach F, Munzing S, Allmeling AM, Gerlach JT, Behr J, Dorger M: **Cell size of alveolar macrophages: an interspecies comparison.** *Environ Health Perspect* 1997, **105:**1261–1263.
30. Abram CL, Lowell CA: **The diverse functions of Src family kinases in macrophages.** *Front Biosci* 2008, **13:**4426–4450.
31. Lin T, Bost KL: **STAT3 activation in macrophages following infection with Salmonella.** *Biochem Biophys Res Commun* 2004, **321:**828–834.
32. Looyenga BD, Hutchings D, Cherni I, Kingsley C, Weiss GJ, MacKeigan JP: **STAT3 Is Activated by JAK2 Independent of Key Oncogenic Driver Mutations in Non-Small Cell Lung Carcinoma.** *PLoS One* 2012, **7**.
33. Sablina AA, Chumakov PM, Kopnin BP: **Tumor suppressor p53 and its homologue p73 alpha affect cell migration.** *J Biol Chem* 2003, **278:**27362–27371.
34. Berton S, Belletti B, Wolf K, Canzonieri V, Lovat F, Vecchione A, *et al:* **The tumor suppressor functions of p27(kip1) include control of the mesenchymal/amoeboid transition.** *Mol Cell Biol* 2009, **29:**5031–5045.
35. Kobayashi T, Hino S, Oue N, Asahara T, Zollo M, Yasui W, *et al*: **Glycogen synthase kinase 3 and h-prune regulate cell migration by modulating focal adhesions.** *Mol Cell Biol* 2006, **26:**898–911.
36. Ip CK, Wong AS: **p70 S6 kinase and actin dynamics: a perspective.** *Spermatogenesis* 2012, **2:**44–52.
37. Roger L, Gadea G, Roux P: **Control of cell migration: a tumour suppressor function for p53?** *Biol Cell* 2006, **98:**141–152.
38. Huang C, Rajfur Z, Borchers C, Schaller MD, Jacobson K: **JNK phosphorylates paxillin and regulates cell migration.** *Nature* 2003, **424:**219–223.
39. Lee MH, Koria P, Qu J, Andreadis ST: **JNK phosphorylates beta-catenin and regulates adherens junctions.** *FASEB J* 2009, **23:**3874–3883.
40. Yoon JH, Kim HE, Choi JY, Bae HJ, Lee SG: **Caffeoylserotonin suppresses THP-1 monocyte adhesion and migration via inhibition of the integrin beta1/FAK/Akt signalling pathway.** *Fitoterapia* 2012.
41. Baruzzi A, Caveggion E, Berton G: **Regulation of phagocyte migration and recruitment by Src-family kinases.** *Cell Mol Life Sci* 2008, **65:**2175–2190.
42. Donaldson K, Brown GM, Brown DM, Bolton RE, Davis JG: **Inflammation generating potential of long and short fiber amosite asbestos samples.** *Br J Ind Med British* 1989, **46:**271–276.
43. Rao GV, Tinkle S, Weissman DN, Antonini JM, Kashon ML, Salmen R, *et al*: **Efficacy of a technique for exposing the mouse lung to particles aspirated from the pharynx.** *J Toxicol Environ Health A* 2003, **66:**1441–1452.

doi:10.1186/1743-8977-9-47
Cite this article as: Schinwald *et al.*: Use of silver nanowires to determine thresholds for fibre length-dependent pulmonary inflammation and inhibition of macrophage migration *in vitro*. *Particle and Fibre Toxicology* 2012 **9**:47.

Use of silver nanowires to determine thresholds for fibre length-dependent pulmonary inflammation and inhibition of macrophage migration *in vitro*

Supplementary Material:

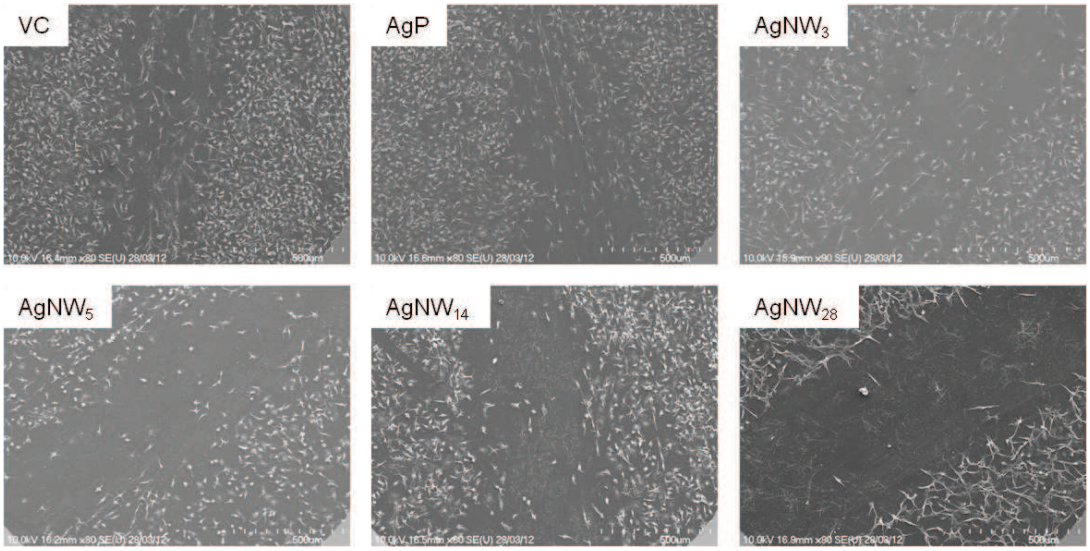

Figure S1: 24 hour wound healing assay in BMMs. SEM images showing the closer of the wound after 24 hour at different treatments with AgNW.

Table S1: Phosphoproteomic analysis of BMMs exposed to AgNW. A phospho- kinase array (R&D) was performed to screen the phosphorylation state of 46 kinases in BMMs after treatments with AgNW. Relative pixel density in % compared to VC is shown for all kinases measured (n=1).

	VC	$AgNW_3$	$AgNW_5$	$AgNW_{14}$
p38 a	100	74.85336	159.0873	121.9645
ERK 1/2	100	93.41407	86.15658	74.33238
JNK pan	100	107.5308	82.98289	86.15175
GSK -3 a/b	100	288.9975	256.3521	327.8246
MEK1/2	100	115.8622	97.57284	129.8732
MSK 1/2	100	77.76693	96.80675	79.47691
Akt 473	100	221.5099	137.8032	261.4832
mTOR	100	94.12129	92.45151	138.5429
CREB	100	52.63563	29.98924	78.0085
HPS27	100	128.6365	131.5996	141.1714
AMPK a2	100	175.9596	105.3152	140.0264
β-Catenin	100	306.2233	249.1231	293.5133
Chk-2	100	54.88571	97.62734	103.0031
Src	100	86.62845	87.61551	178.408
Lyn	100	52.63225	45.04333	67.13648
Lck	100	43.72153	32.89619	171.7983
Fyn	100	51.26141	57.08296	104.4002
Yes	100	50.55822	72.43423	108.4889
Frg	100	69.26241	111.4022	132.6036
Hck	100	100.0667	132.3898	162.4953
FAK	100	96.46324	132.2894	126.2003
STAT2	100	126.9072	97.20593	120.5616
STAT3	100	109.6658	101.5223	247.599
STAT 5a	100	115.5917	122.0649	135.4271
STAT5 b	100	93.40943	90.0274	117.703
STAT5 A/B	100	121.4369	116.3074	154.2314
STAT7	100	110.9859	93.45342	112.7044
p53 S392	100	83.20326	356.6267	198.7431
p53 S 46	100	105.0083	189.0473	147.1997
p53 S15	100	38.12322	190.13	152.7404
Akt 308	100	131.3407	172.3985	161.1092
p70 S6 T421/S424	100	134.2128	104.9497	134.3285
p70S6 T229	100	93.99121	142.352	136.8473
cJun	100	107.2125	141.3437	160.8311
PLC-γ1	100	263.5613	266.5383	363.6785
Pyk -2	100	126.6551	115.0751	152.8664
p27 T198	100	0.000239	459.7914	326.2103
p27 T157	100	107.9484	480.6506	363.2138
paxillin	100	159.0782	250.3517	152.2328
RSK1/2/3	100	87.01548	99.49556	89.35632
RSK1/2 S221 S227	100	78.24321	111.3611	104.9323
STAT1	100	123.3307	100.8336	170.8514
STAT4	100	85.94709	101.5377	160.658
eNOS S1177	100	156.1881	173.3605	94.30464
p70 S6 kinase T389	100	100	74681710	3.26E+08

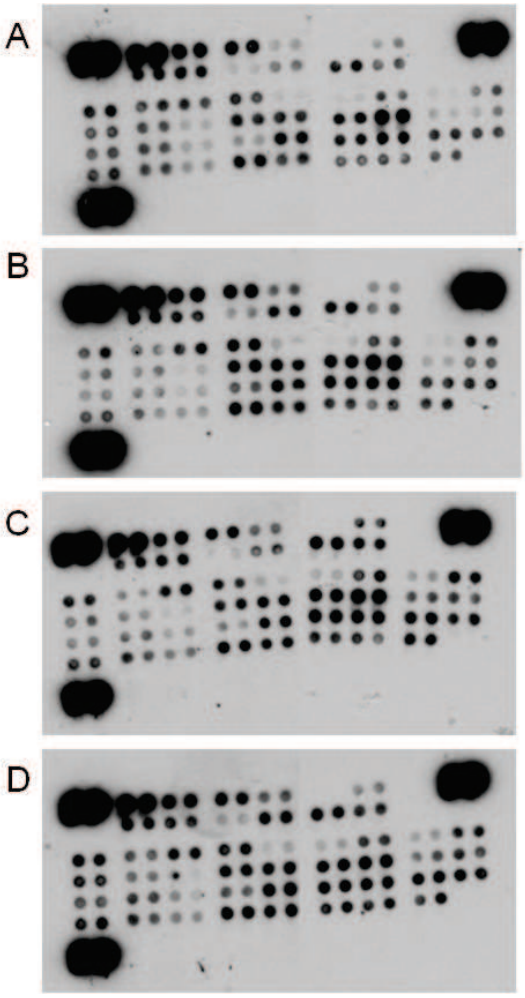

Figure S2: Phospho-kinase array immunoplots. A) VC, B) $AgNW_3$, C)$AgNW_5$, D) $AgNW_{14}$.

Research article under revision:

Schinwald A, Donaldson K, Campbell C. **Minimal oxidation of pristine graphene and loss of inflammogenicity with residence in the lung**. Submitted to Nanotoxicology.

Minimal Oxidation and Inflammogenicity of Pristine Graphene with Residence in the Lung

Anja Schinwald[1], Fiona Murphy[2], Alexandros Askounis[3], Vasileios Koutsos[3], Khellil Sefiane[3], Ken Donaldson [1], Colin J. Campbell[4*]

[1]MRC/University of Edinburgh, Centre for Inflammation Research, Queen's Medical Research Institute, 47 Little France Crescent, Edinburgh EH16 4TJ, UK

[2]MRC Toxicology Unit, Hodgkin Building, PO Box 138, University of Leicester, Lancaster Road, Leicester, LE1 9HN, UK

[3]Institute for Materials and Processes, School of Engineering, The University of Edinburgh, King's Buildings, Mayfield Road, Edinburgh, EH9 3JL, United Kingdom.

[4]EaStCHEM, School of Chemistry, University of Edinburgh, Edinburgh, EH9 3JJ, UK

***Corresponding Author:**

EaStCHEM, School of Chemistry, University of Edinburgh, Edinburgh, EH9 3JJ, UK

Tel: +44-131-651-3049. Fax: +44-0131-650-6453. E-mail: colin.campbell@ed.ac.uk

Keywords: Pristine Graphene, Oxidation, Horseradish peroxidase, biodegradation, lung inflammogenicity.

Abstract

Two-dimensional graphitic carbon, graphene is a new form of nanomaterial with great potential in a wide variety of applications. It is therefore crucial to investigate the behavior of graphene in biological systems to assess potential adverse effects that might follow from inhalation exposure. In this study we focused on medium term effects of graphene in lung tissue by investigating the pulmonary inflammation 6 weeks after pharyngeal aspiration of unoxidised multi-layered graphene platelets (GP) in mice and assessed their biopersistence in the lung tissue using Raman spectroscopy. Additionally, GP degradation *in vitro* was examined after horseradish peroxidase (HRP) treatment up to 1 week. Building on our previous report showing acute inflammation in mice lungs at 1 day, pristine GP showed minimal inflammation in mouse lungs after 6 weeks even though no degradation of GP in lung tissue was observed and large deposits of GP were evident in the lungs. Raman analysis of GP in tissue sections showed minimal oxidation and *in vitro* examinations of enzymatic oxidation of GP via HRP and H_2O_2 showed only slight increases in I_D/I_G ratio and the appearance of the Raman D'-band at 1620 cm^{-1} (surrogates of graphene oxidation). Our results showing non-inflammogenicity at medium timepoints have important implications in the hazard identification of GPs following inhalation exposure and for their use in biomedical applications. Additionally, the biopersistence of pristine GP *in vivo* with no associated inflammation could open the way to applications in tissue engineering and drug delivery.

Introduction

Graphene is a two dimensional honeycomb lattice of carbon atoms which has been hailed as 'a rapidly rising star' and 'the mother of all graphitic forms'(Geim and Novoselov 2007). The physicochemical properties of graphene including its high elasticity, flexibility and adaptability make it a promising tool for a range of biomedical applications including drug delivery and tissue engineering as structural reinforcement of films, hydrogels and other scaffold materials (Sanchez et al. 2011). As tissue engineering material it is important to assess the extent to which graphene is stable *in vivo* and for safe handling and medical application of graphene it is crucial to assess its toxicological profile. Graphene is defined as a nanomaterial, and can be further classified as a high aspect ratio nanomaterial due to its width-to-diameter ratio which is higher than 10:1 (Hankin and Poland 2012). Recent *in vivo* studies on the toxicity of graphene and its derivatives, including graphene oxide (GO) have shown that pristine graphene nanoplatelets with a diameter of ≥5 μm lead to acute inflammation in the lung after aspiration exposure in mice due to its extended lateral dimensions (Schinwald *et al.* 2012a). In contrast, in the nanometer size range, pristine graphene produced minimal lung inflammation whilst GO caused severe and persistent lung injury (Duch *et al.* 2011). The resistance of carbon nanomaterials to biological degradation is a major concern for their potential *in vivo* toxicity but recent investigations have shown that carbon nanomaterials, including graphene oxide and oxidized carbon nanotubes, are degraded by oxidase enzymes including horseradish peroxidase and neutrophil myeloperoxidase (hMPO) *in vitro* and *in vivo* (Kagan *et al.* 2010; Kotchey *et al.* 2011; Shvedova *et al.* 2012) causing them to exhibit less inflammatory potential. Functional groups and structural defects introduced during oxidative processes have been shown to play a major role in acute lung toxicity and reduction of oxygenated carbon functionalities and annealing of defects have been shown to minimize the inflammatory potential (Duch *et al.* 2011; Fenoglio *et al.* 2008).

Our study aimed to investigate the medium term pulmonary effects of pristine GP after aspiration exposure in relation to *in vivo* oxidation and degradation of pristine GP in lung tissue. The correlation between the biological effect study and the investigation of the material oxidation *in vivo* is based on the

link between the decrease in biological effect with increased degradation of material due to oxidation. To aid in the interpretation of *in vivo* data, additional *in vitro* enzymatic degradation of pristine GP via horseradish peroxidase and chemical oxidation were also performed. The GP used in this study possess a high lateral dimension (≥5 μm) and are therefore classified under the term high aspect ratio nanomaterials (HARN). In a previous study we showed that the GP used in the present study were inflammogenic following short term *in vivo* exposure, due to their extended lateral dimension (Schinwald *et al.* 2012a). Furthermore, the translocation of deposited long asbestos fibres from the lung to the pleural space is a prerequisite for the development of fibre-related pleural diseases and there has been concern that HARN, including CNT and various forms of nanofibres, could have the potential to show asbestos-like pathogenicity in the pleural space due to their extended lateral dimensions (Murphy *et al.* 2011; Schinwald *et al.* 2012b) in addition to adverse health effects in the lung. It has been proven that CNT can translocate to the pleural space after aspiration exposure and subsequently induce a pleural inflammatory response (Murphy et al. 2012) however so far we do not know whether extended micrometer sized platelet shaped particles would be able to translocate to the pleural space after inhalation exposure. Therefore, the second aim of our study was to examine the translocation of GP to the pleural space up to 6 weeks post aspiration exposure in order to identify whether GP pose a similar risk as fibrous materials in inducing pleural diseases after inhalation exposure.

Materials and Methods

Characterization of Graphene PlateletsThe particles investigated in this study consisted of few-layered graphene platelets (GP) and nanoparticulate carbon black (CB) as previously described in Schinwald et al. (Schinwald *et al.* 2012a) (Table 1). CB (Printex 90) was purchased from Evonik Degussa GmbH, Germany and used as an amorphous carbon particle control with known toxicological profile. GP were

produced via chemical exfoliation and purchased from Cheaptubes.com. The size distribution of the GP ranged from 5 μm (57.4%) to 30 μm (0.3%) projected area diameter in vehicle solution with an aerodynamic diameter of 1.33 to 3.26 μm, respectively (Schinwald *et al.* 2012a). The aerodynamic diameter is based on a theoretic calculation of GP suspended in vehicle control using a projected area diameter. GP consisted of up to 10 sheets of graphene, and are therefore classified as few-layered GP. The thickness of the GP aggregates was measured by atomic force microscopy (AFM) and visulised by scanning electron microscopy (SEM) (details see below). Trace metal and endotoxin levels were previously tested and reported in (Schinwald *et al.* 2012a). CB and GP stock solution was prepared at 1 mg/mL in 0.5% BSA/saline for *in vivo* work and dispersed by sonication in an ultrasonicating water bath at 230 V, 50 Hz, 350W (FB11002, Fisherbrand, Thermo Fisher Scientific, Inc., MA, USA) for 6 h to break up aggregates. Detailed characterization can be found in Schinwald et al. (Schinwald *et al.* 2012a).

Scanning electron microscopy of CB and GP

GP were dispersed in 0.5% BSA (heat-shocked fractionate) (Sigma-Aldrich, Poole, UK)/saline at a concentration 50 μg/ml by ultrsonication. The suspension was filtered onto an Isopore™ membrane filter (Millipore), dried and gold sputter coated. Scanning electron microscopy was carried out using a Hitachi S-2600N digital scanning electron microscope (Oxford Instruments, Oxfordshire, UK).

Light microscopy of GP

For light microscopy images a concentration of 100 μg/ml was used to demonstrate the dispersion of the materials. 10 μl of GP solution were mixed with 10 μl of glycerol (Sigma-Aldrich, Poole, UK) to reduce the motion of GP. The suspension was placed on glass slide and covered with a glass coverslip and sealed. Images were captured at x100 magnification using QCapture Pro software (Media Cybernetics).

Atomic force microscopy (AFM) for thickness measurement of GP

GP samples were prepared at a concentration of 0.1 mg/ml (diluted) and 1mg/ml (concentrated) in 0.5 % BSA/saline solution and sonicated for 6 hours before use. Freshly cleaved mica (atomically flat) was used as a substrate. A thin film was formed on the substrate using spin coating at 4000 rpm, for 90 sec. Atomic force microscopy was carried out on a Bruker Multimode/ Nanoscope IIIa AFM (Bruker AXS, Santa Barbara, CA).The scanners used were a J-scanner (x-y scan range ca. 140 microns) and an E-scanner (x-y scan range ca. 14 microns). RTESP Bruker cantilevers were used in these measurements with nominal spring constant of 40 N/m, resonance frequency of 300 kHz and nominal tip radius of 8 nm, as specified by the manufacturer. The measurements were performed under tapping mode in air at room temperature. Acquired images were post-processed by simple flattening and analyzed using the software Scanning Probe Image Processor (SPIP, Image Metrology, Hørsholm, Denmark).

In vivo

Experimental animals

Nine week old female C57BL/6 strain mice (Harlan, UK) were used in this study. Mice were kept in a group size of five in standard caging with sawdust bedding within a pathogen-free Home Office approved facility. Mice were maintained on a normal 12 hour light and dark cycle. Prior to the treatment mice were kept for 7 days in the facility to acclimatise. The work was carried out by staff holding a valid UK Home Office personal licence under a Home Office approved project licence.

Pharyngeal aspiration, pleural and broncho-alveolar lavage

The given particle dose for pharyngeal aspiration was 50 µg per mouse of CB and GP in 0.5% BSA/ saline. The dose of 50 µg was selected to allow direct comparison to a previous study investigating the medium term effects of CNT aspiration. Vehicle control was 0.5% BSA/saline. Mice were anesthetized with isoflurane and the tongue was gently held in full extension while 50 µl of particle suspension was

pipette onto the base of the tongue (Rao *et al.* 2003) The tongue was held extended until at least two breaths were complete. To stimulate inhalation and to induce a gasp reflex the nasal cavities of the mice were covered. Mice were observed until full recovery.

Mice were sacrificed 24 hour (n=4), 1 week (n=4) and 6 weeks (n=7) post exposure by terminal anaesthesia by injection of a single dose of 0.5 ml of pentobarbitone (200 mg/ml) into the peritoneal cavity followed by exsanguinations via the abdominal aorta. The pleural space was lavaged with three 1 ml washes of sterile saline and kept on ice. After the pleural cavity was lavaged the thoracic cavity was exposed and the trachea cannulated using a 23 gauge needle and legated. The lungs were lavaged three times with 800 µl of ice-cold sterile saline. The first lavage was retained separately and the subsequent lavages were pooled.

Differential cell count/ total protein and lactate dehydrogenase measurement

To separate the cellular fraction from the supernatant the lavage fluid from BAL and pleural lavage was centrifuged for 5 minutes at 2000 g at 4°C in a Mistral 3000i centrifuge (Thermo Fisher Scientific, Inc., MA, USA). Total cell count was performed using a NucleoCounter (ChemoMetec, 7 A/S, Allerød, Denmark) and cyto-centrifugation with following Diff-Quik staining using Diff-Quik stainset (Dade Behring Gmbh, Marburg, Germany) were prepared for differential cell counts. In the supernatant, membrane integrity using the Cytotoxicity Detection Lactate Dehydrogenase kit (Roche Diagnostics Ltd., Burgess Hill, UK) and protein content using the bicinchoninic acid (BCA) protein assay (Sigma-Aldrich, Poole, UK) were measured following the manufacturer's instructions.

Dissection of lung, diaphragm and chestwall

For histological examination the lungs and heart were removed on-block and fixed by installation of 10% ice-cold formalin without foregoing lavage and submerged in fixative for a period of 4 hours prior to processing. The heart was removed and the lung separated into individual lobes and transferred to 70% ethanol for 24 hour. The tissue was embedded in paraffin, sectioned and stained with H&E to show gross

pathology and Pico-Sirius Red (PSR) to show collagen deposition. Images at 20x magnification were taken to show higher maginification areas of the lung sections.

The diaphragm and the lower right posterior portion of the chest wall, approximately an area of 1cm x 0.5 cm along the spine was cut out from the mice after lavage, washed in ice-cold saline and fixed for 4 hours in 30% formalin. The tissue was excised from the surrounding tissue and either embedded in paraffin, sectioned and stained with Haematoxylin & Eosin (H&E) for gross pathology or prepared for scanning electron microscopy (SEM).

Lung tissue for Raman Spectroscopy

Raman spectroscopy on lung tissue embedded in paraffin was used to measure oxidation of pristine GP *in vivo*. In addition to the lung samples collected in this study we used lung samples from a previous study to compare the oxidation state of GP in lung tissue after 24 hour, 1 week and 6 weeks aspiration exposure (Schinwald *et al.* 2012a). The procedure of the 24 hour and 1 week aspiration exposure was identical to the procedure used in this study; therefore direct comparison of the results can be performed.

Incubation of GP with Horseradish peroxidase and H_2O_2

The following protocol for HRP oxidation of GP was adapted from Kotchey et al.(Kotchey *et al.* 2011). Two milliliter of 0.125 wt% GP were dispersed in double distilled water and dispersed by sonication in an ultrasonicating water bath at 230 V, 50 Hz, 350W (FB11002, Fisherbrand, Thermo Fisher Scientific, Inc., MA, USA) for 2 h to break up aggregates. Lyophilized HRP type VI was solubilized in 1x phosphate buffered saline (PBS) (PAA, Austria) at 0.390 mg/ml and 4 ml were added to the GP dispersion and 3.5 ml of PBS for a total volume of 9.5 ml. H_2O_2 (Sigma Aldrich, Poole, UK) was added to give a final concentration of 40 μM. For the 24 hour incubation time H_2O_2 was added every hour for 12 hours, for 1

week incubation time H_2O_2 was added daily. Controls included GP incubation with HRP (- H_2O_2) (control I) and GP incubation with H_2O_2 (-HRP) (control II).

Plasma oxidation of GP was performed in a SPI Plasma Prep III plasma etcher, at 60W, for times between 5 mins and 60 mins (as indicated).

Raman Spectroscopy

Samples for *in vitro* oxidation of GP via HRP and H_2O_2 were prepared by adding 10 µl of GP at day 0, 1 and 7 on a quartz microscope slide and drying. For *ex-vivo* measurement lung tissue embedded in paraffin was used to record GP oxidation. Areas of GP deposited in lung tissue were identified by visual inspection. All spectra were collected on a Renishaw *inVia* Raman microscope using an excitation wavelength of 514 nm. Samples were scanned from 1000 to 2000 cm^{-1} to visualize D and G bands. Spectra were collected with a 120 s exposure; for *ex-vivo* measurements and pristine GP at 0h a total of 20 locations were selected per sample. For *in vitro* oxidation via HRP and plasma oxidation a total of 6 locations were selected per sample.

Statistical analysis

Graphs are shown as the mean ± s.e.m and these were analysed using one-way analysis of variance (ANOVA). P-values greater than 0.05 were not considered significant based on one- way ANOVA variation among column means and no post tests were calculated. Multiple comparisons were analysed using Tukey-HSD method (GraphPad InStat Software Inc., 629 CA, USA). Raman spectra are shown as mean and standard deviation (OriginLab 8.5 Software).

Results

Characterization of GP

Characteristics and specifications of GP are summarised in Table 1 (more information can be found in (Schinwald *et al.* 2012a). Morphology of multilayered GP was examined using scanning electron microscopy (SEM) (Table 1) and dispersion of the GP was examined using light microscopy (Supporting Information Figure S1). Thickness of GP aggregates was measured using atomic force microscopy and showed an average thickness of approximately 175±60 nm (further details see supporting information Figure S2 and S3) whereby variations in the height are due to inhomogeneity of the orientation of the GP on the surface.

Pathological response at a 6 week timepoint after single aspiration exposure in mice

To determine whether multilayered graphene platelets (GP) caused inflammation to a greater extent than graphene in nanoparticulate form (disjointed sheets) (Carbon Black, CB), the inflammatory response after aspiration exposure to CB or GP were measured 6 weeks post-exposure. The lungs were lavaged and the cell types present quantified. The total cell number, consisting mainly of alveolar macrophages with a small proportion of granulocytes (neutrophils, basophils and eosinophils) as well as granulocytes on their own was measured in the broncho-alveolar lavage (BAL) fluid (Figure 1A). Exposure to GP or CB caused no significant increase in the total cell number ($p= 0.2660$,; one-way ANOVA) however, the total granulocyte number was significantly increased when compared to vehicle control (Figure 1A and Table S2). However, this statistical significance, does however not represent a biologically significant increase since the percentage of granulocytes in the BAL fluid only increased from 1 % in the VC treated mice to 3.7 % in the GP treated mice. Comparison between the extent of inflammation at 24 hour, 1 week and 6 weeks time points as previously published in Schinwald et al. (Schinwald *et al.* 2012a) is shown in the supplement (Supplementary Figure S4). This figure demonstrates the decrease of inflammation measured

as total granulocytes in the lung lavage fluid after GP aspiration. Histopathological changes in the lung sections 6 weeks post aspiration were examined in lung sections stained with haematoxylin/Eosin (H&E) and compared to VC. No granuloma formations, infiltration of inflammatory cells or epithelial hyperplasia was observed in lung section of GP exposed mice (Figure 1B) which is indicative of a lack of inflammogenicity. Assaying for lung fibrosis indicated by collagen deposition was determined using Picrosirius Red staining but no increase in collagen deposition was observed in association with (Figure 1C) substantial accumulations of GP in the alveolar airspaces (see black arrow Figure 1 B,C). In addition to CB, the results were compared to the inflammatory response of carbon nanotubes (CNT; graphene in the form of layered tubes) with a mean length of 36 μm, as previously reported in Murphy et al. (Murphy *et al.* 2012). Experimental procedure and dose of the CNT study was identical to the procedures used here and characterization of the CNT sample can be found in the supplement (Table S1) and Murphy et al. (Murphy *et al.* 2012). Mice aspirated with CNTs showed substantial inflammation at 24 hour and 1 week and a decrease in inflammation at 6 weeks which was comparable to the VC (Supplement Figure S4) as reported in Murphy et al. (Murphy *et al.* 2012). In histological sections, mice treated with CNTs showed strong interstitial thickening and remodeling of the alveolar spaces, collagen deposition and lymphocyte infiltrates at a 6 week timepoint as reported in Murphy et al. (Murphy *et al.* 2012) (Supplement Figure S5).

Pleural response to pulmonary exposure

To identify whether GP translocate to the pleura following pulmonary exposure, the tissue and alveolar macrophages lying immediately beneath the visceral pleura were examined in histological sections. No accumulations of GP were seen subjacent to the visceral pleura (data not shown). Additionally the pleural space was lavaged and the extent of inflammation measured at the timepoints 24 hour, 1 week and 6 weeks. At all timepoints no significant influx of inflammatory cells was measured compared to vehicle

controls (Supplement Figure S6A). This was verified by failure to detect aggregations of inflammatory cells or granuloma formation by scanning electron microscopy (SEM) examination of the mesothelial surface of the parietal pleura (Supplementary Figure S6B-C). The translocation of GP was compared to CNT at the 6 week timepoint as shown in the supplement figure S6A, B. Aspiration of CNT led to translocation to the pleural space at the 6 week timepoint as measured by increase in the total cell number and total granulocyte number and accumulation of inflammatory cells on the mesothelial surface of the parietal pleura as reported in Murphy et al. (Murphy *et al.* 2012) (Supplement Figure S6F).

Oxidation of GP in the lung tissue

Degradation of GP via enzymatic oxidation in lung tissue was assessed using Raman microspectroscopy. Section of lungs embedded in paraffin blocks from mice exposed to GP for 24 hour, 1 week and 6 week via pharyngeal aspiration were used. Characteristic graphene Raman spectra were recorded from GP within the sections enabling us to directly probe for oxidized graphitic material; data are presented as average spectra from 20 locations (Figure 2A and Supplement Figure S7). Oxidation is known to increase the ratio of the D (1360 cm^{-1}) band, which indicates disorder in sp^2-hybridized carbon systems to the G band (1580 cm^{-1}). Graphene spectra recorded in lung sections showed no significant difference between I_D/I_G at the different timepoints, indicating that no systematic oxidation had taken place over the period of 6 weeks (Figure 2A insert). Spectra from lung sections also showed vibrations at 1300 cm^{-1} and 1440-1460 cm^{-1} characteristic of paraffin wax spectra at 20°C due to the CH_2 twisting band and overtones of the CH_2 bending, respectively (Zheng and Du 2006). Background spectra from the paraffin block did not interfere with the specific Raman spectra for GP.

Enzymatic oxidation of GP via Horseradish peroxidase

To determine the capability of peroxidases to oxidize GP, *in vitro* oxidation of GP was studied using the enzyme horseradish peroxidase (HRP). The active site of HRP, Fe(III) porphyrin IX has been reported to be analogous to leukocytic peroxidase in the oxidation of graphenic carbon (Kotchey *et al.* 2012). The suspensions with GP, HRP and H_2O_2 were left for 24 hour (H_2O_2 added every hour for 12 h) and 1 week (H_2O_2 added every day) at room temperature and Raman spectra were recorded to measure the change in the extent of oxidation of GP via the ratio I_D/I_G as well as a disorder induced Raman D'-band at 1620 cm^{-1}, indicating imperfect crystalline order (Malard *et al.* 2009). Control samples included GP without HRP and GP without H_2O_2. Between 0 hours and 24 hours the D:G ratio showed a modest increase from 0.12:1 to 0.22:1, however the disorder induced D'-band was recorded in three out of six spectra for HRP+ H_2O_2 treated samples and was not observed in untreated pristine samples. The spectra recorded after 1 week incubation with HRP were similar to the spectra recorded after 24 hour with the exception of one spectrum, which showed an substantial increase in D:G ratio to 0.76:1 indicating extensive oxidation of GP (Figure 2 B). Raman spectra from control samples were similar to those from pristine GP (data not shown). All averaged spectra with standard deviation are shown in the supplement (Supplement Figure S8).

Chemical oxidation of GP via plasma ashing

To compare the spectroscopic data of enzymatic oxidation of GP to that of a chemical oxidation, O_2 plasma oxidation of the GP was performed. Raman spectra of chemical oxidized GP were recorded after 5, 10, 15, 40 and 60 min of plasma oxidation. An increase in the ratio of D:G band (0.12:1 (0 min), 0:22:1 (5 min), 0.24:1 (10 min), 0.27:1 (15 min), 0.19:1 (40 min) and 0:25:1 (60 min)) and a disorder induced Raman D'-band at 1620 cm^{-1} appeared indicating imperfect crystalline order and increase in the degree of oxidation of the GP (Figure 2C) (Malard *et al.* 2009). All averaged spectra with standard deviation including plasma oxidation up to 60 min are shown in the supplement (Supplement Figure S9).

Discussion

The aim of this study was to investigate the medium term pulmonary inflammogenicity of pristine GP in relation to its biopersistence *in vivo*; parallel *in vitro* studies using intense enzymatic oxidation were also carried out. Additionally the evidence for translocation of GP from the distal regions of the lung to the pleural space with subsequent pleural inflammation was investigated. The latter study aimed to shed light onto whether GP might have the potential to cause asbestos like effects in the pleural space after inhalation exposure. We hypothesized that GP used in this study would lead to an extended inflammatory response similar to that seen with CNT due to their extended lateral dimensions which caused frustrated phagocytosis at earlier timepoints and possible diminished clearance from the lung (Schinwald *et al.* 2012a).

The findings on the medium term inflammatory effects of pristine GP in the lung of mice after aspiration exposure showed minimal inflammation, or granulomatous aggregations of inflammatory cells in the bronchial and alveolar regions, and no alveolar wall thickening or fibrosis. This contrasts with carbon nanotubes, which did show all of these types of effect at these timepoints in mice at the same mass dose (Murphy *et al.* 2012). Even though little is known so far of the pulmonary toxicity of GP, it has been shown that the *in vivo* toxicity of graphene- based materials is closely associated with their surface characteristics as summarized in Yang et al.(Yang et al. 2012). Duch et al. showed that graphene oxide and aggregated pristine GP caused sustained pulmonary inflammation *in vivo* compared to well-dispersed pristine GP.(Duch *et al.* 2011). The lack of pulmonary inflammogenicity after exposure to GP in medium term studies is in contrast to recent studies on pulmonary effects of CNT, which reported that CNT have the potential to cause severe lung fibrosis and persistent inflammation after aspiration exposure at a 6 week timepoint (Mercer *et al.* 2011; Murphy *et al.* 2012; Shvedova *et al.* 2005; Wang *et al.* 2011). Both CNT and GP are composed of graphene yet show very different effects in the lungs and so further study is warranted to elucidate the underlying mechanisms for differences in the inflammatory response to CNT and GP. Furthermore it has been shown that fiber-shaped CNT can translocate to the pleural space after aspiration exposure leading to persistent inflammation and granuloma formation at the surface of the

parietal pleura, similar to that seen after asbestos fibre treatment (Mercer *et al.* 2010; Murphy *et al.* 2012). GP used in this study did not accumulate in the sub- visceral pleural tissue up to 6 weeks after aspiration exposure and no inflammatory response was measured in the pleural space up to 6 weeks post exposure. The absence of inflammation in the pleural space does not necessarily exclude the possibility of translocation of very small GP that are able to negotiate the parietal pleural stomata from reaching the pleural space but being cleared (Donaldson *et al.* 2010). It might be argued that while GP had not reached the pleural space by 6 weeks they would get there eventually. However translocation of CNT from the airspaces of mice to the pleural space has been seen at 28 days (Mercer *et al.* 2010) and 6 weeks (Murphy *et al.* 2012) and so we see no reason to conclude that GP translocation might only begin after 6 weeks. The difference in translocation behavior of CNT and GP could be explained by their differing morphology, whereby the fibrous structure of CNT could facilitate translocation as needles are more likely to penetrate cell layers (Mercer *et al.* 2010). In the case of GP, the platelet shape with its extended lateral dimension and no sharp, penetrating tip could limit translocation. However, one limitation of this study is the use of a single sample of GP with a wide distribution of lateral diameter up to 25 µm. We cannot exclude that other forms of GP with one dimensions near the threshold fibre length for retention in the pleura -5 µm-(Schinwald *et al.* 2012b) might be more likely to translocate and be retained in the pleural space.

Biopersistence is a major contributing factor to the toxicity of carbon- based materials and is dependent on the surface functionalisation of these materials (Liu *et al.* 2010; Osmond-McLeod *et al.* 2011). Recent studies on the degradation of oxidized carbon nanomaterials by Kagan and coworkers have shown that enzymatic oxidation *in vivo* and *in vitro* leads to the disruption of the carbon structure in highly oxidized graphene as well as highly oxidized SWCNT and MWCNT (Allen *et al.* 2008; Kagan *et al.* 2010; Kotchey *et al.* 2011). In these studies of enzymatic degradation, the carbon nanomaterials were subjected to chemical oxidation prior to the enzymatic treatment in order to facilitate peroxidase mediated degradation via the interaction of positively charged residues of hMPO with the carboxyl surface of the

nanotubes. Based on these studies our aim was to examine the degree of oxidation of non-oxidised pristine GP *in vivo* up to 6 weeks in lung tissue as well as *in vitro* using horseradish peroxidase which acts as a surrogate for leukocyte peroxidase as previously decribed (Kotchey *et al.* 2011). Raman spectroscopic evaluation of oxidative defects in pristine GP present in lung sections *in vivo* revealed that GP did not undergo oxidative change. This is in line with results published on the biopersistence of pristine CNT and reduced graphene oxide, showing less effective biodegradation by peroxidase compared to oxididized CNT (Kagan *et al.* 2010; Kotchey *et al.* 2011). A possible explanation between the degradation of pristine and oxidized carbonaceous nanomaterials has been stated by Kotchey et al. as being a lack of binding sites for enzymes on the surface of pristine CNT and GP compared to oxidized surfaces with its covalently attached oxygen functional groups (epoxides, negative charged carboxyl groups) facilitating strong interaction with enzymes (Kagan *et al.* 2010; Kotchey *et al.* 2011). A recent study has shown that MPO- deficient mice show increased pulmonary inflammation and impaired clearance after pharyngeal aspiration of oxidized SWCNT due to impaired degradation compared to wild type mice (Shvedova *et al.* 2012). However the importance of MPO in nanomaterial degradation is questionable since neutrophils play only a minor role in phagocytosis and clearance of deposited nanomaterials in the lungs, the bulk of particle clearance being mediated through alveolar macrophages (Lehnert and Morrow 1985). The persistence of large accumulations of GP was very obvious at 6 weeks with no neutrophils in the lavage fluid. Therefore, a role for MPO in the dissolution, breakage and clearance of these particles seems most unlikely. Studies on the peroxidase activity of alveolar macrophage in rats during pulmonary inflammation have shown that alveolar macrophages acquire peroxidase activity from multiple sources during pulmonary inflammation but only 0.8% of all macrophages were positive for cytoplasmic peroxidase in normal rats (Shellito *et al.* 1987). Therefore future studies to clarify the impact of alveolar macrophages, if any, on biodegradation of graphenic nanomaterials are a priority.

In parallel with the studies on degradation of pristine GP *in vivo* we examined the potential enzymatic oxidation of GP *in vitro* using HRP and H_2O_2, as a surrogate for MPO as described in Kotchey et al. (Kotchey *et al.* 2011). No significant increase in I_D/I_G ratio was observed but another band, the D' band, located at 1620 cm^{-1} appeared, which is documented in literature to be linked to substantial defects in the graphene structure (Kudin *et al.* 2008; Malard *et al.* 2009). Additionally, the recording of one spectrum showing a substantial increase in the I_D/I_G ratio after 1 week HRP treatment leads to the conclusion that the oxidation process may be intrinsically non-linear and that this introduces a large variability to the process. Minimal oxidation was seen in pristine GP treated *in vitro* with the peroxidase, but the extent of degradation was not comparable to complete dissolution of the graphene structure of oxidized GP after 20 days HRP H_2O_2 treatment reported in Kotchey et al. (Kotchey *et al.* 2011). Therefore, the timeframe for oxidation of pristine graphene appears to be much longer than for oxidized graphene. This is in line with the lack of oxidation we describe up to 6 weeks post exposure *in vivo* and the self-evident persistence of GP in lungs evident as large accumulations of particles in the histological section. However, from our study we cannot exclude the possibility that a fraction of GP were being oxidized, comminuted and then cleared from the lungs and therefore not detected in our study. Future studies have to be performed to investigate which fraction of GP are deposited in the lung or translocate to extra-pulmonary tissue. We showed that the absence of a biological effect of GP after a 6 weeks timepoint was not correlated with a degradation via oxidation and subsequent clearance of the deposited GP.

Conclusion

The findings of our study show that pristine GP has reduced inflammogenicity in a 6 week study compared to 24 hour and 1 week studies and is non-fibrotic. This has important implications for potential biomedical and technological applications of GP. Oxidative degradation of GP *in vivo* does not account for the lack of inflammation since no change in the I_D/I_G ratio in the Raman spectrum occurred, indicating

no oxidation of pristine GP up to 6 weeks in lung tissue and in addition large accumulations were plainly seen in lung sections. I*n vitro* oxidation of GP via HRP showed only minimal oxidation of GP indicating that pristine graphenic nanomaterials are more biopersistent and may behave differently *in vivo* to their oxidized counterpart. This study suggests that further research is warranted into biodegradation of pristine and oxidised carbonaceous nanomaterials via enzymatic oxidation, in particular by alveolar macrophages.

Supporting Information. Light microscopy images of GP. AFM analysis of GP aggregates. CNT characterization. Data on lung inflammation of CB, GP and CNT (24 hour, 1 week, 6 weeks), pleural translocation and SEM images of chestwall samples; Averaged raman spectra with standard deviation from GP in lung tissue, from *in vitro* HRP+ H_2O_2 treatment and chemical oxidation.

Author Contributions

A.S., K.D. and C.J.C. initiated, designed, directed and performed all experiments (excluding AFM) and took responsibility for planning and writing the manuscript. F.A.M. contributed to designing the experiments and writing the manuscript. A.A.,V.K. and K.S. prepared samples for AFM experiments and performed AFM measurements and analysis.

Funding Sources

The research was funded by the Colt Foundation (A.S. and K.D.), The Department of Health (F.A.M.), EaStCHEM and Leverhulme Trust (C.J.C.) and Eric Birse Charitable Trust and Materials, Physics and Nanosciences COST Action MP1106 (A.A.,V.K. and K.S.).

Notes

The authors declare no competing financial interest.

ACKNOWLEDGMENT

We are grateful to O. Nerushev, A. Gromov and K. Fisher for technical support with the Raman spectrometer and chemical oxidation of GP.

ABBREVIATIONS

BAL, Broncho alveolar lavage fluid; CB, Carbon Black; CNT, carbon nanotubes; GO, Graphene oxide; GP, Graphene Platelets; HARN, High aspect ratio nanotubes; H&E, Hematoxylin & Eosin; HRP, Horseradish peroxidase; MPO, myeolperoxidase.

Reference List

1. Allen, B. L., Kichambare, P. D., Gou, P., Vlasova, I. I., Kapralov, A. A., Konduru, N., Kagan, V. E., and Star, A. (2008). Biodegradation of single-walled carbon nanotubes through enzymatic catalysis. *Nano. Lett.* **8**(11), 3899-3903.

2. Donaldson, K., Murphy, F. A., Duffin, R., and Poland, C. A. (2010). Asbestos, carbon nanotubes and the pleural mesothelium: a review of the hypothesis regarding the role of long fibre retention in the parietal pleura, inflammation and mesothelioma. *Part Fibre. Toxicol.* **7:5.**, 5.

3. Duch, M. C., Budinger, G. R., Liang, Y. T., Soberanes, S., Urich, D., Chiarella, S. E., Campochiaro, L. A., Gonzalez, A., Chandel, N. S., Hersam, M. C., and Mutlu, G. M. (2011). Minimizing oxidation and stable nanoscale dispersion improves the biocompatibility of graphene in the lung. *Nano Lett.* **11**(12), 5201-5207.

4. Fenoglio, I., Greco, G., Tornatis, M., Muller, J., Rayrnundo-Pinero, E., Beguin, F., Fonseca, A., Nagy, J. B., Lison, D., and Fubini, B. (2008). Structural defects play a major role in the acute lung toxicity of multiwall carbon nanotubes: Physicochemical aspects. *Chemical Research in Toxicology* **21**(9), 1690-1697.

5. Geim, A. K., and Novoselov, K. S. (2007). The rise of graphene. *Nat. Mater.* **6**(3), 183-191.

6. Hankin, S. M., and Poland, C. A. (2012). High Aspect Ratio Nanomaterials. *Aerosols Handbook*, 229-248.

7. Kagan, V. E., Konduru, N. V., Feng, W., Allen, B. L., Conroy, J., Volkov, Y., Vlasova, I. I., Belikova, N. A., Yanamala, N., Kapralov, A., Tyurina, Y. Y., Shi, J., Kisin, E. R., Murray, A. R., Franks, J., Stolz, D., Gou, P., Klein-Seetharaman, J., Fadeel, B., Star, A., and Shvedova, A. A. (2010). Carbon nanotubes degraded by neutrophil myeloperoxidase induce less pulmonary inflammation. *Nat. Nanotechnol.* **5**(5), 354-359.

8. Kotchey, G. P., Allen, B. L., Vedala, H., Yanamala, N., Kapralov, A. A., Tyurina, Y. Y., Klein-Seetharaman, J., Kagan, V. E., and Star, A. (2011). The Enzymatic Oxidation of Graphene Oxide. *ACS Nano* **5**(3), 2098-2108.

9. Kotchey, G. P., Hasan, S. A., Kapralov, A. A., Ha, S. H., Kim, K., Shvedova, A. A., Kagan, V. E., and Star, A. (2012). A Natural Vanishing Act: The Enzyme-Catalyzed Degradation of Carbon Nanomaterials. *Acc. Chem. Res.*

10. Kudin, K. N., Ozbas, B., Schniepp, H. C., Prud'homme, R. K., Aksay, I. A., and Car, R. (2008). Raman spectra of graphite oxide and functionalized graphene sheets. *Nano Letters* **8**(1), 36-41.

11. Lehnert, B. E., and Morrow, P. E. (1985). Characteristics of alveolar macrophages following the deposition of a low burden of iron oxide in the lung. *J Toxicol Environ Health* **16**, 855-868.

12. Liu, X. Y., Hurt, R. H., and Kane, A. B. (2010). Biodurability of single-walled carbon nanotubes depends on surface functionalization. *Carbon* **48**(7), 1961-1969.

13. Malard, L. M., Pimenta, M. A., Dresselhaus, G., and Dresselhaus, M. S. (2009). Raman spectroscopy in graphene. *Physics Reports-Review Section of Physics Letters* **473**(5-6), 51-87.

14. Mercer, R. R., Hubbs, A. F., Scabilloni, J. F., Wang, L., Battelli, L. A., Friend, S., Castranova, V., and Porter, D. W. (2011). Pulmonary fibrotic response to aspiration of multi-walled carbon nanotubes. *Part Fibre. Toxicol.* **8:21.**, 21.

15. Mercer, R. R., Hubbs, A. F., Scabilloni, J. F., Wang, L., Battelli, L. A., Schwegler-Berry, D., Castranova, V., and Porter, D. W. (2010). Distribution and persistence of pleural penetrations by multi-walled carbon nanotubes. *Part Fibre. Toxicol.* **7:28.**, 28.

16. Moller, W., Brown, D. M., Kreyling, W. G., and Stone, V. (2005). Ultrafine particles cause cytoskeletal dysfunctions in macrophages: role of intracellular calcium. *Part Fibre Toxicol.* **2:7.**, 7.

17. Murphy, F. A., Poland, C. A., Duffin, R., Al-Jamal, K. T., Ali-Boucetta, H., Nunes, A., Byrne, F., Prina-Mello, A., Volkov, Y., Li, S. P., Mather, S. J., Bianco, A., Prato, M., MacNee, W., Wallace, W. A., Kostarelos, K., and Donaldson, K. (2011). Length-Dependent Retention of Carbon Nanotubes in the Pleural Space of Mice Initiates Sustained Inflammation and Progressive Fibrosis on the Parietal Pleura. *American Journal of Pathology* **178**(6), 2587-2600.

18. Murphy, F. A., Poland, C. A., Duffin, R., and Donaldson, K. (2012). Length-dependent pleural inflammation and parietal pleural responses after deposition of carbon nanotubes in the pulmonary airspaces of mice. *Nanotoxicology.*

19. Osmond-McLeod, M. J., Poland, C. A., Murphy, F., Waddington, L., Morris, H., Hawkins, S. C., Clark, S., Aitken, R., McCall, M. J., and Donaldson, K. (2011). Durability and inflammogenic impact of carbon nanotubes compared with asbestos fibres. *Part Fibre. Toxicol.* **8:15.**, 15.

20. Rao, G. V., Tinkle, S., Weissman, D. N., Antonini, J. M., Kashon, M. L., Salmen, R., Battelli, L. A., Willard, P. A., Hoover, M. D., and Hubbs, A. F. (2003). Efficacy of a technique for exposing the mouse lung to particles aspirated from the pharynx. *J Toxicol. Environ. Health A.* **66**(15), 1441-1452.

21. Sanchez, V. C., Jachak, A., Hurt, R. H., and Kane, A. B. (2011). Biological Interactions of Graphene-Family Nanomaterials - An Interdisciplinary Review. *Chem. Res Toxicol.*

22. Schinwald, A., Murphy, F. A., Jones, A., MacNee, W., and Donaldson, K. (2012a). Graphene-based nanoplatelets: a new risk to the respiratory system as a consequence of their unusual aerodynamic properties. *ACS Nano* **6**(1), 736-746.

23. Schinwald, A., Murphy, F. A., Prina-Mello, A., Poland, C. A., Byrne, F., Movia, D., Glass, J. R., Dickerson, J. C., Schultz, D. A., Jeffree, C. E., MacNee, W., and Donaldson, K. (2012b). The Threshold Length for Fiber-Induced Acute Pleural Inflammation: Shedding Light on the Early Events in Asbestos-Induced Mesothelioma. *Toxicol. Sci.* **128**(2), 461-470.

24. Shellito, J., Sniezek, M., and Warnock, M. (1987). Acquisition of Peroxidase-Activity by Rat Alveolar Macrophages During Pulmonary Inflammation. *American Journal of Pathology* **129**(3), 567-577.

25. Shvedova, A. A., Kapralov, A. A., Feng, W. H., Kisin, E. R., Murray, A. R., Mercer, R. R., St Croix, C. M., Lang, M. A., Watkins, S. C., Konduru, N. V., Allen, B. L., Conroy, J., Kotchey, G. P., Mohamed, B. M., Meade, A. D., Volkov, Y., Star, A., Fadeel, B., and Kagan, V. E. (2012). Impaired Clearance and Enhanced Pulmonary Inflammatory/Fibrotic Response to Carbon Nanotubes in Myeloperoxidase-Deficient Mice. *Plos One* **7**(3).

26. Shvedova, A. A., Kisin, E. R., Mercer, R., Murray, A. R., Johnson, V. J., Potapovich, A. I., Tyurina, Y. Y., Gorelik, O., Arepalli, S., Schwegler-Berry, D., Hubbs, A. F., Antonini, J., Evans, D. E., Ku, B. K., Ramsey, D., Maynard, A., Kagan, V. E., Castranova, V., and Baron, P. (2005). Unusual inflammatory and fibrogenic pulmonary responses to single-walled carbon nanotubes in mice. *American Journal of Physiology-Lung Cellular and Molecular Physiology* **289**(5), L698-L708.

27. Wang, X., Xia, T., Ntim, S. A., Ji, Z. X., Lin, S. J., Meng, H., Chung, C. H., George, S., Zhang, H. Y., Wang, M. Y., Li, N., Yang, Y., Castranova, V., Mitra, S., Bonner, J. C., and Nel, A. E. (2011). Dispersal State of Multiwalled Carbon Nanotubes Elicits Profibrogenic Cellular Responses That Correlate with Fibrogenesis Biomarkers and Fibrosis in the Murine Lung. *ACS Nano* **5**(12), 9772-9787.

28. Yang, K., Li, Y., Tan, X., Peng, R., and Liu, Z. (2012). Behavior and Toxicity of Graphene and Its Functionalized Derivatives in Biological Systems. *Small.*, 10.

29. Zheng, M., and Du, W. (2006). Phase behavior, conformations, thermodynamic properties, and molecular motion of multicomponent paraffin waxes: A Raman spectroscopy study. *Vibrational Spectroscopy* **40**, 219-224.

Table legend:

Table 1. Characterization of CB and GP, adapted from Schinwald et al.(Schinwald *et al.* 2012a) and scanning electron micrograph of GP in 0.5% BSA/saline solution. * Aerodynamic diameter from Moller et al. (Moller et al. 2005).

A)

	Carbon Black	Graphene Platelets
Projected diameter [µm] (mean± s.e.m.)	0.01 ± 0.01	5.64 ±4.56
Number of layers	-	1-10
Surface area [m^2/g]	253.9	~100
Density [g/cm^3]	~1.9	~2
EPR [Arbitrary Units]	451.3± 52.2	867.3±77.5
Aerodynamicdiameter [µm] (t=0.1 µm)	<=2.5*	1.33-3.26
Average aggregate thickness [nm]		178± 57
Source	Evonik Degussa GmbH	Cheaptubes.com

B)

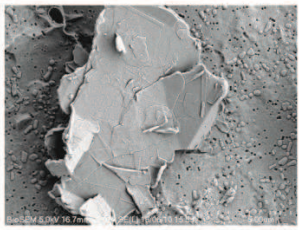

Figures:

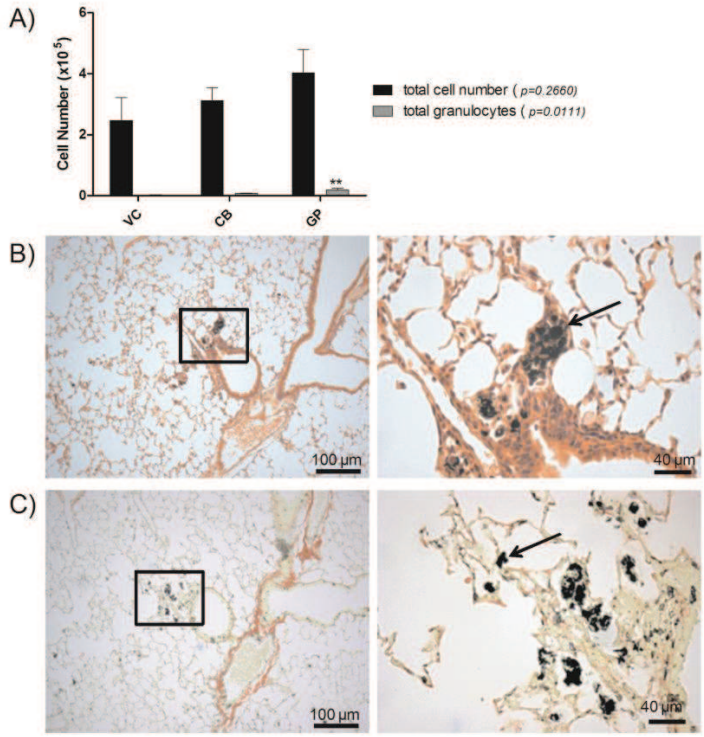

Figure 1**.** Response to GP in the lungs at 6 weeks post aspiration. C57BL/6 mice were exposed to VC, CB and GP by pharyngeal aspiration. A) At 6 weeks the lungs were lavaged and total cell number and granulocyte (neutrophils, eosinophils, basophils) number were measured. No significant difference was measured for total cell number between the VC, CB and GP (total cell number $p= 0.2660$) however the total granulocytes was significantly increased in GP treated mice (p= 0.0111 from one-way ANOVA). Data represent mean ± s.e.m. of n=7. Histological lung sections of GP treated mice stained with H&E (B) and picrosirius red (C) with higher magnification callouts. No granuloma formations, lymphocyte infiltrates or increase in collagen were observed despite extensive deposition of GP is visible (as indicated by the black arrows).

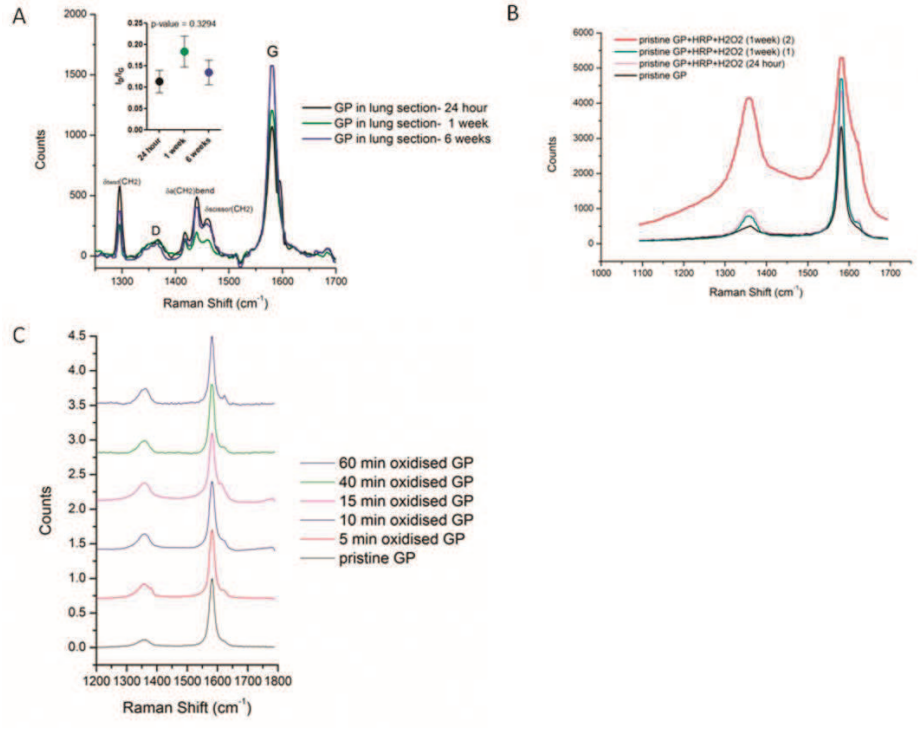

Figure 2. Raman spectroscopy of GP in lung sections, after enzymatic treatment using HRP and chemical oxidation. A) Raman spectra of GP in lung section embedded in paraffin from mice exposed for 24 hour, 1 week and 6 weeks to GP via pharyngeal aspiration. Characteristic D (1360 cm^{-1}) and the G band (1580 cm^{-1}) of graphene can be seen. Spectra at 1290 cm^{-1} and 1450 cm^{-1} is characteristic for paraffin wax. No statistically significant change in the ratio of I_D/I_G was measured as shown in the insert. Data represent mean of 20 spectra. B) Raman spectra of pristine GP and GP incubated with HRP and H_2O_2 for 24 hour and 1 week. An increase in the D-band and D'-band at 1620 cm^{-1} was observed at 24 hour and 1 week compared to pristine spectra however no significant increase in I_D/I_G ratio was measured. For the 1 week timepoint one spectrum was recorded with an increase in D:G ratio to 0.76:1. C) Raman spectra of oxygen plasma treated GP for 5, 10, 15, 40 and 60 min. Increase in D- band and disorder induced Raman D'-band at 1620 cm^{-1} indicating imperfect crystalline order. Data represent mean of 6 spectra.

Supplement:

Minimal oxidation and inflammogenicity of pristine graphene with residence in the lung

Anja Schinwald, Fiona Murphy, Alexandros Askounis, Vasileios Koutsos, Khellil Sefiane, Ken Donaldson , Colin J. Campbell

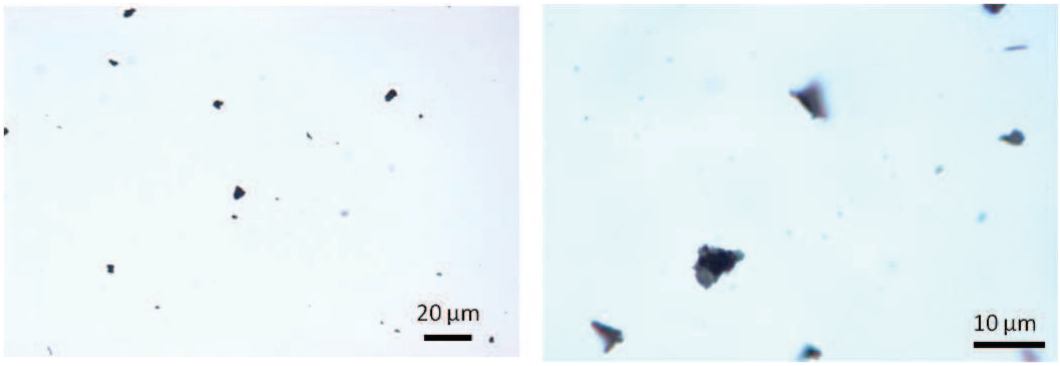

Fig S1. Light microscopy images of GP in 0.5% BSA/saline at 100 µg/ml (aspirated dose).

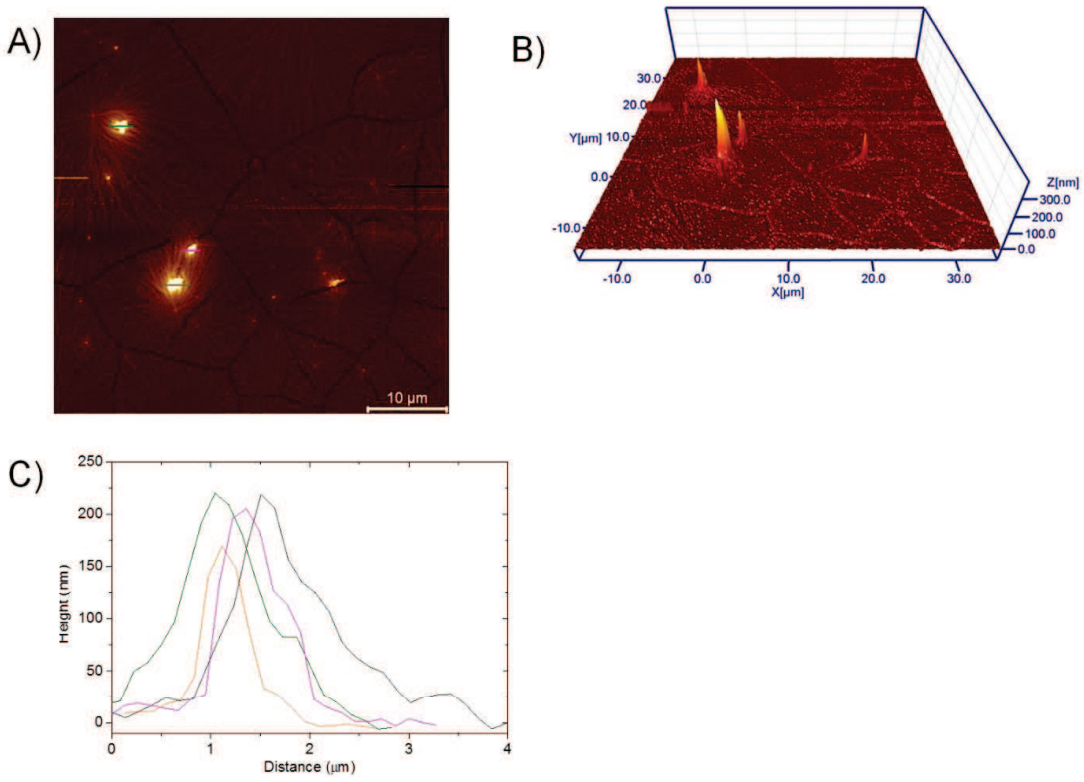

Fig S2: Thickness measurement of the GP-aggregates at 0.1 mg/ml concentration. A) Typical topography image where the contrast has been adapted to simultaneously exhibit the graphene platelets (brighter areas) and the underlying BSA layer. B) 3D image of the same area.

A flat dendritic BSA structure with cracks (probably grain boundaries) is found on the sample surface. On top of this structure a scatter of GP can be readily identified as the taller features. Typical height profiles of the platelets acquired according to the lines in (A) are presented in (C). The average height of the GP-aggregates at this concentration was calculated to be 178 ±57 nm. Apart from the possible polydispersity in thickness and diameter, variations of the value could be affected by the following reasons: 1) stacking of more GP on top of each other on the surface and 2) folding of the graphene and 3) platelets oriented ('sitting') at a different angle on the surface. The third reason appears to be the most significant as the platelets are not completely flat on the substrate. These measurements are compatible with ca 100 nm thickness for the GP-aggregates in suspension as these are the lower values that we measure.

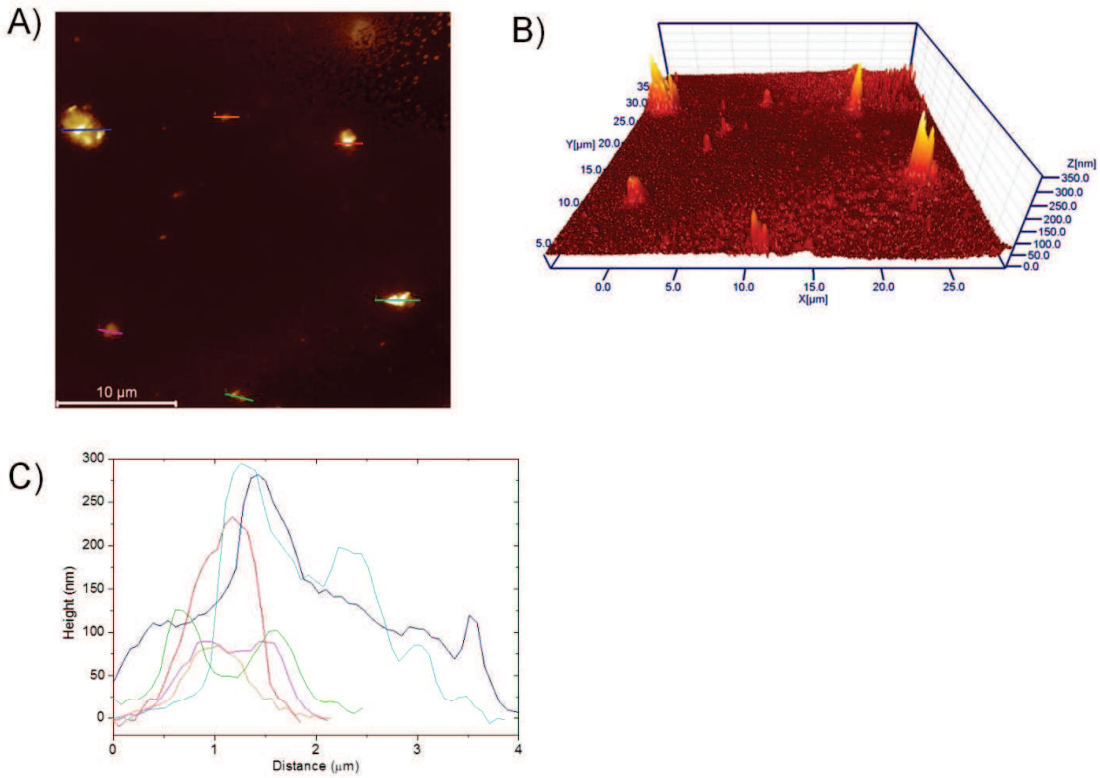

Fig S3: Thickness measurement of the GP-aggregates at 1 mg/ml concentration. A) Typical topography image where the contrast has been adapted to simultaneously exhibit the graphene platelets (brighter areas) and the underlying BSA layer. B) 3D representation of the same area. In this case, the protein appears to have formed multilayers. On top of these layers (compared to diluted solution- figure S2) more GP-aggregates can be identified, due to higher concentration. Typical height profiles acquired according to the lines in (A) are presented in figure (C). The average height of the platelets at such samples was calculated to be 171±64 nm.

Table S1. Characteristics and morphology of the Carbon Nanotube samples used as a comparison in this study. Table adapted from Murphy et al. 2012 [1].

	Carbon Nanotubes
Diameter (nm)	165.02 ± 4.68
Length (µm)	Mean 36
% fibre greater than 15 µm	84.26
Source	University of Manchester [Dr. I. Kinloch]

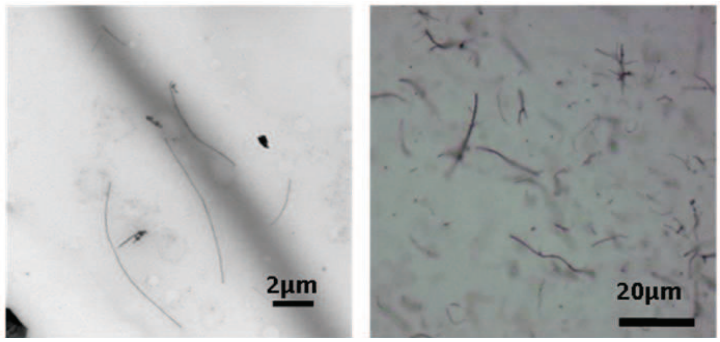

Table S2. Number of monocytes/macrophages and granulocytes after pharyngeal aspiration of 50 µg/mouse CB and GP 6 weeks post aspiration.

	Monocytes/ Macrophage	Neutrophiles	Eosinophiles	Lymphocytes	Total cell number	Total Granulocytes	% total Granulocytes
VC 1	324				324	0	0
VC 2	346	2			348	2	0.574713
VC3	330	4			334	4	1.197605
VC 4	348	2			350	2	0.571429
VC 5	324	0			324	0	0
VC 6	308	3		1	312	4	1.282051
VC 7	410	2			412	2	0.485437
CB 1	336	2			338	2	0.591716
CB 2	320	10			330	10	3.030303
CB 3	360	11		1	372	12	3.225806
CB 4	330	4			334	4	1.197605
CB 5	304	10			314	10	3.184713
CB 6	432	15		3	450	18	4
CB 7	378	10			388	10	2.57732
GP 1	350	4			354	4	1.129944
GP 2	380	18	1	2	400	20	5
GP 3	380	20			400	20	5
GP 4	320	4			324	4	1.234568
GP 5	350	9		1	360	10	2.777778
GP 6	244	14			258	14	5.426357
GP 7	356	22			378	22	5.820106

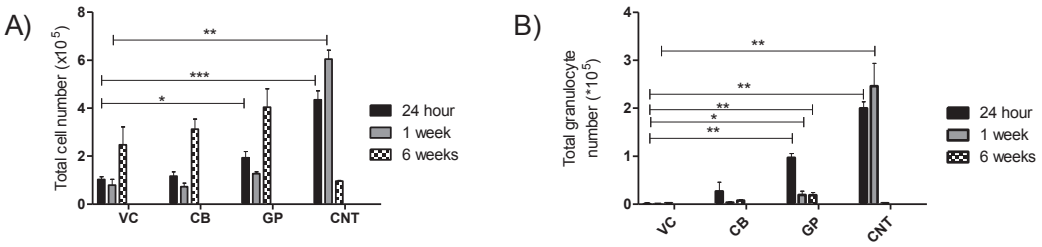

Fig S4: Time- dependent inflammatory response in the lungs after aspiration exposure to CB, GP and CNT. The inflammatory response in the lungs after exposure via pharyngeal aspiration was examined. At 24 hour, 1 week and 6 weeks post exposure the lungs were lavaged and total cell number (A) and total granulocyte number (B) was measured. Decrease in total granulocyte number after GP exposure from 24 hour to 6 weeks is shown (B). Data from 24 hour and 1 week timepoint are obtained from Schinwald et al. [2] CNT showed significant increase of inflammation at 24 hour and 1 week, which decreased at 6 weeks to a level comparable to VC. CNT data was obtained with permission from Muphy et al. [1]. Significance versus vehicle control **P <0.01. Data represent mean ± s.e.m. of n = 4.

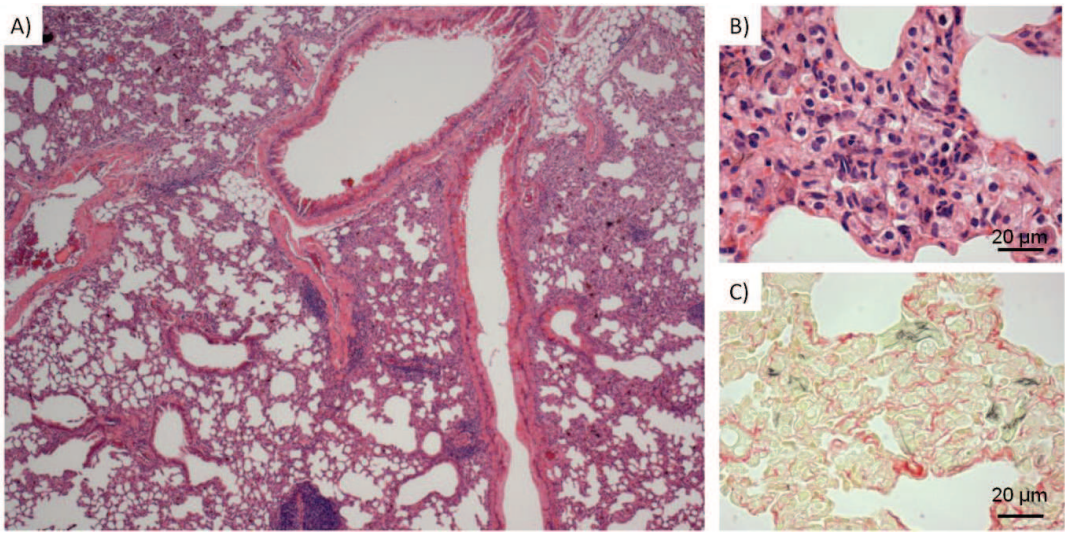

Fig S5: Lung pathology 6 weeks post aspiration to CNT. A) Low magnification overview (2.5x) of a histological section stained with H&E to demonstrate gross pathology. Extensive lymphocyte infiltrates and extreme interstitial thickening (B) and collagen deposition (C) was observed. Long CNT are identified within the lymphocyte aggregates. Figures with permission from Murphy et al. [1].

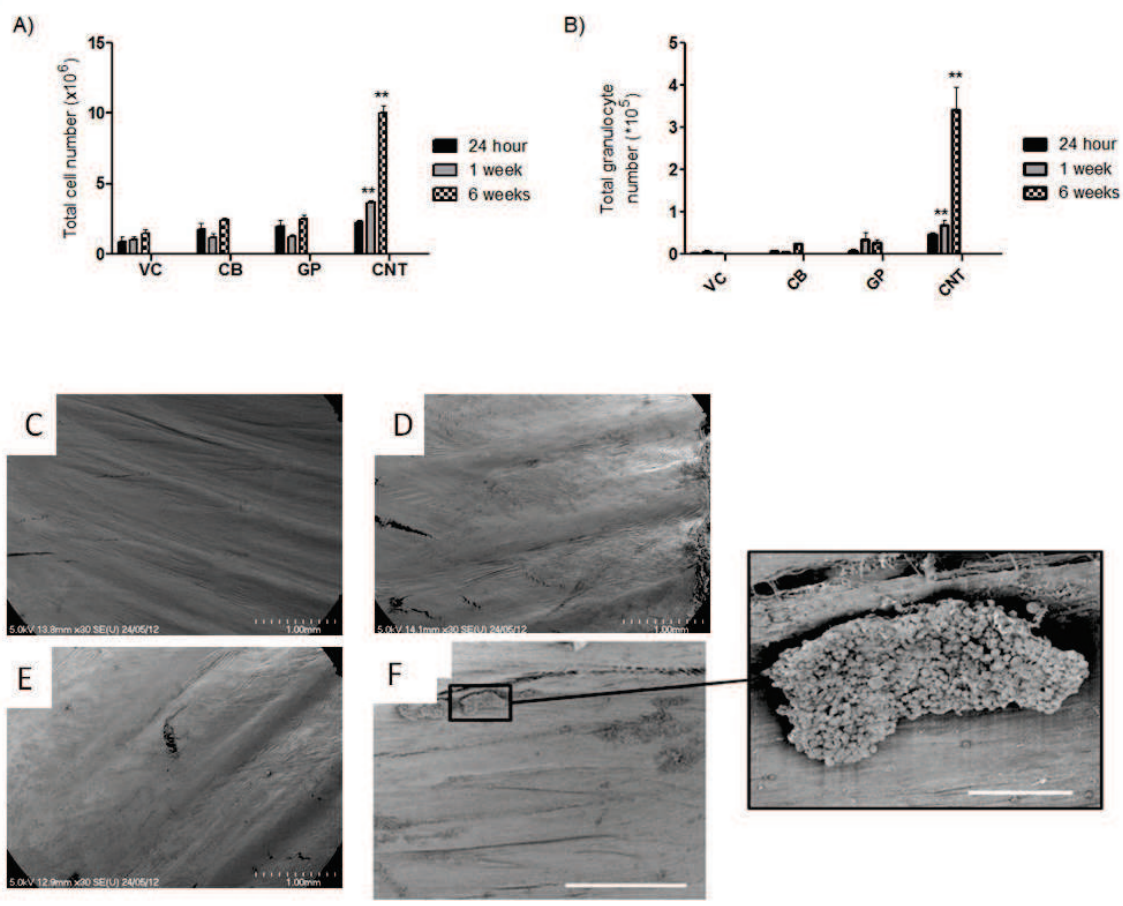

Fig S6: Inflammatory response in the pleural cavity after pulmonary exposure to CB, GP and CNT. The inflammatory response in the pleural cavity after CB, GP and CNT exposure via pharyngeal aspiration was examined. At 24 hour, 1 week and 6 weeks post exposure the pleural cavity was lavaged and total cell number (A) and total granulocyte number (B) were measured. Data represent mean ± s.e.m. of n = 4. CNT data obtained with permission from Murphy et al. [1]. The chestwall was examined by scanning electron microscopy (SEM) to identify lesion formation after pulomary exposure to CB (D) and GP (E). Normal mesothelium was observed in all treatments which was comparable to VC (C). F) To illustrate an inflammatory response on the parietal pleura after aspiration exposure, SEM of parietal pleura after aspiration to 50 µg/mouse CNT at a 6 week timepoint is shown. Aggregates of inflammatory cells are present on the mesothelial surface indicating a translocation of CNT to the pleural space; this image was obtained with permission from Murphy et al. [1].

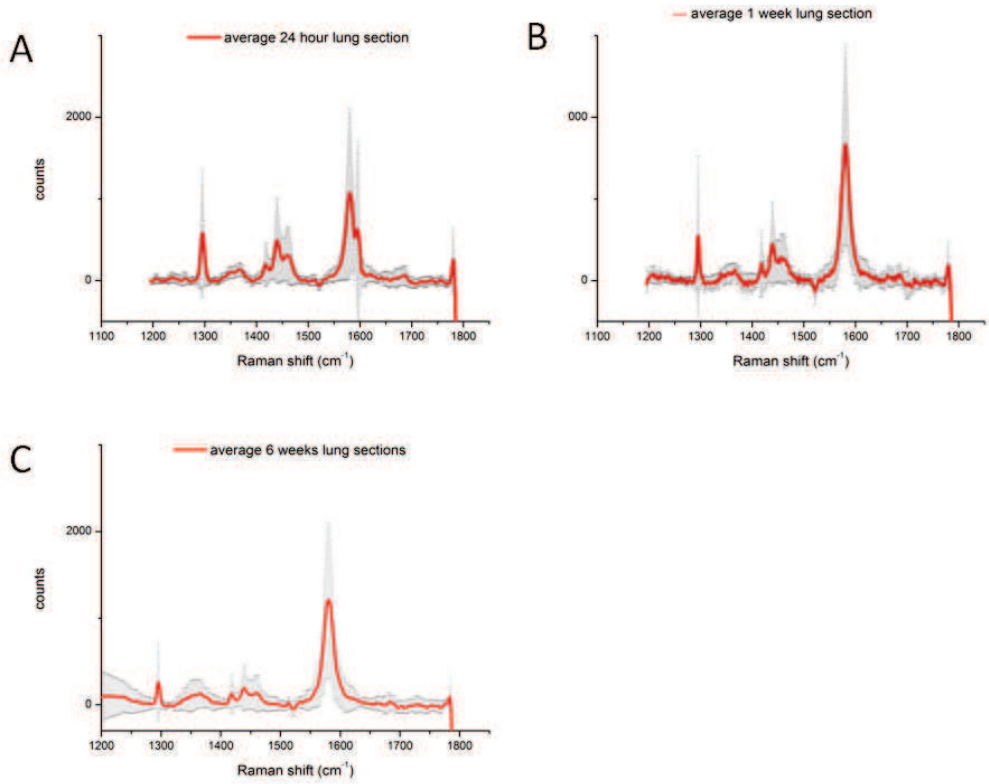

Fig S7. Raman spectra from GP in lung tissue after 24 hour (A), 1 week (B) and 6 weeks post exposure (C). Average and standard deviation of 20 locations is shown.

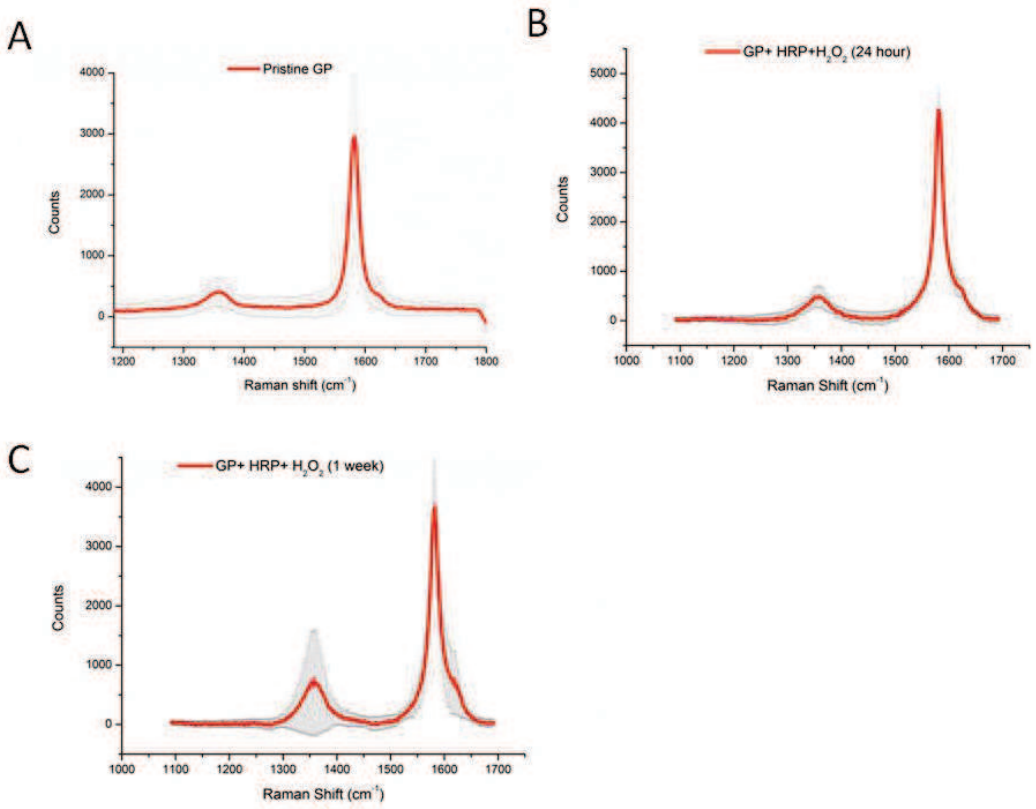

Fig S8. Raman spectra from pristine GP (A) and GP treated with HRP and H_2O_2 for 24 hours (B) and 1 week (C). Average and standard deviation of 20 locations (pristine) and 6 locations (HRP treatment) are shown.

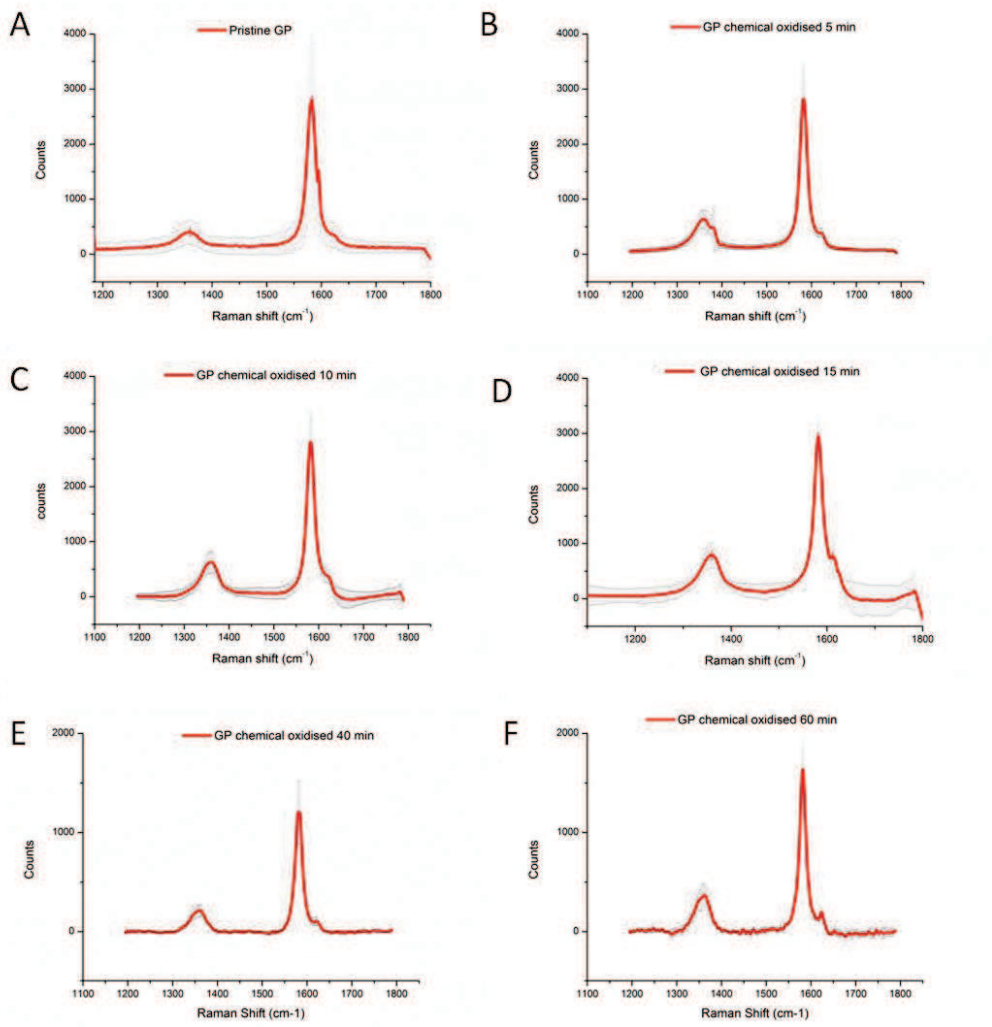

Fig S9. Raman spectra from pristine GP (A) and chemical oxidised GP using oxygen plasma for 5 min (B), 10 min (C), 15 min (D), 40 min (E) and 60 min (F).Average and standard deviation of 6 locations is shown.

Reference List

1. Murphy, F. A.; Poland, C. A.; Duffin, R.; Donaldson, K. Length-dependent pleural inflammation and parietal pleural responses after deposition of carbon nanotubes in the pulmonary airspaces of mice. *Nanotoxicology.* **2012**.

2. Schinwald, A.; Murphy, F. A.; Jones, A.; MacNee, W.; Donaldson, K. Graphene-based nanoplatelets: a new risk to the respiratory system as a consequence of their unusual aerodynamic properties. *ACS Nano* **2012,** *6* (1), 736-746.

Review article under submission:

Schinwald A, Cherrie JW, Poland CA, Donaldson K. **Fibre length and mesothelioma – new science illuminates an old question and highlights new risks.** Submitted to Environmental International.

Fibre Length and Mesothelioma: *Using new science to illuminate an old question and highlight new risks*

A. Schinwald [1*], J. W. Cherrie [2,3], C. A.Poland[2], R. J. Aitken [2,4], K. Donaldson [1,2]

[1]MRC/University of Edinburgh, Centre for Inflammation Research, Queen's Medical Research Institute, 47 Little France Crescent, Edinburgh EH16 4TJ, UK

[2]Institute of Occupational Medicine, Research Avenue North, Riccarton, Edinburgh EH14 4AP, UK

[3]University of Aberdeen, Division of Applied Health Sciences, Royal Aberdeen Children's Hospital, Aberdeen AB25 2ZD, UK

[4]IOM Singapore, 30 Raffles Place, #17-08 Chevron House, Singapore, 048622

*Corresponding author: Anja Schinwald, University of Edinburgh, Centre for Inflammation Research, Queen's Medical Research Institute, 47 Little France Crescent, Edinburgh EH16 4TJ, UK
Email: a.schinwald@sms.ed.ac.uk
Phone: 0044 131 242 9102

Keywords: Nanofibres; asbestos fibres; fibre length; mesothelioma.

Abstract

The hazardous potential of fibrous materials was first recognized at the turn of the 20th century and later studies indicated the importance of fibre dimension in the development of diseases from inhaling asbestos fibres. The definition of a fibre for the purposes of occupational health and safety has existed now for over forty years and is based around strict morphological criteria for length and diameter defining what is and what is not, a fibre. However the scientific basis of this definition, in particular the length threshold, is shrouded in uncertainty and it is the purpose of this article to discuss the basis of this in light of recent advances in nanotechnology. These advances have allowed a critical evaluation of the role of fibre length that is shown to have surprising concordance with the original fibre definition and its serendipitous grounding in particle toxicology.

In addition to helping solve critical questions surrounding fibre definition and toxicology, nanotechnology also presents new concerns in terms of hazard and potential for occupational exposure, with key questions raised as to the suitability of current detection methods for determining airborne concentrations. The challenges for accessing workplace exposure raised by these new breed of industrial fibres is summarised in this article as well as new methods that may need to be adopted to assess their exposure.

1. Introduction: Fibres, Exposure and Disease

The hazardous potential of fibrous materials, in particular asbestos, has long been known although it was only with the widespread use of asbestos fibres at the turn of the 20th century that the strong link between occupational asbestos exposure and health problems was defined. As the use and exposure to asbestos continued through much of the 20th century, so did the increasing incidence of asbestos related disease, which resulted in the eventual classification of asbestos as a carcinogen by the International Agency for research on Cancer (IARC) in 1977 (1977). This was followed by bans on crocidolite and amosite asbestos in the UK (1985) (Bottomley 1985) and later a ban on chrysotile asbestos (Prescott 1999). Currently asbestos is banned in over 50 countries around the world. The basis of the pathogenicity that has so affected the industrialised world and resulted in the banning of asbestos has been the subject of numerous research studies spanning many decades and several of these seminal studies along with key events in asbestos history and regulation are summarised in figure 1. Of the diseases linked to asbestos exposure, asbestosis, a fibrotic lung disease affecting those with heavy exposure to asbestos was the first reported (Cooke 1924) and subsequently tackled using dust control measures. Later, lung cancer was linked to asbestos exposure by Sir Richard Doll and this was seen to be also associated with asbestosis. In Doll's cohort of 105 asbestos workers, 18 developed lung cancer of which 15 were associated with asbestosis (Doll 1993). Whilst lung cancer is also associated with many other risk factors including smoking (Darnton *et al.* 2006), mesothelioma is almost exclusively associated with asbestos. This is a uniformly fatal cancer of the pleural or peritoneal mesothelium; mesothelioma is rarely found in individuals not previously exposed to asbestos although can occur in rare instances after chronic pleural inflammation, radiation therapy and exposure to certain carcinogenic chemicals (see review by Cugell and Kamp (Cugell and Kamp 2004)).

1.1 Evaluation of Fibres in Workplace Air

It has long been recognised that the majority of particles of retained in the lungs are relatively short, typically less than 7 µm (Walton 1982). During the first half of the 20th Century dust sampling in the workplace developed from simple gravimetric assessments of "total" dust to microscopic particle counting methods designed to focus the evaluation on the finer fraction of the aerosol, which was considered more biologically relevant. At this time the konimeter and thermal precipitator were widely used to collect short-term dust samples directly onto a glass substrate to facilitate the counting process. Particles with diameter between 0.5 µm and 5 µm were generally counted and the concentration was expressed in terms of "particle counts per cubic centimetre" (ppcc) or "million particles per cubic foot" (mppcf).

When occupational hygienists first began assessing exposure to asbestos, regulations which were implemented for silica dust were used. These regulations were based on mass dose, neglecting the fibre shape as a determining factor relevant for pathogenicity. However, in the earliest toxicological studies with asbestos there was a suspicion that long fibres were more pathogenic than short ones. For example, Walton (Walton 1982) cites a study by Beger reporting that asbestos fibres with a length of 25-109 µm were found in a patient who died from asbestosis, indicating the possibility of selective retention of long fibres, which might be important in the observed development of disease. A series of animal inhalation studies and studies on lung material from asbestosis cases were performed to investigate the length fraction of asbestos fibres responsible for asbestosis (KNOX and BEATTIE 1954a; KNOX and BEATTIE 1954b; VORWALD *et al.* 1951). The inhalation models indicated a fibre length of 20-50 µm caused peribronchiloar fibrosis whereas human asbestosis cases showed that fibres up to 15 µm caused severe asbestosis (KNOX and BEATTIE 1954a; KNOX and BEATTIE 1954b). Burdett (1998) reports on a survey undertaken in 1938 at the J. W. Roberts Ltd. factory at Armley in Leeds where particle and fibre concentrations (longer than 0.5 µm and longer than 5 µm) were reported (Burdett 1998). In 1957 the Asbestosis Research Council (ARC) was formed by the main asbestos manufacturing companies in Britain, and at the outset they agreed that asbestos dust

measurements should focus on fibres longer than 5 µm. As late as 1960 limits on occupational exposure in Britain was specified as particle counts 177 ppcc for asbestos and the same value for dusts containing more than 50% free crystalline silica. In 1969 the ARC published the membrane filter method for measuring airborne asbestos dust, which was sampled onto a filter that after sampling was rendered transparent so that the fibres could be counted using a phase contrast optical microscope (Asbestosis Research Council 1968). A fibre was defined and counted as a structure less than 3 µm in diameter (based on the ability of the fibre to penetrate to the alveoli), longer than 5 µm (based on the presumed hazardous nature of longer fibres) and had a length to diameter ratio more than 3:1 (to focus on fibrous shaped particles). Around the same time the British Occupational Hygiene Society (BOHS) published a standard for chrysotile asbestos based on this new method (BOHS 1968) to prevent the formation of asbestosis and lung cancer in asbestos exposed workers which was later described by the US National Institute for Occupational Safety and Health as "the first modern approach to the setting of an asbestos standard" (1976). Indeed this fibre definition was later used by the World Health Organisation in the 1985 Reference Method for Measuring Airborne Man-made Mineral Fibres (1985). The membrane filter method has evolved in the subsequent years but the fibre definition has remained unchanged at <3 µm in diameter > 5 µm in length and a length to diameter ratio more than 3:1.

1.2. Critical Fibre Dimensions for Mesothelioma

The link between asbestos exposure and mesothelioma was suspected as early as 1943 (Tweedale 2002) however the association was only finally confirmed by Wagner and colleagues in 1960 (Wagner *et al.* 1960). This study described 33 cases of mesothelioma in the Cape Asbestos fields in South Africa and made a clear link to their asbestos exposure. The relative rarity of mesothelioma in animals exposed to asbestos by inhalation, as is the case for humans, meant that meaningful experimental studies of the mechanism of mesothelioma following inhalation exposure were impracticable. This problem was only overcome in the seventies in an extensive series of studies by

Merle F. Stanton and co-workers at the National Cancer Institute in the USA. This group were the first to develop a high yield toxicology assay of mesothelioma, using it to determine the fibres types and dimensions important for mesothelioma. The approach used was direct pleural implantation, which depending on dose, produced up to 100% mesotheliomas in some groups (Lippmann 1994) in a relatively short time. Inhalation of asbestos in rodent exposure studies yields most frequently zero and at best, a few percentages of animals with mesothelioma after lifetime inhalation of high levels of asbestos.

In the publications arising from this approach, Stanton first described the role of fibre length, diameter and composition for a range of fibrous materials including asbestos, fibrous glass and aluminium oxide (Stanton and Wrench 1972). The findings related asbestos type and dimensions, especially diameter, to pathogenicity and it was clear that asbestos samples with a substantial number of fibres longer than 10-20 µm were most efficient in producing mesothelioma. Whilst long asbestos fibres of different types seemed to be similarly potent, a number of glass fibres containing a large proportion of fibres >10-20 µm induced much less carcinogenic response that might be anticipated from the long fibres present. Whilst not discussed to any great extent, this observation preceded the role of biopersistence that was to emerge and dominate the fibre pathogenicity paradigm in the future (Donaldson *et al.* 2010). Ten years later, Stanton had accumulated considerably more data and was able to conclude that:

> *'…The probability of pleural sarcoma (mesothelioma) correlated best with the number of fibers that measured 0.25 µm or less in diameter and more than 8 µm in length, but relatively high correlations were also noted with fibers in other size categories having diameters up to 1.5 µm and lengths greater than 4 µm….'. (Stanton et al. 1981)*

In other words, thin fibres shorter than 4 µm were low in mesothelioma potential whilst those 4-8 µm long were almost as effective as those that were longer than 8 µm and those beyond 8 µm did

not cause a very more marked increase in carcinogenicity described. Pathology studies using direct instillation or inhalation of synthetic vitreous fibres, whilst not an efficient way to produce mesotheliomas (see below) confirmed the general lack of pathogenicity of short fibres. Kuschner *et al.* (Kuschner and Wright 1974) used vitreous fibres that were ground to be much shorter than the parent long fibre material; the short fibres showed virtually no pathology in rats when instilled but there was severe fibrosis with the long fibre material. Davis *et al.* ground long amosite asbestos to shortness and again found virtually no pathology with the short after years of inhalation exposure; in contrast lung cancer, fibrosis and a single mesothelioma were reported in animals inhaling the long parent material (Davis *et al.* 1986a).

However Timbrell argued that asbestos fibres from the Northwest Cape in Africa had virtually no fibres greater than 10 µm although numerous mesothelioma cases had been reported (Timbrell 1982).

It should be borne in mind that, since the Stanton experiments were achieved using direct implantation of fibres, they effectively by-passed the normal mechanisms whereby fibres depositing in the airspaces actually reach the pleura. There is, in our opinion, a strong likelihood that this translocation process is itself length-dependant and that the potential for longer fibres to reach the pleura from the airspaces is likely limited since very long fibres would - I) have a higher likelihood of depositing before they reach the distal sub-pleural alveoli; II) find it physically difficult to penetrate through the sub-pleural alveoli to the pleural space due to their length. This is also in keeping with the argument that inhaled long fibres may not reach the pleural space. This problem is likely to have affected a number of studies where the peritoneal assay of mesothelioma was used (Bolton *et al.* 1982a; Bolton *et al.* 1982b; Davis *et al.* 1986b; Davis *et al.* 1986c), although the limitations of this assay, including the one highlighted here, were raised (Johnson 1993; Rossiter 1991). For example a large study examining the role of fibre dimensions and biopersistence in mesothelioma has shown length of >20 µm in biopersistent fibres as the length class best related to mesothelioma development (Miller *et al.* 1999). However, such evidence as exists suggests that fibres longer than

15 µm are very rarely found in the parietal pleura and that short fibres < 5 µm are most common (Boutin *et al.* 1996); the predominant fibre length found in the pleural mesothelioma tissue is 5 µm and less (Suzuki *et al.* 2005). A review by Lippmann of animal and human studies in relation to mesothelioma development (Lippmann 1993) concluded that:

> *'..fibres shorter than 5 µm appear to be ineffective, whist an appreciable fraction longer than 10 µm appear to be unnecessary..'*

Taking all these studies into account, it seems that the length of the most pathogenic fraction of fibres is between 5-10 µm. It can therefore be seen that indirectly, using the poly-dispersed length distributions of fibres of various sorts and correlation analyses, research in the 20th century reached the conclusion that the threshold length for mesothelioma was 5 µm.

2. Recent Experimental Demonstration of a Threshold Length for Pleural Inflammation

As discussed above, naturally occurring fibres are always poly-dispersed for length with the exception of milled fibres that can all be short, but all long fibre samples may contain short material in addition to longer fibres of varying lengths. This has always provided an obstacle to clarifying the threshold length for biological effects of fibres. However the advance of materials science and nanotechnologies has enabled the production of tight length distributions of nanofibres; this in turn offers the possibility of precise determination of the threshold length for pleural retention/inflammation. There has been concern that nanofibres or high aspect ratio nanomaterials (HARN) may pose an asbestos-like hazard (Donaldson *et al.* 2010; Maynard *et al.* 2006) and so it is paradoxical that nanotechnology might hold the key to determining the threshold length for fibre effects in the pleura; a possibility indicated in 2008 by one of the authors (Poland *et al.* 2008). The problem that all naturally occurring and man-made vitreous fibres (MMVF) have a wide distribution of length, along with non-fibrous material in the case of synthetic vitreous fibres, meant that only estimations of the potential threshold length could previously only be made from statistical analyses

of complex datasets e.g. (Stanton and Wrench 1972). However, in a 2012 study by some of the authors, silver nanofibres which were made by the nanotechnological polyol process provided five distinct length classes, with mean lengths (range) of 3 (0.5-4.5), 5 (0.5- 8.5), 10 (5.5- 15.5), 14 (2.5-30.5) and 28 µm (20.5-60.5) (Schinwald *et al.* 2012b); importantly the diameter of the different length samples was closely similar and the composition was identical so the only variable was the length. In addition nickel nanowires in two length classes (4 and 20 µm) and carbon nanotubes in two length classes (2 and 13 µm) (Murphy *et al.* 2011; Poland *et al.* 2012; Schinwald *et al.* 2012b) were used to further investigate the cut-off length for acute pleural inflammation in mice. A method of direct intrapleural instillation of very small masses of the nanofibres was used followed by sampling of the pleural space for evidence of acute inflammation (results summarised in Figure 2). Whilst acute inflammation is not mesothelioma and mesothelioma is in fact diagnosed after a long lag-time after first exposure (Yang *et al.* 2008), we believe that short-term inflammation may predict long-term effects. This is argued on the basis that 1) only retained fibres can cause inflammation so inflammation is indicative of retention (Murphy *et al.* 2011) and that only retained fibres could cause mesothelioma; 2) inflammation is implicated in the development of cancer for a range of agents and specifically for asbestos (Kane 1996; Nagai and Toyokuni 2010).

The instillation of a range of fibres within tightly defined length ranges echoes Stanton & Wrench's work with poly-dispersed fibres decades earlier and the results here similarly showed a differential response in terms of pleural inflammation as shown in figure 2. Here we see length dependent inflammation with a very clear threshold for fibres ≥ 5µm in length inducing pleural inflammation whereas none of the shorter fibres (≤ 4 µm) produced an inflammatory response despite considerably different chemical composition. Above the length threshold the response flattened off which may be a consequence of long fibres aggregating in the restrictions of the pleural space. This is the first study showing a quantitative association between fibre length and pleural inflammation using fibres of different kinds in tightly defined length classes. The identified threshold length of 5 µm (Schinwald *et al.* 2012b) provides persuasive experimental toxicological confirmation of a

hypothetical length threshold that had evolved over the previous half century and so represents an important step forward.

2.1. Why Should Mesothelioma Show Such a Distinct Length Threshold?

The explanation for such a dramatic threshold lies in the method of clearance of particles from the pleural space. Whilst several theories for fibre transfer to the pleura exist (Miserocchi *et al.* 2008), the mechanism are not well understood, yet it is apparent that a proportion of all particles that reach the lung periphery transit through to the pleura and clear from the pleural space through stomata that are restricted in size in all mammals to between 2 and 10 µm (Donaldson *et al.* 2010; Murphy *et al.* 2011). Fibres may penetrate through the pleural tissues from sites of deposition in sub-pleural alveoli (Mercer *et al.* 2010). In any case particles that clear through the stomata accumulate in specific mediastinal lymph nodes (Murphy *et al.* 2011). Compact particles that reach the periphery of the lungs are elutriated by their passage through the airways to be less than about 3 µm and so particles of this size that find their way into the pleural space exit readily through the stomata. Fibres longer than 5 µm are still aerodynamically small and reach the distal lung where they can translocate to the pleura. However, their length means they cannot negotiate the stomata and so become trapped and accumulate at the parietal pleura where they can trigger inflammation and could directly cause genotoxicity in mesothelial cells leading in the long term to mesothelioma if the fibres are biopersistent (Donaldson *et al.* 2010). Since the stomata are tightly defined in size there is likely to be a sharp threshold with the physical dimension of the fibres.

2.2. A Single Length Threshold for Lung and Pleural Effects?

The preceding discussion specifically concerns mesothelioma but it is important to understand whether the same fibre length threshold would apply to asbestos-related disease in the lung airways and parenchyma. The pleura is an unusual target for particles yet asbestos and other fibres uniquely

affect this compartment in terms of causing pleural effusion, plaques and mesothelioma; whilst pleural fibrosis is not unique to fibres, fibre are peculiarly potent in inducing this effect compared to other particles. It has been demonstrated that shorter fibres reach the pleura because of translocation/penetration from the site of deposition in sub-pleural airspaces (Mercer *et al.* 2010). As discussed above, the mechanism of size dependent retention in the pleura, constrained due to stomatal size, may also mean that there is a shorter threshold length for inflammation in the pleural space than in the parenchyma. In the airspaces frustrated phagocytosis of macrophages, as demonstrated in figure 3, is the primary mechanism of length-dependent inflammation (Donaldson *et al.* 2010) and this may possess a different length threshold compared to the pleural threshold. Recent data indicate that the same silver nanowires described here have 14 µm as a length threshold for pulmonary inflammation, which is longer than that for the threshold for pleural inflammation (Schinwald *et al.* 2012a). A precautionary approach for exposure assessment would however suggest that the best length standard would be the shortest one, the pleural threshold, since it would protect against lung and pleural effects.

3. The Existing Standard and the New Generation of Industrially Relevant Fibres and Nanofibres

The current Health and Safety Executive standard on asbestos fibre sampling is based on the definition for 'fibres' by the British Occupational Hygiene Society in 1968 whereby countable fibres were defined as particles with a length > 5 µm as determined by a standard membrane filter method (BOHS 1968), which was revised 1971 to include an aspect ratio of 3:1 and a width of < 3 µm in the definition of a fibre (ARC Technical Note No. 1) as described by the WHO reference scheme for man-made mineral fibres (MMMF) in 1985 (World Health Organisation 1985). This standard was chosen arbitrarily to 'allow a margin of safety below the limits of 10-20 µm for pathogenic fibres', the best current opinion held at that point in time (Walton 1982). In the intervening years there has been a suggestion using statistical and deductive evidence of a value for the threshold length but it is

only in the 2012 paper lead by one of the authors that a threshold length for pleural inflammation was finally demonstrated (Schinwald *et al.* 2012b). This was, paradoxically, only achievable by nanotechnological methods for making fibres in clear-cut length categories, whilst the potential asbestos-like threat posed by such novel nanofibres was highlighted early (Royal Society 2004; Service 1998). It is extraordinary that the standard for pathogenic fibres set in 1968, drawn from investigations of workers exposed to various forms of asbestos fibres and early *in vivo* studies on rodents using fibres with a wide distribution of length and set to provide a 'margin of safety,' coincided so accurately with the actual threshold length. If the length had been set higher then hazardous fibres would not have been counted and if it had been set lower an unnecessary penalty could have been applied to industries to comply with an overly-rigorous standard. The fact that synthetic nanofibres were used to define the length threshold highlights that a whole new generation of fibres made from novel materials by nanotechnological methods are being synthesised or are under test for use in industry. There is therefore a distinct possibility that workforces will be exposed to some of these nanofibres in workplace air and hygiene will be mandatory. As summarized by Donaldson *et al.*, high aspect ratio nanomaterials including carbon nanotubes have an exceptionally high annual product growth rate (Donaldson *et al.* 2011). For example, carbon nanotubes (CNT) are now manufactured in more than 140 companies around the world and the main application sector for CNTs is semiconductors and electronics although applications range from sporting goods and military equipment to medical applications and aerospace (futuremarketsinc.com 2012).

3.1. New Fibres and New Measurement Challenges

Currently, to assess inhalation exposure to fibres, air is drawn through a filter onto which the fibres are deposited. The fibres are then counted using an optical microscopy according to a defined method; there are several variants of this method but one widely used approach is that published by

the World Health Organisation (WHO 1997). Only fibres with diameters less than 3 µm with a length greater than 5 µm and an aspect ratio of at least 3:1 are counted. The method incorporates counting rules governing size (as above), number of areas scanned (fields of view), number of fibres scanned, number density of fibres on the collection substrate, and how to deal with "bundled" or overlapping fibres. Typically in assessing occupational exposures, something of the order of 50 to 100 fields of view are counted. Efforts to automate this measurement have not generally been found to be effective and so this process is typically carried out manually and an experienced assessor may count such a sample in around 10 minutes.

The scope of application of the World Health Organisation (WHO) method is broad and it is considered to be appropriate for all natural and synthetic fibres, including the various asbestos varieties, other naturally occurring mineral fibres and synthetic vitreous fibres (WHO 1997). Carbon nanotubes (CNT) and other nanofibres could be considered to fall within the scope of the WHO method and it has been suggested that fibre counting could be an appropriate method to assess exposure to CNT and other types of HARN (2007). However there are several problems with this approach as summarised:

- Optical microscopy is very insensitive for very fine fibres (of diameters less than 200-300 nm) so given that the diameter of nanofibres are in the nano-range and so, substantially less than 300 nm, these would not generally be detected (although bundles, ropes or other aggregations of nanofibres may be).
- Scanning or Transmission electron microscopy may overcome the resolution limitation of optical methods using much higher magnification (2007). However since the size of the field of view is inversely proportional to the square of the magnification used, many more individual field would have to be counted in order to assess the same proportion of the sample. An increase in magnification of 10 would decrease the size of the field of view by 100.

- A further complexity is the higher magnifications employed would (as intended) detect very fine fibres which would not be observed by optical microscopy. This would lead to difficulties in making comparison with limit values for fibres set using optical microscopy.
- Finally, it is clear that many of the forms CNT's observed are highly entangled. Strict application the WHO counting rules would require that touching fibres would not be counted.

Relatively few published studies have attempted to measure particle release and / or occupational exposure to CNTs in workplace settings. Maynard *et al.* looked at the exposures associated with production of single walled carbon nanotubes (SWCNT) and in a simulated mixing operation (Maynard *et al.* 2004). Han *et al.* measured the release of multi-walled carbon nanotubes (MWCNT) during CNT manufacture and in a laboratory scale mixing process (Han *et al.* 2008) whilst Bello *et al.* reported on exposure to CNT during machining of advanced composites containing carbon nanotubes (Bello *et al.* 2009). In addition, Johnson *et al.* measured the release of fullerenes (C60), MWCNT and carbon black during laboratory tasks, weighing and sonication (Johnson *et al.* 2010) and Tsai *et al.* reported measurements during the CNT production by CVD (Tsai *et al.* 2009). A range of measurement approaches were used by these investigators. For example, Bello *et al.* collected samples from the air on to a filter for electron microscopy analysis, but no fibres were identified during the analysis (Bello *et al.* 2009). In contrast, Johnson *et al.* observed clumped MWCNT on filter sample taken close to a laboratory sonication process but did not quantify these (Johnson *et al.* 2010). Other investigators used condensation particle counters (CPC), optical particle counters (OPC) and scanning mobility particle sizers (SMPS) to try to detect the release of CNT although these devices provide no morphological information and are not able to distinguish fibres from other types of particles. Only Han *et al.* used an approach based on the WHO method whereby they collected samples on to a filter, which were analysed by TEM to quantify fibre concentrations. However, despite this, it is clear that in this study not all of the formal WHO counting rules were applied, yet

no statement concerning compliance of these rules was made. Specifically many of the images shown in the paper indicate clumped or overlapping fibres but it is not stated whether or not these were counted. Fibres counted were short; the maximum length of fibres observed was reported as 1.5 µm, which is too small to be considered a fibre under the WHO criteria, where the minimum length of a fibre is 5 µm. Of the samples taken, the 'fibres' were only found in one scenario, blending, and were found on both personal and area samples. The reported number concentration was very high (193.6 and 172.9 fibre.ml^{-1}), although this was reduced by four orders of magnitude when a control system (enclosure) was applied. The German 'Frauenhofer-Informationszentrum Raum und Bau' published guidelines to measure fibrous particles (including chrysotile and amphibolasbest-fibres) using a raster-electron microscopy approach coupled with energy dispersive X-ray analysis (Verein Deutscher Ingenieure 2004). The detection limit of this method is 300 fibres per m^3. These studies indicate that there is potential for applying fibre counting measurement approaches, either by using TEM or perhaps even SEM in order to quantify more effectively the level of exposures however, significant effort will be required to turn this into a viable (e.g. efficient), routine method. Despite these limitations no alternative approaches for assessing fibre number concentration for nanofibres have yet been developed and it is difficult to see how quantification of fibre number concentration could be achieved if not by a method derived from the WHO approach.

Whilst number concentration is the standard and most robust metric for reporting exposure to fibres, mass has classically been used for quantifying all other particulates and for CNT, assessment of release and or exposure in terms of mass has been reported in the literature. Mass based exposure measurements are recommend in the recent NIOSH Current Intelligence Bulletin-Occupational Exposure to Carbon Nanotubes and Nanofibers (NIOSH 2010). The NIOSH approach is based on analysis by NIOSH method 5040 for Diesel Particulate Matter as Elemental carbon (Birch 2002), which by its nature is non-specific for fibrous materials or even carbon nanotubes. This method is based on a thermal-optical analysis technique for organic and elemental carbon (OC and EC). The analysis quantifies total carbon (TC) in a sample as the sum of OC and EC. NIOSH claim an

upper limit of quantitation (LOQ) of NIOSH Method 5040 of 7 $\mu g.m^{-3}$. At the current time there is very little published experience about this method or its utility in quantifying exposure to CNT.

A recent review of approaches to detect and analyse CNT concluded that the ELPI spectrometer may have some utility in this respect (2010). Various off line measurement approaches reviewed by Tantra *et al.* concluded that none were immediately appropriate for measurement of occupational exposure (Tantra and Cumpson 2007). Currently there is no consensus on the most appropriate approach. While mass measurements are clearly possible, much more work is need to routinely detect and quantify CNT and other fibrous nanomaterials.

4. Conclusions

Exposure to pathogenic fibres has left a legacy of disease and suffering that is still with us today. The methods of assessing exposure were developed long before toxicity studies identified the morphological parameters that make fibres hazardous. The method published by the British Occupational Hygiene Society defined countable (relevant) fibres as having a length of 5-100 µm, an aspect ratio of 3:1 and a width of < 3 µm. The lower length cut-off was based on the best available evidence and was chosen arbitrarily to 'allow a margin of safety below the limits of 10-20 µm for pathogenic fibres', the best current opinion held at that point in time (Walton 1982). This has proven serendipitous as the 5 µm cut-off for countable fibres appears to fall exactly at the threshold for fibre retention and pleural effects; with cut-off being both rigorous enough to identify pathogenic fibres whilst not being unduly stringent and encompassing shorter fibres of lower pathogenicity.

Such toxicological corroboration of the current definition and standard is heartening however the very materials technology that allowed the further investigation of this threshold length also heralds new challenges in assessing exposure to new nanofibres. Whilst the threshold length appears to hold firm for nano and non-nano fibres alike, the methods for counting such fibres must be suitable for counting of the small diameter nanofibres, which are beyond the optical resolution of phase contrast optical microscopy. New methods that take heed of the standard counting rules for fibres have been

suggested but the practicality of such methods compared to the robustness and efficiency of the phase contrast optical microscopy still requires investigation.

When considering the interaction between toxicology and exposure science, it is evident that the development of a fibre standard represents a strong synergy between the two disciplines that has allowed the identification of the most appropriate metric and assessment criteria. Wherever possible, such synergy should continue and this is more and more evident when considering the challenges of nanotechnology.

Acknowledgements

This work was funded by the Colt Foundation (A.S. and K.D.).

Figure Legends

Figure 1: Time line of key publications, standards and legislation surrounding fibres.

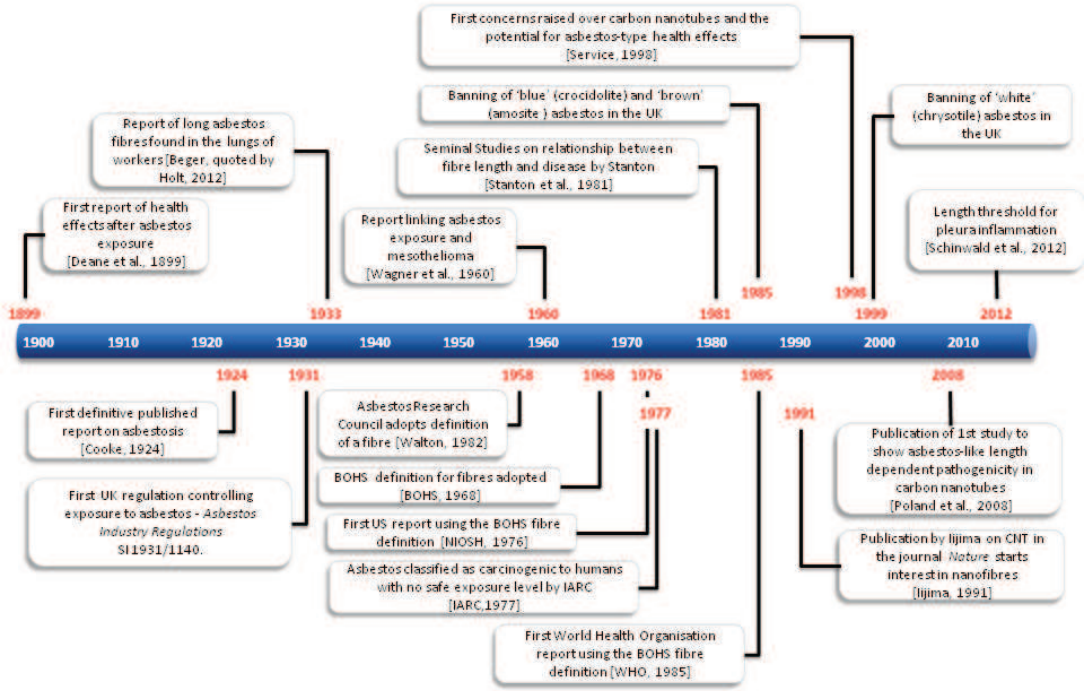

Figure 2: The vertical axis shows the number of neutrophilic leukocytes in the pleural lavage indicative of inflammation. The horizontal axis shows the mean length. There was tight distribution about the mean for all samples expect nanotubes samples which were more dispersed. All labels show the mean length as a subscript - AgNW= Silver nanowires; NiNW = Nickel nanowires; NT= carbon; VC = vehicle control; NPCB = nanoparticulate carbon black; AgP = Silver nanoparticles. Figure from (Schinwald *et al.* 2012b) with permission; see further details (Schinwald *et al.* 2012b).

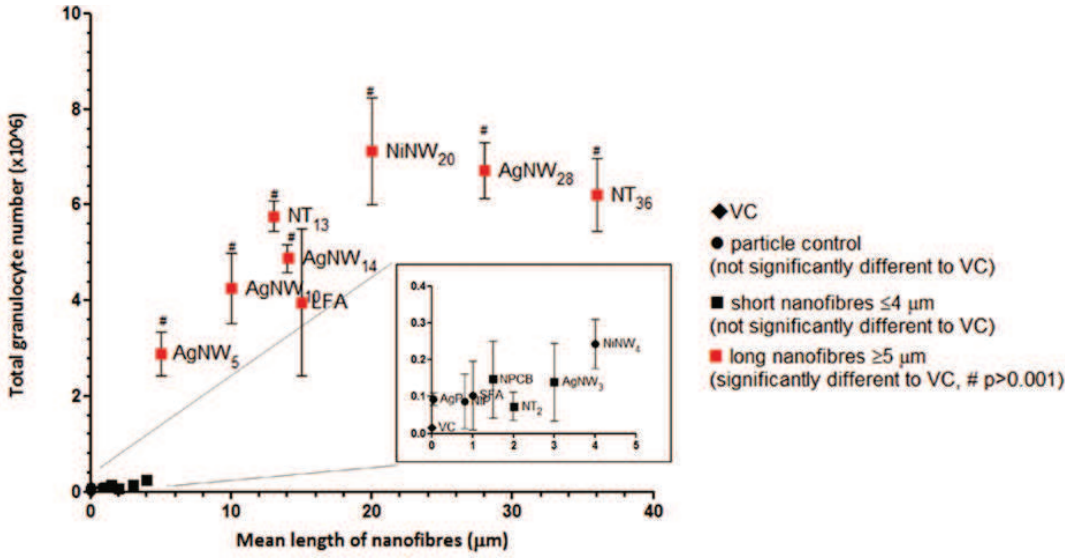

Figure 3: Frustrated phagocytosis by amosite asbestos fibres. Image of rat alveolar macrophages (NR8383 cell line; white arrow) attempting to phagocytose long amosite asbestos fibres (white chevron). The resultant elongation of the cells as demonstrated by the black arrows is the frustration of the macrophage as they attempt to fully enclose the fibre which is much longer than itself. Reproduced with permission from (Donaldson *et al.* 2011).

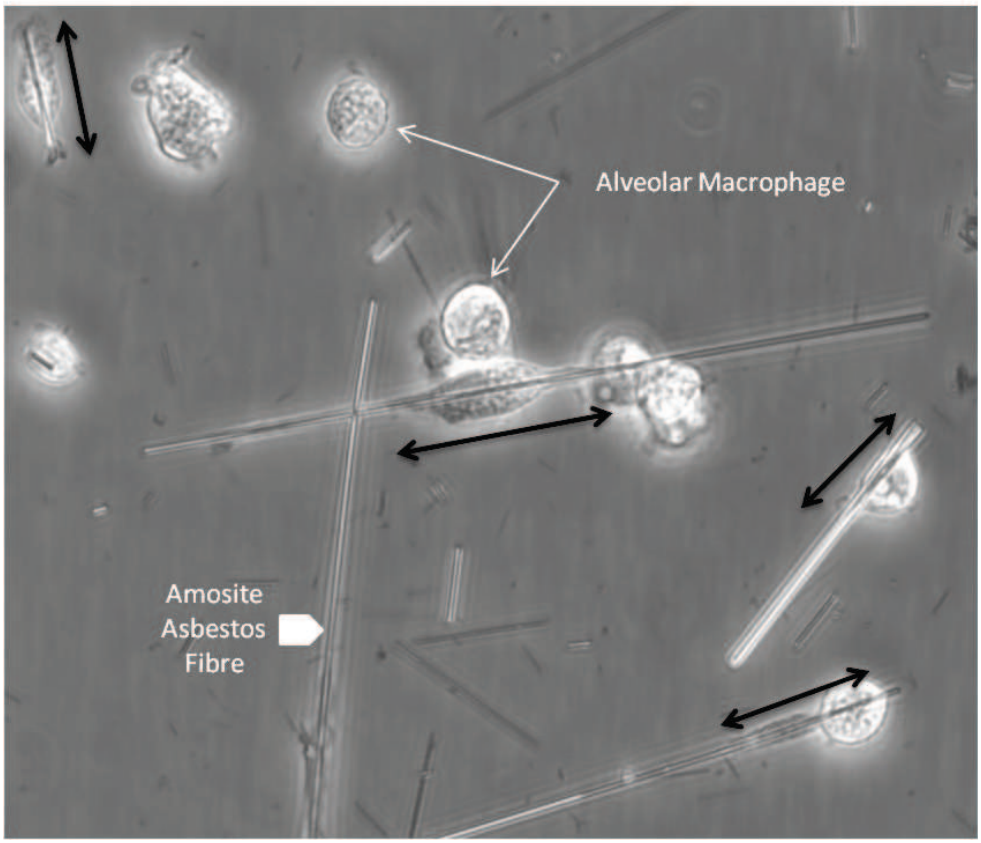

Reference List

Revised Recommended Asbestos Standard. 1976. U.S. Department of Health, Education, and Welfare. Public Health Service, Centre for Disease Control, National Institute for Occupational Safety and Health.

Asbestos. IARC Monographs on the Evaluation of the Carcinogic Risks to Humans. 14, 1-106. 1977. International Agency for Research on Cancer 1977.
Ref Type: Report

Reference Methods for Measuring Airborne Man-made Mineral Fibres (MMMF). 1985. World Health Organization. Regional Office for Europe. Copenhagen.

Nanotechnologies – Part 2: Guide to safe handling and disposal of manufactured nanomaterials. PD 6699-2:2007. 2007. British Standards Institution.
Ref Type: Report

Engineered Nanomaterials Feasibility of establishing exposure standards and using control banding in Australia, Commonwealth of Australia. 2010. SAFEWORK Australia (SWA). 1-9-2010.

Aitken, R. J., Peters, S. A. K., Jones A.D., and Stone, V. (2011). Regulation of Carbon Nanotubes and Other High Aspect Ratio Nanoparticles: Approaching this Challenge from the Perspective of Asbestos. In *International Handbook on Regulating Nanotechnologies* (G.A.Hodge, D.M.Bowman, and A.D.Maynard, Eds.).

Asbestosis Research Council (1968). The measurement of airborne asbestos dust by the membrane filter method. Technical note 1. *Asbestosis Research Council*.

Bello, D., Wardle, B. L., Yamamoto, N., deVilloria, R. G., Garcia, E. J., Hart, A. J., Ahn, K., Ellenbecker, M. J., and Hallock, M. (2009). Exposure to nanoscale particles and fibers during machining of hybrid advanced composites containing carbon nanotubes. *Journal of Nanoparticle Research* **11**(1), 231-249.

Birch, M. E. (2002). Occupational monitoring of particulate diesel exhaust by NIOSH method 5040. *Appl. Occup. Environ Hyg.* **17**(6), 400-405.

BOHS (1968). Hygiene standards for chrysotile asbestos dust. *Ann Occup. Hyg.* **11**, 47-69.

Bolton, R. E., Davis, J. M. G., Donaldson, K., and Wright, A. (1982a). Variations in the Carcinogenicity of Mineral Fibers. *Annals of Occupational Hygiene* **26**(1-4), 569-582.

Bolton, R. E., Davis, J. M. G., Donaldson, K., and Wright, A. (1982b). Variations in the Carcinogenicity of Mineral Fibers. *Annals of Occupational Hygiene* **26**(1-4), 569-582.

Bottomley, P. Health and Safety. The Asbestos (Prohibitions) Regulation 1985. 910, 2844-2847. 12-6-1985. The Stationery Office Limited, UK.

Boutin, C., Dumortier, P., Rey, F., Viallat, J. R., and De, V. P. (1996). Black spots concentrate oncogenic asbestos fibers in the parietal pleura. Thoracoscopic and mineralogic study. *Am J Respir. Crit Care Med.* **153**(1), 444-449.

Burdett, G. (1998). A comparison of historic asbestos measurements using a thermal precipitator with the membrane filter-phase contrast microscopy method. *Annals of Occupational Hygiene* **42**(1), 21-31.

Cooke, W. E. (1924). Fibrosis of the lungs due to the inhalation of asbestos dust. *British Medical Journal* **1924**, 147.

Cugell, D. W., and Kamp, D. W. (2004). Asbestos and the pleura - A review. *Chest* **125**(3), 1103-1117.

Darnton, A. J., McElvenny, D. M., and Hodgson, J. T. (2006). Estimating the number of asbestos-related lung cancer deaths in Great Britain from 1980 to 2000. *Annals of Occupational Hygiene* **50**(1), 29-38.

Davis, J. M., Addison, J., Bolton, R. E., Donaldson, K., Jones, A. D., and Smith, T. (1986a). The pathogenicity of long versus short fibre samples of amosite asbestos administered to rats by inhalation and intraperitoneal injection. *Br. J Exp. Pathol.* **67**(3), 415-430.

Davis, J. M., Addison, J., Bolton, R. E., Donaldson, K., Jones, A. D., and Smith, T. (1986b). The pathogenicity of long versus short fibre samples of amosite asbestos administered to rats by inhalation and intraperitoneal injection. *Br. J Exp. Pathol.* **67**(3), 415-430.

Davis, J. M. G., Addison, J., Bolton, R. E., Donaldson, K., and Jones, A. D. (1986c). Inhalation and Injection Studies in Rats Using Dust Samples from Chrysotile Asbestos Prepared by A Wet Dispersion Process. *British Journal of Experimental Pathology* **67**(1), 113-129.

Deane, L. (1899). Report on the health of workers in asbestos and other dusty trades. HM Chief Inspector of factories and Workshops. *Annual Report for 1898*, 171-172.

Doll, R. (1993). Mortality from lung cancer in asbestos workers 1955. *Br. J Ind. Med.* **50**(6), 485-490.

Donaldson, K., Murphy, F., Schinwald, A., Duffin, R., and Poland, C. A. (2011). Identifying the pulmonary hazard of high aspect ratio nanoparticles to enable their safety-by-design. *Nanomedicine. (Lond).* **6**(1), 143-156.

Donaldson, K., Murphy, F. A., Duffin, R., and Poland, C. A. (2010). Asbestos, carbon nanotubes and the pleural mesothelium: a review of the hypothesis regarding the role of long fibre retention in the parietal pleura, inflammation and mesothelioma. *Part Fibre. Toxicol.* **7:5.**, 5.

futuremarketsinc.com (2012). Applications Chart for nanotubes companies: Nanomaterials Chart #9: Nanotubes. *Online Source: http://www. futuremarketsinc. com/index. php?option=com_content&view=article&id=196:applications-chart-for-nanotubes-companies&catid=21&Itemid=58 (date accessed 21. 11. 2011)*.

Han, J. H., Lee, E. J., Lee, J. H., So, K. P., Lee, Y. H., Bae, G. N., Lee, S. B., Ji, J. H., Cho, M. H., and Yu, I. J. (2008). Monitoring multiwalled carbon nanotube exposure in carbon nanotube research facility. *Inhalation Toxicology* **20**(8), 741-749.

Iijima, S., and Ichihashi, T. (1993). Single-Shell Carbon Nanotubes of 1-Nm Diameter. *Nature* **363**(6430), 603-605.

Johnson, D. R., Methner, M. M., Kennedy, A. J., and Steevens, J. A. (2010). Potential for Occupational Exposure to Engineered Carbon-Based Nanomaterials in Environmental Laboratory Studies. *Environmental Health Perspectives* **118**(1), 49-54.

Johnson, N. F. (1993). Limitations of inhalation, intratracheal and intracoelomic routes of administration for identifying hazardous fibrous materials. In *Fibre Toxicology* (D.B.Warheit, Ed.), pp. 43-72. Academic Press, San Diego.

Kane, A. B. (1996). Mechanisms of mineral fibre carcinogenesis. *IARC Sci. Publ.*(140), 11-34.

KNOX, J. F., and BEATTIE, J. (1954a). Distribution of mineral particles and fibers in the lung after exposure to asbestos dust. *AMA. Arch. Ind. Hyg. Occup. Med.* **10**(1), 30-36.

KNOX, J. F., and BEATTIE, J. (1954b). Mineral content of the lungs after exposure to asbestos dust. *AMA. Arch. Ind. Hyg. Occup. Med.* **10**(1), 23-29.

Kuschner, M., and Wright, A. (1974). The effcts of intratracheal instillation of glass fiber of varying sizes in guinea pigs. *Occupational Exposure to Fibrous Glass. Proceedings of a Symposium Presented by the Center of Adult Education, University of Maryland, College Park, Maryland*, 151-168.

Lippmann, M. (1993). Biophysical factors affecting fiber toxicity. In *Fibre Toxicology* (D.B.Warheit, Ed.), pp. 259-303. Academic Press, San Diego.

Lippmann, M. (1994). Deposition and Retention of Inhaled Fibers - Effects on Incidence of Lung-Cancer and Mesothelioma. *Occupational and Environmental Medicine* **51**(12), 793-798.

Maynard, A. D., Aitken, R. J., Butz, T., Colvin, V., Donaldson, K., Oberdorster, G., Philbert, M. A., Ryan, J., Seaton, A., Stone, V., Tinkle, S. S., Tran, L., Walker, N. J., and Warheit, D. B. (2006). Safe handling of nanotechnology. *Nature* **444**(7117), 267-269.

Maynard, A. D., Baron, P. A., Foley, M., Shvedova, A. A., Kisin, E. R., and Castranova, V. (2004). Exposure to carbon nanotube material: Aerosol release during the handling of unrefined single-walled carbon nanotube material. *Journal of Toxicology and Environmental Health-Part A* **67**(1), 87-107.

Mercer, R. R., Hubbs, A. F., Scabilloni, J. F., Wang, L., Battelli, L. A., Schwegler-Berry, D., Castranova, V., and Porter, D. W. (2010). Distribution and persistence of pleural penetrations by multi-walled carbon nanotubes. *Part Fibre. Toxicol.* **7:28.**, 28.

Miller, B. G., Searl, A., Davis, J. M. G., Donaldson, K., Cullen, R. T., Bolton, R. E., Buchanan, D., and Soutar, C. A. (1999). Influence of fibre length, dissolution and biopersistence on the production of mesothelioma in the rat peritoneal cavity. *Annals of Occupational Hygiene* **43**(3), 155-166.

Miserocchi, G., Sancini, G., Mantegazza, F., and Chiappino, G. (2008). Translocation pathways for inhaled asbestos fibers. *Environ. Health.* **7:4.**, 4.

Murphy, F. A., Poland, C. A., Duffin, R., Al-Jamal, K. T., Ali-Boucetta, H., Nunes, A., Byrne, F., Prina-Mello, A., Volkov, Y., Li, S. P., Mather, S. J., Bianco, A., Prato, M., MacNee, W., Wallace, W. A., Kostarelos, K., and Donaldson, K. (2011). Length-Dependent Retention of Carbon Nanotubes in the Pleural Space of Mice Initiates Sustained Inflammation and Progressive Fibrosis on the Parietal Pleura. *American Journal of Pathology* **178**(6), 2587-2600.

Nagai, H., and Toyokuni, S. (2010). Biopersistent fiber-induced inflammation and carcinogenesis: lessons learned from asbestos toward safety of fibrous nanomaterials. *Arch. Biochem. Biophys.* **502**(1), 1-7.

NIOSH (2010). Draft Current Intelligence Bulletin on Occupational Exposure to Carbon Nanotubes and Nanofibres. *National Institute for Occupational Safety and Health, Centre for Disease Control and Prevention*.

Poland, C. A., Byrne, F., Cho, W. S., Prina-Mello, A., Murphy, F. A., Davies, G. L., Coey, J. M., Gounko, Y., Duffin, R., Volkov, Y., and Donaldson, K. (2012). Length-dependent pathogenic effects of nickel nanowires in the lungs and the peritoneal cavity. *Nanotoxicology.* **6**, 899-911.

Poland, C. A., Duffin, R., Kinloch, I., Maynard, A., Wallace, W. A., Seaton, A., Stone, V., Brown, S., MacNee, W., and Donaldson, K. (2008). Carbon nanotubes introduced into the abdominal cavity of mice show asbestos-like pathogenicity in a pilot study. *Nat. Nanotechnol.* **3**(7), 423-428.

Prescott, J. The Asbestos (Prohibitions) (Amendment) Regulations 1999. 2373. 24-8-1999. The Stationery Office Limited, UK.

Rossiter, C. E. (1991). Fibre carcinogenesis studies: intra-cavitary studies cannot assess risk to man. *Mechanisms of Fibre Carcinogenesis*, 567-578.

Royal Society. Nanoscience and nanotechnologies: opportunities and uncertainties . 2004. Royal Society Publications.

Schinwald, A., Chernova, T., and Donaldson, K. (2012a). Use of silver nanowires to determine thresholds for fibre length-dependent pulmonary inflammation and inhibition of macrophage migration in vitro. *Part Fibre Toxicol.* **9**(1), 47.

Schinwald, A., Murphy, F. A., Prina-Mello, A., Poland, C. A., Byrne, F., Movia, D., Glass, J. R., Dickerson, J. C., Schultz, D. A., Jeffree, C. E., MacNee, W., and Donaldson, K. (2012b). The Threshold Length for Fiber-Induced Acute Pleural Inflammation: Shedding Light on the Early Events in Asbestos-Induced Mesothelioma. *Toxicol. Sci.* **128**(2), 461-470.

Service, R. F. (1998). Nanotubes: The next asbestos? *Science* **281**(5379), 941.

Stanton, M. F., Layard, M., Tegeris, A., Miller, E., May, M., Morgan, E., and Smith, A. (1981). Relation of Particle Dimension to Carcinogenicity in Amphibole Asbestoses and Other Fibrous Minerals. *JNCI* **67**(5), 965-975.

Stanton, M. F., and Wrench, C. (1972). Mechanisms of Mesothelioma Induction with Asbestos and Fibrous Glass. *Journal of the National Cancer Institute* **48**(3), 797-&.

Suzuki, Y., Yuen, S. R., and Ashley, R. (2005). Short, thin asbestos fibers contribute to the development of human malignant mesothelioma: pathological evidence. *International Journal of Hygiene and Environmental Health* **208**(3), 201-210.

Tantra, R., and Cumpson, P. (2007). The detection of airborne carbon nanotubes in relation to toxicology and workplace safety. *Nanotoxicology* **1**(4), 251-265.

Timbrell, V. (1982). Deposition and Retention of Fibers in the Human-Lung. *Annals of Occupational Hygiene* **26**(1-4), 347-369.

Tsai, S. J., Hofmann, M., Hallock, M., Ada, E., Kong, J., and Ellenbecker, M. (2009). Characterization and Evaluation of Nanoparticle Release during the Synthesis of Single-Walled and Multiwalled Carbon Nanotubes by Chemical Vapor Deposition. *Environmental Science & Technology* **43**(15), 6017-6023.

Tweedale, G. (2002). Asbestos and its lethal legacy. *Nat. Rev. Cancer.* **2**(4), 311-315.

Verein Deutscher Ingenieure. VDI 3492. Messen von Innenraumluftverunreinigungen - Messen von Immissionen - Messen anorganischer faserförmiger Partikeln - Rasterelektronenmikroskopisches Verfahren. 2004. Verein Deutscher Ingenieure, Beuth Verlag GmbH.

VORWALD, A. J., DURKAN, T. M., and PRATT, P. C. (1951). Experimental Studies of Asbestosis. *Ama Archives of Industrial Hygiene and Occupational Medicine* **3**(1), 1-43.

Wagner, J. C., SLEGGS, C. A., and MARCHAND, P. (1960). Diffuse pleural mesothelioma and asbestos exposure in the North Western Cape Province. *Br. J Ind. Med.* **17:260-71.**, 260-271.

Walton, W. H. (1982). The Nature, Hazards and Assessment of Occupational Exposure to Airborne Asbestos Dust - A Review. *Annals of Occupational Hygiene* **25**(2), 117-&.

WHO (1997). Determination of airborne fiber number concentration: a recommended method by phase contrast microscopy. WHO, Geneva, Switzerland, ISBN: 924 1544961. *WHO*.

World Health Organisation. Reference Method for Measuring Airborne Man-Made Mineral Fibres (MMMF). 1985. WHO Regional Office for Europe.

Yang, H. N., Testa, J. R., and Carbone, M. (2008). Mesothelioma Epidemiology, Carcinogenesis, and Pathogenesis. *Current Treatment Options in Oncology* **9**(2-3), 147-157.

Review article under submission:

Donaldson K, Poland CA, Murphy FA, MacFarlane M, Chernova T**, Schinwald A. Pulmonary toxicity of carbon nanotubes and asbestos – similarities and differences.** Submitted to Advanced Drug Delivery Reviews.

Pulmonary toxicity of carbon nanotubes and asbestos – similarities and differences

Ken Donaldson[1*], Craig A. Poland[2], Fiona A. Murphy[3], Marion MacFarlane[3], Tatyana Chernova[3], Anja Schinwald[1]

[1]MRC/University of Edinburgh
Centre for Inflammation Research
Queen's Medical Research Institute
47 Little France Crescent
Edinburgh EH16 4TJ, UK

[2]Institute of Occupational Medicine
Research Avenue North
Riccarton
Edinburgh

[3]MRC Toxicology Unit
Hodgkin Building
Lancaster Road
Leicester LE1 9HN
United Kingdom

*Corresponding author
Email Ken.donaldson@ed.ac.uk
MRC/University of Edinburgh
Centre for Inflammation Research
Queen's Medical Research Institute
47 Little France Crescent
Edinburgh EH16 4TJ, UK
0131 242 6580

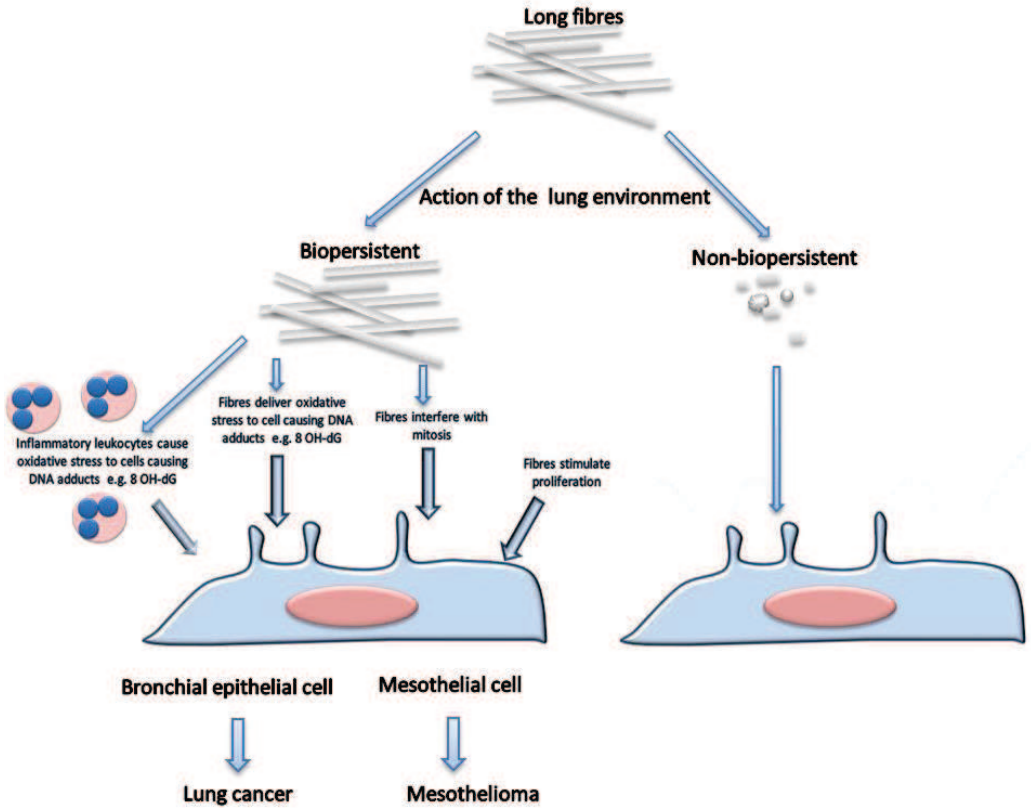

Graphical abstract

1 Introduction

Fibres are very useful to industry and the archetypal industrial fibre was asbestos, first mined in bulk at the end of the 19th century in Canada and rapidly incorporated into many products, structures and buildings. The pandemic of disease that was a consequence of the mining and use of asbestos was met by a huge research effort into toxicology and experimental pathology which attempted to understand how asbestos was pathogenic and what characteristics of the fibre were involved. The banning of asbestos on safety grounds resulted in increased use of 'asbestos substitute' fibres, which had similar or higher performance than asbestos in insulation or other properties; most of these fibres were glassy and eventually classified as Synthetic Vitreous Fibres (SVF). A considerable thrust of research into the relationship between structure of natural and synthetic fibres and their toxicity took place in the 1980s and 90s culminating in 'the fibre pathogenicity paradigm' (FPP). The FPP is a structure:toxicity model that has stood the test of time and it predicts the potential pathogenicity of fibres. The FPP highlights thinness, length and biopersistence as the factors that determine pathogenicity. The overarching question in the modern era of nanotoxicology is whether nanofibres of different types, especially carbon nanotubes in the context of the present article, conform to the FPP. This article describes the FPP and uses it as a framework for assessing the similarities and differences between asbestos and CNT.

2 Not all carbon nanotubes are in the form of fibres

CNT can exist as particles if they have defects and therefore 'grow' as tangles, like balls of string. Whilst the CNT in such bundles are tubular, they are particulate as far as cells are concerned, since the bundles of tubules are in a compact form. However, if the CNT have few defects, the tubules can grow straight and the CNT can adopt a fibrous, high-aspect shape [1,2]. We have demonstrated that the long CNT behave like fibres causing effects such as frustrated phagocytosis leading to pathogenicity, whilst short or tangled ones do not behave like fibres in this sense [2-4]. It is therefore important to define whether any CNT exposure is to CNT in the form of fibres or particles and for these reasons, the following discussion pertaining to CNT and the FPP only relates to CNT in a fibrous shape.

3 Pathogenic effects of fibres

Exposure to asbestos causes the human diseases shown in Figure 1, demonstrating the unique proclivity of asbestos in causing pathogenic effects in the pleura as well as in the lungs themselves. In animals, asbestos and some other fibres cause similar types of pathology. Asbestosis is a bilateral interstitial fibrosis with accumulation of fibrous/scar tissue in the interstitium of the lung,

obstructing the diffusion of gas from the blood to the airspaces and restricting lung expansion. Bronchogenic carcinoma is a malignant cancer of the cells lining the bronchi or airways and is the same as the lung cancer that is common in smokers. Mesothelioma is an unusual tumour arising from the mesothelium lining the pleural space that is slow–growing and that does not metastasise and so is well- advanced before diagnosis leading subsequently to a very poor prognosis. Pleural fibrosis is a diffuse accumulation of scar tissue in the pleura that may lead to pleural effusion, an accumulation of fluid in the pleura seen in individuals exposed to asbestos. Pleural plaques are raised hard fibrous lesions that arise on the parietal pleura that are smooth and composed of a basketwork of pure collagen; they are almost acellular that do not appear to cause any adverse effects on the lungs. Since, in the classical toxicology, paradigm response follows dose it is evident that fibres depositing in the lungs accumulate to high dose at various sites in the lining epithelial cells and parenchyma, leading to the pulmonary effects and that they accumulate in the pleura, where they cause the pleural pathologies described in Figure 1 and below.

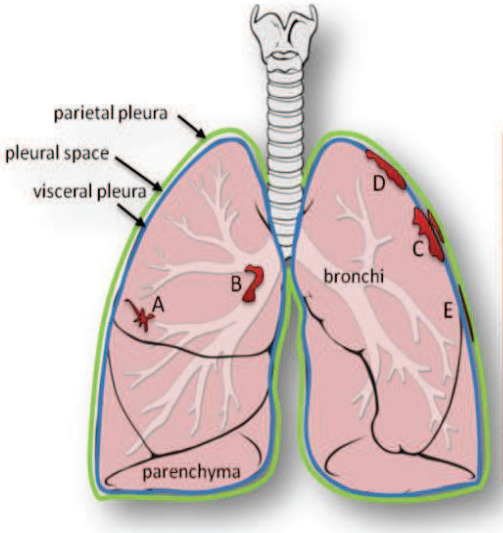

Label	Pathology	Site
A	Asbestosis	Parenchyma
B	Bronchogenic carcinoma (lung cancer)	Bronchi
C	Mesothelioma	Pleurae
D	Pleural fibrosis	Pleurae
E	Pleural plaque	Parietal pleura

Figure 1 Diagram showing the situation of the types of pathology caused by fibres

4 Fibre characteristics and disease; the fibre pathogenicity paradigm

Not all fibres are equally pathogenic as pathogenicity depends on the structure and composition. Decades of fibre toxicology have led to an over-arching fibre toxicology structure:activity paradigm involving diameter, length and biopersistence that is reviewed elsewhere [5,6] termed the Fibre

Pathogenicity paradigm (FPP). The FPP recognises the geometry of fibres as their most important toxicological characteristic and not the chemical make-up, except in so far as the composition makes a contribution to biopersistence (see later). Independence from composition means that the paradigm embraces fibres composed of a number of diverse materials including amphibole and serpentine asbestos, vitreous and ceramic fibres and an organic fibre (reviewed in [5]).

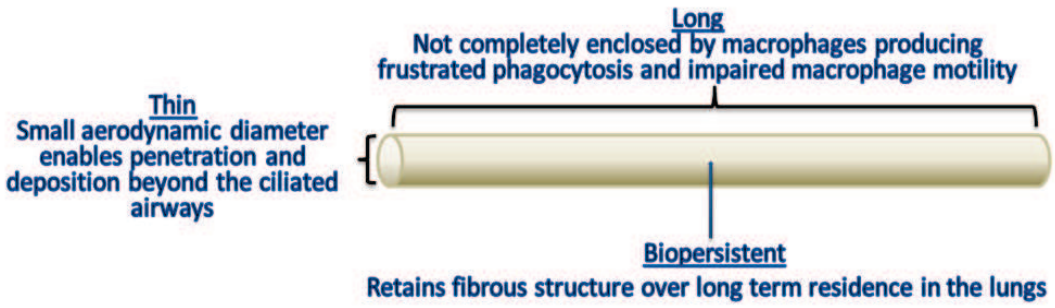

Figure 2 Diagram summarising the fibre pathogenicity paradigm. Three biophysical characteristics govern whether a fibre will be pathogenic – length, thinness and biopersistence (see text for clarification)

3.1 Diameter

The central role of diameter is in the important relationship it has with aerodynamic diameter (D_{ae}) which dictates the efficiency and site of pulmonary deposition [7]. The fact that fibres longer than 50μm can reach and deposit beyond the ciliated airways is explained on the basis that, regardless of length, the D_{ae} of a straight fibre is around 3 times its actual diameter [6]. Thin fibres equal to or less than about 1μm in diameter are therefore 'respirable' and can deposit beyond the ciliated airways. Clearance from beyond the ciliated airways is effected by slow, macrophage-mediated clearance and so fibres which deposit there have the potential to contribute most to build-up of dose.

3.2 Length

Length impacts little on D_{ae} [8] of respirable fibres except when length is sufficient to cause interception, a mechanism of particle where the tip of a fibre makes contact with the wall, resulting in deposition. This means that long fibres can readily penetrate beyond the ciliated airways. The evidence demonstrating that length is a key factor in pathogenicity of fibres comes from a number of sources but the best data are from experimental toxicological studies where it is possible to

characterise the length of the fibres in the exposure or isolate length categories and assess their effects; this approach contrasts with the poorly-characterised nature of human exposures. In the seventies Stanton implanted fibres of various types and lengths directly onto the pleural mesothelial surface [9,10] and identified that carcinogenicity was related to biopersistent fibres longer than about 8μm [9]. Davis et al. exposed rats for one year to long and short amosite asbestos fibres and there was a substantial tumour and fibrosis response in the rats exposed to the long amosite, but virtually no response in rats exposed to the short amosite [11]. Adamson et al. used long and short crocidolite and following deposition in mouse lungs reported fibrosis [12] and proliferative responses [13] at the pleura with the long, but not the short samples. The mouse peritoneal cavity has been used as a model of direct mesothelial exposure and much greater toxic [14], inflammatory [15] and granuloma-generating [16] responses were evident in mice that were exposed to long fibres than was seen with shorter fibres. In vitro systems have also demonstrated the greater potency of long compared to short fibres in assays of pro-inflammatory and genotoxic activity [17-19].

Length also affects retention, with long fibres being retained with a much longer retention half-time than short fibres [20,21]. In the lungs this is a consequence of :-

a) long fibres not being completely enclosed by macrophages [22] leading to frustrated phagocytosis (see below) and inflammation producing chemotaxins that retain the long fibre-loaded macrophages [4] preventing migration to the mucociliary escalator
b) direct effects of long fibres in inhibiting macrophage locomotion [23].
c) long fibres that reach the pleural space being retained at the parietal pleura stomata [3].

3.3 Biopersistence

The biopersistence of a particle is defined as its ability to resist damage or modification that would substantially alter its structure within tissue such as the lungs. Since long fibres are the effective dose (see above), it is the action of the lung milieu on long fibres that is most important for fibre-specific effects. Non-biopersistent fibres that do not release toxic ions or other components undergoing dissolution dissolve, break and shorten. However a soluble fibre releasing toxic/reactive components may generate localised or even systemic accumulation and toxicity; this especially applies to contaminating bioavailable metals [24]. Soluble ion release has been shown to be a cause of toxicity for particles [25]. The role of biopersistence in fibre effects is well understood and has been shown to have a profound effect on the clearance and toxicity of fibres [21]. For example McConnell and colleagues reported on a long-term (78 wk) inhalation study comparing SVF of differing solubilities, with insoluble amosite asbestos on an equal fibre number basis. They found that the type and severity of pulmonary and pleural effects differed between the samples in direct

relation to *in vitro* dissolution rates - "the faster the dissolution, the lower were the cumulative lung burdens and the less severe the effects" [26]. Within the lung, the less durable fibres may split longitudinally, as seen with fibrils of chrysotile asbestos, or break transversely as in the case of glass fibres making it possible for these to be cleared by alveolar macrophages leading to the removal of long fibre dose. Alternatively they may dissolve in the milieu of the lung, especially the acidic environment of macrophage phagolysosomes resulting in weakening and breakage.

The use of such results in developing safer insulation products by altering biodurability is well described in a review article by Hesterberg [27] and shows the importance of considering physico-chemical properties in designing materials that are 'benign-by-design' which is of great relevance to manufactured nanomaterials.

For the above reasons the durability of carbon nanotubes has come under scrutiny. In one study, single walled carbon nanotubes were exposed to a simulated phagolysosmal fluid (pH 4.5) for 90 days in vitro (with the addition of H2O2 to simulate the oxidising environment). The conclusion was that durabilty was dependent on nanotube functionalization with carboxylated nanotubes undergoing degradation leading to length reduction whilst unmodified, ozone-treated, and aryl-sulfonated nanotubes did not [28]. The suggested explanation for this was that the act of carboxylation causes damage to the graphenic backbone resulting in the formation of active sites that provide points of attack for further oxidative degradation [29]. A similar mechanism may have been in action when carboxylated single-walled carbon nanotubes were shown to be catalytically degraded over several weeks by horseradish peroxidase whilst hypochlorite and reactive radical intermediates of myeloperoxidase also catalysed the degradation of single-walled carbon nanotubes in vitro [30].

Using a similar in vitro approach, Osmond-McLeod and colleagues [31] compared the durability of 1 single walled carbon nanotube sample and 3 multi-walled carbon nanotube samples to that of soluble and non-soluble control fibres. They found that after 24 weeks agitation in simulated phagolysosmal fluid (pH 4.5) the control fibres behaved as expected with the bio-soluble glass fibres and chrysotile asbestos both losing appreciable mass whilst the durable amosite asbestos did not. Three out of 4 of the carbon nanotubes tested showed no or minimal loss of mass or change in fibre length or morphology but one multi-walled carbon nanotube sample lost 30% of its original mass within the first three weeks of incubation, after which there was no further loss. The authors then, assuming no reduction in fibre mass, injected these samples into the peritoneal cavity of mice and noted that a loss of mass and fibre shortening was accompanied by a loss of pathogenicity when compared to fibres incubated briefly. This approach mirrored a similar study by Donaldson [32] whereby non-biopersistent fibres pre-treated in a physiological buffer at pH 5.0 or 7.0 to mimic

residence in the lung lost some inflammogenic potential. What these studies show is that similarly to pathogenic and non-pathogenic fibres, carbon nanotubes can vary in their durability and this has implications for their long-term residence and toxicity. Interestingly, surface modification of the carbon nanotubes is a major factor in enhancing biosolubility and hence offers a method of reducing potential toxicity.

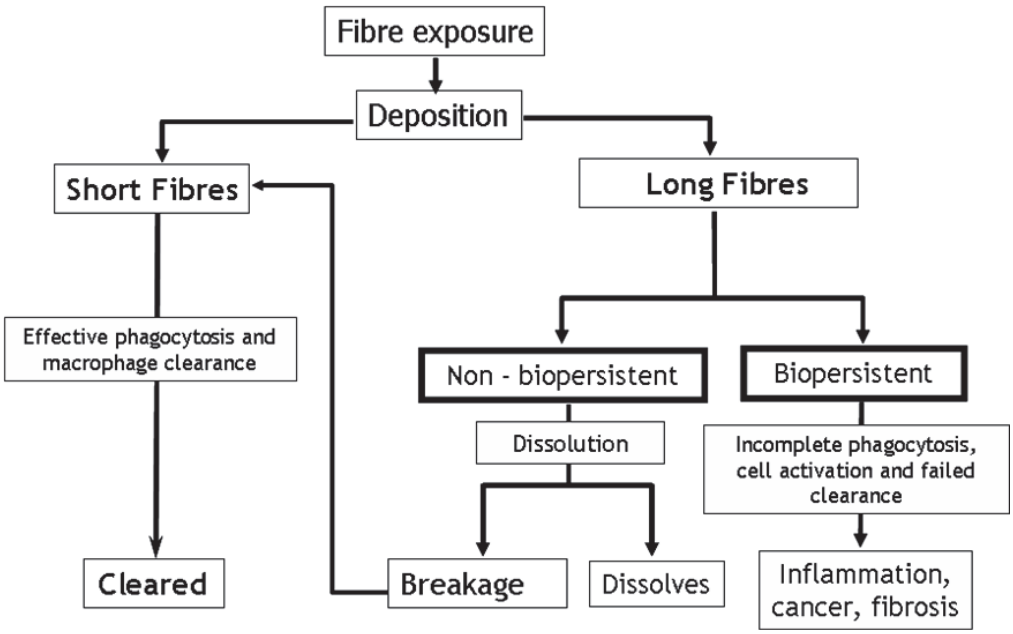

Figure 3 Summary of how length and biopersistence interact to lead to the accumulation of long biopersistent fibres as the effective dose for inflammation, cancer and fibrosis.

5 Fibres and the lungs

The accumulation of long fibres in lung tissue can lead to numerous adverse responses including oxidative stress, inflammation and genotoxicity which if sustained may manifest as more severe lung pathologies including fibrosis, i.e. asbestosis, and lung tumours [33]. Although lung disease associated with CNT exposure has yet to be identified in human populations, rodent studies

examining the pulmonary toxicity of CNT have revealed a pattern of effects similar to those observed following exposure to asbestos including acute neutrophilic inflammation [34,35], cytokine production [35], granulomatous inflammation [36,37], interstitial thickening [38] and fibrosis [35,39]. No study has as yet reported the presence of lung tumours in CNT-exposed animals primarily due to the short-term nature of the majority of these studies; however short-term endpoints such as inflammogenicity and fibrogenicity may have the potential to predict long-term carcinogenicity [40].

Considerable evidence suggests that reactive oxygen species (ROS) such as hydrogen peroxide (H_2O_2), superoxide anion ($O2^-$) and the hydroxyl radical ($HO^{\cdot}$), and reactive nitrogen species (RNS), which can be generated directly by the fibres themselves or indirectly through interactions with inflammatory cells, are important mediators of asbestos toxicity [41,42]. Direct release of free radicals from the asbestos fibres is mediated by iron integrated into the crystalline structure of the asbestos fibres which can contribute to redox-cycling reactions leading to the production of damaging hydroxyl radicals [43]. Similarly in a number of studies the pro-inflammatory response to CNT in the lung has been attributed to the presence of contaminating transition metals, a by-product CNT synthesis, or structural defects in the CNT generating free bonds in the graphenic backbone of the CNT [44].

A second mechanism by which asbestos fibres can increase lung ROS and oxidative stress is by activating inflammatory cells recruited to the site of asbestos deposition. As discussed above, a low aerodynamic diameter will allow deposition of even very long fibres beyond the ciliated airways in the pulmonary regions of the lung, where clearance is mediated by alveolar macrophages. However, if fibres exceed the maximal length a macrophage can enclose (~15 µm see [23]) the macrophage will be unable to successfully remove the fibre and become 'frustrated'/pro-inflammatory. Frustrated phagocytosis is accompanied by the release of oxidants [45] and cytokines [46,47] as well as lysosomal destabilisation [48], increasing recruitment of inflammatory cells to the lungs and activating the surrounding epithelial cells, leading to an inflammatory response. The ability of long CNT to stimulate frustrated phagocytosis in macrophages *in vitro* has been described in studies which have shown specific length-dependent increases in the release of superoxide anion and pro-inflammatory cytokines after macrophages were treated with long fibre-containing CNT samples [4,46].

Asbestos-induced free radicals activate signalling cascades and cause DNA damage that results in altered gene expression and cellular toxicity important in the pathogenesis of asbestos associated

pulmonary diseases [49]. Alternatively fibres may also prove to be directly genotoxic where long fibres may physically interfere with mitosis by interacting with the mitotic spindle and chromosome segregation resulting in aneuploidy in daughter cells [33]. There is evidence analogous to asbestos that CNT can interfere with normal mitosis leading to the induction of aneuploidy. Treatment of airway epithelial cells with SWCNT in vitro led to a variety of genetic abnormalities including multiple mitotic spindle poles, anaphase bridges and aneuploidy [50]. Due to the small diameter of the SWCNT the authors proposed that the similarity in structure may have allowed the incorporation of the SWCNT into the mitotic spindle leading to abnormal cell division. Fibres can also stimulate proliferation that contributes to neoplastic change [51] (Figure 4).

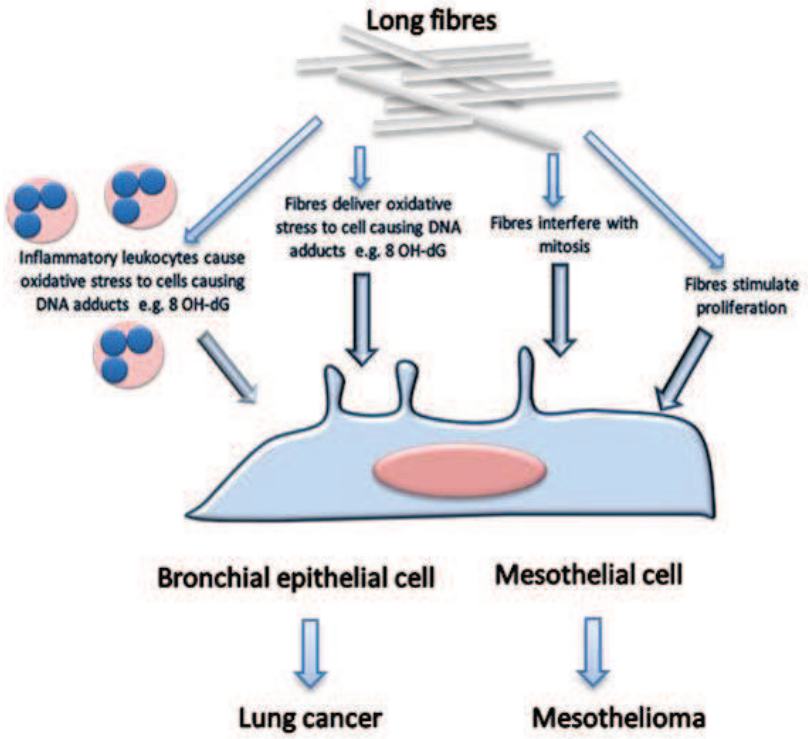

Figure 4 Diagram summarising the hypothesised mechanistic events mediated by long fibres that lead to genotoxic and carcinogenic effects in bronchial epithelial or the mesothelial target cells.

6 Fibres and the pleura

Anatomy and function of the pleural space

The pleura is the serous membrane that covers the lung parenchyma, the mediastinum, the diaphragm and the rib cage. The pleura is divided into the visceral pleura which covers the lung parenchyma with its interlobar fissures and the parietal pleura which lines the inside of the thoracic cavities. The parietal pleura is composed of connective tissue layers covered by a monolayer of flat and cuboidal mesothelial cells [52]. The pleural space is the cavity between the visceral and parietal pleura and contains a film of pleural fluid which acts as a lubricant during respiratory movements while avoiding direct contact between visceral and parietal mesothelial surfaces, thus preventing cell damage. Pleural fluid or lymph drains from the parietal pleura via numerous lymphatic vessels in the pleural connective tissue layer which start off as gaps within the endothelial lining, called lymphatic stomata. These stomata have a diameter of 2-12 µm and are predominantly found in the dorsal, caudal intercostal spaces and to a lesser degree in the ventro-cranial region of the pleura [53]. Across mammalian species there is a remarkable consistency in the reported size of stomata on the diaphragm or parietal pleura as summarized in [54]. Through stomata the pleural fluid flows directly into the lumen of the lymphatic vessels [55] which run along the intercostal spaces and drain towards nodes near the head of the ribs.

The report confirming the link between asbestos exposure and mesothelioma development in the pleural space appeared in 1960 by Wagner et al. [56] who made a connection between asbestos exposure and mesothelioma in the asbestos fields in North Western cape province [56]. In addition to mesothelioma, other forms of pleural diseases such as pleural effusion, a build-up of pleural fluid due to an imbalance of influx and efflux of fluid in the pleural space [57], and pleural plaques, areas of hyaline fibrosis, were recognised as asbestos exposure-related disease in the pleural space.

In an extensive study by Stanton & Wrench in 1972 the role of fibre length, diameter and composition of a range of fibrous materials including asbestos, fibrous glass and aluminium oxide was investigated. The fibres were surgically introduced onto the pleural surface in a gelatine pledget [58,59] and the pathological outcome was that carcinogenicity was related to fibres with a length between 10 and 80 µm and a diameter below 2.5 µm; it was notable that the physiochemical properties of the fibre samples had no influence on the carcinogenicity outcome [58,59]. A threshold length ≥ 10 µm for pathogenic fibres was hypothesised and became known as the 'Stanton hypothesis'. This was modified downwards when Timbrell showed that exposure to asbestos fibres from the Northwest Cape in Africa with virtually no fibres greater than 10 µm was associated with numerous mesothelioma cases [60] .

This length-dependent relationship of fibre exposure in the pleural space and disease development was recently further investigated by one of the authors (FM), comparing the severity of pleural

inflammation in response to carbon nanotubes or amosite asbestos fibres after direct intra-pleural injection [61]. The study compared different forms of multi-walled CNT including two tangled and a short CNT, which were composed of non-fibrous material and two long CNT, with a mean length of 13 μm and up to 56 μm. Short and long amosite asbestos fibres (SFA/LFA) and nanoparticulate carbon black (NPCB) were included as control fibres/particles [62]. This study demonstrated that CNT, like asbestos, exhibit length-dependent pathogenicity. This was evident in the findings that long CNT caused a substantial inflammatory response in the pleural space and granuloma formation on the diaphragm and parietal mesothelial layer up to 24 weeks, similar to the response observed after exposure to LFA fibres. Even though this study provided valuable insight into the inflammatory potential of CNT, the threshold length for pleural inflammation could not be determined. Therefore, a follow up study used silver nanowires and nickel nanowires purpose-synthesised in very distinct length classes [54] was carried out. This study revealed a cut-off length for nanowires in causing acute pleural inflammation after direct intra-pleural injection, with 4 μm being non-inflammogenic and ≥ 5 μm being inflammogenic [54]. This clear threshold can be explained by the clearance mechanism from the pleural space through stomata as discussed above. Even though the study on the threshold length was a short term inflammation study, the results can predict long term effects based on the above argument that only retained fibres can cause inflammation and inflammation is implicated in the development of asbestos related cancer [33,63]. Overall, the latest studies performed on predicting the pathogenicity of newly designed high aspect ratio nanomaterials in relation to asbestos fibre exposure in the pleural space showed that nanofibres may pose an asbestos-like hazard if they are if they are long enough to be retained as well as biopersistent. Although carbon nanotubes were not available in strict length classes the generality of the length threshold for nanofibres was demonstrated and it may be assumed that any fibre or nanofibre that is longer than 5μm, is less than 1um in diameter and is biopersistent poses a risk of causing asbestos –like pathogenicity i.e. causing flung fibrosis, lung cancer and pleural disease including mesothelioma and pleural fibrosis.

7 Use of the peritoneal cavity to study mesothelioma –inducing potential

The peritoneal cavity has long been used as a model for fibre pathogenesis spanning the eras of asbestos, synthetic vitreous fibres and most recently, engineered nanofibres. The rationale for the model is simple yet often misinterpreted and misunderstood. It can be summarised by the fact that some fibres cause pathogenic effects in the pleural space and can give rise to mesothelioma but it is difficult to introduce fibres into the pleural space, although this issue has recently been much

improved via a direct injection technique developed by some of the authors [3]. The peritoneal cavity is the other mesothelium-lined coelomic cavity and therefore provides an easily –accessed and logical surrogate for the pleural cavity. The clearance mechanisms from the pleural space and the peritoneal cavity are strikingly similar being mediated through size (2 to 12 μm [64]) restricted clearance via pore-like structures called stomata which overlie a specialised network of sub-mesothelial lymphatic channels (reviewed in [5]). The relevance of this similarity in structure and clearance mechanisms between these two serosal cavities is that particles which cannot negotiate the narrow (2-12 μm) stomatal openings are retained where they can interact with the mesothelium as well as inflammatory cells and generate a pathogenic response.

The peritoneal assay has been used for decades and was initially used to compare between asbestos types. Long -term studies focused on the development of mesothelioma as the endpoint of interest whilst shorter term ones examined inflammation and fibrosis. Although there were early acute high dose studies it was the studies of the late 1980's to early 2000's which marked the main use of the peritoneal assay for the purpose of understanding the basis of fibre pathogenicity. One such study is that of Moalli [16] who looked at the role of length on the acute toxicity of asbestos fibres to the mesothelium using a single injected dose of long or short crocidolite or silica/ titanium dioxide as non-fibrous toxic and non-toxic particles respectively. The authors noted that within 6 hours the short asbestos fibres, silica and titanium dioxide particles (all <μm in size) were cleared through the stomata without causing an inflammatory reaction or mesothelial injury. In stark contrast, the long asbestos fibres were trapped at the draining stomata and provoked an intense inflammatory reaction including accumulation of activated macrophages at the mesothelial surface and localised mesothelial cell death [16]. In a later study, the authors showed that 5 daily injections of short fibres eventually blocked the stomata and short fibres were then retained [14]. These studies first showed that retention and accumulation of long fibres at the mesothelial surface is key to the elicitation of inflammation/ fibrosis. Whilst early studies showed the role of length and in fibre toxicity in the peritoneal cavity the general applicability of the length paradigm was later shown for carbon nanotubes and other nanofibres [2]. The first study published using the peritoneal model for carbon nanotubes [65] used a susceptible p53 +/- mouse model to study the ability of carbon nanotubes to generate mesothelioma. The authors injected a large dose (3 mg) of long carbon nanotubes into the peritoneal cavity or crocidolite as a positive control and C60 fullerenes as a carbon control. The authors reported large granuloma formation and the induction of mesothelioma in the asbestos and carbon nanotube-treated mice yet a minimal response in the fullerene treated mice. However, the exceptionally large dose resulted in the formation of large agglomerates (reported as 50-200μm in diameter), drawing the relevance of such results into question. Shortly after this a study was

published using wild-type mice and much lower doses (50μg/mouse) of long carbon nanotubes in comparison to compact nanotubes with, carbon black as well as short and long amosite asbestos as controls. Similarly to the Moalli study, this work showed length dependent retention of long carbon nanotubes and asbestos but not short at the mesothelial surface resulting in a rapid induction of inflammation, accumulation of macrophages leading to the formation of foreign body giant-cell granulomas [2]. The importance of the consideration of length was evident in a study where carbon nanotubes were injected into the peritoneal cavity of rats at a dose of 2 or 20 mg and observed over a period of 24 months for mesothelioma. The results showed no significant mesothelioma yield [66] but the carbon nanotubes used were very short , 0.7μm in length, far shorter than the fibres used in the Moalli or Poland studies. Currently, the it is not known if the early inflammatory and fibrotic response to CNT in the peritoneal cavity are portents for the induction of mesothelioma. However the similarity in response to asbestos and role of length in the structure:toxicity relationship seen for carbon nanotubes still raises considerable concerns and shows the need for targeted definitive studies.

As a model, the peritoneal cavity is useful but interpretation of results should be performed with care and in light of these caveats. Specifically these are that injection into it is non-physiological and at high dose and dose-rate, the dose normally reaching the pleura from the distal airspaces at very low dose rate and dose. In addition, biopersistence as it impacts the fibre in transit from the deposition site to the pleura (dealt with elsewhere in this article) is not taken into consideration during direct injection and fibre diameter which is important for fibre deposition into the lung may not be taken into account. However all models are subject to caveats and this does not diminish their utility as long as they are taken into consideration during interpretation.

8 Molecular changes associated with asbestos or CNT in the pleural mesothelium

***7.1 in vitro* findings** The molecular mechanisms leading to mesothelial cell transformation and the development of mesothelioma are unclear. It has been suggested that there may be a gradual progression from mesothelial hyperplasia to mesothelioma, with intermediate stages characterised by the presence of fibrous adhesions and pleural nodular lesions [16,67] thus highlighting the likely role for chronic inflammation in mesothelioma carcinogenesis. However, characterization of the sequential changes preceding the onset of mesothelioma in animal models is limited and therefore as yet the key molecular mechanisms driving these events are unknown.

Efforts have been made to delineate the molecular mechanisms contributing to the transformation of mesothelial cells using *in vitro* models. After direct interaction with mesothelial cells, asbestos fibres trigger a number of signalling cascades involving mitogen-activated protein kinases (MAPK) and nuclear factor-kappa B (NF-κB) [68,69]. The activation of MAPK and NF-κB signalling pathways, either directly by binding of asbestos fibres to surface signalling receptors or indirectly via oxidative stress, has been shown to cause the activation of multiple transcription factors such as activator protein-1 (AP-1) which promote cellular responses such as proliferation and pro-inflammatory changes [70]. In particular, the sustained activation of MAPK signalling in asbestos-exposed mesothelial cells has been linked to the induction of Fra-1, a component of the AP-1 complex that is causally related to anchorage-independent growth in mesothelioma cells [71]. To date, even less has been done to examine the pro-carcinogenic changes induced in mesothelial cells upon exposure to CNT. However, similar to asbestos fibres, direct effects of SWCNT and MWCNT on normal and malignant mesothelial cells include a decrease in cell viability, activation of pro-inflammatory transcription factors and pro-inflammatory MAPK pathway activation [72,73].

Although direct exposure of mesothelial cells to asbestos fibres *in vitro* has been shown to induce sustained signalling pathway activation [74,75], inflammatory mediator production [76], oxidative stress [77], genotoxicity and chromosomal changes [78,79], exposure of normal human mesothelial cells to asbestos fibres *in vitro* has not been shown to lead to cell transformation. The essential role played by the chronic inflammatory environment in tumorigenesis has been demonstrated by Wang *et al* [80] who examined the transformation potential of erionite, a naturally occurring long biopersistent fibre which causes mesothelioma in man and rodents [81-83]. While erionite alone had no effect on mesothelial cell transformation, a cocktail of pro-inflammatory cytokines, IL-1β and TNFα, could stimulate anchorage-independent growth of mesothelial cells in soft agar; a marker of mesothelial cell transformation [80]. The pro-inflammatory cytokine, TNFα, has also been shown to inhibit asbestos-induced cell death by activating the NF-κB signalling pathway in mesothelial cells [76]. This led the authors to propose that the activation of NF-κB and subsequent activation of multiple pro-survival genes allows mesothelial cells with asbestos-induced DNA damage to divide and proliferate rather than die and, if key genetic alterations accumulate, to eventually develop into mesothelioma [76].

The pro-inflammatory cytokines which support cell transformation may be released by the mesothelial cells upon direct exposure to pathogenic fibres [76], or alternatively be released from immune cells recruited to the area to clear the fibres. A recent study demonstrated that, although

the mesothelial cells were refractory to treatment with CNT directly, exposure to conditioned media from macrophages undergoing frustrated phagocytosis after treatment with long fibres stimulated a potent pro-inflammatory response from the mesothelial cells [84]. It is well documented that cross-talk between macrophages and mesothelial cells is important in the normal inflammatory and repair processes in the serosal cavities [85]; however, if these processes are aberrantly sustained due to the presence of biopersistent fibres, they may also help to promote the development of mesothelioma. This highlights the need to examine both the effects of direct interactions between fibres and mesothelial cells and also the role of the activated immune cells on normal mesothelial cells when considering the molecular mechanisms leading from mesothelial cell activation to transformation.

***7.2 in vivo* findings** Most *in vivo* studies that have assessed the carcinogenic hazard of CNT in intact or genetically modified rodents have been limited to obtaining histological evidence of tumour development [84,86-88]. Although the histological changes observed are similar to those induced by asbestos exposure in murine models and faithfully replicate human mesothelioma, the molecular mechanisms involved and how they compare with asbestos-induced tumours in animals or humans are yet to be investigated. It is well documented that CNT cause sustained inflammation of the parietal pleura [84,89,90]. However, recent studies have highlighted that the molecular changes underlying CNT-induced carcinogenesis need to be examined in the context of a cross-talk and co-dependence of different cell types in the exposed tissues. Up-regulation of genes encoding cytokines (IL-1β, IL-6) in macrophages after injection of MWCNT in the rat peritoneal cavity [91], and an elevated release of cytokines and chemokines as part of the inflammatory response to intratracheal instillation of CNT in mice [92], suggest that mesothelial cells are subjected to persistent stimulation by inflammatory factors. The recruitment of macrophages to the exposure site (e.g. subcutaneously injected MWCNT in the model used by Yang et al) is a continuous process [93] that would be accompanied by persistent interaction of the inflammatory factors with membrane molecules, for example RTKs and growth factor receptors, causing sustained activation of pro-oncogenic pathways and eventually leading to epithelial-mesenchymal transition (EMT) [94]. Alternatively, an epigenetic switch could provide another mechanism whereby CNT-induced carcinogenesis develops following chronic inflammation. In support of this, our recent *in vivo* findings have shown a sustained activation of STAT3 in CNT-induced inflammatory lesions in a pleural instillation model (unpublished data) and, in another independent study, STAT3 activation was demonstrated to connect chronic inflammation and cancer *via* an epigenetic switch *in vitro* [95]. In addition, the tissue response to MWCNT exposure *in vivo* (intratracheal instillation) included changes in apoptosis- related proteins

(p53 and caspase-3) and tissue damage-associated proteins (COL1A1, MMP-2 and MMP-9) [92]; importantly, these matrix proteins are also known to be a part of the chronic inflammation-cancer axis [94].

9 Conclusion regarding the similarities and differences between asbestos and CNT.

Since asbestos types are not all the same composition or pathogenicity and they conform to the FPP, it makes more sense to aim to conclude whether or not CNT conform to the FPP in terms of benchmarking them against asbestos. In terms of pathogenicity and mechanism CNT produce oxidative stress, inflammation, toxicity and genotoxicity and produce fibrosis in medium term studies and these are similar to the effects of asbestos. Importantly the effect of asbestos are length depended and so are some of the effects of CNT, making them compliant with the FPP for a pathogenic fibre. Carbon nanotubes can be manufactured as tight tangles of nanotubes that are essentially particles, or as high aspect ratio 'fibres' [1]. Effects of CNT as particles would be limited to the lungs (fibrosis and cancer) but CNT as fibres would have pulmonary effects but also affect the pleura (fibrosis and mesothelioma). Importantly, to conform to the FPP, these effects would be anticipated to be length-dependent. Exposure of the both the pleural cavity [3] and the peritoneal cavity as a model mesothelium [2], revealed that long carbon nanotube fibres had the ability to produce inflammation and fibrosis that was similar to that produced by long asbestos. In contrast, neither short asbestos fibres nor short or tangled CNT caused any significant inflammation or fibrosis in the two cavities. Frustrated phagocytosis of long fibres as it likely applies to asbestos and carbon nanotubes is illustrated in Figures 2 and 3. Biopersistence is the other key component of the FPP and pristine carbon nanotubes are durable using *in vitro* assay [31]. However there is some evidence that highly oxidised single wall carbon nanotubes can be further broken down by the enzyme peroxidase [96] although the is doubtful that CNT encounter this enzyme to any great extent at a plausible inhalation exposure; it is also that non-oxidised multi-walled CNT, the most common form of CNT in industrial use, would be affected by this enzyme. Therefore in terms of the fibre pathogenicity paradigm, it is possible for carbon nanotubes to be pathogenic by being thin, long and biopersistent. However it should be noted that CNT exist in forms that are non-fibrous would not be expected to comply with the paradigm for a pathogenic fibre and would not produce fibre-specific pathology in the pleura.

Reference List

1. Donaldson K, Duffin R, Murphy FA, Poland C. Utilising the concept of the biologically effective dose to define the particle and fibre hazards of carbon nanotubes. Chapter 3.in The toxicology of carbon nanotubes.Eds Ken Donaldson, Craig A.Poland, Rodger Duffin, James Bonner.Cambridge University Press, Cambridge. 63-72. 2012.

Ref Type: Generic

2. Poland CA, Duffin R, Kinloch I, Maynard A, Wallace WA, Seaton A *et al*.: **Carbon nanotubes introduced into the abdominal cavity of mice show asbestos-like pathogenicity in a pilot study.** *Nat Nanotechnol* 2008, **3:** 423-428.

3. Murphy FA, Poland CA, Duffin R, Al Jamal KT, Ali-Boucetta H, Nunes A *et al*.: **Length-dependent retention of carbon nanotubes in the pleural space of mice initiates sustained inflammation and progressive fibrosis on the parietal pleura.** *Am J Pathol* 2011, **178:** 2587-2600.

4. Murphy FA, Schinwald A, Poland CA, Donaldson K: **The mechanism of pleural inflammation by long carbon nanotubes: interaction of long fibres with macrophages stimulates them to amplify pro-inflammatory responses in mesothelial cells.** *Part Fibre Toxicol* 2012, **9:** 8.

5. Donaldson K, Murphy FA, Duffin R, Poland CA: **Asbestos, carbon nanotubes and the pleural mesothelium: a review of the hypothesis regarding the role of long fibre retention in the parietal pleura, inflammation and mesothelioma.** *Part Fibre Toxicol* 2010, **7:** 5.

6. Donaldson K. The inhalation toxicology of p-aramid fibrils. Critical Reviews In Toxicology (Pre-print available on the web). 2009.

Ref Type: Generic

7. Kreyling WG, Moller W, Semmler-Behnke M, Oberdorster G. Particle dosimetry: Deposition and clearance from the respiratory tract and translocaton to extra-pulmonary sites. Chapter 3: in Particle Toxicology.Eds.Donaldson, K.and Borm, P.CRC Press, Boca Raton USA . 47-74. 2007.

Ref Type: Generic

8. Walton WH. Chapter 5. Airborne dusts. In: Mineral Fibers and Health (Liddell D, Miller K, eds).Boca Raton, FL:CRC Press,., 55-77. 1991.

Ref Type: Generic

9. Stanton MF, Laynard M, Tegeris A, Miller E, May M, Kent: **Carcinogenicity of fibrous glass: pleural response in the rat in relation to fiber dimension.** *Journal Of The National Cancer Institute* 1977, **58:** 587-603.

10. Stanton MF, Layard M, Tegeris A, Miller E, May M, Morgan E *et al*.: **Relation of particle dimension to carcinogenicity in amphibole asbestoses and other fibrous minerals.** *Journal Of The National Cancer Institute* 1981, **67:** 965-975.

11. Davis JG, Addison J, Bolton RE, Donaldson K, Jones AD, Smith T: **The pathogenicity of long versus short fiber samples of amosite asbestos administered to rats by inhalation and intraperitoneal injection.** *British Journal Of Experimental Pathology* 1986, **67:** 415-430.

12. Adamson IY, Letourneau HL, Bowden DH: **Comparison of alveolar and interstitial macrophages in fibroblast stimulation after silica and long or short asbestos**

1. *Lab Invest* 1991, **64:** 339-344.

13. Adamson IY, Bakowska J, Bowden DH: **Mesothelial cell proliferation after instillation of long or short asbestos fibers into mouse lung**

4. *Am J Pathol* 1993, **142:** 1209-1216.

14. Goodglick LA, Kane AB: **Cytotoxicity of long and short crocidolite asbestos fibers invitro and invivo.** *Cancer Research* 1990, **50:** 5153-5163.

15. Donaldson K, Brown GM, Brown DM, Bolton RE, Davis JG: **Inflammation generating potential of long and short fiber amosite asbestos samples.** *British Journal Of Industrial Medicine* 1989, **46:** 271-276.

16. Moalli PA, Macdonald JL, Goodglick LA, Kane AB: **Acute injury and regeneration of the mesothelium in response to asbestos fibers.** *American Journal Of Pathology* 1987, **128:** 426-445.

17. Donaldson K, Li XY, Dogra S, Miller BG, Brown GM: **Asbestos-stimulated tumor-necrosis-factor release from alveolar macrophages depends on fiber length and opsonization.** *Journal Of Pathology* 1992, **168:** 243-248.

18. Hill IM, Beswick PH, Donaldson K: **Differential release of superoxide anions by macrophages treated with long and short-fiber amosite asbestos is a consequence of differential affinity for opsonin.** *Occupational And Environmental Medicine* 1995, **52:** 92-96.

19. Donaldson K, Golyasnya N: **Cytogenetic and pathogenic effects of long and short amosite asbestos.** *Journal Of Pathology* 1995, **177:** 303-307.

20. Coin PG, Roggli VL, Brody AR: **Persistence of long, thin chrysotile asbestos fibers in the lungs of rats**

4. *Environ Health Perspect* 1994, **102 Suppl 5:** 197-199.

21. Searl A, Buchanan D, Cullen RT, Jones AD, Miller BG, Soutar CA: **Biopersistence and durability of nine mineral fibre types in rat lungs over 12 months.** *Ann Occup Hyg* 1999, **43:** 143-153.

22. Poland CA, Byrne F, Cho WS, Prina-Mello A, Murphy FA, Davies GL *et al*.: **Length-dependent pathogenic effects of nickel nanowires in the lungs and the peritoneal cavity.** *Nanotoxicology* 2011.

23. Schinwald A, Chernova T, Donaldson K. Use of silver nanowires to determine thresholds for fibre length-dependent pulmonary inflammation and inhibition of macrophage migration in vitro. 2012. Part Fibre Toxicol. 9:47. 2012.

Ref Type: Generic

24. Giovanni M, Ambrosi A, Pumera M: **Direct determination of bioavailable molybdenum in carbon nanotubes.** *Chemistry* 2011, **17:** 1806-1810.

25. Cho WS, Duffin R, Poland CA, Duschl A, Oostingh GJ, MacNee W *et al*.: **Differential pro-inflammatory effects of metal oxide nanoparticles and their soluble ions in vitro and in vivo; zinc and copper nanoparticles, but not their ions, recruit eosinophils to the lungs.** *Nanotoxicology* 2011.

26. Mcconnell EE, Axten C, Hesterberg TW, Chevalier J, Miiller WC, Everitt J *et al*.: **Studies on the Inhalation Toxicology of Two Fiberglasses and Amosite Asbestos in the Syrian Golden Hamster. Part II. Results of Chronic Exposure**

1. *Inhal Toxicol* 1999, **11:** 785-835.

27. Hesterberg TW, Anderson R, Bernstein DM, Bunn WB, Chase GA, Jankousky AL *et al*.: **Product stewardship and science: safe manufacture and use of fiber glass.** *Regul Toxicol Pharmacol* 2012, **62:** 257-277.

28. Liu X, Hurt RH, Kane AB: **Biodurability of Single-Walled Carbon Nanotubes Depends on Surface Functionalization.** *Carbon N Y* 2010, **48:** 1961-1969.

29. Allen BL, Kotchey GP, Chen Y, Yanamala NV, Klein-Seetharaman J, Kagan VE *et al*.: **Mechanistic investigations of horseradish peroxidase-catalyzed degradation of single-walled carbon nanotubes.** *J Am Chem Soc* 2009, **131:** 17194-17205.

30. Kagan VE, Konduru NV, Feng W, Allen BL, Conroy J, Volkov Y *et al*.: **Carbon nanotubes degraded by neutrophil myeloperoxidase induce less pulmonary inflammation.** *Nat Nanotechnol* 2010, **5:** 354-359.

31. Osmond-McLeod MJ, Poland C, Murphy FA, Waddington L, McCall MJ, MOrris H *et al*.. Durability and inflammogenic impact of carbon nanotubes compared with asbestos fibres. Particle and Fibre Toxicology (in press). 2011.

Ref Type: Generic

32. Donaldson K: **Biological-activity of respirable industrial fibers treated to mimic residence in the lung.** *Toxicology Letters* 1994, **72:** 299-305.

33. Kane AB: **Mechanisms of mineral fibre carcinogenesis.** *in Mechanisms of Fibre Carcinogenesis Edited by Kane AB, Boffetta P, Saracci R and Wilbourn JD* 1996, 11-34.

34. Muller J, Huaux F, Moreau N, Misson P, Heilier JF, Delos M *et al*.: **Respiratory toxicity of multi-wall carbon nanotubes**

1. *Toxicol Appl Pharmacol* 2005, **207:** 221-231.

35. Shvedova AA, Kisin ER, Mercer R, Murray AR, Johnson VJ, Potapovich AI *et al*.: **Unusual inflammatory and fibrogenic pulmonary responses to single-walled carbon nanotubes in mice**

1. *Am J Physiol Lung Cell Mol Physiol* 2005, **289:** L698-L708.

36. Shvedova AA, Kisin ER, Murray AR, Johnson VJ, Gorelik O, Arepalli S *et al*.: **Inhalalation versus aspiration of single walled carbon nanotubes in C57/Bl6 mice: Inflammation, fibrosis, oxidative stress and mutagenesis.** *Am J Physiol Lung Cell Mol Physiol* 2008, **295:** L552-L565.

37. Lam CW, James JT, McCluskey R, Hunter RL: **Pulmonary toxicity of single-wall carbon nanotubes in mice 7 and 90 days after intratracheal instillation.** *Toxicol Sci* 2004, **77:** 126-134.

38. Porter DW, Hubbs AF, Chen BT, McKinney W, Mercer RR, Wolfarth MG *et al*.: **Acute pulmonary dose-responses to inhaled multi-walled carbon nanotubes.** *Nanotoxicology* 2012.

39. Mercer RR, Hubbs AF, Scabilloni JF, Wang L, Battelli LA, Friend S *et al*.: **Pulmonary fibrotic response to aspiration of multi-walled carbon nanotubes.** *Part Fibre Toxicol* 2011, **8:** 21.

40. Donaldson K, Brown GM, Brown DM, Bolton RE, Davis JM: **Inflammation generating potential of long and short fibre amosite asbestos samples**
11. *Br J Ind Med* 1989, **46:** 271-276.

41. Kamp DW: **Asbestos-induced lung diseases: an update.** *Transl Res* 2009, **153:** 143-152.

42. Mossman BT, Churg A: **Mechanisms in the pathogenesis of asbestosis and silicosis.** *Am J Respir Crit Care Med* 1998, **157:** 1666-1680.

43. Gilmour PS, Brown DM, Beswick PH, MacNee W, Rahman I, Donaldson K: **Free radical activity of industrial fibers: Role of iron in oxidative.** *Environmental Health Perspectives* 1997, **105:** 1313-1317.

44. Muller J, Huaux F, Fonseca A, Nagy JB, Moreau N, Delos M *et al*.: **Structural defects play a major role in the acute lung toxicity of multiwall carbon nanotubes: toxicological aspects.** *Chem Res Toxicol* 2008, **21:** 1698-1705.

45. Hansen K, Mossman BT: **Generation of superoxide (O2-.) from alveolar macrophages exposed to asbestiform and nonfibrous particles**
2. *Cancer Res* 1987, **47:** 1681-1686.

46. Brown DM, Kinloch IA, Bangert U, Windle A, Walter DM, Walker GS *et al*.. An in vitro study of the potential of carbon nanotubes and nanofibres to induce inflammatory mediators and frustrated phagocytosis. Carbon 45, 1743-1756. 2007.
Ref Type: Generic

47. Ye J, Shi X, Jones W, Rojanasakul Y, Cheng N, Schwegler-Berry D *et al*.: **Critical role of glass fiber length in TNF-alpha production and transcription factor activation in macrophages.** *American Journal Of Physiology* 1999, **276:** L426-L434.

48. Hamilton RF, Wu N, Porter D, Buford M, Wolfarth M, Holian A: **Particle length-dependent titanium dioxide nanomaterials toxicity and bioactivity.** *Part Fibre Toxicol* 2009, **6:** 35.

49. Kamp DW, Graceffa P, Pryor WA, Weitzman SA: **The role of free radicals in asbestos-induced diseases. [Review] [212 refs].** *Free Radical Biology & Medicine* 1992, **12:** 293-315.

50. Sargent LM, Shvedova AA, Hubbs AF, Salisbury JL, Benkovic SA, Kashon ML *et al*.: **Induction of aneuploidy by single-walled carbon nanotubes.** *Environ Mol Mutagen* 2009, **50:** 708-717.

51. Driscoll KE. Effects of fibres on cell proliferation, cell activation and gene expression. in Mechanisms of fibre carcinogenesis.IARC Scientific Publicatoin No 140.Eds Kane AB, Boffetta P, Saracci R, Wilbourn JD. 73-96. 1996.
Ref Type: Generic

52. Mutsaers SE: **The mesothelial cell.** *Int J Biochem Cell Biol* 2004, **36:** 9-16.

53. Shinohara H: **Distribution of lymphatic stomata on the pleural surface of the thoracic cavity and the surface topography of the pleural mesothelium in the golden hamster.** *Anat Rec* 1997, **249:** 16-23.

54. Schinwald A, Murphy FA, Prina-Mello A, Poland CA, Byrne F, Movia D *et al*.: **The Threshold Length for Fiber-Induced Acute Pleural Inflammation: Shedding Light on the Early Events in Asbestos-Induced Mesothelioma.** *Toxicol Sci* 2012, **128:** 461-470.

55. Mueller KM: **Principles of anatomy and pathology of the pleura.** In *Pleural Diseases*. 7 edition. Edited by Loddenkemper R, Antony VB. European Respiratory Society Journals Ltd; 2002.

56. Wagner JC, SLEGGS CA, MARCHAND P: **Diffuse pleural mesothelioma and asbestos exposure in the North Western Cape Province.** *Br J Ind Med* 1960, **17:260-71.:** 260-271.

57. Owens MW, Milligan SA: **Pleuritis and pleural effusions.** *Curr Opin Pulm Med* 1995, **1:** 318-323.

58. Stanton MF: **Some etiological considerations of fibre carcinogenesis.** In *Biological Effects of Asbestos*. 8 edition. Edited by Bogovski P, Timbrell V, Gilson J. World Health Organization, International Agency for Research on Cancer; 1973:289.

59. Stanton MF, Wrench C: **Mechanisms of mesothelioma induction with asbestos and fibrous glass.** *J Natl Cancer Inst* 1972, **48:** 797-821.

60. Timbrell V: **Fibres and carcinogenesis.** *J Occup Health Soc Aust* 1983, **3:** 3-12.

61. Murphy FA, Poland CA, Duffin R, Al-Jamal KT, Ali-Boucetta H, Nunes A *et al*.: **Length-Dependent Retention of Carbon Nanotubes in the Pleural Space of Mice Initiates Sustained Inflammation and Progressive Fibrosis on the Parietal Pleura.** *American Journal of Pathology* 2011, **178:** 2587-2600.

62. Poland CA, Duffin R, Kinloch I, Maynard A, Wallace WA, Seaton A *et al*.: **Carbon nanotubes introduced into the abdominal cavity of mice show asbestos-like pathogenicity in a pilot study.** *Nat Nanotechnol* 2008, **3:** 423-428.

63. Nagai H, Toyokuni S: **Biopersistent fiber-induced inflammation and carcinogenesis: Lessons learned from asbestos toward safety of fibrous nanomaterials.** *Archives Of Biochemistry And Biophysics* 2010, **502:** 1-7.

64. Schinwald A, Murphy FA, Prina-Mello A, Poland CA, Byrne F, Movia D *et al*.: **The threshold length for fiber-induced acute pleural inflammation: shedding light on the early events in asbestos-induced mesothelioma.** *Toxicol Sci* 2012, **128:** 461-470.

65. Takagi A, Hirose A, Nishimura T, Fukumori N, Ogata A, Ohashi N *et al*.: **Induction of mesothelioma in p53+/- mouse by intraperitoneal application of multi-wall carbon nanotube.** *J Toxicol Sci* 2008, **33:** 105-116.

66. Muller J, Delos M, Panin N, Rabolli V, Huaux F, Lison D: **Absence of carcinogenic response to multi-wall carbon nanotubes in a 2-year bioassay in the peritoneal cavity of the rat.** *Toxicol Sci* 2009, kfp100.

67. Fraire AE, Greenberg SD, Spjut HJ, Dodson RF, Williams G, Lach-Pasko E *et al*.: **Effect of erionite on the pleural mesothelium of the Fischer 344 rat.** *Chest* 1997, **111:** 1375-1380.

68. Zanella CL, Posada J, Tritton TR, Mossman BT: **Asbestos causes stimulation of the extracellular signal-regulated kinase-1 mitogen-activated protein-kinase cascade after phosphorylation of the epidermal growth-factor receptor.** *Cancer Research* 1996, **56:** 5334-5338.

69. Shukla A, Timblin C, BeruBe K, Gordon T, McKinney W, Driscoll K *et al*.: **Inhaled particulate matter causes expression of nuclear factor (NF)- kappaB-related genes and oxidant-dependent NF-kappaB activation in vitro.** *Am J Respir Cell Mol Biol* 2000, **23:** 182-187.

70. Zanella CL, Timblin CR, Cummins A, Jung M, Goldberg J, Raabe R *et al*.: **Asbestos-induced phosphorylation of epidermal growth factor receptor is linked to c-fos and apoptosis.** *Am J Physiol* 1999, **277:** L684-L693.

71. Ramos-Nino ME, Timblin CR, Mossman BT: **Mesothelial cell transformation requires increased AP-1 binding activity and ERK-dependent Fra-1 expression.** *Cancer Res* 2002, **62:** 6065-6069.

72. Pacurari M, Yin XJ, Zhao J, Ding M, Leonard SS, Schwegler-Berry D *et al*.: **Raw single-wall carbon nanotubes induce oxidative stress and activate MAPKs, AP-1, NF-kappaB, and Akt in normal and malignant human mesothelial cells.** *Environ Health Perspect* 2008, **116:** 1211-1217.

73. Pacurari M, Yin XJ, Ding M, Leonard SS, Schwegler-Berry D, Ducatman BS *et al*.: **Oxidative and molecular interactions of multi-wall carbon nanotubes (MWCNT) in normal and malignant human mesothelial cells.** *Nanotoxicology* 2008, **2:** 155-170.

74. Yang H, Rivera Z, Jube S, Nasu M, Bertino P, Goparaju C *et al*.: **Programmed necrosis induced by asbestos in human mesothelial cells causes high-mobility group box 1 protein release and resultant inflammation.** *Proc Natl Acad Sci U S A* 2010, **107:** 12611-12616.

75. Broaddus VC, Yang L, Scavo LM, Ernst JD, Boylan AM: **Asbestos induces apoptosis of pleural mesothelial cells via reactive oxygen species.** *Molecular Biology of the Cell* 1996, **7:** 2032.

76. Yang HN, Bocchetta M, Kroczynska B, Elmishad AG, Chen YB, Liu ZM *et al*.: **TNF-alpha inhibits asbestos-induced cytotoxicity via a NF-kappa B-dependent pathway, a possible mechanism for asbestos-induced oncogenesis.** *Proceedings Of The National Academy Of Sciences Of The United States Of America* 2006, **103:** 10397-10402.

77. Swain WA, Faux SP. **Activation of p38 MAP Kinase by Crocidolite in Mesothelial Cells is Dependent upon Oxidative Stress**. Ann.Occup.Hyg. 46 Suppl 1, 136-139. 2002.
Ref Type: Generic

78. Xu LX, Flynn BJ, Ungar S, Pass HI, Linnainmaa K, Mattson K *et al*.: **Asbestos induction of extended lifespan in normal human mesothelial cells: interindividual susceptibility and SV40 T antigen.** *Carcinogenesis* 1999, **20:** 773-783.

79. Lechner JF, Tokiwa T, LaVeck M, Benedict WF, Banks-Schlegel S, Yeager H, Jr. *et al*.: **Asbestos-associated chromosomal changes in human mesothelial cells.** *Proc Natl Acad Sci U S A* 1985, **82:** 3884-3888.

80. Wang YH, Faux SP, Hallden G, Kirn DH, Houghton CE, Lemoine NR *et al*.: **Interleukin-1 beta and tumour necrosis factor-alpha promote the transformation of human immortalised mesothelial cells by erionite.** *International Journal of Oncology* 2004, **25:** 173-178.

81. Wagner JC, Skidmore JW, Hill RJ, Griffiths DM: **Erionite exposure and mesotheliomas in rats.** *Br J Cancer* 1985, **51:** 727-730.

82. Maltoni C, Minardi F, Morisi L: **Pleural mesotheliomas in Sprague-Dawley rats by erionite: first experimental evidence.** *ENVIRONMENTAL RESEARCH* 1982, **29:** 238-244.

83. Dikensoy O: **Mesothelioma due to environmental exposure to erionite in Turkey.** *Current Opinion in Pulmonary Medicine* 2008, **14:** 322-325.

84. Murphy FA, Schinwald A, Poland CA, Donaldson K: **The mechanism of pleural inflammation by long carbon nanotubes: interaction of long fibres with macrophages stimulates them to amplify pro-inflammatory responses in mesothelial cells.** *Part Fibre Toxicol* 2012, **9:8.:** 8.

85. Mutsaers SE, Whitaker D, Papadimitriou JM: **Stimulation of mesothelial cell proliferation by exudate macrophages enhances serosal wound healing in a murine model.** *American Journal Of Pathology* 2002, **160:** 681-692.

86. Takagi A, Hirose A, Nishimura T, Fukumori N, Ogata A, Ohashi N *et al*.: **Induction of mesothelioma in p53+/- mouse by intraperitoneal application of multi-wall carbon nanotube.** *J Toxicol Sci* 2008, **33:** 105-116.

87. Sakamoto Y, Nakae D, Fukumori N, Tayama K, Maekawa A, Imai K *et al*.: **Induction of mesothelioma by a single intrascrotal administration of multi-wall carbon nanotube in intact male Fischer 344 rats.** *Journal of Toxicological Sciences* 2009, **34:** 65-76.

88. Takagi A, Hirose A, Futakuchi M, Tsuda H, Kanno J: **Dose-dependent mesothelioma induction by intraperitoneal administration of multi-wall carbon nanotubes in p53 heterozygous mice.** *Cancer Sci* 2012, **103:** 1440-1444.

89. Murphy FA, Poland CA, Duffin R, Al Jamal KT, Ali-Boucetta H, Nunes A *et al*.: **Length-dependent retention of carbon nanotubes in the pleural space of mice initiates sustained inflammation and progressive fibrosis on the parietal pleura.** *Am J Pathol* 2011, **178:** 2587-2600.

90. Schinwald A, Murphy F, Prina-Mello A, Poland C, Byrne F, Glass J *et al*.: **The threshold length for fibre-induced acute pleural inflammation: shedding light on the early events in asbestos-induced mesothelioma.** *Toxicol Sci* 2012.

91. Nagai H, Okazaki Y, Chew SH, Misawa N, Yamashita Y, Akatsuka S *et al*.: **Diameter and rigidity of multiwalled carbon nanotubes are critical factors in mesothelial injury and carcinogenesis.** *Proc Natl Acad Sci U S A* 2011, **108:** E1330-E1338.

92. Park EJ, Roh J, Kim SN, Kang MS, Han YA, Kim Y *et al*.: **A single intratracheal instillation of single-walled carbon nanotubes induced early lung fibrosis and subchronic tissue damage in mice.** *Arch Toxicol* 2011, **85:** 1121-1131.

93. Yang M, Meng J, Cheng X, Lei J, Guo H, Zhang W *et al*.: **Multiwalled carbon nanotubes interact with macrophages and influence tumor progression and metastasis.** *Theranostics* 2012, **2:** 258-270.

94. Bremnes RM, Al Shibli K, Donnem T, Sirera R, Al Saad S, Andersen S *et al*.: **The role of tumor-infiltrating immune cells and chronic inflammation at the tumor site on cancer development, progression, and prognosis: emphasis on non-small cell lung cancer.** *J Thorac Oncol* 2011, **6:** 824-833.

95. Iliopoulos D, Jaeger SA, Hirsch HA, Bulyk ML, Struhl K: **STAT3 activation of miR-21 and miR-181b-1 via PTEN and CYLD are part of the epigenetic switch linking inflammation to cancer.** *Mol Cell* 2010, **39:** 493-506.

96. Kagan VE, et al. Carbon nanotubes degraded by neutrophil myeloperoxidase induce less pulmonary inflammation. Nature Nanotechnology Advance online publication April 4th 2010. 2010.

Ref Type: Generic